THE UNIVERSITY
of ADELAIDE

Corrosion Detection:
A Fibre Optic Approach

by

Roman KOSTECKI

THESIS

presented for the degree of

DOCTOR OF PHILOSOPHY

in the

FACULTY OF SCIENCE, SCHOOL OF PHYSICAL SCIENCES

UNIVERSITY OF ADELAIDE

May 2017

To Ethan and Cosette

I am (we all are) a small link in the chain of human endeavour, of humanity. It is up to each of us to choose what kind of link we want to be, and always strive to better ourselves.

> **– Dad**

> *"Always dream and shoot higher than you know you can do. Dont bother just to be better than your contemporaries or predecessors. Try to be better than yourself."*

> **– William Faulkner**

> *"Using no way as way. Having no limitation as your only limitation."*

> **– Lee Jun-fan (a.k.a. Bruce Lee)**

Contents

Declaration

I certify that this work contains no material which has been accepted for the award of any other degree or diploma in my name in any university or other tertiary institution and, to the best of my knowledge and belief, contains no material previously published or written by another person, except where due reference has been made in the text. In addition, I certify that no part of this work will, in the future, be used in a submission in my name for any other degree or diploma in any university or other tertiary institution without the prior approval of the University of Adelaide and where applicable, any partner institution responsible for the joint award of this degree.

I give consent to this copy of my thesis when deposited in the University Library, being made available for loan and photocopying, subject to the provisions of the Copyright Act 1968.

The author acknowledges that copyright of published works contained within this thesis resides with the copyright holder(s) of those works.

I also give permission for the digital version of my thesis to be made available on the web, via the University's digital research repository, the Library Search and also through web search engines, unless permission has been granted by the University to restrict access for a period of time.

Signed:

Dated: 23rd May, 2017

Abstract

The University of Adelaide

Faculty of Science

School of Physical Sciences

Doctor of Philosophy

by Roman Kostecki

Corrosion is a multi-billion dollar problem faced by industry. High acquisition costs associated with modern military and civilian aircraft coupled with tighter budgets has resulted in the need for greater utilisation of existing aircraft fleets. With advancing aircraft age there is increased possibility that protective coatings will break down or be damaged, resulting in exposure of the base material to the environment and an increased possibility of corrosion. Corrosion is most difficult to detect in inaccessible metallic structures within aircraft. Monitoring these areas requires a sensor capable of spatially resolved detection of corrosion (distributed measurements), so that the location of the detected corrosion can be determined. Optical fibre based sensors are inherently suited to distributed sensing and are typically in the order of only a few hundred microns in diameter making them very lightweight and suitable for embedding in otherwise inaccessible corrosion-prone areas.

This thesis describes the development of an optical fibre based corrosion sensing element. Transition of exposed-core microstructured optical fibres from soft glass to silica is shown to provide a platform for optical fibre sensors requiring long term and/or harsh environmental applications while providing real time analysis anywhere along the fibres length. The portion of light guided outside of the glass core, often described as the 'evanescent field,' is affected by the refractive index and absorption characteristics of the surrounding medium. Functionalising this core with chemosensors sensitive to corrosion by-products, turns the light guiding fibre into a corrosion sensing element, with which in-situ kinetic measurements of accelerated corrosion in simulated aluminium aircraft joints is demonstrated. This provides a fibre optic approach for detection of corrosion inside the hidden part of structures and opens up new opportunities for distributed optical fibre chemical sensing with a capacity for long-term application in harsh environments.

Acknowledgements

It is very difficult to find the right words to thank all the people whom, explicitly or not, helped me realise this work. I will try, but apologise to anyone that I have forgotten.

I acknowledge the Australian Defence Science and Technology Group (DSTG) (under the Signatures, Materials and Energy Corporate Enabling Research Program) for financial support and for providing the accelerated corrosion laboratory facilities. This work was performed in part at the OptoFab node of the Australian National Fabrication Facility utilising Commonwealth, South Australian and New South Wales State Government funding. The atomic force and scanning electron microscopy work was performed at Adelaide Microscopy. The majority of this work was performed at the amazing facilities provided by the Institute for Photonics and Advanced Sensing and the School of Physical Sciences at the University of Adelaide.

I am truly grateful for all of the support and guidance provided by my supervisors, Tanya Monro and Heike Ebendorff-Heidepriem, both of whom I consider to be my greatest mentors. I am extremely fortunate to have had the opportunity to do this work under the supervision of two people with such inspirational drive and passion for knowledge and discovery. Thank you Tanya Monro for your awe-inspiring ability to ask the right question just when I need it most, and thank you Heike Ebendorff-Heidepriem for always having your door open to me no matter how busy you were.

I would like to express my appreciation to Claire Davis and Grant McAdam from the DSTG for trusting me to do this project as well as providing guidance and all of our discussions. Thank you also for your organisation and participation in the accelerated corrosion experiments performed at the Fishermans Bend laboratories. A very special thank you goes to Sabrina Heng and Alex François, both of whom have provided invaluable discussions and taught me so much about experimental procedures and scientific techniques. I also thank Peter Henry, Stephen Warren-Smith, and Erik Schartner for your contribution to the fibre fabrication, as well as Kristopher Rowland and Tze (Herbert) Foo for your helpful discussions.

My special thanks goes to my loved family whom have surely contributed to this achievement, and especially to my late father for his words of wisdom during our discussions and to my mother for her intensity and love. Finally, I thank myself for choosing this course in life, the journey has been amazing so far.

Publications

Overview

- The research during candidature led to eleven journal publications.

- Ten of these papers were published in high ranked journals such as ACS Applied Materials & Interfaces (2015 Impact factor: 7.145), Physical Review Applied (2015 Impact factor: 4.061), RSC Advances (2015 Impact factor: 3.289), Optics Express (2015 Impact factor: 3.148), and Optics Materials Express (2015 Impact factor: 2.657).

- One further paper has been been prepared for submission.

- The silica exposed-core microstructured optical fibre (ECF) work [1] was published in a feature issue (Specialty Optical Fibers) of Optical Materials Express, and was chosen by the Optical Society of America for inclusion in 'Spotlight on Optics'.

- The above mentioned ECF paper was the top download from Optical Materials Express in the first month of publication, and remained a top 10 downloaded paper for the first four months.

- The work has directly benefited nine other National Health and Medical Research Council (NHMRC), Australian Research Council (ARC), industry funded, and overseas funded projects in research areas for medical [2–9] and national security [10, 11].

- This research was discussed in the recently opened 'ARC Centre of Excellence for Nanoscale BioPhotonics' proposal to the ARC as being a platform that will be used to create distributed and multiplexed assays, opening a pathway for measuring biochemical gradients within organisms.

- The research contributed to 15 conference presentations at leading national and international conferences; including presentations at the Australian Conference on Optical Fibre Technology (ACOFT), the International Conference on Materials for Advanced Technologies (ICMAT), and was presented at the 2014 International Conference on Optical Fibre Sensors (OFS) as well as the 2016 SPIE Smart Structures/NDE conference, which are leading international events for material technology, optical fibre sensing, and structural health monitoring research.

Thesis Related Publications

Highlights of the work contained in this thesis narrative have been published in the papers listed below. This list of papers is ordered in a way that reflects the order of this thesis, and includes the related chapter numbers of the thesis. A copy of the papers have been included in the Appendix.

1. Chapters 1, 2, 4 & 5 – Appendix A

   R. Kostecki, H. Ebendorff-Heidepriem, S. C. Warren-Smith, G. McAdam, C. Davis and T. M. Monro, "Optical Fibres for Distributed Corrosion Sensing - Architecture and Characterisation," Key Eng. Mat. **558**, 522-533 (2013).

   [**Cited by: 3**[*]]

2. Chapters 4 – Appendix B

   R. Kostecki, H. Ebendorff-Heidepriem, S. C. Warren-Smith, and T. M. Monro, "Predicting the drawing conditions for microstructured optical fiber fabrication," Opt. Mater. Express **4**, 29 – 40 (2013).

   [**Impact Factor: 2.657**[†]**, Cited by: 23**[*]]

3. Chapters 4 & 6 – Appendix C

   S. Heng, M. Nguyen, R. Kostecki, T. M. Monro and A. D. Abell, "Nanoliter-scale, regenerable ion sensor: sensing with a surface functionalized microstructured optical fiber," RSC Adv. **3**, 8308 – 8317 (2013).

   [**Impact Factor: 3.289**[†]**, Cited by: 23**[*]]

4. Chapters 4 & 5 – Appendix D

   R. Kostecki, H. Ebendorff-Heidepriem, C. Davis, G. McAdam, S. Warren-Smith, and T. M. Monro, "Silica exposed-core microstructured optical fibers," Opt. Mater. Express **2**, 1538 – 1547 (2012).

   [**Impact Factor: 2.657**[†]**, Cited by: 30**[*]]

---

[*] Google Scholar (October 2016)
[†] Impact Factor from 2015

5. Chapter 6 – Appendix E

R. Kostecki, H. Ebendorff-Heidepriem, S. Afshar V., G. McAdam, C. Davis, and T. M. Monro, "Novel Polymer Functionalization Method for Exposed-Core Optical Fiber," Opt. Mater. Express **4**, 1515 – 1525 (2014).

[**Impact Factor: 2.657**†**, Cited by: 7***]

6. Chapter 6 – Appendix F

E. P. Schartner, G. Tsiminis, A. François, R. Kostecki, S. C. Warren-Smith, L. V. Nguyen, S. Heng, T. Reynolds, E. Klantsataya, K. J. Rowland, A. D. Abell, and H. Ebendorff-Heidepriem, and T. M. Monro, "Taming the Light in Microstructured Optical Fibers for Sensing," Int. J. Appl. Glass. Sci. **6**, 229 – 239 (2015).

[**Impact Factor: 1.843**†**, Cited by: 7***]

7. Chapters 4 & 7 – Appendix G

S. C. Warren-Smith, R. Kostecki, L. V. Nguyen, and T. M. Monro, "Fabrication, splicing, Bragg grating writing, and polyelectrolyte functionalization of exposed-core microstructured optical fibers," Opt. Express **22**, 29493 – 29504 (2014).

[**Impact Factor: 3.148**†**, Cited by: 13***]

8. Chapter 7 – Appendix H (Conference Paper)

R. Kostecki, H. Ebendorff-Heidepriem, C. Davis, G. McAdam, T. Wang, and T. M. Monro, "Fiber Optic Approach for Detecting Corrosion," Smart Struct. NDE 9803, 55 (2016).

Prepared for Submission

9. Chapter 6 – Appendix I

R. Kostecki, S. Heng, A. M. Mak, H. Ebendorff-Heidepriem, A. D. Abell, and T. M. Monro, "Control of Molecular Recognition with Nano-Environment Effects," *Journal paper prepared for submission.*

Journal Publications not within Scope of Thesis

10. Not within scope of thesis – Appendix J

C. Perrella, H. P. Griesser, P. S. Light, <u>R. Kostecki</u>, T. M. Stace, A. G. White, H. Ebendorff-Heidepriem, T. M. Monro, and A. N. Luiten, "Demonstration of Exposed Core Fibre Platform for Two-Photon Rubidium Spectroscopy," Phys. Rev. Applied **4**, 014013 (2015)

[**Impact Factor: 4.061†, Cited by: 4***]

11. Not within scope of thesis – Appendix K

S. Heng, C. McDevitt, <u>R. Kostecki</u>, J. Morey, B. Eijkelkamp, H. Ebendorff-Heidepriem, T. M. Monro, and A. D. Abell, "Microstructured Optical Fiber-based Biosensors: Reversible and Nanoliter-Scale Measurement of Zinc Ions," ACS Appl. Mater. Interfaces **8**, 12727 – 12732 (2016)

[**Impact Factor: 7.145†**]

12. Not within scope of thesis – Appendix L

S. C. Warren-Smith, J. Wei, M. Chemnitz, <u>R. Kostecki</u>, H. Ebendorff-Heidepriem, T. M. Monro, and M. A. Schmidt, "Third harmonic generation in exposed-core microstructured optical fibers," Opt. Express **24**, 17860 – 17867 (2016).

[**Impact Factor: 3.148†**]

Conference Presentations During Candidature

1. <u>R. Kostecki</u>, H. Ebendorff-Heidepriem, C. Davis, G. McAdam, T. Wang, and T. M. Monro, "Fiber Optic Approach for Detecting Corrosion," in [*Sensors and Smart Structures Technologies for Civil, Mechanical, and Aerospace Systems* (Las Vegas, USA)], (Mar. 2016).

2. <u>R. Kostecki</u>, S. Heng, H. Ebendorff-Heidepriem, A. Abell, and T. M. Monro, "Thin-Film Polymer Functionalization of Optical Fiber Enabling Multiligand Chemosensing," in [*8th International Conference on Materials for Advanced Technologies & 4th Photonics Global Conference* (Singapore)], ICMAT15-A-3719, (Jun. 2015).

3. <u>R. Kostecki</u>, S. Heng, H. Ebendorff-Heidepriem, A. D. Abell, T. M. Monro, "Thin-Film Polymer Functionalisation of Optical Fibre Enabling Multiligand Chemosensing," in [*Australian Nanotechnology Network Early Career Workshop* (Sydney, Australia)], (Jul. 2014).

4. <u>R. Kostecki</u>, S. Heng, H. Ebendorff-Heidepriem, A. D. Abell, T. M. Monro, "Functionalization of exposed core fibers with multiligand binding molecules for fluorescence based ion sensing," in [*23rd International Conference on Optical Fibre Sensors* (Santander, Spain)], (Jun. 2014).

5. E. Klantsataya, A. François, A. Zuber, V. Torok, <u>R. Kostecki</u>, and T. M. Monro, "Exposed core microstructured optical fiber surface plasmon resonance biosensor," in [*Optical Fibers and Sensors for Medical Diagnostics & Treatment Applications XIV* (San Francisco, USA)], (Feb. 2014).

6. C. Whittaker, <u>R. Kostecki</u>, W. Zhang, A. Martinez, S. Yamashita, H. Ebendorff-Heidepriem, T. M. Monro, and S. Afshar V., "Carbon nanotube functionalised exposed-core fibre," in [*International Conference on Nanoscience and Nanotechnology* (Adelaide, Australia)], (Feb. 2014).

7. <u>R. Kostecki</u>, H. Ebendorff-Heidepriem, and T. M. Monro, "Surface Functionalisation of Silica Exposed-Core Fibre with Thin Film Polymer," in [*International Conference on Nanoscience and Nanotechnology* (Adelaide, Australia)], (Feb. 2014).

8. S. C. Warren-Smith, <u>R. Kostecki</u>, H. Ebendorff-Heidepriem, and T. M. Monro, "Fabrication and splicing of exposed core microstructured optical fibres," in [*2013 Australian and New Zealand Conference on Optics and Photonics* (Perth, Australia)], (Dec. 2013).

9. <u>R. Kostecki</u>, H. Ebendorff-Heidepriem, E. P. Schartner, P. C. Henry, and T. M. Monro, "Experimental Verification of a Mathematical Model for the Draw Process of Microstructured Optical Fibers," in [*7th International Conference on Materials for Advanced Technologies* (Singapore)], ICMAT13-A-1875, (Jul. 2013).

10. S. Heng, M. Nguyen, <u>R. Kostecki</u>, T. M. Monro, and A. D. Abell, "Nanoliter-scale, regenerable ion sensor: sensing with surface functionalized microstructured optical fiber," in [*Optical Sensors 2013* (Prague, Czech Republic)], Proc. SPIE 8774, 877403 (May 2013).

11. <u>R. Kostecki</u>, E. P. Schartner, H. Ebendorff-Heidepriem, P. C. Henry, and T. M. Monro, "Fabrication of Suspended and Exposed Core Silica Fibres for Sensing Applications," in [*37th Australian Conference on Optical Fibre Technology* (Sydney, Australia)], (Dec. 2012).

12. D. G. Lancaster, D. J. Ottaway, P. C. Henry, <u>R. Kostecki</u>, and T. M. Monro, "Air-clad holmium-doped silica fibre laser," in [*37th Australian Conference on Optical Fibre Technology* (Sydney, Australia)], (Dec. 2012).

13. <u>R. Kostecki</u>, H. Ebendorff-Heidepriem, S. C. Warren-Smith, G. McAdam, C. Davis and T. M. Monro, "Optical Fibres for Distributed Corrosion Sensing - Architecture and Characterisation," in [*4th Asia-Pacific Workshop on Structural Health Monitoring* (Melbourne, Australia)], (Dec. 2012).

14. S. C. Warren-Smith, G. Nie, J. Kobelke, <u>R. Kostecki</u>, L. A. Salamonsen, and T. M. Monro, "Suspended core optical fibers for biological applications using UV wavelengths," in [*22nd International Conference on Optical Fibre Sensors* (Beijing, China)], (Oct. 2012).

15. <u>R. Kostecki</u>, H. Ebendorff-Heidepriem, G. McAdam, C. Davis and T. M. Monro, "Optical Fibre Distributed Sensing - Architecture, Response and Characterisation," in [*Conference on Optics Atoms and Laser Applications* (Melbourne, Australia)] (Nov. 2011).

List of Tables

List of Figures

List of Abbreviations

1

Introduction

> *"The greater danger lies not in setting our aim too high
> and falling short; but in setting our aim too low, and
> achieving our mark."*
>
> **– Michelangelo**

Corrosion is a multi-billion dollar problem in industry [12, 13]. An increasing recognition of potential cost savings by early warning of corrosion problems has led to an increasing focus on corrosion monitoring as part of preventive and predictive maintenance. The high acquisition costs associated with modern military and civilian aircraft coupled with tighter budgets has resulted in the need for greater utilisation of existing aircraft fleets. Typically, military aircraft have a planned life-of-type of 25–30 years. In Australia, in many cases, almost twice this time is achieved before the aircraft is retired [14]. For civilian aircraft flying today, approximately 20% are considered to be ageing, and as that number increases so does the need for heightened fleet monitoring by airlines and manufacturers [15] and continued intense focus and surveillance of these activities by regulatory agencies [16].

With advancing aircraft age there is an increased possibility that protective coatings will break down or be damaged, resulting in exposure of the base material to the environment and an increased possibility of corrosion [15]. The continual cycling of the structure also increases the possibility of structural fatigue damage, which constitutes one of the most significant safety concerns due to the potential for corrosion to combine with structural fatigue [17]. While inspection and preventive maintenance attempts are made to prevent and reduce the effect of corrosion, in practice it is impossible to completely avoid. It is therefore essential that corrosion processes are monitored so that repair time and costs are minimised, and the structure is maintained in a safe operating condition.

Corrosion is most difficult to detect in the inaccessible metallic structure of an aircraft, such as lap joints, stiffeners and under sealant beads, since access to these areas usually requires time consuming and therefore costly disassembly [14]. Such areas are recognised as being particularly prone to corrosion, due to the possibility of creating a micro-environment within the crevice between the plates, accelerating the corrosion process [17]. Current non-destructive inspection methods are typically based on the use of a hand held ultrasonic probe which tests material thickness. To reliably detect material thinning, ultrasonic probes require a 5–10% loss in material thickness and so are not suitable for measuring localised or isolated material thinning. By the time such a dramatic loss in material thickness is detected by these probes, the damage caused by corrosion may be too severe to repair, and so the component often needs to be replaced [14]. Clearly a more proactive approach is needed to detect the initial onset of corrosion within these difficult to inspect areas.

Detecting corrosion in these inaccessible areas requires the ability for measuring localised corrosion regardless of where it is located, which requires a sensor capable of spatially resolved detection (distributed measurement) of corrosion. To achieve this, a monitoring system with the ability to detect the onset and location of corrosion could be embedded within these inaccessible areas. Detecting corrosion requires a sensor capable of measuring the changes that occur as a result of the corrosion process, such as corrosion induced chemical changes of the metallic structure. Optical fibre based sensors offer several inherent advantages when applied to structural platforms; they are immune to electro magnetic interference (EMI), easily networked, inherently suited to distributed sensing, and are typically in the order of only a few hundred microns in diameter making them very lightweight and suitable for embedment in inaccessible corrosion-prone areas. A number of fibre optic systems have been developed for single point corrosion monitoring, but only a few of these systems have exploited the capability of optical fibres for distributed measurements. Many of the aircraft fuselage components are fabricated from aluminium-based alloys, hence aluminium ions (Al^{3+}) are of particular interest because they are not only an indicator of the onset of corrosion [14], but also have the potential to be an environmental hazard [18].

1.1   Aims of Thesis

This thesis describes research associated with developing a robust optical fibre based sensor capable of detecting corrosion anywhere along the fibre length while embedded in the structure of an aircraft. The project aims were to find an approach where a fibre optic evanescent field sensor could be used to detect corrosion while embedded inside the harsh conditions of a corroding aircraft joint.

1.2   Detecting Corrosion

According to ISO8044:1999 [19] corrosion is defined as an interaction between a metal and its environment that results in changes in the properties of the metal, and which may lead to significant impairment of the function of the metal, the environment, or the technical system, of which these form a part. There are two essential requirements for the corrosion process to occur, which are: a susceptible alloy / metal, and; a corrosive environment [20].

The corrosive environment is provided by a conductive solution, such as airborne salt and water. The susceptible metal can be exposed to the corrosive environment by mechanical damage to protective coatings, such as paint, during aircraft use or maintenance or by the breakdown of protective coatings with time due to other environmental factors. The susceptible metal is gradually destroyed by chemical and/or electrochemical reaction with the corrosive environment. As shown in Fig. 1.1, the changes that occur (therefore the possible measurands) due to corrosion are:
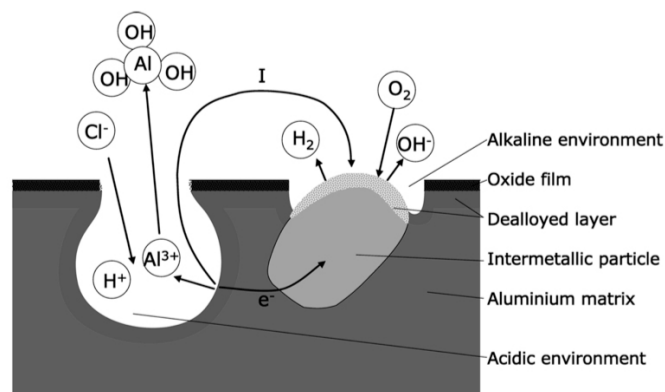
Figure 1.1 – Image from [20] showing a generalised illustration on pitting corrosion of aluminium alloys.

- pH

- oxygen level

- moisture content

- presence of salt contaminants

- production of corrosion products

The first four are measurands that indicate the environment has changed, providing conditions susceptible to corrosion, however do not provide a direct measurement of the corrosion itself. Therefore the measurement of corrosion products is preferred to directly detect and monitor the progress of the corrosion process. Many aircraft components, including the fuselage, are fabricated from aluminium-based alloys. Therefore, a unique by-product of the corrosion process will be Al^{3+} [14].

The current practice is to routinely disassemble the aircraft for visual inspection of corrosion, which is time consuming and therefore costly both in terms of aircraft down-time and maintenance personnel. When corrosion is found it is to removed, regardless of whether it poses a risk to structural integrity [14]. In some cases, the process of disassembly damages the panels even when they are not corroded which adds further costs. Therefore, a corrosion monitoring system is expected to reduce costs by reducing inspection time, decreasing damage and repair time, and increasing aircraft availability. There are power and weight restrictions associated with aircraft, and so a detection system also needs to have very low power consumption and be light weight. For nondestructive detection of corrosion of an aluminium fuselage, the system needs to be capable of detecting corrosion anywhere within the inaccessible preferential corrosion areas of long joints and beads of an aircraft fuselage. Ideally an aircraft corrosion detection system would be also capable of:

- measuring the onset of corrosion; so that the effect of protective measures or changes in process variables can be evaluated under actual operating conditions.

- rapid response; so that solutions of urgent problems to be tested and applied immediately.

- yield reproducible and accurate data, and should respond to the propensity of the operating environment to induce corrosion.

- monitoring actual corrosion of a component as it occurs.

- continuous detection and measurement of minor changes in the corrosion rate at the early stages of degradation.

1.3 Benefits of Fibre Optic Techniques

The channelling and manipulation of light through an optical fibre and monitoring any variation(s) of the output is the basic concept of optical fibre sensor methods. Fibre optic sensors represent a technology base that can be applied to a multitude of sensing applications. The following are some characteristic advantages of fibre optics that make their use especially attractive for sensors [21]:

- nonelectrical;

- explosion proof;

- compatible with remote sensing applications;

- small size and very light;

- allow access into normally inaccessible areas;

- potentially easy to install;

- immune to radio frequency and EMI;

- can be interfaced with data communication systems;

- capable of secure data transmission;

- potentially resistant to ionising radiation.

Most physical properties can be sensed optically with fibres. Light intensity, displacement (position), temperature, rotation, sound, strain, magnetic field, electric field, radiation, flow, liquid level, chemical / biological analysis, and vibration are just some of the phenomena that can be sensed [21]. In particular, optical fibres have
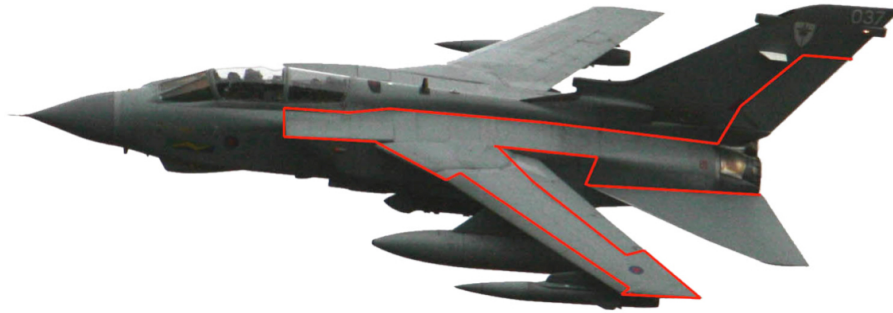
Figure 1.2 – Image from [25] showing the concept of aircraft fitted with a distributed optical fibre sensor in ▮ – red.

advantage of being flexible and lightweight enough for use in confined and inaccessible spaces, with the capacity to sense the position where corrosion is occurring along the length of a single fibre (distributed sensing) [22–24]. Those areas on an aircraft that are particularly prone to corrosion have been identified as being at lap joints and under sealant beads [14]. The concept of an aircraft fitted with a distributed optical fibre sensor is shown in Fig. 1.2.

Techniques by which the fibre optic sensor measurements can be made are broadly grouped in three categories depending on the physical extent of the sensing (Sec. 1.3.1), the role of the optical fibre in the sensing process (Sec. 1.3.2), and how the sensing is accomplished (Sec. 1.3.3) [26]. These broad groups in terms of corrosion sensing are further expanded on in the following sections.

1.3.1   Extent of Sensing

Fibre optic sensors are typically termed either point sensors or distributed sensors. In the case of a point sensor, the role of the fibre is only to bring light to and from a transducer which is typically at the end of the fibre. An example of a point sensor is remotely measuring pressure or temperature using interferometry at the ends of optical fibres. In the case of a distributed sensor, sensing is performed along the fibre length [27]. Hence, the physical extent of corrosion sensing using optical fibres is based on whether the fibre will operate as a single point sensor or over a distribution of points.

1.3.2   Role of the Optical Fibre

The role of optical fibres in sensing applications is typically separated into two categories, depending on whether the measurand acts externally or internally to the light guiding properties of the fibre. When transducers are external to the light guiding properties of an optical fibre, and the fibre is used to register and transmit the sensed quantity, then the optical fibre sensor is termed an extrinsic sensor. When sensors are embedded into or form a part of the light guiding property of the fibre, then it is termed an internal or intrinsic sensor. Intrinsic optical fibre sensors often involve some modification to light guiding characteristics, such as using fibre Bragg gratings (FBGs) or propagation loss from micro–bending to sense strain, or measuring rotation using counter–propagating beams within an optical fibre coil, and can provide long-range distributed sensing [28]. Some examples of extrinsic sensors are using fibre to fibre couplers to sense displacement, and absorption cells to sense chemistry effects [27].

1.3.3   Means of Sensing

Fibre optic sensors are generally based on measuring an intensity, wavelength or phase change in the guided light due to interaction or interference, and so are termed either intensity or interferometric sensors. Techniques used for intensity based sensors include light scattering (both Rayleigh and Raman), spectral transmission changes such as attenuation of transmitted light due to absorption or additional signal due to fluorescence, micro–bending or radiative losses, changes in reflection, and changes in the modal properties of the fibre. A few of the interferometric type sensors which have been demonstrated tend make use of magneto–optic, the laser–Doppler, or Sagnac effects [27].

1.4   A Brief History of Microstructured Optical Fibres as Sensors

Optical fibres have come an exceedingly long way since Dr Charles Kao's Nobel Prize winning work on reducing fibre propagation losses in the 1960s [29]. He realised that the losses of optical fibres at that time were orders of magnitude above the fundamental limit set by unavoidable density fluctuations in the glass, known as Rayleigh scattering. It was soon realised that a major issue was the purity of the glass, and that silica was a good candidate material for lower propagation losses. These ideas were taken seriously

by several research groups, and already by 1973 at Corning, Dr Robert Maurer and his colleagues Dr Donald Keck and Dr Peter Schultz showed that optical fibres can be used as a practical telecommunications technology with optical losses as low as 2 dB/km [30]. To achieve this they developed the flame hydrolysis deposition sintering process to create optical fibres with an oxide doped fused silica core and fused silica cladding. By 1974, Dr John MacChesney with his colleague Dr Paul O'Connor invented the modified chemical vapour deposition (MCVD) process [31] at Bell Labs, which has been key to low-cost commercial manufacture of telecommunications optical fibre, fuelling the explosion in fast reliable worldwide communications and the internet. Today, silica telecom fibres are regularly being made with losses close to the fundamental limit ($\sim$0.2 dB/km at near-infrared (NIR) wavelengths) [32] with over a billion kilometres of optical fibre wound around the globe, used for transmitting enormous amounts of information very quickly and at astonishingly low-cost. There can be no doubt that the pioneering work of Kao, Maurer, and MacChesney has had an enormous impact on technology and our lives.

Around the same time as Maurer and his colleagues were working on ways to use silica for optical fibres, Dr Peter Kaiser and Dr Enrique Marcatili were working on a new concept which has become known as MOFs [33], shown in Fig. 1.3. The core of these fibres was effectively suspended in an air cladding surrounded by a solid jacket
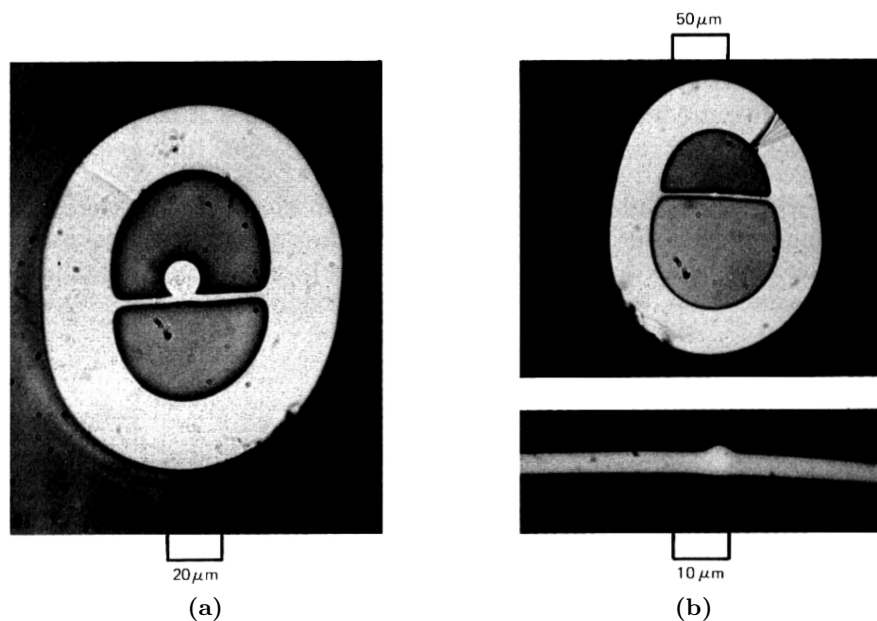
Figure 1.3 – Photographs from [33] showing the first (a) multimode and (b) single mode (top) microstructured optical fibres (MOFs), developed at Bell Labs in 1972. (b)(bottom) Magnified core region of the single mode MOF.

by using a thin supporting glass web. Their idea was to use structural form along the length of the silica material to provide the effective refractive index needed for light confinement. This meant that a single low loss material could be used to guide light by total internal reflection, removing the need to modify the composition of the silica as is necessary with conventional core–cladding or graded index fibres. At the time the motivation was still to produce low loss optical fibres for telecommunications or integrated optical circuits (IOCs). However, the low losses obtained with the MCVD process soon overtook single material MOFs, and interest in structured fibres faded for the next two decades.

At Bellcore in the late 1980s, Dr Eli Yablonovitch noticed losses in semiconductor lasers and other devices arising from light emitted at unwanted frequencies. In 1987, Yablonovitch and Dr Sajeev John of Princeton University independently showed that these types of losses would not occur in a medium with band gaps which prevented these frequencies of light from propagating [34, 35]. They proposed that such a medium could be produced by introducing voids in a transparent material to create a periodic structure, with the material and the voids having different refractive indices. This pattern resembled a crystal lattice and so they decided to use the words "photonic crystal" to describe these kinds of structures with band gaps for electromagnetic waves. Spurred on by these concepts, Yablonovitch, Dr Thomas Gmitter, and Dr Kok-Ming Leung (a theorist from Polytechnic University) worked together on developing and testing different periodic designs with spacing on the scale of a few millimetres for microwave wavelengths [36–38]. Following their success, several groups during the 1990s worked on extending this concept to the visible and infrared wavelengths. This photonic crystal work led to renewed interest in MOFs when Dr Jonathan Knight, Dr Tim Birks, and Prof Philip Russell at the University of Southampton demonstrated the first photonic crystal fibre (PCF) in 1996 [39], shown in Fig. 1.4. The fabrication technique was described by the group a year earlier [40], which involved stacking macroscopic silica capillary tubes together into a hexagonal lattice to form a preform with millimetre-scale features and then pull this preform to a fibre with micron-scale features on a drawing tower (stack and draw method).

Since their conception, PCFs (also known as holey or microstructured fibres) have been shown to provide a host of interesting and technologically enabling optical prop-

erties. Unlike conventional optical fibres, PCFs are typically made of a single material, and with the appropriate cross-sectional design, the structure can enable a broad range of highly unusual and tailorable optical properties [41]. This is because of the way the guided light interacts with the cladding region, where the high refractive index contrast between the material and small air hole features combine to form a strongly wavelength dependent effective cladding index. The work started in the 1990s led to several groups working out that with suitable selection of glass or polymer material and geometry the dispersion, nonlinearity, birefringence, polarisation, evanescent field and mode area of the propagating light can be optimised to specific applications. This has led to innovations in air-guiding photonic band gap fibres (PBGFs) (also known as hollow-core fibre) [42], supercontinuum generation [43], fibre lasers [44], terahertz wave guiding [45], fibres with high numerical apertures [46, 47]. MOFs are also an excellent candidate for new high-capacity transmission multicore telecommunications fibres [48], as they can guide a single mode at all wavelengths (endlessly single mode).

In 1999, while working on light propagation modelling for PCFs at the University of Southampton, Dr Tanya Monro developed a highly efficient and flexible approach to model the way the light is guided, which could easily be used to explore the modal properties of different fibre geometries. This model became a valuable tool in the development of PCF technology, and by using it Monro noticed that the holes of PCFs do not need to be filled with air to guide light but instead could be used to create an evanescent field device [49]. Monro showed that the portion of guided light (often described as "evanescent field") protruding into the holes of the structure can be
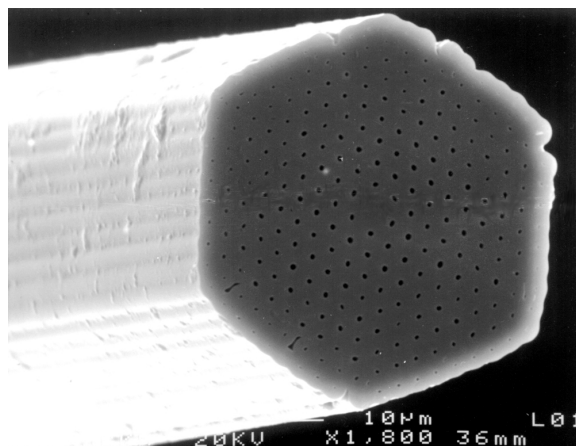
Figure 1.4 – Image from [39] showing the first PCF, produced at the University of Southampton in 1996.

affected by the characteristics of the medium within these holes, providing opportunities for exploiting the interaction of light with gases and liquids [50]. In this regard, the fibre geometry can provide extremely long interaction lengths without the need for large volumes. A couple of years later, in 2001, Monro went on to describe the type of sub-wavelength sized suspended silica rod fibre geometry needed to gain a significant fraction of guided light power in the holes outside of the glass (power fraction (PF)) [51].

During the early 2000s, PCFs made using compound glass for nonlinear applications [52], such as ultrafast optical switching for telecommunications, and polymer for data communications [53] were also being investigated. Unlike silica, compound glasses (also known as soft glass) and polymers have softening temperatures low enough to extrude the preform rather than use the stack and draw method, making it possible to produce new MOF geometries proportional to the design of the extrusion die. In 2002, Monro demonstrated the first MOF made using the extrusion method [54, 55], shown in Figs. 1.5(a)–(b). This fibre was produced using a chalcogenide glass preform, and was the first example of a suspended-core microstructured optical fibre (SCF) with the type of geometry needed to gain a significant PF, described by Monro the year before [51]. The SCF geometry has a high air filling fraction with a small core suspended on a number of thin struts. Unlike glass nano-wires [56, 57], this design provides a means for obtaining uniform micrometer–nanometer scale suspended 'wires' while protecting the highly sensitive core, and long lengths can be fabricated by drawing the structured extruded preform.

Over the next few years, the SCF extrusion and fibre drawing methods became well

(a)   (b)   (c)
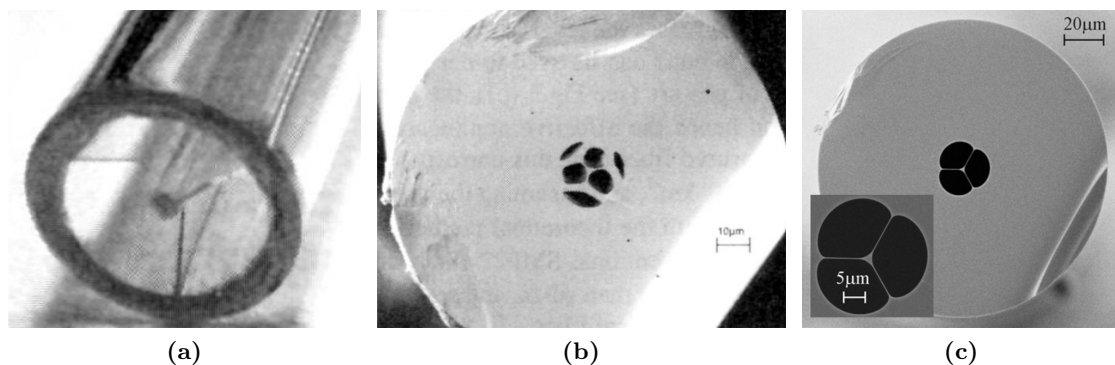
Figure 1.5 – Images from [55] showing the first (a) extruded preform and (b) SCF, developed at the University of Southampton in 2002. (c) Image from [58] of SCF produced by the same group in 2004.

established. Being joined by glass chemistry expert Dr Heike Ebendorff-Heidepriem, the Monro group at the University of Southampton developed the methods to produce uniformly structured, long length SCFs with smaller core sizes, single mode, and higher PF properties. Figure 1.5(c) shows the well defined geometry, with Ø1.7 µm core, of the SCFs being produced by the group in 2004 [58, 59]. The fibres were made in three steps. First, the structured preform and a jacket tube were produced using the extrusion method. Next, the structured preform, which had an outer diameter (OD) of about 16 mm, was reduced in scale on a fibre drawing tower to a cane of about 1.7 mm OD. In the last step, the cane was inserted into a jacket tube, and this assembly was drawn to the final fibre (cane-in-jacket method).

Another breakthrough occurred in 2004, five years after Monro's ideas that PCFs could be used to create an evanescent field device [49, 50], when Dr Jesper Jensen at the Technical University of Denmark demonstrated highly efficient evanescent field detection of fluorophore-labeled biomolecules in aqueous solutions positioned in the air holes of a PCF [60]. A year later Jensen demonstrated selective detection of fluorophore-labeled antibodies from aqueous samples by using a sensor layer immobilised by physisorption inside the air holes of a polymer MOF [61]. In these experiments, the excitation laser light was focused on the side (short axis) of the fibre, and the emitted fluorescence collected from the end face of the core. This showed that emitted fluorescence at the core surface could tunnel through the evanescent field and be guided along the core. The MOF was produced by drilling six holes in a poly(methyl methacrylate) (PMMA) rod to produce the preform (drill method), which was then drawn down to a fibre with core and hole diameters of ∼60 µm, shown in Fig. 1.6(a). The functionality of the MOF was illustrated by selectively detecting labeled antibodies in micro-litre volumes of aqueous solutions in the air holes of the fibre, shown by Fig. 1.6(b). At this time, in the mid 2000s, many groups around the world began investigating the use of different types of MOFs for the development of novel biological [60–62] and gas [63–66] MOF–based sensors.

Spurred on by the advances being made with MOF based technologies, Monro founded a new group at the University of Adelaide focusing on the design, fabrication and application of soft glass optical fibres, starting out as the Centre of Expertise in Photonics (CoEP) in early 2005 which later became the Institute for Photonics & Advanced

Sensing (IPAS) in 2009. In 2007, while working on his PhD thesis at the University of Adelaide under the supervision of Monro, Dr Stephen Warren-Smith developed a general model for both in-fibre excitation and fluorescence recapturing of filled MOFs by their core guided modes [67, 68]. This model showed that fluorescence emission at the surface of the fibre core has a higher coupling efficiency into the backward modes, which was experimentally verified using quantum dot (QD) labeled proteins. This meant the portion of modal field overlap surrounding the core (the PF) could be used to both excite the QDs from one end of the fibre and recapture the resulting emission at the core surface for measurement at the same end. In the following year, in 2008 while also working at the Adelaide based Monro group, Dr Yinlan Ruan demonstrated that the chemistry shown by Bhatia *et al.* [69] for covalent attachment of proteins to a glass surface, could be used to provide functionality to glass SCFs [70]. To do this, Ruan silanised the internal hole surfaces of a lead silicate glass SCF (including the core), similar to the one shown in Fig. 1.5(c), with thiol-terminal silanes and heterobifunctional crosslinkers having different reactive groups on each end. The cross-linking layer formed by this method was subsequently used to connect antibodies to the silane layer at the glass surface. The antibodies that Ruan used were conjugated with 100 nm QDs which were used as a fluorescence label to measure the effectiveness of the immobilisation procedure. These ideas shown by Warren-Smith and Ruan led to reduction of the minimum detectable concentration of QDs by optical fibres to 10 pM, and made it possible to detect single nanoparticles in sub-cellular fluid volumes [71].

| (a) | (b) |
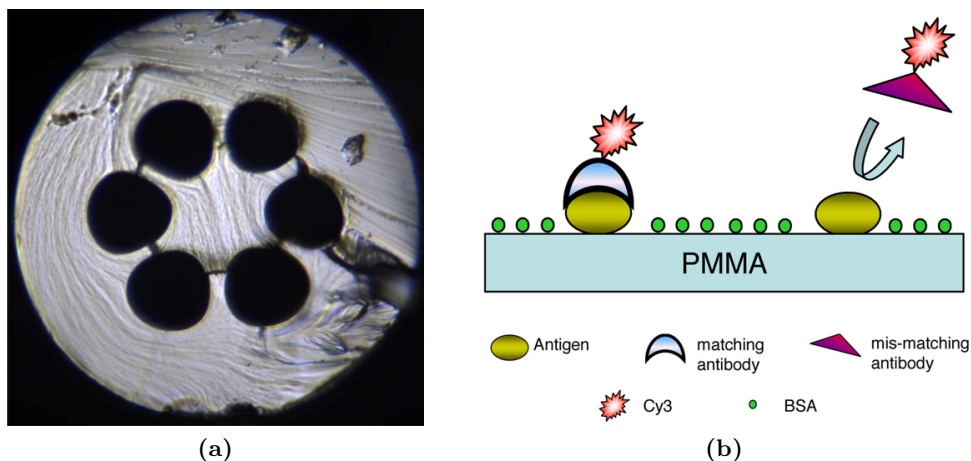
Figure 1.6 – Images from [61] showing; (a) the end-face of the MOF used in the experiments. The outer diameter is 300 μm and the air hole diameter is 60 μm, and; (b) schematic presentation of the capture processes utilised in the selective detection of the antibodies. α-streptavidin-Cy3 was captured by streptavidin molecules directly immobilised on the PMMA core surface while the mis-matching α-CRP-Cy3 molecules are washed out.

1.5   Corrosion Sensing: State of the Art

This section summarises corrosion sensing methods found in literature, and critical evaluation in terms of fibre optic distributed sensing using these methods. A summary of this section is given in Table 1.1 on page 28.

1.5.1   Intensity Methods

There has been some interest in extrinsic fibre optic sensing using probes for reflectance, polarised reflectance [72], fluorescence (discussed in Sec. 1.5.6), mechanical failure [73], and Raman spectroscopy. Also, intrinsic methods include evanescent wave absorption spectroscopy with which Namkung *et al.* [74–76] has published several papers and presented at conferences work on Fourier transform infrared spectroscopy (FTIR) techniques for periodic remote sensing and structural health monitoring of normally inaccessible structural components and areas. Although this technique might be adaptable to distributed sensing, it does not seem to have any advantages over the distributed fluorescence methods discussed in Sec. 1.5.6.

Although reflectance and polarised reflectance could be setup in a multiplexed arrangement, this does not seem to be cost effective or be practically compatible with the need to detect the onset of corrosion in any location. Similarly, although Raman spectroscopy using sampling fibres [77] or with the application of a surface enhanced Raman spectroscopy (SERS) active substrate at the end of a fibre as a probe [78, 79] has been successfully shown to work in the literature, these methods are not cost effective or practically compatible with distributed sensing.

1.5.2   Fibre Bragg Grating (FBG) Methods

There has been successful micro-bending methods using fibres with long-period FBG to detect expansion of polymer films that swell due to pH or moisture changes [80–82]. Although this seems like a reasonable approach, since it might be possible to engineer a polymer material which has specificity with respect to aluminium ions, fixed position FBGs do not seem to be able to provide a distributed sensor capable of measuring corrosion anywhere along the fibre length. During and following the application of heat

to metallic components, FBG sensors can also be used to detect temporal and spatial temperature variations due to hidden corrosion [83]. Although this thermography technique seems possible, the method requires thermal stimulation which adds to the cost and complexity of the system, and are not practically capable of detecting actual corrosion as it occurs in any environment.

Ultrasonic signal generators and sensors can be applied in-situ to monitor corrosion in hidden or hard to reach locations [84, 85]. The principle of operation is based on Rayleigh-Lamb waves at ultrasonic frequencies that can be made to propagate over or through a given structure. The detected return signal, that is bounced or deflected back, can be used to deduce material characteristics such as surface defects, corrosion, and material thickness. A FBG ultrasound detection system incorporating a fibre ring laser has been developed for this purpose [86]. The basic idea is to use FBG sensors as acoustic receivers of ultrasonic Lamb waves [86, 87]. The spectral response of FBGs subjected to the ultrasonic field have been theoretically and numerically investigated [88], and related work with respect to spatially resolved acoustic measurement as a diagnostic framework for structural health monitoring has been done at the Australian Defence Science and Technology Group (DSTG) [89]. This concept could be susceptible to temperature changes, have cross-talk issues, ghost reflections, blind zones, requires the additional cost of an ultrasonic signal generator, and may need several measurements to obtain reliable data.

The development of a reflective, gold coated long-period FBG based sensor for the measurement of chloride ions (Cl^-) in solution has been shown [90]. The approach has explored creating a portable, low-power device, developed with the potential for installation in concrete structures to determine the ingress of Cl^-, operating through measuring the refractive index change by the FBG response. When there is a concentration change leading to a refractive index change in the surrounding medium, the effective refractive index of the cladding mode changes and therefore a definite shift in the central wavelength. The work done showed that the sensitivity of this sensor could be further enhanced by coating it with gold nano-particles and thereby utilising the surface plasmon resonance (SPR) effect, enhancing the sensitivity to changes in the refractive index of the material surrounding the sensing region. It seems feasible that a transduction coating on this type of sensor which changes refractive index in the presence of Al^{3+},

such as chitosan [91] with specificity, could be used as a corrosion sensor. However, this method does not seem to be able to provide a continuous distributed method without a dynamic FBG.

1.5.3   Brillouin Scattering Methods

Brillouin scattering based fibre optic sensors could be used [92] to extend the FBG concepts to a distributed sensor. Strain and temperature distributed sensing through Brillouin scattering in single mode fibres (SMFs) has been demonstrated [93] in different tests to understand the influence of different fibre coatings and embedding techniques. In that work, pressure tests were performed on a pipe with inhomogeneous strengthening layout. The Brillouin strain data was compared with conventional strain gauges and a data comparison between the developed Brillouin technique and resistive strain gauges confirmed that the Brillouin technique is very effective for composite materials strain monitoring.

Brillouin gain has also been investigated both experimentally and numerically in azimuthally symmetric optical fibres with cores that are acoustically inhomogeneous due to the doping required to establish optical waveguides with the desired properties [94]. There seems to be an opportunity to develop a MOF with optimised Brillouin gain, and hence improved sensitivity for distributed sensing, while still maintaining low loss. This type of new fibre could provide the basis of a new type of distributed corrosion sensor with the potential to not only utilise transduction mechanisms for local strain or refractive index differential measurements along the fibre, but also have the ability to map strain and corrosion pitting on a surface using ultrasonic Lamb waves.

Recent work on Brillouin optical time-domain reflectometry (OTDR) distributed temperature sensors show 1.2 cm spatial resolution for distributed temperature measurements over a 20 m polarisation maintaining fibre [95]. The authors claim that the sensing range can be expanded to 100 m, but a kilometre range remains highly questionable, since the polarisation is unlikely to be maintained over this distance. Also, this method does not provide a whole distribution map, where it is claimed by Song *et al.* [96] that the approach suffered from noises coming from the analog signal processing applied for high-speed position sweep, which deteriorated the practicality of the sensor in

terms of measurement accuracy. In that paper, the authors showed an alternate method incorporating differential frequency modulation, and claimed their result of 20 Hz is the highest repetition rate ever reported in distributed Brillouin sensors, albeit with a spatial resolution of about 80 cm.

1.5.4 Electromagnetic & Electrical Resistance Methods

Electromagnetic and electrical resistance methods have been successfully used for corrosion sensing and structural health monitoring, however the concepts are not practically compatible with fibre optics. Some of these methods are;

- Pulsed eddy current (PEC) [97] uses a pulse of electric current through a drive coil to induce a multi-frequency mix of eddy currents. Low frequency eddy currents can penetrate a conductive structure more deeply, providing a basis for buried corrosion detection.

- Magnetometers and superconducting quantum interference devices (SQUIDs) [98] have been demonstrated for quantitative measurements of both corrosion activity and material loss in aircraft aluminium alloys. SQUIDs provide sufficient spatial resolution for the distribution of hidden corrosion currents, which can be mapped [99].

- Magnetic flux leakage (MFL) [100] is one of the oldest and most commonly used technique for detecting corrosion in the pipe wall as well as pipeline features like welds, valves, supports, attachments, etc. MFL data is processed for detecting (isolating) defect or feature signal and characterising it for the purpose of sizing or assigning a template. The characterisation of the defects is based on primary and secondary parameters of the radial MFL signature. Primary parameters are axial and circumferential spread and amplitude of the signature.

- A micro electro mechanical system (MEMS) [101] based multifunctional wireless environmental monitoring chip has been demonstrated with successful results from integrated temperature, humidity and gas sensors. The authors state that it is planned to incorporate additional sensing functionalities such as corrosion and gas flow velocity in later sensor models.

Electrochemical methods typically use electrochemical change by electron transfer as the mode for detection, however the concepts are not practically compatible with fibre optics. Some of these include;

- Linear polarisation resistance method [102], limited to ionic conducting liquids where the electrical conductivity (or inversely the resistance) of a given fluid can be related to its corrosiveness. This principle can also be applied at the interface between a given metal and its environment.

- Galvanic [103] and thin film micro-sensors [104] use the well known principles of galvanic corrosion incorporated into a bimetallic sensor.

- The electrochemical noise (ECN) methodology [105] involves the measurement of electrochemical transient or noise produced by the corrosion process. This is accomplished by measuring potential noise by monitoring the potential difference of two identical electrodes, and/or measuring current noise by monitoring current fluctuations, utilising a zero resistance ammeter of two identical shorted electrodes.

- Electrochemical impedance spectroscopy (EIS) [106] is a technique for continuous measurement of the corrosion rate and corrosion pitting behaviour [107] which can be determined by quantifying the polarisation resistance. EIS is also used as a method for evaluating commercially applied organic protective coatings [108] and other corrosion inhibitors.

- Electrochemical emission spectroscopy (EES) [109] is a modified electrochemical noise technique, developed for nondestructive, real-time corrosion rate measurements. This technique differs from standard measuring techniques in that it uses signals generated by the corroding system. It can detect the onset and re-passivation of a previously localised corrosion site.

1.5.5   Radiation Methods

Radiation methods have typically used high-energy radiation, such as X-ray which is ionising, or low frequency terahertz or microwaves which can penetrate outer protective layers to effectively image hidden corrosion. These wavelengths are not practically compatible for distributed corrosion detection using fibre optics. Some of the radiation based methods used for detecting corrosion include;

- X-ray methods to detect corrosion and cracks involve the use of tomograms or tomography in which the surface images are reconstructed from the various slices taken. The method is particularly effective in detecting inter-granular corrosion [110].

- Corrosion and material thickness can be monitored by employing microwave radiation methods. This approach seems to provide good results for detecting corrosion under paint and other materials [111].

- Terahertz radiation is capable of detecting hidden corrosion under surfaces, surface roughness of metals, and used to evaluate composites [112]. The National Aeronautics and Space Administration (NASA) has investigated methods using terahertz radiation for detecting hidden corrosion such as might be found underneath the heat barrier tiles. This method was able to detect corrosion under 5 cm thick space shuttle tiles, using a time domain processing procedure with terahertz radiation in samples ranging from small lab samples to an actual space Shuttle [113].

1.5.6   Fluorescence Intensity Methods

Initial work on the fluorometric detection of Al^{3+} as an indicator of aluminium corrosion was conducted by the Australian Defence Science and Technology Group (DSTG), part of Australia's Department of Defence, in conjunction with Monash University in the early 2000s. These experiments focussed on the use of conventional large core multi-mode fibres (MMFs). As part of this research a range of different permeable polymer systems, doped with a compound that fluoresces in the presence of Al^{3+} were evaluated. The most promising of these, a flexible polyurethane (PU) the main constituent of which is a polyether [14], was shown by Dr Grant McAdam in 2005. The polymer was doped with a fluorescent compound, 8-hydroxyquinoline (8-HQ), which reacts with Al^{3+} to form a rigid octahedral complex that fluoresces at 516 nm under ultraviolet (UV) excitation at around 360–390 nm.

The doped polymer was dip-coated onto the distal end of a conventional large core optical fibre to create a sensing polymer bead at the fibre tip. This bead was exposed to 8-HQ in solution to allow the dopant to diffuse into the polymer, and then
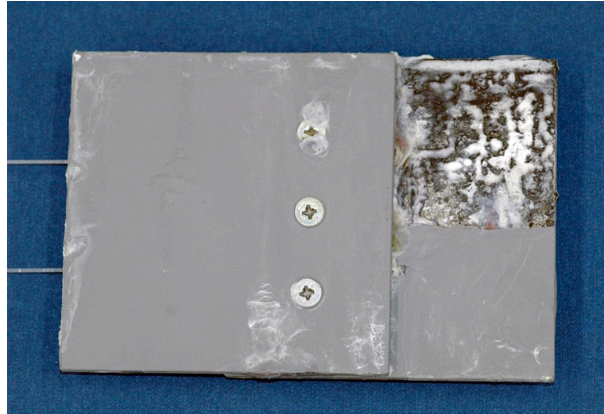
Figure 1.7 – Simulated lap-joint after exposure in salt spray chamber for 2 weeks.

allowed to dry naturally prior to placement into the channel of a simulated lap joint in a region where the corrosion protective coating had been removed. This lap joint was then placed in a salt spray chamber for a period of 14 days to accelerate the corrosion process, as shown in Fig. 1.7. The sensing fibre was excited using a UV light emitting diode (LED) light source and the back-reflected fluorescence measured via a 3 dB coupler using a micro spectrophotometer (Ocean Optics). A schematic diagram of the experimental set-up is shown in Fig. 1.8(a). The measured back fluorescence as a function of exposure time in the salt-spray chamber is plotted in Fig. 1.8(b).

For this case, where the bead is attached to the end of an optical fibre, there are fewer physical constraints on the properties of the permeable coating used to contain the fluorescent species compared to a distributed sensor. Ideally, it would be preferable to

(a)

(b)
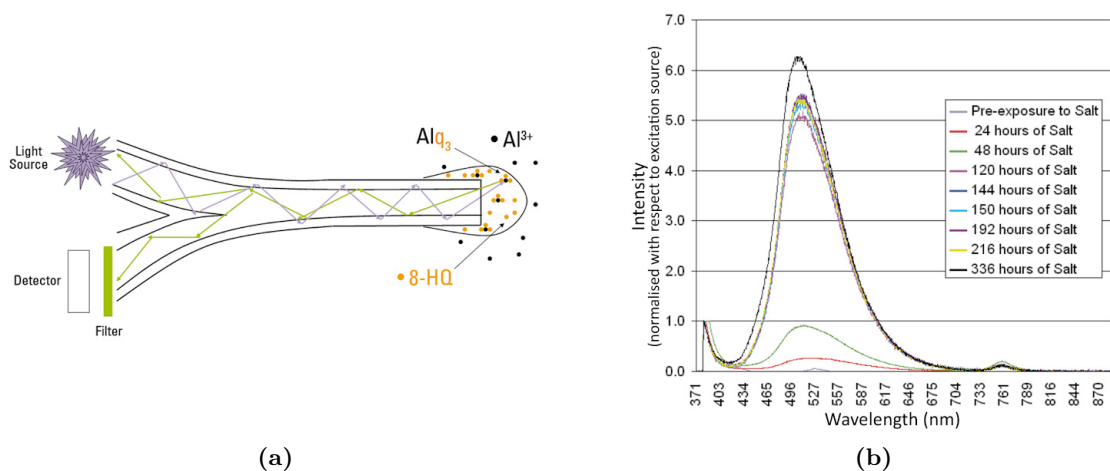
Figure 1.8 – (a) Schematic for point detection from a doped polymer bead, and (b) the measured back reflected fluorescence from the fibre tip as a function of exposure time in the salt spray chamber.

create sensitivity to Al^{3+} by coating the fibre along the length, thus creating a distributed sensor rather than a local (point) sensor. To make distributed measurements the fraction of guided light propagating along the outside of the core needs to be accessed, which requires careful tailoring of the cladding to optimise the light/fluorophore interaction.

1.5.7   Distributed Sensing with Optical Fibres

For spatially resolved mapping of analyte, a technology should permit the determination of the analyte as a function of position along the sensing element length. Fibre optics provide a unique solution to this problem. Distributed sensors using extended-length continuously sensitive optical fibres can offer detection schemes that have no counterpart in conventional sensor technologies. A sensor is termed 'distributed' here if it operates with a continuous extended length sensing element and is capable of determining variations in a parameter along the entire length of the fibre as a continuous function of distance [114] or spatially averaged [115].

The first type of distributed optical fibre sensor was devised by Dr Michael Barnoski in 1976 at Hughes Research Laboratories using optical time-domain reflectometry (OTDR) [114]. The OTDR method is shown in Fig. 1.9. A pulsed laser is coupled into a section of fibre via a directional coupler, used to couple the returned backscattered light fraction to a test fibre and avalanche photodiode (APD) detector. For uniform fibres, the detected component varies as the product of the launched power and the bi-directional attenuation between the source and detec-
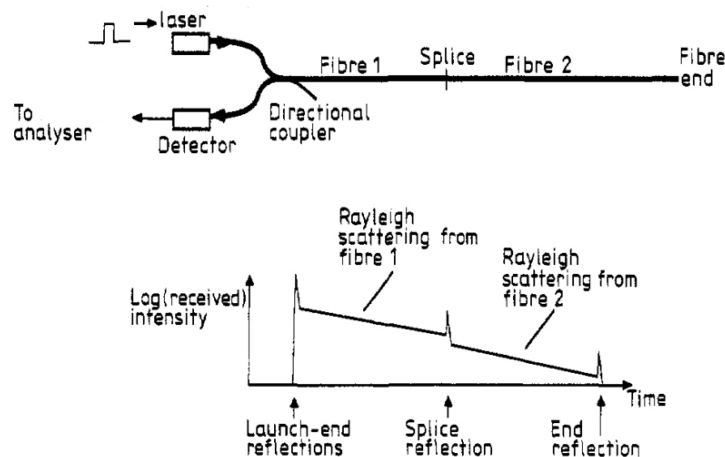
Figure 1.9 – Image from [116] showing the basic concept of OTDR with (top) the optical arrangement and (bottom) the OTDR return signal.

tor, since the scattering coefficient does not vary significantly along the length. This makes the method extremely useful for measuring spatial variations of fibre attenuation.

The concept of optical fibre distributed sensing of an analyte was first discussed by Dr Lee Blyler of Bell Labs at the 1988 International Conference on Optical Fibre Sensors (OFS) [117]. The work Blyler demonstrated utilised MMFs made from silica and plastic clad with a dye-doped silicone acrylate. This rubbery silicone cladding was shown to have a distinct advantage for chemical sensing applications since small molecule chemical species could diffuse through the cladding very rapidly. The dye used to dope the cladding was sensitive to changes in pH, and Blyler used this to show that absorption loss changes which occur anywhere along the fibres length could be detected in a spatially averaged manner. Ten years latter, Dr Radislav Potyrailo of General Electric combined the ideas of Barnoski and Blyler to create an extended length distributed sensor capable of determining the location and local concentration of an analyte along an optical fibre [118].

The concept of distributed detection of fluorescence from 8-HQ complex with Al^{3+} in solution was demonstrated by Dr Elena Sinchenko in 2010 at Swinburne University in conjunction with the DSTG [119]. By using a large solid core (200 µm) MMF made from silica with the cladding removed, it was shown that OTDR could be used to not only detect the presence of Al^{3+} but also locate the position of this fluorescence 80 m along the fibres length. Figure 1.10(a) shows the setup, where photon counts were accumulated by the time-gated electronics in bins of 2 ns width, which

(a)   (b)
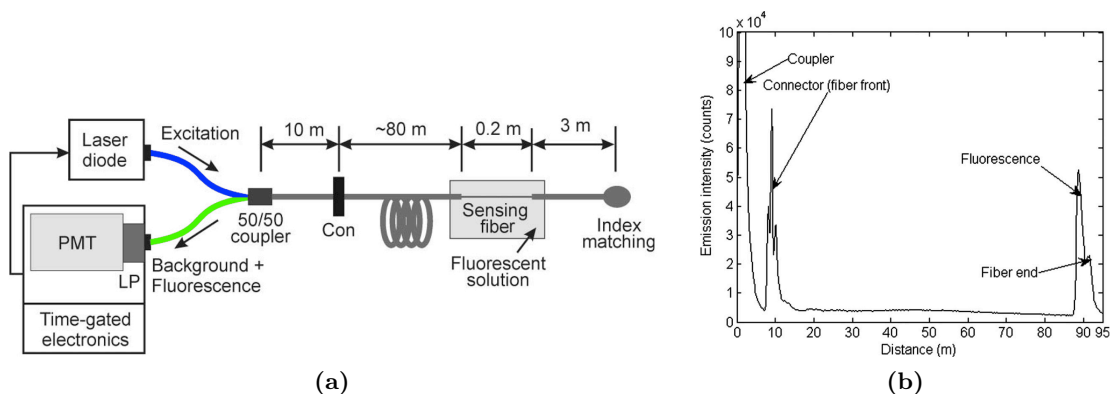
Figure 1.10 – (a) OTDR setup for distributed measurements of Al^{3+} (LP, long pass; Con, connector) in solution using a MMF silica fibre with 200 µm core; with which the (b) time of flight resolved fluorescence response of the 8-HQ complex within solution corresponds to detection position along the fibre [119].

corresponds to a length resolution along the fibre of 0.2 m, assuming a propagation velocity of 2×10^8 ms^{-1}. An accumulation time of 10 min was used to obtain adequate signal-to-noise discrimination. These photon bin accumulations corresponded to the return time of flight of the fluorescence that originate at a distance along the fibre. The signal detected is shown in Fig. 1.10(b), which represents the time domain response of the detection system when the de-clad fibre section was immersed in a 5×10^{-3} M solution of the 8-HQ complex.

This OTDR experiment, conducted at Swinburne University, and described in detail in Ref. [119], shows that distributed fluorescence detection of cations, and in particular Al^{3+}, is possible. The PF from the guided light propagating along the outside of the core could be used to excite the 8-HQ complex and the fraction of emitted florescence recaptured by the fibre core could be measured by the time-gated electronics. Further work by Sinchenco demonstrated that the MMF could be used to perform *in situ* detection of corrosion in a model aluminium lap joint [120, Chap. 7]. However, using such a large core MMF meant that less than 0.1% of the total optical power propagates outside the core. In fact, the PF increases as a function of core diameter where smaller core sizes have increased power [121]. Further explanation of how the fraction of guided light power propagating outside the core changes with core size is discussed in the next chapter, Sec. 2.3.3.

1.5.8 Suspended-Core MOF (SCF) Fluorescence Based Sensing

Unlike sub-wavelength diameter optical fibre made by tapering a commercial fibre (glass nano-wires) [57] (Fig. 1.11(a)), a MOF [41] provides a means for obtaining long lengths of uniform micrometre–nanometre scale suspended and protected cores. A protected core geometry is necessary for sensing in harsh environments, such as the application of corrosion sensing within an aluminium structure. In particular, the SCF [122] design, which consists of a small glass core suspended by thin struts inside voids within the fibre, has found extensive use in chemical sensing applications [121, 123]. For these fibres the PF that is outside the glass overlaps with the voids, and by controlling the size of the core, this overlap between the light and the voids can be adjusted. If the voids of the fibre are then filled with liquids or gases this controllable interaction allows sensing measurements to be performed, using methods such as direct absorption [66] or various

fluorescent techniques [121, 122]. These SCFs dramatically improve fluorescence-based fibre sensors by making use of the increased PF provided by the micrometre scale core size and therefore increased sensor performance. Figure 1.11(b)-1.11(c) shows a SCF based on undoped high purity fused silica known as Heraeus Suprasil F300HQ silica (F300HQ).

Figure 1.11(b) shows the overall suspended-core structure, with the polymer coating removed. This example has an OD of 270 µm, although smaller sizes can easily be achieved. An enlargement of the core and holes region in the centre of the fibre is shown in Fig. 1.11(c), where the core of the fibre is the small triangular element in the centre of the image (highlighted by the green box), suspended on three thin struts. The three black voids are the holes within the fibre cross-section, which form the cladding region used to provide the refractive index contrast needed for light confinement, and can also be used as sample chambers. Each hole effective diameter is 12.4 µm, defined as the diameter of a circle whose area is equal to the cross sectional area of the hole. The web thicknesses are at least 0.16 µm, while the core has an effective diameter of 1.7 µm, defined as the diameter of a circle whose area is equal to a triangle that fits wholly within the core area [124].

While SCFs have provided a highly sensitive sensing platform exploiting the significant fraction of guided power located within the holes [66, 67, 121, 125–127], the closed structure makes it impossible to use them for distributed sensing applications. This is because sensing with SCFs relies on filling the fibre from one or both ends,

(a)   (b)   (c)
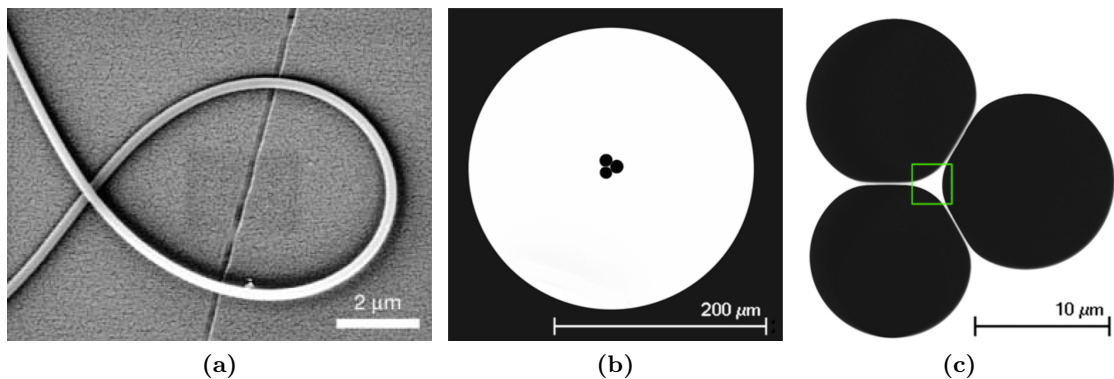
Figure 1.11 – Scanning electron microscope (SEM) cross section images of (a) glass nano-wire from Ref. [57]; (b) the silica SCF with a OD of 270 µm; and, (c) an enlarged image of the core and hole region, where the core is highlighted by the ▊ – green box, having an effective diameter of 1.7 µm [3].

and difficulty exists when attempting to ensure stable optical coupling while filling [2]. In principle, SCFs offer the potential for easier filling compared to PCFs, since PCF cladding holes provide very small air filling fraction when the core is small [128]. In practice though, the time needed to fill SCFs depends on the required interaction length and size of the holes. For example, it takes ~7 hrs for gas diffusion [66] or ~100 min for water [129] to fill 1 m of SCF with Ø8 µm holes at standard temperature and pressure. To overcome this, fabrication techniques that expose the core were demonstrated in 2007 by micro-machining fluidic side-channels at several locations along the fibre length [130–133], which results in short exposed regions in the order of tens of microns. This provides access to the core by the analyte, making it useful for real time sensing applications, but is still not practical for distributed sensing applications where long lengths are required. To overcome this problem, Dr Stephen Warren-Smith [134] at the University of Adelaide (using soft glass) and Dr Felicity Cox at the University of Sydney [135] (using polymer) independently created the first example of an exposed-core microstructured optical fibre (ECF) in 2007. A scanning electron microscope (SEM) image of the soft glass ECF made by Warren-Smith is shown on the right hand side of Fig. 1.12. This was done by effectively opening up one of the voids within the preform before drawing to fibre. These ECFs can allow the guided light to interact with the surrounding medium anywhere along the length. This method provides the ability to fabricate ECFs hundreds of metres long with a fixed microstructured cross section.
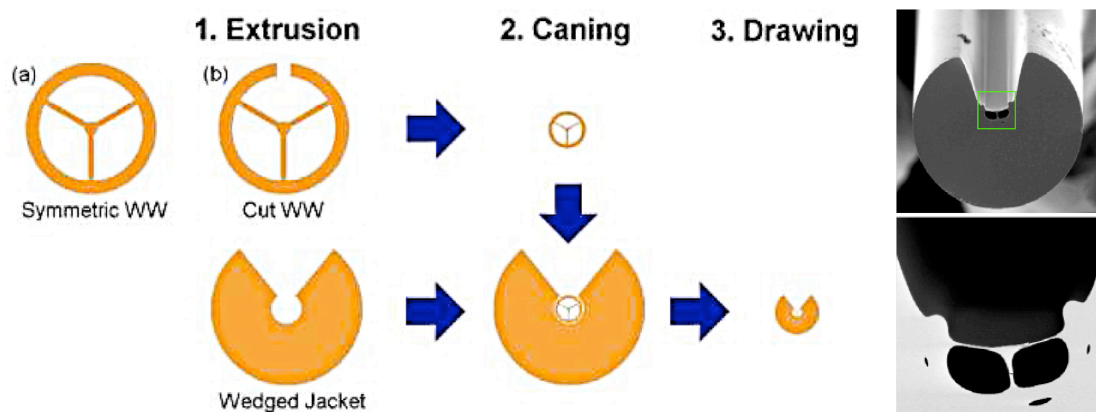
Figure 1.12 – (Left) Schematic diagram of Schott F2 soft glass (F2) ECF fabrication process, with SEM images of (top-right) the resulting ECF with an OD of ~160 µm; with an enlargement of the area highlighted by the ▌ – green box (bottom-right) showing the core, hole and strut structured region, where the core has an effective diameter of ~3.0 µm [134].

The fabrication of ECFs is challenging due to their asymmetric cross section. The method using soft glass involved modification of the established cane-in-jacket process [124] by introducing a wedge in the preform fabrication process [134]. These fibres were initially produced in F2, which has a glass transition temperature low enough to make it practical for extruding the structured preform [136]. The process, summarised in Fig. 1.12, involved extruding a F2 billet into a SCF structured preform at high temperature and pressure. The SCF preform was then drawn to a cane ($\sim$1 mm diameter) using a draw tower, which was inserted into an extruded F2 wedged jacket. The cane-in-jacket was then drawn to fibre with an OD of $\sim$160 µm diameter (top-right of Fig. 1.12) where the $\sim$3 µm effective diameter core, in the exposed region highlighted by the green box, is suspended by three thin struts [134]. An enlarged view of the ECF structured region of the fibre is shown in the bottom-right view of Fig. 1.12.

Warren-Smith showed that the ECF has fast response and is capable of real-time sensing anywhere along the fibre length, making this type of fibre ideal for distributed sensing. It was demonstrated that fluorescence emission coupled into the backward modes of a MOF core has higher efficiency compared to the forward modes [68, 137]. This means that fluorescence measurements are enhanced when evaluating the back reflected signal, as shown by the schematic in Fig. 1.13. Figure 1.14 shows the result of the demonstrated fluorescence based distributed sensing by performing OTDR measurements using ECFs. Fabrication of these small-core ECFs was a significant milestone in the development of a distributed fibre optic corrosion sensor. For the first time, small core distributed fluorescence measurements became possible [138], where the increased PF from the guided light propagating outside the small core could be accessed anywhere
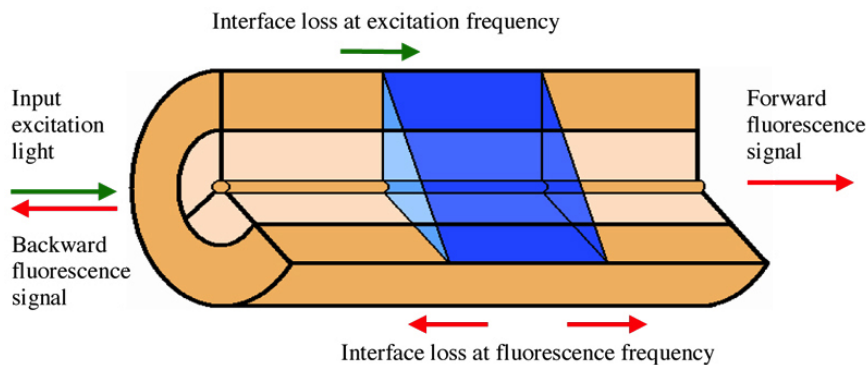
Figure 1.13 – Schematic from Ref. [137] of an ECF with a section immersed in a liquid. Liquid interface losses exist for the excitation light entering the liquid filled section and for the fluorescence exiting the liquid filled section.
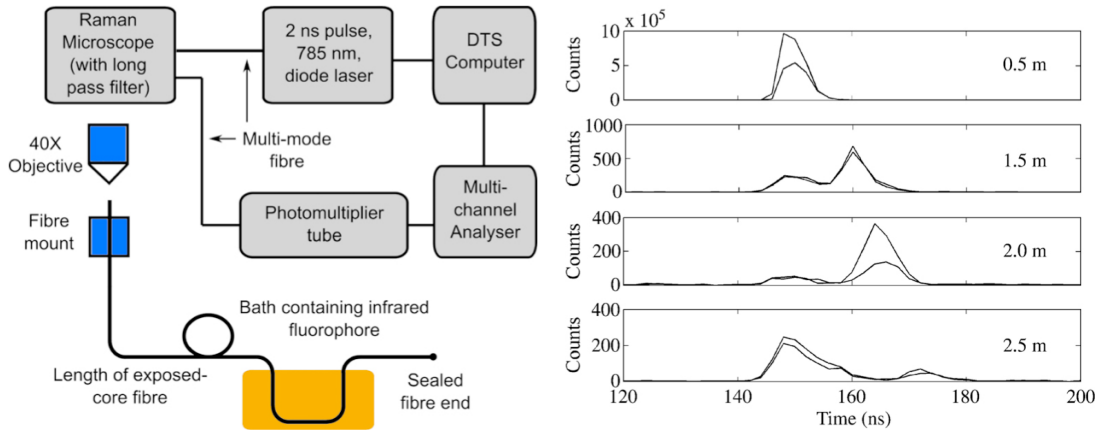
Figure 1.14 – From [138] demonstrating the use of ECFs for fluorescence-based distributed sensing. This was achieved by performing OTDR measurements using an ECF immersed in a fluorescent solution.

along its length, whilst still being protected by the outside jacket. Unfortunately, it was found that the F2 material was not suitable for long term use and/or harsh environments [134, 139], where the fibre loss increased by 0.4 ± 0.048 dBm^{-1}day^{-1} while in storage. These loss and deterioration issues associated with the soft glass material from which they were fabricated precluded their long-term practical use under harsh conditions.

1.5.9 Summary of Methods

A summary of the corrosion sensing methods discussed in this chapter are summarised in Table 1.1. Of these varying approaches, further development of the fluorescent method described in Secs. 1.5.6 and 1.5.8 has many benefits over the others. In particular, fabrication of ECFs and their application to excite and perform distributed measurements of the emission from fluorophores in solution is significant towards the development of a distributed fibre optic corrosion sensor. This means that fluorophores with specificity to Al^{3+} could be used to detect corrosion. The obvious next step was to find a way to create a practical ECF / fluorophore combination as a sensing element for the detection of corrosion in harsh conditions while embedded in a simulated joint.

Table 1.1 – Summary of Corrosion Sensing Methods

Method	Conclusion	Section
Reflectance, Polarised Reflectance Spectroscopy	-Requires multiplexing and so is not cost effective or practically compatible with the requirements.	1.5.1
Evanescent Wave Absorption Spectroscopy	-Does not have any advantages over fluorescence methods.	1.5.1
Raman Spectroscopy	-Requires multiplexing and so is not cost effective or practically compatible with the requirements.	1.5.1
Micro-bending (Bragg Grating)	-Fixed position Bragg gratings are not able to provide a continuous distributed measurement and so is not practically compatible with the requirements.	1.5.2
Thermography (Bragg Grating)	-Requires thermal stimulation which adds to cost and complexity of the system, and is not practically compatible with the requirements.	1.5.2
Ultrasonic Lamb Waves (Bragg Grating)	-Susceptible to temperature changes, has cross-talk issues, ghost reflections, blind zones, and requires the additional cost of an ultrasonic signal generator. Several measurements are needed for reliable data.	1.5.2
Refractive Index Change (Bragg Grating)	-Does not seem to be able to provide a continuous distributed method without a dynamic Bragg grating.	1.5.2
Stimulated Brillouin Scattering	-There is an opportunity to develop a corrosion/chemical sensor with a MOF that optimises Brillouin gain, hence improved sensitivity for distributed sensing, while still maintaining low loss.	1.5.3
Electromagnetic / Electrical Resistance / Electrochemical / Radiation	-These methods are not practically compatible with the requirements.	1.5.4 1.5.5
Fluorescence	-Demonstrated method for distributed corrosion sensing, requiring improvement to handle the harsh environmental exposure.	1.5.6 1.5.8

1.6   Thesis Structure

This research advances optical fibre sensing technology with the objective to develop a fibre optic approach for detecting the initiators and/or by-products of corrosion within an aluminium structure. This thesis shows the significant progress that was necessary to achieve this objective. In the next chapter, the requirements for using fibre optics in this way are discussed and the design parameters are described, along with material options and their properties. A technique was established for the fabrication of suitable polymer (Chapter 3) and silica MOFs (Chapter 4). This required understanding of the details of the draw process beyond what is achievable by trial and error, which required the ability to predict the experimental drawing parameters needed to produce the desired final geometry. A method to apply an analytical model developed by Fitt *et al.* [140] to determine the draw conditions needed to produce multi-hole symmetric and asymmetric MOFs is described in Chapter 4. This fabrication methods was used to fabricate the first silica ECF, the characterisation of which is shown in Chapter 5.

Although these newly developed silica ECFs provided a robust fibre optic sensing platform, a transduction method was also needed for the specific detection of Al^{3+}. To achieve this, sensor molecules that fluoresce when combined with Al^{3+} where immobilised onto the surface of the MOF exposed core (also known as functionalisation). Chapter 6 shows a new method for functionalising, by applying a thin film polymer doped with sensor molecules to the surface of the ECF core. It was found that the thin film polymer method has several advantages over traditional covalent bonding techniques, when fluorescent sensor molecules are used. These developments were then used to create an optical fibre based sensor for corrosion detection of aluminium in accelerated laboratory tests of simulated aircraft joints, shown in Chapter 7.

> ## 2
> # Methods and Material for MOF Corrosion Sensor

"If you wish to make an apple pie from scratch, you
must first invent the universe."

– Carl Sagan

Further development of optical fibre fluorescence sensing described in the last chapter has merit for this project. Fluorescence was shown to be practical when combined with ECFs, with the capacity for distributed measurements. To decide whether to iterate from the past work done by Warren-Smith and Sinchenko or change tactics, it was important to understand why the soft glass ECF had loss and deterioration issues. The ECF material used for fluorescence based distributed sensing prior to this work was F2, which is known to not be as mechanically or chemically robust as silica or polymer [141]. Hence, the discussion and results shown in this chapter is intended to gain a quantitive understanding of the critical requirements as well as available fabrication techniques and materials that could be used for MOF sensing elements for use in distributed detection of corrosion.

2.1 The Process of Producing MOFs

All optical fibres are produced by heating and drawing down a preform from an initial diameter of the order of centimetres to the desired final diameter using a fibre drawing tower. This process is shown in Fig. 2.1(a). For MOFs with longitudinal air holes this draw process typically includes a mechanism by which the pressure difference of the holes and atmosphere is maintained to ensure the holes collapse or expand to achieve the desired final geometry. Some common ways to produce MOF preforms include using extrusion [136, 142] (Fig. 2.1(b)), sol-gel casting [143, 144], ultrasonic drilling [66, 145] or stack and draw methods [39, 146, 147], which resemble a large-scale form of the final desired fibre geometry. The fibre drawing tower is then used to feed the preform at a
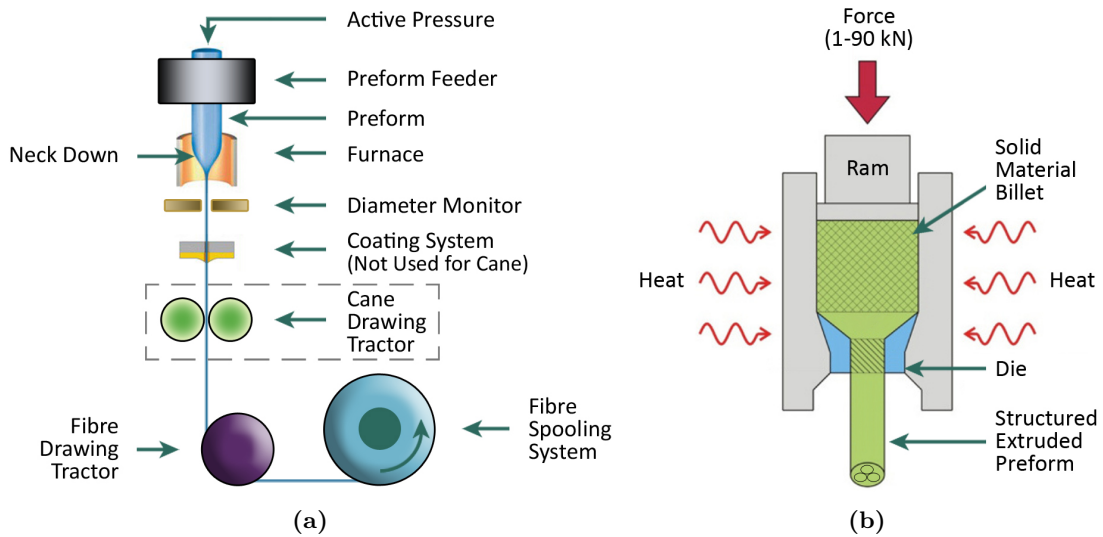
Figure 2.1 – Schematics showing (a) the draw process of cane or fibre from preform, including the neck down region inside the furnace, and; (b) the preform extrusion setup and process [142].
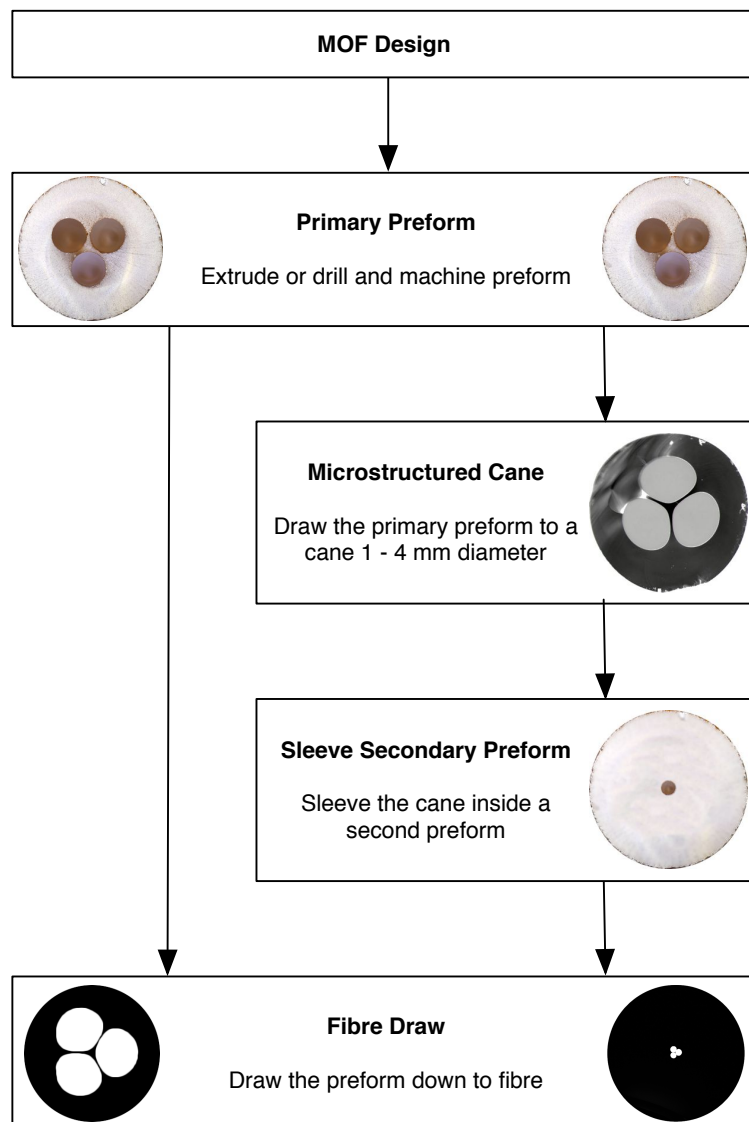
Figure 2.2 – Schematic of MOF fabrication procedure, showing the two main fabrication options.

fixed rate into a furnace, which heats the material to an appropriate viscosity, so it can taper down to the final fibre diameter (usually of the order of hundreds of micrometers) by drawing the fibre below the furnace at a faster rate.

The process of drawing the preform directly to fibre is termed a 'one step process', as shown on the left side of Fig. 2.2. It is also common to use two steps in the drawing of fibres to achieve smaller core sizes than can be realised by the one step process [124, 134]. The 'two step process', shown on the right side of Fig. 2.2, involves firstly caning the preform to the order of millimetres, inserting this cane into a jacket, and then drawing down the cane-in-jacket to fibre.

2.2   Description of Materials

Ultimately, the corrosion sensing element needs to withstand the corrosive environment while detecting the progress of corrosion within the joints and beads of an aircraft fuselage. To produce a distributed fibre optic corrosion sensor capable of withstanding these intended harsh conditions, fibre materials other than soft glass needed to be investigated. Both polymer and silica have material properties that make them attractive for optical fibre sensing applications [141, 148]. PMMA polymer optical fibres (POFs) have high elastic strain limits, high fracture toughness, and high flexibility in bending, and so initial work was performed to determine the suitability of polymer to create a robust optical fibre based distributed corrosion sensor (see Chapter 3). On the other hand, silica is known to be reliable under a range of processing and use environments, with relatively better mechanical and thermal stability [141] (see Sec. 2.2.3). Highly homogeneous, high purity bulk material is commercially available, which has led to the development of low loss silica telecom fibres ($\sim$0.2 dB/km at NIR wavelengths) [32]. Both polymer [135] and silica [66] SCFs have already been developed by other researchers, and working in multiple directions with these two materials provided a risk reduction for the project.

As an initial step, the transmission characteristics of bulk F2 soft glass, F300HQ silica, and PMMA polymer were measured using ultraviolet–visible spectroscopy (UV-Vis) to understand what could be expected when producing optical fibres from these materials. The results for these UV-Vis measurements are shown in Fig. 2.3. This graph indicates that F300HQ silica has better overall transmission properties compared to PMMA and
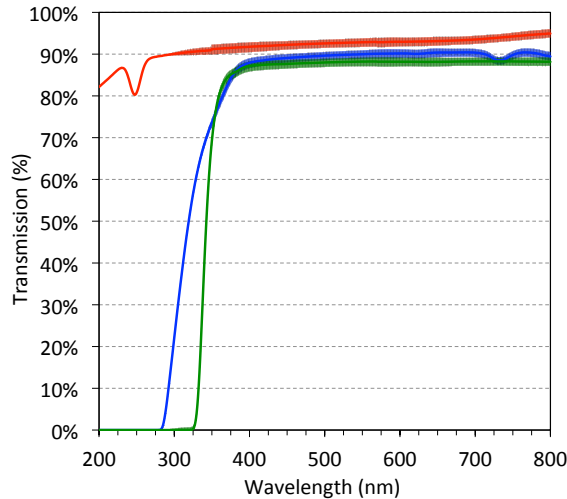
Figure 2.3 – Comparison of the (█ – green) soft glass (F2 - 31.33 mm thickness), (█ – red) silica (F300HQ - 31.97 mm thickness) and (█ – blue) polymer (PMMA - 33.95 mm thickness) bulk material transmission using UV-Vis. Error bars are included in the plot.

F2, which have similar transmission characteristics in the range 200–800 nm. Other known properties from the manufacturer or literature is shown in the following sections.

2.2.1   Schott F2 Lead Silicate

F2 is part of the family of compound glasses, also known as 'soft glass'. A significantly useful feature of F2 is that it has relatively high transmission at visible wavelengths while having a transition temperature (T_g) that is considerably lower than that of silica. This makes it useful for producing low loss MOF [150] using the extrusion method, and so in the past has become common for use as fibre optic sensors. While the material

Table 2.1 – Typical properties of Schott F2 lead silicate glass [149]

Property	F2
Density (g/cm^3)	2.65
Sensitivity to Humidity, 30 hrs (%)	<0.3
Glass Surface Stain Formation, pH=4.6	No
Acid Resistance (hours)	>100
Alkali Resistance (hours)	>4
Phosphate Resistance (hours)	>4
Transition Temperature T_g (°C)	569
Refractive Index (at 589.29 nm)	1.62
Light Transmission at 400 nm, 10 mm thick (%)	94.6

specifications shown in Table 2.1 show good bulk material stain, acid, and alkali resistance, the transmission properties of SCF and ECF produced from this material tends to degrade very quickly compared to fibres where the core is protected. Another property to consider when choosing F2 for sensing applications is that it absorbs and therefore is not transparent at UV wavelengths, therefore precluding the use of many biological or fluorescent sensing molecules that are excited by UV.

2.2.2 PMMA Polymer

One advantage of using polymer MOFs for sensing applications is that the sensing layer can be directly physisorbed to the light guiding core surface by electrostatic interactions. For example, polymers containing negatively charged side chains readily adsorb positively charged adsorbates. Alternatively, negatively charged adsorbates are attracted to polymer that contains positively charged side chains. However, the low transition temperature (e.g. ~90℃ for PMMA) makes polymer MOFs impractical for use in high temperature environments or for high power light transmission, and like F2 is not transparent at UV wavelengths. Nevertheless, PMMA has been used extensively for the production of POFs, and so was chosen as the material used for the work described in this thesis. This material is described by manufacturers as being transparent at visible wavelengths, unaffected by moisture, able to be heat formed, and offers a high strength to weight ratio.

In brief PMMA is manufactured by two different production processes [153]. Cast PMMA, as the name suggests, is manufactured by a process whereby methyl methacrylate monomer (MMA) liquid is pumped into a mould. The mould and monomer is then submerged in warm water where the process of polymerisation takes place. The result is rigid PMMA, also known more generically as Acrylic. The surface finish of cast PMMA is smooth, since it is cast in a smooth mould. On the other hand, extruded PMMA is manufactured by a continuous production process whereby PMMA pellets are fed through an extrusion barrel. As the pellets progress through the heated zones of the extruder barrel the heat increases until the pellets melt into a molten mass. This molten mass is pushed forward into a conical shaped die and outwards through a round die to produce a molten rod which is then cooled. The specifications of both cast and extruded PMMA are shown in Table 2.2. The main differences in the specifications of the cast and

extruded material are the tensile elongation at break, 2% (cast) vs. 4.5% (extruded), the forming temperature 170℃ (cast) vs. 149℃ (extruded), and the operating temperature for the cast material can be twenty degrees higher than for the extruded material.

Table 2.2 – Typical properties of cast [151] and extruded [152] PMMA

Property	Cast	Extruded
Density (g/cm^3)	1.18	1.19
Water Absorption, 24 hrs (%)	0.3	0.2
Tensile Elongation at Break (%)	2	4.5
Flexural Strength (MPa)	83 − 117	117
Compressive Strength (MPa)	Unknown	149
Forming Temperature (℃)	170	149
Vicat Softening Point (℃)	Unknown	105
Max Operating Temperature (℃)	65 − 93	71
Refractive Index (at 589.29 nm)	1.48 − 1.50	1.49
Min Broadband Light Transmission (%, 10 mm)	92	92
Chemical Resistance		

Limited Resistance to:	Resistance to:
- Acetic Acid (5%) - Chromic Acid - Ethyl Alcohol (30%) - Gasoline - Hydrogen Peroxide (>40%) - Isopropyl Alcohol - Methyl Alcohol (30%) - Nitric Acid (40%)	- Ammonium Chloride - Ammonium Hydroxide - Battery Acid - Calcium Chloride (Sat.) - Calcium Hypochlorite - Citric Acid (20%) - Cottonseed Oil - Detergent Solution - Diesel Oil - Ethylene Glycol - Glycerine - Heptane - Hexane - Hydrochloric Acid - Hydrogen Peroxide (<40%) - Kerosene - Mineral Oil - Nitric Acid (10%) - Olive Oil - Soap Solution (Mild dish soap) - Sodium Carbonate (20%) - Sodium Chloride (10%) - Sodium Hydroxide (<60%) - Sodium Hypochlorite (5%) - Sulfuric Acid (<30%) - Transformer Oil - Turpentine - Water
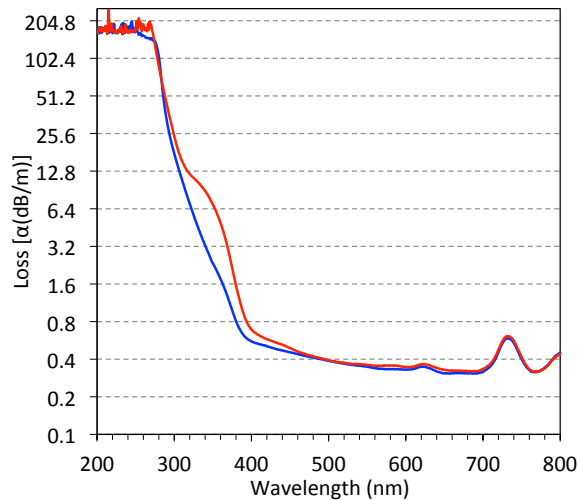
Figure 2.4 – UV-Vis loss comparison of (▌ – red) cast PMMA billet from supplier and (▌ – blue) extruded PMMA billet from supplier.

To determine the difference in transmission properties of cast and extruded PMMA, UV-Vis measurements of these materials was conducted using samples ∼35 mm thick. The results of these measurements is shown in Fig. 2.4, which indicates that the loss is similar for wavelengths above 400 nm, however for the cast PMMA there is an additional loss peak centred at around 380 nm.

2.2.3 Silica

It is generally accepted that "if you can do it in silica; do it in silica ... given silica's high strength, very low loss, industrial acceptance, and market incumbency" [154]. Silica has a relatively low refractive index, which can improve the sensitivity of evanescent field sensors, since reducing the index contrast (Δn) at the core-cladding boundary increases the power fraction to the analyte or functionalised surface [121]. A relatively low intrinsic nonlinearity makes silica excellent for low or high power optical fibre applications. The most striking feature of silica is the broad transparent area that covers the complete visible spectrum and extends far into the infrared and ultraviolet regions. The intrinsic UV and infrared (IR) absorption edges in silica glass are located at around 180 nm and 3.5 µm wavelengths, respectively. Like other glasses, metallic impurities cause the UV edge to shift to longer wavelengths, and the presence of hydroxide (OH^-) caused by water introduces absorption just below the IR edge. The strongest of these is the fundamental O–H stretching band with peak wavelength at 2.73 µm.

To modify the absorption characteristics of silica materials, manufacturers produce highly homogeneous materials using vapour deposition with varying amounts of OH^-, Cl^-, and fluorine. Viscosity is also significantly affected by trace impurities [156]. Alkalis and halogens such as sodium and chloride lower viscosity while small amounts of aluminium and refractory metals like molybdenum increase viscosity [155]. Hence, the method of manufacture is an important consideration for defining processing temperature. F300HQ material is made using vapour deposition with silicon tetra-chloride ($SiCl_4$) as the starting material, which produces a material that has excellent transmission properties from 400–1100 nm, because of the very low OH^-, and is designed for the most demanding optical performance applications. On the other hand, light weight quartz (LWQ) silica material is melted from quartz crystals which have a variety of impurities including high OH^- but is a cheaper alternative to the F300HQ. The specifications of these two materials are shown in Table 2.3, and Fig. 2.5 shows the difference in the viscosity curves of these two materials, with F300HQ having a lower viscosity due to the Cl^- content. For the experiments with silica shown in this thesis, the cheaper LWQ was chosen for initial trials and then once the method was established the F300HQ was used.

While silica has many advantageous characteristics, the T_g of silica (∼1150℃) makes it challenging to use extrusion techniques established for producing preforms from soft glass or polymer. In 2007, Webb *et al.* showed that silica SCFs could be fabricated by

Table 2.3 – Typical properties of electrically fused mineral quartz and synthetic fused silica material [155].

Property	Electrically Fused Quartz	Synthetic Fused Silica
Density (g/cm^3)	2.203	2.201
Flexural Strength (MPa)	67	67
Compressive Strength (MPa)	1150	1150
Softening Temperature (℃)	1710	1600
Annealing Temperature (℃)	1220	1100
Max Operating Temperature (℃)	1160	950
Refractive Index (at 589.29 nm)	1.458	1.458
Min Broadband Light Transmission (%, 10 mm)	93	93
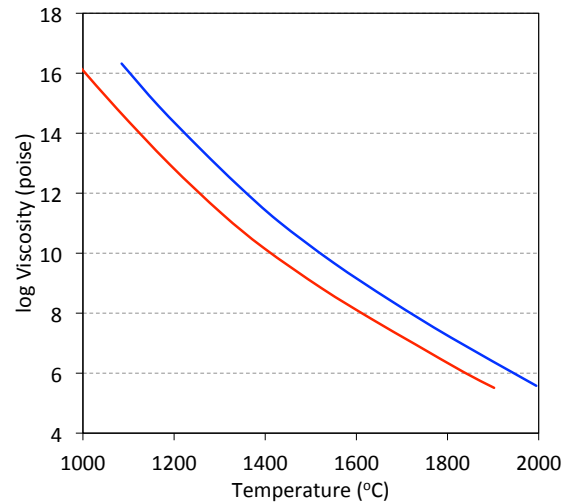
Figure 2.5 – Comparison of synthetic fused silica (▮ – red), and electrically fused mineral quartz (▮ – blue) materials [155, 157].

using ultrasonic drilling to define the air holes in a solid silica rod, which is then caned and drawn inside a jacket tube into fibre, using a conventional fibre drawing tower [66]. This method was shown to produce a three hole SCF structure, as shown in Fig. 2.6. The shape of the holes were manipulated during the draw by applying a vacuum around the cane, which introduced a pressure differential between the holes inside the cane and the surrounding air space. Thus, the holes were expanded and the strut length increased by introducing a pressure differential between the holes inside the cane and the outside space.
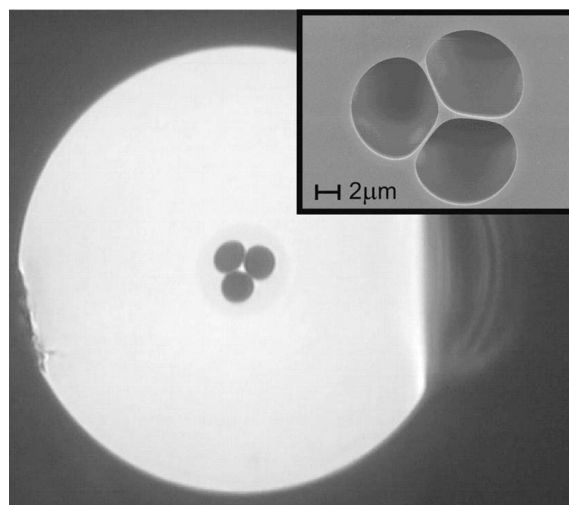
Figure 2.6 – Cross section of silica SCF produced by Webb *et al.* [66]. Inset shows a SEM image of the core area.

2.2.4   Summary of Materials

Table 2.4 shows a comparison of fibre characteristics using F2 soft glass, PMMA poly-
mer, or F300HQ silica materials for MOFs from past research. The ticks and crosses
indicates results from past published MOF production showing if the material is suit-
able for; producing exposed-core fibre; mechanical flexibility; reproducible cleaves; harsh
environments, and has relativity low loss suitable for sensing using spectroscopic tech-
niques. Gaps in knowledge are shown by the question marks. This comparison shows
that while polymer ECFs have been developed by other researchers [135], further work
was still needed to understand if PMMA polymer could be used in harsh environments
and would have suitable characteristics in terms of loss or cleaving. Also, while a method
to produce silica SCFs was shown by Webb *et al.* [66], further work was needed to de-
velop silica ECFs, and characterising these fibres in terms of aircraft fuselage corrosion
sensing and applicability to the harsh environment.

Table 2.4 – Comparison of MOFs produced from soft glass, silica and polymer.

Material	Exposed Core	Flexible	Repeatable Cleaving	Harsh Environments	Low Loss 400–800 nm
F2 Schott Glass	✔	✘	✔	✘	✔
F300HQ Silica	?	✘	✔	?	✔
PMMA Polymer	✔	✔	?	?	?

2.3   Target Fibre Specifications

While developing ECFs in potentially a more mechanically or chemically robust material,
such as silica and/or polymer, it is important to understand what core size would be
suitable and fibre loss acceptable for distributed detection of corrosion. Even though
reducing the core size can increase PF, PF alone cannot be used to optimise fluorescence-
based optical fibre sensors [137]. The following sections describe the distributed sensing
fibre design in terms of PF, fluorescence capture fraction (FCF) into guided modes of
the fibre, range, loss, modes, and field distributions. All of these factors needed to be
considered together to analyse the effectiveness of the fibre's being produced.

2.3.1   Optical Time-Domain Reflectometry (OTDR) Fibre Sensor Model

The light propagating in an optical fibre is affected by the fibre attenuation proper-
ties, which is discussed further in Chapter 5. It is important to understand how the
distributed attenuation profile of the fibre affects the power available for OTDR based
measurements. The concept of an OTDR distributed measurement using optical fibre is
based on detecting the backscattered power as a function of the position (z) along the
fibre, which is given by,

$$P_d(z) = SP(0) e^{\left[- \int_0^z \left(\alpha'(z') + \alpha''(z') \right) \mathrm{d}z' \right]}$$

(1)

where,

$P_d(z)$ is the power detected at the detector;

S is the fractional part of pulse scattered and guided by the fibre going in the
reverse direction;

$P(0)$ is the initial power of the coupled pulse at $z = 0$;

α'' is the position dependent loss coefficient for the backscattered pulse;

α' is the position dependent loss coefficient for the forward pulse.

The position dependent loss coefficients, α' and α'', are related to the average attenuation
coefficient, α, with,

$$\alpha = \frac{\int_{z_0}^z \left(\alpha'(z') + \alpha''(z') \right) \mathrm{d}z'}{2(z - z_0)}$$

(2)

Since the attenuation properties of a fibre can be obtained from power measurements
as,

$$10 \log_{10} \frac{P_d(z)}{P_d(z_0)} = \text{Attenuation in [dBm}^{-1}]$$

(3)

then Eqs. (1), (2) and (3) form the basis for determining what the limit of detection
is for a particular intrinsic fibre attenuation, or what the minimum intrinsic fibre

attenuation needs to be for some choice of overall sensing length.

The time scale can be converted to propagation distance in the fibre by multiplying by the phase velocity of the pulse in the core. Hence, it is useful to describe how the pulse travels along the optical waveguide to understand the fibres dispersion properties. The basic description is shown here, for a more thorough description one should see Ref. [158]. Considering the response for an optical pulse having the Gaussian envelope of the form,

$$f(t) = A e^{\left[-\left(\dfrac{t}{t_{\text{in}}}\right)^2 + i\omega_0 t\right]} \tag{4}$$

is injected into a step index fibre, where ω_0 is a centre angular frequency, t_{in} is the input pulse width and A is a constant. With Eqs. (1) and (4), the pulse waveform at the detector $(g_d(t,z))$ after the pulse undergoes a reflection (backscattering) at some position z is,

$$g_d(t,z) = \frac{S(\omega)A}{\sqrt{t_d/t_z}} e^{\left[-\alpha z - \left(\dfrac{(t - \beta' z)}{t_d}\right)^2 + i[\omega_0 t - \beta_0 z + \vartheta_r(t,z)]\right]} \tag{5}$$

where,

$$t_d = \sqrt{t_z^2 + \left(\frac{2}{t_z}\beta'' z\right)^2} \quad ; \quad t_z = \sqrt{t_{\text{in}}^2 + \left(\frac{2}{t_{\text{in}}}\beta'' z\right)^2} \tag{6}$$

and,

$$\vartheta_r(t,z) = \frac{2\beta'' z}{t_z^2}\left(\frac{t - \beta' z}{t_d}\right)^2 - \frac{1}{2}\tan^{-1}\left(\frac{2\beta'' z}{t_z^2}\right) \tag{7}$$

$S(\omega)$ in Eq. (5) is the fractional part of the backscattered pulse, and compared to S in Eq. (1) is also a function which includes any additional distortions induced by the backscatter event, β is the propagation constant, $\beta' = \mathrm{d}\beta/\mathrm{d}\omega$ and $\beta'' = \mathrm{d}^2\beta/\mathrm{d}\omega^2$. In Eq. (5), α is the average attenuation coefficient which can also be replaced with the position dependant loss coefficient from Eq. (2).

Equations (5) to (7) provide the basis for understanding the distributed sensor not

only in terms of the attenuation, but also the fibres dispersive properties. Since the power $P(0) \propto \int f(t)\, \mathrm{d}t$ (from Eq. (4)), and $P_d(z) \propto \int g_d(t, z)\, \mathrm{d}t$ from Eqs. (1) and (5), by the constant A, then,

$$\text{Attenuation in [dBm}^{-1}] = \frac{P_d(z)}{P_d(z_0)} = \frac{\displaystyle\int_{-\infty}^{\infty} g_d(t, z)\, \mathrm{d}t}{\displaystyle\int_{-\infty}^{\infty} g_d(t, z_0)\, \mathrm{d}t} \tag{8}$$

Thus, the one model can be used to optimise different fibre sensing architectures in terms of attenuation (α), dispersion (t_z) and any additional distortions induced by the backscatter event ($S(\omega)$).

The fabrication of a MOF with the core exposed along the whole length provides near-instantaneous measurements of fluorescence intensity while additionally allowing the opportunity for spatial measurements along the length of the fibre through temporal detection methods such as OTDR [134].

2.3.2   Distributed Sensing: Range vs Loss

The power P at an axial light propagation distance z along a fibre can be written as,

$$P(z) = P_0 10^{\frac{-\alpha z}{10}} \tag{9}$$

where P_0 is the initial input power, and α is the average characteristic fibre attenuation (see Eq. (2)) in dBm^{-1}. By assuming that both the excitation light propagation and the fluorescence propagation have the same attenuation, the loss of the fibre can be determined by fitting a set of measured OTDR intensities to the rearranged equation,

$$\log_{10}\left[P(z)\right] = -\frac{\alpha z}{10} + \log_{10}[P_0] \tag{10}$$

where with $z = 2L$, L is the position along the fibre of an observed OTDR intensity. Equation (10) represents the linear regression line of OTDR intensities.

$P(2L)$ is the fluorescence power expected at the detector from a position L along the fibre, and P_0 is the fluorescence power expected at the detector from a fibre with zero length ($L = 0$). P_0 is now related to the excitation power by factors assumed to

be constant, such as excitation coupling efficiency, fluorophore quantum efficiency, and fluorescence coupling efficiency.

As a function of L, Eq. (10) becomes,

$$L = \frac{5}{\alpha} \log_{10} \left(\frac{P_0}{P(2L)} \right) \tag{11}$$

This result can be extrapolated to determine the length of fibre that could be used for particular characteristic fibre loss,

$$L_{\mathrm{max}} = \frac{5}{\alpha} \log_{10} \left(\frac{P_0}{P_{\mathrm{min}}} \right) \tag{12}$$

With P_{min} as the minimum detectable peak height required to detect a OTDR fluorescence signal, and P_0/P_{min} is the SNR. We see from Eq. (12) that the maximum length for OTDR detection is strongly effected by the fibre loss (α) and weakly effected by the SNR, P_0/P_{min}. To show this, Eq. (12) can be rewritten as,

$$L_{\mathrm{max}} = c\,\alpha^{-1} \qquad \text{where} \qquad c = 5\log_{10}(\mathrm{SNR}) \tag{13}$$

and so,

$$L_{\mathrm{max}} \propto \alpha^{-1} \qquad \text{and} \qquad 10^{L_{\mathrm{max}}} \propto \mathrm{SNR} \tag{14}$$

Figure 2.7 shows four plots of L_{max} as a function of α, at SNRs of 3, 30, 300 and 3000. These results show that a decrease in fibre loss will increase the practical OTDR
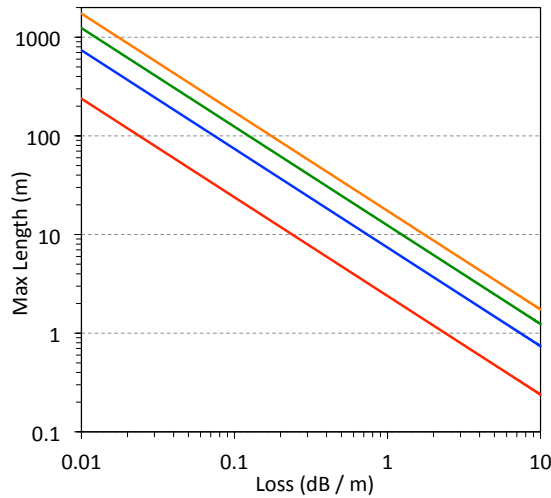
Figure 2.7 – Log–Log plot of L_{max} as a function of loss (α), at signal-to-noise ratios (SNRs) of 3, 30, 300 and 3000 shown in ▮ – red, ▮ – blue, ▮ – green and ▮ – orange respectively.

detectible length by the same amount. For example, halving the fibre loss doubles the maximum practical length, and reducing it by an order of magnitude will increase the practical maximum length by an order of magnitude. On the other hand, orders of magnitude improvement in the SNR would be required to double the maximum practical length. This shows that the majority of gain in practical OTDR length can be achieved by reducing the fibre loss. Nevertheless, it is also beneficial to make any practical improvements to SNR, since an improvement in SNR from 3 to 30 will more than double $L_{\max}$, whereas the practical difficulty of improving SNR from 30 to 300 might outweigh the benefits. For example, improving coupling and using better detectors are some easy and cost effective ways of improving SNR, and it is possible to enhance SNR if the noise is random by averaging the measurement.

2.3.3 Core Size and Power Fraction Relationship

Using the equations described in Ref. [137], a theoretical estimate of PF propagating outside a circular silica core (air suspended rod (ASR) model), for core diameters ranging from 460 nm to 10 µm was calculated. The excitation and fluorescence wavelengths used for this study were 375 nm and 516 nm respectively, being the excitation and fluorescence wavelengths of the 8-HQ complex, and for the region surrounding the silica core a refractive index of $n = 1.33$ was used. As a first approximation, the coupled incident beam waist was set at the same diameter as the core, which is reasonable for micron scale (> 1 µm) core diameters. The total PF that propagates outside the core, of all propagating modes excited by the incident beam as a function of the core diameter, is shown by the red curve in Fig. 2.8(a). This PF curve shows that for core diameters less than 4 µm the fraction of power available for fluorophore excitation starts to significantly increase, being 0.3 and 2.1% at 4 and 2 µm diameters respectively. For core sizes below 1 µm in diameter there is another significant PF increase, where the calculated values are 2.8 and 17% at 1 µm and 460 nm diameters respectively. The corresponding FCF is shown by the blue curve in Fig. 2.8(a). The FCF is defined as the fraction of fluorescent photons that are coupled to the guided mode(s) of the fibre. Although the total PF was used to calculate the FCF, for simplicity only the FCF into the fundamental mode (HE11) of the fibre was considered for the special case of an attenuation-free fibre of infinite length. This FCF curve varies from a minimum of 1.1% to a maximum of 1.7%.
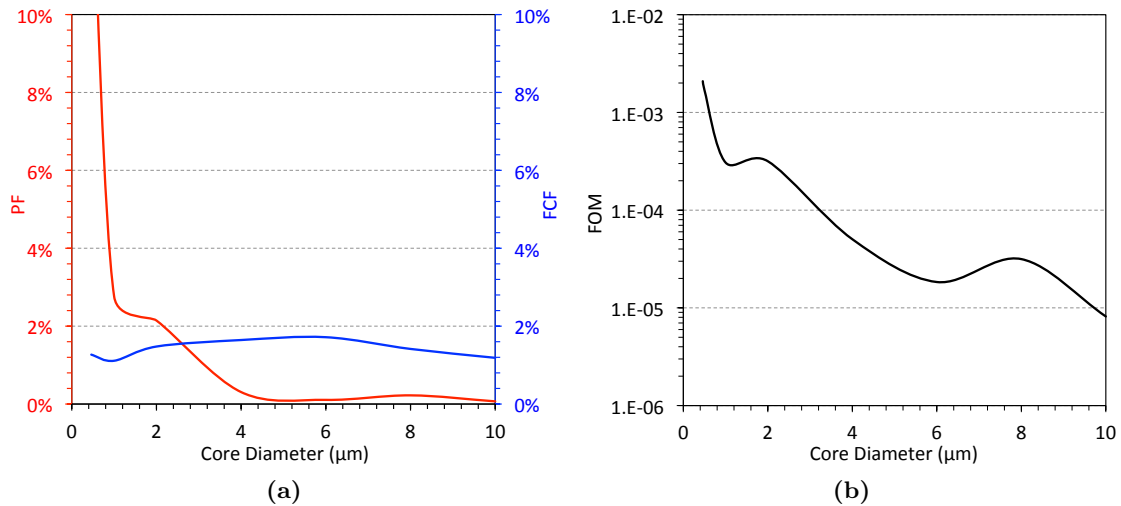
Figure 2.8 – (a) [█ - Red] Fraction of guided light power propagating outside a silica core as a function of core diameter assuming Gaussian beam excitation, and [█ - Blue] the corresponding fluorescence capture fraction into the fundamental mode; and (b) the figure of merit as a combination of both.

The intensity of fluorescence that is measured from the backward propagating modes of the fibre is the result of both the incident excitation power and the number of fluorescence photons recaptured. These quantities can be brought together to provide a better understanding of the overall performance of the sensor as a function of the core diameter by defining a figure of merit (FOM)=(PF)·(FCF) [121]. This FOM is shown in Fig. 2.8(b), where we observe an order of magnitude increase in sensor performance between the peaks at 8 and 2 μm, and no significant change in performance from 2 to 1 μm. Another factor, which will influence the FOM, is the fibre loss, which increases with smaller core diameters (and therefore greater PF) due to the increased scattering resulting from surface imperfections. More details and characterisation of optical fibre loss is discussed in Chapter 5.

2.3.4   Field Distribution and Power

While the FOM can be used to understand the overall performance of the fibre sensor, more work is needed to calculate a more accurate FCF. This is because for many mode sensing fibres, fluorescence capture is mostly through the higher order modes. In fact, Warren-Smith *et al.* show in Ref. [159] that the contribution of the higher order modes is such that fluorescence capture efficiency becomes insensitive to core diameter with an increase in number of modes. This means that larger core diameters,

with potentially less loss and therefore longer practical OTDR length, could have the desired SNR characteristics to be effective as an optical fibre based sensor for corrosion. As the effective core diameter is increased the number of modes increases, hence the fibre design in terms of number of modes and mode distribution were studied.

To show the core size / number of modes relationship, the ASR model was used to calculate the number of modes with:

$$M \approx \frac{4V^2}{\pi^2} \tag{15}$$

where

$$V = 2\pi\frac{a}{\lambda}\sqrt{n_1^2 - n_2^2} \tag{16}$$

and a is the core radius.

Figure 2.9 shows these number of modes for core diameters of 0.9375 µm, 1.875 µm, 3.75 µm, and 7.5 µm. To gain an understanding of the amount of power fraction in the exposed hole of an ECF, and how this power fraction changes with core size, numerical simulations were performed using full vector finite element method (FEM) in the commercial package COMSOL 3.4. This numerical simulation of the field distributions provides the z-component of the Poynting vector (S_z), from which the power percentage
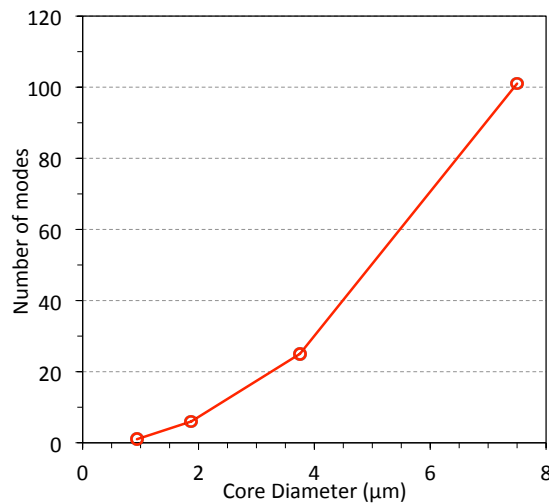
Figure 2.9 – Number of modes in circular optical fibre.

can be calculated as,

$$P_\% = 100 \cdot \left(\frac{\int_H S_z \, dA}{\int_\infty S_z \, dA} \right) \tag{17}$$

using trapezoidal rule integration over the domains. For the holes the refractive index used was $n_2 = 1$, the wavelength used was $\lambda = 1550\,\text{nm}$ at which the silica refractive index is $n_1(\lambda) = 1.444$. These simulations were done using the SEM cross section image of a fabricated ECF shown later in this thesis in Fig. 5.22(a), and scaling down the geometry in 50% steps to obtain $P_\%$ for effective core diameters of 7.5 µm (*full size*), 3.75 µm (*half size*), 1.875 µm (*quarter size*), and 0.9375 µm (*eighth size*). Since the number of modes able to propagate in these simulated fibres increases with increasing core size, the number of modes simulated was 12, 12, 6, and 1 for the four core diameters respectively. The field distribution of S_z as well as the power percentage ($P_\%$) is shown on the following six pages and discussed afterwards. The fibre was found to be single-mode at 0.9375 µm core diameter (shown in Fig. 2.10), and only the mode distributions shown for the 1.875 µm core diameter (Fig. 2.11) were found to propagate by the simulation. This is the same number of modes that were predicted by the ASR model shown in Fig. 2.9.
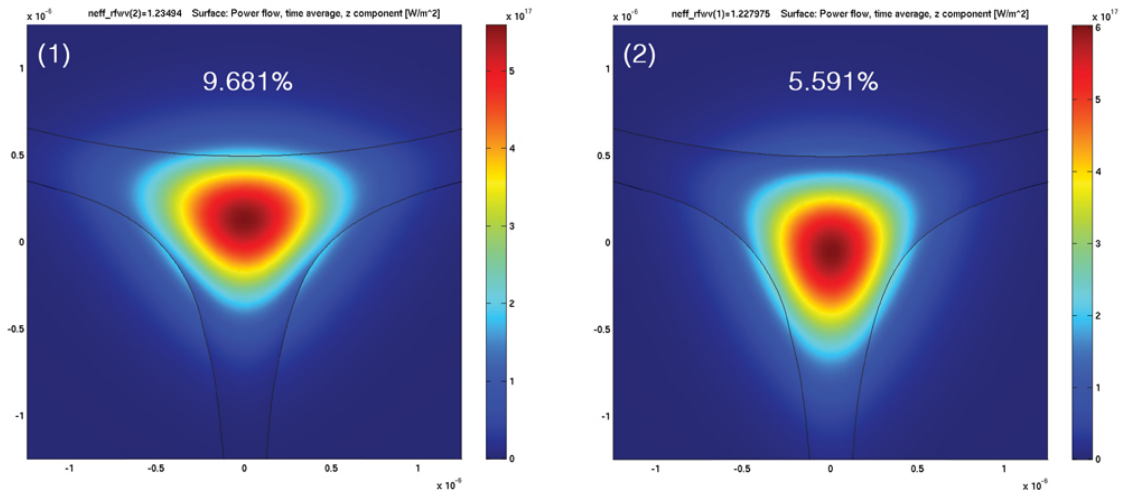
Figure 2.10 – Distribution of Poynting vector z-component of 0.9375 µm effective core diameter ECF from *eighth size* SEM cross section image. Percentage of power in the exposed hole region for each mode is shown.
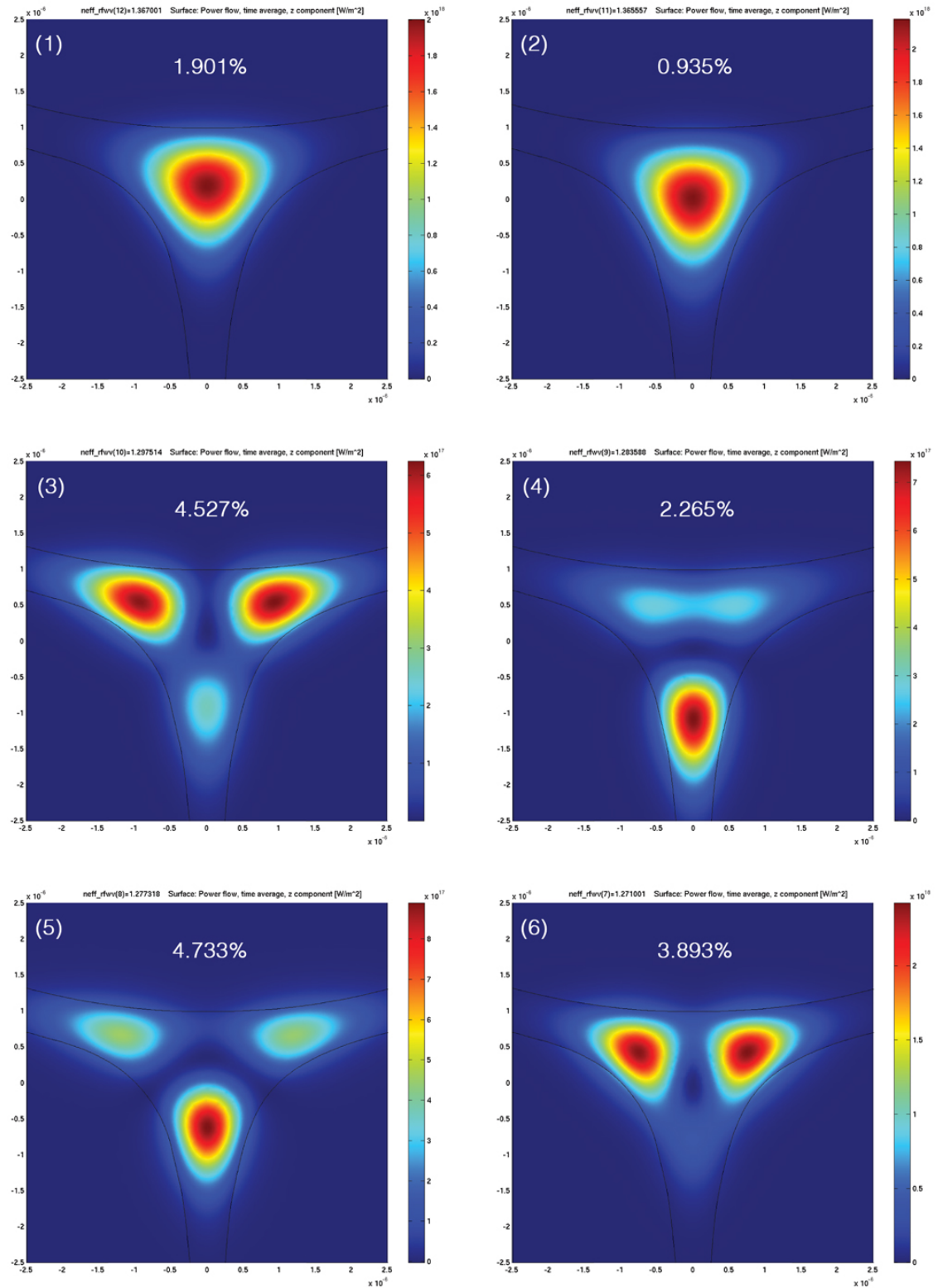
Figure 2.11 – Distribution of Poynting vector z-component of 1.875 µm effective core diameter ECF from *quarter size* SEM cross section image. (1)–(6) represent the effective refractive index order, with (1) and (2) being the fundamental mode. Percentage of power in the exposed hole region for each mode is shown.
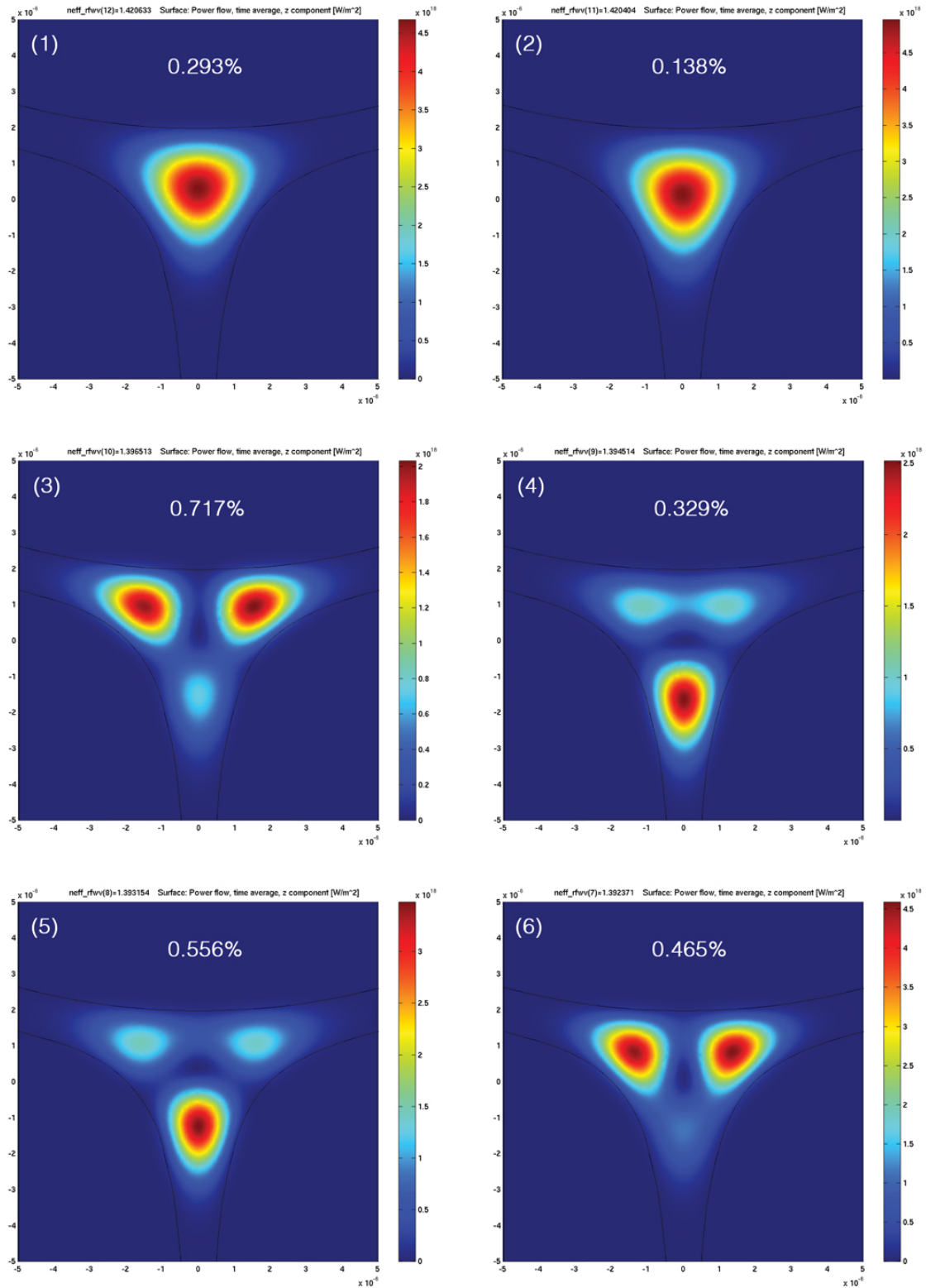
Figure 2.12 – Distribution of Poynting vector z-component of 3.75 μm effective core diameter ECF from *half size* SEM cross section image. (1)–(6) represent the effective refractive index order, with (1) and (2) being the fundamental mode. The percentage of power in the exposed hole region for each mode is shown.
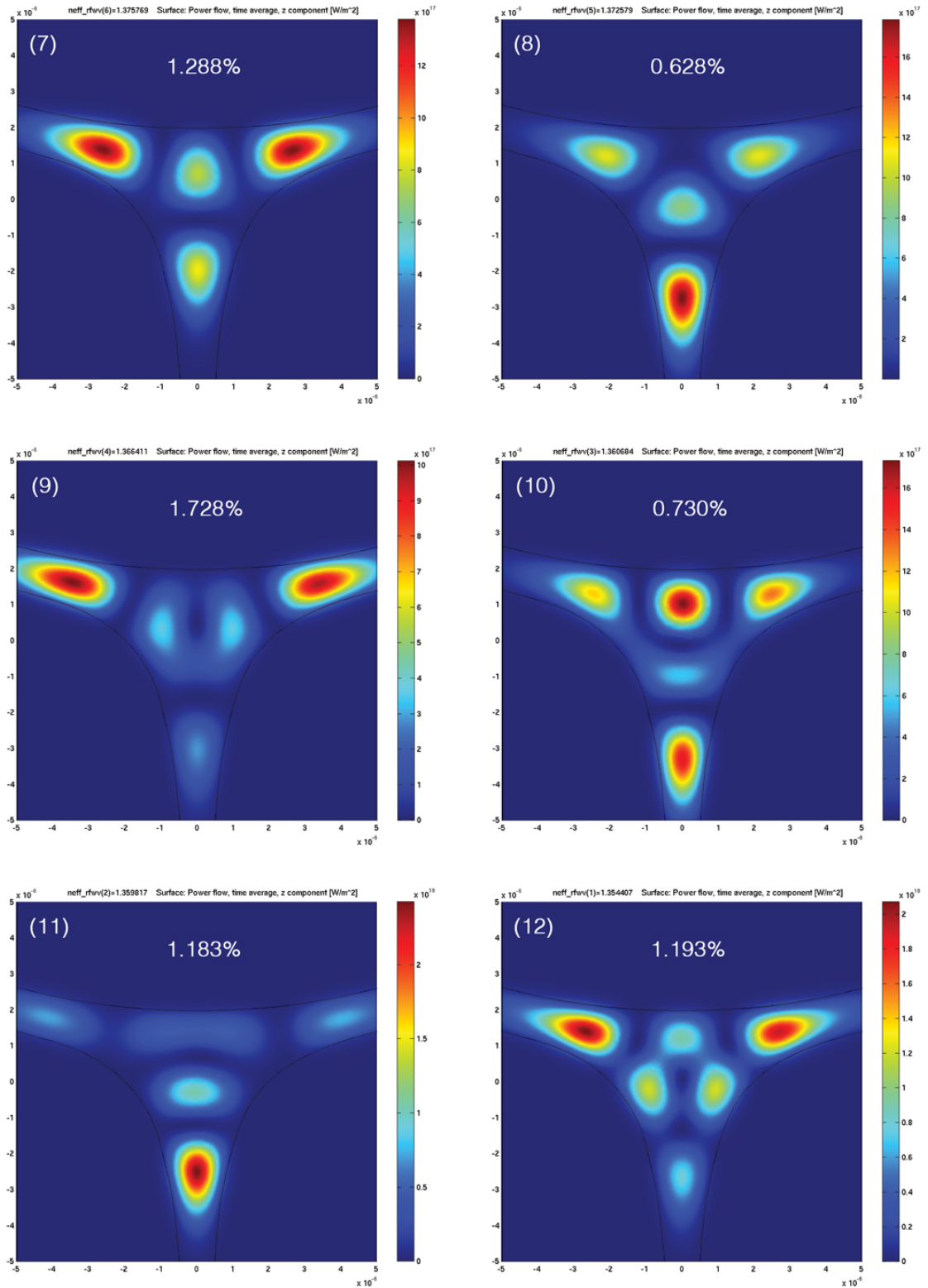
Figure 2.13 – Distribution of Poynting vector z-component of 3.75 µm effective core diameter ECF from *half size* SEM cross section image. (7)–(12) represent the effective refractive index order. The percentage of power in the exposed hole region for each mode is shown.
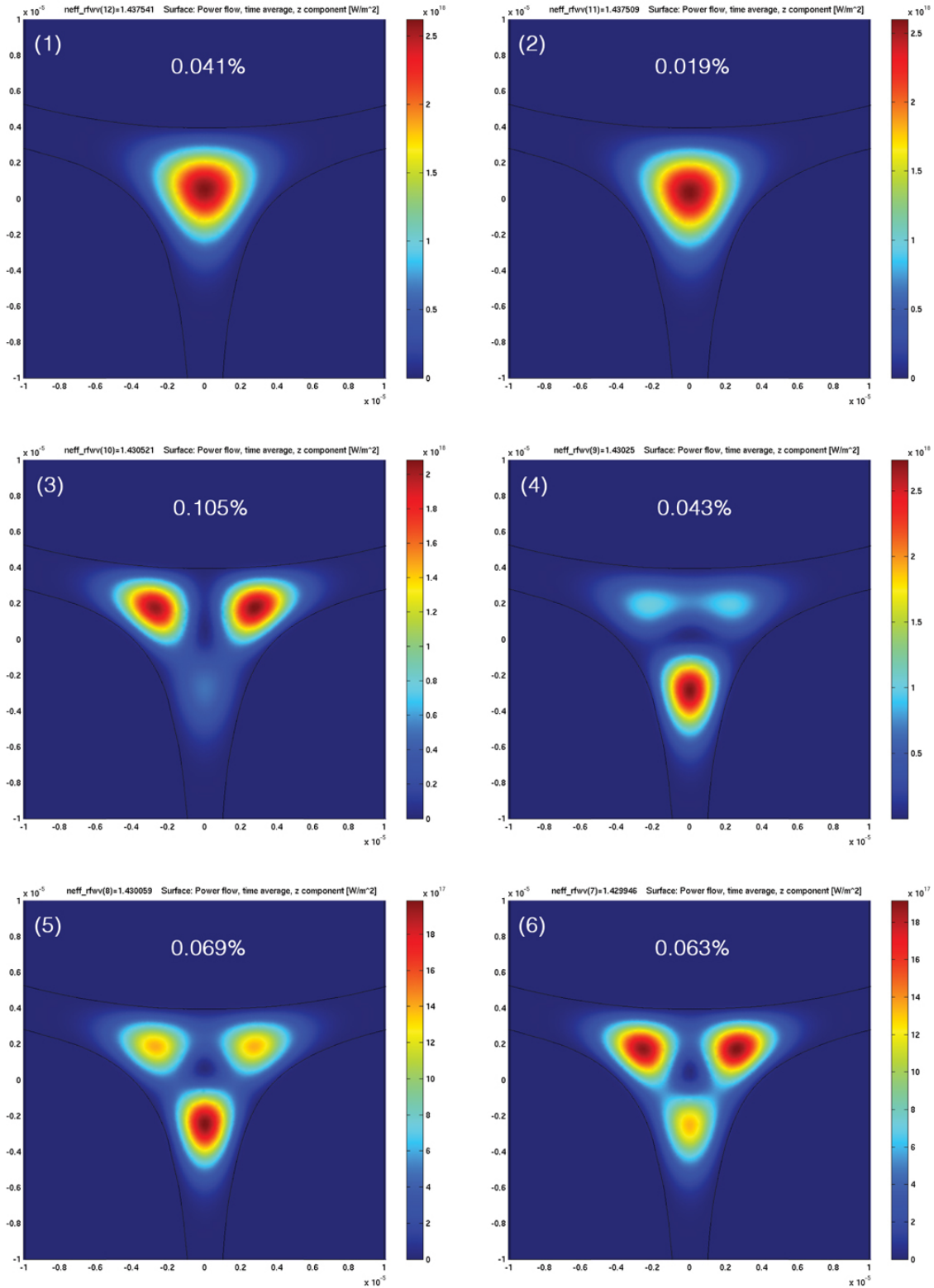
Figure 2.14 – Distribution of Poynting vector z-component of 7.5 µm effective core diameter ECF from *full size* SEM cross section image. (1)–(6) represent the effective refractive index order, with (1) and (2) being the fundamental mode. The percentage of power in the exposed hole region for each mode is shown.
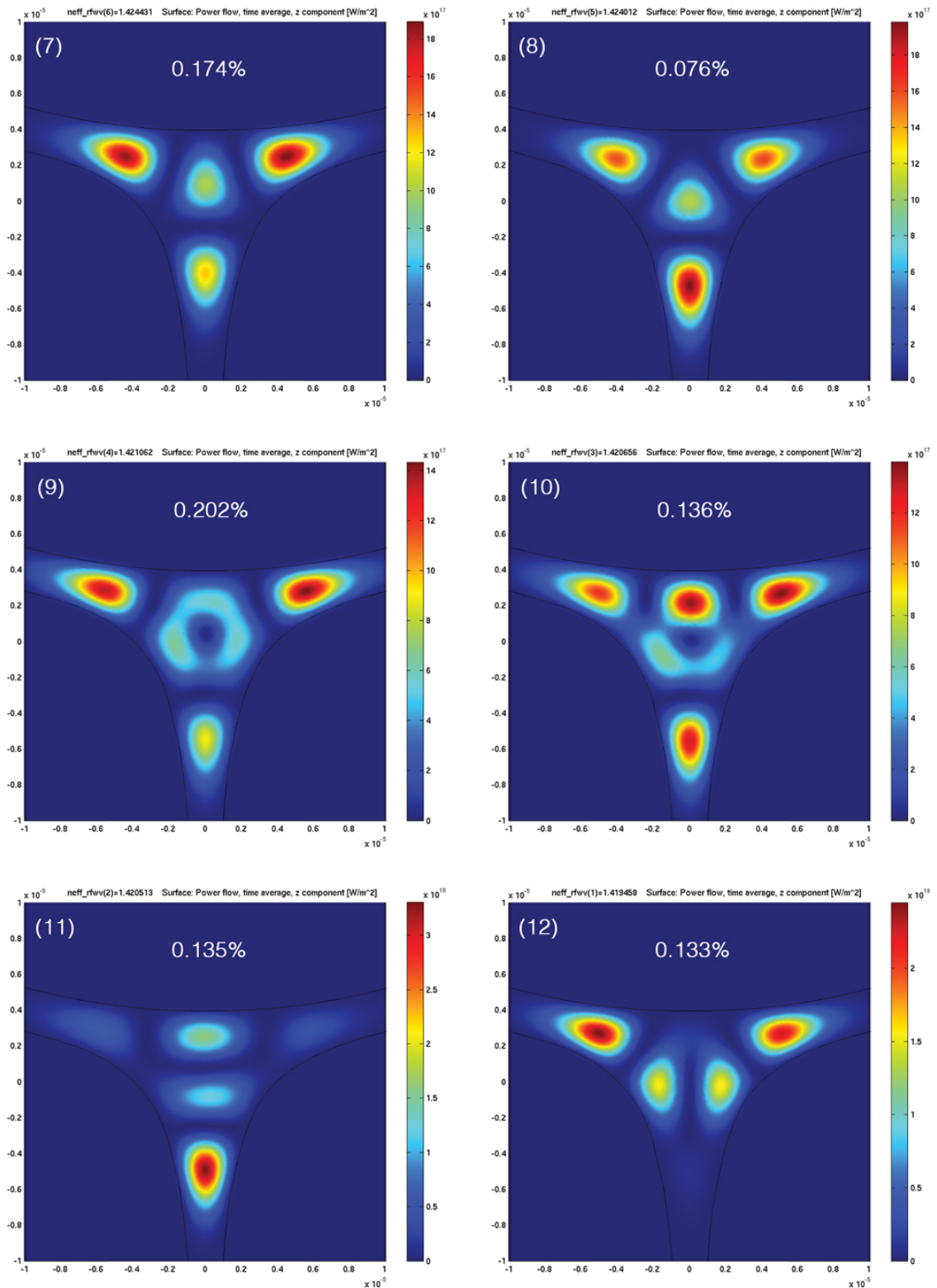
Figure 2.15 – Distribution of Poynting vector z-component of 7.5 µm effective core diameter ECF from *full size* SEM cross section image. (7)–(12) represent the effective refractive index order. The percentage of power in the exposed hole region for each mode is shown.
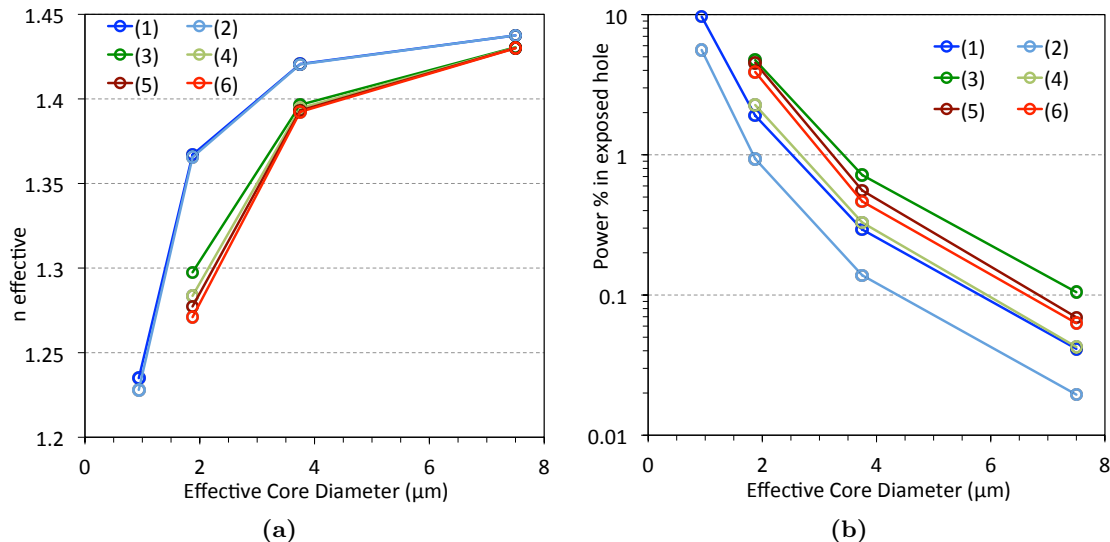
Figure 2.16 – As a function of the core diameter; (a) the effective refractive indexes plotted in order and, (b) the percentage of power in the exposed hole region plotted in effective refractive index order. (1) − (6) refers to modes.

Figure 2.16 shows a summary of how reducing the core diameter influences both the effective refractive index (n_{eff}) and the percentage of power for the first six modes. These results show that while the power percentage of the fundamental mode in the exposed hole increases as the fibre core size is reduced, for larger core diameters this power percentage increases for higher order modes. Inversely, since the mode overlap with the hole is relatively larger for higher order modes, the coupling efficiency for fluorescence capture is also increased for higher order modes. One should also keep in mind that an excitation light source with a gaussian power distribution cross section will couple mostly into the fundamental mode of the sensing fibre.

2.3.5   Summary of Target Fibre Specifications

Section 2.3 demonstrates that the best practical results for an optical fibre sensing element could be obtained by a fibre that has low loss. The loss of the fibre will impact most on the fibre's practical OTDR length. While PF improves light overlap with the sensing environment, that increased overlap can also increase loss due to increased scattering. Therefore, the initial plan was to produce an ECF that has a relatively large core diameter (∼10 µm) with relatively low loss for ∼100 m practical OTDR length (∼0.1 dB/m). Essentially, the core diameter needs to be small enough so that there is sufficient PF to excite sensing molecules at the core surface but not excessively impact the fibre's loss. This requires careful balancing. While not done as part of this project, further theoretical work could potentially be done in the future to find the optimum core geometry that has the best loss, PF, and fluorescence capture efficiency ratio.

3

Polymer MOF Fabrication

*"It is scientific only to say what is more likely and what
less likely, and not to be proving all the time the
possible and impossible."*

– Richard Feynman

This chapter shows the results associated with experiments towards producing a practical polymer ECF. As discussed in the previous chapter, polymer has a T_g low enough to make extrusion of structured preforms a possibility. The first part of this chapter shows the results of experiments related to extruding PMMA billets, followed by polymer fibre fabrication and cleaving results.

3.1   Extruding Structured Preforms

There is no reliable viscosity curve for polymer, such as for many glasses, hence it is not possible to look up exactly which settings to use for the extrusion process when working with polymer. In fact, the viscosity of PMMA varies between manufactures and production methods. Hence, systematic extrusion work with polymer to determine a viscosity curve was needed. For this purpose a procedure was developed by Ebendorff-Heidepriem *et al.* [160], which can provide the required data to plot a provisional viscosity curve for the used polymer type. In this case the material used was extruded PMMA.

This procedure for determining the PMMA viscosity makes use of the extrusion machine, which provides a detailed force profile and the extrusion machine furnace can be set to within ± 2℃. Typically the extruded diameter, D_{rod}, is larger than the die exit diameter, D_{die}, and the ratio of the diameters is used as a measure for the die swell, $B = D_{\text{rod}}/D_{\text{die}}$. The affect of temperature and ram speed on the die swell is given

as [160],

$$B = a + b \ln F = a + b \left(\ln K + \frac{E}{RT} + n \ln v_0 \right) \qquad (18)$$

where F is the force, v_0 is the ram speed, n is a measure for the degree of shear thinning, K is a constant for a specific die geometry (the die constant), T is the absolute die temperature, E is the activation energy for the flow process, R is the gas constant, and a and b are linear regression constants for die swell as a function of $\ln F$. Die swell is a useful measurement which effectively connects the die constant, temperature and ram speed. From Eq. (18) we expect that the die swell should increase as v_0 increases, where at a particular ram speed there is expected to be no die swell.

From Eq. (18) we have the relationship,

$$\ln F \quad = \quad \ln K + \frac{E}{RT} + n \ln v_0 \quad = \quad \frac{m}{T} + c \qquad (19)$$

By setting a constant ram speed, whilst stepwise varying the temperature, it is possible to plot the linear relationship between $\ln F$ and inverse temperature shown by Eq. (19) and determine the slope (m) and intercept (c) from the regression line. A typical force profile at constant temperature is shown in Fig. 3.1, which shows that time is needed for steady state applied force as the flow of material through the die reaches a steady state.
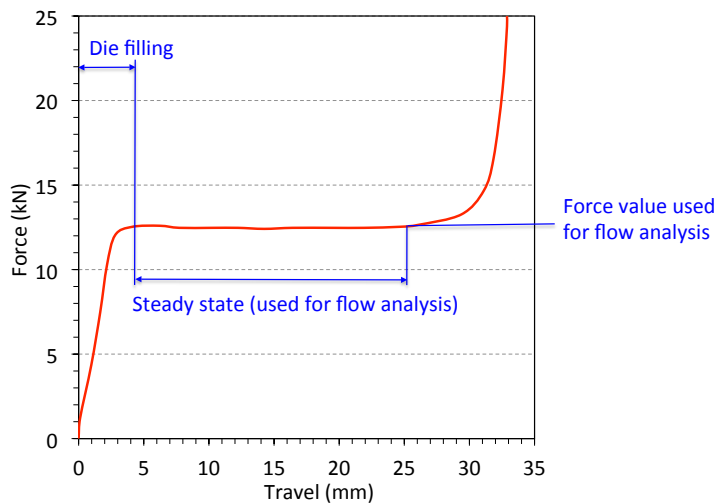
Figure 3.1 – From [142], a typical force profile of an extrusion trial that produced an F2 lead-silicate glass rod of 10 mm diameter from a 30 mm diameter billet using 531°C die temperature and 0.2 mm/min ram speed.
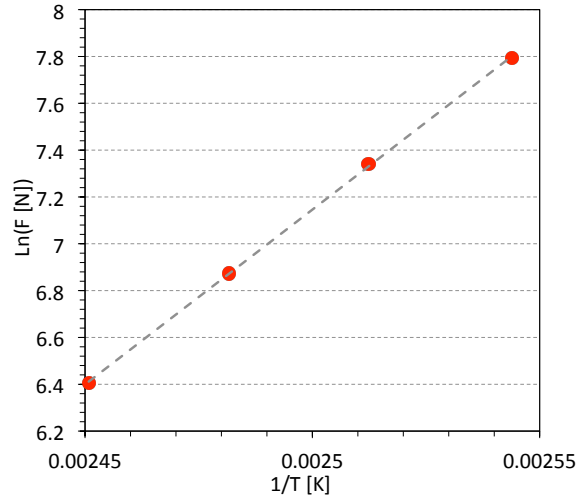
Figure 3.2 – Viscosity result of PMMA extrusion, $\ln F$ as a function of inverse temperature, by Ebendorff-Heidepriem *et al.* [160].

Figure 3.2 shows an example from Ref. [160] of a plot created using the process described above which gives,

$$\ln(F) = \frac{14566}{T[\mathrm{K}]} - 29.256 \tag{20}$$

These previous results led to polymer preforms that were visibly smooth, as shown by Fig. 3.3 although the final SCF produced from these preforms had very high loss at 10–15 dB/m at visible wavelengths. For the aims of this project it was necessary to improve on that result by producing a polymer SCF with 1–2 orders of magnitude less loss. To work out the ideal temperature for PMMA extrusion experiments described here, an initial guess for temperature was taken from from the previous work described above using Eq. (20).
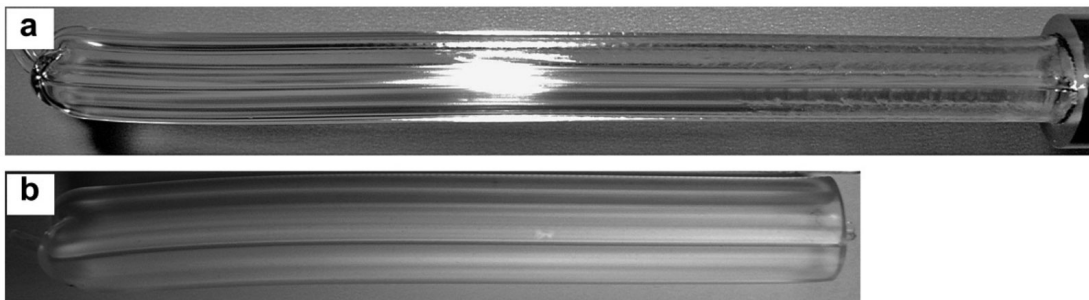
Figure 3.3 – Structured preforms extruded at (a) 175℃ and (b) 165℃ using the same billet size and PMMA material quality. The left end corresponds to the start of extrusion. The two preforms are shown at the same scale, their outer diameters are (a) 15 mm and (b) 16 mm, respectively [160]. The die size used was 15 mm.

3.2   Extrusion of Cast PMMA Material

Since the tensile strength, operating and forming temperatures are higher for clear cast PMMA relative to clear extruded PMMA, initial thoughts were that this material might have some useful benefits for MOFs, such as the possibility of producing relatively low loss fibre. Clear PMMA rods at 3 cm diameter (density of 1.18 g/cm^3) were purchased from Professional Plastics Pte. Ltd. [Singapore]. These rods were cut into billets of approximately 32 mm length, ends polished to 1200 grit, sonic cleaned with Methanol and rinsed of with demineralised water, dried/annealed at 90℃ for 135 hrs, then stored in a nitrogen filled glovebox. These billets were subsequently used for the experiments described in this section.

From the results described in Ref. [160], an initial attempt was made to produce an extruded rod using a Ø10.2 mm die with temperatures set at 160/160/210℃ (Top/Middle/Bottom). At these parameters the cast PMMA material did not extrude, with the force building up to 10 kN, at which time the experiment was aborted. The extrusion force profile is shown in Fig. 3.4. The only material that exited the die was a small amount in the shape of a flower, approximately Ø2 cm max, as shown in Fig. 3.5(a). This was found at the exit of the die, but was not attached to the bulk inside which did not look like it has taken the form of the internal die radius. This suggested that the material was highly deformed by the high pressure, but did not flow. Since the forming temperature of cast material is higher than that of extruded material,
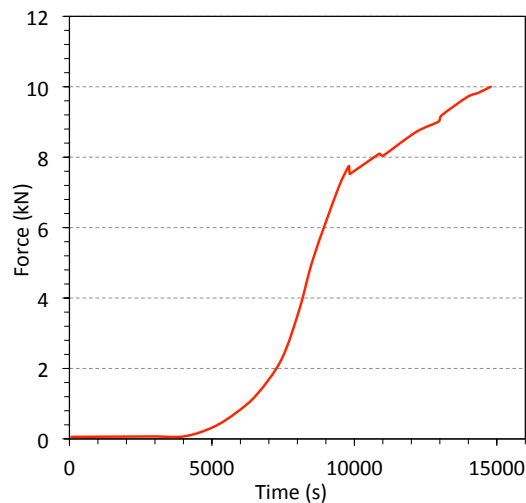
Figure 3.4 – Cast PMMA extrusion force plot as function of time at 160/160/210℃ (top/middle/bottom) set temperatures.

(a)   (b)
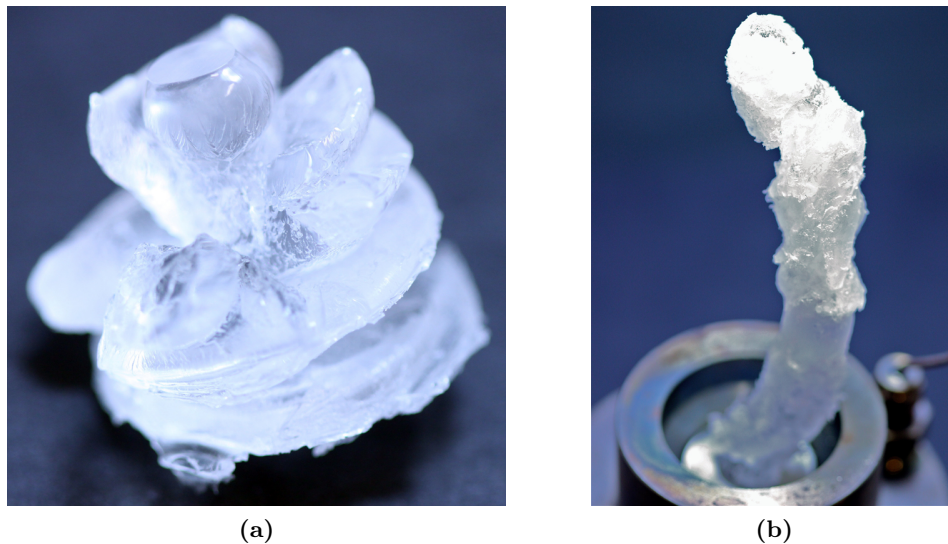
Figure 3.5 – Die exit material from cast PMMA extrusion attempts at (a) 160℃ and (b) 180℃.

it was thought the T_g of the cast material may also be higher, hence the extruding temperature which suits this cast material needed to be found.

The next step was to raise the temperature in 5℃ increments with the ram at constant feed rate and measure the force profiles. Figure 3.6 shows the force results for the PMMA extrusion at incrementally increased temperatures. The green, blue and orange curves show the results for 165/165/215℃, 170/170/220℃ and 175/175/225℃ (Top/Middle/Bottom) temperatures at 0.2 mm/min ram speed, where the experiment was aborted above 6 kN. At 180/180/230℃ and 0.2 mm/min ram speed, the force oscillated around 5.5–5 kN for about 7 mm then dropped to around 4 kN and fluctuated
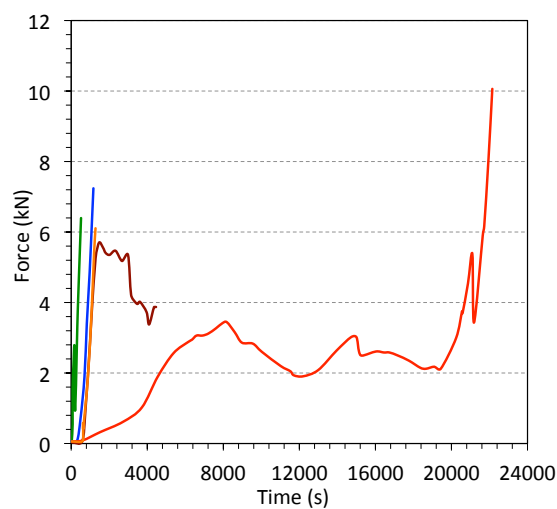
Figure 3.6 – Cast extrusion force plot as function of time at (▊ – green) 165/165/215℃, (▊ – blue) 170/170/220℃, (▊ – orange) 175/175/225℃ (top/middle/bottom) set temperatures and 0.2 mm/min ram speed. (▊ – dark red) and (▊ – red) were done at 0.2 mm/min and 0.05 mm/min respectively with set temperature at 180/180/230℃.

between 3.5–4 kN for a further 6 mm, as shown by the dark red curve in Fig. 3.6. The ram speed was then changed to 0.05 mm/min for the remainder of the billet, shown by the red curve.

The resulting extrusion was extremely rough and fractured, with the shape of a dried tree branch and bark, as shown by Fig. 3.5(b) and Figs. 3.7(a)–(b). The material at the inlet of the die also looked extremely fractured, as shown by Fig. 3.7(c). Using the force and temperature results from Fig. 3.6 and Eq. (19) as a starting point, then for $T = 180°C = 453.15K$, $\ln(F) = 2.88$. Therefore, using $F = 4$ kN at 180℃ with 0.2 mm/min from the result shown in Fig. 3.6, Eq. (19) becomes,

$$\ln(4000[\text{N}]) = 8.29405 = 2.88788 + a = \frac{14566}{453.15[\text{K}]} - 29.256 + a$$

therefore for the cast PMMA material,

$$\ln(F) = 14566\frac{1}{T[\text{K}]} - 23.8498 \tag{21}$$

For $F = 1$ kN, Eq. (21) predicts that $T = 200°C$. Hence, a series five temperatures at 5℃ increments in the range of 190–210℃ was chosen for the next extrusion experiment. A program for the extrusion machine was created to extrude a 70 mm long billet of the new PMMA material in five even extrusion lengths, where the temperature was allowed

| (a) | (b) | (c) |
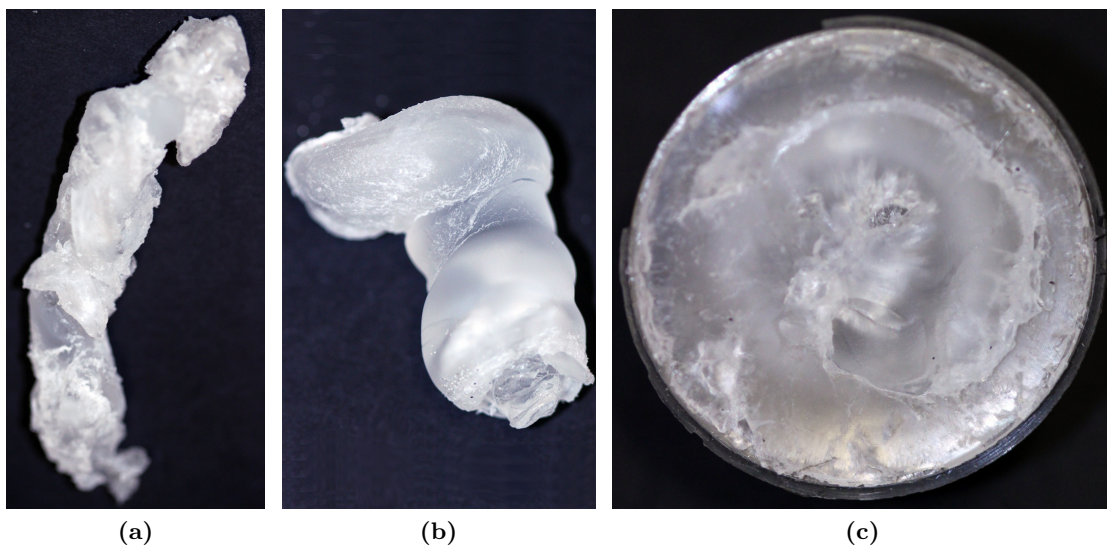
Figure 3.7 – ((a) and (b)) Die exit material and (c) die entry material from cast PMMA extrusion attempt at 180℃.

to stabilise for 30 mins between each step. During the stabilisation the ram was held at a constant force of 50 N.

The blue line in Fig. 3.8(a) shows the force results, with the temperature for each step in the series shown in orange. The 190℃ result did not show any steady state of the force curve, which might have been due to the die filling. Also, something seemed to have gone wrong with the result at 210℃, for which the cause was unknown. At the other three temperatures, 195–205℃, the force curve increases to a maximum then begins to level off with some fluctuations. For these three temperatures, the mean force across the levelling off area was calculated, as shown in red. The viscosity curve using these three temperatures is shown in Fig. 3.8(b). This viscosity curve showed that for a target force of 1 kN, 235℃ would be required, from the formula,

$$\ln(F) = \frac{6117.1}{T[\text{K}]} - 5.1211 \tag{22}$$

As was the case with the 160–180℃ experiment, the extruded material from the 190–210℃ experiments was also badly deformed and bark like in appearance. There was some material left in the die, shown in Fig. 3.9(a), which was dissected in half and the cross sectional faces polished, as shown in Fig. 3.9(b). Figure 3.9(a) shows that most of the material had expanded to fill out the sleeve, however there are still some areas which could expand further. In Fig. 3.9(b) it is possible to see why the extruded
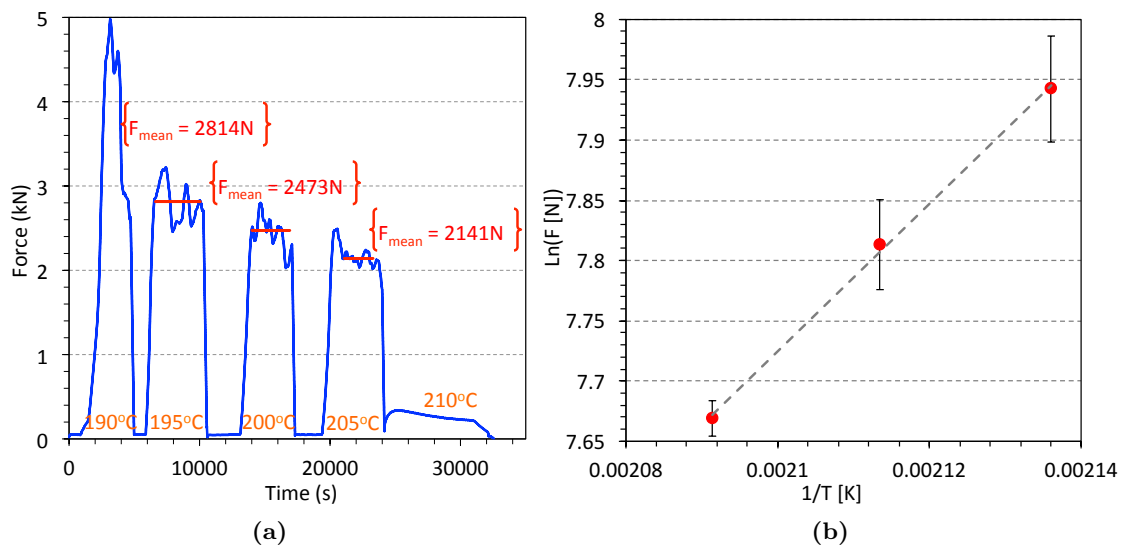
Figure 3.8 – (a) Series of force curves and (b) viscosity result ($\ln F$) as a function of inverse temperature for cast PMMA extrusion from 190–210℃ at 0.2 mm/min extrusion speed.
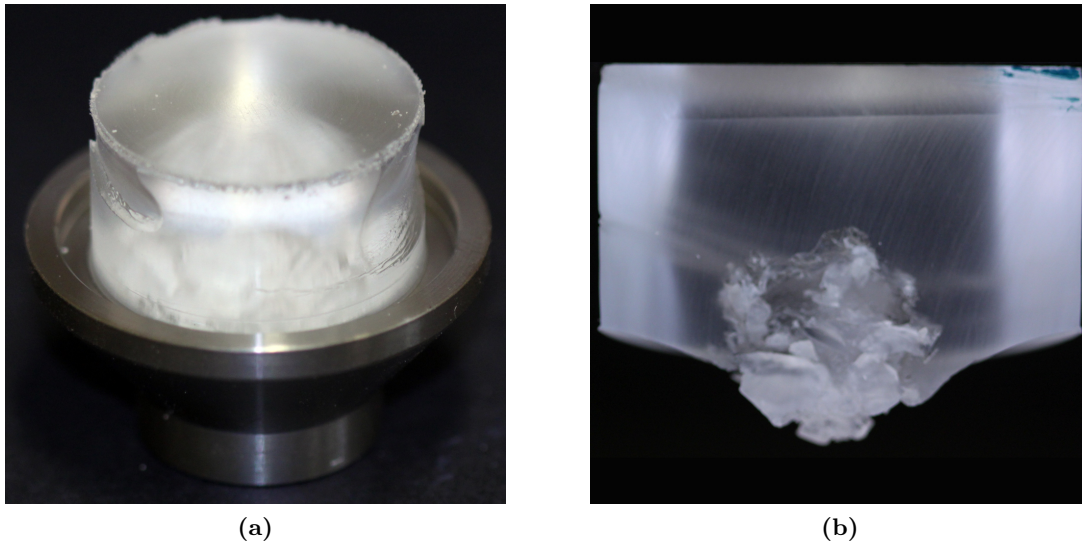
Figure 3.9 – (a) Remaining PMMA material in extrusion die. (b) Cross section of the material from the extrusion die.

material looks so rough, since the polymer is fracturing in the area around the Ø10 mm die outlet, through which it is being forced.

The viscosity experiment was done again with the temperature range of 225–245℃, the results for which are in Fig. 3.10(a), which showed that a 1 kN was generated at around 245℃ instead of 235℃ as expected. It was also found that the program needed to be changed to hold the ram at constant position instead of constant pressure, since the ram was being pushed back up 10–12 mm at the holding force of 50 N. This is probably also the reason that the previous result at 210℃ failed (Fig. 3.8). The viscosity curve
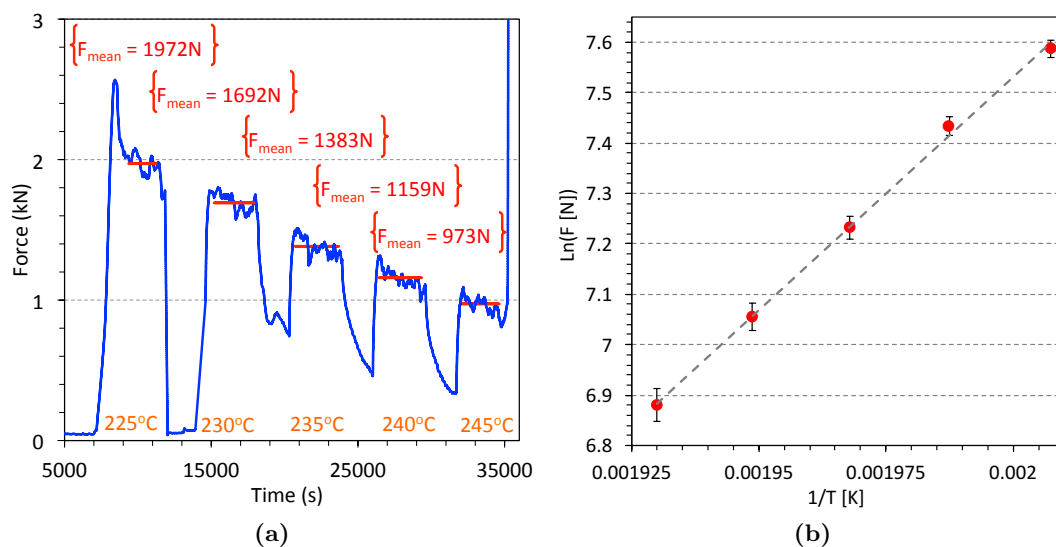
Figure 3.10 – (a) Series of force curves and (b) viscosity result (ln(F)) as a function of inverse temperature for cast PMMA extrusion from 225–245℃ at 0.2 mm/min extrusion speed.
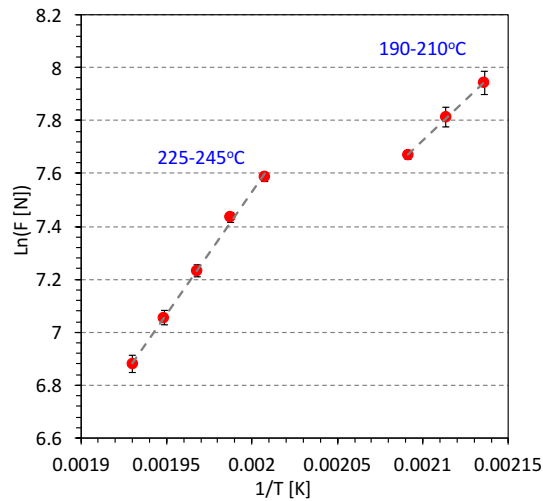
Figure 3.11 – Combined plot of viscosity curves from Figs. 3.8 and 3.10.

from these results is shown in Fig. 3.10(b) which indicates that 244℃ is needed for a
1 kN extruding force at the 0.2 mm/min rate, given by,

$$\ln(F) = \frac{9245}{T[\text{K}]} - 10.959 \tag{23}$$

The viscosity curve for the 225–245℃ experiment, together with the viscosity curve for
the 195–205℃ experiment is shown in Fig. 3.11. This difference in the viscosity curves
of the two experiments was not expected, since there should be a linear correlation
between all of these points. The extruded material from the 225–245℃ experiments was
also badly deformed and bark like in appearance, as shown in Fig. 3.12. One possible
reason why the extrusion viscosity curves from the two experiments were different could
be related to the fracturing occurring in the area around the Ø10 mm die outlet, through
which it is being forced, as shown in Fig. 3.9.

Figure 3.12 – Die exit material from cast PMMA extrusion force flow analysis (225–245℃).

3.2.1   Deformation Experiments of Cast PMMA Material

To provide some additional understanding towards the cast PMMA extrusion temperature, softening experiments were performed at a range of temperatures to determine at which temperature the polymer shows deformation. Five millimetre thick coins of Ø5cm cast PMMA billet were used with a support on two sides, leaving a 38 mm spacing so that the material could sag in the centre (shown in Fig. 3.13(a)). Since the viscosity curve from the extrusion experiment showed that the temperature required should be 235℃, and the target of 1 kN force was reached at 245℃, the starting temperature of 240℃ for the softening experiment was selected. At this temperature, deflection of the polymer coin along with considerable blistering at the material surfaces was observed, as shown in Fig. 3.13(h). The amount of deflection was still much less than expected for an extrusion temperature, therefore the temperature was increased to 250℃, where the deflection increased (shown in Fig. 3.13(i)) and the blistering was much worse. This surface blistering, as shown in Fig. 3.14, seemed to be the limiting factor which needed to be better understood, so another experiment at lower temperatures was restarted.

A new 5mm thick piece of material was setup as before, and the softening experiment was started from 165℃ and increased in 10℃ increments, as shown in Fig. 3.13. These observations showed that there was only a slight deflection for this temperature range, although no blistering was visible during the experiment. The material was then left in the furnace at 200℃ for 1.5 hrs, at which time the material had again blistered at

(a) 25℃   **(b)** 165℃   **(c)** 175℃

(d) 185℃   **(e)** 195℃   **(f)** 205℃

(g) 215℃   **(h)** 240℃   **(i)** 250℃
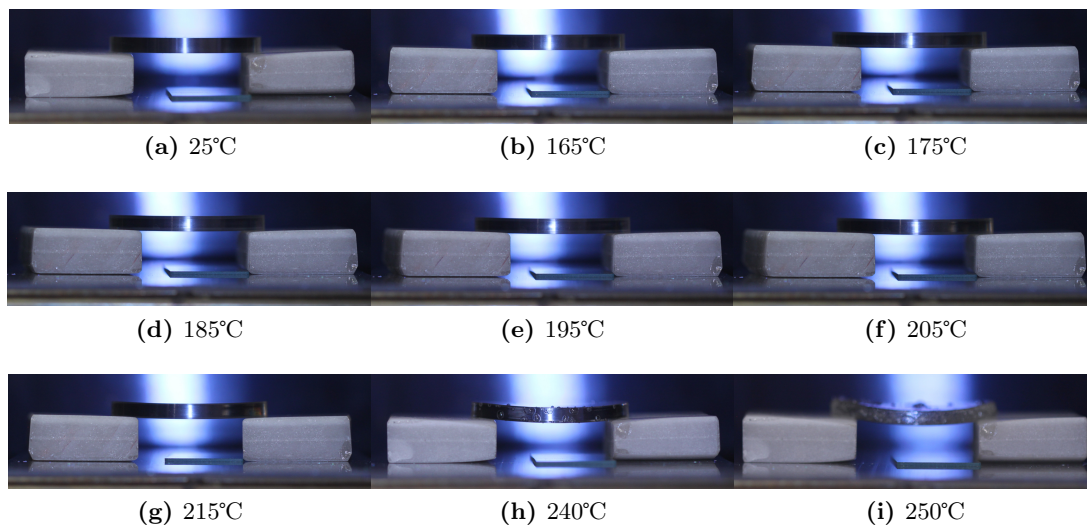
Figure 3.13 – Softening experiment of cast PMMA material.

Figure 3.14 – Blistering of PMMA at 250℃.

the surface. The reason for the blistering is not known at this stage, although it seems that something in the material was evaporating and causing thin layers to separate from the bulk material at the surface. This might be due to the material not being dried properly (at 95℃ for 96 hrs) before storage in the nitrogen filled glovebox. Hence, subsequent experiments were performed to find a temperature $> 95℃$ at which the material could be dried without blistering. It was found that this cast PMMA material had surface blistering after 16 hrs at 175℃, however did not show any signs of surface blistering at 150℃. After leaving the 5 mm thick coin to dry for 24 hrs at 150℃, the temperature was raised back up to 175℃, where no signs of blistering was noticed after 1hr, however after 16hrs the material was again significantly surface blistered.

While there might be a way to extrude cast PMMA, these experiments were not continued as part of this project as the challenges involved outweighed the possible benefit towards the project aims. The next step in understanding what might be causing the surface blistering is to do differential scanning calorimetry (DSC) measurements using the simultaneous thermal analyser (STA) to determine the materials thermal properties and measure the amount of mass loss with temperature. A simultaneous X-ray photoelectron spectrometry (XPS) and DSC or a residual gas analyser (RGA) could be used to examine the composition of the gases leaving the material when it is heated to determine what might be causing the blistering. Another possible approach to producing cast PMMA SCF and ECFs is to drill the polymer billet rather than using extrusion techniques [61].

3.3   Extrusion of Extruded PMMA material

3.3.1   Thick Wall Extrusion

As described in Sec. 2.1, the typical method for producing relatively smaller core MOFs is to use a cane-in-jacket two step process. To attempt to make an extrusion that could be used for drawing relatively small core SCFs in one step, removing the need to produce a cane, a so called 'thick wall' extrusion die was fabricated as shown in Fig. 3.15. Experiments were conducted to attempt to produce SCF preforms with the thick wall extrusion die using extruded PMMA billets.

A Ø5 cm extruded PMMA billet taken from the storage cabinet and dried at 95℃ for 65 hrs prior to the extrusion process. With N_1, D_1, and L_1 being the number, diameter and length of the die holes respectively, the die constant described in Eq. (18) was calculated as [142],

$$K = \frac{128L_1}{\pi N_1 D_1^4} \text{ where } K = 0.29, \text{ with}$$

$$N_1 = 570, \ D_1 = 1.0 \text{ mm}, \ L_1 = 4 \text{ mm} \tag{24}$$

which is similar to two step process dies; i.e. 10/2 jacket ($K = 0.2$) or SCF thin wall

(a)

(b)

Figure 3.15 – Thick wall suspended-core extrusion die.

($K = 0.4$) extrusion dies [142]. Hence, since a feed rate of 0.05 mm/min was used in Sec. 3.2 for the jacket or thin wall extrusions from Ø3 cm billets, 0.018 mm/min was chosen for the Ø5 cm billet being used for the thick wall die. Based on other polymer extrusion work [160] it was decided to start with top and mid zone temperatures at 160℃ and the bottom zone set to 210℃.

The extrusion produced with this thick wall die was straight, however the outside surface finish was extremely rough with a fine bark type finish, as shown in Fig. 3.16. Figure 3.16(b) shows the end, where the first 16 mm had a smooth outer surface with a great deal of bubbles trapped within the fused thick wall. After this initial smooth section, the outside face of the extrusion wall was rough, as can be seen in Fig. 3.16(a).

A cross section was cut 38 mm from the end, which is shown in Figs. 3.17(a)–(b), were a plume of gas bubbles were visible close to the extrusion outside surface. Several more sections were cut and it was found that Fig. 3.17 is typical with respect to a steady stream of bubbles which follows the extrusion length within the first few millimetres of the surface. The core, shown in Fig. 3.17(b), started to form at 38 mm from the end and looked continuous for the remainder of the extrusion length, although the struts had a slight rough speckled appearance.

The section closer to the end of the extrusion was further examined, where

(a)   (b)
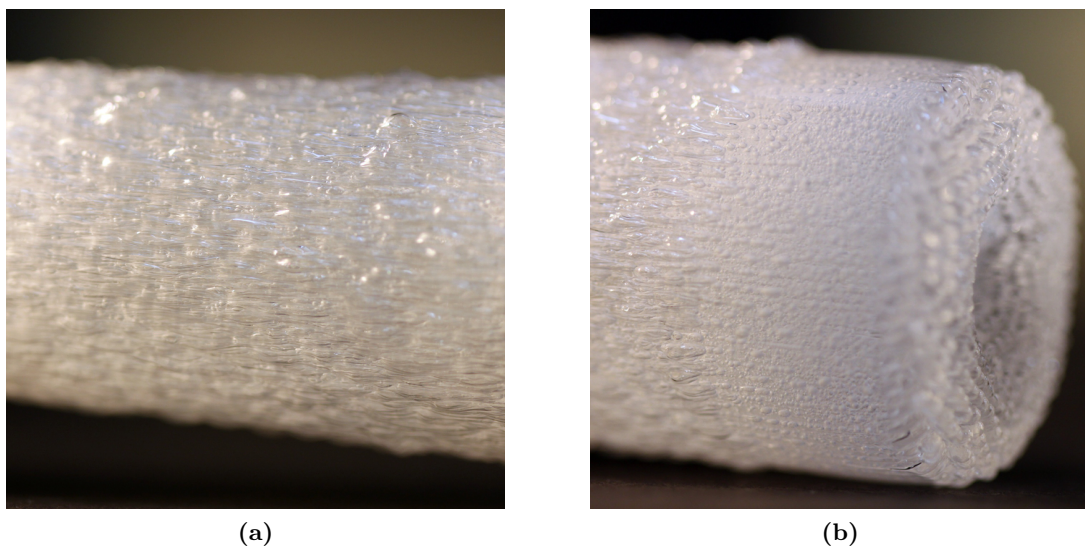
Figure 3.16 – Images of the outer surface finish of the PMMA thick wall extrusion (a) side and (b) start.
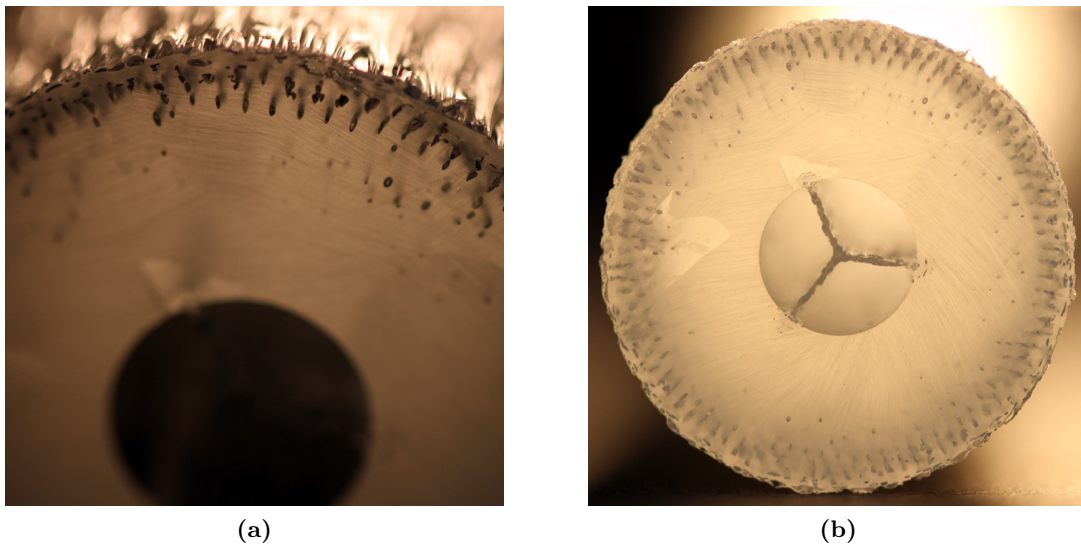
Figure 3.17 – Cross sections of thick wall extrusion showing (a) bubbles under surface and (b) the well formed core.

Fig. 3.18(a) shows a close-up. This closeup shows the bubbles are starting at the outside edge sections of the die. The majority of these bubbles are going to the surface and the remainder remained in the region close to the surface, as was seen in the section closer to the start of the extrusion (Fig. 3.17).

To better see what was going on at the die exit, a section of the material as seen in Fig. 3.18(a) was cut down to the die. It can be seen from Fig. 3.18(b) that the majority of the bubbles originated from the outside edge of the die and swirl towards the core, and a continuous thinning line also formed within the material at the remaining die
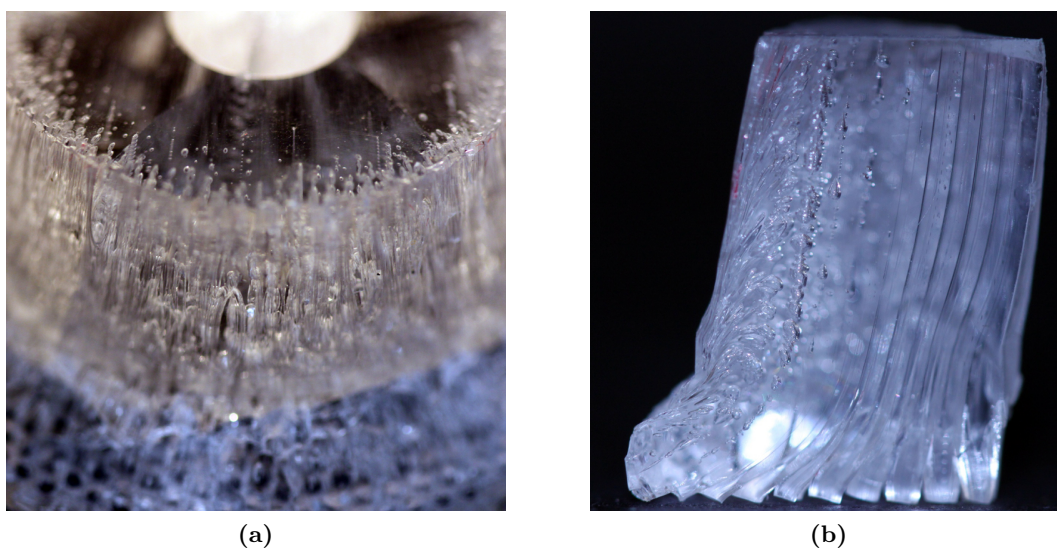
Figure 3.18 – Thick wall extruded material close to die exit (a) cross section and (b) longitudinal section.

(a)   (b)
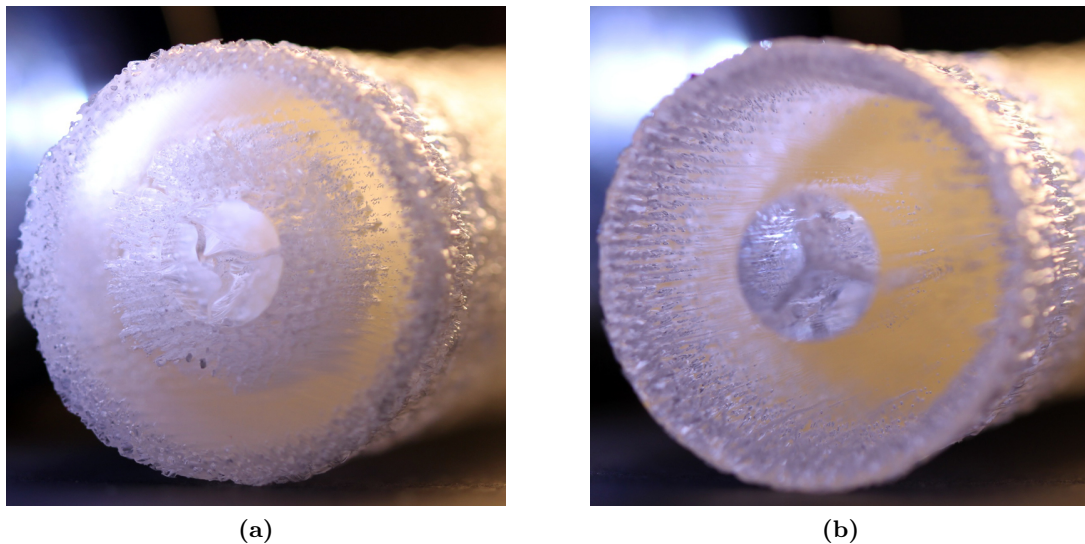
Figure 3.19 – Cross sections of thick wall extrusion showing areas (a) with gas plume close to core area and (b) without gas plume.

holes. When looking through the extrusion with backlight, there was an appearance of darker and lighter sections periodically alternating along its length, although the distances between these areas was not uniform. A section taken through the middle of one of these dark areas, as shown in Fig. 3.19(a), revealed a plume of bubbles surrounding the core. Another section through one of the lighter areas, as shown in Fig. 3.19(b), showed no bubbles in this area.

Figure 3.20 shows a plot of the force as a function of travel for the thick wall extrusion. The peak at the start is unusual, and further work is needed to better understand what occurs as the material flows through the die. This could be done in the future by comparing the extrusion cross section profile with the force plot in the travel domain.
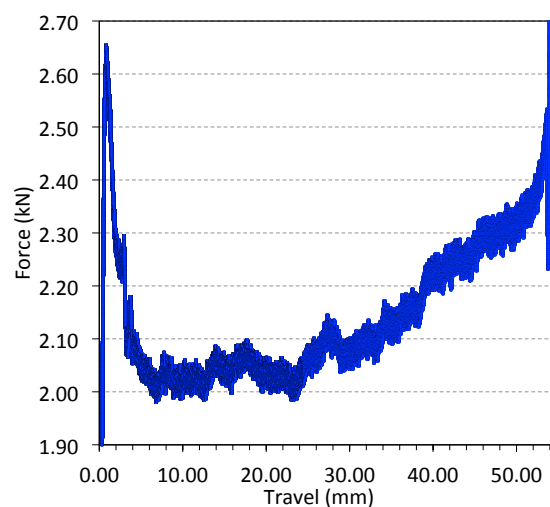
Figure 3.20 – Thick wall extrusion force plot as function of travel.

3.3.2   Thin Wall Extrusion

To create an initial practical PMMA fibre for characterisation purposes, a structured SCF thin wall extrusion and 10/2 jacket (i.e. outer diameter measures $\sim$ Ø10 mm and the inner diameter measures $\sim$ Ø2 mm) were produced for drawing down to fibre using the cane-in-jacket method. The material used for both the SCF thin wall and sleeve extrusions was Ø3 cm billet taken from the nitrogen glovebox. In the case of the SCF thin wall extrusion, the temperatures where set at 170℃ for the top and mid zones and at 220℃ for the bottom zone, whereas for the sleeve the temperatures were set at 165℃ for the top and mid zones and at 215℃ for the bottom zone. These temperatures were previously successful for the production of PMMA SCF in 2007 [160].

Figure 3.21 shows the profiles obtained from the extrusions, where the outside and inside faces of the SCF thin wall extrusion was rough although the core looked to have a smooth outer surface. Also, the struts looked straight with a clear smooth finish, without any buckling. Subsequently, the outside surface of the SCF thin wall extrusion was polished prior to caning, which was found to work well for the bare fibre extrusion previously produced and drawn to fibre. Similarly, the surface finish of the sleeve was rough, and gas bubbles close to the inner diameter were noticed along the length of the extrusion, as shown in Fig. 3.22. Comparing this extrusion result, shown in Fig. 3.23,

| (a) | (b) |
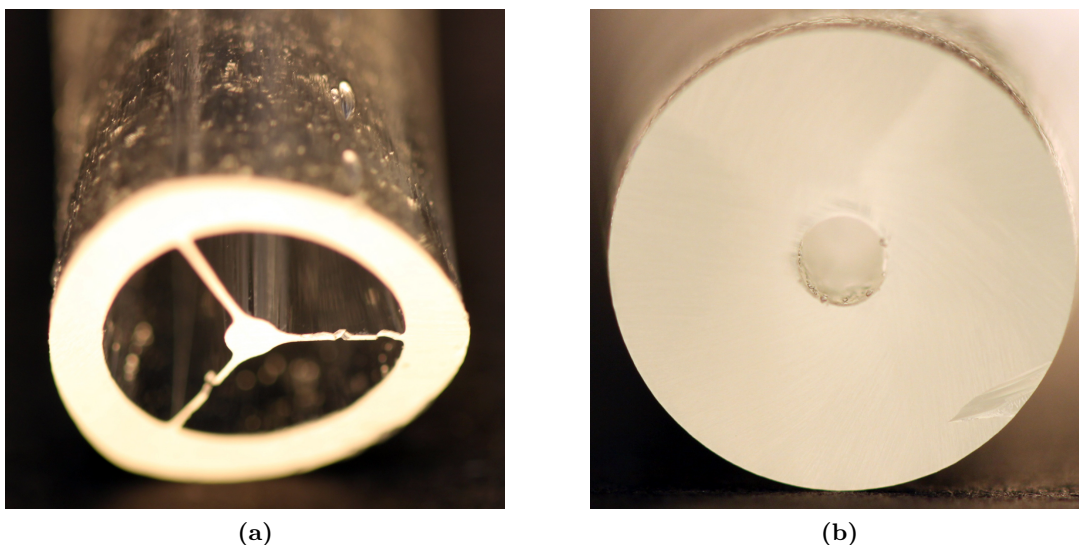
Figure 3.21 – (a) PMMA suspended-core thin wall extrusion profile and surface finish; and (b) PMMA Sleeve produced using a 10/2 (ratio) die. The outer diameter measures $\sim$ Ø10 mm and the inner diameter measures $\sim$ Ø2 mm.
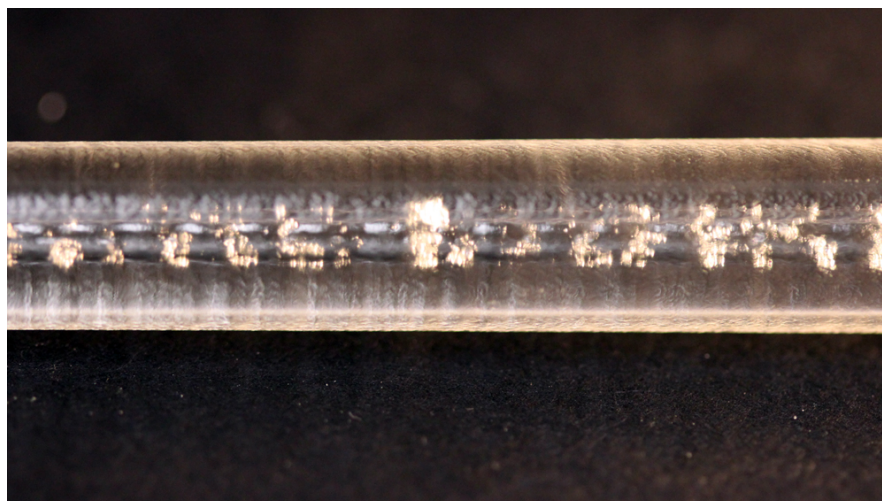
Figure 3.22 – The 10/2 PMMA sleeve with air bubbles along the length, near the inner diameter.

with the work published in 2007 (Fig. 3.3), there was additional roughness associated with this recent attempt and the bubbling effect in the sleeve was unexpected. This result also had much more tapering than the results obtained in 2007.

3.3.3 PMMA Suspended-Core MOF (SCF)

Experiments were done to better understand the draw tower temperature profile related to the polymer caning and fibre draw process, which the viscosity of the polymer depends on. This is because drawing tower furnaces do not exhibit a constant temperature but an axial temperature gradient/profile [161, 162]. This means that the polymer viscosity varies with the temperature gradient/profile within the furnace [163], preform size and the feed rate. Figure 3.24(a) shows an example of the temperature profile in the draw tower furnace used for the polymer fibre work. This temperature profiling was done for soft glass, and so is at a higher temperature than is used for polymer fibre drawing.
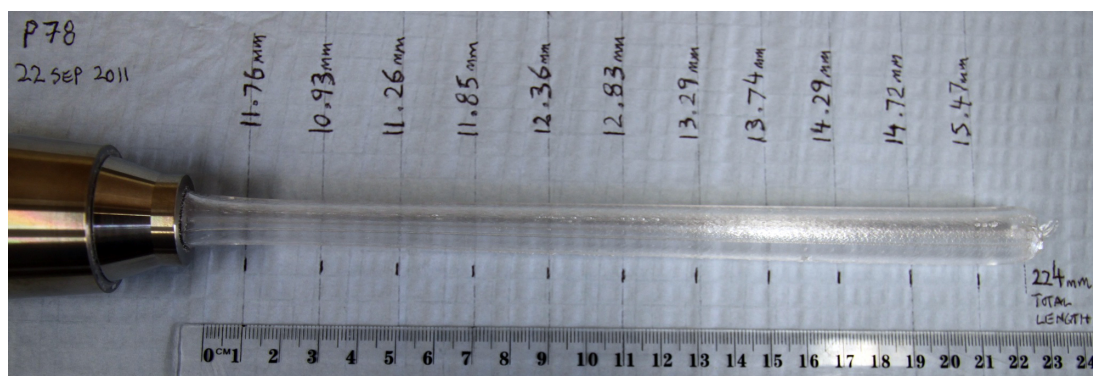
Figure 3.23 – PMMA thin wall extrusion length and diameter measurements.
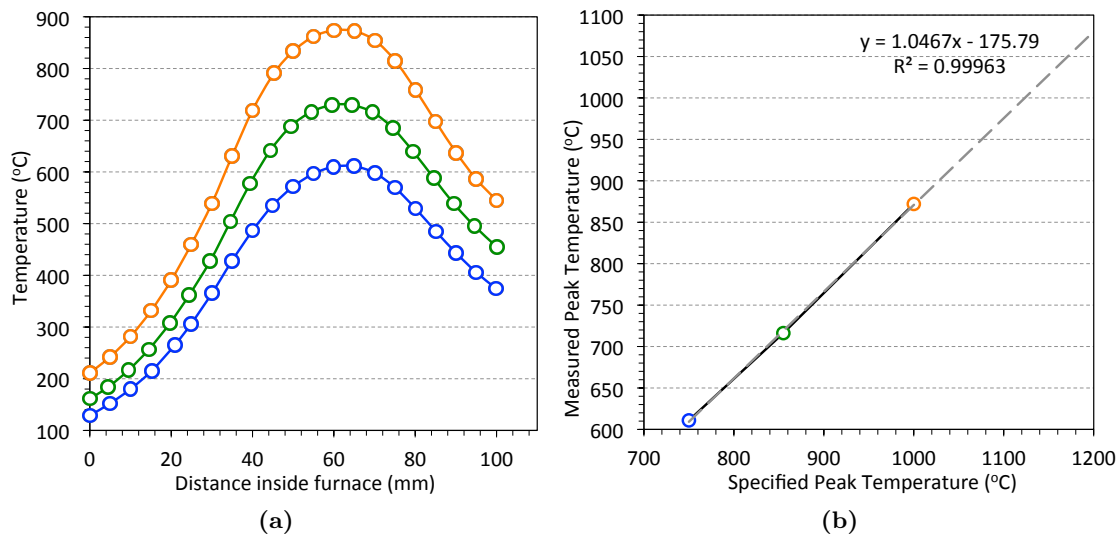
Figure 3.24 – (a) Temperature profiles measured inside soft glass tower furnace at (▮ – blue) 750℃, (▮ – green) 855℃, and (▮ – orange) 1000℃ furnace temperatures. (b) Plot and linear fit of peak measured temperatures as a function of set temperatures. The distance inside furnace was measured from the top of the furnace outer casing.

From these profiles, the peak temperatures are shown in Fig. 3.24(b) as a function of the temperature measured by the draw tower temperature sensors which shows that the actual temperature of the polymer would be lower than the measured temperature on the tower, where the offset is linear.

The first step towards producing the polymer SCF was to cane the thin wall extrusion so that the structure could be placed inside the jacket to draw down to fibre. The result of the cane produced is shown in Fig. 3.25. The burrs visible on the inside of the structure are only at the surface, and arise from the polishing technique used to create a plane
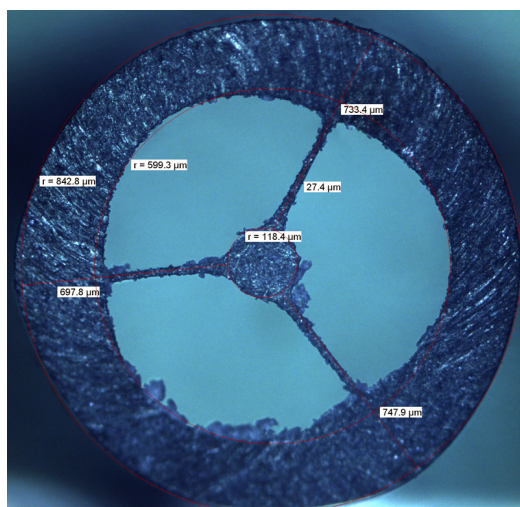
Figure 3.25 – PMMA cane from thin wall preform.

surface for the image. The final cane geometry remained approximately the same as the thin wall extrusion, although reduced to Ø1.7 mm which could be inserted into the jacket. The PMMA SCF was drawn to Ø340–400 µm. Images of the final fibre produced are shown in the next section which discussed cleaving experiments.

3.4   PMMA Fibre Cleaving

One of the main challenges with respect to polymer fibres is being able to produce a quality cleave with reproducibility. Quality cleaves are important to check the fibre structure during drawing, as well as being able to couple light into the core for characterisation measurements and sensing applications. In the case of glass, the crack cleaving method is used since the glass is brittle. Polymer is different to glass since it is elastic and malleable, stretching under load, which means it needs to be cut. The published method which is shown to have the best cleaving results for POFs is hot cleaving [164]. It has also been shown [165] that a UV laser cleaving method produces excellent results when used with porous polymer fibre structures. Another method which has been discussed but discounted in several papers, is to cool the fibre before cleaving. Therefore, hot, laser, and cold cleaving methods where tried and compared to find a suitable method for the PMMA SCF produced.

Figure 3.26 – Hot cleave setup. The hotplate was used to heat the lower teflon block and blade, and the upper teflon block was preheated in the oven.

3.4.1   Polymer Hot Cleaving

The initial setup for the hot cleaving attempt is shown in Fig. 3.26, where a standard V-sharpened razor blade was used. A hot plate was used to heat the lower teflon block and blade, and the upper teflon block was preheated in an oven. The fibre was placed in the slot of heated teflon block, and left for 1 min so the fibre reached the same temperature as the blocks before slowly moving blade down through fibre. Attempts were made at cleaving using this setup at both ∼80℃ and ∼100℃, the results for which are shown by Fig. 3.27(a) and Fig. 3.27(b) respectively. These results show that the overall cleave quality achieved using this method was extremely poor, with a great deal of distortion to the fibre geometry. An increase in temperature (120℃) was tried, the result of which is shown in Fig. 3.28. While this result was better, there was still a lot of distortion of the fibre geometry.

The distortion of the fibre suggested that the material was being squashed by the blade, so the blade was chisel sharpened at a small angle to try to avoid distortion to the fibre geometry. This new blade is shown in Fig. 3.29(a). This chisel sharpened blade design did produce better results, where the overall fibre geometry is reasonably well maintained, shown in Fig. 3.29(b). However, when the fibre core area was examined with transmission, shown in Fig. 3.29(c), it is evident that the core area is multifaceted

(a)   (b)
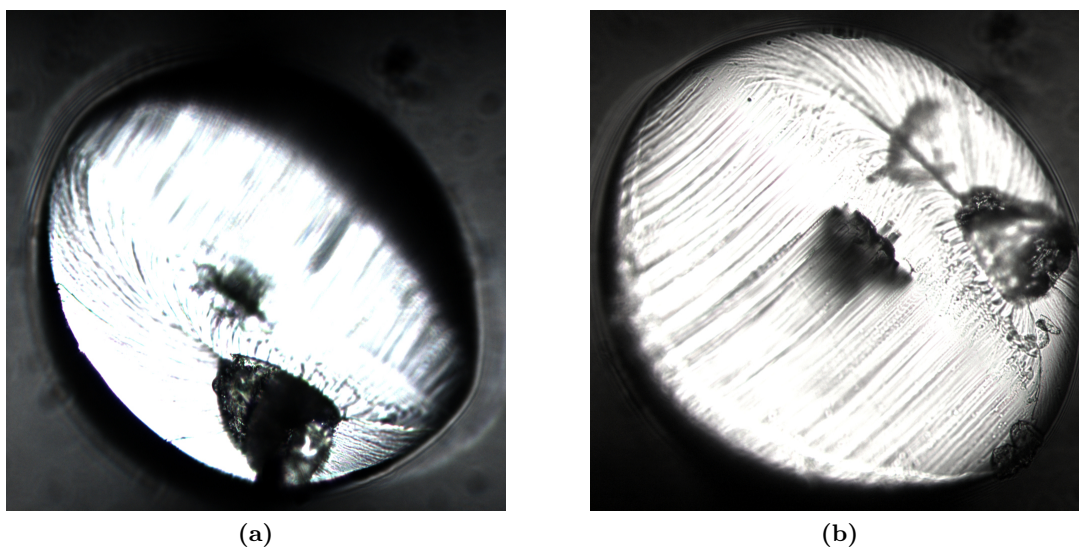
Figure 3.27 – Hot cleaves using V-ground sharpened blade, where; (a) At ∼80℃, fibre placed in slot of teflon block, waited 1 min before slowly moving blade down through fibre; and (b) the same method tried at ∼100℃.

(a)   (b)
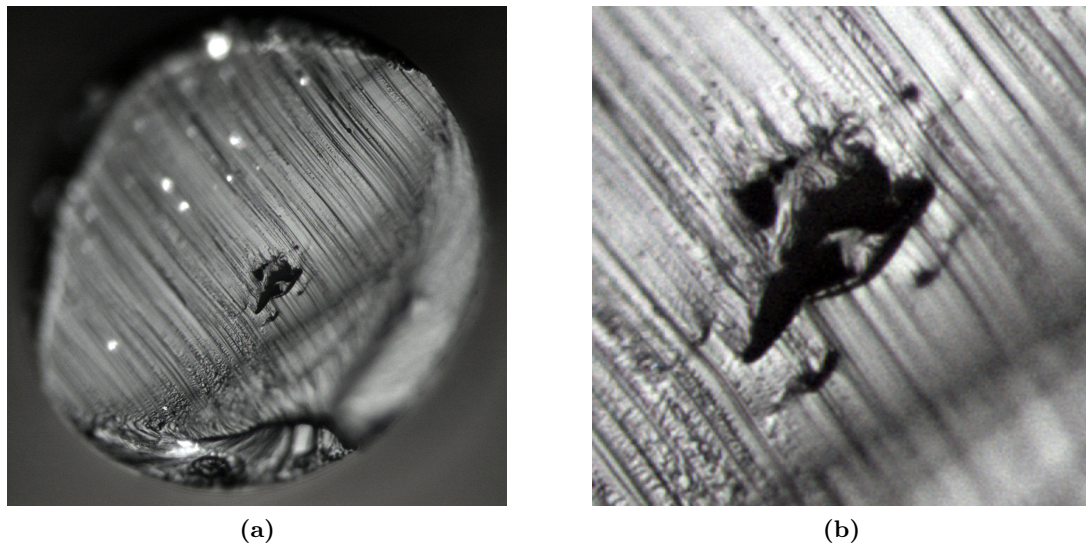
Figure 3.28 – Hot cleave at 120℃ using V-ground sharpened blade, where (a) shows the overall result and (b) shows a closeup of the fibre core area.

rather than the required single plane for optimum coupling and transmission conditions. This multifaceted cleave at the core, will cause the light to scatter and therefore reduce coupling efficiency.

This result using a chisel sharpened blade suggested that the best quality in cleaving PMMA fibre might be achieved by hot cleaving with a extremely small angle chisel sharpened blade, however the tip of steel blades tend to roll over at very small angles, causing a blunt leading edge. Therefore, a ceramic blade chisel sharpened to $\sim 1°$ was tried. Unfortunately, the tip of this ceramic blade reached a minimum of about 10 µm after which it could not be further sharped due to the material being brittle. The

(a)   (b)   (c)
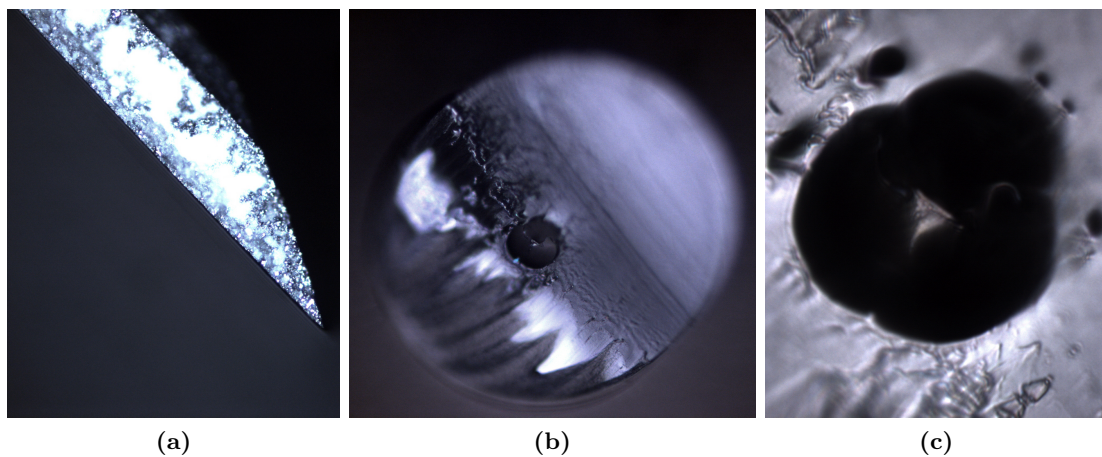
Figure 3.29 – Hot cleaving attempt at ∼80℃ with chisel sharpened blade, where; (a) shows the new blade geometry created; (b) shows the overall cleave quality, and (c) shows the core area in transmission.

resulting cleave was much rougher than that produced by a steel blade sharped at a 12°
angle.

3.4.2   Laser Cleaving

Laser cleaving experiments were attempted using a high power laser at 532 nm. The
results, shown in Figs. 3.30(a)–(c), were very poor quality since the absorption of polymer
caused the surrounding material to also melt and ablate, thus distorting the structure.

(a)   **(b)**   **(c)**
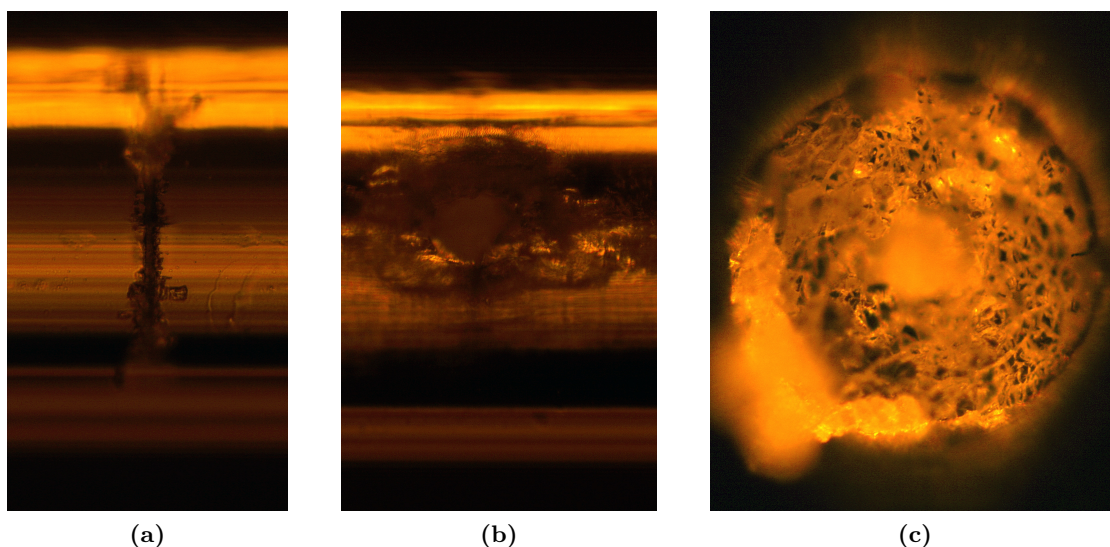
Figure 3.30 – Laser cleaving attempts using 532 nm, where; (a) shows the polymer fibre partially cut; (b)
shows a hole cut through the polymer fibre; and (c) shows the overall cleave quality using a
laser

3.4.3   Polymer Cold Cleaving

For an initial attempt at cold cleaving, the fibre, chisel sharpened blade and teflon
block were placed in liquid nitrogen and cooled for 3 mins to ~70K. The blade was
then used to cut through the cooled fibre. The overall cleave quality and core area
in transmission of the cleaved end of the fibre are shown in Figs. 3.31(a) and 3.31(b)
receptively. Although focusing and imaging the whole end of the fibre was difficult, this
cleaving method produced a reasonable result at the core which looks to be in one plane.

In another method, the fibre was first scored with a blade, then placed in liquid
nitrogen for 3 mins, then removed from the liquid nitrogen and snapped off at the score
location. This cleaving method consistently produced the best results with respect to
the core being in one plane. Figures 3.32(a) and 3.32(b) show the overall cleave quality

<div align="center">(a)   (b)</div>
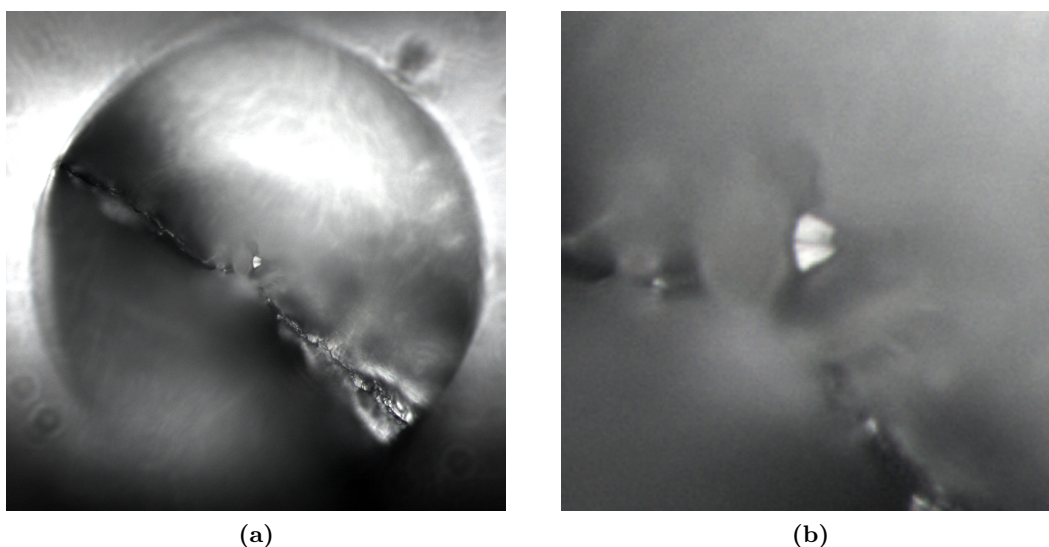
Figure 3.31 – Cold cleave (∼70K) of PMMA by placing fibre in slot of teflon block, cooled for 3 mins with chisel sharpened blade which was then used to cut through the cooled fibre. (a) Shows the overall cleave quality and (b) shows the core area in transmission.

<div align="center">(a)   (b)</div>
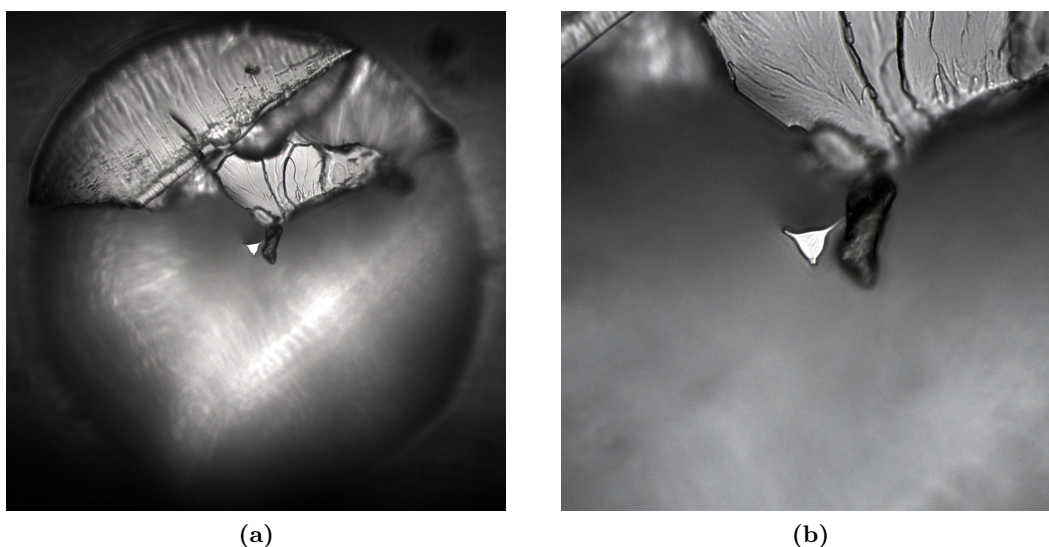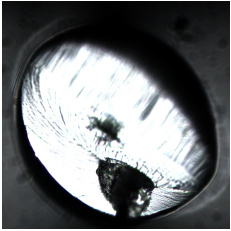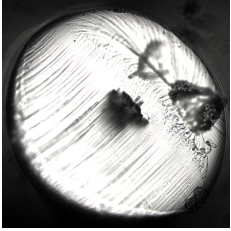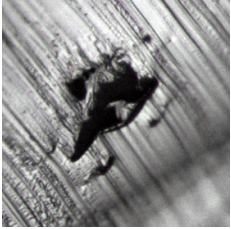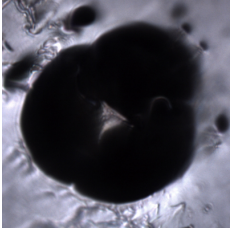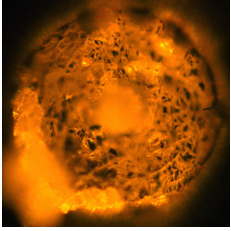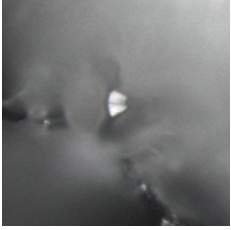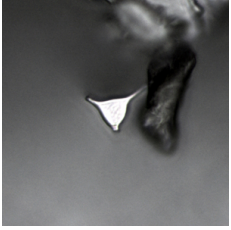
Figure 3.32 – Cold cleaving attempts at ∼70K, where the fibre was firstly scored with a blade, placed in the liquid nitrogen for 3 minutes then snapped at the score location; (a) shows the overall result; and (b) shows a closeup of the core in transmission.

and a close-up of the core area respectively. The main concern was that the outer solid region was not in a single plane. The differences in height of the outside area caused most of this area to be out of focus so the hole structure around the core is not visible in this image, however were not collapsed.

3.4.4 Summary of Cleaving Results

Table 3.1 shows a summary of the cleaving attempts which shows that the best cleaving result was achieved when using cold cleave score and snap method. Characterisation of the fibre is shown in Chapter 5.

Table 3.1 – Summary of PMMA SCF cleaving results

Type	Method	Result
Hot (80℃)	V-ground sharpened blade	
Hot (100℃)	V-ground sharpened blade	
Hot (120℃)	V-ground sharpened blade	
Hot (80℃)	chisel sharpened blade	
Laser	532 nm	
Cold (70K)	chisel sharpened blade	
Cold (70K)	score and snap	

3.5   Summary and Conclusions

This chapter has shown the results towards producing a practical polymer fibre for corrosion sensing. For the aims of this project, it was necessary to show that SCF with orders of magnitude less loss than previous published results [160] could be fabricated. It was thought that using cast PMMA might be a way to achieve this lower loss target, since the tensile strength, operating and forming temperatures are higher for cast PMMA relative to extruded PMMA. While the cast polymer had a T_{g} low enough to make extrusion of structured preforms a possibility, a suitable viscosity for extruding cast PMMA could not be found. Future work attempting to extrude cast PMMA could involve DSC and STA measurements to get a better understanding of the materials thermal properties, or drilling the cast material to produce a preform for drawing SCFs could be a less challenging option.

An attempt was shown to produce relatively smaller core size SCFs by a one step process using extruded PMMA material. Instead of the typical cane-in-jacket approach, the process involved using a 'thick wall' extrusion die. While an extrusion was produced, the surface finish of the extrusion was extremely rough due to small bubbles that were formed and trapped during the process. This roughness makes the extrusion unsuitable for optical fibre production as rough surfaces cause transmission loss, and further work is needed to gain an understanding of what is occurring to cause bubbles as the material flows through the die. Extrusions for an SCF using the typical two step cane-in-jacket approach were also produced from extruded PMMA material, and successfully drawn to fibre.

Several different cleaving methods were attempted to find a technique that produces a quality cleave reproducibly. These included hot, laser, and cold cleaving methods. While reasonable results were achievable with hot cleaving, the best result was found to be the cold (70 K) score and snap cleaving. This cold cleaving method produced consistent results with respect to the core being in one plane, which is important for maximising coupling into the fibre. Further characterisation of the PMMA SCF transmission properties are shown in Chapter 5.

4

Silica MOF Fabrication

"Each problem that I solved became a rule, which
served afterwards to solve other problems."

– René Descartes

The production of SCF and ECFs in silica has many inherent advantages as well as challenges. A way to predict the draw process parameters was needed to provide insight into the nature of the process, which is especially useful when preform lengths are relatively short such as those produced by the drilling process, the length of which are limited by the drill length. The advantages of having analytic equations for the fibre draw process are these equations allow prediction of processing parameters such as temperature and pressure to achieve desired final MOF geometries. This avoids the need for systematic scanning of drawing parameters such as temperature and pressure during the fibre draw. Given that each time the drawing conditions are changed it takes time for the draw process to stabilise, which reduces the fibre yield possible from the preform.

Models describing the draw process of MOFs has already been done by several studies [166–169]. Instead of repeating such descriptions, this chapter shows how the analytical model provided by Fitt *et al.* [140] can be used to predict suitable fibre draw conditions when applied to multi-hole MOF geometries. This model, describing the process of a single axisymmetric hole fibre, was shown to give excellent agreement to a range of capillary drawing experiments, providing practical guidelines useful in design and control of capillary fabrication [140, 161, 170]. The results shown here provide experimental validation of the ability for the Fitt model to predict the parameters needed for fabrication of symmetric and asymmetric multi-hole fibre structures. In particular, this chapter shows the predictive nature of this model when applied to fabrication of three hole symmetric SCFs, such as that shown by Webb *et al.* [66], and leads to the first two hole asymmetric silica ECFs [1].

4.1   Silica Fibre Preforms

For fabrication of silica MOFs described in this chapter, the ultrasonic drilling method
to produce preforms was used. Drilling was chosen since it has been demonstrated to
be a relatively simple method to create three hole structures [66] compared to the more
widely used stacking method, and after cleaning the surface quality is satisfactory to
produce fibres with relatively low losses [171]. Examples of drilled preforms produced as
part of this project are shown in Fig. 4.1, which were 100 mm long. For such relatively
short preforms a hollow handle (∼60 cm long) was welded to the preform. This handle
is used to ensure the drive mechanism for feeding the preform is kept well away from
the high temperatures of the furnace. The holes of the preform were pressurised by
attaching the top of the handle to the nitrogen supplied pressure system controlled by
the furnace. To create this type of arrangement, the preform or sleeve (Fig. 4.2(d))
was first welded to the hollow handle (Fig. 4.2(a)) and a solid silica drop-off weight
(Fig. 4.2(e)). This drop-off weight is used in the initial stages of setting up the fibre
draw, to form a neck down of the preform to fibre.

For the two step process (cane-in-jacket method), sufficiently long enough cane was
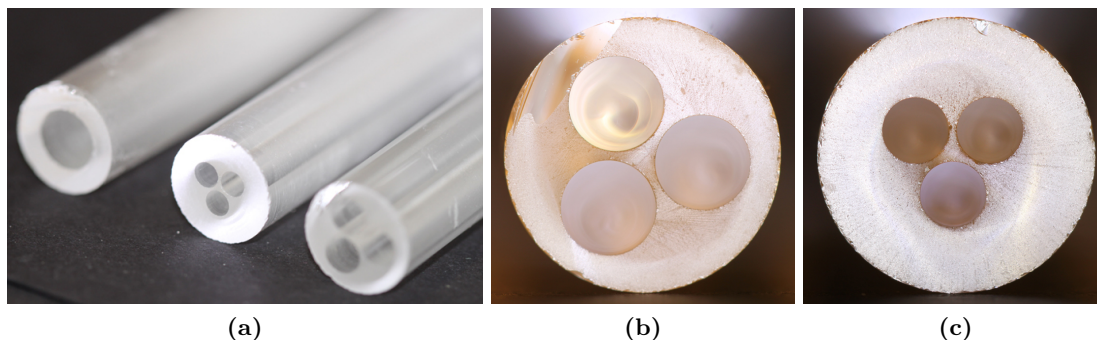
Figure 4.1 – Images of (a) 3 preforms drilled will different size holes, (b) cross section of 100 mm long,
Ø12 mm diameter silica rod drilled with three Ø4.2 mm holes, and (c) cross section of
100 mm long, Ø12 mm diameter silica rod drilled with three Ø2.9 mm holes.

Figure 4.2 – Handle setup for silica MOF draw process, made up of (a) a hollow silica tube which is (b)
tapered at the top to suit the gas pressure attachment and attached to the (d) structured
preform and (e) drop-off weight. (c) Pressure relief or active vacuum fitting.

Figure 4.3 – Closeup of cane sealed into handle.

inserted into the handle and sleeve. The gap between the outside of the cane and wall of the handle was then sealed at the top of the handle using high temperature sealing putty (Resbond 907GF) capable of withstanding upto 1300℃ (Fig. 4.2(b)), a closeup of which is shown in Fig. 4.3. This setup ensures that the pressure applied at the top of the handle inflates the cane while allowing the gas in the gap between the cane and sleeve to escape. To ensure that the pressure in the handle did not buildup, a relief fitting was also welded into the side (Fig. 4.2(c)) which could have been attached to vacuum; although vacuum was not used in the experiments.

4.2   Practical Understanding of the Draw Process

When fabricating structured optical fibres it is important to control the size and shape of the hole structure in a finished MOF. This is because when the MOF is drawn down to the typical 100–250 µm diameter from the typically 10–25 mm diameter preform, the structure experiences substantial external deformation under draw tension. A range of deformation patterns compared to the initial preform structure can occur:

- hole collapse: the holes are partially or totally closed;

- hole expansion: the hole diameter is increased relative to fibre outer diameter; and

- hole shape changes: originally circular hole may become non-circular.

Such deformations may lead to favourable or disadvantageous alteration of the fibre's optical properties. The extensive range of possibilities means that to fabricate MOFs

in an efficient manner, it is essential that these draw conditions can be predicted accurately. Hence, the first step was to find the parameters needed to control the structure during the draw process and achieve the target structure.

To understand how the draw parameters affect the hole structure of the fibre, systematic experiments were performed. These experiments involved varying the temperature (material viscosity) or internal hole pressure parameters while keeping the others constant during the draw process. The method used to create the preforms was to ultrasonically drill solid silica rod to define the air holes. These first set of experiments were done using LWQ, to avoid using up high grade material during the initial stages. After drilling, these preforms were etched for 15 minutes in a buffered hydrofluoric acid (BHF) solution, 6 volumes of ammonium fluoride (NH_4F) 40% solution – 1 volume of hydrofluoric acid (HF). This solution is commonly used in the electronics industry for etching silica wafers, due to its well known etch rate of 100–250 nm/min. The resulting reaction with the silica is $SiO_2 + 6\,HF \longrightarrow H_2SiF_6 + H_2O$, where the H_2SiF_6 dissolves into the BHF solution.

A 6 m fibre drawing tower, with a temperature range of 1800–2200℃, was used to draw the preforms to fibre. The preform used for these initial experiments, shown in Fig. 4.1(c), was made using 10 cm long Ø12 mm silica rods, drilled with three Ø2.9 mm holes, where the centres of the holes form an equilateral triangle with a 0.3 mm web between them. A series of fibres were produced at varying internal hole pressures (p_0) from 100 to 1600 Pa at fixed furnace temperature (2020℃), feed rate ($W_f = 1.5$ mm/min), and outer fibre diameter ($h_2 = 220$ µm) which was maintained by setting the draw tower draw speed (W_d) to automatically maintain the outer diameter. The pressure was then initially set to 100 Pa for the first 16 mm of preform, then raised to 200, 400, 800, 1600 and 3200 Pa for subsequent 16 mm preform lengths. The fibre lengths for each segment ranged from 40–45 m with a total of 257 m drawn. Except for the 3.2 kPa segment where the pressure was too high and so continued to expand uncontrollably, the pressure and draw speed settled to become approximately steady within 8 mm of preform and remained steady up until the pressure was changed for the next segment. The images shown in Fig. 4.4 were taken from the end of each of these segments. These results showed that the initial preform geometry is kept relatively constant (internal holes remain circular) at ∼800 Pa (equilibrium pressure). Below

and above this 800 Pa equilibrium pressure the geometry shows hole collapse and hole expansion respectively.

To understand if a change to the fibre diameter significantly effected the size and shape of the hole geometry, another pressure series of fibres with outer diameter (h_2) at 160 µm was produced using LWQ. For this pressure series, the internal holes pressures were varied from 200 to 2000 Pa, while the same temperature and feed rates (2020℃, $W_f = 1.5$ mm/min) were used. As done previously, the pressures where raised from 200 Pa to 400, 800, 1200, 1600 and 2000 Pa in 16 mm reform length increments. The images shown in Fig. 4.5 were taken from the end of each of these segments. These results also showed that the initial preform geometry is kept relatively constant (internal holes remain circular) at ∼800 Pa, with hole collapse and hole expansion above and below this equilibrium pressure respectively. This indicated that the change from 220 µm to 160 µm external fibre diameter did not significantly alter the effect that internal hole pressure has on the size and shape of hole geometry.

With success of the above pressure series experiments using the low quality LWQ material, the next step was to perform experiments to understand the draw process using high quality silica which is more suitable for fabricating the exposed-core corrosion

(a) 100 Pa **(b)** 200 Pa **(c)** 400 Pa **(d)** 800 Pa **(e)** 1.6 kPa
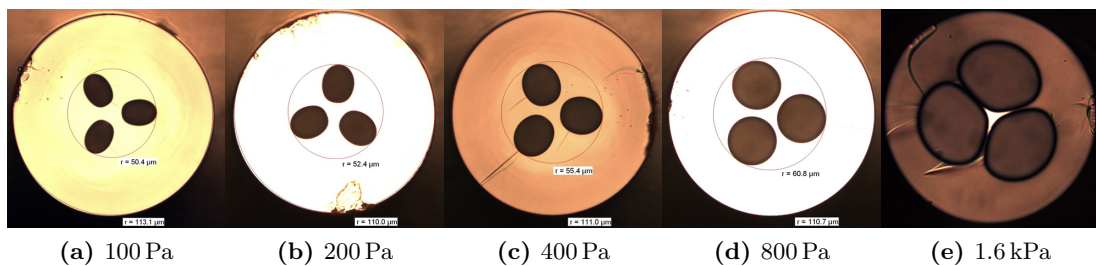
Figure 4.4 – Microscope images of SCF pressure series cross sections, drawn to outside diameter of 220 µm using feed rate of 1.5 mm/min, and furnace temperature of 2020℃, using LWQ.

(a) 200 Pa **(b)** 400 Pa **(c)** 800 Pa **(d)** 1.2 kPa **(e)** 1.6 kPa **(f)** 2 kPa
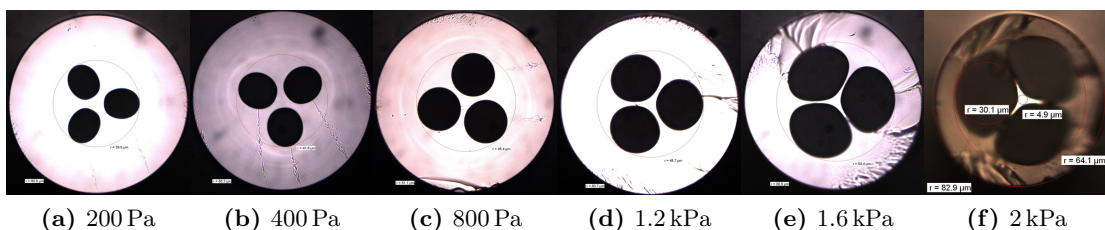
Figure 4.5 – Microscope images of SCF pressure series cross sections, drawn to outside diameter of 160 µm using feed rate of 1.5 mm/min, and furnace temperature of 2020℃, using LWQ.

sensing fibre. High purity F300HQ fused silica (Heraeus Quarzglas GmbH & Co.KG) was chosen for this purpose. The first step was to replicate the previous LWQ pressure series results by using the higher grade material, and then produce a series of fibres with varying temperature while keeping the other parameters constant. For this purpose, the preforms were produced using the drilling technique in the same way as was done in the previous set of experiments, shown in Fig. 4.1(c). Since the temperature dependance of viscosity for the two materials is different, the preform was first heated to 1920℃ and slowly raised in 10℃ increments until the tension of the 'drop-off' was similar to the LWQ drop. This occurred at 2000℃.

A series of fibres were produced at varying internal hole pressures (p_0) from 200 to 2000 Pa at fixed furnace temperature (2000℃), feed rate ($W_f = 1.5$ mm/min), and outer fibre diameter ($h_2 = 160$ µm) which was maintained by setting the draw tower draw speed (W_d) to automatically maintain the outer diameter. The pressure was initially set to 200 Pa then raised to 400, 800, 1200, 1600, and 2000 Pa in 16 mm preform length intervals. At 2000 Pa the fibre continued to expand uncontrollably, which could be seen by the draw speed increasing, and the experiment was stopped. The results of this pressure series, produced using F300HQ material, is shown in Fig. 4.6. As was the case for the pressure series produced using LWQ material, these results

(a) 200 Pa   **(b)** 400 Pa   **(c)** 800 Pa   **(d)** 1.2 kPa   **(e)** 1.6 kPa   **(f)** 2 kPa
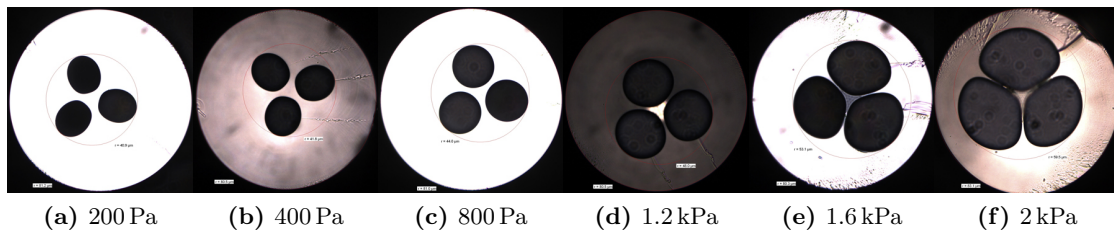
Figure 4.6 – Microscope images of SCF pressure series cross sections, drawn to outside diameter of 160 µm using feed rate of 1.5 mm/min, and furnace temperature of 2000℃, using F300HQ.

(a) 1920℃   **(b)** 1960℃   **(c)** 2000℃   **(d)** 2040℃   **(e)** 2080℃
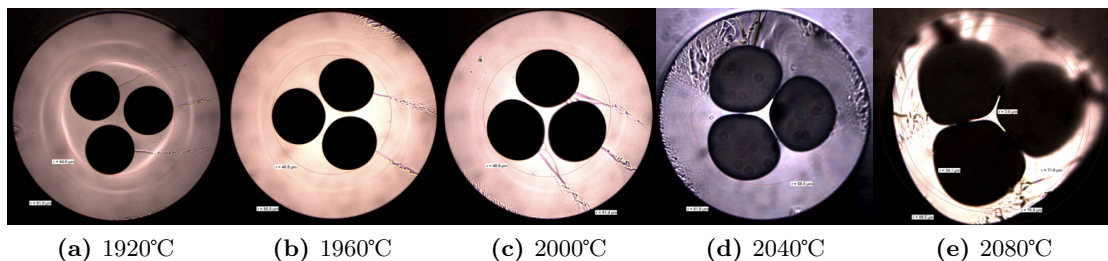
Figure 4.7 – Microscope images of SCF temperature series cross sections, drawn to outside diameter of 160 µm using feed rate of 1.5 mm/min, and hole pressure at 1.2 kPa, using F300HQ.

also show that the initial preform geometry is kept relatively constant (internal holes remain circular) at ~800 Pa, with hole collapse and hole expansion below and above this equilibrium pressure respectively. This is an indication that the material viscosities during the draw process of these fibres produced from LWQ and F300HQ materials were similar, since the deformation of the holes is also related to the viscosity of the material.

To understand how the holes deform with varying viscosity, a temperature series was produced from 1920℃ to 2080℃ in 40℃ increments. This ensured that the result could be compared to the same set of parameters used during the pressure series at 2000℃. In this case the pressure was kept constant at 1.2 kPa. As with the pressure series, the feed rate ($W_f = 1.5$ mm/min) and outer fibre diameter ($h_2 = 160$ µm) were also kept constant. The results of this temperature series are depicted in Fig. 4.7, which shows that the initial preform geometry is kept relatively constant (internal holes remain circular) somewhere between 1920℃ and 1940℃, with hole collapse and hole expansion above and below this temperature respectively. Also, as was expected, the geometry of the fibre drawn at 2000℃ during the temperature series was similar to the fibre drawn at 1.2 kPa during the pressure series, since all the parameters at these points were the same.

4.3 Simplified Model of the Draw Process: The *Fitt Model*

In theory, the set of Navier-Stokes coupled differential equations can be used to describe the neck down region viscous fluid flow of the MOF draw process to model the shape of the final expected fibre geometry [166, 167]. These equations describe how the velocity, pressure, temperature, and density of a moving fluid are related, as well as how these quantities are transferred inside the physical system due to diffusion and convection. Solving these equations for MOF production becomes a computationally intensive numerical problem due to the large set of parameters involved in the fibre draw process. To overcome this, suitable approximations and generalisations have been studied to develop useful draw process predictive models [168].

In 2002, starting from the Navier-Stokes and convection-diffusion equations, Fitt *et al.* [140] derived and experimentally validated a general model describing the draw process of a capillary (Fitt model), which is capable of including the effects of internal

hole pressurisation, surface tension and all of the other effects useful for predicting the draw process. The Fitt model assumes that viscosity alone is a function of temperature, ignoring some of the weak dependance [172] that temperature has on physical quantities such as material density, surface tension, thermal conductivity and specific heat, since the material viscosity typically varies by orders of magnitude over a relatively modest temperature range. Also, although the Fitt model accounts for physical effects such as diffusive and convective heat transfer, some simplifications are made where the terms in the equations are small, such as ignoring viscous dissipation, and that the optically thin fibre absorbs radiation directly from the surrounding furnace and re-radiates heat back to the furnace. With these approximations and appropriate choice of practical boundary conditions for fibre drawing purposes, a set of analytical equations for the case of a capillary was developed.

There have been several studies utilising the methods described by Fitt *et al.* [140], such as models to; determine the drawing domain of internal hole pressurisation when applied to a square lattice geometry [173], include the effects of preform rotation [170, 174, 175] and self pressurisation [161], and asymptotic analysis of surface tension and internal hole pressurisation affects on the drawing process [176]. Here, it is demonstrated how the Fitt model can be used as a practical predictive tool to produce multi-hole symmetric and asymmetric fibre structures, and provides the first experimental validation of these analytical equations when applied to MOFs rather than simple capillaries.
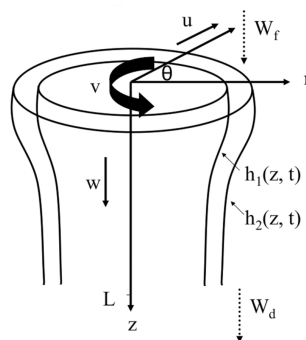
Figure 4.8 – Representation of the parameters involved when drawing a simple capillary structure. Adapted from [161].

4.3.1 The Fitt Model

A simplified representation (simple capillary structure) of the fibre draw process described by Fitt *et al.* [140] is shown in Fig. 4.8. Even though this representation is simplified there are still may variables involved, where,

p_0 [Pa], internal hole overpressure (above atmospheric pressure);

h_1 [m], the inner diameter;

h_2 [m], the outer diameter;

h_{10} [m], the initial inner preform diameter;

h_{20} [m], the initial outer preform diameter;

μ [Pa.s], temperature dependent material viscosity;

γ [Nm^{-1}], surface tension;

W_f [ms^{-1}], the feeding speed for the preform;

W_d [ms^{-1}], the drawing speed for the fibre;

L [m], the draw down (neck down) length [162, 177];

z [m], the distance along the axis from the start of the neck down region.

The Fitt model equation describing the internal diameter (h_1 [m]) of the single axisymmetric hole fibre depicted in Fig. 4.8, is given by [140],

$$h_1(p_0) = \exp\left(\frac{-\beta z}{2L} - P \exp\left(\frac{-\beta z}{L}\right)\right) \left[h_{10}\exp(P) - G\int_0^z \exp\left(\frac{-\beta u}{2L} + P \exp\left(\frac{-\beta u}{L}\right)\right) \mathrm{d}u\right]$$

$$G = \frac{\gamma}{2\mu W_f} \quad , \quad P = \frac{p_0 L}{2\beta\mu W_f} \quad , \quad \beta = \ln\left(\frac{W_d}{W_f}\right) \tag{25}$$

where, the heating zone length (L [m]) is defined by Eq. (25) as the neck down region where the changes are integrated over $0 \leq z \leq L$ for the drawn fibre case.

4.3.2 Temperature Dependence of Viscosity and Surface Tension

Knowing the temperature dependence of material viscosity is a major part of practically applying a model to the fibre drawing process. For F300HQ material in the temperature range $1673 \,\mathrm{K} \leq T \leq 2773 \,\mathrm{K}$ the viscosity, experimentally measured by Urbain *et al.* [178] and discussed by Doremus [179] and Voyce *et al.* [170], is given by,

$$\mu = 5.8 \times 10^{-8} \ \exp\left(\frac{515400}{RT}\right) \quad [\mathrm{Pa.s}] \tag{26}$$

where R is the gas constant and T [K] is the glass temperature. To find closed form solutions of Eq. (25) it is necessary that the temperature of the glass is assumed constant. However, a drawing tower furnace does not exhibit a constant temperature but an axial temperature gradient/profile [162, 170]. This means that the glass viscosity varies with the temperature gradient/profile within the furnace [163]. One should also consider that temperature profiles can vary between drawing towers and furnace designs.

To determine the temperature profile inside the preform for the conditions prevailing within our draw tower, a thermocouple was inserted in the centre of a drilled F300HQ glass rod. The measurements of the thermocouple temperature were taken for Ø12 mm and Ø20 mm rods at 5 mm intervals along the central axis of the furnace, ensuring
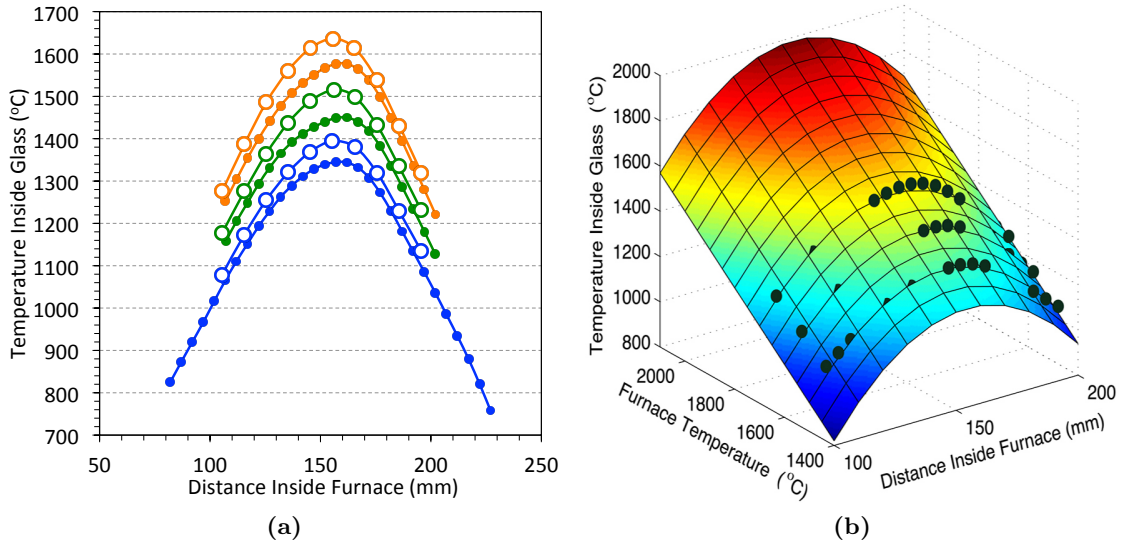
Figure 4.9 – (a) Temperature profiles measured inside (small dots) Ø12 mm and (large dots) Ø20 mm rods at (■ – blue) 1500℃, (■ – green) 1600℃, and (■ – orange) 1700℃ furnace temperatures. (b) Surface of 2×1 degree polynomial (Eq. (27)) fitted to the Ø12 mm results shown by green dots. The distance inside furnace was measured from the top of the furnace outer casing.

thermal equilibrium at each measured point. For furnace temperature measurements, the draw tower was equipped with a pyrometer located next to a furnace element and targeted at the inner sleeve of the furnace. Figure 4.9(a) shows the results of the thermocouple temperatures measured at 1500℃, 1600℃, and 1700℃ furnace temperatures, shown in blue, green and orange respectively, where the small and large dots correspond to the measured points for the Ø12 mm and Ø20 mm rods respectively. The three furnace temperatures were chosen so the results could be extrapolated to typically higher fibre drawing temperatures.

These temperature profile results show that the temperature measured inside the silica glass tube is lower for smaller diameters. Larger diameter preforms are closer to the surrounding heating element, placing the outside of the glass in a hotter part of the furnace [163], which results in a hotter temperature inside the preform and shows the role that glass thermal conductivity has in the heat transfer process. For the three Ø12 mm silica rod temperature profiles, the 2×1 degree polynomial given by,

$$T_\mathrm{m} = -3634 + 43.71\,\xi + 1.073\,T_\mathrm{f} - 0.1416\,\xi^2 - 2.404 \times 10^{-5}\,\xi\,T_\mathrm{f} \tag{27}$$

fits the curves with R^2 of 0.9899, where T_m is the measured temperature, T_f is the furnace temperature, and ξ is the distance inside the furnace from top of the outer casing. The surface given by Eq. (27) is shown in Fig. 4.9(b) together with the three sets of measured points. Similarly, for the three Ø20 mm silica rod temperature profiles, the 2×1 degree polynomial given by,

$$T_\mathrm{m} = -4704 + 51.79\,\xi + 1.537\,T_\mathrm{f} - 0.1551\,\xi^2 - 2.201 \times 10^{-3}\,\xi\,T_\mathrm{f} \tag{28}$$

fits the curves with R^2 of 0.9957.

For calculations shown in this chapter, the surface tension of silica is assumed constant at 0.31 Nm^{-1} [180–182], since it varies weakly with temperature within the fibre drawing range.

4.3.3   Defining the Geometry and Analytical Solution

The Fitt model describes a capillary draw process for which the geometry change during drawing is defined as the ratio [183],

$$C = \frac{h_1 h_{20}}{h_2 h_{10}} \tag{29}$$

where h_{10} and h_{20} are the preform inner and outer diameters. This ratio provides a comparison of the final fibre geometry ratio (h_1/h_2) to the initial preform geometry ratio (h_{10}/h_{20}) of the inner and outer diameters. When $C = 1$ the hole geometry is preserved. If $C > 1$ the hole expands from the original geometry, and the hole experiences collapse when $C < 1$. With Eq. (25) and the external fibre diameter (h_2 [m]) given by [140],

$$h_2 = h_{20} \; \exp\left(\frac{-\beta}{2}\right) \quad , \tag{30}$$

Eq. (29) becomes,

$$C(p_0) = \frac{\exp\left(-P\exp\left(-\beta\right)\right)}{h_{10}} \left[h_{10}\exp(P) - G \int\limits_0^z \exp\left(\frac{-\beta u}{2L} + P\exp\left(\frac{-\beta u}{L}\right)\right) \mathrm{d}u \right] \tag{31}$$

for the $z = L$ drawn fibre case. To obtain a closed form Eq. (31), Eq. (30) assumes that the draw down ratio (β) is independent of inner diameters, which can only be valid for small hole changes compared with the initial preform geometry.

Equation (31) is simple to calculate using mainstream software, such as Excel or Matlab. Since the geometry change ratio (C) describes a capillary draw process, a method to relate the geometry of a multi hole MOF to a capillary needed to be established. Four different definitions to relate the ratio C from experimental results shown in Sec. 2.1 using Eq. (29) with the predicted value of $C(p_0)$ using Eq. (31) were investigated. These are,

- **Circle:** define h_1 and h_{10} as the diameter of a circle that fits tightly around the inner holes, as shown in Fig. 4.10(a);

- **Area:** define h_1 and h_{10} as the diameter of a circle which has the same area as the area of the three holes ($d = 2\sqrt{A_{\text{total}}/\pi}$), as shown in Fig. 4.10(b);

(a)   **(b)**   **(c)**
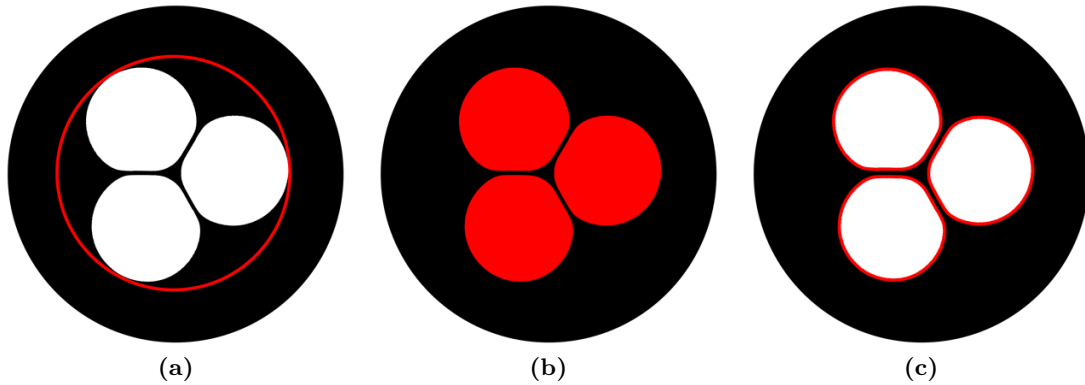
Figure 4.10 – Geometry relationship definitions shown in ▮ – red; being (a) circle, (b) area, and (c) perimeter.

- **Perimeter:** define h_1 and h_{10} as the diameter of a circle which has the same perimeter as the total perimeters of the three holes ($d = P_{\text{total}}/\pi$), as shown in Fig. 4.10(c); and

- **Hydraulic:** define h_1 and h_{10} as the hydraulic diameter ($d = A_{\text{total}}/P_{\text{total}}$) from the three inner holes, calculated from the area (Fig. 4.10(b)) and perimeter (Fig. 4.10(c)).

4.4   Comparing the Model with Experiment

As discussed in Sec. 4.3.2, although the furnace temperature is known, it is not the actual glass temperature. The actual temperature of the glass in the neck down region was less than the furnace temperature, due to axial and radial temperature gradients. Also, as discussed in Sec. 4.3 several assumptions were made to arrive at Eq. (25). It was therefore expected that not all of the contracting effects due to surface tension are completely accounted for in the Fitt model described in Sec. 4.3.1, which would lead to the actual internal hole overpressure (p_0) being different to the pressure measured by the draw tower control system (p_{f}). Because of these uncertainties, pressure (p_ϵ) and temperature (T_ϵ) offsets were included such that $p_0 = p_{\text{f}} + p_\epsilon$ and $T = T_{\text{f}} + 273.15 + T_\epsilon$, and fitted to the experimental data. The outside diameters, h_2 and h_{20} were measured directly. The neck down region length (L) was measured from the preforms after fibre drawing as being 0.039 m. The results of this comparison is shown in Fig. 4.11, and summarised in Table 4.1 including 95% confidence interval for the offsets. These results show that the circle and hydraulic definitions have the worst correlation to experiments,
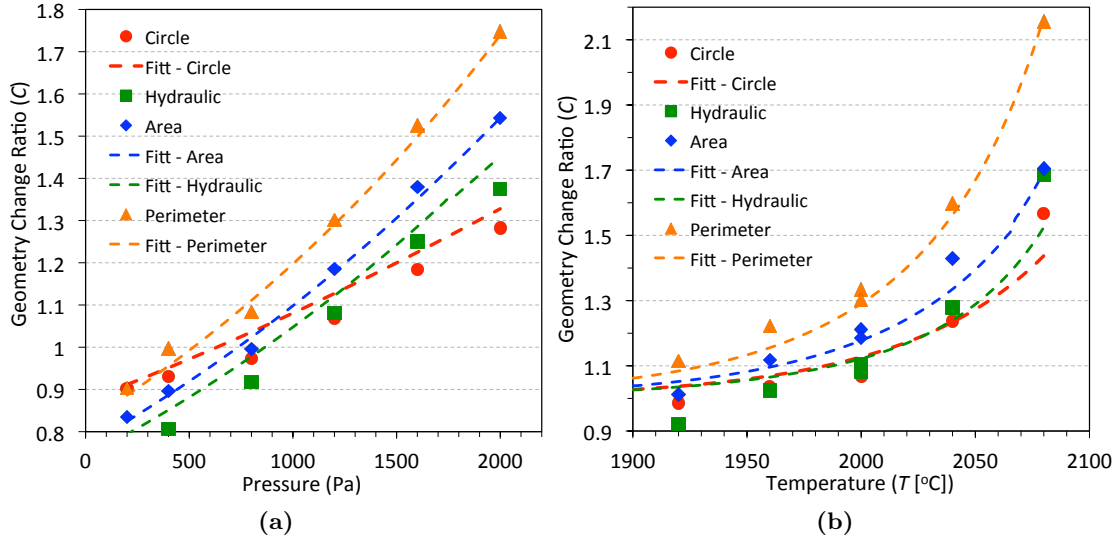
Figure 4.11 – Fitt model vs experimental results using circle (■ – red), area (■ – blue), perimeter (■ – orange), and hydraulic (■ – green) defined inner diameters.

Table 4.1 – Summary of offsets and goodness of fit from Fig. 4.11. SSE is sum of squared errors, and RMSE is the root mean square error.

Definition	Offset T_ϵ	Offset p_ϵ	SSE	R^2	RMSE
Circle	-181.5°C $\pm$22.6	-445.8 Pa $\pm$210.3	0.03102	0.9217	0.0557
Area	-147.5°C $\pm$8.2	-479.9 Pa $\pm$70	0.01222	0.9849	0.03496
Perimeter	-141.1°C $\pm$7.6	-375.8 Pa $\pm$80.4	0.01368	0.9905	0.03699
Hydraulic	-151.2°C $\pm$16.7	-431.2 Pa $\pm$131.6	0.04944	0.9358	0.07032

with $R^2 = 0.9217$ and $R^2 = 0.9358$ respectively. The area and perimeter relationships are the better way to define the geometry, with $R^2 = 0.9849$ and $R^2 = 0.9905$ respectively. Defining the geometry relationship using the perimeter definition was chosen since the temperature offset was closer to the furnace temperature described in Sec. 4.3.2. The peak temperature offset calculated from Eq. (27) at a furnace temperature of 2000°C gives an offset of -123°C, which is remarkably close to the value obtained, $T_\epsilon = -141.1$°C, considering that only a step temperature profile is assumed in the model.

In Sec. 4.3.3, Eq. (30) assumes that the outside diameter (h_2) is independent of pressure, which leads to a closed form geometry change ratio (Eq. (31)) being independent of outside diameter. This is because the approximation of Eq. (30) given by the Fitt model leads to the outside diameter (h_2) only being dependant on the draw down ratio ($\beta = W_d/W_f$; i.e. draw speed divided by feed speed) and so independent of inner diameters, which can only be valid for small hole changes compared with the initial preform geometry. It is interesting to compare this with the experimental results

to verify if the assumptions are valid in this respect. The draw tower pressure and draw speed data obtained during the pressure series discussed in Sec. 4.2 are shown in Fig. 4.12, where the blue line shows the pressure applied to the holes of the preform and the red line shows the draw speed. At the start of the experiment, where the automatic diameter control was switched off, a constant draw speed of $\sim$4 m/min was used while the pressure was switched on and allowed to stabilise to 200 Pa. The automatic diameter control was then switched on with a target outside diameter of 160 µm and the draw increased in speed until the target diameter was reached, at $\sim$8 m/min. As the pressure was increased to 400, 800 and 1200 Pa the draw speed did not increase, showing that within this range of hole expansion the outside diameter (h_2) of the final fibre is indeed independent of pressure. When the pressure was increased to 1.6 kPa the draw speed started to increase, which is due to the automatic diameter control compensating for an increase in fibre diameter by increasing the draw speed and as a result the set fibre diameter is maintained. After this initial increase, the draw speed reduced back towards the 8 m/min draw speed, showing that although the system experienced some instability there was tendency for the draw speed to remain constant. At the end of the fibre draw experiment the draw speed started to increase quickly, where the fibre draw is no longer in a steady state regime at the end of the preform.

These experimental results provide evidence that the assumptions made to arrive at Eq. (25) and Eq. (30) are within the range of pressures used and for moderate geometry
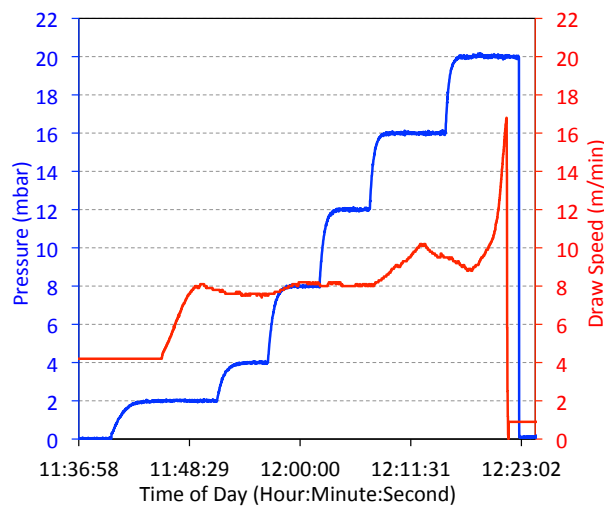
Figure 4.12 – Draw tower data, showing (▮ – blue) the pressure applied to the holes of the preform, and (▮ – red) the draw speed which was set to automatically maintain a constant outside fibre diameter.

change ratios (up to $C \sim 2$), giving greater confidence in the Fitt model to predict the parameters which need to be considered for practical fibre drawing. The validation that the geometry change ratio (Eq. (31)) is independent of the MOFs outside diameter for moderate geometry change ratios leads to the proposition that it should be possible to create asymmetric structures where the cross sectional wall thickness surrounding the holes could be made non-axisymmetric.

4.5   Predicting Fibre Draw Parameters

4.5.1   Suspended-Core MOF: Symmetric Structures

The predictive nature of Eq. (31) is most useful for fabrication of MOFs. Equipped with the temperature and pressure offsets, the aim was to produce a fibre with a similar structure but smaller scale and core size, for which the cane-in-jacket method [124] was required. The process is to first cane the preform (shown in Fig. 4.13(a)) to the order of millimetres, insert this cane into a rod (jacket), and then draw down the cane and jacket to fibre, which requires the successful application of the right combination of parameters to achieve the desired final fibre structure. Another preform was fabricated and drawn down to fibre using the cane-in-jacket method.

For the cane, the feed rate needs to be greatly increased and the draw speed greatly reduced to achieve the lower draw down ratio. For this a feed rate of 6.4 mm/min was chosen, with the targeted outside diameter for the cane being Ø0.95 mm maximum. The aim was to pre-expand the holes during the caning process, for which a geometry change ratio of $C = 1.55$ was chosen. Using Eq. (31) the predicted pressure (p_f) needed to achieve this was 3.5 kPa at a furnace temperature of 1980℃. A microscope image
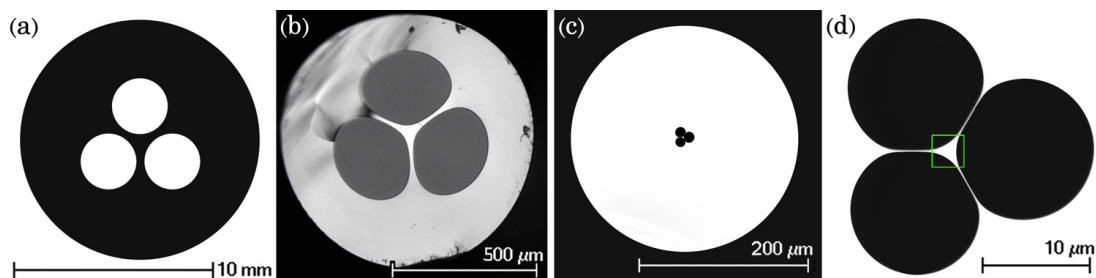
Figure 4.13 – (a) Cross section of the preform fabricated from Ø12 mm F300HQ rod; and, microscope image of (b) the cane; and, scanning electron microscope images of (c) the silica SCF cross section measured to be Ø270 µm with (d) and enlarged image of the holes and core having effective diameters of 40.5 µm and 1.7 µm respectively.

of the resulting cane structure is shown in Fig. 4.13(b), from which the outer diameter was measured as Ø0.91 mm with the hole region diameter Ø0.87 mm. Applying the definition discussed in Sec. 4.3.3, the geometry change ratio (Eq. (29)) obtained for this cane was $C = 1.50$, which agrees well with the target $C = 1.55$.

A jacket was made by drilling a Ø1 mm hole centrally located in Ø12 mm F300HQ rod into which the cane was placed. The setup of the cane and jacket arrangement was made to ensure pressure was only applied to the three holes of the cane, as described in Sec. 2.1. The aim was to draw down the cane and jacket to a SCF with core size of Ø1.5–2.0 µm and target outside diameter of Ø270 µm. A geometry change ratio of $C = 1.8$ was chosen to further expand the cane holes, for which Eq. (31) predicted the pressure (p_f) needed to achieve this was 2.7 kPa at a furnace temperature of 2000℃ and feed rate of 1.5 mm/min. A single 80 m long length of SCF was fabricated using those parameters, as shown by the SEM images in Figs. 4.13(c)–4.13(d) from which the outer diameter was measured as being Ø270 µm with the hole region diameter Ø40.5 µm. Applying the definition discussed in Sec. 4.3.3, the geometry change ratio (Eq. (29)) obtained for this fibre was $C = 1.97$, which is ∼10% deviation from what was calculated by the model. The core, shown by the green box in Fig. 4.13(d), was measured as having a effective diameter of Ø1.7 µm, defined as the diameter of a circle whose area is equal to a triangle that fits wholly within the core area [124].

4.5.2   Exposed-Core MOF: Asymmetric Structures

Another preform was fabricated as before, however this time a 1.8 mm wide slot cut along the length of one hole to fabricate a fibre with the core exposed along the length, as shown in Fig. 4.14(a). The aim was to produce this type of asymmetric structure to a final maximum outside diameter of 200 µm, by directly drawing down the preform to fibre. Looking at the series of fibres discussed in Sec. 4.4, a furnace temperature of 2000℃ was chosen with an aim of expanding the holes to achieve a geometry change ratio of $C = 1.4$. Using Eq. (31) the predicted pressure (p_f) needed to achieve this was 1.40 kPa, at a preform feed rate of 1.5 mm/min. A single 127 m long uncoated ECF (Fig. 4.14(b)) was fabricated using a pressure of 1.40 kPa and the dimensions of this fibre were measured from SEM images, shown in Figs. 4.14(b–d), being Ø202 µm (measured at the maximum) with the hole region diameter of the two holes being

Ø143.1 µm. The central web thickness (between the holes) is 0.85 µm minimum, while the webs each side of the core are 1.10 µm minimum thickness. The core, shown by the green box in Fig. 4.14(c) and enlarged in Fig. 4.14(d), has an effective diameter of 10.0 µm. This is the first time the fabrication of a silica MOF with the core exposed along the whole length was achieved [1].

As shown in Fig. 4.14(b), the outside of this asymmetric structure no longer resembles the preform from which it was made (Fig. 4.14(a)). This is caused by surface tension increasing the initial gap provided by the 1.8 mm slot in the preform and significantly changing the geometry, adding a degree of complexity not accounted for in the Fitt model or in the way the geometry is defined (Sec. 4.3.3). Therefore, C was not calculated from measurements (Eq. (29)) and compared to the model, since a consistent method for such a measurement could not be found and further work is needed to understand, account for, and predict such geometry changes in the draw process. Nevertheless, since the outside diameter does not contribute in the calculation of C given by the Fitt model (Eq. (31)), it was still possible to predict the pressure needed, fabricate this asymmetric structure, and create a fibre useful for the intended application [184].

The above experiment used a one step drawing process from preform to fibre. To achieve a small core size, the two step cane-in-jacket method was tried next. For this another preform was fabricated, as discussed above for the ECF, and drawn down to fibre using the cane-in-jacket method discussed in Sec. 4.5.1. The jacket was made by drilling a Ø1 mm hole centrally located in a Ø12 mm F300HQ rod and cutting a 1.8 mm wide slot along the length of the hole, ensuring that this slot only overlapped the hole by 0.25 mm to make sure a lip remained to hold the cane. The cane was placed into the
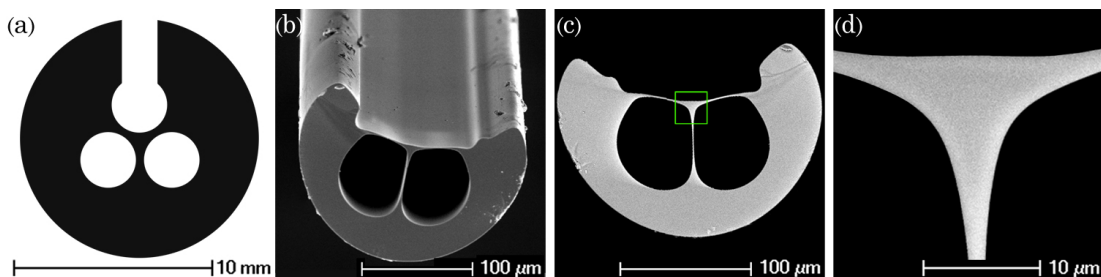
Figure 4.14 – (a) Cross section of the preform fabricated from Ø12 mm F300HQ rod; and, SEM images of (b) the silica ECF with (c) the cross section measured at the maximum to be Ø202 µm; and, (d) an enlarged image of the core having an effective diameter of 10.0 µm.

jacket ensuring that the jacket slot lined up with the cane slot. The setup of the cane and jacket arrangement was made to ensure that the cane would remain orientated correctly with the slot of the jacket during drawing, as well as ensuring that pressure was only applied to the two holes of the cane. Although the cane was successfully produced with an outside diameter of ~1 mm, drawing this cane with jacket to fibre was not successful. It was found that the holes collapsed for pressures < 3.5 kPa, and that pressures higher than this caused the struts of the exposed hole to break. To understand this further, the impact of surface tension on the fibre draw process was investigated using the Fitt model.

4.5.3   Impact of Surface Tension on Fibre Draw

The impact of surface tension when drawing MOFs is particularly apparent for asymmetric structures, such as the ECF, where the final geometry of the fibre can be dramatically altered compared to the preform shape due to surface tension. Figure 4.14(b) shows how the outside of the fibre has been altered from the circular shape of the initial preform to a D shape due to surface tension. Surface tension also acts on the holes during fibre drawing.

Surface tension is defined as the force acting a line of unit length, where the force is parallel to the surface but perpendicular to the line. When the surface is curved, as in the case of the holes, there is a pressure difference normal to the surface caused by surface tension. This pressure difference acting on the hole can be determined from the Young–Laplace equation as,

$$\Delta p = \gamma \left(\frac{1}{r_x} + \frac{1}{r_y} \right) \tag{32}$$

where Δp is the pressure difference (known as Laplace pressure), γ is surface tension, and r is the radius of the hole in the cross sectional xy plane of the preform. Equation (32) shows that the pressure difference caused by surface tension, increases with reduced hole radius. This means that holes with relatively larger initial size should require less internal pressure during fibre draw. To test this, the Fitt model (Eq. (31)) was used to calculate the pressure needed to produce SCFs with various size canes.
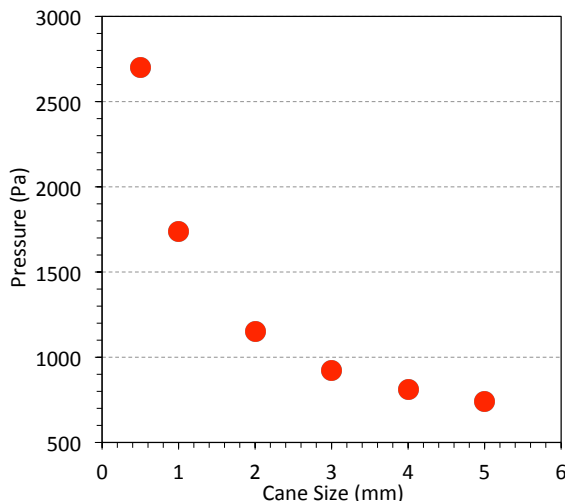
Figure 4.15 – Plot of calculated pressure required to produce fibre without geometry change (i.e. $C = 1$) from different size canes with initial geometry as shown in Fig. 4.13 on page 96.

The pressures were calculated using Eq. (31) for cane shown in Fig. 4.13(b) as the initial geometry. The cane sizes used ranged from 1 to 5 mm outer diameters, with hole region diameters scaling to maintain the same geometry. The final hole region diameter of 19.5 µm was used with geometry change ratio of $C = 1$, furnace temperature of 2000℃ and preform feed rate of 1.5 mm/min. Figure 4.15 shows a plot of the pressure needed to keep the holes from collapsing relative to the initial cane geometry. These results show that for smaller cane hole sizes the internal pressure needed to produce the same final fibre geometry exponentially increases. This is because of the slope of hole change with pressure at the temperature used, due to the $1/r$ dependance shown in Eq. (32). If this slope is high, small changes in pressure has large effect on expansion of the holes. It is important to consider this when drawing MOFs, and in particular ECFs with small cores, since the need to use higher internal pressures, with higher hole change slope, can lead to difficulties in maintaining a controlled state.

4.5.4   Small Core Exposed-Core MOFs

Since larger cane sizes reduce the need for higher pressure to expand the holes during fibre drawing another attempt was made to produce an ECF with small core using a larger cane size. Another preform was fabricated, as shown in Sec. 4.5.2 (Fig. 4.14(a)), for a cane with targeted OD of Ø2.9 mm maximum, and feed rate of 7.5 mm/min. The aim was to again expand the holes slightly during the caning process, for which a geometry change ratio of $C = 1.25$ was chosen. Using Eq. (31) the predicted pressure

(p_{f}) needed to achieve this was 1.64 kPa at a furnace temperature of 2000℃. A microscope image of the resulting cane structure is shown in Fig. 4.16(a), which was measured as Ø2.8 mm (at the maximum) with the hole region diameter Ø1.48 mm.

A jacket was made by drilling a Ø2.9 mm hole centrally located in a Ø12 mm F300HQ rod and cutting a 1.8 mm wide slot along the length of the hole, into which the cane was placed ensuring that the sleeve slot lined up with the cane slot. The setup of the cane and jacket arrangement was again made to ensure that the cane would remain orientated correctly with the slot of the jacket during drawing, as well as ensuring that pressure was only applied to the two holes of the cane. The aim was to draw down the cane and jacket to a ECF with a core size of Ø1.5–2.0 µm and target outside diameter of Ø150 µm. We chose a geometry change ratio of $C = 1.3$, since the holes of the cane were already expanded, for which Eq. (31) predicted the pressure (p_{f}) needed to achieve this was 1.80 kPa at a furnace temperature of 2000℃ and feed rate of 1.5 mm/min. A single 80 m long length of ECF was fabricated using those parameters, as shown by the SEM images in Figs. 4.16(b)–4.16(c). This fibre outer diameter was measured using these SEM images as being Ø152 µm (measured at the maximum) with the hole region diameter Ø19.1 µm. The core of this fibre, shown by the green box in Fig. 4.16(c), was measured as having a effective diameter of Ø1.7 µm. C was not calculated from measurements (Eq. (29)) and compared to the model, since this asymmetric structure no longer resembles the preform due to surface tension effects on the outside geometry.

The fabricated asymmetric ECF structures have extremely non-axisymmetric cross sectional wall thicknesses about the hole structure for which Eq. (31) was used to calculate the parameters. Since in the Fitt model the outside diameter is independent of pressure and surface tension, the parameters needed to make these structures could be
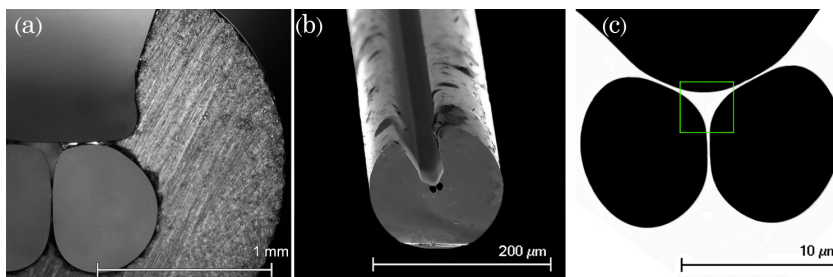
Figure 4.16 – Microscope image of (a) the cross section of a cane which was used in a two step (cane-in-jacket) process to produce a asymmetric silica ECF shown by SEM images (b); and, (c) an enlarged image of the core having an effective diameter of 1.7 µm.

predicted, within the geometry change ratio (C) limits of the types of asymmetric and symmetric multi-hole fibre structures shown here.

4.6   Summary and Conclusions

The ability to predict the experimental drawing parameters needed to produce desired final MOF geometries requires a practical understanding of the draw process beyond what is achievable by trial and error. This chapter described how to use the analytical model provided by Fitt *et al.* [140] to determine the draw conditions needed to produce multi-hole MOFs. The results showed that although the Fitt model describes a capillary draw process, it provided powerful and practical insights when applied to more complex multi-hole symmetric and asymmetric structures. By understanding the draw process, both in terms of the draw tower temperature profile and establishing a method to relate the geometry of a multi-hole MOF to a capillary, it was found that analytical equations given by the Fitt model could predict the drawing conditions needed to produce the chosen structures.

This better understanding of the draw process and application of the analytical equations (published Ref. [185], see Appendix B) were used to fabricate the first silica ECF (published Ref. [1], see Appendix D). For this type of asymmetric structure it was found that the outside no longer resembles the preform from which it was made, due to surface tension effects. These effects add a degree of complexity not accounted for in the Fitt model or in the way the geometry is defined and further work is needed to understand and account for such geometry changes in the draw process. Nevertheless, it was still possible to predict the pressure needed, fabricate this asymmetric structure, and create the type of desired ECF geometry targeted towards distributed corrosion sensing.

> **5** —

> # Characterisation of Fabricated Fibres

"Measure what is measurable, and make measurable
what is not."

– Galileo Galilei

To understand if the new polymer and silica SCF and ECFs were suitable for distributed sensing in harsh environmental conditions, characterisation in terms of transmission and environmental stability was needed. As shown in Chapter 2, the lower the loss in transmission properties of the fibre, the greater the capacity for distributed measurement. This chapter shows the results of methods used to surface profile, determine the loss and deterioration characteristics in transmission properties of the fabricated fibres.

5.1   Optical Fibre Attenuation

Attenuation of an optical fibre, also known as transmission loss, is the reduction in intensity of the transmitted light with respect to distance travelled along the core. Characterising optical fibres in terms of attenuation is important, as it is the main limiting factor in transmission of the sensing signal across long distances. There are two principle attenuation mechanisms in MOFs, being

- absorption: intrinsic – determined by the electronic transitions of the material where photon energy exceeds the network band gap energy (UV cut-off), and lattice (multi-phonon) vibrations of the material network (IR cut-off); extrinsic – caused by impurities and defects which absorb different wavelengths of light,

- and scattering: intrinsic – caused by dielectric inhomogeneities and impurities (Rayleigh scattering); extrinsic – caused by defects, bubbles, rough surfaces, etc. type scattering centres.

The optical power, P, at a propagation distance z with respect to the optical power at position z_0 a fibre can be expressed as,

$$P(\lambda, z) = P(\lambda, z_0) e^{\left[-\int_{z_0}^{z} \mathrm{d}z'\, \alpha'(z') \right]}$$

$$= P(\lambda, z_0) e^{-\alpha(z - z_0)} \tag{33}$$

where the general loss coefficient, $\alpha'(z')$, may be position dependent. If the loss coefficient $\alpha'(z')$ is constant, then Eq. (33) reduces to Beer's law. The conventional technique for determining the attenuation of an optical fibre is known as 'cut-back measurement'. This technique involves measuring the optical power emanating from the end of a fibre of length z, then shorten the fibre and measure the power at length z_0, as shown in Fig. 5.1. The attenuation coefficient (α) can be calculated by fitting these measurements to Eq. (33). Cut-back measurements performed in this fashion eliminate Fresnel reflection and provide the average total attenuation which is dependent on the length $z - z_0$, and is typically expressed in units of dB per unit length. The cut-back measurements were performed while the fibre was on this drum, using the light from a 100 W halogen light bulb source with power curve of approximately Gaussian distribution and peak power at 800 nm. This light source was coupled into one end of the cleaved fibre core, while the light emitting from the other end of the core was imaged onto the grating of a Ando AQ6315E optical spectrum analyser (OSA) such that the power was maximised before each measurement.
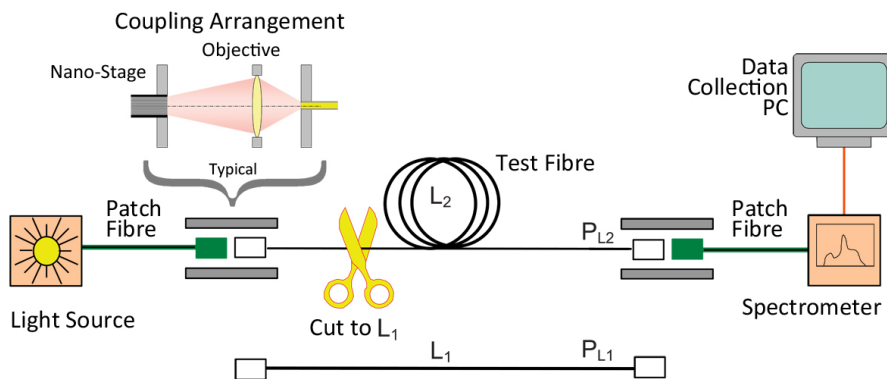
Figure 5.1 – Schematic of cutback attenuation measurement. (Step 1) Measure output power $P_{L2}(\lambda)$ of length L_2; (Step 2) Cut test fibre to L_1 and measure output power $P_{L1}(\lambda)$. Use Eq. (33) to determine the fibre attenuation α in dB per unit length.

5.2   Deterioration in Optical Fibre Transmission

The corrosion sensing application of the ECFs involves the detection of an analyte suspended in liquid. Also, when preparing the fibre for this application, solvents such as acetone, isopropanol, methanol and water will need to be used to clean the core of dust or other particulates deposited on the surface, as well as prepare the core for functionalisation. Deterioration in the transmission properties of the MOF can occur as a result of changes in the mechanical characteristics, such as pitting or micro-fracturing, and/or compositional characteristics at the core surface, causing light scattering effects [186, 187]. The build up of dust or other particulates onto the light guiding core can also cause the guided light to be scattered [188].

This deterioration in the transmission properties of the ECF are expected to increase the attenuation of the fibre over time. A modified version of Eq. (33), to include time dependant attenuation (ξ), can be expressed as,

$$P(\lambda, z, t) = P(\lambda, z_0, 0) e^{-\alpha(z - z_0) - \xi(t, z - z_0)} .$$

(34)

A technique for determining the average deterioration on the transmission properties of ECFs involves performing time based measurements of the optical power emanating from the end of a fibre, with length z exposed to a test environment. These measurements can then be fitted to,

$$P(\lambda, t) = P(\lambda, 0) e^{-\xi t z} .$$

(35)

The setup for this type of time based measurement is shown in Fig. 5.2, where the test fibre is exposed to a test environment. Before this type of time based measurement could be performed, the stability of the setup needed to be established. This is because any variations in the light source, coupling, or measuring equipment can lead to measurements that indicate fluctuations in the setup rather than the fibre. The next section shows characterisation of the setup.
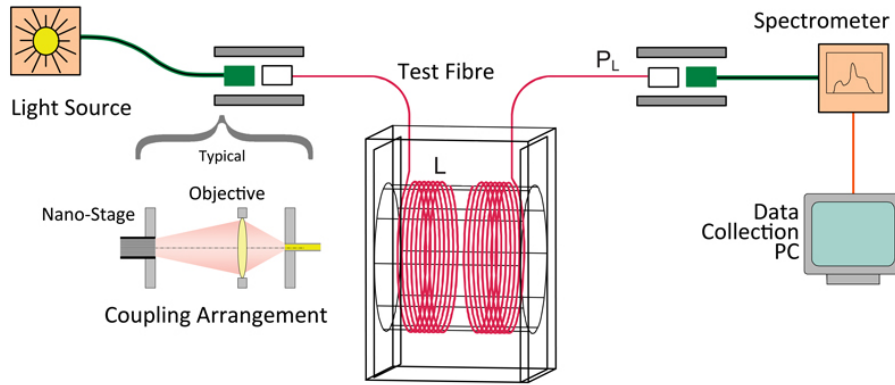
Figure 5.2 – Setup to perform time based measurements to determine the effect that an environment has on deterioration of transmission properties of an optical fibre.

5.3   Measurement Equipment Stability

The equipment stability measurements were performed using the setup shown in Fig. 5.1 with a 5 mW 532 nm laser light source. To measure the stability of coupling the light source to the OSA, the light source was coupled into a SMF patch cable which was screwed directly into the OSA and the power measured every 15 seconds for 30 minutes. The result of this measurement is shown in Fig. 5.3 which demonstrates that this part of the setup has an error of ± 0.1 dBm, which should be minimised by averaging several points when performing cut-back or time based transmission deterioration measurements.

To measure the stability of methods used for cut-back measurements and time
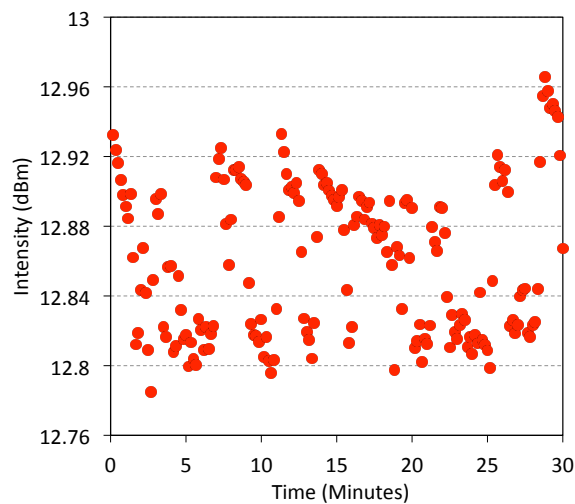
Figure 5.3 – Equipment stability measurement of coupled 5 mW 532 nm laser light source, OSA, and SMF patch cable.

(a)   (b)
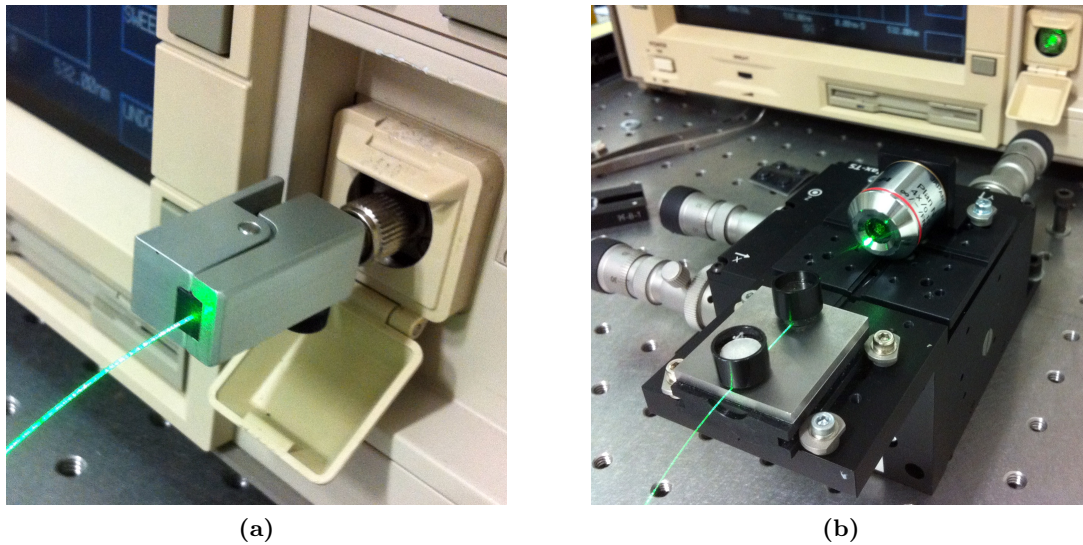
Figure 5.4 – (a) Bare fibre coupler and (b) free-space methods tested for coupling into the OSA.

based measurements of the deterioration in transmission properties of the MOF fibres produced, lengths of polymer clad bare fibre made from F2 were used. For these types of measurements, a method to image the light from the core onto the grating of the OSA was needed. The errors from two methods to achieve this were compared. The first of these was a commercially available bare fibre coupler, shown in Fig. 5.4(a). The other was a free-space method, by using a stage with ×4 objective to focus the light emanating from the end of the core onto the grating of the OSA, shown in Fig. 5.4(b).

The light source was coupled into a 1.5 m length of cleaved fibre, setup into the
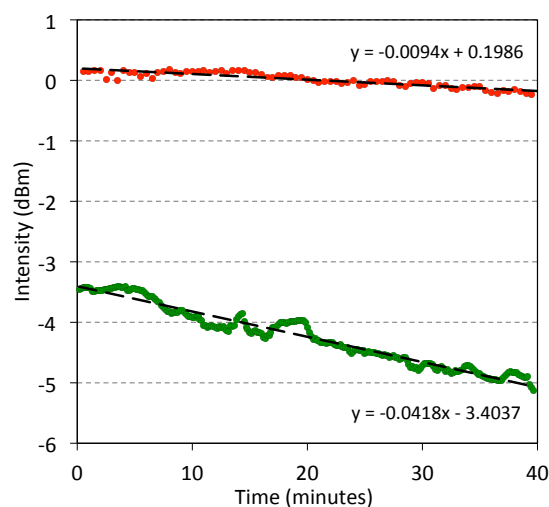
Figure 5.5 – Comparison of coupling stability into OSA using bare fibre coupler (∎ – green) and free-space (∎ – red) methods.

OSA using the bare fibre coupler, and measurements were recorded every 15 seconds for 40 minutes. The experiment was repeated using the free-space method. Results from these experiments are compared in Fig. 5.5, which shows that over 40 minutes the measurement using the bare fibre coupler drifts 1.5 dBm, whereas the free-space method has five times less drift at 0.3 dBm.

When doing cut-back measurements, the fibre needs to be removed, cleaved, and restored to the OSA for the next measurement. To measure how accurately the two methods realigned with the OSA, experiments were performed to measure how the power changed when the fibre was removed and replaced. The results of these measurements is shown in Fig. 5.6, which shows that realignment of the light from the end of the fibre is 6.5 times improved using the free-space method, at ± 0.1 dBm. These two experiments, comparing the bare fibre coupler and free-space methods, show that the free-space method has ~ 5 times better measurement stability compared to the bare fibre coupler.

The other stability measurement that needed to be considered is the time required for the setup to settle, such as settling of the threads on the stage, which could lead measurement error. To perform such a measurement, the laser light source was coupled into another 1.5 m length of fibre, and the free-space method was used to image the output of the fibre into the OSA. Figure 5.7 shows the stability of the setup when left overnight, which indicates that settling time is required after the initial coupling of
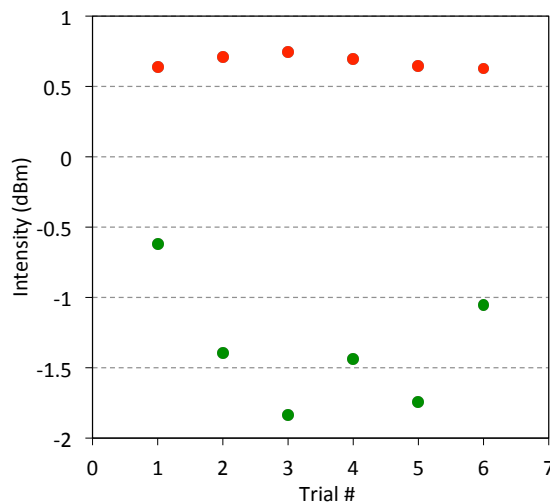
Figure 5.6 – Comparison of bare fibre coupler (∎ – green) and free-space (∎ – red) re-coupling error into OSA.
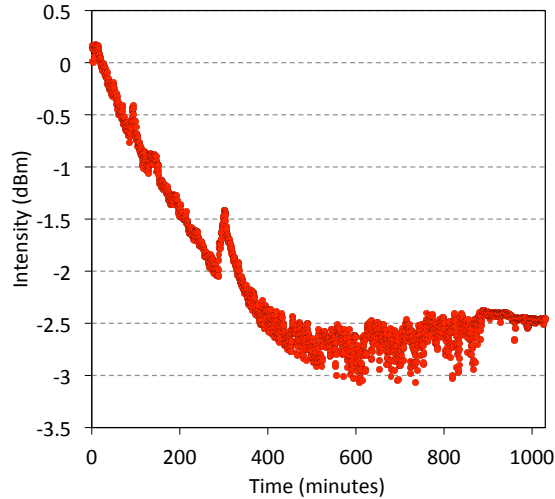
Figure 5.7 – Long term stability of measurement setup.

the fibre to prevent misleading results. In particular, the first part of the curve shows an almost linear drop in intensity of ~ 1 dBm over the two hour period directly after coupling, which could cause lower than actual loss to be measured. The result shows that approximately 15 hours is needed for the setup to settle.

5.4 Uncertainty in Loss and Deterioration Measurements

As described in the previous sections, the measurements from loss or deterioration in transmission properties can be fitted to Eqs. (33) and (35) respectively. Since dB is a logarithmic unit, the fitting to these equations is linear in dB. A straight line is fitted through a set of n points by using the least squares method, and for loss measurements we are primarily interested in the slope β_1 of the line in the linear model given by [189],

$$Y = \beta_0 + \beta_1 X + \varepsilon \tag{36}$$

with an experimental region $X_1 \leqslant X \leqslant X_n$. Using $\widehat{Y_i}$ to estimate the expected value of Y_i $(E(Y_i))$, the variance of the data set is,

$$S^2 = \left(\frac{1}{n-2}\right) \sum_{i=1}^{n} (Y_i - \widehat{Y_i})^2 \tag{37}$$

which provides an unbiased estimator for the population variance σ^2. Hence, the standard deviation (σ) of an unbiased point estimator $\widehat{\beta}_1$ is given by,

$$\sigma_{\widehat{\beta}_1} = \sqrt{\frac{\sum\limits_{i=1}^{n}(Y_i - \widehat{Y}_i)^2}{(n-2)\sum\limits_{i=1}^{n}(X_i - \bar{X})^2}} \tag{38}$$

and for a $100(1-\vartheta)$ percent confidence interval (CI) for the slope,

$$CI_{\widehat{\beta}_1} = t_{\vartheta/2,n-2}\,\sigma_{\widehat{\beta}_1} \tag{39}$$

for a t distribution with $n-2$ degrees of freedom.

5.5   Loss Measurements

5.5.1   Polymer Fibre Loss

The light guiding properties of the polymer fibre produced was assessed by performing cutback loss measurements. Figure 5.8(a) shows the results of the cutback measurements on approximately 12 m of the PMMA bare fibre together with the bulk material loss for comparison. For the PMMA SCF the score and snap cold cleave method was used and the results are shown in Fig. 5.8(b). In each case the loss of these PMMA
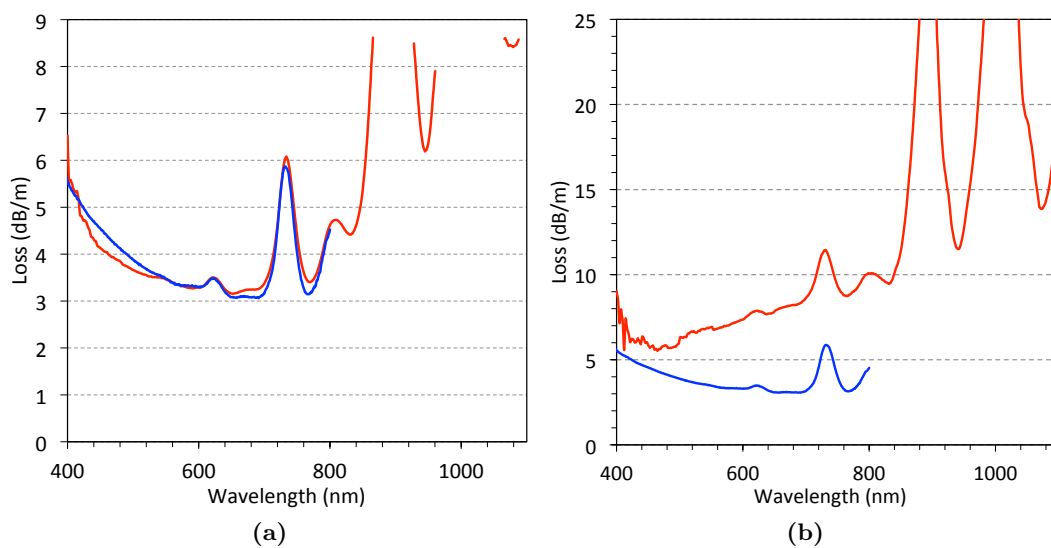
Figure 5.8 – PMMA broadband cutback loss measurements (■ – red) of (a) bare unstructured fibre and (b) the SCF fibre shown in Fig. 3.32 of Chapter 3. The bulk material loss is shown for comparison by the blue (■) curve.

fibres was very high, with the bare fibre having loss between 3–4 dB/m and the SCF having loss between 5–10 dB/m at visible wavelengths. Both fibres showed increasing high losses peaks beyond 700 nm. The measured loss of the PMMA SCF fibre is much higher than the bulk loss, which is 3.6 dB/m at 532 nm. In the SCF case, it was found that loss centres along the length of the fibre caused the transmission along the core to terminate, and it was found that only several short 1.5 m lengths of fibre could be used for the cutback measurements. For the sections of fibre where the core could not be seen at the transmitted end of the fibre, many discrete loss centres were visible due to light scattering along the length, as shown in Fig. 5.9(a). Figure 5.9(b) shows an image of the transmitted light from the core and a haze of light being transmitted by the sleeve section of the fibre. For these loss measurements the light from the fibre core into the OSA was isolated by using a pin-hole.

Investigation of the cause of the catastrophic loss centre in the polymer SCFs was a challenge, and while isolation these regions for imaging was tried they could not be found. Figure 5.10 shows two sections of the Ø237 µm core in the cane. There were bubbles found inside the core, as shown by the two circled regions to the left of Fig. 5.10(a), and another type of unknown artefact shown to the right of Fig. 5.10(a). Twelve bubbles were counted at varying focus depths in a 465 µm length region of the core, as shown in Fig. 5.10(b). The core of the drawn SCF was measured at Ø6.0 µm which gives a draw-down ratio of 0.0253, equating to this 465 µm region becoming

(a)   (b)
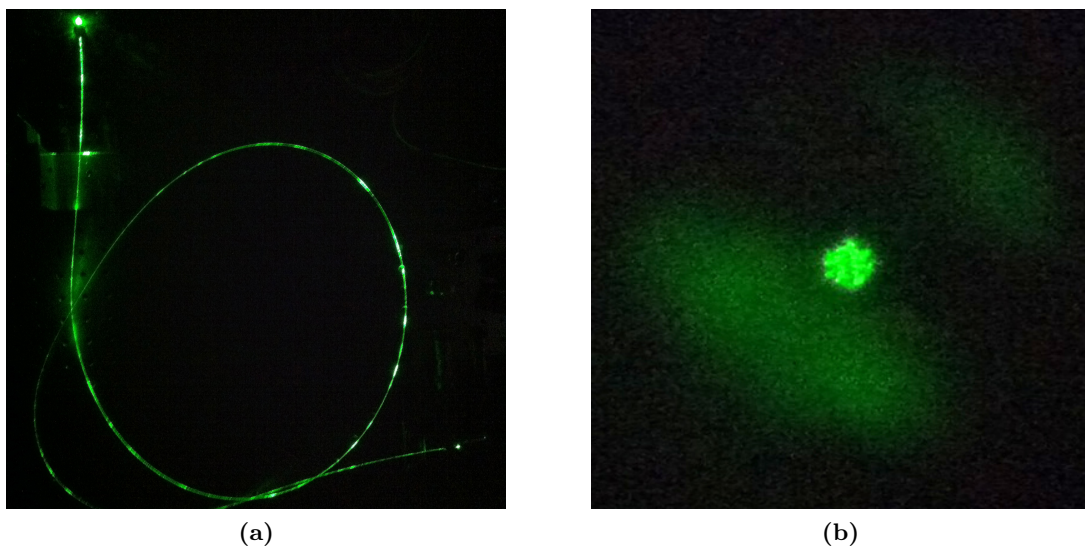
Figure 5.9 – (a) Photograph showing loss centres and (b) far field image of transmission from coupled PMMA SCF.

18.4 m long. Hence, assuming an approximate even length distribution of the bubbles, this equates to a bubble being spaced every ∼1.53 m which is close to the observed catastrophic loss centre spacing in the fibre. This shows that the catastrophic loss centres can be attributed to these air bubble imperfections in the fibre core which would be causing loss due to light scattering. It is not clear why these bubbles form during the process. One possible explanation could be that there is still some residual moisture remaining in the material after drying. The elimination of these bubbles would be required to achieve long lengths of fibre without catastrophic loss centres.

A UV-Vis spectrum of the extruded PMMA preform was obtained and compared to the bulk material billet, shown in Fig. 5.11. This result shows that the extrusion has three times the loss, compared to the bulk material in the region 400–600 nm. Clusters of bubbles along with some other artefacts were observed at ×10 and ×20 magnification on the surface of the extrusion, although none were found within the material bulk. Bubbles may have still been present within the material bulk, since there was a limitation of only being able to view inside the extrusion with ×10 magnification due to its size. Hence, the additional loss of the extruded preform, shown in Fig. 5.11, might also be due to the additional loss scattering centres generated by small air bubbles.

(a)   (b)
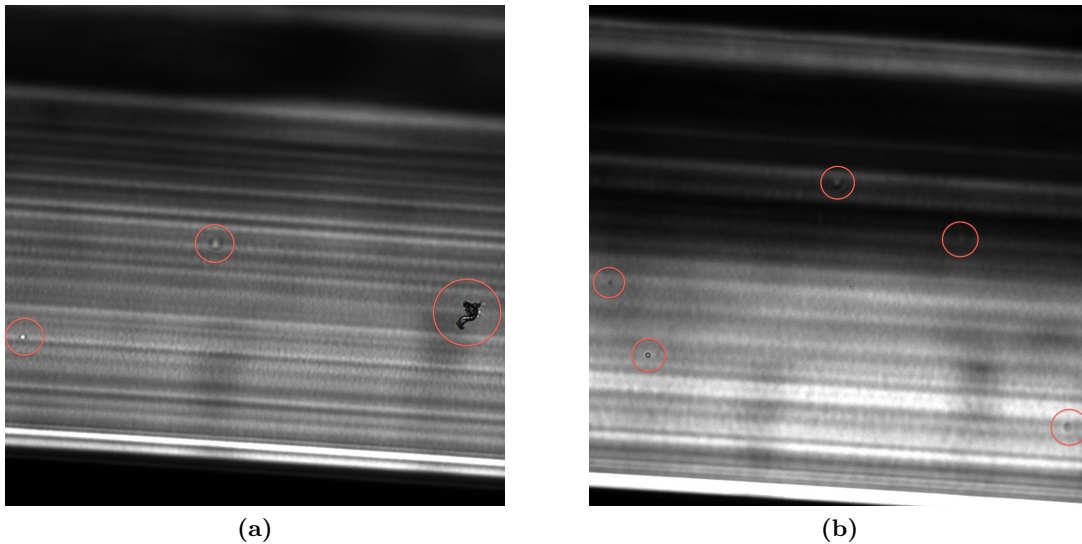
Figure 5.10 – Microscope images of loss centres (shown by ◯ – red circles) in the core (∅237 μm) of the PMMA cane at ×20 magnification, where (a) shows a region of the cane with loss centres, and (b) shows a 465 μm long region where 12 ∅4 μm bubbles were counted.
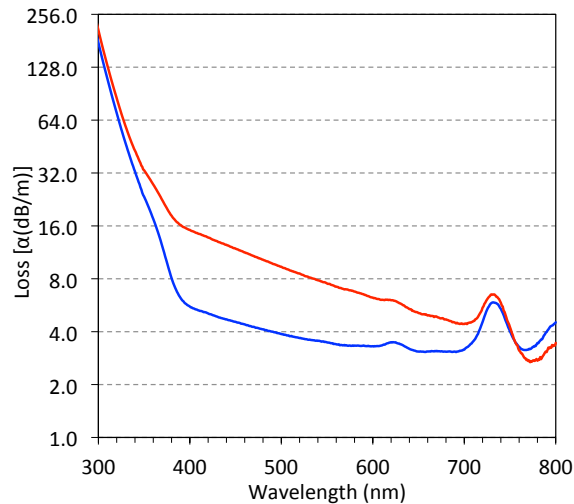
Figure 5.11 – UV-Vis loss of (■ – blue) as supplied extruded PMMA billet and (■ – red) after extruding material to a ⌀10 mm rod.

5.5.2   Silica Suspended-core MOFs Loss

To assess the light guiding properties of the silica fibres produced, cut-back measurements were performed. After fabrication, the fibres discussed in the last chapter were stored in the laboratory, exposed to air, on a high density PU foam drum with 1 m circumference. Comparison of broadband loss (400 – 1750 nm) from SCFs drawn using LWQ and F300HQ with similar geometries being produced with similar draw parameters; such as viscosity and pressure (SCFs shown on pages 85 and 86) are shown by the green and blue spectra in Fig. 5.12 respectively. While the loss of these SCFs
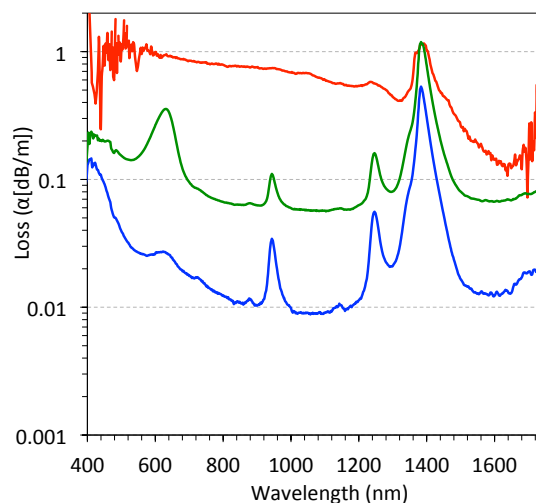
Figure 5.12 – Cutback loss measurements of SCFs drawn using (■ – green) LWQ material (see page 85) using 31 m length with ⌀7.5 μm core, (■ – blue) F300HQ material (see page 86) using 54 m length with ⌀7.5 μm core, and (■ – red) small core (⌀1.7 μm) F300HQ (see page 96) using 9 m length.

are extremely low for a MOF, the overall loss of the SCF produced using LWQ material (0.057 dB/m at 1064 nm) is more than six times higher than the fibre produced using F300HQ (0.009 dB/m at 1064 nm). This higher loss of the LWQ SCF is expected, since LWQ material is produced from mineral quartz whereas the F300HQ material is produced from synthetic fused silica [157]. The presence of OH^- within the fibres causes an increase in attenuation at 950, 1244, and 1383 nm wavelengths. These ions occur in the glass because water molecules enter the material through a chemical reaction during the manufacturing process or environmental humidity [190]. This loss in optical fibres due to OH^- groups is known as the water peak absorption areas. In addition, the increased attenuation at 635 nm is caused when rapidly cooled silica has strained bonds, which can be cleaved upon ionising radiation to form non-bridging oxygen hole centres (NBOHC) [191].

The red loss spectra in Fig. 5.12 is from cut-back measurements of the small core (Ø1.7 µm) SCF shown on page 96. Although the loss of this fibre is nearly two orders of magnitude higher than the SCF produced with a Ø7.5 µm core size using the same F300HQ material. This greater PF means that more of the propagating light interacts with small imperfections on the core surface, which leads to an increase in scattering loss [124]. Section 2.3.4 included more discussion about field distribution of the guided modes, and Sec. 5.9 shows that the preform etching is likely to be the dominant cause.

5.5.3   Silica Exposed-Core MOF Loss

After fabrication, the large core (Ø10 µm, page 98) ECF was stored in the laboratory, exposed to air, on a high density PU foam drum with 1 m circumference. While the fibre was on the drum, cutback fibre loss measurements were performed by coupling the light from a 100 W halogen light bulb source with power curve of approximately Gaussian distribution and peak power at 800 nm, into one end of the ECF. At the other end, the light from the core was imaged onto the grating of the Ando AQ6315E OSA such that the power was maximised before each measurement. The fibre loss measurement results taken directly after fibre draw, shown by the red spectrum in Fig. 5.13(a), were 1.12±0.15 dB/m, 1.10±0.08 dB/m and 1.43±0.39 dB/m at 532 nm, 900 nm and 1550 nm respectively. Further work is required to determine the cause of the increased loss at longer wavelengths. For another fibre loss measurement taken 26 days after fibre draw,
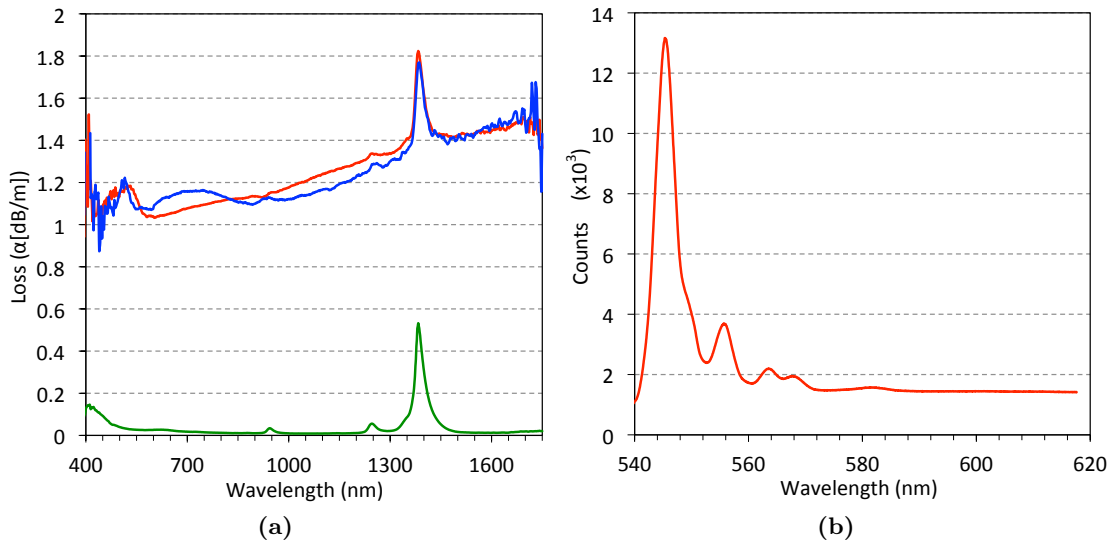
Figure 5.13 – (a) Loss of silica ECF, broadband cutback measurements taken 26 days apart (▌ – red & ▌ – blue) compared to silica SCF with similar core size (▌ – green) ; and, (b) fibre Raman peaks at 532 nm.

shown by the blue spectrum in Fig. 5.13(a), the results were observed to be the same within a 95% confidence interval. As a comparison, the fibre loss measurement results for the SCF (Fig. 5.12(blue)) produced in the same way, with material from the same bulk stock, and with similar core, web and hole sizes as for the ECF, is shown by the green spectrum in Fig. 5.13(a). This SCF result, being ∼2 orders of magnitude lower compared to the ECF, shows that confinement loss is negligible in the total loss of the ECF, and therefore additional surface scattering loss, either from the process of cutting the slot, airborne particulates depositing on the surface of the core [188] before or after fibre drawing, or the etching process when preparing the preform is the most likely dominant cause of the additional loss (see Sec. 5.9). For ECFs previously produced in F2 [134] (n ∼1.62) with a core size of ∼ Ø3 µm, the fibre loss measurements taken directly after fibre draw were 5.54±0.20 dB/m, 2.25±0.26 dB/m and 2.50±0.34 dB/m at 532 nm, 900 nm and 1550 nm respectively.

5.6 Silica ECF Fluorescence

Another factor which can restrict the detection limit of a fibre optic sensor is the amount of Raman and fluorescence peaks generated within the glass [121] which depends on the wavelength and power of the light source. Given enough power and with a sensitive enough detector, the Raman spectrum corresponding to the energy of the probed vibrational modes of the silica is expected, whereas fluorescence is an indication

of impurities and/or structural defects within the silica material. To detect the Raman and any potential fluorescence peaks, a 25 mW laser excitation light source at commonly used 532 nm was coupled into a 1 m long exposed-core fibre using a $60\times$ objective via a dichroic mirror. The signal collected from the fibre was imaged using the same objective, passed through the dichroic mirror and filtered using a 532 nm long pass filter, and measured using a Horiba iHR550 Imaging Spectrometer with Synapse CCD Detector. The peaks observed at 545 nm, 550 nm, 555 nm, 562 nm, 566 nm and 580 nm, shown in Fig. 5.13(b), correspond to well known Raman peaks of silica at $490\,\mathrm{cm}^{-1}$, $605\,\mathrm{cm}^{-1}$, $800\,\mathrm{cm}^{-1}$, $1050\,\mathrm{cm}^{-1}$, $1190\,\mathrm{cm}^{-1}$ and $1600\,\mathrm{cm}^{-1}$ respectively, previously used for sensing applications [192]. The absence of any fluorescence peaks shows that the silica material has negligible fluorescence at 532 nm for the excitation power and detector sensitivity used. For fluorescence or Raman spectroscopy sensing applications these peaks generated within the glass might affect the detection limit, depending on the excitation and emission wavelengths of interest.

5.7 Environmental Stability of Silica Exposed-Core MOF

In previous studies, for the ECFs produced using F2 [134, 139] with a $\sim \varnothing 3\,\mu\mathrm{m}$ core, it was found that the fibre loss increased by $0.4\pm0.048\,\mathrm{dBm}^{-1}\mathrm{day}^{-1}$, even when stored in a dry nitrogen filled environment. It is thought that this deterioration in the transmission properties of the fibre occurs due to changes in the properties at the core surface, such as particulate deposits [188], micro-fracturing [186] and/or increased roughness [187] induced by exposure to the environment. Since the deterioration found in the F2 ECFs was rapid, it could easily be measured by comparing standard cutback loss measurements over time. However, as shown in the previous section no loss was observed after 26 days for the silica exposed-core fibre.

To measure the exposure induced deterioration in the transmission properties of the silica ECF, a length of fibre was setup as described Sec. 5.2. Instead of performing cutbacks, the transmitted power spectrum, in dBm, was recorded from 350–1750 nm every two minutes. With the fibre in air, this setup was left for 15 hrs so that the measured power stabilised to within $\pm0.05\,\mathrm{dBm}$, then used to take time based measures of the power. Changes over time in the transmission characteristics can be fitted to Eq. (35), where ξ is the loss in dB/day. An assumption for these measurements is that

the deterioration measured comes from changes along the ECF length, not just the cleaved ends of the fibre, as the area exposed along the length is much greater than the area at the ends. As a sanity check, a laboratory-grade patch cord optical fibre assembly was setup in the same way, to ensure that the measured losses were not coming from the light source or other parts of the setup; where no deterioration was detected.

The result of ξ_λ (Eq. (35)) for a 4.2 m length of the ECF exposed to air for 180 hrs is shown in Fig. 5.14(a), where the 95% CI is also shown in black. This result shows that there is a sharp loss peak at 515 nm, equivalent to $0.043\,\mathrm{dBm^{-1}day^{-1}}$, and a broad loss from $\sim$450 nm to $\sim$900 nm with a peak of $0.023\,\mathrm{dBm^{-1}day^{-1}}$. At wavelengths $\sim$900 nm to $\sim$1340 nm the loss is at $\sim$0.0043 $\mathrm{dBm^{-1}day^{-1}}$, and drops below the detection limit of the experiment for wavelengths $> \sim$1340 nm. The air exposure induced deterioration in the transmission properties of the silica ECF is lower than the CIs for cutback measurements, as shown in Fig. 5.13(a), and $\sim$2 orders of magnitude better than for the previously reported ECFs produced in F2.

This measurement was repeated for a 1 m length of the silica ECF with a 8 cm centrally located section of the fibre submersed in Milli-Q water, shown in Fig. 5.14(b), where the transmission properties of the fibre is reduced by $\sim$0.067 $\mathrm{dBm^{-1}day^{-1}}$ for wavelengths shorter than 1450 nm. When this was repeated with methanol, it was observed that the transmission properties of the silica ECF was significantly affected across
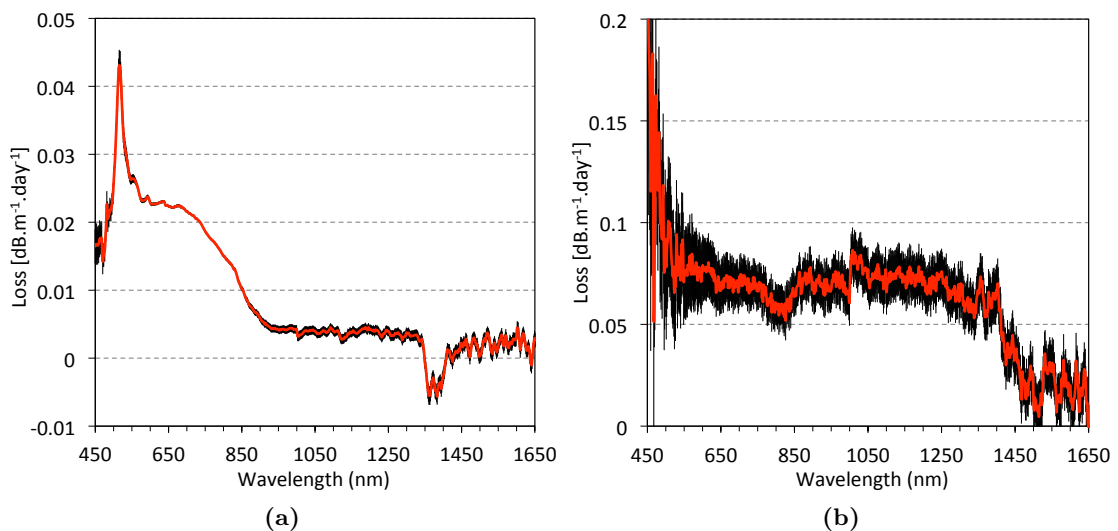
Figure 5.14 – Deterioration in the transmission properties of the silica ECF when exposed to (a) air; and, (b) water. The 95% confidence interval is shown in black.

all the measured wavelengths (350–1750 nm), at a rate of 12.8–$16.8\,\mathrm{dBm}^{-1}\mathrm{hr}^{-1}$. This deterioration in the transmission properties is expected to come from changes in the mechanical and/or compositional characteristics at the core surface, causing light scattering effects.

5.8 Surface Measurements

The silica ECF serves as a useful platform for understanding the causes of deterioration in the transmission properties, providing access to the core for post exposure surface analysis. To determine the differences between the mechanical and compositional characteristics of the exposed core surfaces, a NT-MDT Ntegra Solaris atomic force microscopy (AFM) + near-field scanning optical microscope (SNOM) with Smena head for tapping mode atomic force microscopy (TMAFM) measurements was used. Initial broad area surface profile measurements were also taken using a ContourGT-K1 (Fig. 5.15(a)–(b)) coherence scanning interferometry (CSI). The CSI measures the intensity of the light as the interferometic objective is actuated in the vertical direction (z–axis) and finds the interference maximum. Each pixel of the sensor measures the intensity of the light and the fringe envelope obtained is used to calculate the position of the surface, as shown in Fig. 5.15(b).
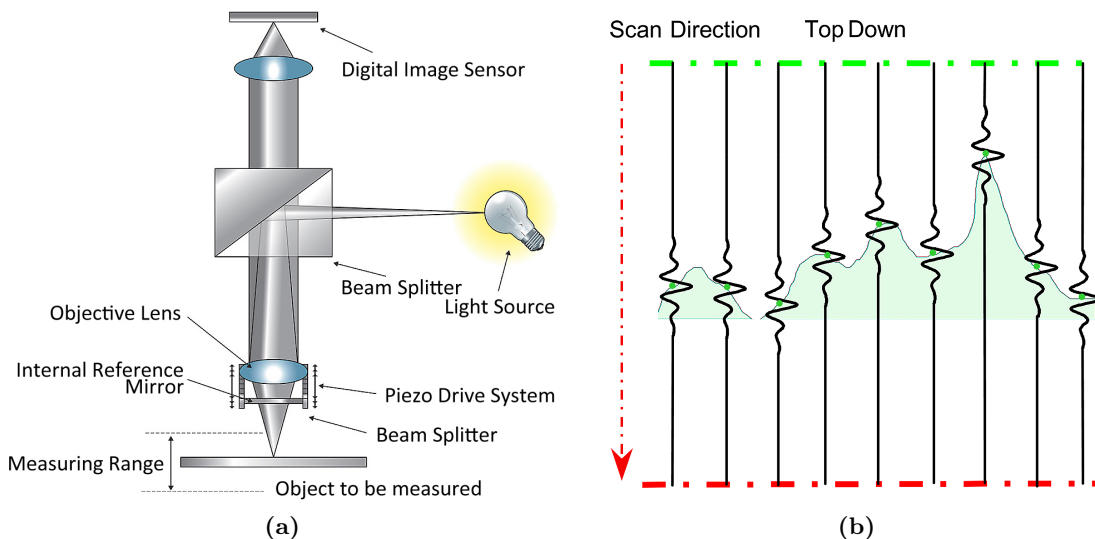
Figure 5.15 – (a) Schematic of CSI; and (b) CSI measures the intensity of the light as the interferometic objective is actuated in the vertical direction (z–axis) and finds the interference maximum. (from Ref. [193])
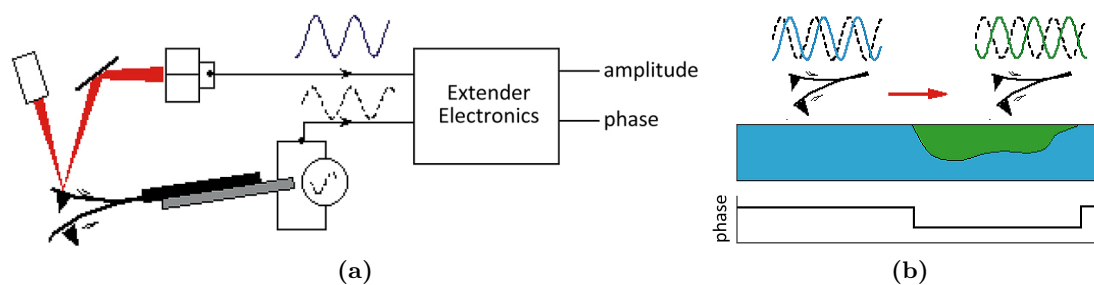
Figure 5.16 – TMAFM schematics where (a) shows the topology measure scheme and (b) shows the phase shift measure scheme which can be thought of as a delay in the oscillation of the cantilever as is moves up and down in and out of contact with the sample.

Nanometer-scale topographical and phase mapping of the ECF core surfaces was performed using a TMAFM, as shown in Fig. 5.16(a). As the tip is brought close to the sample surface, the vibrational characteristics (i.e., the force constant, resonance frequency, phase angle, and amplitude) of the cantilever change due to the tip-sample interaction and any contamination layer on the sample surface.

In TMAFM a surface region of larger amplitude damping is recorded as being higher in topography, and the phase refers to the phase shift which can be thought of as a delay in the oscillation of the cantilever as is moves up and down in and out of contact with the sample, as shown in Fig. 5.16(b). This means that the phase is really a measure of the energy dissipation involved in the contact between the tip and the sample, which depends on a number of factors, including such features as variations in composition, hardness, adhesion, friction, viscoelasticity and also contact area. Therefore, as the contact area is dependent on the slope of the sample, the phase image can also contain some topographic contributions. Understanding of the contribution of the individual factors to the phase shift is not simple, and it is a crucial issue of TMAFM studies how one can relate the contrasts of height and phase images recorded, to physical properties of samples. Despite the complications involved in interpretation, phase contrast is a commonly used technique for mechanical and composition characterisation of sample surfaces.

5.8.1   Surface Mechanical and Compositional Characteristics

Figures 5.17(a–c),(d–f) and (g–i) show the TMAFM phase and topology results of a
$25\,\mu m \times 25\,\mu m$ section across the core for the ECF exposed to air for 19 days, Milli-
Q water for 72 hrs and methanol for 2 hrs respectively. For the core area exposed to
air, the nanometer scale spikes in the topology and phase shift suggest small hardened
impurities within the surface structure, while the bulk of the material is homogeneous
in composition with nanometer scale roughness. For the core exposed to water, large
peaks measuring $> 100\,nm$ in height and several microns across the surface suggest that
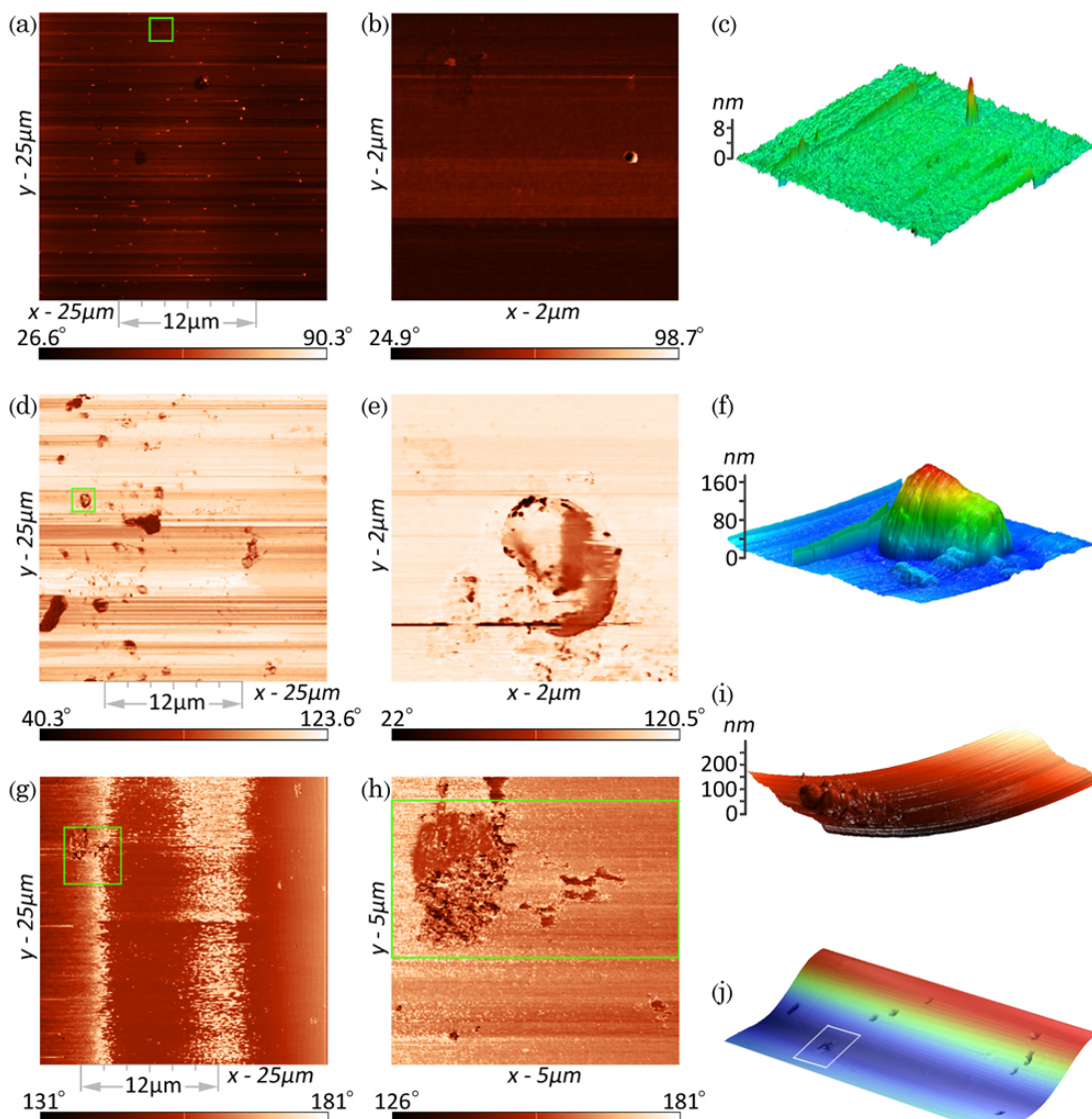
Figure 5.17 – TMAFM images of the ECFs exposed to (a–c) air, (d–f) water and (g–i) methanol with (j) a
CSI image along the methanol exposed core region. (a), (d) and (g) show the phase images
across the core region indicated by the 12 μm area on the x-axis, with [(b), (e) and (h)
respectively] enlarged phase images of the area shown by the green box; and, (c), (f) and (i)
showing their respective topologies.

impurities from the water have been deposited onto the core. The darkest areas in the phase image show up on the topology to be slightly lower than the surrounding bulk, which may also be an indication of surface damage such as micro-fracturing [186]. The results for the core exposed to methanol shows micron scale areas with large phase shifts where the topology image indicates an increase in height. The methanol exposed-core area was further investigated using a CSI, shown in Fig. 5.17(j), which indicates micrometer scale pitted sections along the core instead of the increase in height observed by the TMAFM. It is known that topology height reversal can occur for AFM images when the tip is strongly affected by capillary forces and also by tip-sample van der Waals attraction [194]. In this interaction regime, the phase shift shows to be more negative on more hydrophilic regions, and suggests pitting or micro-fracturing of the methanol exposed sample, which is confirmed by the CSI results.

5.8.2   Exposed-Core MOF in Saturated Salt Solution

Another experiment, exposing the fibre to a saturated salt solution was also performed to determine the effect that the salt might have on the deterioration of the transmission properties of the ECF when being tested in a salt spray chamber. Figure 5.18(a) shows the deterioration of the transmission properties of the fibre at one of the wavelengths (1445 nm) while submersed in a saturated sodium chloride (NaCl) solution. The black dots of Fig. 5.18(a) are measurements of the power
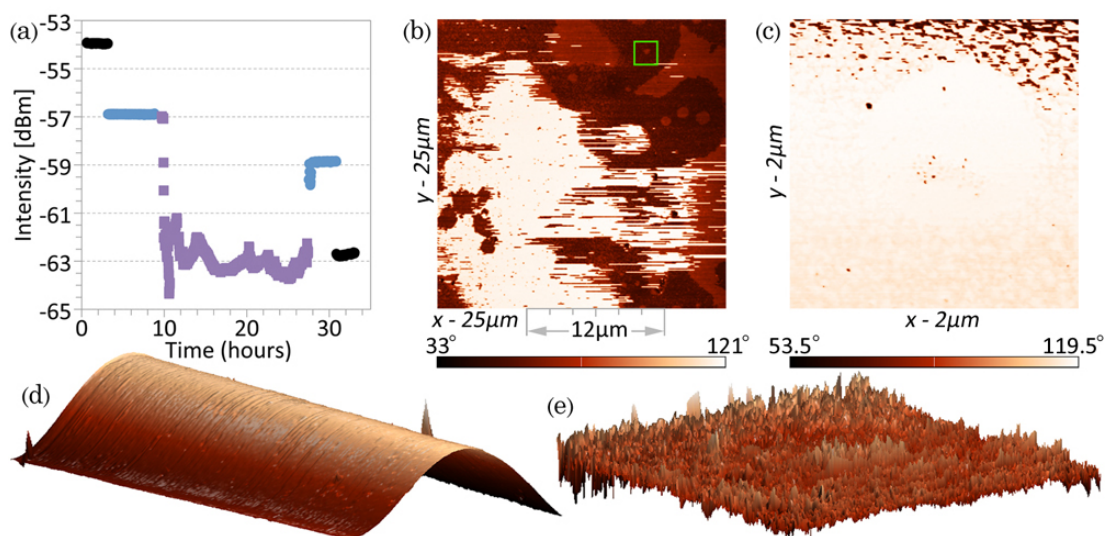
Figure 5.18 – Results of exposed-core MOF, where an 8 cm section has been submersed in saturated NaCl solution. (a) Shows the measured power over time; (b) shows the phase image across the core region indicated by the 12 µm area on the x-axis, with (c) being an enlarged phase image of the area shown by the green box; and, (d) and (e) showing their respective topologies.

in air, the blue dots are the measured power in water and the square violet dots are the measured power while an 8 cm section was submersed in the saturated salt solution.

These results show that for the first few minutes the power remained close to what was measured in water, the transmission characteristics then quickly declined and became erratic for the remaining time in the NaCl solution. When the fibre was placed back in water, the transmitted power increased and settled about 2 dBm below the power level measured before the NaCl solution experiment, and reduced a further 4 dBm when the fibre was removed from the water and allowed to dry. This erratic transmission behaviour of the fibre submersed in the NaCl solution is likely to be caused by salt crystals, which could form as a result of capillary action combined with evaporation where the fibre enters and exits the solution. Figure 5.19 shows how salt crystals formed along the fibre at these two interfaces.

The TMAFM phase image of a $25\,\mu m \times 25\,\mu m$ section across the core is shown in Fig. 5.18(b), where the core area is indicated by the 12 µm area on the x–axis. In this image the total phase difference is 88°. The streaking of the image at 121° might be an indication that loose particles are interfering with the tip during the measurement, and with subsequent attempts the streaking became more apparent. The surface topology along the 12 µm core area shows a surface with nano scale structure and only a couple of larger 180 nm spikes. Also, the phase image (Fig. 5.18(c)) of the $2\,\mu m^2$ region shown by the green square in Fig. 5.18(b), shows the majority of the area to have the same
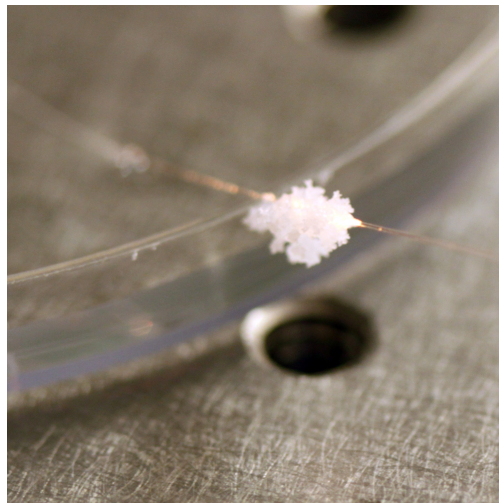
Figure 5.19 – Salt crystallisation on fibre due to capillary action from the saturated NaCl solution.

phase characteristics with only a few small areas, measuring tens of nanometers, having large phase shifts of 66°. The topology of this area, shown in Fig. 5.18(e), indicates nano scale (±1.5 nm) rough structure. These results seem to indicate that something has accumulated on the surface, which is probably the NaCl, and it is not clear if the silica has been damaged in any way.

5.9 Characterisation of Preform Etching

The cut-back measurements of the ECF, shown in Fig. 5.13, has orders of magnitude greater loss compared to the SCFs initially produced (shown in Fig. 5.12). It was thought that the method of BHF etching used could have effected the loss by changes to roughness and composition at the preform surface which might led to scattering centres. To understand the effect of BHF etching, a small drilled section of the preform was cut in half along its length, and both halves were sonic cleaned in methanol and then Milli-Q water. One of these halves was then etched for 30 minutes using the process described for etching silica preforms, and cleaned again in methanol and Milli-Q water. These two halves were mounted on a glass slide (shown in Fig. 5.20) so the surface topology of the drilled holes of both samples could be measured using the CSI surface profiler. The un-etched sample showed an root mean square (RMS) surface roughness of $\sim$1.5 µm, with some larger grooves perpendicular to the hole, as shown in Fig. 5.21(a). The surface of the etched sample had become microporous (Fig. 5.21(b)), where the material was removed by the etching process in a random pattern with $\sim$ 7.5 µm features. An inkblot test on the etched surface also confirmed the porous nature, as the ink spread due to capillary action.

Another ECF was produced from an initial 20 mm diameter silica rod, where the
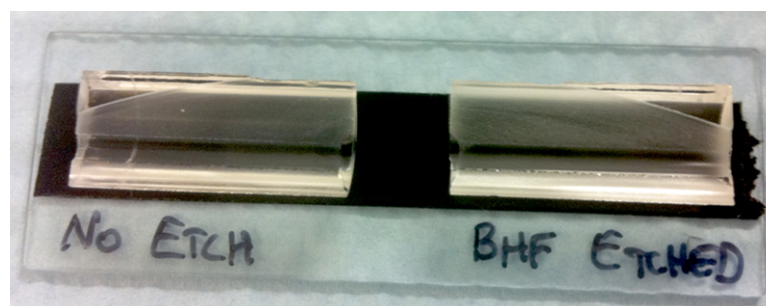
Figure 5.20 – Samples measured to understand the affect of the BHF etch.
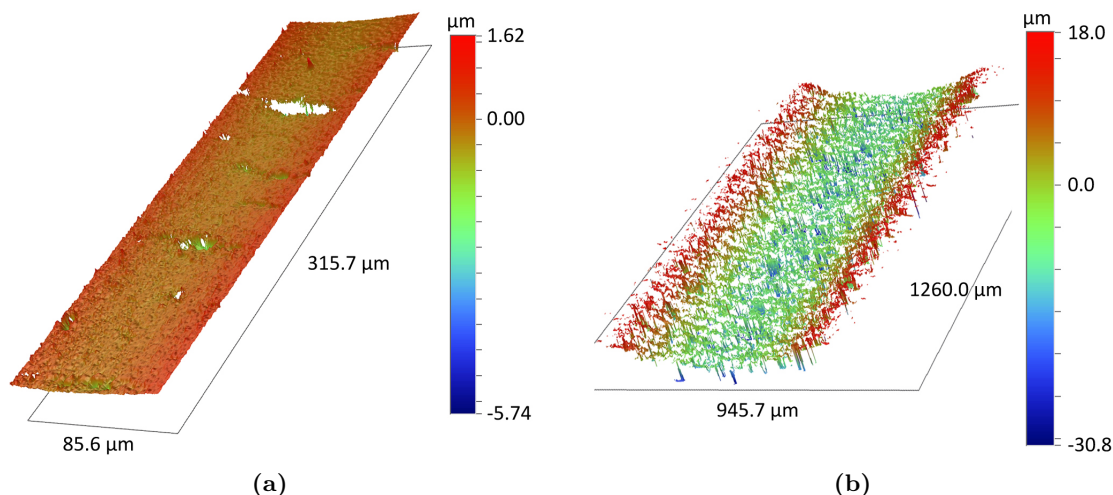
Figure 5.21 – CSI surface topology profiles of (a) un-etched sample with surface roughness of ∼1.5 μm plus some larger grooves; and (b) the microporous BHF etched sample.

preform was cleaned by submersion in 70% nitric acid instead of using the BHF etch method described earlier. The geometry and loss of this ECF is shown in Figs. 5.22(a) and 5.22(b) respectively. This result shows more than an order of magnitude less loss than the previously produced ECF. This shows that the higher loss of the preciously produced etched ECF is likely to have been caused by the etching process. The nanometer scale spikes shown in Figs. 5.17(a–c) are likely to have been caused by particles becoming trapped on the surface of the preform during the draw process, because of the rough porous nature of the etched exposed core. This type of loss was not experienced
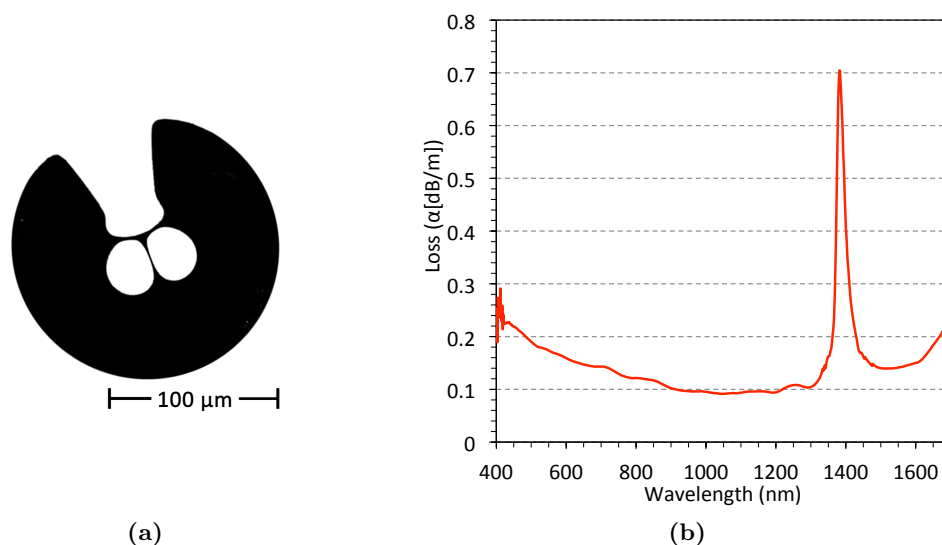
Figure 5.22 – (a) Contrast enhanced SEM image of (silica material shown in black) F300HQ ECF cross section with 7.5 μm effective core diameter and 160 μm outside diameter, and (b) loss (cutback) measurement of this fibre.

by the etched enclosed SCF, having a similar core size to the ECF, which is an indication that the surface was protected from particulate contamination of the surface during the draw process. This lower loss has the potential to increase the OTDR distributed sensing range, as discussed in Sec. 2.3.2. At this 0.1–0.15 dB/m loss level the achievable distributed sensing range would be about $80-100$ m at SNR of 30.

5.10 Evanescent Field Spectroscopy

In Sec. 5.1, Eq. (33) describes the power at a particular wavelength (P_λ) at an axial light propagation distance (z) along a fibre, which can be rewritten as,

$$P_\lambda(z) = P_{\lambda,0} \cdot e^{-\alpha \cdot z} \tag{40}$$

where $P_{\lambda,0}$ is the initial input power, and α is the absorption coefficient in dBm^{-1} of the fibre. This absorption coefficient (α) is made up of absorption of the light propagating inside the silica core and the light propagating outside the core (the PF).

Taking a reference absorption measurement of the fibre, without the presence of the analyte of interest,

$$P_{\lambda,1}(z) = P_{\lambda,0} \cdot e^{-\alpha_1 \cdot z} \tag{41}$$

and comparing this to the absorption measurement of the fibre in the presence of the analyte (assuming the initial power remains the same),

$$P_{\lambda,2}(z) = P_{\lambda,0} \cdot e^{-(\alpha_1 + \alpha_\mathrm{a} \cdot P_\mathrm{f})z} = P_{\lambda,0} \cdot e^{-\alpha_1 \cdot z - \alpha_\mathrm{a} \cdot z \cdot P_\mathrm{f}} \tag{42}$$

where α_a is the analyte absorption coefficient and P_f is the power fraction in the analyte, then with Eqs. (41) and (42).

$$\frac{P_{\lambda,1}(z)}{P_{\lambda,2}(z)} = \frac{P_{\lambda,0} \cdot e^{-\alpha_1 \cdot z}}{P_{\lambda,0} \cdot e^{-\alpha_1 \cdot z - \alpha_\mathrm{a} \cdot z \cdot P_\mathrm{f}}} = \frac{\cancel{P_{\lambda,0}} \cdot \cancel{e^{-\alpha_1 z}}}{\cancel{P_{\lambda,0}} \cdot \cancel{e^{-\alpha_1 z}} \cdot e^{-\alpha_\mathrm{a} \cdot z \cdot P_\mathrm{f}}} = \frac{1}{e^{-\alpha_\mathrm{a} \cdot z \cdot P_\mathrm{f}}} \tag{43}$$

$$\therefore \quad \frac{P_{\lambda,2}(z)}{P_{\lambda,1}(z)} = e^{-\alpha_\mathrm{a} \cdot z \cdot P_\mathrm{f}} \qquad \therefore \quad \ln\left(\frac{P_2}{P_1}\right) = -\alpha_\mathrm{a} \cdot z \cdot P_\mathrm{f} \tag{44}$$

we get the power fraction as,

$$P_{\mathrm{f}} = \frac{-1}{\alpha_{\mathrm{a}} \cdot z} \cdot \ln\left(\frac{P_2}{P_1}\right) \tag{45}$$

Equation (45) shows that the ECF can be used to measure the absorption characteristics of an analyte using the PF, and if the absorption coefficient of the analyte is known then the PF can be calculated. This is particularly useful for understanding how much of the transmitted light is available for interacting with the analyte, and a way of experimentally validating calculated field distributions (also see Appendix J).

5.10.1   Evanescent Field Absorption of Water

Since the wavelength dependant absorption coefficient of water is well documented [195], water was chosen for an initial absorption measurement using the ECF, to test the ability for evanescent field absorption spectroscopy. Broadband light was coupled to the ECF core, as discussed in Sec. 5.1, and the transmitted power in dBm was measured ten times from 400 nm to 1750 nm in 1.35 nm increments. The transmitted power was then measured ten times with an 8 cm section of the fibre submersed into MilliQ water. The average of each of these ten measurements was calculated for each of the measured wavelengths, where the difference of these averages is shown by the red spectra in Fig. 5.23. The result of this absorption measurement clearly shows the 1445 nm absorption peak expected for pure water. The blue spectra shown in Fig. 5.23 is the known water absorption from Pope *et al.* [195]. There is a clear discrepancy of 2–3 dB/m
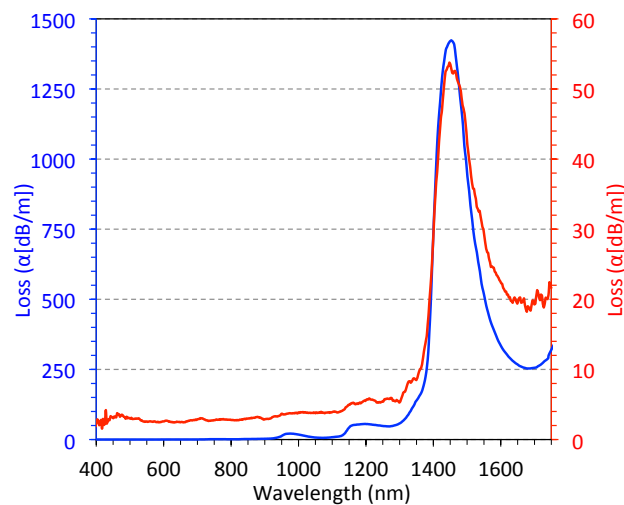
Figure 5.23 – The result when using the silica ECF (10 µm core) as a evanescent field spectroscopy sensor in water (▌ – red), compared to the published absorption of water from Ref. [195] (▌ – blue).

across all the lower wavelengths. This discrepancy is most likely due to the change in refractive index, and therefore PF, because the transmitted powers were taken initially in air and then in water. Nevertheless, the power faction can be approximated at the 1445 nm water peak, since this discrepancy of a few dB/m is negligible. The ratio between the ECF result and published absorption results shows that the evanescent field PF of the exposed part of the fibre is $\sim 3.5\%$ in water.

5.10.2   Evanescent Field Fluorescence Measurements

Rhodamine B in solution was used to test the ability to use the silica ECF for measuring recaptured fluorescence propagating in the backward direction from fluorophores surrounding the core. While Rhodamine B does not complex with ions, it is an efficient fluorescent dye that fluoresces strongly at ~ 583 nm (max) when excited around 562 nm (max) in water [196], and therefore useful for initial characterisation. To do this, a 532 nm laser excitation light source was coupled into the fibre using a $60\times$ objective via a dichroic mirror. The fluorescence signal collected from the fibre was imaged using the same objective, passed through the dichroic mirror and filtered using a 532 nm long pass filter, and measured using a Horiba iHR550 Imaging Spectrometer with Synapse CCD Detector, as shown in Fig. 5.24(a).
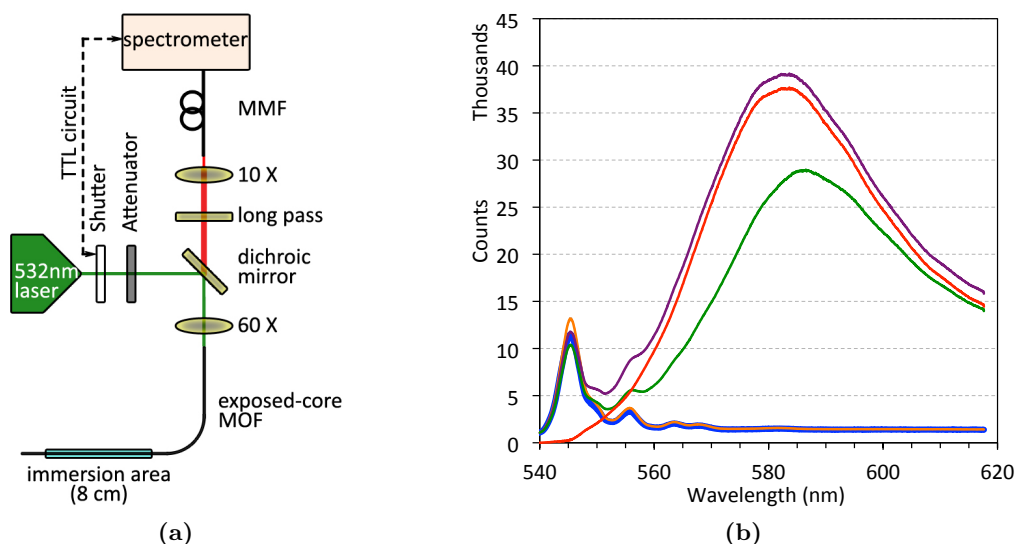
Figure 5.24 – (a) The setup used for ECF based back reflected fluorescence measurements. (b) Result of fluorescence experiment using Rhodamine B where the ▌ – orange and ▌ – blue curves are the background spectra of the fibre in air and fibre submersed in water respectively. The ▌ – violet and ▌ – green curves are the spectra when the fibre is submersed in 1 μM and 10 μM solution of Rhodamine B respectively. The ▌ – red curve shows the water background subtracted result of 1 μM Rhodamine B.

The results of the fluorescence experiment are shown in Fig. 5.24(b), where the background spectra of the fibre in air and the fibre submersed in water are shown by the orange and blue curves respectively. These background peaks are characteristic of Raman from the silica. The Rhodamine B was then added to the water to achieve a 1 µM solution of Rhodamine B, which is shown by the violet curve. The solution was then increased to 10 µM, shown by the green curve, where the fluorescence signal was lower with the higher concentration. This reduction in fluorescence signal was also seen for subsequent increase in concentration to 100 µM and 1 mM. Reduction in the measured fluorescence intensity with higher concentrations suggests that fluorescence quenching of the Rhodamine B is occurring [197].

5.11   Summary and Conclusions

Characterisation in terms of transmission and environmental stability of the fabricated polymer and silica SCF and ECFs were performed to understand if these fibres were suitable for distributed sensing in harsh environmental conditions. The methods used included; cut-back measurement to determine the fabricated fibre loss; measurement of the deterioration in transmission properties of the fibre over time; surface profiling of the preform and fibre core to ascertain the possible causes of the losses; and, measurement of the PF percentage as well as testing the ability for the silica ECF to recapture fluorescence using evanescent field PF excitation.

For the polymer SCF, it was found that there were catastrophic loss centres along the length of the fibre. These loss centres were investigated using a microscope, and were attributed to small air bubble imperfections in the fibre core which cause loss due to light scattering. Further investigation showed that small air bubbles were present in the extrusion, and that the extrusion had increased loss compared with the bulk material before extrusion. On the other hand, the silica SCF was found to have particularly good transmission properties, with loss as low as 9 dB/km at NIR wavelengths, which is extremely low for a MOF. While the loss of the first silica ECF produced was found to be 2–5 times better than ECFs previously produced using F2, the loss was still ∼2 orders of magnitude higher than the silica SCFs. This additional loss for the silica ECF compared to the SCF was investigated and found to be attributed to the BHF cleaning method used on the preform before drawing to fibre. This BHF cleaning method

does not etch the silica surface smoothly, but instead causes the surface to become microporous which is likely to have trapped particulates on the surface of the ECF core during the draw process. When another silica ECF was drawn from a preform that was cleaned using nitric acid instead of BHF, it was found to have an order of magnitude less loss compared to the first silica ECF produced, and at ~0.1 dB/m at NIR wavelength this loss is low enough to achieve distributed sensing over a distance of 80–100 m at SNR of 30.

Experiments to measure air exposure induced deterioration in the transmission properties showed the silica ECF had ~2 orders of magnitude less susceptibility in transmission loss over time compared with previously produced F2 ECFs. These measurements were also repeated with the silica ECF in methanol, water, and saturated salt solution. In all these cases, there was an increase in transmission loss over time compared to the air result and, for the water and saturated salt solution, this was attributed to particulates deposited on the core surface. For the methanol case, the TMAFM and CSI results indicated that the methanol causes pitting or micro-fracturing of the silica.

Evanescent field spectroscopy results using the silica ECF showed that in water there is ~3.5% PF at the exposed part of the fibre, which was used to excite fluorophores in solution and recapture the resulting fluorescence for measurement. This fluorescence measurement was done by coupling the excitation light source into the core at one end of the silica ECF and measuring the fibre collected fluorescence signal from the fibre core at the same end of the ECF. All of the results with the silica ECF showed potential towards the project aims of a fibre capable of distributed detection of corrosion within the harsh environment of an aircraft fuselage. Alternatively, the polymer fibre produced had substantial challenges to overcome in terms of fabrication and reducing loss. Therefore, the remainder of the project concentrated on further developing the silica ECF for corrosion sensing.

6

Functionalisation of Exposed-Core MOFs

"To raise new questions, new possibilities, to regard old problems from a new angle, requires creative imagination and marks real advance in science."

– Albert Einstein

To detect an analyte using light, it is necessary for the analyte to change the propagation characteristics of the light in a specific way that can be measured. While the most straightforward sensing architecture can be to make use of absorption or Raman spectroscopy techniques [198], as shown in the previous chapter, problems can occur when dealing with; mixtures with spectral overlap, analyte with weak or no determinable signals, and/or solution condition dependance. These problems can be overcome by using a sensor molecule (detector or probe) that specifically recognises the analyte of interest, and either uses the guided light to provide a detectable signal of the recognition event (such as fluorescence) or changes the properties of the medium through which the light is guided (such as refractive index). For the detection of Al^{3+}, as an indicator of aluminium corrosion, sensor molecules that fluoresce when complexed with the ion are available. The advantage of using such a fluorescent indicator is that they can be specific and sensitive to very low concentrations of Al^{3+}; for example detection of concentrations as low as 30 nM have been reported [199]. Although mixing sensor molecules with a sample is a simple method for the detection of analyte, it does not allow for the potential to use MOFs directly without the need for pre-mixing. To enable such direct sensing measurements, it is necessary to immobilise these sensor molecules on the surface of the MOF exposed core, which is known as surface functionalisation.

While silica ECFs offer advantages of lower loss, higher damage thresholds, easier cleaving (compared with polymer), and potential for integration with commercial interrogation devices [7], they do not allow for a sensing layer to be directly physisorbed

onto the surface. For glass MOFs it is necessary to use some initial chemical interactions often referred as covalent binding (also known as grafting) or physical interactions (adsorption, physisorption or chemisorption) between the core surface and deposited layers [198]. The choice of the surface functionalisation method is as important in defining sensing performance as the transduction mechanism being used, and dictated by the physical and chemical properties of both the core surface and the sensing layer to be deposited. Functionalisation methods traditionally used include silanes [3, 200, Appendix C] or polyelectrolytes [201, 202], which provide a functional group on the surface to which the sensor molecules can be covalently attached.

Some important factors to consider when choosing a functionalisation method are the conditions in which the sensor is to be used and any additional optical losses that might occur as a result. Polyelectrolytes have been found to wash off in acidic conditions [123], and so this method was not included in this study towards developing a robust optical fibre based distributed sensor capable of detecting corrosion in the structure of an aircraft. This is because of the acidic environment in the local of aluminium corrosion, as shown in Fig. 1.1. Another consideration is the use of fluorescent sensing molecules which form multiligand complexes, such as 8-HQ that forms an octahedral complex with Al^{3+} (Sec. 1.5.6), and the effect that restricting their mobility by covalently bonding to the core surface might have on their ability to form a complex. In this chapter, the fabricated silica ECFs are characterised in terms of fluorescence-based sensing using a covalent bonding functionalisation method. Also, the development of a new one step functionalisation process for optical fibre sensing applications, by applying thin film ($\sim$ 50 nm) PMMA doped with sensor molecules to a silica ECF, is described and compared to covalent bonding.

6.1   Fluorescent Indicators and Binding of Aluminium Ions

Reactions ligands with Al^{3+} are characterised by polymerisation, slow ligand exchange rates, and extensive hydrolysis in aqueous solution. Its preferred coordination number is 6, producing octahedral complexes. All metals and metal ions are Lewis acids (electron pair acceptors; electrophiles) that have incomplete valence electron shells. They complex with Lewis bases (electron pair donors; nucleophiles), which are therefore effective ligands, e.g. small molecules or ions that have at least one electron pair that can be

donated. Al^{3+} is the hardest trivalent metal ion (hard Lewis acid), and is highly electropositive, not easily polarised, and prefers to coordinate with hard Lewis bases that can donate electrons to its vacant electron orbitals. The most stable Al^{3+} complexes are with multi-dentate ligands with nitrogen or oxygen donors [203, 204]. The term denticity, from Latin for tooth, denotes the number of donor atoms the chelator uses in metal binding. The term chelator, from the Greek word for claw of a crab, refers to a compound that binds a metal ion through at least two functional groups, where each group donates a pair of electrons to form a heterocyclic ring encompassing the metal. To form a ring, the ligand must have at least two donor atoms. Chelators having hydroxy and azo groups that complex Al^{3+} have been used in the fluorometric detection of Al^{3+} [205, 206]. The following are examples of chelators possessing these groups, used to combine with the ECF for Al^{3+} detection.

6.1.1 8-hydroxyquinoline

8-hydroxyquinoline (8-HQ) is an aromatic nitrogen compound characterised by a double-ring structure, containing a benzene fused to pyridine at two adjacent carbon atoms, with the formula C_9H_7NO (Fig. 6.1(left)). This compound has a hydrogen atom that is replaceable by a metal, and gains its fluorescent nature by forming a dative bond between the metal and hetrocyclic nitrogen atom, enabling formation of a six-membered chelate ring with Al^{3+}. It is a bidentate ligand which forms stable multi-ligand complexes with several metal ions [207]. For example, metal ions with 2^+ charge form a bis[8-hydroxyquinoline]metal(II), whereas a 3^+ charge metal ion forms a tris[8-hydroxyquinoline]metal(III), as shown in Fig. 6.1 for the Al^{3+} case. The rigid octahedral complex that forms between three 8-HQ molecules and Al^{3+} fluoresces strongly at 516 nm
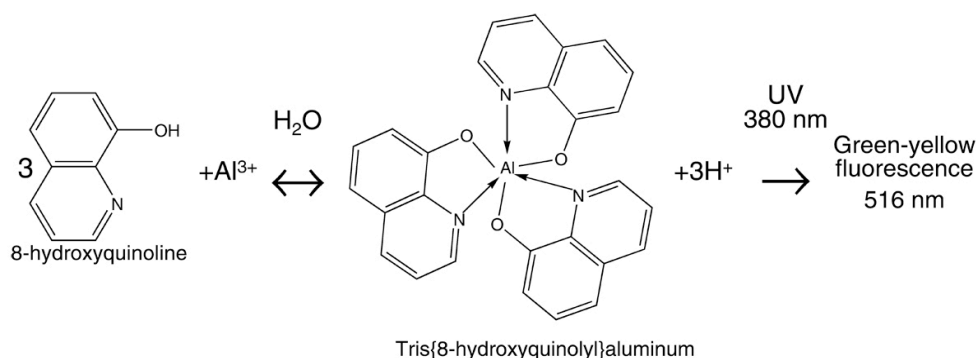
Figure 6.1 – Reaction sequence for 8-HQ with Al^{3+} from Ref. [14].

(max) when excited by UV light in the range 360 to 390 nm [208], although has also been shown to work effectively when using a 405 nm excitation light source [119].

6.1.2   Lumogallion

Lumogallion ($C_{12}H_9ClN_2O_6S$), shown in Fig. 6.2(a), has a specific reactivity to the trace amount of all inorganic aluminium, gallium, and niobium species [209] in wide pH range (from 2.0 to 5.7) and an extremely high stability constant when complexed with Al^{3+} (5.62×10^7) [210]. It has been reported that nM level detection of Al^{3+} in solution is possible using Lumogallion [211]. When not complexed, the molecule exhibits weak fluorescence at 567 nm (max) when excited at ~ 507 nm, and strongly fluorescent upon complexation (Fig. 6.2(a)). Lumogallion is a derivative of 2,2'-Dihydroxyazobenzene (i.e. includes sulfonic acid, chloro, and additional hydroxy groups), with which Al^{3+} can form a complex by replacing the hydrogen atoms of the hydroxy groups. When the Al-Lumogallion complex is formed, the increased rigidity reduces non-radiative losses and dative bonds with the nitrogen atoms induce molecular polarisation making the complex fluoresce strongly [212] when excited with green light.

To enable surface attachment, the derivative of Lumogallion with formula $C_{13}H_{10}N_2O_5$ (see Ref. [123]) was used, as shown in Fig. 6.2(b). This derivative contains a carboxyl moiety in place of the sulfonic acid of lumogallion to allow ready attachment to a glass surface. It also lacks the chloro substituent of lumogallion to improve the hydrophilicity of the molecule. This derivative of Lumogallion was produced by Dr Sabrina Heng at The University of Adelaide.
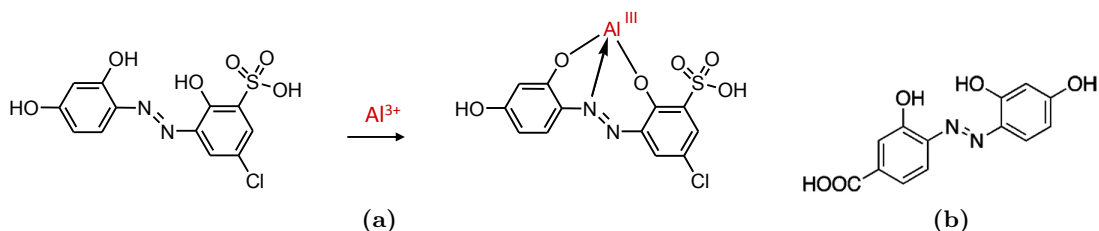
Figure 6.2 – (a) Reaction sequence for Lumogallion with Al^{3+} [123, 211], and (b) Lumogallion analog with carboxyl moiety functional group in place of the sulfonic acid for ready glass surface attachment.

6.1.3   Spirobenzopyran

A spiropyran appended with a crown ether (spirobenzopyran (SP)) allows photochromatic control between ion binding and non-ion binding states [213–216]. This type of sensing molecule can be reversibly photo-switched between ring-opened form, which is fluorescent when the metal ion is bound (Fig. 6.3(c)–(d)), and ring-closed form, which is non-fluorescent and doesn't bind to metal ions (Fig. 6.3(a)–(b)). Cations coordinated by the crown moiety of the ring-opened form are subject to intramolecular interactions with the merocyanine phenoxide anion, as shown in Fig. 6.3(c), inducing strong fluorescence at ~ 630 nm (max) when excited with ~ 532 nm. Isomerisation of the ring-closed form (spirocyclic isomer), as shown in Fig. 6.3(a)–(b), to ring-opened form (merocyanine isomer) occurs in dark conditions, but is promoted most strongly by the presence of UV light at $\lambda \approx 365$ nm. The cation-bound ring-opened form readily reverts to the ring-closed form on exposure to visible light, releasing the bound metal ion. This provides an opportunity to control Al^{3+} complexation, by simply irradiating with either UV or visible light. Weak background fluorescence from the ring-closed form, without
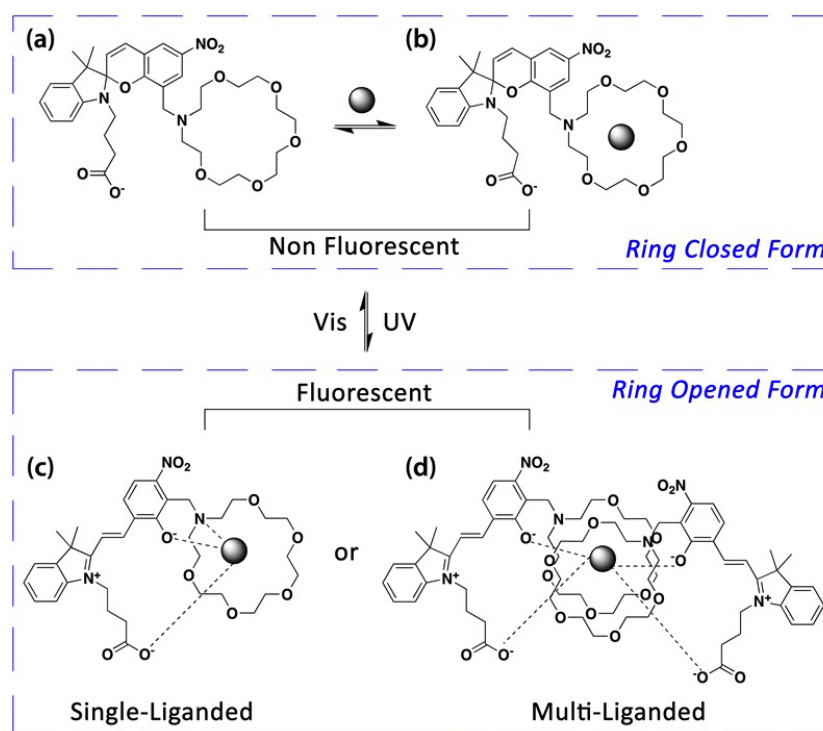
Figure 6.3 – Metal ion (M) interaction with spirobenzopyran (SP) according to the model proposed by Kimura *et al.* [215] Compound (b) represents the closed form of the SP–M complex prior to irradiation with UV light. Compounds (c) and (d) represent the opened and fluorescent form of the SP–M complexes (single- or multi- linganded versions respectively) after irradiation with UV light ($\lambda \approx 365$ nm).

the presence of cations, also provides a powerful self-indicating internal reference feature
for analytical measurements [217]. This is because change in fluorescence is due to
cations coordinated by the crown moiety.

Experiments involving SPs with several different size crown ether's, and therefore
binding affinities to cations other than Al^{3+} were tried before a suitable spiropyran
based sensing molecule for Al^{3+} was found. The spiropyran analog with 1-Aza-18-crown-
6 attached to the indolic nitrogen, as shown in Fig. 6.3(a), was found to multi-ligand
bind to Al^{3+} (Fig. 6.3(d)). To achieve this, a carboxylated chain was incorporated into
the sensor design as an additional binding site. All of these SP based sensing molecules
shown in the following experiments were produced by Dr Sabrina Heng at The University
of Adelaide.

6.2   Covalent Functionalisation

Covalent functionalisation refers to the creation of covalent bond between the glass core
surface and the sensing molecule to be immobilised. A popular way in achieving this is
to exploit OH^{-} on glass surfaces [200, 218, 219] (also polymers [220] and metals [221]).
Among the different attachment chemistries available shown in Fig. 6.4, which include
phosphonates, carboxylates, catechols, alkenes or alkynes, and amines, silanes are the
most popular. This is because the chemical modification is performed by a simple
reduction reaction followed by the widely used organosilane chemistry to introduce
diverse functional groups such as perfluoroalkyl, amino, and sulfhydryl for surface
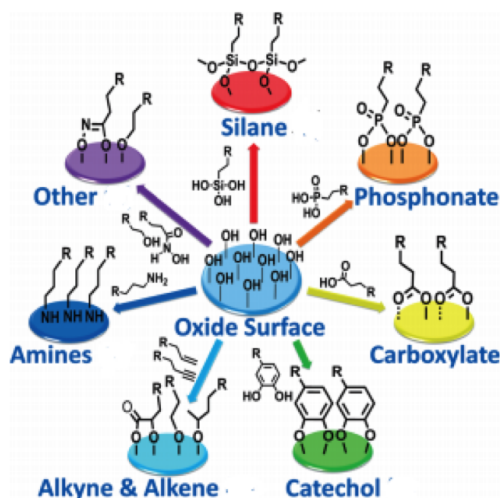
Figure 6.4 – Available surface modification processes for oxide surfaces, from Ref. [218]

passivation or further sensing molecule immobilisation.

The attachment mechanism of silane, shown in Fig. 6.5, relies first on the hydrolysis of the silane to be deposited by water molecules already adsorbed by the polar sensors surface which presents hydroxyl groups, creating the corresponding hydroxysilane. Hydrogen bonds are formed between the hydroxysilane and the surface hydroxyl groups while lateral reordering allows the formation of a single monolayer before the condensation between the Si-OH groups to form the stable Si-O-Si bonds. This is what should be happening in theory, however silanes are very sensitive to moisture which can strongly affect their ability to form a perfect monolayer. Depending on the deposition method and the moisture exposure during the coating process, cross linking between silanes can occur during the condensation phase, resulting in the creation of a network rather than a monolayer. Another factor which can influence the quality of the silane layer is the initial surface density of OH^- groups onto the sensor surface. A low surface density inevitably results in low reproducibility in the deposition process. These OH^- groups can be generated onto the sensor surface prior the deposition process by plasma activation [222] or extensive cleaning of the surface with acids [223].

Silanes can be deposited either in solution [223] or in vapour phase [224, 225]. The
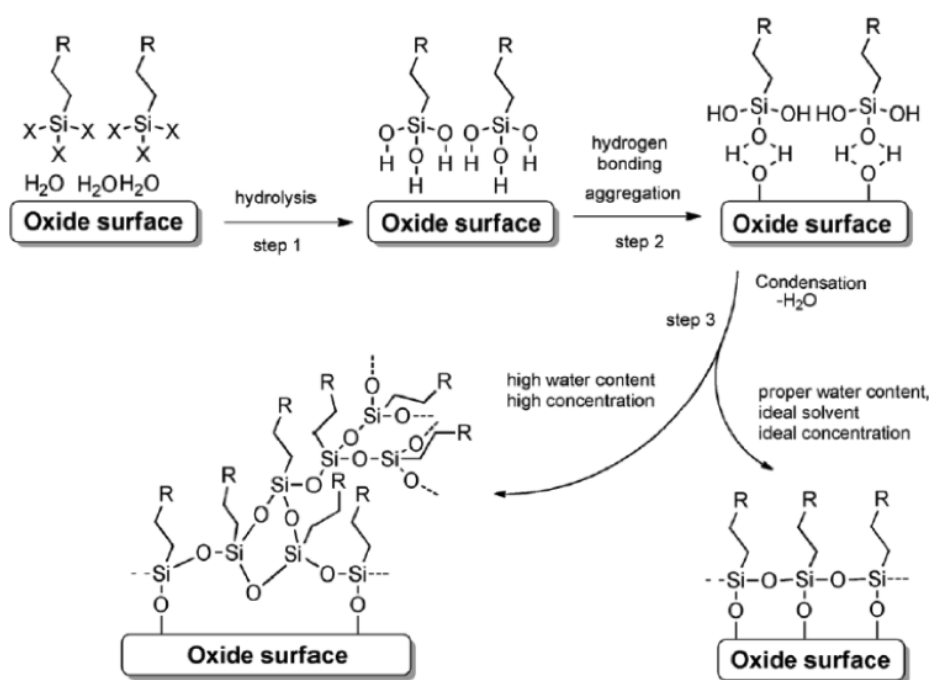
Figure 6.5 – Schematic of silane immobilisation mechanism, from Ref. [218]

solution deposition process involves simply exposing the freshly prepared core surface into milli-molar silanes concentration in anhydrous solvent such as Toluene [200, 223], yielding a full silane coating in minutes to hours. Concentration of the silane in solution is also crucial in achieving an homogeneous film without cross-linking [226]. The vapour phase deposition requires more equipment as it involves placing the sensor surface in a vacuum chamber under a reduced pressure of silane vapour [227]. This technical limitation makes solution deposition of silanes the typical choice for functionalisation of silica surfaces.

6.2.1   Functionalisation of MOF exposed core using silane

The fibre used for these experiments was the silica ECF, fabricated [185] with 7.5 µm effective core diameter, as shown in the previous chapter (Fig. 5.22). To couple the sensing molecules to the exposed core surface, 3-aminopropyltriethoxysilane (APTES) was used. This silane covalently bonds to hydroxyl groups (OH^-) on the silica core surface to provide free amine groups for covalent bonding with a carboxylic acid group of the sensing molecule [200]. The fibre was prepared for APTES functionalisation by flame sealing the holes at each end, then clean and hydroxylate the outer surface by immersion in 70% nitric acid for 16 hrs followed by 2 hrs in 70/30 piranha solution. After rinsing and drying, the prepared fibre was immersed in 5% APTES-toluene solution for 2 hrs, then rinsed with toluene and acetonitrile. This silane functionalised fibre was then immersed in a solution of sensing molecule + acetonitrile + HATU[‡] + *N,N*-diisopropylethylamine (DIPEA) for 20 hrs and rinsed with acetonitrile. The HATU and DIPEA are used as a coupling agent to generate an active ester from the carboxylic acid group for covalent attachment to the amine group of the silane [228]. The detailed step by step procedure is described below. The container used for this chemistry was a long (1 m) test tube with Ø8 mm inner diameter, specifically made for this purpose from borosilicate glass (Pyrex). The fibres were not removed from the container until the functionalisation procedure was complete, and the chemistry was done in a fume hood and room temperature (∼23℃).

[‡] 1-[Bis(dimethylamino)methylene]-1H-1,2,3-triazolo[4,5-b]pyridinium 3-oxid hexafluorophosphate

1. Seal the ends of the ECFs (~ 0.8 m lengths) using a hot flame torch.
   ($\sim$1800℃ - such as oxy/acetylene.)

2. Place the sealed fibres into the test tube.
   (The rest of the procedure is done using the test tube without removing the fibre.)

3. Fill with concentrated nitric acid (70%) and leave overnight (16 hrs).

4. Remove the nitric acid and rinse twice with Millipore water, by filling then removing the water. Leave the test tube filled with water until preparation of the piranha solution is complete.

5. Prepare a 70/30 (v/v) piranha solution (concentrated sulfuric acid (98%) and hydrogen peroxide (30%)).
   CAUTION - Piranha solution must be prepared and handled with great care as it is an extremely strong oxidising agent, capable of quickly dissolving organic material.

6. Remove the water from the test tube, fill with the prepared piranha solution and leave for 2 hrs.
   Note: Bubbles from the piranha solution reaction will attach to the fibre(s) and cause them to lift out of solution. To prevent this a loose cap, such as a small glass slide, should be placed over the top of the test tube.

7. Remove the piranha solution, and rinse twice with Millipore water, by filling then removing the water. Then, rinse twice with acetone (high performance liquid chromatography (HPLC) grade).

8. Place the test tube in an oven at $\sim$150℃ for 20 mins.

9. Remove from the oven and leave to cool for a few minutes. Check that there is no condensation at the sealed end of the test tube. If condensation is noticed, then rinse with acetone again and repeat the drying step.

10. Fill with anhydrous toluene.

11. Prepare a (5%) solution of APTES in anhydrous toluene (v/v), inside a nitrogen filled (dry) glove box.

12. Remove the toluene from the test tube, fill with the APTES solution and leave for 2 hrs.

13. Remove the APTES solution, rinse twice with anhydrous toluene, and then rinse twice with acetonitrile (HPLC grade). Leave the test tube filled with acetonitrile until preparation of the sensing molecule solution is complete.

14. Prepare a solution of 75 µM sensing molecule with 100 µM HATU + DIPEA, i.e. the coupling agent needs to be in excess of the sensing molecule. For example, the lumogallion (molecular mass: 344.72) can be prepared from 2.6 mg/100 mL in acetonitrile, then add 17.5 µL HATU and 3.8 mg DIPEA.

15. Remove the acetonitrile from the test tube, fill with the sensing molecule solution, and leave for 20 hrs.

16. Remove the solution and rinse twice with acetonitrile. Leave the test tube filled with acetonitrile until ready to use the fibre for sensing experiment.

Some of the challenges with this functionalisation chemistry is making sure the surface is kept clean and free from moisture, and how to achieve long lengths of homogeneously functionalised fibres. The results for silane functionalisation of the silica ECF are shown in the following sections.

6.2.2 Covalent Attachment of Lumogallion

As described in Sec. 6.1.2, the lumogallion used for attachment to the silica ECF is a derivative that was characterised and compared to the commercially available lumogallion in Ref. [123]. Those published cuvette measurements showed that the fluorescence from the surface attachable derivative is similar to that of the commercially available form, with the added advantage of linear increase in emission with increasing aluminium concentration. The minimum detectable concentration of Al^{3+} in solution was found to be ~ 500 nM. Comparison of slides and F2 SCF (core diameter ~ 1.7 µm), functionalised with the lumogallion derivative using polyelectrolytes showed a 10-fold decrease in sensitivity for the SCF case. This decrease in sensitivity was attributed to a high surface density of the fluorophore on the fibre, causing large background fluorescence from the uncomplexed fluorophore. Nevertheless, lumogallion is a good candidate as a first attempt to functionalise the ECF for detection of Al^{3+}, since it was
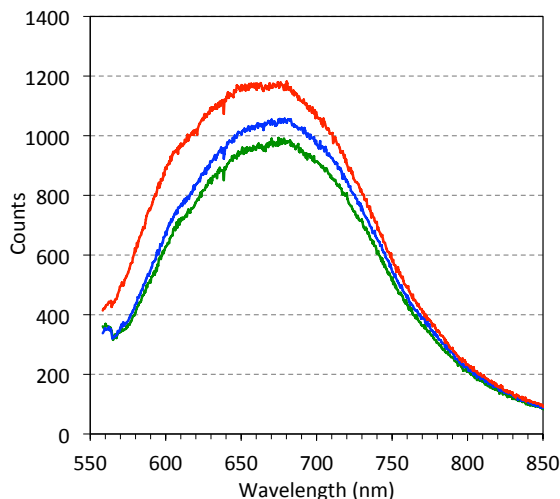
Figure 6.6 – Back reflected spectra of ECF functionalised with lumogallion using silane, where the ■ – green, ■ – blue, and ■ – red curves are the results from the fibre before immersion (background measurement), immersed in a solution containing Al^{3+} dissolved in water, and immersed in a solution containing Al^{3+} dissolved in acetonitrile respectively.

previously used for functionalising the F2 SCFs.

To characterise covalent functionalisation of the lumogallion derivative using silane, using the method shown in Sec. 5.10.2, the back reflected fluorescence from the lumogallion functionalised ECF (60 cm total length) was measured with a 8 cm immersed in saturated solutions (100 g/L) of $KAl(SO_4)_2 \cdot 12\,H_2O$ (Al^{3+} solution). Figure 6.6 shows the results of these measurements, where the green, blue, and red spectra are the back reflected fluorescence from the fibre before immersion (background measurement), immersed in Al^{3+} dissolved in water, and immersed in Al^{3+} dissolved in acetonitrile. While the fluorescence response is slightly better when the Al^{3+} is in acetonitrile solvent, the result is still only a few hundred counts increase over background. These results show that response of the lumogallion to a saturated solution of Al^{3+} is limited when covalently attached to the fibre core.

6.3   Physical Functionalisation

Physical functionalization is a method for immobilisation of sensing molecules which doesn't depend on the chemistry of the surface and can be exploited virtually on every material. Although the process is relatively simple, it is unlikely to result in a single self-assembled monolayer due to the attachment mechanisms involved. One particular approach is to use charged polymers in solution, often called polyelectrolytes (PE).
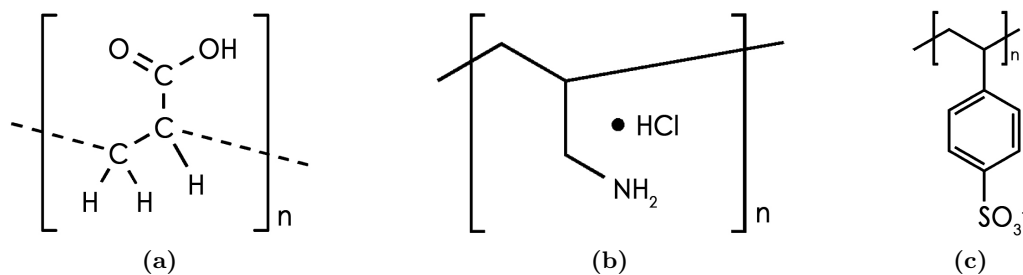
Figure 6.7 – Examples of polyelectrolytes (a) poly(acrylic acid), (b) poly(allylamine hydrochloride), (c) poly(styrene sulfonate).

A large variety of PEs are available, the most common of which are poly(acrylic acid) (PAA) (with carboxylic functional group), poly(allylamine hydrochloride) (PAH) (with amino functional group), and poly(styrene sulfonate) (PSS), depicted in Fig. 6.7.

Polyelectrolytes are either positively or negatively charged. Deposition of PE layers is done following a layer by layer process where a first PE layer with a charge opposite to the intrinsic surface charge of the substrate is deposited in solution, then followed by a rinsing step and a second PE layer with opposite charge compared to the previously deposited PE layer [230] as shown in Fig. 6.8. The process can be repeated multiple times to stack layers onto any substrate, resulting in an increase of the functional groups density onto the sensor surface. These free functional groups are then available on the surface for subsequent attachment of a sensing molecule with the corresponding group. Since the deposition process relies exclusively on electrostatic forces, the deposition of PE layers is only dependent on the intrinsic charges of the surface rather
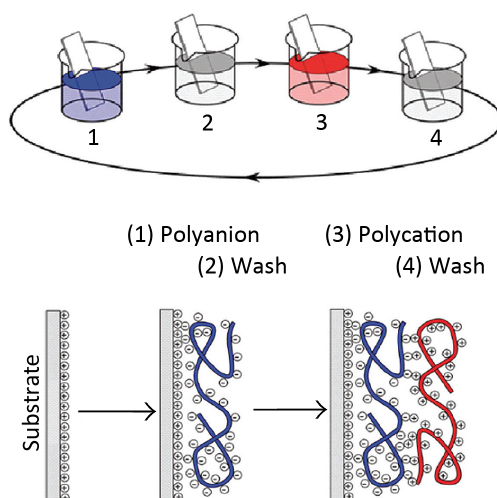
Figure 6.8 – Depiction of the layer by layer deposition process used for polyelectrolytes coating, from Ref [229].

than its chemical nature, as required by the covalent bonding method. This versatility means that PE coatings have been used for MOF based sensing applications involving; SPR with metallic coatings [201, 231], polymer whispering-gallery mode (WGM) microspheres [232, 233], and functionalisation of suspended glass cores with molecular beacons for deoxyribonucleic acid (DNA) detection [11, 234] and fluorophores for ion detection [123]. Appendix K shows a combination of PEs and liposomes used to create a biocompatible sensing platform using the silica ECF.

6.4   8-HQ Doped Thin Film Polymer

In 2013, Rowland *et al.* showed a solvent evaporation deposition method for the internal coating of silica capillaries with doped polymer to create capillary resonators for optofluidic refractometric sensors [235]. In that work, the principle of capillary forces was used to load a solution of dissolved polymer (poly(benzyl methacrylate) (PBzMA)) into the capillary which leaves behind a thin film as the solvent evaporates. It was also shown that a fluorescent die (Nile Red) could be mixed with the dissolved PBzMA to coat the inner surface of the capillaries with a doped polymer thin film ($\sim$400 nm). These ideas by Rowland *et al.* led to the question; is it possible to use a polymer thin film doped with fluorescent indicators as a functionalisation method? It has been shown that polymers can be thought of as a highly viscous fluid subject to molecular diffusion [236, 237]. Therefore, it was thought that the polymer matrix might provide an environment on the surface of the ECF that allows diffusion of Al^{3+} and mobility of multiligand binding fluorophores, such as 8-HQ, as long as these fluorophores are also sufficiently trapped by the polymer matrix.

For thin film functionalisation, PMMA was chosen since it has a refractive index of 1.49 (at 620 nm), which is closer to that of silica (1.46 at 620 nm) compared with polystyrene (1.59 at 620 nm) or PBzMA (1.57 at 620 nm). Higher refractive indices at the core surface can lead to more PF [137, 139], however it is also important to consider possible increased light scattering losses as a greater portion of guided light travels outside the core and coupling of excited fluorescence back to the guided modes of the fibre core. While fluorocarbon based polymers (such as poly(tetrafluoroethylene) (PTFE); DuPont brand name Teflon) have refractive indices lower than silica, finding a way to dissolve these types of polymers could pose a challenge. PMMA is known to be soluble

in dichloromethane (DCM), which evaporates very quickly (boiling point 39.6℃), and PMMA is often used for doped thin film optical devices [238–240]. To understand if 8-HQ doped within a polymer film could complex with Al^{3+}, a drop of 8-HQ doped PMMA (concentration of 3:100 by weight) was placed on a glass slide.

It was noticed that the PMMA+8-HQ on glass slide was lifting off the glass after several minutes of being submersed in aqueous solution. This suggested that the polymer was not bonding to the glass substrate, but instead just sitting on the surface where the water was able to penetrate between the coating and substrate, breaking the adhesion. In this case, PMMA granules with a density of 1.20 g/cm^3 from Polysciences Inc. were used. To determine if bonding improvement could be achieved using cast polymer, as well as reduced background due to impurities, a 24.65 g PMMA clear cast rod with a density of 1.18 g/cm^3, also known as a 'plexiglass rod' (Professional Plastics Pte. Ltd. [Singapore]) was dissolved in 1 ltr of DCM to produce a PMMA solution. The solubility of this cast PMMA is thought to be 30 mg/ml in DCM. 6 mg of 8-HQ was dissolved in 1 ml of DCM and 1 ml of the PMMA solution, making a concentration of $30_{(8\text{-HQ})} : 100_{(\text{PMMA})}$ by weight. A drop of this PMMA+8-HQ solution was then placed at each end of a glass slide and allowed to set for 15 mins at room temperature. The glass slide was cut in half, and one of these pieces was placed in Al^{3+} solution for 2.5 hrs during which time the PMMA+8-HQ remained attached to the glass slide.
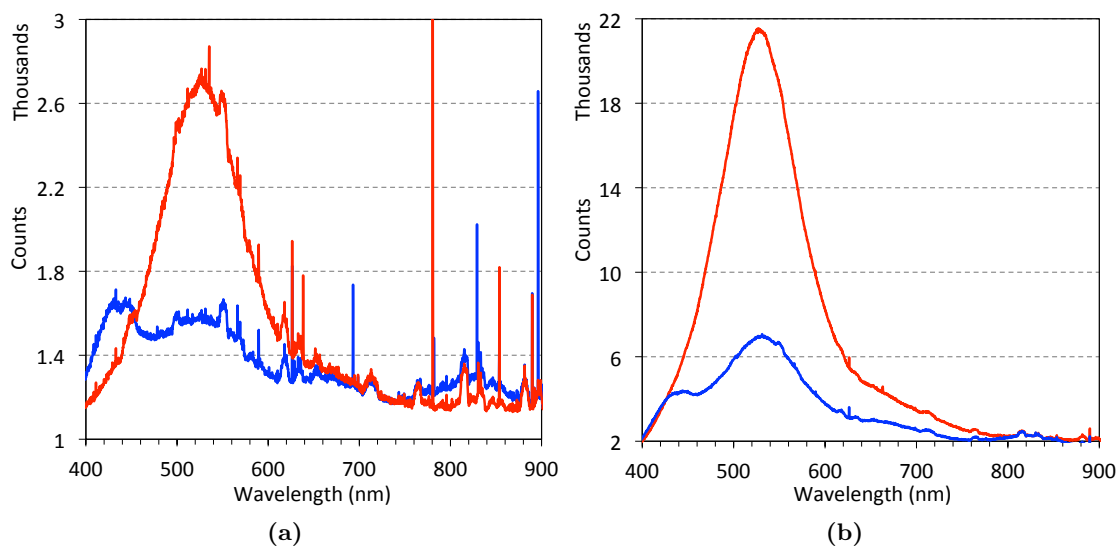
Figure 6.9 – Back reflected spectra at 355 nm excitation wavelength of PMMA+8-HQ drop on glass slide, not exposed to Al^{3+} solution (■ – blue) and exposed to Al^{3+} solution for 2.5 hrs (■ – red), with (a) 5 mW excitation power, and (b) 35 mW excitation power.

The back reflected spectra from each of the PMMA+8-HQ drops on the glass slide was measured using a 355 nm excitation light source and Horiba iHR550 Imaging Spectrometer with Synapse CCD Detector via a 400 nm long pass filter, shown in Fig. 6.9. The blue spectra show the results when the drop was not exposed to Al^{3+} solution, and the red spectra show the results when the drop was exposed to Al^{3+} solution for 2.5 hrs, using 5 mW excitation power (Fig. 6.9(a)) and 35 mW excitation power (Fig. 6.9(b)). The results confirm that the Al^{3+} is able to complex with the 8-HQ doped within the PMMA drop on the slide. It is assumed that the cations are able to permeate the PMMA and that the 8-HQ molecules are able to move within the polymer matrix to complex with the cations.

6.4.1   One Step Functionalisation Process

The PMMA+8-HQ solution, at a concentration of $30_{(8\text{-}HQ)} : 100_{(PMMA)}$ by weight, was next used to coat the ECF. One end of the fabricated silica ECF (Fig. 6.10(a)), with an effective core diameter of 7.5 μm, was fed through a silicone septum (Aireka Scientific Co., Ltd) fitted to the bottom of an open-end vial. This setup, shown by the schematic in Fig. 6.10(b), was then used to coat the outside of the ECF including the exposed core region. The PMMA+8-HQ solution was placed into the vial ($\sim$5 mm depth), and the fibre was pulled through the solution and silicone septum by hand (at $\sim$8 m/min) to leave behind a $\sim$50 nm coating of the doped PMMA on the core surface (Fig. 6.10(c)). Uniformity of the polymer layer is critically important for optical performance of the

(a)   (b)   (c)
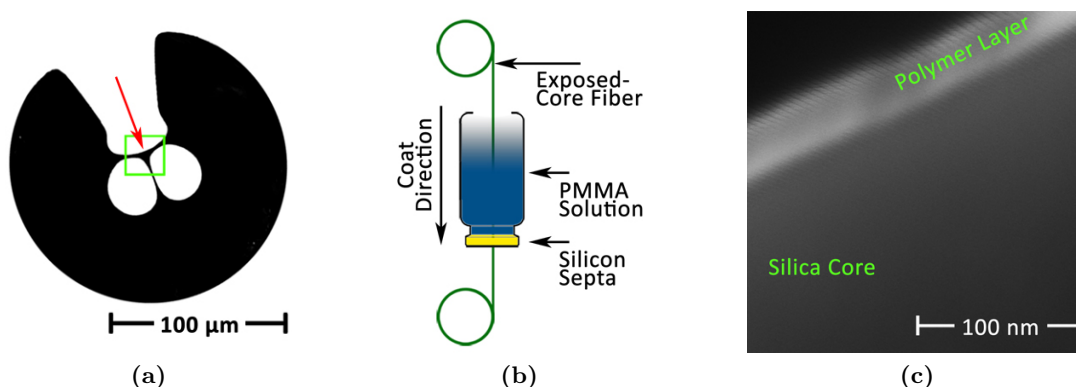
Figure 6.10 – (a) Contrast enhanced SEM image of (silica material shown in black) ECF cross section, having an effective core diameter of 7.5 μm (core location shown by ▮ – green box). (b) A schematic of the thin-film polymer coating method used to coat the outside of the ECF including the exposed core region. (c) Close-up SEM of the outside edge of the exposed core (▮ – red arrow in Fig. 6.10(a)) with 50 nm polymer coating (light grey).

device. Measured results from SEM images of six samples, from the centre and 10 cm in from the ends of two individually coated 1 m lengths of fibre, showed the coating thickness on the outside edge of the exposed core to be in the range 43–46 nm with measurement uncertainty of ± 9 nm. The coating procedure was performed in a laboratory chemical fume hood at room temperature ($\sim 21°C$), without additional curing.

6.5   Characterisation of Thin Film Polymer Layer

6.5.1   Functionalised Fibre Loss

To determine the impact of polymer coating on propagation loss, cutback fibre loss measurements were performed using a 100 W halogen broadband source with an approximately Gaussian-distributed intensity profile and peak power at 800 nm. The before and after polymer coating loss measurements are shown by the blue and red lines in Fig. 6.11 respectively, and summarised in Table 6.1 for 532 nm, 1064 nm, and 1550 nm wavelengths. These results show an increase of $\sim$10–20 times after applying the polymer layer. The difference between these coated and uncoated fibre
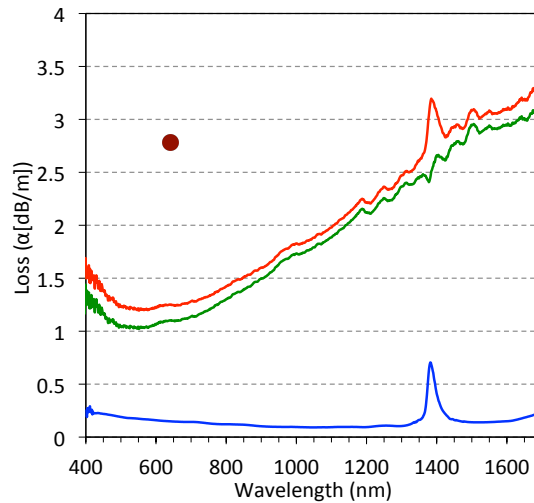
Figure 6.11 – Broadband cutback loss measurements of silica ECF, before (∎ – blue) and after polymer (PMMA+8-HQ) coating (∎ – red). The difference between the coated and uncoated fibre loss $\alpha_{\text{after}} - \alpha_{\text{before}}$ is shown in ∎ – green. Cutback loss measurement at $\lambda = 640$ nm for un-doped PMMA coated ECF (dark-red dot ●).

Table 6.1 – Loss measurements for silica ECF (Fig. 6.10(a))

Wavelength (nm)	Uncoated (dB/m)	Coated (dB/m)
532	0.178	1.04
1064	0.092	1.82
1550	0.141	2.94

loss measurements $(\alpha_{\text{after}} - \alpha_{\text{before}})$ is shown by the green line in Fig. 6.11.

Understanding the reasons the polymer layer adds to the overall loss, and finding ways to reduce these losses, can significantly improve the distributed sensor practical range, as shown in Chapter 2. The loss of a fibre is given by,

$$\alpha_{\text{fiber}}(\lambda) \; = \; \left(\frac{\varepsilon_0}{\mu_0}\right)^{\frac{1}{2}} \frac{\int_{\infty} n^{\text{r}} \alpha |\mathbf{E}|^2 \, \mathrm{d}A}{\int_{\infty} \mathbf{E} \times \mathbf{H}^* \cdot \hat{\mathbf{z}} \, \mathrm{d}A} \tag{46}$$

where $n^{\text{r}}(x,y)$ and $\alpha(x,y)$ are the refractive index and material loss distribution, $\mathbf{E}(x,y)$ and $\mathbf{H}(x,y)$ are the electric and magnetic field distributions, and $\mathbf{z}$ is along the optical axis of the fibre. This guided mode loss includes all loss mechanisms, such as absorption and scattering. The change in loss of the guided mode due to the addition of the polymer layer can be written as,

$$\alpha_{\text{after}} - \alpha_{\text{before}} \; = \; \left(\frac{\varepsilon_0}{\mu_0}\right)^{\frac{1}{2}} \frac{\int_{\text{layer}} n^{\text{r}} \alpha |\mathbf{E}|^2 \, \mathrm{d}A}{\int_{\infty} \mathbf{E} \times \mathbf{H}^* \cdot \hat{\mathbf{z}} \, \mathrm{d}A} \tag{47}$$

where we have assumed the mode distribution has not changed due to addition of the layer, since it is very thin (~ 50 nm). In Eq. (47), $\alpha(x,y)$ includes loss of polymer material, α_{m}, and any loss due to scattering or inhomogeneity added during fabrication, α_{f}, hence $\alpha(x,y) = \alpha_{\text{m}} + \alpha_{\text{f}}(x,y)$. As a result, Eq. (47) can be rewritten as,

$$\alpha_{\text{after}} - \alpha_{\text{before}} \; = \; \left(\frac{\varepsilon_0}{\mu_0}\right)^{\frac{1}{2}} \left(\frac{n^{\text{r}}_{\text{m}} \alpha_{\text{m}} \int_{\text{layer}} |\mathbf{E}|^2 \, \mathrm{d}A}{\int_{\infty} \mathbf{E} \times \mathbf{H}^* \cdot \hat{\mathbf{z}} \, \mathrm{d}A} + \frac{\int_{\text{layer}} n^{\text{r}}(x,y) \alpha_{\text{f}}(x,y) |\mathbf{E}|^2 \, \mathrm{d}A}{\int_{\infty} \mathbf{E} \times \mathbf{H}^* \cdot \hat{\mathbf{z}} \, \mathrm{d}A} \right) \tag{48}$$

or alternatively,

$$\left(\frac{\mu_0}{\varepsilon_0}\right)^{\frac{1}{2}} \frac{(\alpha_{\text{after}} - \alpha_{\text{before}}) \int_{\infty} \mathbf{E} \times \mathbf{H}^* \cdot \hat{\mathbf{z}} \, \mathrm{d}A}{n^{\text{r}}_{\text{m}} \int_{\text{layer}} |\mathbf{E}|^2 \, \mathrm{d}A}$$

$$= \; \alpha_{\text{m}} + \frac{\int_{\text{layer}} n^{\text{r}}(x,y) \alpha_{\text{f}}(x,y) |\mathbf{E}|^2 \, \mathrm{d}A}{n^{\text{r}}_{\text{m}} \int_{\text{layer}} |\mathbf{E}|^2 \, \mathrm{d}A}$$

$$= \; \alpha' \tag{49}$$

where α' is the overall layer loss. Equation (49) can be used to determine the loss induced from applying the polymer layer, as a function of the guided mode field distribution fraction, by measuring $\alpha_{\text{after}} - \alpha_{\text{before}}$ and calculating electric and magnetic fields of the fibre propagation mode.

To calculate the electric and magnetic fields, numerical simulation was performed on the fibre core profile taken from an SEM image, with a 50 nm polymer layer added to the exposed hole side of the core, using full vector FEM in the commercial package COMSOL 3.4. For example, Fig. 6.12(a) shows the FEM result for the z-component power flow $(\mathbf{S}_z = \mathbf{E} \times \mathbf{H}^* \cdot \hat{\mathbf{z}})$ distribution at $\lambda = 532$ nm of the fundamental mode, with refractive indices of the air holes, silica core, and polymer layer being $n_{\mathrm{holes}} = 1$, $n_{\mathrm{silica}} = 1.4607$, and $n_{\mathrm{layer}} = 1.4947$ respectively (Fig. 6.12(b)). The cutback measurements (see Fig. 6.11) were used together with the fundamental mode FEM calculations with silica and PMMA material wavelength dependent refractive indices $(n_{\mathrm{m}}^{\mathrm{r}})$ to determine α' for 405 nm, 532 nm, 640 nm, 790 nm, 980 nm, 1064 nm, and 1550 nm wavelengths. The green dots in Fig. 6.13 plot the results for these seven wavelengths which show a trend of reducing attenuation with increased wavelength. To investigate this λ dependence, α' was fitted to the function,

$$\alpha' = \sum_{i=0}^{4} \frac{a_i}{\lambda^i} \tag{50}$$

which revealed the experimental values of α' could be fitted with either of the following
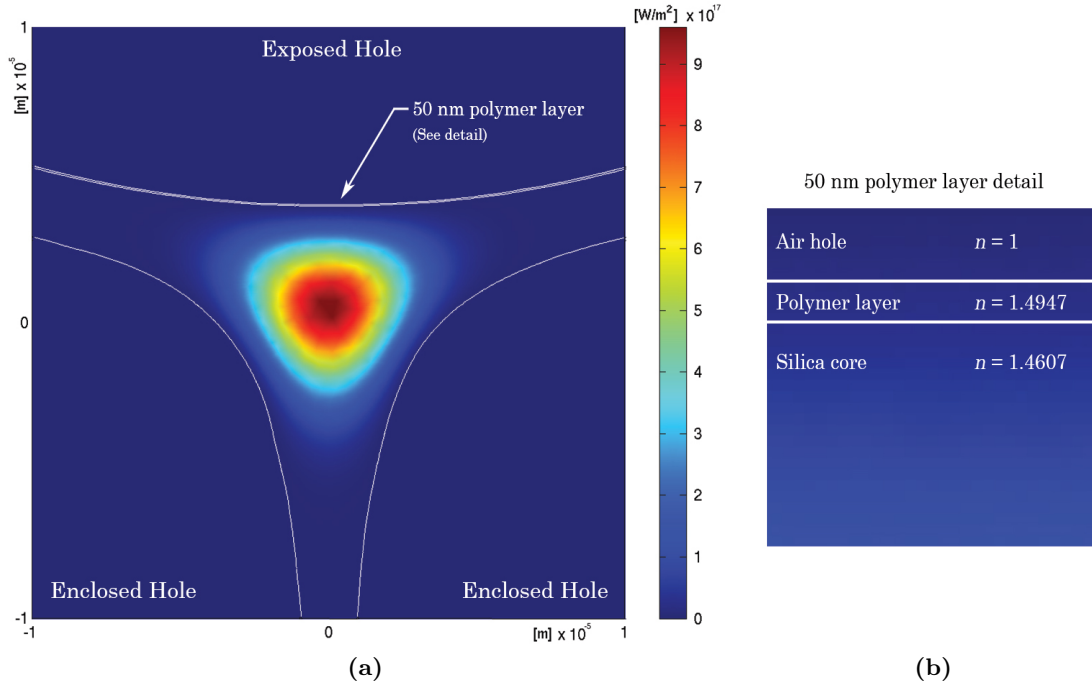
Figure 6.12 – (a) Numerical simulation result for the z-component power flow $(\mathbf{S}_z)$ distribution at $\lambda = 532$ nm of the fundamental mode using full vector FEM. The fibre core profile (shown by white outline) taken from SEM image. (b) Detail of the of the refractive index profile used for the simulation.

two functions,

$$\alpha_1' = \left(\frac{2049.04}{\lambda} + \frac{413.27}{\lambda^4} + 6988.35 \right) \qquad \left[R^2 = 0.997 \right] \qquad (51)$$

$$\text{and} \qquad \alpha_2' = \left(\frac{1272.97}{\lambda^3} + 8001.75 \right) \qquad \left[R^2 = 0.994 \right] \qquad (52)$$

with λ in µm, and α' in dB/m units, shown by the red and blue lines respectively in Fig. 6.13. The fit of these functions could not be improved by allowing $a_2 \neq 0$.

Equation (51) shows wavelength dependencies of the form known to originate from intrinsic material light scattering. In general terms, material density changes cause intrinsic light scattering which is termed as Tyndall, Mie, and Rayleigh scattering originating from constituents of sizes $r > 40\lambda$, $\lambda/20 < r < 40\lambda$, and $r < \lambda/20$ respectively [241]. On the other hand, Eq. (52) has λ^{-3} dependence which is described by Roberts *et al.* [242] as applying to surface roughness at all length scales. For suspended and free-standing nanowires, increased field strength at the surface leading to larger roughness scattering type loss [187, 243] has also been shown to have core size dependence of $\alpha \propto d^{-3}$ [124].

The fact that both functions α_1' and α_2' fit the experimental data indicates that any function α' given by $\alpha' = \rho\alpha_1' + (1 - \rho)\alpha_2'$ where $\rho \in [0, 1]$ fits the data as well. To
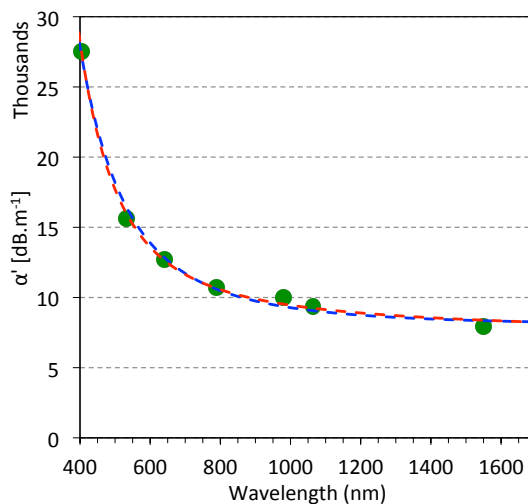
Figure 6.13 – (green ●) Plot of loss induced from applying the polymer layer, α' in Eq. (49), using cutback measurements ($\alpha_{\text{after}} - \alpha_{\text{before}}$, Fig. 6.11) for 405 nm, 532 nm, 640 nm, 790 nm, 980 nm, 1064 nm, and 1550 nm wavelengths. Plot of fitted λ dependent functions Eq. (51) (▮ – red) and Eq. (52) (▮ – blue).

determine ρ, we compare the coefficient of Rayleigh scattering that has been measured for bulk PMMA [244] with the coefficient of λ^{-4} in Eq. (51), which appears to be 5×10^6 times bigger than actual value as reported in [244]. To investigate the possibility that the added 8-HQ is contributing to additional Rayleigh scattering, another length of the ECF was coated with a thin film (~ 50 nm) of un-doped PMMA using the same method as described above. The loss of this PMMA coated ECF was measured at $\lambda = 640$ nm using the cutback method, which was found to be 2.78 dB/m compared to 1.25 dB/m measured for the PMMA+8-HQ, shown by the dark-red dot and red line in Fig. 6.11 respectively. This reveals that 8-HQ is not the cause of the additional loss from the thin film layer, instead helping to reduce the overall attenuation. Also, the λ^{-1} Mie type scattering in Eq. (51) cannot be due to intrinsic properties of the thin film, since this would suggest constituents with sizes orders of magnitude larger than the layer thickness. This implies that $\rho \approx 0$, since Eq. (51) cannot be describing intrinsic material properties of the thin film layer as being the predominant cause for the additional loss, and so does not contribute to the loss function α' in terms of intrinsic material light scattering.

To investigate surface roughness scattering type loss described by Eq. (52), a CSI was used to measure the roughness of the ECF core surface before and after polymer coating. Before coating the roughness along a 20 µm length of the core was found to be $S_z = 0.394$ nm, whereas after coating $S_z = 0.873$ nm, where,

$$S_z = |\max_A Z(x,y)| + |\min_A Z(x,y)| \tag{53}$$

The additional measured roughness at the core surface, together with Eq. (52) having an $\alpha \propto \lambda^{-3}$ dependence [242], indicates that the source of the added attenuation from the polymer layer is primarily due to surface roughness. Such roughness has been shown to arise from excited surface capillary waves (SCWs) [242], where small ripples on the surface are frozen in at the time of fibre fabrication. The amplitude of SCWs is dictated by equilibrium thermodynamics with surface tension (γ) providing a restoring force. During material phase transition these SCWs freeze [245], leaving a surface roughness proportional to inverse surface tension ($S_z \propto \gamma^{-1}$) [242, 246]. Both the PMMA ($\gamma = 0.032$ Nm^{-1} [247]) and DCM ($\gamma = 0.026$ Nm^{-1} [248]) used for the thin film coating have surface tensions an order of magnitude lower than for the silica ($\gamma = 0.31$ Nm^{-1} [182]) used to fabricate the ECF. This relatively low surface tension

for the polymer coating gives rise to higher amplitude SCWs, leading to additional sur-
face roughness and therefore additional loss. Hence, improvements may be possible by
finding ways to increase the surface tension of polymer mixtures used for the thin film
coating.

6.5.2   Air Exposure Induced Deterioration

The impact of deterioration on the transmission properties of the functionalised fibre,
resulting from exposing the functionalised fibre to air, was measured using the same
procedure detailed in Sec. 5.7. A 4 m long PMMA+8-HQ functionalised fibre was cou-
pled to a 100 W halogen broadband source with an approximately Gaussian-distributed
intensity profile and peak power at 800 nm. At the other end, the light from the core
was imaged onto the detector of an OSA and the transmitted power spectrum, in dBm,
was recorded from 350–1750 nm every two minutes. This procedure was performed in a
laboratory at room temperature ($\sim$21℃), with the fibre in air, where the setup was left
long enough ($\sim$6 hours) so that the measured power stabilised to within $\pm$0.05 dBm,
then used to take time based measures of the power for 180 hours. Any changes over
time (t) in the transmission characteristics were then fitted to the equation Eq. (35)
where ξ is the loss in dB m^{-1}day^{-1}. For comparison the result for the uncoated ECF
from Fig. 5.14 (with 10 µm core diameter), in Sec. 5.7, is shown by the red line in
Fig. 6.14. The result of $\xi(\lambda)$ (Eq. (35)) for the thin-film functionalised fibre, shown by
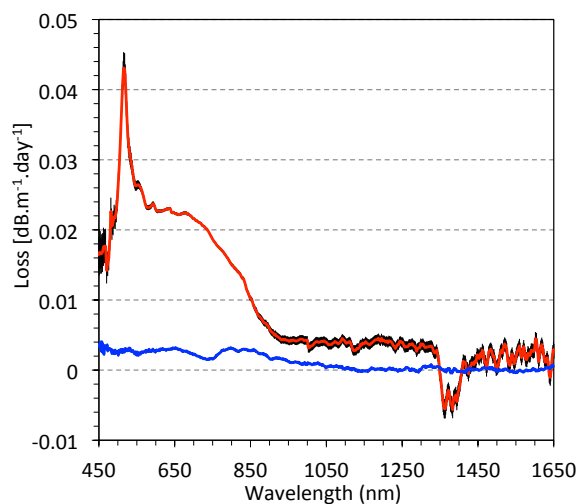
Figure 6.14 – Deterioration in the transmission properties of the air exposed uncoated (▌ – red), from
Sec. 5.7 with 10 µm core diameter) and thin-film polymer functionalised (▌ – blue). silica
ECF. The 95% confidence interval is shown in black. For the thin-film polymer functionalised
fibre result, the confidence interval is approximately the same as the line thickness.

the blue line in Fig. 6.14, shows a significant improvement compared to the uncoated fibre.

This deterioration in the transmission properties is expected to come from changes in the mechanical and/or compositional characteristics at the core surface, causing light scattering effects [186–188]. When the core diameter is reduced these light scattering effects are expected to increase, as a greater portion of guided light travels outside the core. However, this result shows an order of magnitude less deterioration in transmission properties even though the core diameter of this functionalised fibre is smaller (7.5 µm) compared to the uncoated ECF from Sec. 5.7 (10 µm). This shows that the thin film coating is providing a protective function for the core surface. For example, at $\lambda = 532$ nm the air induced deterioration in the transmission properties of the thin-film functionalised fibre (3×10^{-3} dB m^{-1}day^{-1}) is an order of magnitude better than for the uncoated result. This is significant for optical fibre sensors requiring long term and/or harsh environmental applications while providing long length light interaction with the analyte of interest.

6.5.3   Sensing Measurements

To test the ability of the coated fibre to detect Al^{3+}, an 18 mW laser excitation light source with a wavelength of 375 nm was coupled into the core of an 80 cm long PMMA+8-HQ functionalised fibre using an aspheric lens (f=2.75 mm, NA=0.55) via a dichroic mirror. The back reflected light collected from the coated fibre core was imaged using the same lens, passed through the dichroic mirror, 425 nm long pass filter and $\times 4$ objective, and characterised using a Horiba iHR550 Imaging Spectrometer with Synapse CCD Detector. The exposed-core region of the coupled fibre was then exposed to Al^{3+} by immersing the outside of a 23 cm long central section of the fibre in Al^{3+} solution, and the back reflected spectra were measured immediately after immersion and again after 1 hour of immersion. The setup is shown by the schematic in Fig. 6.15(a). The measured result before immersion subtracted from the after immersion results is presented in Fig. 6.15(b), which shows the fluorescence peak of 8-HQ complexed with Al^{3+} [208] increasing over time. This result demonstrates the ability of a thin polymer film functionalised fibre to detect Al^{3+}, with the potential for corrosion detection, and confirms sufficient mobility of the 8-HQ within the polymer matrix to allow complexation.
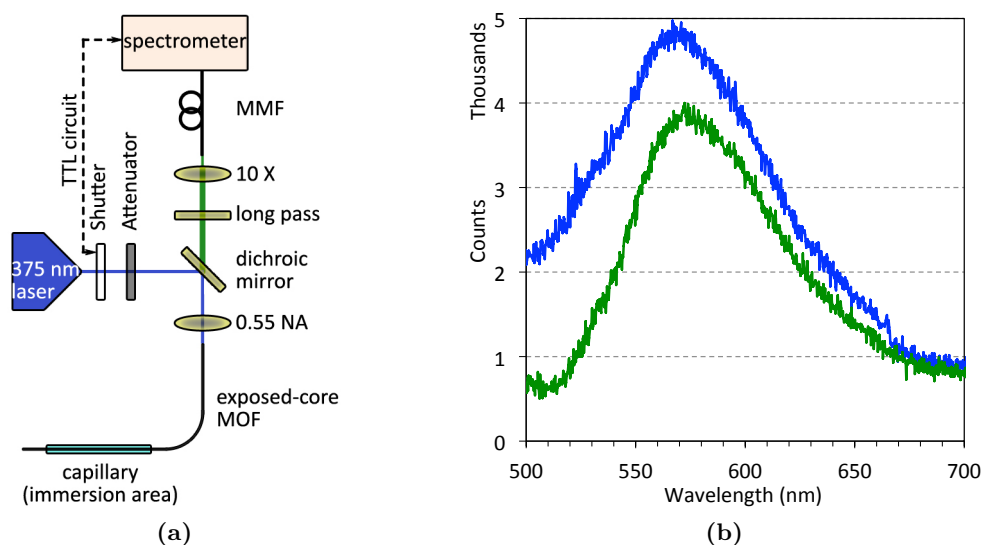
Figure 6.15 – (a) Setup used to test the ability of the coated fibre to detect Al^{3+} (MMF is multimode fibre). (b) Background subtracted back reflected spectra of the functionalised fibre directly after immersion in Al^{3+} solution (▮ – green) and after 1 hour of immersion in solution (▮ – blue).

6.6 Functionalisation with Lumogallion Doped Thin Film

It has been shown that lumogallion (Lumo) is an effective chemosensor for Al^{3+} detection. To test a PMMA+Lumo functionalised fibre, PMMA solution was prepared to make a concentration of $30_{(Lumo)} : 100_{(PMMA)}$ by weight. However, because lumogallion is a mostly polar molecule it was found that it does not dissolve well in the non-polar DCM solvent. Therefore, to achieve the 30:100 ratio a sonic bath and vortex mixture were used several times until the participants in the mixture were no longer visible. A 600 mm long ECF was thin film functionalised with this solution.

The functionalised fibre was coupled to a 532 nm (15 mW) laser and the back reflected spectra of the unexposed fibre recorded, the result of which is shown in Fig. 6.16(a). For this and subsequent measurements, 10 spectra were recorded using 10 ms exposure in 20 ms intervals, and the average of these ten spectra is shown by the red spectrum. Then a 100 mm long section along the fibre, was immersed in a Al^{3+} solution. Back reflected spectra from the fibre were measured straight after immersion, shown in Fig. 6.16(b), where the spectral intensity was increasing over the course of the 10 measurements showing a fluorescence peak due to the lumogallion complexing with Al^{3+}. For measurements recorded after 5 minutes and again after 45 minutes, shown by Figs. 6.16(c) and 6.16(d) respectively, there was a reduction in the fluorescence peak.
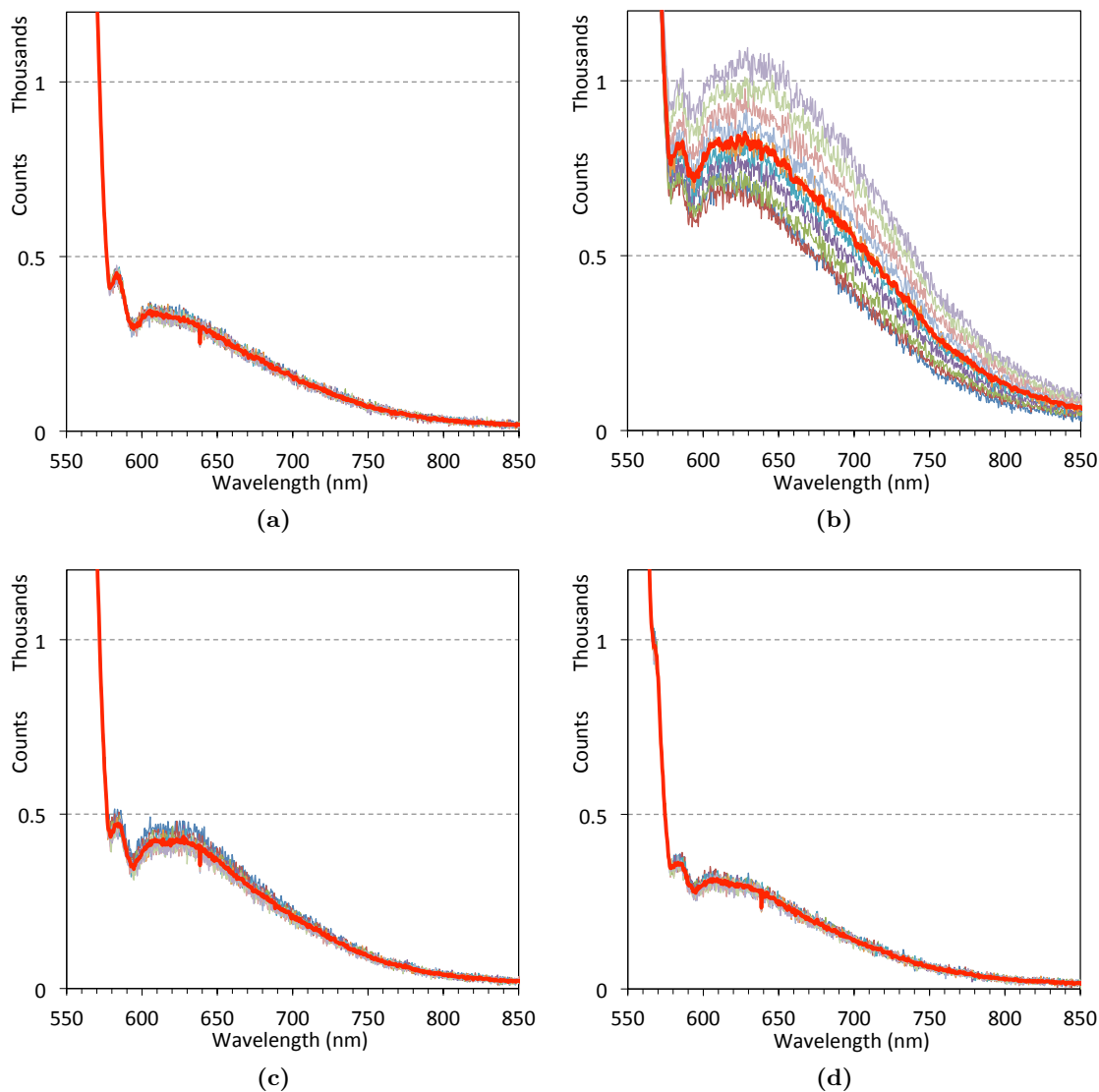
Figure 6.16 – PMMA + Lumo functionalised ECF back reflected fluorescence measurements (a) dry, (b) straight after adding Al^{3+} solution, (c) after 5 minutes, and (d) after 45 minutes.

A 2 cm section, 0.6 m along the length of the functionalised fibre, was submersed in the Al^{3+} solution and the fluorescence spectra measured every 30 seconds and normalised to the silica Raman peak at 548 nm. Figure 6.17 shows the fluorescence peak values, at 649 nm. These results show that the fluorescence signal from the lumogallion is significantly decreasing over time. Further experiments with doped polymer drops on glass slides showed that the lumogallion leaches out of the polymer when in aqueous solution. This shows the importance of using non-polar sensing molecules, which remain trapped in the polymer layer, as was the case for the 8-HQ.
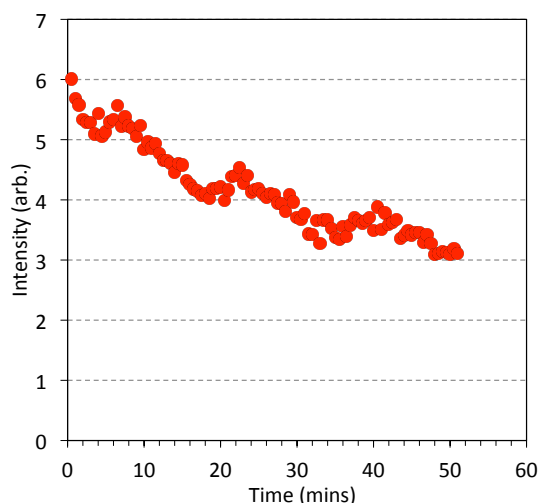
Figure 6.17 – Fluorescence peak values of back reflected spectra at 532 nm excitation wavelength from ECF with lumogallion doped PMMA coating submersed in solution containing Al^{3+}.

6.7 Comparison of Functionalisation Methods using Spiropyran

A real advantage would be the ability to control the selectivity of ion binding for a particular ion, without the need to change the chemical structure of the sensor molecule. This could be achieved by immobilising the sensor molecule onto a suitable surface and use the local molecular environment (nano-environment) around the sensor to control the way the molecule interacts with the analyte. This is because the incorporation of a substance into a nanoscale space can dramatically alter its chemical properties [249–251], providing a means to control host-guest interactions and similar molecular recognition events [252–256].

Multiligand chelation of SP has been found to be highly dependent on the ionophore that is appended to SP and these structures in turn show a degree of molecular flexibility. Chelation of these sensors can be changed by binding to a surface or by altering solvent conditions which can affect the behaviour of the ring-opened isomer [257, 258]. This molecular flexibility makes SP an ideal system to probe effects of the nano-environment in which the sensor is embedded. By using a single sensor molecule to measure and compare binding to each cation when (i) in solution, (ii) covalently bonded to a surface, or (iii) embedded within a thin film polymer, the effect of the different nano-environments on molecular recognition can then be characterised. The SP sensor molecule used for surface attachment onto the ECF shown in this section was found to have affinity towards calcium ions (Ca^{2+}) and Al^{3+} as single- and multiligand complex respectively.

6.7.1   Binding and Fluorescence Behaviour in Solution

The solution behaviour of ring-opened form of the SP sensor was studied by measuring fluorescence intensity at 25°C and pH 7.0 using 96 well plates with the excitation wavelength at 532 nm, after UV irradiation ($\lambda \approx 365$ nm) for 5 min. The Al^{3+} and Ca^{2+} metal ion solutions were prepared by dissolving the respective sulfate or perchlorate salt in HPLC-grade acetonitrile. Jobs method [259] was used to establish stoichiometry, where the relative fluorescence response was plotted (Fig. 6.18(a)) as a function of the corresponding reagent molar fractions given by $x = C_S/(C_M + C_S)$, with C_M and C_S being the metal ion and sensor concentrations respectively, and $(C_M + C_S) = 100$ μM. This plot depicts the increase in analytical signal with the ligand molar ratio until a maximum is reached where the signal diminishes. Linear fits to the two parts of the curve, one with positive slope due to the increase of the complex proportion in solution and the other with negative slope, are also shown in Fig. 6.18(a). The stoichiometric molar fraction (SF), obtained from the intersection of these linear fits, was found to be $SF_{Al} = 0.68$ and $SF_{Ca} = 0.40$ for Al^{3+} and Ca^{2+} respectively. This indicates that two sensor molecules are used to form the SP–Al^{3+} complex, whereas only one sensor is needed for the SP–Ca^{2+} complex.
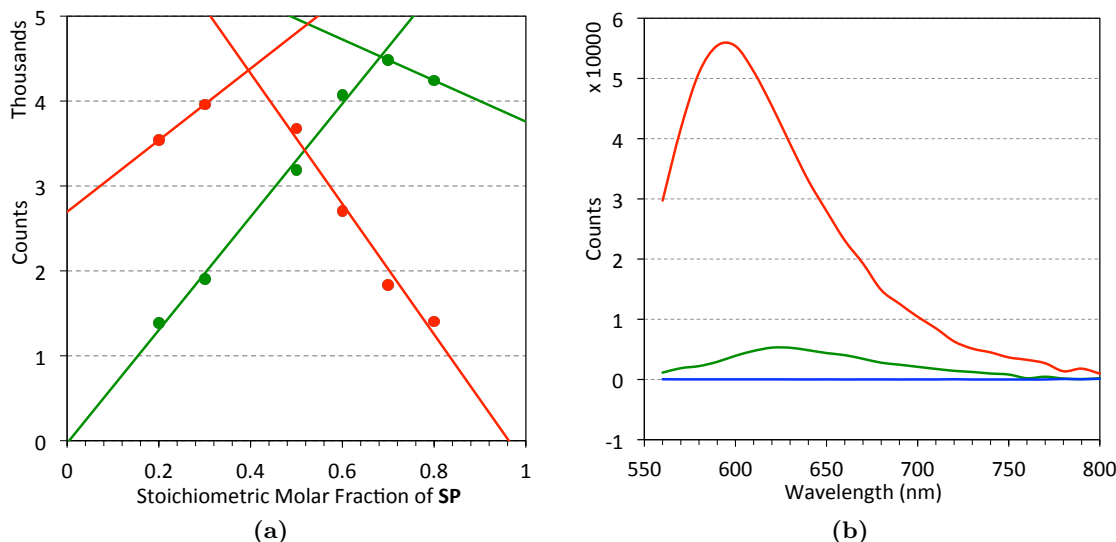
Figure 6.18 – Solution measurements of SP in ring-open form. (a) Job plot of sensor to metal ion stoichiometry, with relative fluorescence response of (●) SP–Ca^{2+} and (●) SP–Al^{3+} at various molar fractions. Linear fits of the positive and negative sides for (▮) SP–Ca^{2+} and (▮) SP–Al^{3+} indicate the SFs are $SF_{Ca} = 0.40$ and $SF_{Al} = 0.68$ respectively. (b) Solution measurements using 532 nm excitation, where the blue, red, and green spectra are the fluorescence response from (▮) SP without the presence of cations, (▮) SP–Ca^{2+} complex, and (▮) SP–Al^{3+} complex respectively.

Fluorescence intensity measurements of ring-opened SP in acetonitrile solution without cations as well as separate solutions containing 10 µM Ca^{2+} and Al^{3+} are shown in Fig. 6.18(b) by the blue, red, and green spectra respectively. These results show that fluorescence from the SP–Al^{3+} multiligand complex (green) was an order of magnitude lower than fluorescence measured from the SP–Ca^{2+} single-ligand complex (red). Compared to these two complexes, no fluorescence was noticeable from SP in solution without the presence of metal ions (blue).

It is generally understood that formation of single-ligand or multiligand crown–metal complexes depend on the cation size relative to the size of crown ether, where larger cations tend to form multiligand complexes with two or more sensor molecules [260]. However contrary to that general understanding, the SF measurements (Fig. 6.18(a)) show that the smaller Al^{3+} cation binds to SP as a multiligand complex ($2\times SP : 1\times Al^{3+}$) while only one sensor molecule is needed to form the complex with the larger Ca^{2+} cation, which has approximately twice the ionic radii of Al^{3+}. This suggests that multiligand chelation may also be related to cation charge. Further work to understand this was done by theoretical chemist Dr. Adrian Mak at the Agency for Science, Technology and Research (A*STAR) Institute of High Performance Computing (IHPC) in Singapore, and is shown in the jointly prepared manuscript in Appendix I.

6.7.2 Fluorescence Behaviour when Covalently Bound

To characterise the effect that attaching the sensor to a substrate has on the ability to detect ions, the SP sensor was covalently bonded to the ECF surface and the fluorescence response measured. The silica ECF surface was cleaned and hydroxylated by immersion in nitric acid followed by piranha solution. This was followed by covalently bonding silane to the surface OH^- groups, which provided free amine groups at the surface for subsequent covalent attachment to the carboxylic acid group of SP. Fluorescence response from the surface of this covalently functionalised fibre was then measured.

Fluorescence from the ring-closed and ring-opened forms of the SP sensor on the surface of the fibre core were measured in separate 10 µM Al^{3+} and Ca^{2+} solutions, as well as acetonitrile without metal ions as a control. The Al^{3+} and Ca^{2+} solutions were prepared by dissolving the respective sulfate or perchlorate salt in HPLC-grade

acetonitrile, and the measurements were performed at 25℃ and pH 7.0. To measure the fluorescence response from the SP sensor in ring-closed form on the surface, the fibre was first exposed to 532 nm light coupled into the core for 15 seconds before performing the measurements. For the fluorescence response measurements from the sensor in ring-opened form, the fibre was first exposed to UV from the side (λ_{peak} = 365 nm) for 5 minutes before performing the measurements. A single covalently functionalised fibre was used for all of these experiments, which preserves the optical fibre coupling conditions. This is possible due to photochromism of the sensor, enabling reversible switching between ion-binding and ion-release states [3], and therefore removing the need to change the fibre between measurements. The functionalised fibre was rinsed with acetonitrile between the Ca^{2+} and Al^{3+} measurements. This rinsing was done while exposing the fibre to 532 nm light coupled into the core to ensure the SP sensors on the surface were in the ring-closed form to facilitate releasing of any bound metal ions.

The results of these fluorescence intensity measurements of SP from the ECF core surface are shown in Fig. 6.19. The violet, orange, and brown spectra show the ring-closed form and the blue, red, and green spectra show the ring-opened form in solutions of acetonitrile without cations, Ca^{2+} in acetonitrile, and Al^{3+} in acetonitrile respectively. These results show that the SP sensor molecules are at the light guiding core surface
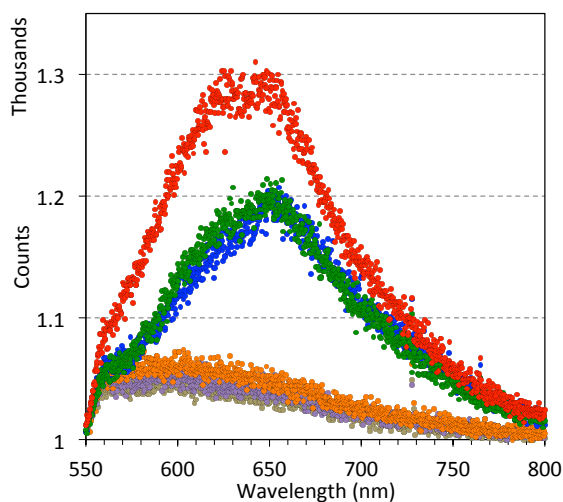
Figure 6.19 – Fluorescence intensity measurements of ECF with the SP sensor molecule covalently attached to the light guiding core. The ■ – violet, ■ – orange, and ■ – brown spectra are fibre in solutions of acetonitrile without cations, Ca^{2+} in acetonitrile, and Al^{3+} in acetonitrile respectively, with the SP sensor in ring-closed form on the surface. The ■ – blue, ■ – red, and ■ – green spectra are fibre in solutions of (■) acetonitrile without cations, Ca^{2+} in acetonitrile, and Al^{3+} in acetonitrile respectively, with the SP sensor in ring-opened form on the surface.

of the ECF. Fluorescence intensity from the ring-opened form of the SP sensor on the surface is the same for both the reference solution not containing any cations (blue) and the solution containing Al^{3+} (green). This shows that covalent bonding of the SP sensors onto the surface hindered the molecules ability for multiligand binding. For the experiment with solution containing Ca^{2+} (red), the fluorescence of the ring-opened SP sensor on the surface clearly increased over the ring-closed reference measurments (blue). This shows that the SP sensor is able to bind to ions on a single-ligand basis to form the SP–Ca^{2+} complex at the surface. Comparing the intensity ratio of SP–Ca^{2+} complex (red) to the uncomplexed SP reference (blue) from this result (Fig. 6.19) and the solution measurement result shown in the previous section (Fig. 6.18(b)), we see there is a 5×10^4 reduction in the SP–Ca^{2+} complex fluorescence intensity for the surface bound case.

6.7.3   Fluorescence Behaviour from Thin Film Polymer

To characterise the effect that placing the SP sensor in a macromolecular environment has on molecular recognition, a thin film polymer doped with the SP sensor was coated onto the ECF surface and the fluorescence response measured. Fluorescence response from the thin-film functionalised fibres was then measured using the setup described in Sec. 5 and shown in Fig. 5.24(a). Initial results of fast diminishing fluorescence intensity when the thin-film functionalised fibre was placed in acetonitrile based analyte solutions showed again that solvent polarity is an important consideration to avoid leaching of a doped thin film. Experiments on glass slides confirmed leaching of the sensor, rather than break down of the polymer, was the most likely cause of the diminishing signal in the presence of acetonitrile. Hence, the analyte was changed to separate 1 mM Milli-Q water based Al^{3+} and Ca^{2+} solutions and Milli-Q water without metal ions as a control. The Al^{3+} and Ca^{2+} solutions were prepared by dissolving the respective sulfate or perchlorate salt in Milli-Q water, and the measurements were performed at 25℃ and pH 7.0.

To avoid contamination from trapped cations between measurements of each analyte sample, three separate doped thin-film coated ECFs were used to measure fluorescence intensity from the ring-closed and ring-opened forms of the SP sensor in the polymer film. This is because, even though the thin film can be thought of as a highly viscous fluid subject to molecular diffusion [236], it also creates a nano-environment that can

trap molecules [261]. To measure the fluorescence response from the SP sensor in ring-closed form within the polymer film, the fibre was first exposed to 532 nm light for 15 seconds before performing the measurements. For the fluorescence response measurements from the SP sensor in ring-opened form, the fibre was first exposed to UV (λ_{peak} = 365 nm) for 5 minutes before performing the measurements.

The results of these fluorescence intensity measurements are shown in Fig. 6.20, where the violet, orange, and brown spectra show the ring-closed form and the blue, red, and green spectra show the ring-opened form in solutions of water without cations, Ca^{2+} in water, and Al^{3+} in water respectively. These measurements show there was a significantly improved signal for all the analytes from the SP doped thin film polymer compared to the covalently functionalised results (Fig. 6.19). Most significantly the result demonstrates strong fluorescence from the thin film in response to Al^{3+} solution. This shows the SP sensor molecule has increased mobility within this physically absorbed environment compared to covalent bonding. The macromolecular polymer chains hold the SP sensor within the nano-environment while providing the conditions needed for diffusion, solvation, and therefore complexation. Even though this SP sensor molecule is not readily soluble in water, the thin-film polymer provides a nano-environment where solvation can occur. For the thin-film polymer we also observed an increased signal from the smaller Al^{3+} atom compared to Ca^{2+}, which is in contrast with the
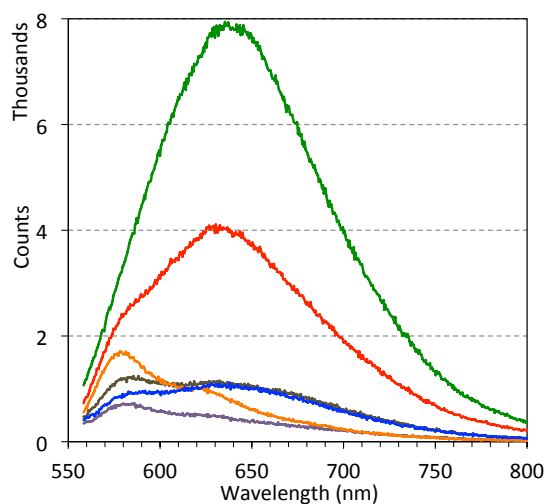
Figure 6.20 – Fluorescence intensity measurements of ECF with SP sensor molecules doped thin film polymer coated on the light guiding core. The violet, orange, and brown spectra are fibre in solutions of (■) water without cations, (■) Ca^{2+} in water, and (■) Al^{3+} in water respectively, with the SP sensor in ring-closed form in the thin film. The blue, red, and green spectra are fibre in solutions of (■) water without cations, (■) Ca^{2+} in water, and (■) Al^{3+} in water respectively, with the sensor in ring-opened form in the thin film.

solution measurements (Fig. 6.18(b)). Since dispersion interaction (London dispersion force) between the sensor, cations, and polymer macromolecules is proportional to intermolecular distance (r^{-6}), the larger Ca^{2+} atoms are subject to lower London dispersion force compared with smaller Al^{3+}. This shows that the dispersion contribution to solvation energy [262, 263] can significantly change complexation behaviour, and suggests that the polymer chains can act as a solvent. The mobility [236] and dispersive properties of the polymer macromolecules reduce the degree of complexation with larger cations, while the SP molecule is weakly bound to the polymer nano-environment.

The hindrance of Ca^{2+} binding within the PMMA layer is surprising considering that single-ligand complexation of Ca^{2+} poses less demands on the mobility of the SP sensor molecule compared to multi-molecule complexation with Al^{3+}. When SP is embedded in polymer, the cations have to diffuse from the analyte solution to the surface of the polymer film and then into the polymer matrix to be bound to SP. If diffusion of SP would determine the rate of cation binding then it would be more greatly affected when binding with Al^{3+}, as two SP ligands have a reduced probability of binding compared to one SP ligand. However, it is not observed that Al^{3+} binding to the SP sensor molecule in PMMA is hindered in this way, compared to Ca^{2+}. Therefore, this hindrance is attributed not to a difference in SP mobility but to a difference in the mobility of the cations. The larger ionic radius for Ca^{2+} (114 pm) compared to Al^{3+} (68 pm) is anticipated to relatively decrease the ability of Ca^{2+} to diffuse within the PMMA matrix, which would diminish the efficiency to form SP–Ca^{2+} complexes in PMMA.

Photoswitching experiments were performed with the thin-film coated fibres to understand if ion binding and release could be optically controlled and fluorescence from the complexed and uncomplexed states of the SP molecule remained reliable over respective cycles. The switching cycle involved measuring the passive SP in ring-closed form ('off') after long (15 second) exposure to 532 nm laser light, and then measuring the active SP in ring-opened form ('on') after exposure to UV light for 5 minutes. This was done while the thin-film coated fibres were coupled to the setup with the 10 cm section immersed in the analytes. Each measurement consisted of ten 0.1 second exposure to the 532 nm excitation light source with 0.1 second intervals, the spectra of which were integrated and summed together then normalised to the average of the seven 'on' ring-opened form of SP measured while the fibre was in water without cations.

Figure 6.21 shows the results of these photoswitching experiments, where the 'off' and 'on' measurements of the thin film functionalised fibres are shown by the empty circle (○) and filled circle (●) respectively. The blue, red, and green circles in Fig. 6.21 show results from the fibre when in solutions of water without cations, Ca^{2+} in water, and Al^{3+} in water respectively. When the fibres were in water (blue) or Al^{3+} in water (green), the 'on' and 'off' fluorescence intensity was approximately the same for each measurement. However when the fibres were in water with Ca^{2+} (red), the 'on' and 'off' fluorescence intensities steadily increased over subsequent measurements. Further experiments are needed to better understand this increasing fluorescence with the Ca^{2+} analyte. The increase may be due to increased concentration over time of these relatively larger cations in close proximity with the sensor molecules within the polymer matrix.

After performing the 'on' and 'off' switching experiments, each of the fibres was left in dark conditions while in the water, Ca^{2+}, or Al^{3+} solutions for 1 hr, 1.5 hrs, and 17 hrs respectively, and then a final 'on' signal measured, shown by the squares (■) in Fig. 6.21. These dark conditions results show the fluorescence response of the sensor in water returning back to the first 'on' measurement, and the response to Ca^{2+} remaining reasonably constant with the last 'on' measurement. For Al^{3+}, there is a significant increase over the last 'on' measurement ($\sim 25\%$), which may be due to the
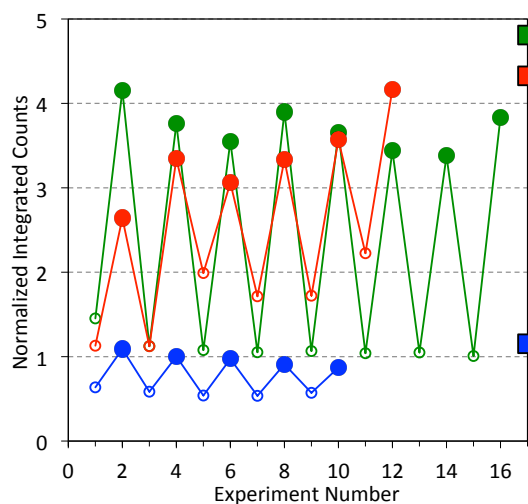
Figure 6.21 – Photoswitching of the thin-film functionalised ECF. Each point represents a measurement of (○) the passive 'off' ring-closed form or (●) the active 'on' ring-opened form of the SP sensor molecules. The blue, red, and green shows the results from the fibre when in solutions of (●) water without cations, (●) Ca^{2+} in water, and (●) Al^{3+} in water respectively. The last result (■) in each case was measured after leaving the fibres in water, Ca^{2+}, or Al^{3+} analytes in dark conditions for 1 hr, 1.5 hrs, and 17 hrs respectively.

long duration (17 hrs) enabling deeper penetration of the cations, and therefore higher complexation yield. The results show that the sensor molecules are trapped within nano-environment of the polymer matrix. The binding process and fluorescence response of the sensor–polymer layer is maintained over many switching cycles.

6.8   Summary and Conclusions

Sensor molecules that fluoresce when complexed with Al^{3+} are available, which can be used for the detection of Al^{3+} as an indicator of corrosion. An advantage of using a fluorescent indicator is that they can be specific and sensitive to very low (30 nM) concentrations of Al^{3+}. To enable direct sensing measurements, it is necessary to immobilise these sensor molecules on the surface of the MOF exposed core, which is known as surface functionalisation.

The results of this chapter show that mobility of sensing molecules is an important consideration when choosing a surface functionalisation method. The fluorescence signal from covalently attached single-ligand binding sensing molecules, such as lumogallion with Al^{3+} or SP with Ca^{2+}, was found to be only a few hundred counts above background. This low signal significantly reduces the SNR which impacts on the distributed sensing range when applied to distributed corrosion sensing, and would require very sensitive detectors which add to the cost of the system. Covalent bonding hinders the ability for sensing molecules to form multiligand complexes with Al^{3+}, as shown by the covalent bonding experiments using SP in Sec. 6.7.2. To overcome these problems associated with covalent attachment of sensing molecules, a new one step functionalisation method was developed, using thin film polymer doped with sensor molecules.

A doped thin polymer film ($\sim$50 nm) eliminates the need for functional groups on the surface of the silica core for sensor molecule attachment, and offers the prospect of being applied during the fibre drawing process. This method integrates the polymer, silica, and sensor molecule properties to create a distributed sensor capable of detecting an analyte of interest anywhere along the fibre length. The technique was successfully applied to the detection of Al^{3+} in solution by applying a thin film doped with either 8-HQ or SP multiligand binding sensing molecules. These experiments showed sufficient

mobility in the PMMA matrix to allow interaction of the sensing molecules with the analyte of interest. This functionalisation method for optical fibre sensors has the potential to be applied not only to detecting corrosion, but also a variety of sensing applications such as environmental hazard detection or detection of analytes within biological samples.

The air induced deterioration in transmission properties of the thin film functionalised ECF was shown to be an order of magnitude reduced compared to the un-coated result shown in the last chapter. The protective function of this coating is a practical improvement for any use of these fibres, particularly for photonic applications were environmental protection is needed while maintaining access to the guided light. Cutback measurements showed a ∼10–20 times increase in loss after applying the polymer layer. Analysing the overall loss of the polymer layer, by calculating the field distribution normalised attenuation of the layer, it was shown that the source of the added attenuation from the polymer layer is primarily due to surface roughness. Such roughness arises from excited SCWs, which become frozen in during material phase transition. Further work is needed to find ways of improving the functionalised surface, and exploit the method for more complex sensing molecules and applications.

7

Corrosion Sensing with Exposed-Core MOF

*"Everything must be made as simple as possible. But
not simpler."*

– Albert Einstein

Having established the fabrication and functionalisation of suitable optical fibres for the detection of Al^{3+}, the next step was to test the ability of these fibres for sensing actual corrosion.

7.1   Detecting Corrosion

Measurements were performed to test the ability of the ECF coated with the 8-HQ doped PMMA to detect Al^{3+}. Each measurement was done with 50 ms pulses of light from 18 mW 375 nm laser. Two separate experiments were performed, the first of which was to again immerse a section of the ECF in a solution containing Al^{3+} and the second experiment used a second section of ECF in a corroded simulated aluminium aircraft joint. This was done so the two measurements could be directly compared. For consistency, one longer length of ECF was coated and then cut, with half used on each of the experiments.

For the first experiment the exposed-core region of the coupled ECF was exposed to Al^{3+} by immersing a 23 cm long central section of the fibre in Al^{3+} solution in a capillary. The back reflected spectra were measured before immersion, immediately after immersion and periodically over a 2 hour period. The measured result before immersion subtracted from the after immersion results is presented in Fig. 7.1(a), which shows the fluorescence peaks of 8-HQ–Al^{3+} complex [208] for a series of immersion times. These solution measurements demonstrate the ability of the thin polymer film functionalised fibre to detect Al^{3+}. However, over time the measurement deteriorated
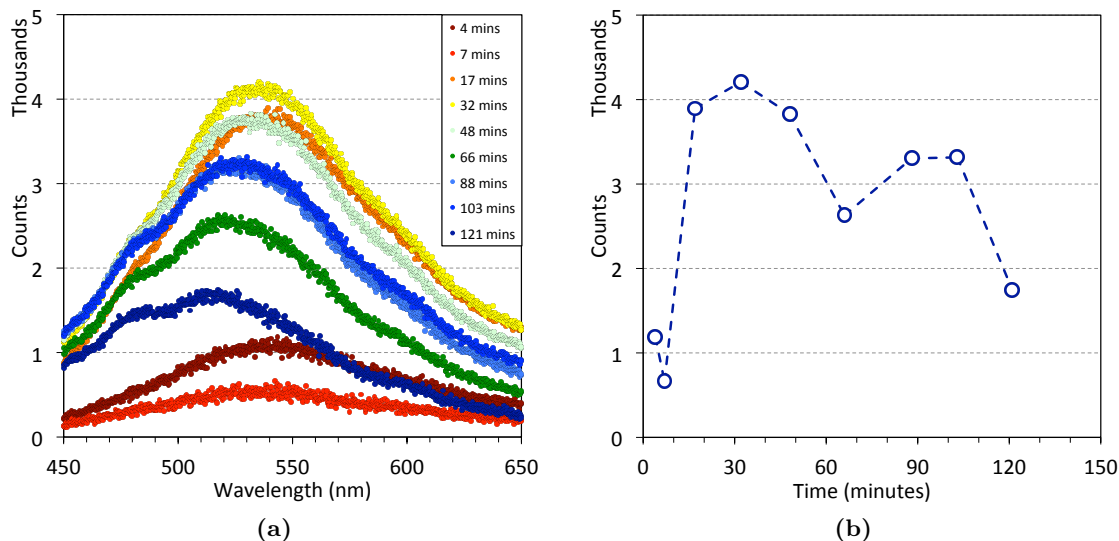
Figure 7.1 – (a) Periodic measurements of the back reflected spectra of the functionalised fibre immersed in solution containing Al^{3+}, and (b) plot of the peak intensities from the measurements shown in Fig. 7.1(a) as a function of time.

after peaking around half an hour after immersion, as shown by a plot of the peak intensities as a function of time in Fig. 7.1(b). The cause of this deterioration is not known, however it may be that the drying saturated solution causes salt crystal formation on the core at the air-liquid interface where the fibre enters and exits the solution.

For the second experiment, a 21 cm long aerospace–grade aluminium plate was machined with 2 mm slots and covered with a top plate of 1 cm thick perspex to allow visualisation of the corrosion. The perspex was drilled with 2 mm holes along the location of the slots so as to allow the ingress of the corrosive atmosphere to the aluminium. The plate was placed in the highly corrosive atmosphere of a salt spray chamber for four days to induce accelerated corrosion of the aluminium. The corroded plate, shown in Fig. 7.2(a) was allowed to dry and then the functionalised ECF was placed inside one of the corroded slots, as shown in Fig. 7.2(b). For a background measurement, the back reflected spectra from the ECF were measured while the plate was dry. The slot of the aluminium plate with the fibre inside was then filled with high purity Milli-Q water and the back reflected spectra measured immediately and again periodically over a 2 hour period.

The measured results with background subtracted are presented in Fig. 7.3(a), which
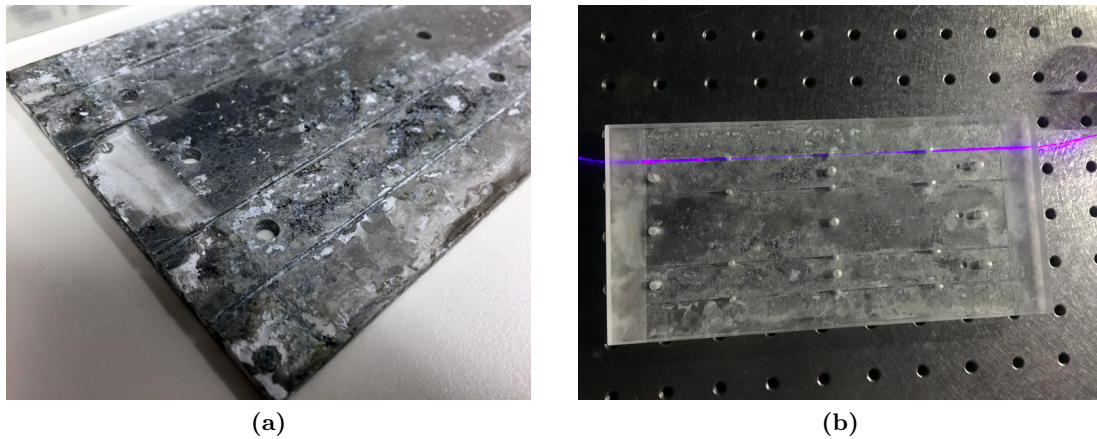
Figure 7.2 – (a) Aerospace grade aluminium plate after four days in the highly corrosive atmosphere of a salt spray chamber. (b) The corroded plate with a functionalised ECF (▌ – purple) inside one of the slots.

shows the fluorescence peaks of 8-HQ–Al^{3+} complex [208] for a series of time intervals after addition of the water. These simulated aluminium aircraft joint measurements demonstrate the ability of the ECF functionalised with a thin polymer film to detect Al^{3+} as a byproduct of corrosion. Figure 7.3(b) is a plot of the peak intensities of these in plate measurements as a function of time, which shows that there was an immediate initial response from the functionalised fibre which then logarithmically increased over the two hour period.

To make this sensing element useful for detecting corrosion within aircraft, a way to
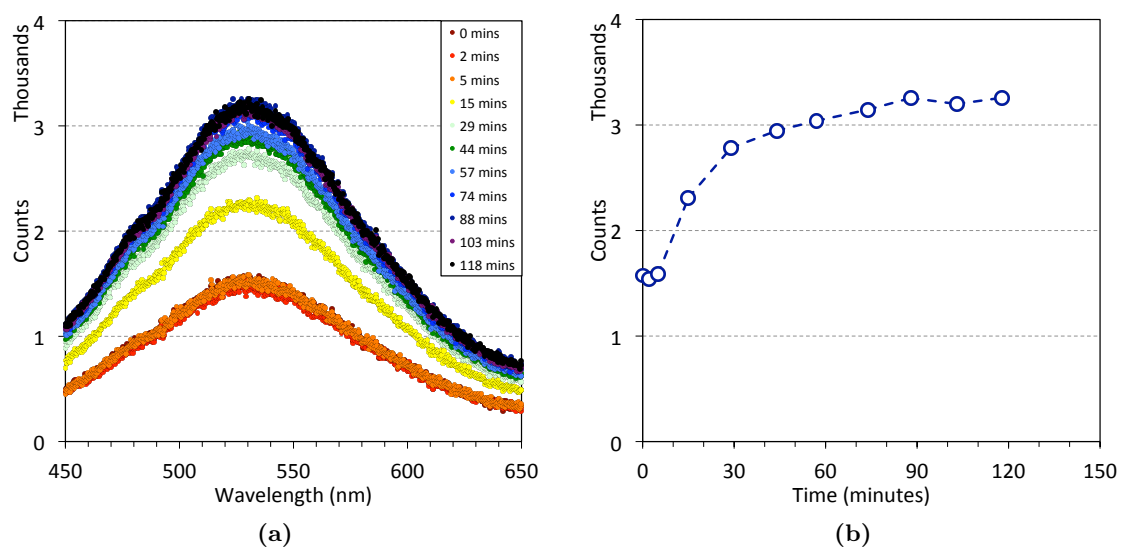
Figure 7.3 – (a) Periodic measurements of the back reflected spectra of the functionalised fibre inside a corroded simulated aluminium aircraft joint, and (b) plot of the peak intensities from the measurements shown in Fig. 7.3(a) as a function of time.

transition from the bulky/flexible equipment typically used for laboratory experiments to a stand-alone/purpose-built setup was necessary. This required finding ways to move away from nano-stage coupling arrangements, instead connectorising the sensing fibre into a small, portable and easy to use system.

7.2   Splicing

One can attempt to solve both the free space optics and coupling problems through the use of splicing. In addition to increasing the ease of use of the sensing fibre, splicing also provides stable permanent coupling, virtually eliminating the effects of thermal expansion. The general idea of splicing is to connect the ECFs to conventional core-clad silica fibres. By connectorising these silica MOF fibres direct 'plug and play' operation of the sensor could be obtained. The initial work on splicing an ECF to SMF was achieved by Warren-Smith using an Ericson arc splicer (FSU 975) [5]. The standard conventional SMF program was used with the exception of a 100 µm offset towards the SMF and manual alignment. Figure 7.4 shows a SEM image of the ECF spliced to SMF. There is core size and numerical aperture (NA) mismatch between the SMF and ECF, so relatively high splice insertion loss is expected compared with splicing SMFs together. The insertion loss was measured to be 3 dB for this fibre at a wavelength of 1550 nm, although modelling results indicated a theoretical insertion loss limit of 0.5 dB [5]. While Fig. 7.4 shows that there is some deformation of the ECF at the splice, as is generally expected for splicing SMF to MOF, the large air holes help to ensure that guidance in the core was still maintained.
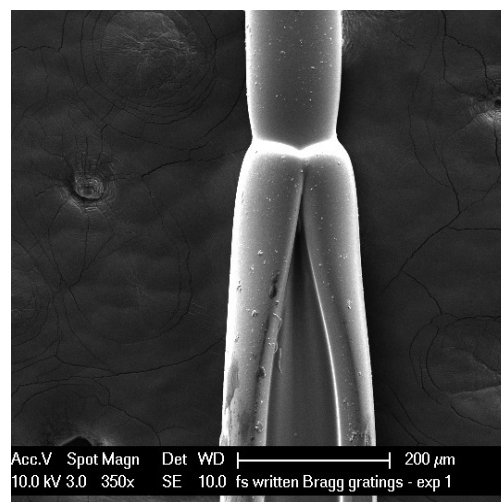
Figure 7.4 – SEM image of ECF spliced to SMF from Ref. [5].

7.2.1   Coupling Losses and Background Signals

While the splice insertion loss of 3 dB is good for coupling the excitation light to the fibre core, compared with freespace coupling, another factor that needed to be considered is the coupling of the fluorescence back into the SMF for measurements. On the one hand, it has been shown that fluorescence in the backward modes of the fibre have a higher efficiency compared to the forward modes [68, 137]. On the other hand, when we consider that the ECF has many hundreds of modes and the SMF only a few at the wavelengths being considered, it becomes apparent that the coupling efficiency of the fluorescence back into the SMF is limited.

While coupling of the excitation light requires a small core, such as that provided by the SMF, high efficiency capture and detection of the fluorescence requires a larger area MMF, shown in Fig. 7.5. Nevertheless, to check this hypothesis and check if back reflected fluorescence could be measured using an SMF, one end of a ECF was spliced to a connectorised SMF. To achieve this a commercially available connectorised SMF patch fibre was cut in half and spliced to a 150 mm length of ECF. The ECF was then functionalised with the 8-HQ doped thin-film technique discussed in the previous section. The functionalised fibre was coupled to a 375 nm (18 mW) laser via the connector of the SMF and the back reflected spectra recorded, shown in Fig. 7.6(a). For this and subsequent measurements, 10 spectra were recorded using 10 ms exposure in 20 ms intervals, and the average of these ten spectra is shown. Then a 100 mm long section along the fibre, was immersed in Al^{3+} solution. The back reflected spectra from the fibre were measured straight after immersion, shown in Fig. 7.6(b), where no change was noticed from the 8-HQ sensing molecule complexing with Al^{3+}. We observe
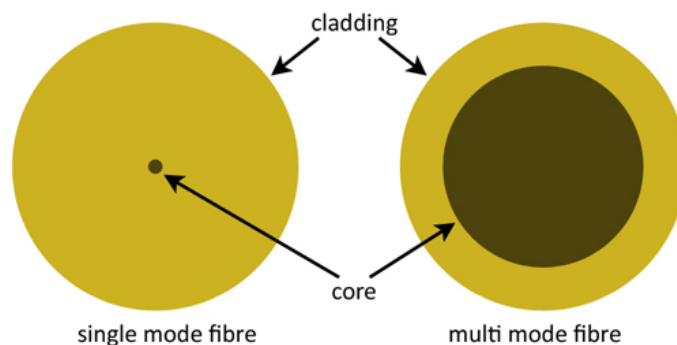
Figure 7.5 – Cross sections of single and multi mode fibres.
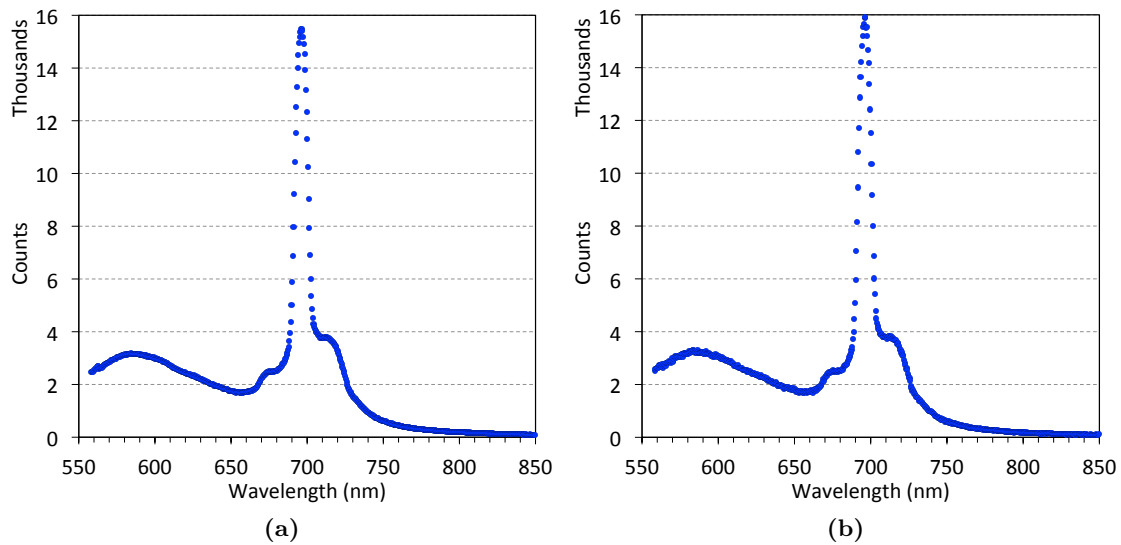
Figure 7.6 – Thin-film functionalised ECF spliced to SMF for coupling. (a) Dry - back reflected measurement, (b) straight after adding Al^{3+} solution - back reflected measurement.

large background fluorescence peaks coming from the device when measuring the back reflected signal, which interferes with any possible measurement of the fluorescence from complexed sensing molecules.

To overcome the back reflected background and limited back reflected fluorescence coupling efficiency into the SMF, a MMF fibre with core diameter of 62.5 µm was spliced to the other end (transmission end) to collect the fluorescence response from the fibre. This setup used an SMF to couple the excitation light into the fibre and MMF to collect the fluorescence produced by the sensing molecules. Initial experiments using this setup were done to test the ability of a fully connectorised system, with the ECF as a sensing element, to detect the onset of corrosion in a simulated aircraft joint.

7.3   Accelerated Corrosion Experiments

7.3.1   Setup

The next step was to put together a proof of concept setup to determine if the SMF and MMF connectorised ECFs can be used for fluorescence detection of Al^{3+}, and then be used for in-situ measurements in the accelerated corrosion tests at DSTG. This was done with a photodetector instead of the Horiba imaging spectrometer to make the setup portable. Several types of silicon (Si) photodetectors were tried, including a
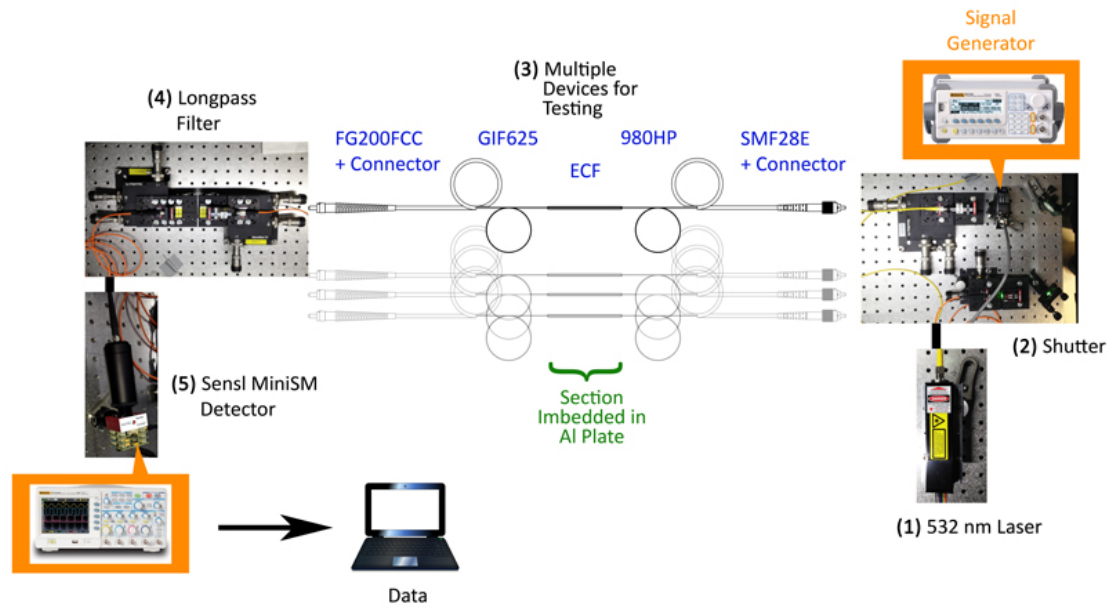
Figure 7.7 – Setup used to prove demonstrator concept, and intended to be used for salt-spray chamber experiments.

Thorlabs PDA36A, however it was found that 'single photon' sensitivity was needed to resolve the signal from noise. A schematic diagram of the experimental setup is shown in Fig. 7.7.

The best result, when comparing several available photodetectors, was found to be with the SensL MiniSM. This detector is capable of single photon detection with a response of around 170 kA/W at 600 nm. Initial results with Rhodamine B on the exposed core, using the setup shown in Fig. 7.7, are shown in Fig. 7.8. The first half of the result from the oscilloscope shows the detector dark counts, and the last part
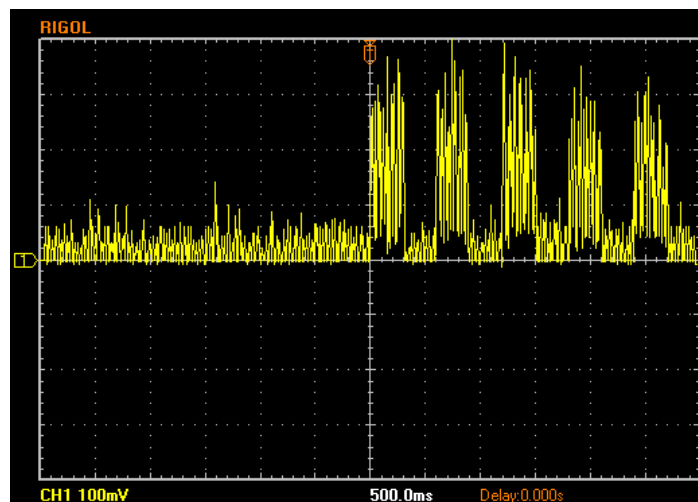
Figure 7.8 – Result of detection response from Rhodamine B, used to determine effectiveness of setup with photodetector.
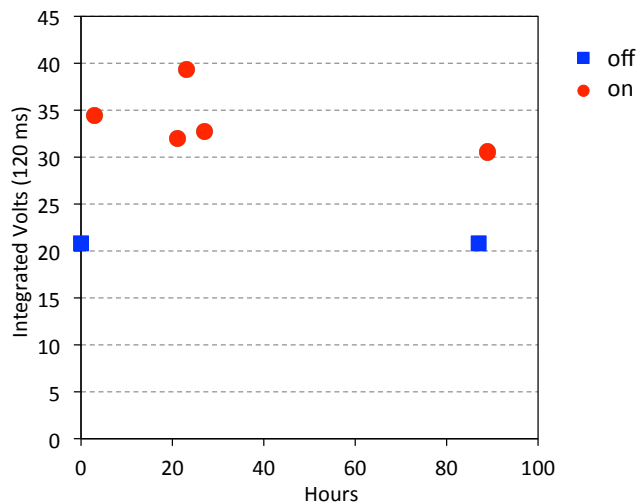
Figure 7.9 – Result of detection response from functionalised device with PMMA doped with SP.

shows the switching experiment where 300 ms pulses were used for the on/off pulses. The increased signal is due to Rhodamine B fluorescence at the surface of the fibre core.

An ECF was functionalised with PMMA+SP and spliced to the setup shown in Fig. 7.7, the results for which are shown in Fig. 7.9. These measurements were obtained by integrating the result from a 120 ms exposure to the 532 nm excitation light, while leaving the setup in dark conditions to allow the SP sensor to open for Al^{3+} interaction. The result shows clear change between the ring-closed and ion bound ring-opened forms ('off' and 'on' states) of the SP sensor molecules.

7.3.2   Experiments

Having determined the feasibility of an all connectorised fibre-optic system, the next set of experiments were to test the system using a simulated aircraft lap-joint supplied by DSTG. A salt spray chamber, shown by Fig. 7.10(a), was used to provide a highly corrosive environment. Four spliced ECFs were fitted to narrow slots cut along the length of the aircraft grade aluminium, and then a perspex cover bolted on top to allow viewing of corrosion. The cover had holes drilled to allow ingress of the corrosive liquid to the aluminium. This plate is shown in Fig. 7.10(b).

One of the fibres was left uncoated, while the other three were thin-film functionalised with PMMA+SP, PMMA+8-HQ, and un-doped PMMA respectively. The excitation and detection apparatus, shown in Fig. 7.7, was placed beside the salt spray chamber

Figure 7.10 – (a) Salt spray chamber used to accelerate the rate of corrosion of the aluminium joints; and, (b) the simulated aircraft joints with four ECFs mounted inside slots of the aluminium plate, and covered with perspex.
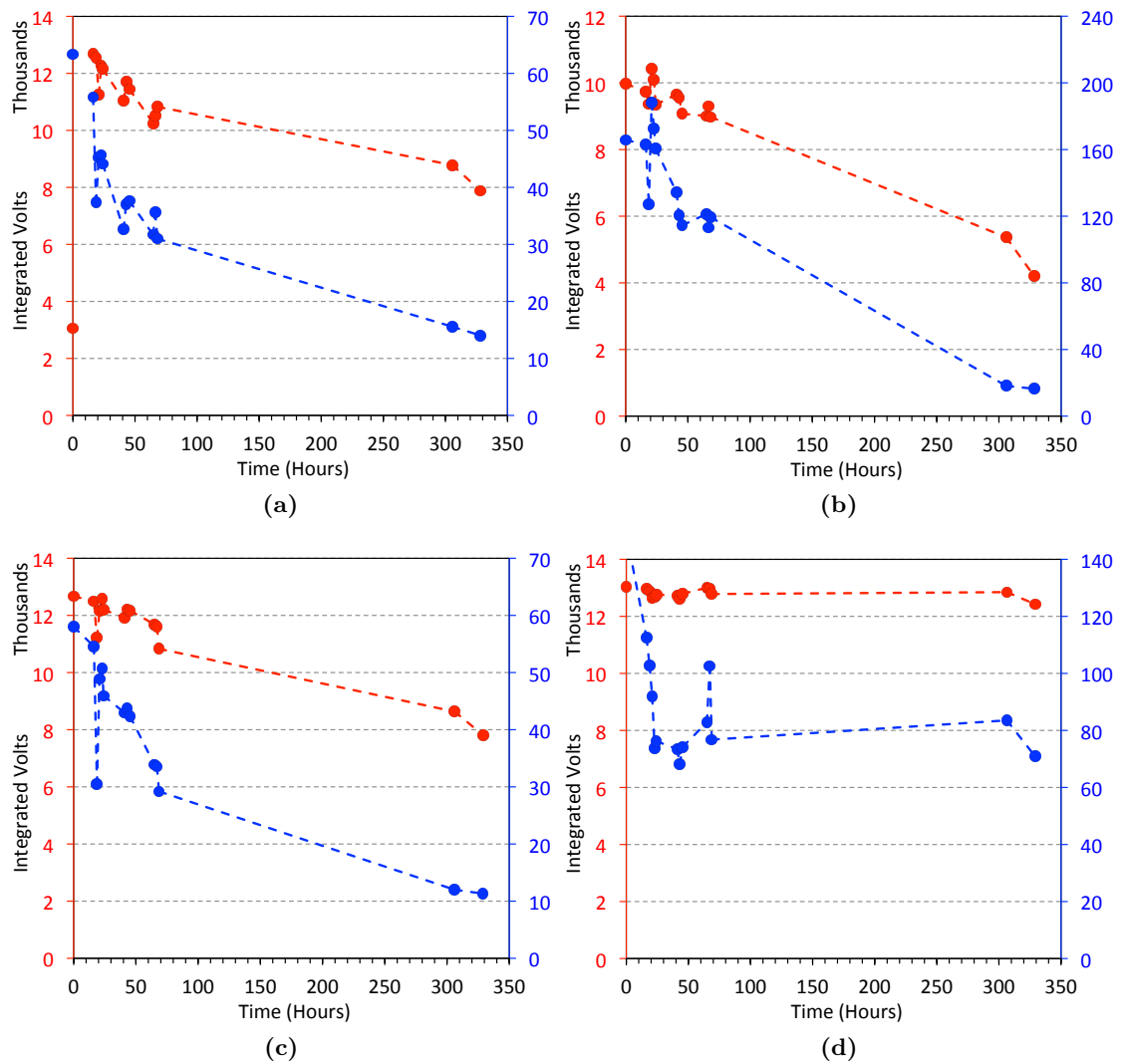
Figure 7.11 – Transmission without (● - red) and with (● - blue) long pass filter of: (a) PMMA+SP thin-film functionalised ECF; (b) PMMA+8-HQ thin-film functionalised ECF; (c) PMMA only thin-film functionalised ECF; (d) uncoated bare silica ECF.

so that in-situ measurements could be performed over time to measure the response of each of the fibres as corrosion progressed in the aluminium plate. A 372 nm excitation light source was used for the PMMA+8-HQ thin-film functionalised fibre, while a 532 nm source was used for the other three. Measurements where taken every two hours during the day for the first three days, left for 10 days and measured again. For each of the fibres, the excitation light source was used together with a long pass filter at the transmitted end of the fibre to measure the fluorescence response, shown by the blue trace in Figs. 7.11. Any changes in the transmission properties of the fibres was also characterised by using the 532 nm light source, shown by the red traces.

The transmission properties of the uncoated bare silica ECF (red curve in Fig. 7.11(d)) showed that the transmission properties of the sensing fibre did not degrade with time during the experiments (14 days). This showed that the ECFs are robust enough to withstand the harsh conditions of the salt spray chamber. For the three thin-film functionalised fibres Figs. 7.11(a)–(c), both the overall transmission properties as well as fluorescence decreased over time. This suggested that the harsh environment might have had an effect on the fibre's thin-film coating in a way that caused losses along the length of the exposed core. During the first few hours, the fibre functionalised with PMMA+8-HQ increased before the signal started to reduce. This may have been an indication that corrosion was detected, before the transmission properties of the fibre diminished.
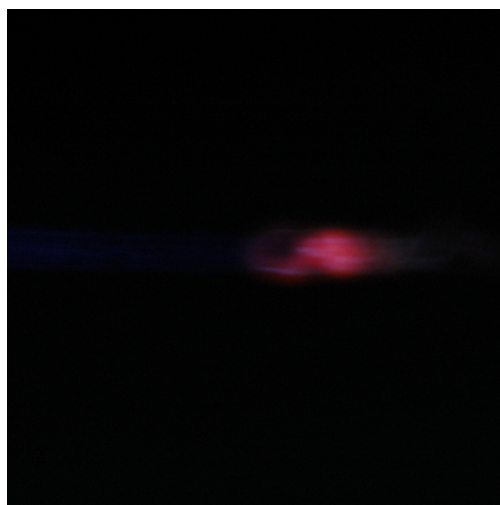
Figure 7.12 – Visual inspection of fluorescence from ECF functionalised with PMMA+SP in plate.

The fibres within the plate were visually inspected to see if scattered fluorescence could be observed from the outside of the fibres through the perspex cover. To achieve this, the salt spray chamber was opened and the excitation light coupled into each of the fibres. For the fibre coated with polymer doped with the 8-HQ sensing molecules, green fluorescence could be observed. Figure 7.12 shows the fluorescence that was observed from the PMMA+SP. This indicated that while the functionalised surfaces are working, the loss induced by the harsh conditions makes the signal difficult to detect along the fibre. This means that the percentage of coupled light guided by the core was being reduced by increasing losses at a faster rate than the increase in fluorescence coming from the sensing molecules. To detect this signal it was necessary to find ways to couple the excitation light into the core as well as collect the fluorescence from the same end of the sensing fibres.

Microscope images of the ECFs within the slots, after the salt spray chamber experiments and after drying, are shown by Figs. 7.13(a) and 7.13(b). The surface of the fibre with the thin-film polymer coating (Fig. 7.13(b)) looks to be much rougher than the surface of the uncoated fibre (Fig. 7.13(a)) which further suggests that the harsh environment might have affected the thin-film, increasing the transmission loss due to scattering effects. Further experiments, such as SEM imaging of the polymer surface to determine if the film has fragmented, are needed to determine the actual nature of the increased loss.

(a)   (b)
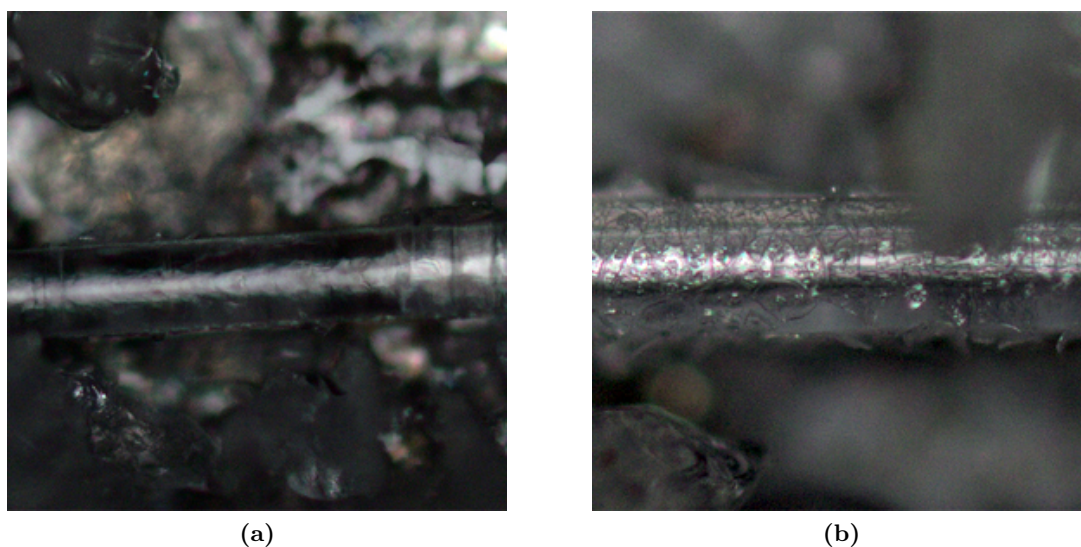
Figure 7.13 – (a) Uncoated ECF in slot after salt spray experiments. (b) Thin-film coated (functionalised) ECF in slot after salt spray experiments.

7.4   Proof of Principle Experiments

Establishment of a method to both couple the excitation light and collect the fluorescence from the same end of the micro-structured sensing fibre was needed. While coupling of the excitation light requires a small core, such as that provided by the SMF, high efficiency capture and detection of the fluorescence requires a larger area MMF, as was shown in Fig. 7.5. Experiments to measure the efficiency of backward fluorescence recapture using SCF, which has a core the same size as the ECF, or a commercially available double clad fibre (DCF) (NUFERN SM-9/105/125-20A) were performed. The DCF fibre has a small inner core (same size as a SMF-28), which can be used to couple the excitation laser light to the sensing fibre, surrounded with an inner clad multi mode region which could be used to collect and guide fluorescence from the higher order modes of the ECF.

Measurements were performed with an ECF in 10 µM solution of Rhodamine-B, results for which are shown in Figs. 7.14, where the blue and red spectra show the result with and without the Rhodamine-B fluorophore respectively. For comparison, the results of a ECF directly coupled via an objective (free-space), and SMF-28 spliced to the ECF, are shown in Figs. 7.14(a) and (b) respectively. Another experiment was performed using the SMF-28 with the polymer cladding removed, to create a double-clad structure with the outer cladding being air. The result of this stripped SMF-28 spliced to the ECF is shown in Fig. 7.14(c). Results of the SCF and DCF spliced to the ECF are shown in Figs. 7.14(d) and (e) respectively. A comparison of each of these results is shown in Fig. 7.14(f), being the ratio of recaptured fluorescence to background of the fibre for 560–640 nm wavelength range. Comparing each of the spliced fibres against the free-space measurement (Fig. 7.14(b)), the results show nearly no fluorescence signal is detectable via the SMF-28. When the cladding is stripped or when using a SCF, the signal is detectable at a ratio of ∼1.5. This is further improved when using the DCF, where the ratio is ∼2, which is approaching the free-space ECF measurement at a ratio of ∼2.7.

These initial results show that excitation of, and fluorescence detection from, the ECF is achievable when spliced with the DCF. It is expected that further improvements would be achieved by using a fully connectorised system with a double clad fibre coupler (DCFC) which would improve the collection optics.
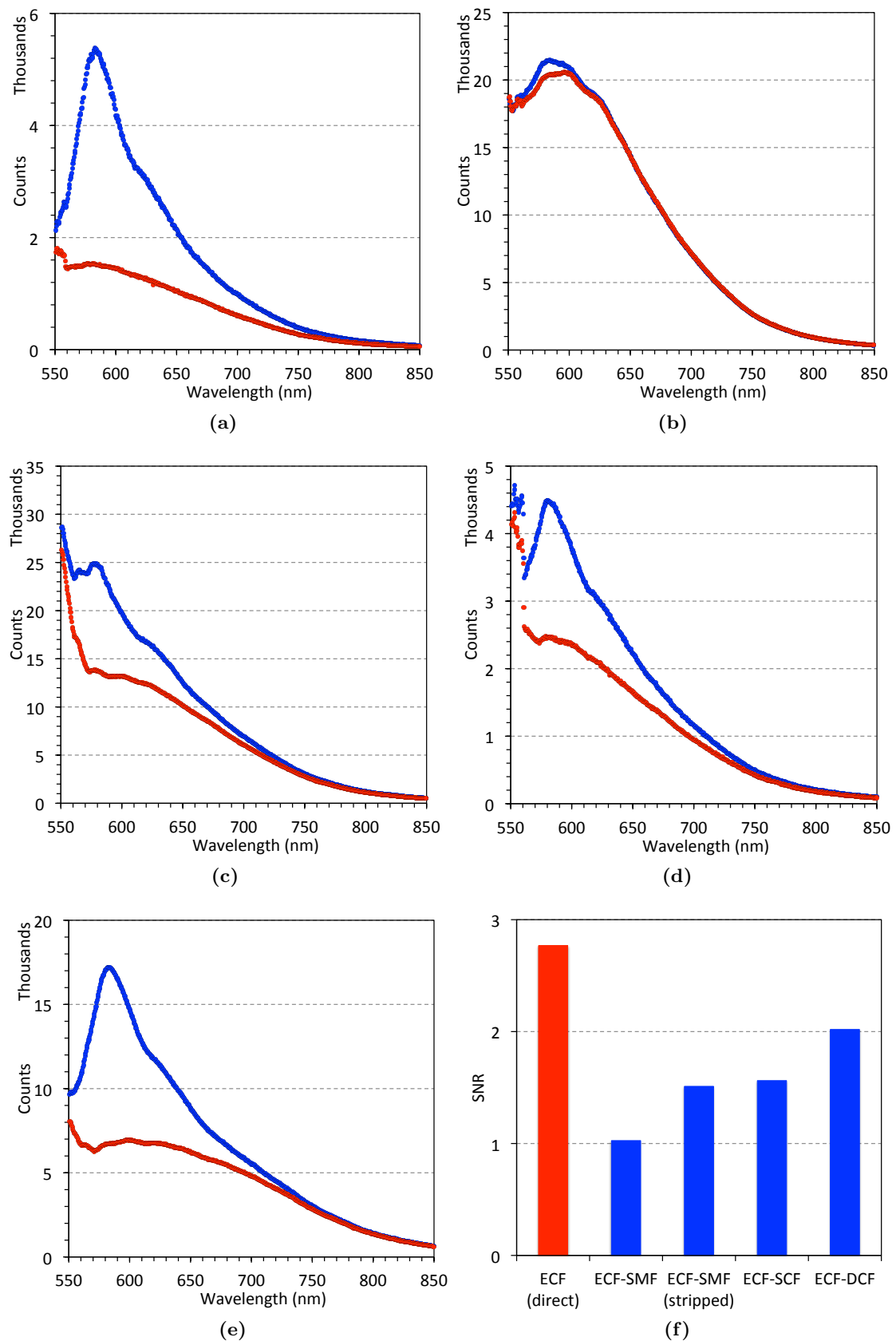
Figure 7.14 – Characterisation experiments of various excitation and collection fibres spliced to the ECF for fluorescence detection. In each case the ● - blue and ● - red spectra show the back reflected result with and without Rhodamine-B fluorophore respectively. Results (a)–(e) are freespace ECF, SMF spliced to ECF, stripped SMF spliced to ECF, SCF spliced to ECF, DCF spliced to ECF respectively. (f) Shows a comparison of these results.

7.5   Integrated Detection Instrumentation (Demonstrator) Design

While the project aims to develop a robust optical fibre based sensor capable of detecting corrosion anywhere along the fibre length was achieved, as shown in Sec. 7.1, more work is needed to turn this into a portable unit capable of being imbedded in the structure of an aircraft. To expand this work to a demonstrator, DSTG extended the program to include transition of this project into an integrated, portable sensor for the detection of Al^{3+} on a representative test article. This requires the design and implementation of an integrated ECF based system that can be used to show potential investors the detection of corrosion in a simulated aircraft lap-joint. The instrumentation, ECF integration and manufacture of the demonstrator is a continuation of the work shown by this thesis, and will be tested using the salt-spray chamber at DSTG to provide an accelerated corrosive environment.

Design of integrated corrosion detection instrumentation, in the form of a demonstrator, is shown in Fig. 7.15. This design incorporates two optical fibre sensor arms (functionalised silica ECF), in corroded and not corroded sections of an aluminium plate. Control of corrosion detection along each arm is done with a NI USB-6000 data acquisition (DAQ) unit via a computer graphical user interface (GUI) which also displays the results. This DAQ switches between each of the arms via a MEMS switch, then pulses the laser (Matchbox 405 nm). The laser pulse is guided along a SMF-28 fibre and transferred to a DCF via a DCFC. The DCF is spliced to the silica ECF which is functionalised with a thin-film polymer doped with 8-HQ, known to fluoresce strongly in the presence of Al^{3+}. The pulse of light guided by the core of the DCF is transferred
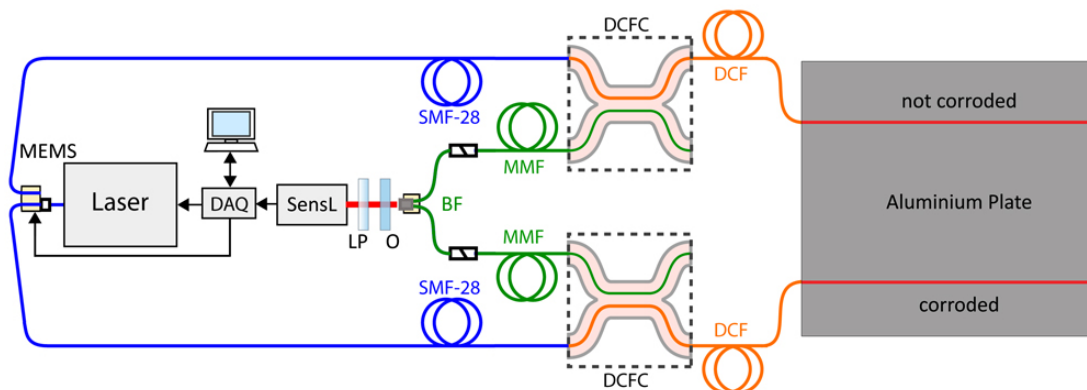
Figure 7.15 – Design of integrated detection instrumentation as a demonstrator

to the core of the functionalised ECF, and any fluorescence recaptured by the ECF is transferred back into the inner cladding of the DCF via the splice. This fluorescence is coupled to a MMF (100 µm bifurcated fibre) via the DCFC and imaged into the detector (SensL MiniSM) via an objective (O) and long-pass filter (LP), which are integrated within a lens tube. The signal from the SensL is processed by the DAQ and the result is displayed on the screen of the computer via the GUI. For the corroded arm, fluorescence is expected to be higher than for the non-corroded arm. This difference provides a differential measurement between the two arms, which provides the means of recognising corrosion within the aluminium plate. This demonstrator is being completed in 2016, and will be available for potential defence collaborators and investors to see a working example of a portable optical fibre sensor capable of detecting corrosion within the inaccessible areas of an aircraft fuselage.

8

Conclusion

"If I have seen further it is by standing on the shoulders
of giants."

– Isaac Newton

The research shown in this thesis advances optical fibre sensing technology with the objective to develop a fibre optic approach for detecting the initiators and/or by-products of corrosion within an aluminium structure. This thesis showed that significant progress in MOF based sensing technologies was necessary to achieve this objective. Results in Chapter 2 demonstrated that the best practical results for an optical fibre capable of distributed sensing should be obtained by an ECF that has low loss. The loss of the fibre impacts most on the fibres practical OTDR length, and while PF improves light overlap with the sensing environment, that increased overlap can also increase loss due to increased scattering. Essentially, the core diameter needed to be small enough so that there is sufficient PF to excite sensing molecules at the core surface but not excessively impact the fibres loss.

In previous research, it was found that F2 material was not suitable for ECFs requiring long term use in harsh environments. The work in Chapter 3 demonstrated that polymer SCFs also had substantial challenges to overcome in terms of fabrication and reducing loss. However, the ECF geometry was successfully transitioned from soft glass to silica with significantly better mechanical and thermal stability as a result. Silica also has high transmission in the UV-Vis-NIR spectral range, making it suitable for a greater range of fluorophores, including 8-HQ. The fibre loss of $\sim$0.1 dB/m at NIR wavelengths was the lowest achieved to date for ECF, which is important to realise long length distributed sensing. The production of these fibres was achieved by first gaining a practical understanding of the draw process beyond what was achievable by trial and error. Chapter 4 described how to use the analytical model provided by Fitt *et al.* [140]

to determine the draw conditions needed to produce multi-hole MOFs. This made it possible to predict the parameters needed to fabricate the first silica ECFs, thereby creating the type of desired asymmetric ECF geometry targeted towards distributed corrosion sensing.

For real time analysis along the ECF length, it was necessary to immobilise the fluorescent sensor molecules on the glass surface of the exposed core. Many strongly fluorescent Al^{3+} sensing molecules, such as 8-HQ, form a multiligand complex with the cation which required the development of a novel surface immobilisation process. For this, a new method to functionalise the ECFs with a thin-film polymer doped with the sensor molecules was developed. This method, demonstrated in Chapter 6, removed the need for surface attachment of functional groups, while integrating the polymer, silica and sensor molecule elements to create a distributed sensor capable of detecting Al^{3+} anywhere along the fibre's length. This surface immobilisation development, using a doped thin-film, offers the prospect of being able to be applied after the furnace stage of the fibre drawing process, for the fabrication of long length functionalised distributed sensing fibres. It was found that the thin-film coating also served a protective function, reducing deterioration in the transmission properties of the silica ECF by a further order of magnitude. Nevertheless, the thin-film had increased fibre loss, due to increased surface roughness arising from excited SCWs becoming frozen in during material phase transition.

Using the silica ECF functionalised with thin-film polymer, Chapter 7 demonstrated an optical fibre based sensor capable of detecting corrosion anywhere along the fibre length. This ECF was also used to develop a stand-alone/purpose-built setup for the detection of corrosion in simulated aircraft joints. To achieve this, single mode conventional fibres were spliced to the ECF for coupling of the excitation light to the core, while multi-mode fibre was spliced to the transmission end of the fibre sensing element to collect fluorescence from the sensing molecules at the functionalised core surface. This meant that standard optical fibre connectors could be used for direct 'plug and play' operation of the sensor. An all fibre-optic system was achieved for in-situ measurements of Al^{3+} corrosion byproducts from a simulated aluminium aircraft lap-joint. These in-situ measurements were performed over time to monitor the response of the sensing fibres as corrosion progressed in the aluminium plate, using DSTGs salt spray chamber. It

was found that the transmission properties of bare silica ECF did not degrade, while the transmission properties of the functionalised fibre decreased over time. While there was an indication that Al^{3+} was detected before the transmission properties of the fibre diminished, the harsh environment effected the transmission, reducing the ability to detect fluorescence from the surface of the ECF sensing element.

8.1 Future Prospects

The work conducted over the past few years, shown in this thesis, has extended the work on using MOFs as sensors. Improvements to the robustness of ECFs and transition into an integrated, portable sensor for the fluorometric detection of Al^{3+} in corroded structures has been demonstrated. However, further development of the ECF sensing element is needed to create a stand alone demonstrator that can be used to show the detection of corrosion in simulated aircraft joints. Double clad type fibres have a small inner core, which can be used to couple the excitation laser light to the sensing fibre, surrounded with an inner clad region which could be used to collect fluorescence from the higher order modes. This should provide the basis for future distributed optical fibre based corrosion sensors, capable of plug-and-play type operation with a stand-alone interrogation unit. To do this, further work is needed to integrate functionalised ECF with connectorised double clad fibres, fibre couplers, detectors and light sources.

While several significant challenges have been overcome, another important step is to combine the sensing element with distributed measurement techniques. This requires careful balancing to find the optimum core geometry that has the best compromise between loss, PF, and fluorescence capture efficiency ratio for distributed measurements. There are significant opportunities in further development of an easy to use model for predicting MOF draw parameters, as well as finding ways to improve the response and reduce the loss functional surfaces on the fibre. Ways of improving the thin-film functionalised surface to reduce loss is needed, such as investigate the use of fluorocarbon based polymers (such as PTFE) instead of using PMMA. Ultimately, low surface tension leads to higher amplitude SCWs and therefore higher loss due to scattering, so further research on increasing the surface tension of thin film polymers could potentially lead to low loss thin film functional coatings. Also, future work could assess the sensitivity of the ECF sensor to changes in refractive index during accelerated corrosion testing.

Further investigation is also needed to understand how to reduce the small air bubbles present in PMMA extrusions, which could potentially lead to lower loss polymer MOFs.

The results shown in this thesis are not limited to just corrosion or just structural health monitoring. These breakthroughs can be adapted to develop new sensors for use in environmental hazard detection, such as water safety, or detect analytes within biological samples. Further work on ensuring biological compatibility can lead to point-of-care *in-vivo* sensing devices for human health monitoring.

APPENDIX A

Paper 1.

Optical Fibres for Distributed Corrosion Sensing – Architecture and Characterisation

Roman Kostecki[1,a], Heike Ebendorff-Heidepriem[1], Stephen C. Warren-Smith[1], Grant McAdam[2], Claire Davis[2] and Tanya M. Monro[1]

[1]Institute for Photonics & Advanced Sensing and School of Chemistry & Physics, University of Adelaide, Adelaide, SA 5005, Australia

[2]Defence Science and Technology Organisation, Fishermans Bend, Victoria, Australia

[a]roman.kostecki@adelaide.edu.au

Abstract. This paper summarises recent work conducted on the development of exposed core microstructured optical fibres for distributed corrosion sensing. Most recently, exposed-core fibres have been fabricated in silica glass, which is known to be reliable under a range of processing and service environments. We characterise the stability of these new silica fibres when exposed to some typical sensing and storage environments. We show the background loss to be the best achieved to date for exposed-core fibres, while the transmission properties are up to ~2 orders of magnitude better than for the previously reported exposed-core fibres produced in soft glass. This provides a more robust fibre platform for corrosion sensing conditions and opens up new opportunities for distributed optical fibre sensors requiring long-term application in harsh environments.

Introduction

The high acquisition costs associated with modern military and civilian aircraft coupled with tighter budgets has resulted in the need for greater utilisation of existing aircraft fleets. Typically, military aircraft have a planned life-of-type of 25–30 years. In Australia, in many cases, almost twice this time is achieved before the aircraft is retired [1]. For civilian aircraft flying today, approximately 20% are considered to be aging, and as that number increases so does the need for heightened fleet monitoring by airlines and manufacturers [2] and continued intense focus and surveillance of these activities by regulatory agencies [3].

With advancing aircraft age there is an increased possibility that protective coatings will break down or be damaged, resulting in exposure of the base material to the environment and an increased possibility of corrosion [2]. The continual cycling of the structure also increases the possibility of structural fatigue damage, which constitutes one of the most significant safety concerns due to the potential for corrosion to combine with structural fatigue [4]. While attempts are made to prevent and reduce the effect of corrosion, in practice it is impossible to completely avoid. It is therefore essential that corrosion processes are monitored so that repair time and costs are minimised, and the structure is maintained in a safe operating condition.

Corrosion is most difficult to detect in the hidden metallic structure of an aircraft, such as lap joints, stiffeners and under sealant beads, since access to these areas usually requires time consuming and therefore costly disassembly [1]. Such areas are recognised as being particularly prone to corrosion, due to the possibility of creating a micro-environment within the crevice between the plates, accelerating the corrosion process [4]. Current non-destructive inspection methods, typically based on the use of a hand held ultrasonic probe, require a 5–10% section loss for corrosion to be reliably detected, at which stage the damage may be too severe to repair, and so the component often needs to be replaced [1]. Clearly a more proactive approach is needed to detect the initial onset of corrosion within these difficult to inspect areas.

Detecting corrosion in these areas is a distributed problem, and therefore requires a detection and/or monitoring system with the potential for distributed measurements, alerting the operator to the onset of corrosion. To monitor corrosion requires a sensor capable of measuring the changes that occur as

a result of the corrosion process. Many of the aircraft fuselage components are fabricated from aluminium-based alloys, hence aluminium (Al) ions are of particular interest because they are not only an indicator of the onset of corrosion [1], but also have the potential to be an environmental hazard [5].

Optical fibre based sensors are inherently suited to distributed sensing [6] and are typically in the order of only a few hundred microns in diameter making them very lightweight and suitable for embedment in inaccessible corrosion-prone areas. In addition they can be functionalised to detect particular species of interest [1] such as Aluminium.

Principles and Background

The Australian Defence Science and Technology Organisation (DSTO) have been collaborating for several years with The University of Adelaide towards the development of a distributed fibre optic detection and monitoring system, capable of identifying corrosion in particularly prone areas of an aircraft fuselage [6]. The collaboration originated under the Centre of Expertise in Photonics (CoEP), and is now incorporated within the Institute for Photonics & Advanced Sensing (IPAS). Ultimately, the optical fibre is intended to be placed in situ and be capable of detecting the onset and monitor the progress of corrosion anywhere along its length within the aircraft fuselage.

Conventional Optical Fibres. Initial work on the fluorometric detection of Al cations by the DSTO in conjunction with Monash University focussed on the use of conventional large core multimode fibres [1]. A range of different permeable polymer systems, doped with a compound that fluoresces in the presence of Al cations, were evaluated. The most promising of these was a flexible polyurethane the main constituent of which is a polyether polymer, poly(oxyethylene-co-oxypropylene), known as 3-PEG. This is a random copolymer of polypropylene oxide and polyethylene oxide with a mole ratio of 1:3. The average molecular weight is of the order of 5000 g.mol^{-1}, and is a cross-linked resin with a stoichiometric amount of 1,6-diisocyanatohexane (also known as hexamethylene diisocyanate, HDI) to produce a soft rubbery like polyurethane referred to as 3-PEG/PU. The 3-PEG/PU can be doped with a fluorescent compound, 8-hydroxyquinoline (8-HQ), which reacts with Al cations form a rigid octahedral complex which fluoresces at 516 nm under UV excitation at 360–390 nm. The reaction chemistry is shown in Figure 1.
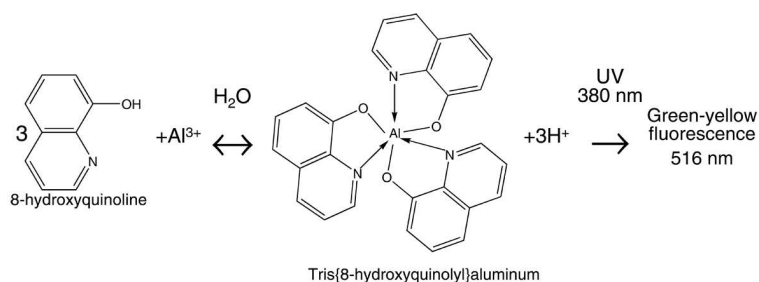
Figure 1. Reaction sequence for 8-hydroxyquinoline with Al cations [1].

The doped 3-PEG/PU was dip-coated onto the distal end of a conventional wide core optical fibre to create a sensing polymer bead at the fibre tip. This bead was exposed to 8-HQ in solution to allow the dopant to diffuse into the polymer, and then allowed to dry naturally prior to placement into the channel of a simulated lap joint in a region where the corrosion protective coating had been removed. This lap joint was then placed in a salt spray chamber for a period of 14 days to accelerate the corrosion process, as shown in Figure 2.

524 **Structural Health Monitoring: Research and Applications**
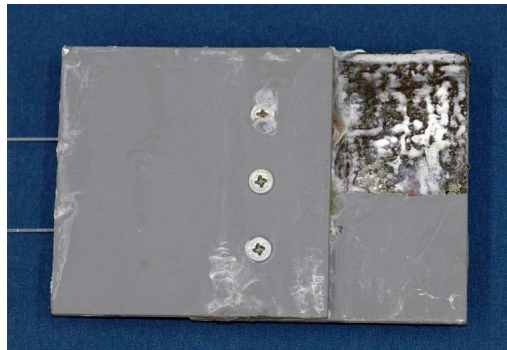
Figure 2. Simulated lap-joint after exposure in salt spray chamber for 2 weeks.

The sensing fibre was excited using an UV LED excitation source and the back-reflected fluorescence measured via a 3dB coupler using a micro spectrophotometer (Ocean optics). A schematic diagram of the experimental set-up is shown in Figure 3(a). The measured back fluorescence as a function of exposure time in the salt-spray chamber is plotted in Figure 3(b).

(a)   (b)
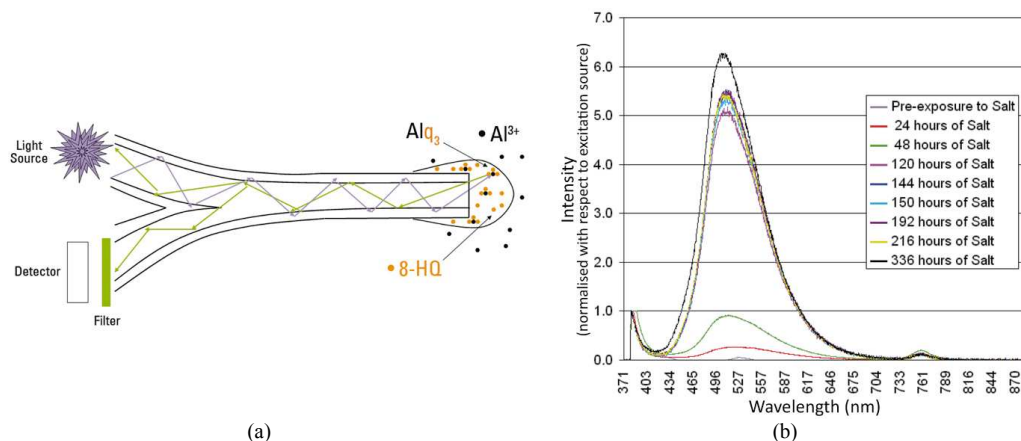
Figure 3. (a) Schematic for point detection from a doped polymer bead, and (b) the measured back reflected fluorescence from the fibre tip as a function of exposure time in the salt spray chamber.

For this case, where the bead is attached to the end of an optical fibre, there are fewer physical constraints on the properties of the permeable coating used to contain the fluorescent species compared to a distributed sensor. Ideally, it would be preferable to create sensitivity to Al cations by coating the fibre along the length, thus creating a distributed sensor rather than a local (point) sensor. In order to make distributed measurements the fraction of guided light propagating along the outside of the core needs to be accessed, which requires careful tailoring of the cladding refractive index to optimise the light/fluorophore interaction.

The concept of distributed detection of fluorescence from 8-HQ complex with Al cations in solution was demonstrated at Swinburne University in conjunction with the DSTO [7]. By using a large solid core (200 μm) silica fibre with the cladding removed, it was shown that Optical Time Domain Reflectometry (OTDR) could be used to not only detect the presence of the Al cations but also locate the position of this fluorescence 80 m along the fibres length. Figure 4(a) shows the setup, where photon counts were accumulated by the time-gated electronics in bins of 2 ns width, which corresponds to a length resolution along the fibre of 0.2 m, assuming a propagation velocity of

2×10^8 m.s^{-1}. An accumulation time of 10 min was used to obtain adequate signal-to-noise discrimination. These photon bin accumulations corresponded to the return time of flight of the fluorescence that originate at a distance along the fibre. The signal detected is shown in Figure 4(b), which represents the time domain response of the detection system when the de-clad fibre section was immersed in a 5×10^{-3} M solution of the 8-HQ complex.

(a)   (b)
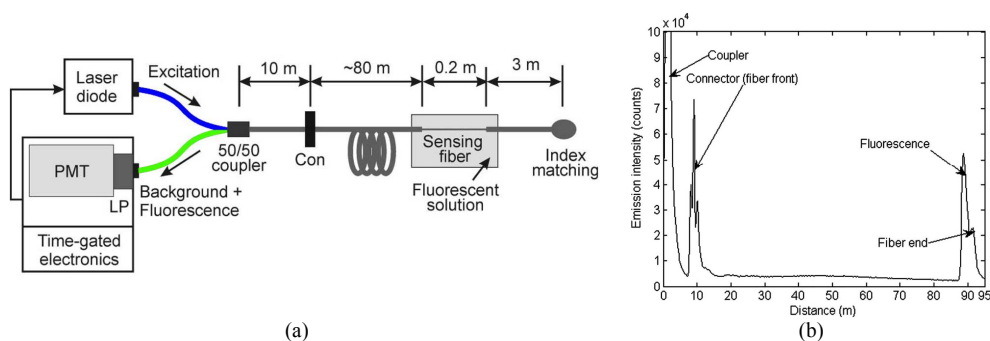
Figure 4. (a) OTDR setup for distributed measurements of Al cations (LP, long pass; Con, connector) in solution using a silica fibre with 200 μm core; with which the (b) time of flight resolved fluorescence response of the 8-HQ complex within solution corresponds to detection position along the fibre [7].

This OTDR experiment, conducted at Swinburne University, and described in detail in Ref. [7], shows that distributed fluorescence detection of the Al cations is possible. The fraction of power from the guided light propagating along the outside of the core was able to be used to excite the 8-HQ complex and the fraction of emitted florescence recaptured by the fibre core could be measured by the time-gated electronics. However, using such a large core diameter (200 μm) less than 0.1% of the total optical power propagates outside the core, making it impractical for applications requiring low detection limits [8]. Nevertheless, it is possible to increase this power fraction by reducing the core diameter.

Figure 5 shows a theoretical estimate [9] of the power fraction propagating outside a circular silica core, for core diameters from 460 nm to 10 μm. The excitation and fluorescence wavelengths used for this study were 375 nm and 516 nm respectively, being the excitation and fluorescence wavelengths of the 8-HQ complex, and for the region surrounding the silica core a refractive index of n = 1.33 was used. As a first approximation, the coupled incident beam waist was set at the same diameter as the core, which is reasonable for micron scale (> 1 μm) core diameters. The total fraction of guided light power (PF) that propagates outside the core, of all propagating modes excited by the incident beam as a function of the core diameter, is shown by the red curve in Figure 5(a). This PF curve shows that for core diameters less than 4 μm the fraction of power available for fluorophore excitation starts to significantly increase, being 0.3 and 2.1% at 4 and 2 μm diameters respectively. For core sizes below 1 μm in diameter there is another significant PF increase, where the calculated values are 2.8 and 17% at 1 μm and 460 nm diameters respectively. The corresponding fluorescence capture fraction (FCF) is shown by the blue curve in Figure 5(a). The FCF is defined as the fraction of fluorescent photons that are coupled to the guided mode(s) of the fibre. Although the total PF was used to calculate the FCF, for simplicity only the FCF into the fundamental mode (HE$_{11}$) of the fibre was considered for the special case of an attenuation-free fibre of infinite length. This FCF curve varies from a minimum of 1.1% to a maximum of 1.7%.
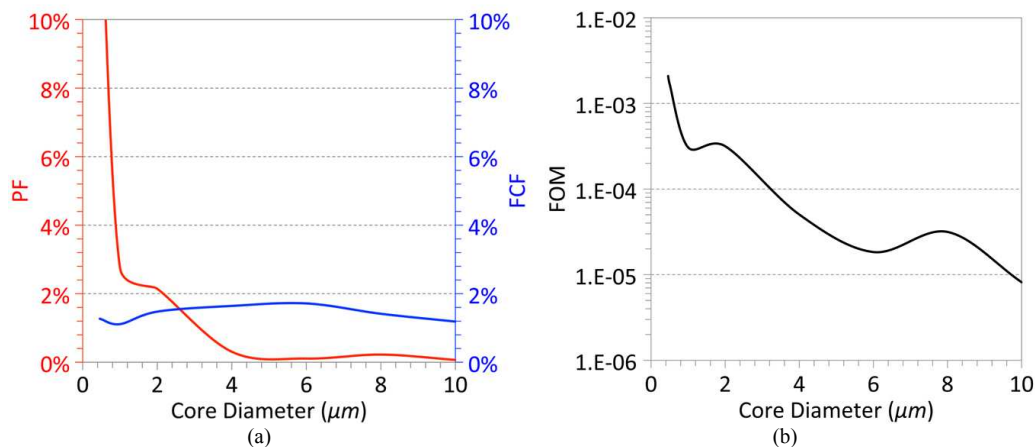
Figure 5. (a) [Red] Fraction of guided light power propagating outside a silica core as a function of core diameter assuming Gaussian beam excitation, and [Blue] the corresponding fluorescence capture fraction into the fundamental mode; and (b) the figure of merit as a combination of both.

The intensity of fluorescence that is measured from the backward propagating modes of the fibre is the result of both the incident excitation power and the number of fluorescence photons recaptured. These quantities can be brought together to provide a better understanding of the overall performance of the sensor as a function of the core diameter by defining a figure of merit, FOM=(PF)(FCF) [8]. This FOM is shown in Figure 5(b), where we observe an order of magnitude increase in sensor performance between the peaks at 8 and 2μm, and no significant change in performance from 2 to 1 μm. Another factor, which will influence the FOM, is the fibre loss, which increases with smaller core diameters (and therefore greater PF) due to the increased scattering resulting from surface imperfections. Previous work [8] has included the effect of fibre loss on the total FOM, and the next step is to include this with respect to this work.

Microstructured optical fibres (MOFs). Unlike glass nano-wires [10], a MOF [11] provides a means for obtaining long lengths of uniform micrometre-nanometre scale suspended and protected cores. A protected core geometry is necessary for sensing in harsh environments such as the application under consideration in this paper. In particular, the suspended-core fibre [12] design, which consists of a small glass core suspended by thin struts inside voids within the fibre, have found extensive use in chemical sensing applications [8, 13]. For these fibres the PF overlaps with the voids, and by controlling the size of the core, this overlap between the light and the voids can be adjusted. If the voids of the fibre are then filled with liquids or gases this controllable interaction allows sensing measurements to be performed, using methods such as direct absorption [14] or various fluorescent techniques [8, 15]. These suspended-core fibres dramatically improve fluorescence-based fibre sensors by making use of the increased PF provided by the micrometre scale core size and therefore increased sensor performance. Figure 6 shows a suspended-core fibre, recently fabricated within IPAS at the University of Adelaide, based on undoped high purity fused silica known as Suprasil F300HQ (Heraeus Quarzglas GmbH & Co.KG).

Figure 6(a) shows the overall suspended-core structure, with the polymer coating removed, this example has an outside diameter of 270 μm, although smaller sizes can easily be achieved. An enlargement of the core and holes region in the centre of the fibre is shown in Figure 6(b), where the core of the fibre is the small triangular element in the centre of the image (highlighted by the green box), suspended on three thin struts. The three black voids are the holes within the fibre cross-section, which form the cladding region used to provide the refractive index contrast needed for light confinement, and can also be used as sample chambers, with each hole diameter being 12.4 μm, defined as the diameter of a circle whose area is equal to the cross sectional area of the hole.

The web thicknesses are at least 0.16 μm, while the core has an effective diameter of 1.7 μm, defined as the diameter of a circle whose area is equal to a triangle that fits wholly within the core area [16].

Figure 6. Scanning electron microscope cross section images of (a) the silica suspended-core fibre with a outside diameter of 270 μm; and, (b) an enlarged image of the core and hole region, where the core is highlighted by the green box, having an effective diameter of 1.7 μm.

While suspended-core fibres have provided a highly sensitive sensing platform [8, 14, 17-20], exploiting the significant fraction of guided power located within the holes, the closed structure makes it impossible to use them for distributed sensing applications. To overcome this, fabrication techniques that expose the core have been demonstrated by micro-machining fluidic side-channels at several locations along the fibre length [21-24], which results in short exposed regions in the order of tens of microns. This provides access to the core by the analyte, making it useful for real time sensing applications, but is still not practical for distributed sensing applications where long lengths are required. To overcome this problem, it has been demonstrated [25, 26] that effectively 'opening up' one of the voids within the fibre during the initial fabrication stages, creating an exposed-core fibre, can allow the guided light to interact with the surrounding medium anywhere along its length. This method provides the ability to fabricate exposed-core fibres hundreds of metres long with a fixed microstructured cross section.

The fabrication of exposed-core fibres is challenging due to their asymmetric cross section, where the method involved modification of the established cane and sleeve process [16] by introducing a wedge in the preform fabrication process [26]. These fibres were initially produced in soft glass (Schott F2) material, which has a glass transition temperature low enough to make it practical for extruding the structured preform [27]. The process, summarised in Figure 7, involved extruding an F2 soft glass billet into a wagon-wheel (WW) structured preform at high temperature and pressure. The WW preform was then drawn to a cane (~1 mm diameter), using a fibre drawing tower, then inserted into an extruded F2 soft glass wedged jacket (sleeve). The cane-in-jacket preform was then drawn to fibre with an outer diameter of ~160 μm diameter (top-right of Figure 7) where the ~3 μm effective diameter core, in the exposed region highlighted by the green box, is suspended by three thin struts [26]. An enlarged view of the exposed core structured region of the fibre is shown in the bottom-right view of Figure 7.
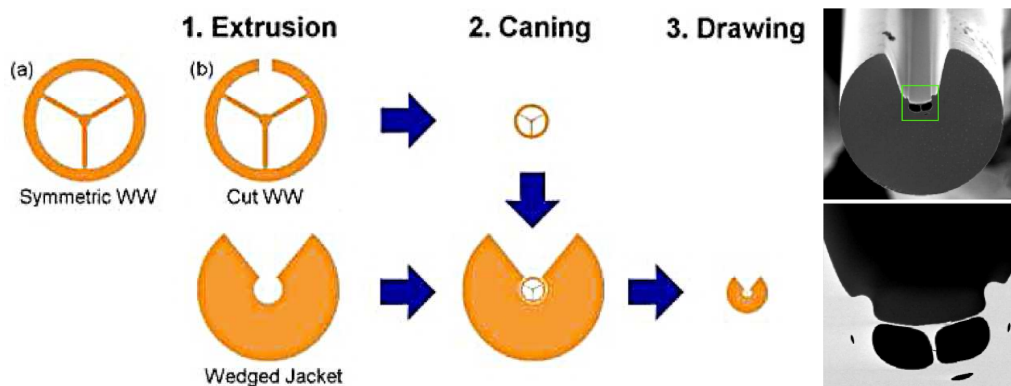
Figure 7. (Left) Schematic diagram of F2 soft glass exposed-core fibre fabrication process, with scanning electron microscope images of (top-right) the resulting exposed-core fibre with a outside diameter of ~160 μm; with an enlargement of the area highlighted by the green box (bottom-right) showing the core, hole and strut structured region, where the core has an effective diameter of ~3.0 μm [26].

Fabrication of these exposed small-core fibres was a significant milestone in the development of the distributed fibre optic corrosion sensor. For the first time, small core distributed fluorescence measurements became possible [6], where the increased fraction of power from the guided light propagating outside the small core could be accessed anywhere along its length, whilst still being protected by the outside sleeve. Since the F2 soft glass is not transparent at UV wavelengths, another fluorophore (lumogallion) with excitation and fluorescence wavelengths at 502 and 588 nm respectively, was used for Al cation detection. Unfortunately, it was found that F2 soft glass was not suitable for long term use and/or harsh environments [26, 28], where the fibre loss increased by 0.4 ± 0.048 dBm^{-1}day^{-1} while in storage. These loss and deterioration issues associated with the soft glass material from which they were fabricated precluded their long-term practical use under harsh conditions.

To produce a distributed fibre optic corrosion sensor capable of withstanding the intended harsh conditions, other fibre materials need to be investigated. Silica is known to be reliable under a range of processing and use environments, with relatively better mechanical and thermal stability [29]. Highly homogeneous, high purity bulk material is commercially available, which has led to silica telecommunications fibres regularly being made with low loss (~0.2 dB/km at NIR wavelengths) [30]. Silica also has high transmission in the UV-Vis-NIR spectral range, making it suitable for a greater range of fluorophores, including 8-HQ. In the next section we report the first silica exposed-core fibres produced, and characterise their environmental stability when exposed to typical sensing and storage environments.

Silica Exposed-Core Fibres

As discussed in the previous section, the rationale behind producing silica exposed-core fibres for corrosion sensing applications was to make a physically robust sensing element for long length distributed sensing applications. The fabrication of a microstructured fibre with the core exposed along the whole length provides near-instantaneous measurements of fluorescence intensity while additionally allowing the opportunity for spatial measurements along the length of the fibre through temporal detection methods such as OTDR [26]. High purity fused silica Suprasil F300HQ was chosen because of its low hydroxide (OH) content and availability with tight geometric tolerances [32]. This material has high transmission in the UV-Vis-NIR spectral range, making it suitable for a range of fluorophores, and is known to be reliable under a range of processing and use environments, with good mechanical and thermal stability [29]. Unlike soft glass, the glass transition temperature of silica is high making it challenging to extrude, and since the exposed-core fibres are asymmetric, new fabrication methods needed to be established.

Fabrication. The silica exposed-core fibre preform, as shown in Figure 8(a), was fabricated by drilling three holes along the length of the fused silica rod, with centres spaced such that they form an equilateral triangle, and a slot was cut along the length of one of the holes. These methods expand on a combination of work previously shown by Webb *et al.* [14] for fabricating silica suspended-core fibres by drilling the preform, and Warren-Smith *et al.* [26] for cutting a thin slot into the side of the symmetric preform (soft glass) in order to expose the core region. The preform was cleaned after drilling using acetone and ultrapure (Milli-Q ™) water, then etched in a buffered hydrofluoric acid solution (BHF), made using 6 volumes of ammonium fluoride (NH_4F, 40% solution) to 1 volume of hydrofluoric acid (HF, 50% solution), with a known etch rate of 100–250 nm/min [33].
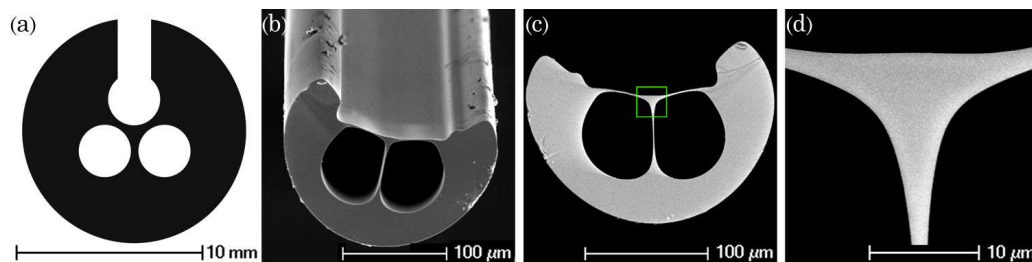
Figure 8. (a) Cross section of the preform fabricated from Ø12 mm F300HQ silica rod; and, scanning electron microscope images of (b) the silica exposed-core fibre with (c) the cross section measured at the maximum to be Ø202 μm; and, (d) an enlarged image of the core having an effective diameter of 10.0 μm [31].

A single long length (> 100 m) of silica exposed-core fibre, as shown in Figure 8(b), was drawn using a 6 m tower with a graphite furnace, positive pressurisation system and automated diameter control. The outside diameter and effective core diameter, as shown in the SEM images of Figures 8(c)-8(d), were measured as 202 and 10 μm respectively. The fibre loss measurement results taken directly after fibre drawing were 1.12±0.15, 1.10±0.08 and 1.43±0.39 dBm^{-1} at 532, 900 and 1550 nm respectively [31]. This relatively large core silica exposed-core fibre was useful to enable surface analysis of the core, and for determining the environmental stability when exposed to some typical sensing and storage environments. For sensing purposes, smaller cores have greater merit, as discussed in the previous section. To fabricate an exposed small-core fibre, a combination of the method used above with the caning and sleeving process, shown in Figure 7, was used. A single long length silica exposed-core fibre, as shown in Figure 9(a), was drawn where the cross section is shown in Figure 9(b) with an outside diameter of 150 μm. Figure 9(c) shows the hole and strut structure which forms the triangular shaped core exposed to the outside environment on one side. The core in this case, shown in Figure 8(d), has an effective diameter of 1.7 μm.
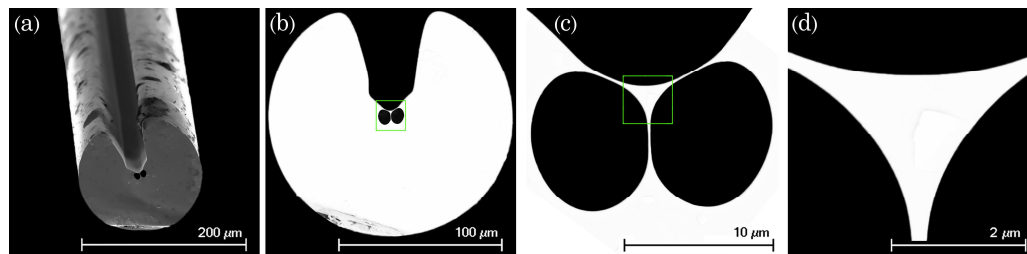
Figure 9. Scanning electron microscope images of (a) the small core silica exposed-core fibre with (b) the cross section measured at the maximum to be Ø150 μm; (c) the structured core, holes and strut region; and, (d) an enlarged image of the core having an effective diameter of 1.7 μm.

Environmental Stability. The silica exposed-core fibre, shown in Figure 8, was used for measuring the deterioration characteristics in transmission properties when exposed to typical sensing and processing environments, where the structure also provides access to the core for post exposure surface analysis. In the case of corrosion detection, it is expected that the fibre might be exposed to the environment, coming in contact with the surrounding air or water.

To measure the exposure induced deterioration in the transmission properties of the silica exposed-core fibre, any changes over time in the transmission characteristics were fitted to the equation,

$$P_{\lambda,t} = P_{\lambda,0}\, 10^{-\xi t/10} \tag{1}$$

where ξ is the loss change in dB/day.

The result of the change in fibre loss (ξ in Eq. (1)) for a 4.2 m length of the exposed-core fibre exposed to air for 180 hrs is shown in Figure 10(a), where the 95% confidence interval is also shown in black. This result shows that there is a sharp loss peak at 515 nm, equivalent to 0.043 $dBm^{-1}day^{-1}$, and a broad loss from 450 to 900 nm with a peak of 0.023 $dBm^{-1}day^{-1}$. At wavelengths from 900 to 1340 nm the loss is at 0.0043 $dBm^{-1}day^{-1}$, and drops below the detection limit of the experiment for wavelengths > 1340 nm. This result shows that the air exposure induced deterioration in the transmission properties of the silica exposed-core fibre is ~2 orders of magnitude better than for the exposed-core fibres produced in F2 soft glass. This measurement was repeated for a 1 m length of the silica exposed-core fibre with an 8 cm centrally located section of the fibre submersed in Milli-Q water. Figure 10(b) shows that the reduction in the transmission properties of the fibre is 0.067 $dBm^{-1}day^{-1}$ for wavelengths shorter than 1450 nm.
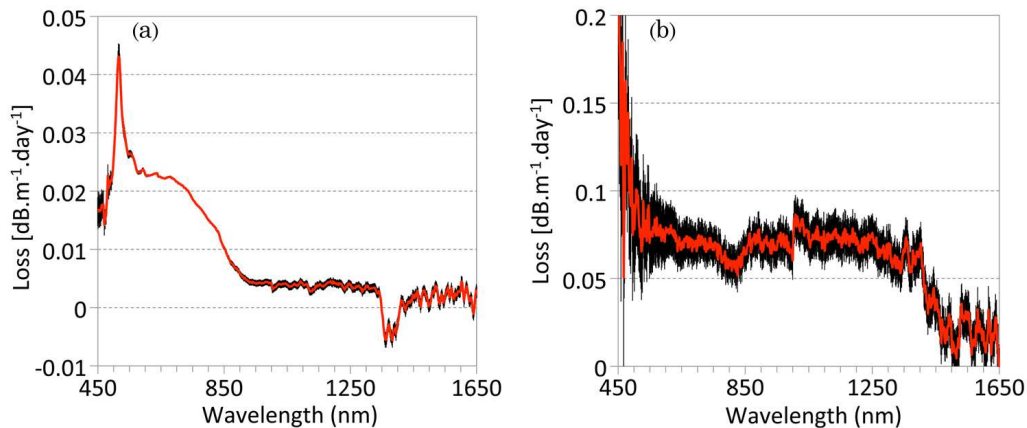
Figure 10. Deterioration in the transmission properties of the silica exposed-core fibre when exposed to (a) air; and, (b) water. The red line shows the change in fibre loss (ξ in Eq. (1)) with the 95% confidence interval shown in black.

This deterioration in the transmission properties is expected to come from changes in the mechanical and/or compositional characteristics at the core surface, causing light scattering effects [34, 35]. When the core diameter is reduced, these light scattering effects are expected to increase, as a greater portion of guided light travels outside the core [19]. Further work is required to quantitatively determine the effect that core size has on the deterioration in the transmission properties of the silica exposed-core fibre.

In order to determine the differences between the mechanical and compositional characteristics of the exposed sample surfaces, nanometre-scale topographical and phase mapping of the exposed-core fibre core surfaces was performed using Tapping Mode Atomic Force Microscopy (AFM). Figures 11(a)–11(c) and 11(d)–11(f) show the AFM phase and topology results of a 25 μm^2 section across the core for the exposed-core fibre exposed to air for 19 days and Milli-Q water for 3 days

respectively. For the core area exposed to air, the nanometre scale spikes in the topology and phase shift suggest small impurities within the surface structure, while the bulk of the material is homogeneous in composition with nanometre scale roughness. For the core exposed to water, large peaks measuring > 100 nm in height and several microns across the surface suggest that impurities from the water have been deposited onto the core. The darkest areas in the phase image show up on the topology to be slightly lower than the surrounding bulk, which may also be an indication of surface damage such as micro-fracturing [34].
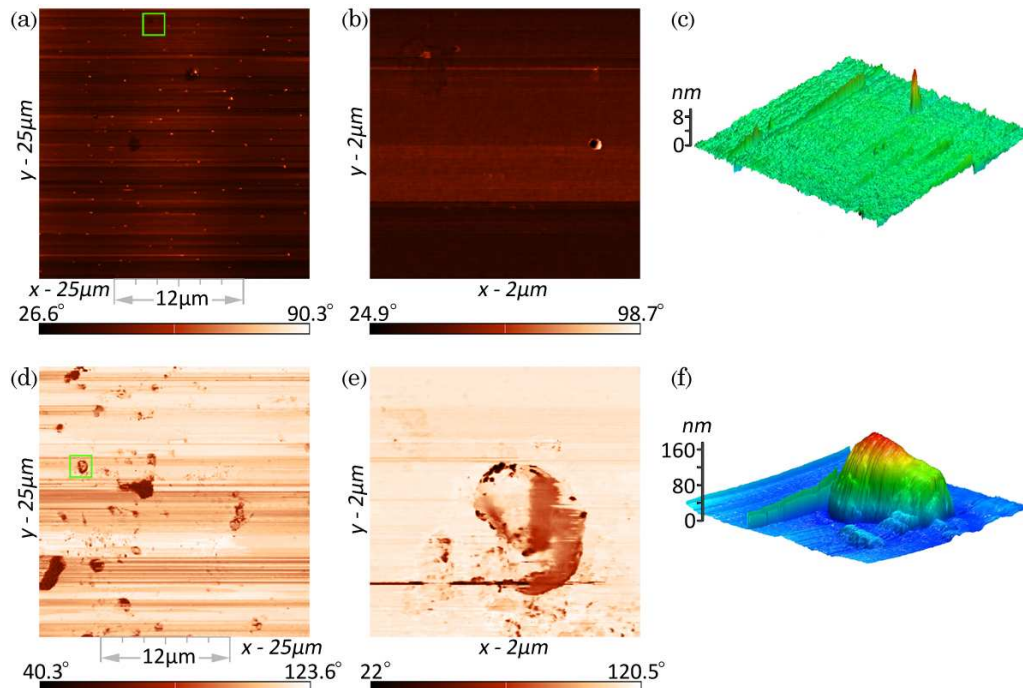
Figure 11. Tapping Mode Atomic Force Microscopy images of the exposed-core fibres exposed to (a)–(c) air, and (d)-(f) water. (a) and (d) show the phase images across the core region indicated by the 12 μm area on the x-axis, with [(b) and (e) respectively] enlarged phase images of the area shown by the green box; and, (c) and (f) showing their respective topologies.

Conclusion

We have summarised recent work done to develop a distributed fibre optic detection and monitoring system, capable of identifying corrosion in particularly prone areas of an aircraft fuselage. This research led to an exposed-core fibre distributed corrosion sensing element produced in lead silicate soft glass, which was found to deteriorate quickly when exposed to the harsh conditions of a simulated corrosive environment, making it impractical for long term use on Defence Platforms. Further work has been presented on newly developed exposed-core fibres fabricated using silica material, which is known to be reliable under a range of processing and service environments. These new silica exposed-core fibres show a relatively low loss with deterioration in the transmission properties being ~2 orders of magnitude better than that for the soft glass version. Although the silica material shows good stability in air and water, the build-up of contaminates on the surface and micro-fracturing are the most likely cause for the degree of deterioration measured.
In the future, further practical issues need to be solved, particularly in how to package the exposed-core fibre such that it is sensitive to Al cations but protected from the harsh environment of an aircrafts fuselage. Further work is also needed to determine if the degree of deterioration measured is sufficiently low for practical application to the intended use on Defence platforms.

532 **Structural Health Monitoring: Research and Applications**

References

[1] G. McAdam, P. J. Newman, I. McKenzie, C. Davis, and B. R. W. Hinton, Fiber optic sensors for detection of corrosion within aircraft, Struct. Health Monit. 4 (2005) 47–56.

[2] J. Hall, Corrosion prevention and control programs for Boeing airplanes, SAE Technical Paper 931259 (1993)

[3] Civil Aviation Safety Regulations 1998, Part 39.001(1), AD/B737/52 Amdt 3 - Corrosion Prevention and Control Program (CPCP) (2011)

[4] I. McKenzie and P. J. Newman, Methods for detection of corrosion in aircraft structures using fiber optic technology, In: Tri-Service Corrosion Conference (1999) 15-19 November, Myrtle Beach, South Carolina.

[5] J. Scancar and R. Milacic, Aluminium speciation in environmental samples: a review, Anal. Bioanal. Chem. 386 (2006) 999–1012.

[6] S. Warren-Smith, E. Sinchenko, P. Stoddart, and T. Monro, Distributed fluorescence sensing using exposed core microstructured optical fiber, IEEE Photon. Technol. Lett. 22 (2010) 1385–1387.

[7] E. Sinchenko, W. E. K. Gibbs, C. E. Davis, and P. R. Stoddart, Characterization of time-resolved fluorescence response measurements for distributed optical-fiber sensing, Appl. Opt. 49 (2010) 6385–6390.

[8] E. P. Schartner, H. Ebendorff-Heidepriem, S. C. Warren-Smith, R. T. White, and T. M. Monro, Driving down the detection limit in microstructured fiber-based chemical dip sensors, Sensors 11 (2011) 2961–2971.

[9] S. C. Warren-Smith, S. Afshar V., and T. M. Monro, Theoretical study of liquid-immersed exposed-core microstructured optical fibers for sensing, Opt. Express 16 (2008) 9034–9045.

[10] L. Tong, R. R. Gattass, J. B. Ashcom, S. He, J. Lou, M. Shen, I. Maxwell, and E. Mazur, Subwavelength-diameter silica wires for low-loss optical wave guiding, Nature 426 (2003) 816–819.

[11] T. M. Monro and H. Ebendorff-Heidepriem, Progress in microstructured optical fibers, Annu. Rev. Mater. Res. 36 (2006) 467–495.

[12] T. M. Monro, S. Warren-Smith, E. P. Schartner, A. Francois, S. Heng, H. Ebendorff-Heidepriem, and S. Afshar V., Sensing with suspended-core optical fibers, Opt. Fiber Technol. 16 (2010) 343–356.

[13] S. C. Warren-Smith, S. Heng, H. Ebendorff-Heidepriem, A. D. Abell, and T. M. Monro, Fluorescence-based aluminum ion sensing using a surface-functionalized microstructured optical fiber, Langmuir 27 (2011) 5680–5685.

[14] A. Webb, F. Poletti, D. Richardson, and J. Sahu, Suspended-core holey fiber for evanescent-field sensing, Opt. Eng. 46 (2007) 010503.

[15] T. M. Monro, S. Warren-Smith, E. P. Schartner, A. Francois, S. Heng, H. Ebendorff-Heidepriem, and S. Afshar V., Sensing with suspended-core optical fibers, Opt. Fiber Technol. 16 (2010) 343–356.

[16] H. Ebendorff-Heidepriem, S. C. Warren-Smith, and T. M. Monro, Suspended nanowires: fabrication, design and characterization of fibers with nanoscale cores, Opt. Express 17 (2009) 2646–2657.

[17] T. G. Euser, J. S. Y. Chen, M. Scharrer, P. S. J. Russell, N. J. Farrer, and P. J. Sadler, Quantitative broadband chemical sensing in air-suspended solid-core fibers, J. Appl. Phys. 103 (2008) 103108.

[18] A. Mazhorova, A. Markov, A. Ng, R. Chinnappan, O. Skorobogata, M. Zourob, and M. Skorobogatiy, Label-free bacteria detection using evanescent mode of a suspended core terahertz fiber, Opt. Express 20 (2012) 5344–5355.

[19] S. Afshar V., S. C. Warren-Smith, and T. M. Monro, Enhancement of fluorescence-based sensing using microstructured optical fibres, Opt. Express 15 (2007) 17891–17901.

[20] Y. Ruan, E. P. Schartner, H. Ebendorff-Heidepriem, P. Hoffmann, and T. M. Monro, Detection of quantum-dot labelled proteins using soft glass microstructured optical fibers, Opt. Express 15 (2007) 17819–17826.

[21] C. M. B. Cordeiro, C. J. S. de Matos, E. M. dos Santos, A. Bozolan, J. S. K. Ong, T. Facincani, G. Chesini, A. R. Vaz, and C. H. B. Cruz, Towards practical liquid and gas sensing with photonic crystal fibres: side access to the fibre microstructure and single-mode liquid-core fibre, Meas. Sci. Technol. 18 (2007) 3075–3081.

[22] C. Martelli, P. Olivero, J. Canning, N. Groothoff, B. Gibson, and S. Huntington, Micromachining structured optical fibers using focused ion beam milling, Opt. Lett. 32 (2007) 1575–1577.

[23] A. van Brakel, C. Grivas, M. N. Petrovich, and D. J. Richardson, Micro-channels machined in microstructured optical fibers by femtosecond laser, Opt. Express 15 (2007) 8731–8736.

[24] J. P. Parry, B. C. Griffiths, N. Gayraud, E. D. McNaghten, A. M. Parkes, W. N. MacPherson, and D. P. Hand, Towards practical gas sensing with micro-structured fibres, Meas. Sci. Technol. 20 (2009) 075301.

[25] F. M. Cox, R. Lwin, M. C. J. Large, and C. M. B. Cordeiro, Opening up optical fibres, Opt. Express 15 (2007) 11843–11848.

[26] S. C. Warren-Smith, H.Ebendorff-Heidepriem, T. C. Foo, R. Moore, C. Davis, and T. M. Monro, Exposed-core microstructured optical fibers for real-time fluorescence sensing, Opt. Express 17 (2009) 18533–18542.

[27] H. Ebendorff-Heidepriem and T. M. Monro, Extrusion of complex preforms for microstructured optical fibers, Opt. Express 15 (2007) 15086–15092.

[28] S. C. Warren-Smith, H. Ebendorff-Heidepriem, S. Afshar V., G. McAdam, C. Davis, and T. Monro, Corrosion sensing of aluminium alloys using exposed-core microstructured optical fibres, Materials Forum 33 (2009) 110–121.

[29] K. Richardson, D. Krol, and K. Hirao, Glasses for photonic applications, Int. J. Appl. Glass Sci. 1 (2010) 74–86.

[30] M. Li and D. Nolan, Optical transmission fiber design evolution, J. Lightwave Technol. 26 (2008) 1079–1092.

[31] R. Kostecki, H. Ebendorff-Heidepriem, C. Davis, G. McAdam, S. C. Warren-Smith, and T. M. Monro, Silica exposed-core microstructured optical fibers, Opt. Mater. Express 2 (2012) 1538–1547.

[32] Heraeus Quarzglas GmbH & Co. KG, Pure Silica Rods for Specialty Fiber Applications, 1st ed. (2012), http://heraeus-quarzglas.com/.

[33] M. Y. Sim and S. Gleixner, Studying the etch rates and selectivity of SiO_2 and Al in BHF solutions, in 2006 16th Biennial University/Government/Industry Microelectronics Symposium (2006), 225–228.

[34] G. Brambilla, F. Xu, and X. Feng, Fabrication of optical fibre nanowires and their optical and mechanical characterisation, Electron. Lett. 42 (2006) 517–519.

[35] G. Zhai and L. Tong, Roughness-induced radiation losses in optical micro or nanofibers, Opt. Express 15 (2007) 13805–13816.

APPENDIX B

Paper 2.

Predicting the drawing conditions for Microstructured Optical Fiber fabrication

Roman Kostecki,[*] **Heike Ebendorff-Heidepriem,**
Stephen C. Warren-Smith, and Tanya M. Monro

Institute for Photonics and Advanced Sensing and School of Chemistry and Physics,
The University of Adelaide, Adelaide, South Australia 5005, Australia
[*]*roman.kostecki@adelaide.edu.au*

Abstract: The efficient and accurate fabrication of Microstructured optical fibers (MOFs) requires a practical understanding of the 'draw process' beyond what is achievable by trial and error, which requires the ability to predict the experimental drawing parameters needed to produce the desired final geometry. Our results show that the Fitt *et al*. fluid-mechanics model for describing the draw process of a single axisymmetric capillary fiber provides practical insights when applied to more complex multi-hole symmetric and asymmetric MOF geometries. By establishing a method to relate the multi-hole MOF geometry to a capillary and understanding how material temperature varies with the draw tower temperature profile, it was found that analytical equations given by the Fitt model could be used to predict the parameters necessary for the chosen structure. We show how this model provides a practical framework that contributes to the efficient and accurate fabrication of the desired MOF geometries by predicting suitable fiber draw conditions.

References and links

1. P. Kasier, E. A. J. Marcatili, and S. E. Miller, "A new optical fiber," Bell Sys. Tech. J. **52**, 265 – 269 (1973).
2. J. C. Knight, T. A. Birks, P. S. J. Russell, and D. M. Atkin, "All-silica single-mode optical fiber with photonic crystal cladding," Opt. Lett. **21**, 1547 – 1549 (1996).
3. T. M. Monro and H. Ebendorff-Heidepriem, "Progress in microstructured optical fibers," Annu. Rev. Mater. Res. **36**, 467 – 495 (2006).
4. W. Q. Zhang, H. Ebendorff-Heidepriem, T. M. Monro, and S. Afshar V., "Fabrication and supercontinuum generation in dispersion flattened bismuth microstructured optical fiber," Opt. Express **19**, 21135 – 21144 (2011).
5. M. Oermann, H. Ebendorff-Heidepriem, D. Ottaway, D. Lancaster, P. Veitch, and T. Monro, "Extruded microstructured fiber lasers," IEEE Photon. Technol. Lett. **24**, 578 – 580 (2012).
6. S. Atakaramians, S. Afshar V., H. Ebendorff-Heidepriem, M. Nagel, B. M. Fischer, D. Abbott, and T. M. Monro, "THz porous fibers: design, fabrication and experimental characterization," Opt. Express **17**, 14053 – 15062 (2009).
7. N. A. Issa, "High numerical aperture in multimode microstructured optical fibers," Appl. Opt. **43**, 6191 – 6197 (2004).
8. B. Gauvreau, F. Desevedavy, N. Guo, D. Khadri, A. Hassani, and M. Skorobogatiy, "High numerical aperture polymer microstructured fiber with three super-wavelength bridges," J. Opt. A. – Pure Appl. Op. **11**, 085102 (2009).

9. T. M. Monro, D. J. Richardson, and P. J. Bennett, "Developing holey fibres for evanescent field devices," Electron. Lett. **35**, 1188 – 1189 (1999).

10. O. S. Wolfbeis, "Fiber-optic chemical sensors and biosensors," Anal. Chem. **80**, 4269 – 4283 (2008).

11. T. M. Monro, S. Warren-Smith, E. P. Schartner, A. François, S. Heng, H. Ebendorff-Heidepriem, and S. Afshar V., "Sensing with suspended-core optical fibers," Opt. Fiber Technol. **16**, 343 – 356 (2010).

12. S. Heng, M.-C. Nguyen, R. Kostecki, T. M. Monro, and A. D. Abell, "Nanoliter-scale, regenerable ion sensor: sensing with a surface functionalized microstructured optical fibre," RSC Adv. **3**, 8308 – 8317 (2013).

13. K. Mukasa, K. Imamura, M. Takahashi, and T. Yagi, "Development of novel fibers for telecoms application," Opt. Fiber Technol. **16**, 367 – 377 (2010).

14. H. Ebendorff-Heidepriem and T. M. Monro, "Extrusion of complex preforms for microstructured optical fibers," Opt. Express **15**, 15086 – 15092 (2007).

15. H. Ebendorff-Heidepriem and T. M. Monro, "Analysis of glass flow during extrusion of optical fiber preforms," Opt. Mater. Express **2**, 304 – 320 (2012).

16. Y. Zhu, R. T. Bise, J. Kanka, P. Peterka, and H. Du, "Fabrication and characterization of solid-core photonic crystal fiber with steering-wheel air-cladding for strong evanescent field overlap," Opt. Commun. **281**, 55 – 60 (2008).

17. H. E. Hamzaoui, L. Bigot, G. Bouwmans, I. Razdobreev, M. Bouazaoui, and B. Capoen, "From molecular pre-cursors in solution to microstructured optical fiber: a sol-gel polymeric route," Opt. Mater. Express **1**, 234 – 242 (2011).

18. A. S. Webb, F. Poletti, D. J. Richardson, and J. K. Sahu, "Suspended-core holey fiber for evanescent-field sens-ing," Opt. Eng. **46** (2007).

19. P. McNamara, D. Lancaster, R. Bailey, A. Hemming, P. Henry, and R. Mair, "A large core microstructured fluoride glass optical fibre for mid-infrared single-mode transmission," J. Non-Cryst. Solids **355**, 1461 – 1467 (2009).

20. J. Lægsgaard and A. Bjarklev, "Microstructured optical fibers – fundamentals and applications," J. Am. Ceram. Soc. **89**, 2 – 12 (2006).

21. A. D. Pryamikov, A. S. Biriukov, A. F. Kosolapov, V. G. Plotnichenko, S. L. Semjonov, and E. M. Dianov, "Demonstration of a waveguide regime for a silica hollow - core microstructured optical fiber with a negative curvature of the core boundary in the spectral region $> 3.5 \mu$m," Opt. Express **19**, 1441 – 1448 (2011).

22. S. E. Rosenberg, H. Papamichael, and I. N. Miaoulis, "A 2-dimensional analysis of the viscous problem of a glass preform during the optical-fiber drawing process," Glass Technol. **35**, 260 – 264 (1994).

23. A. Mawardi and R. Pitchumani, "Optical fiber drawing process model using an analytical neck-down profile," IEEE Photon. J. **2**, 620 – 629 (2010).

24. S. C. Xue, R. I. Tanner, G. W. Barton, R. Lwin, M. C. J. Large, and L. Poladian, "Fabrication of microstructured optical fibers – Part 1 & 2," J. Lightwave Technol. **23**, 2245 – 2266 (2005).

25. G. Luzi, P. Epple, M. Scharrer, C. Fujimoto, C. Rauh, and A. Delgado, "Influence of surface tension and inner pressure on the process of fibre drawing," J. Lightwave Technol. **28**, 1882 – 1888 (2010).

26. A. D. Fitt, K. Furusawa, T. M. Monro, C. P. Please, and D. J. Richardson, "The mathematical modelling of capillary drawing for holey fibre manufacture," J. Eng. Math. **43**, 201 – 227 (2002).

27. R. Kostecki, H. Ebendorff-Heidepriem, C. Davis, G. McAdam, S. C. Warren-Smith, and T. M. Monro, "Silica exposed-core microstructured optical fibers," Opt. Mater. Express **2**, 1538 – 1547 (2012).

28. S. H. K. Lee and Y. Jaluria, "Simulation of the transport processes in the neck-down region of a furnace drawn optical fiber," Int. J. Heat Mass Tran. **40**, 843 – 856 (1997).

29. R. M. Wynne, "A fabrication process for microstructured optical fibers," J. Lightwave Technol. **24**, 4304 – 4313 (2006).

30. C. Voyce, A. Fitt, and T. Monro, "Mathematical model of the spinning of microstructured fibres," Opt. Express **12**, 5810 – 5820 (2004).

31. C. J. Voyce, A. D. Fitt, and T. M. Monro, "The mathematical modelling of rotating capillary tubes for holey-fibre manufacture," J. Eng. Math. **60**, 69 – 87 (2008).

32. C. J. Voyce, A. D. Fitt, and T. M. Monro, "Mathematical modeling as an accurate predictive tool in capillary and microstructured fiber manufacture: The effects of preform rotation," J. Lightwave Technol. **26**, 791 – 798 (2008).

33. C. J. Voyce, A. D. Fitt, J. R. Hayes, and T. M. Monro, "Mathematical modeling of the self-pressurizing mecha-nism for microstructured fiber drawing," J. Lightwave Technol. **27**, 871 – 878 (2009).

34. G. Luzi, P. Epple, M. Scharrer, K. Fujimoto, C. Rauh, and A. Delgado, "Asymptotic analysis of flow processes at drawing of single optical microfibres," Int J. Chem. Reactor Eng. **9** (2011).

35. U. C. Paek and R. B. Runk, "Physical behavior of the neck-down region during furnace drawing of silica fibers," J. Appl. Phys. **49**, 4417 – 4422 (1978).

36. G. Yang, T. Rouxel, J. Troles, B. Bureau, C. Boussard-Plèdel, P. Houizot, and J.-C. Sangleboeuf, "Viscosity of As_2Se_3 glass during the fiber drawing process," J. Am. Ceram. Soc. **94**, 2408 – 2411 (2011).

37. K. Richardson, D. Krol, and K. Hirao, "Glasses for photonic applications," Int. J. Appl. Glass Sci. **1**, 74 – 86 (2010).

38. M.-J. Li and D. A. Nolan, "Optical transmission fiber design evolution," J. Lightwave Technol. **26**, 1079 – 1092 (2008).

39. Heraeus Quarzglas GmbH & Co. KG, http://heraeus-quarzglas.com/, *Pure Silica Rods for Specialty Fiber Applications*, 01st ed. (2012).

40. E. P. Schartner, H. Ebendorff-Heidepriem, S. C. Warren-Smith, R. T. White, and T. M. Monro, "Driving down the detection limit in microstructured fiber-based chemical dip sensors," Sensors **11**, 2961 – 2971 (2011).

41. R. Kostecki, E. P. Schartner, H. Ebendorff-Heidepriem, P. C. Henry, and T. M. Monro, "Fabrication of suspended and exposed core silica fibres for sensing applications," ACOFT - 37th Australian Conference on Optical Fibre Technology (2012).

42. G. Urbain, Y. Bottinga, and P. Richet, "Viscosity of liquid silica, silicates and alumino-silicates," Geochim. Cosmochim. Ac. **46**, 1061 – 1072 (1982).

43. R. H. Doremus, "Viscosity of silica," J. Appl. Phys. **92**, 7619 – 7629 (2002).

44. S. Roy Choudhury and Y. Jaluria, "Thermal transport due to material and gas flow in a furnace for drawing an optical fiber," J. Mater. Res. **13**, 494 – 503 (1998).

45. N. M. Parikh, "Effect of atmosphere on surface tension of glass," J. Am. Ceram. Soc. **41**, 18 – 22 (1958).

46. W. D. Kingery, "Surface tension of some liquid oxides and their temperature coefficients," J. Am. Ceram. Soc. **42**, 6 – 10 (1959).

47. K. Boyd, H. Ebendorff-Heidepriem, T. M. Monro, and J. Munch, "Surface tension and viscosity measurement of optical glasses using a scanning CO_2 laser," Opt. Mater. Express **2**, 1101 – 1110 (2012).

48. A. D. Fitt, K. Furusawa, T. M. Monro, and C. P. Please, "Modeling the fabrication of hollow fibers: capillary drawing," J. Lightwave Technol. **19**, 1924 – 1931 (2001).

49. H. Ebendorff-Heidepriem, S. C. Warren-Smith, and T. M. Monro, "Suspended nanowires: fabrication, design and characterization of fibers with nanoscale cores," Opt. Express **17**, 2646 – 2657 (2009).

50. R. Kostecki, H. Ebendorff-Heidepriem, S. C. Warren-Smith, G. McAdam, C. Davis, and T. M. Monro, "Optical fibres for distributed corrosion sensing – architecture and characterisation," Key Eng. Mat. **558**, 522 – 533 (2013).

51. S. C. Warren-Smith, H. Ebendorff-Heidepriem, T. C. Foo, R. Moore, C. Davis, and T. M. Monro, "Exposed-core microstructured optical fibers for real-time fluorescence sensing," Opt. Express **17**, 18533 – 18542 (2009).

1. Introduction

Microstructured optical fibers [1] (MOFs) are an important class of fiber often with longitudinal air holes that provide a large refractive index contrast used for light confinement [2]. Unlike conventional optical fibers, MOFs with air holes can be manufactured from a single material, and with the appropriate cross-sectional design, the structure can provide a broad range of highly unusual and tailorable optical properties [3]. By the suitable selection of glass or polymer material and geometry the dispersion, nonlinearity, birefringence, polarization, evanescent field and mode area of the propagating light can be optimized to specific applications. This has led to innovations in supercontinuum generation [4], fiber lasers [5], terahertz wave guiding [6], fibers with high numerical apertures [7,8], sensors [9–12], and makes MOFs an excellent candidate for new high-capacity transmission multicore and endlessly single mode telecommunications fibers [13].

All optical fibers are produced by heating and drawing down a preform from an initial diameter of the order of centimeters to the desired final diameter using a fiber drawing tower. For MOFs with longitudinal air holes this draw process includes a mechanism by which the pressure difference of the holes and atmosphere is maintained to ensure the holes collapse or expand to the desired final geometry. Some common ways to produce MOF preforms include using extrusion [14,15], sol-gel casting [16,17], ultrasonic drilling [18,19] or stack and draw methods [2,20,21], which resemble a large-scale form of the final desired fiber geometry. The fiber drawing tower is then used to feed the preform at a fixed rate into a furnace, which heats the material to an appropriate viscosity, so it can taper down to the final fiber diameter (usually of the order of hundreds of micrometers) by drawing the fiber below the furnace at a faster rate. The extensive range of possibilities means that in order to fabricate MOFs in an efficient manner, it is essential that these draw conditions can be predicted accurately.

It is not the intention of this paper to describe the draw process of MOFs, as this has already been done by several studies [22–25]. Instead, we describe how the analytical model provided by Fitt *et al*. [26] can be used to predict suitable fiber draw conditions when applied to multi-hole MOF geometries. This model, describing the process of a single axisymmetric hole fiber,

was shown to give excellent agreement to a range of capillary drawing experiments, providing practical guidelines useful in the design and control of capillary fabrication [26]. The results shown in this paper provide experimental validation of the ability for the Fitt model to predict the parameters needed for fabrication of symmetric and asymmetric multi-hole fiber structures. In particular, we show the predictive nature of this model when applied to fabrication of three hole symmetric suspended-core fiber [18] and two hole asymmetric exposed-core fibers [27]. The advantages of having analytic equations for the fiber draw process are these equations allow prediction of processing parameters such as temperature and pressure to achieve desired final MOF geometries. This avoids the need for systematic scanning of drawing parameters such as temperature and pressure during the fiber draw. Given that each time the drawing conditions are changed it takes time for the draw process to stabilize, which reduces the fiber yield possible from the preform. Such equations can also provide insight into the nature of the process.

2.   The MOF draw process

In theory, the set of Navier-Stokes coupled differential equations can be used to describe the neck down region viscous fluid flow of the MOF draw process to model the shape of the final expected fiber geometry [22,23]. These equations describe how the velocity, pressure, temperature, and density of a moving fluid are related as well as how these quantities are transferred inside the physical system due to diffusion and convection. Solving these equations for MOF production becomes a tedious numerical problem due to the large set of parameters involved in the fiber draw process. To overcome this, suitable approximations and generalizations have been studied in order to develop useful draw process predictive models [24].

In 2002, starting from the Navier-Stokes and convection-diffusion equations, Fitt *et al*. [26] derived and experimentally validated a general model describing the draw process of a capillary (Fitt model), which is capable of including the effects of internal hole pressurization, surface tension and all of the other effects useful for predicting the draw process. The Fitt model assumes that viscosity alone is a function of temperature, ignoring some of the weak dependance [28] that temperature has on physical quantities such as material density, surface tension, thermal conductivity and specific heat, since the material viscosity typically varies by orders of magnitude over a relatively modest temperature range. Also, although the Fitt model accounts for physical effects such as diffusive and convective heat transfer, some simplifications are made where the terms in the equations are small, such as ignoring viscous dissipation, and that the optically thin fiber absorbs radiation directly from the surrounding furnace and re-radiates heat back to the furnace. With these approximations and appropriate choice of practical boundary conditions for fiber drawing purposes, a set of analytical equations for the case of a capillary was developed.

There have been several studies utilizing the methods described by Fitt *et al*. [26], such as models to; determine the drawing domain of internal hole pressurization when applied to a square lattice geometry [29], include the effects of preform rotation [30–32] and self pressurization [33], and asymptotic analysis of surface tension and internal hole pressurization affects on the drawing process [34]. In this paper we demonstrate how the Fitt model can be used as a practical predictive tool to produce multi-hole symmetric and asymmetric fiber structures, and provides the first experimental validation of these analytical equations when applied to MOFs rather than simple capillaries.

2.1. Fitt model

The Fitt model equation describing the internal diameter (h_1 [m]) of a single axisymmetric hole fiber, is given by [26],

$$h_1(p_0) = \exp\left(\frac{-\beta z}{2L} - P\exp\left(\frac{-\beta z}{L}\right)\right) \left[h_{10}\exp(P) - G\int_0^z \exp\left(\frac{-\beta u}{2L} + P\exp\left(\frac{-\beta u}{L}\right)\right) du\right]$$

$$G = \frac{\gamma}{2\mu W_f} \quad , \quad P = \frac{p_0 L}{2\beta\mu W_f} \quad , \quad \beta = \ln\left(\frac{W_d}{W_f}\right) \tag{1}$$

where, μ [Pa.s] denotes the viscosity, p_0 [Pa] denotes internal hole overpressure (above atmospheric pressure), W_f [ms^{-1}] denotes the feeding speed for the preform, W_d [ms^{-1}] denotes the drawing speed for the fiber, z [m] denotes the distance along the axis from the start of the neck down region, γ [Nm^{-1}] denotes surface tension, and the heating zone length L [m] denotes the neck down region [35, 36]. This heating zone length is defined by Eq. (1) as the neck down region where the changes are integrated over $0 \le z \le L$ for the drawn fiber case.

2.2. Materials and equipment

High purity fused silica known as Suprasil F300HQ (Heraeus Quarzglas GmbH & Co.KG) was chosen for experiments. Silica is known to be reliable under a range of processing and use environments, with relatively better mechanical and thermal stability [37]. Highly homogeneous, high purity bulk material is commercially available, which has led to silica telecom fibers regularly being made with low loss (∼0.2 dB/km at NIR wavelengths) [38]. This inherent low loss and relatively low intrinsic nonlinearity makes silica excellent for low or high power fiber applications, with a transmission window from UV to NIR (0.19–2.0 μm) [39]. Also, silica has a relatively low refractive index, which can improve the sensitivity of evanescent field sensors, since reducing the index contrast (Δn) at the core-cladding boundary increases the power fraction to the analyte or functionalized surface [40].

100 mm long fiber preforms were fabricated from Ø12 mm and Ø20 mm F300HQ silica rod, which were drilled with three Ø2.9 mm holes, where the centers of the holes form an equilateral triangle with 3.2 mm sides, and cleaned using the method discussed in Ref. [27]. Drilling was chosen since it has been demonstrated to be a relatively simple method for three hole structures [18] compared to the more widely used stacking method, and after cleaning the surface quality is satisfactory to produce fibers with relatively low losses [41]. The only difference between symmetric suspended-core fiber and asymmetric exposed-core fiber preforms, is that for the exposed-core fiber case a thin slot was cut into the side of the symmetric preform in order to expose the core region [27]. To draw the preform to fiber a 6 m tower with graphite resistance furnace, positive pressurization system and automated diameter control was used.

2.3. Temperature dependence of viscosity and surface tension

Knowing the temperature dependence of material viscosity is a major part of practically applying a model to the fiber drawing process. For F300 silica in the temperature range 1673 K $\le T \le$ 2773 K the viscosity, experimentally measured by Urbain et al. [42] and discussed by Doremus [43] and Voyce et al. [32], is given by,

$$\mu = 5.8 \times 10^{-8} \exp\left(\frac{515400}{RT}\right) \quad [\text{Pa.s}] \tag{2}$$

where R is the gas constant and T [K] is the glass temperature. In order to find closed form solutions of Eq. (1) it is necessary that the temperature of the glass is assumed constant. However, a drawing tower furnace does not exhibit a constant temperature but an axial temperature

gradient/profile [32,36]. This means that the glass viscosity varies with the temperature gradient/profile within the furnace [44]. One should also consider that temperature profiles can vary between drawing towers and furnace designs.

To determine the temperature profile inside the preform for the conditions prevailing within our draw tower, a thermocouple was inserted in the center of a drilled F300HQ silica glass rod. The measurements of the thermocouple temperature were taken for Ø12 mm and Ø20 mm rods at 5 mm intervals along the central axis of the furnace, ensuring thermal equilibrium at each measured point. For furnace temperature measurements, the draw tower was equipped with a pyrometer located next to a furnace element and targeted at the inner sleeve of the furnace. Figure 1(a) shows the results of the thermocouple temperatures measured at 1500 °C, 1600 °C, and 1700 °C furnace temperatures, shown in blue, green and orange respectively, where the small and large dots correspond to the measured points for the Ø12 mm and Ø20 mm rods respectively. The three furnace temperatures were chosen so the results could be extrapolated to typically higher fiber drawing temperatures.
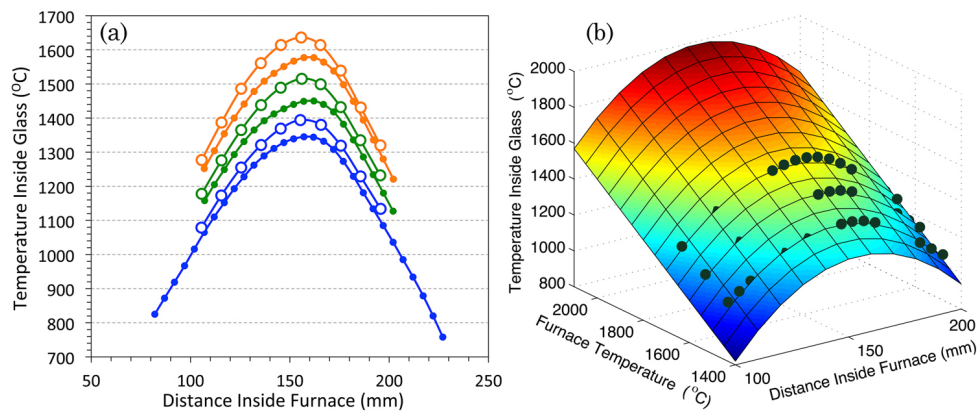
Fig. 1. (a) Temperature profiles measured inside (small dots) Ø12 mm and (large dots) Ø20 mm rods at (blue) 1500 °C, (green) 1600 °C, and (orange) 1700 °C furnace temperatures. (b) Surface of 2×1 degree polynomial (Eq. (3)) fitted to the Ø12 mm results shown by green dots. The distance inside furnace was measured from the top of the furnace outer casing.

These temperature profile results show that the temperature measured inside the silica glass rod is lower for smaller diameters. Larger diameter preforms are closer to the surrounding heating element, placing the outside of the glass in a hotter part of the furnace [44], which results in a hotter temperature inside the preform and shows the role that glass thermal conductivity has in the heat transfer process. For the three Ø12 mm silica rod temperature profiles, the 2×1 degree polynomial given by,

$$T_m = -3634 + 43.71\,\xi + 1.073\,T_f - 0.1416\,\xi^2 - 2.404 \times 10^{-5}\,\xi\,T_f \tag{3}$$

fits the curves with R^2 of 0.9899, where T_m is the measured temperature, T_f is the furnace temperature, and ξ is the distance inside the furnace from top of the outer casing. The surface given by Eq. (3) is shown in Fig. 1(b) together with the three sets of measured points. Similarly, for the three Ø20 mm silica rod temperature profiles, the 2×1 degree polynomial given by,

$$T_m = -4704 + 51.79\,\xi + 1.537\,T_f - 0.1551\,\xi^2 - 2.201 \times 10^{-3}\,\xi\,T_f \tag{4}$$

fits the curves with R^2 of 0.9957.

For calculations shown in this paper, the surface tension of silica is assumed constant at $0.31\ \mathrm{Nm}^{-1}$ [45–47], since it varies weakly with temperature within the fiber drawing range.

2.4. Defining the geometry

The Fitt model describes a capillary draw process for which we define the geometry change during drawing as the ratio [48],

$$C = \frac{h_1 h_{20}}{h_2 h_{10}} \tag{5}$$

where h_{10} and h_{20} are the preform inner and outer diameters. This ratio provides a comparison of the final fiber geometry ratio (h_1/h_2) to the initial preform geometry ratio (h_{10}/h_{20}) of the inner and outer diameters. When $C = 1$ then the hole geometry is preserved. If $C > 1$ then the hole expands from the original geometry, and the hole experiences collapse when $C < 1$. With Eq. (1) and the external fiber diameter (h_2 [m]) given by [26],

$$h_2 = h_{20}\ \exp\left(\frac{-\beta}{2}\right)\quad, \tag{6}$$

Eq. (5) becomes,

$$C(p_0) = \frac{\exp\left(-P\exp(-\beta)\right)}{h_{10}}\left[h_{10}\exp(P) - G\int_0^z \exp\left(\frac{-\beta u}{2L} + P\exp\left(\frac{-\beta u}{L}\right)\right)\mathrm{d}u\right] \tag{7}$$

for the $z = L$ drawn fiber case. To obtain a closed form Eq. (7), Eq. (6) assumes that the draw down ratio (β) is independent of inner diameters, which can only be valid for small hole changes.

Since the geometry change ratio (C) describes a capillary draw process, a method to relate the geometry of a multi hole MOF to a capillary needed to be established. To measure the fabricated structures and calculate C according to Eq. (5), we chose to define the 'hole region diameter' of h_1 and h_{10} as being the diameter of a circle that has the same circumference as the total of all the inner hole perimeters. The outside diameters, h_2 and h_{20} were measured directly. This definition for the inner diameter was found to have a better correlation between Eq. (7) and experimental, compared to other definitions tried such as hydraulic diameter, or the diameter of a circle that fits tightly around the inner holes, or the diameter of a circle that has the same area as the total area of the inner holes.

3. Draw process experimental

3.1. Comparing the model with experiment

Two preforms were fabricated as discussed in Sec. 2.2 and shown in Fig. 4(a), and directly drawn down to fiber at Ø160 μm outside diameter. One of the preforms was used for a series of pressures and the other for a series of furnace temperatures, allowing enough time for the fiber structure to stabilize between each change which typically took approximately 5 minutes. In each case, a preform feed rate of 1.5 mm/min was used, and the draw tower was set to automatically maintain an appropriate draw speed to maintain the target outside diameter. Inner and outer diameters of each fiber structure from the series and the preforms were measured using images from a microscope and applying the definition discussed in Sec. 2.4. The neck down region length (L) was measured from the preforms after fiber drawing as being 0.039 m. Equation (5) was then used to calculate the value for the geometry change ratio (C), which are shown as the dots in Fig. 2. The temperature shown in Fig. 2(b) are the furnace temperatures, and the furnace temperature used for the pressure series (Fig. 2(a)) was 2000 °C.

As discussed in Sec. 2.3, although furnace temperature is known, it is not the actual glass temperature. We expected that the actual temperature of the glass in the neck down region to be less than the furnace temperature, due to axial and radial temperature gradients. Also, as discussed in Sec. 2 several assumptions were made in order to arrive at Eq. (1). It was therefore expected that not all of the contracting effects due to surface tension are completely accounted for in the Fitt model described in Sec. 2.1, which would lead to the actual internal hole over-pressure (p_0) being different to the pressure measured by the draw tower control system (p_f). Because of these uncertainties, pressure (p_ε) and temperature (T_ε) offsets were included such that $p_0 = p_f + p_\varepsilon$ and $T = T_f + 273.15 + T_\varepsilon$, and fitted to the experimental data.
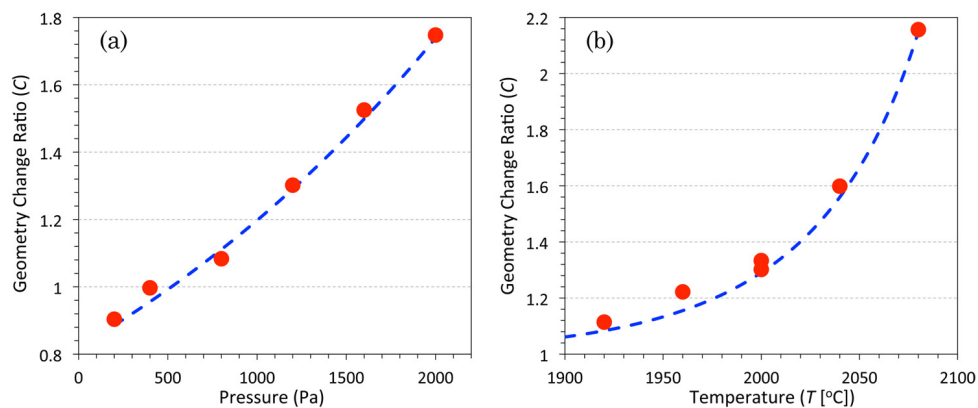
Fig. 2. Experimental (red dots) and model (blue line) for a series of pressures (a) and a series of furnace temperatures (b). For the pressure series (a) the furnace temperature used was 2000 °C at pressures of 200, 400, 800, 1200, 1600, and 2000 Pa. For the temperature series (b), furnace temperatures of 1920, 1960, 2000, 2040, and 2080 °C were used with a fixed pressure of 1200 Pa. The temperature series (b) also includes the 1200 Pa result from the pressure series.

It was found that by using fixed pressure and temperature offsets (± 95% confidence interval) of $p_\varepsilon = -375.8 \pm 80.4$ Pa and $T_\varepsilon = -141.1 \pm 7.6$ K, Eq. (7) fits well with experiment with $R^2 = 0.9905$, as shown by the blue lines in Fig. 2. The peak temperature offset calculated from Eq. (3) at a furnace temperature of 2000 °C gives an offset of -123 °C, which is remarkably close to the value obtained for T_ε considering that only a step temperature profile is assumed in the model.

In Sec. 2.4, Eq. (6) assumes that the outside diameter (h_2) is independent of pressure, which leads to the geometry change ratio (Eq. (7)) being independent of outside diameter. It is interesting to compare this with the experimental results to verify if the assumptions are valid in this respect. The draw tower pressure and draw speed data obtained during the pressure series discussed above are shown in Fig. 3, where the blue line shows the pressure applied to the holes of the preform and the red line shows the draw speed. At the start of the experiment, where the automatic diameter control was switched off, a constant draw speed of 4 m/min was used while the pressure was switched on and allowed to stabilize to 200 Pa. The automatic diameter control was then switched on with a target outside diameter of 160 μm and the draw increased in speed until the target diameter was reached, at 8 m/min. As the pressure was increased to 400, 800 and 1200 Pa the draw speed did not increase, showing that within this range of hole expansion the outside diameter (h_2) of the final fiber is indeed independent of pressure. When the pressure was increased to 1.6 kPa the draw speed started to increase, as the automatic diameter con-

trol measured an increase in fiber diameter and increased the draw speed to compensate. After this initial increase, the draw speed reduced back towards the 8 m/min draw speed, showing that although the system experienced some instability there was tendency for the draw speed to remain constant. At the end of the fiber draw experiment the draw speed started to increase quickly, where the fiber draw is no longer in a steady state regime at the end of the preform.
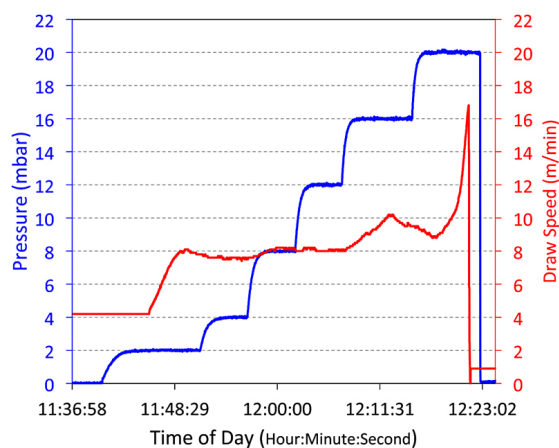
Fig. 3. Draw tower data, showing (blue) the pressure applied to the holes of the preform, and (red) the draw speed which was set to automatically maintain a constant outside fiber diameter.

These experimental results provide evidence that the assumptions made to arrive at Eq. (1) and Eq. (6) are within the range of pressures we used and for moderate geometry change ratios (up to $C \sim 2$), giving greater confidence in the Fitt model to predict the parameters which need to be considered for practical fiber drawing. The validation that the geometry change ratio (Eq. (7)) is independent of the MOFs outside diameter for moderate geometry change ratios leads to the proposition that it should be possible to create asymmetric structures where the cross sectional wall thickness surrounding the holes could be made non-axisymmetric.

3.2. Predicting fiber draw parameters

3.2.1. Suspended-core fibers: symmetric structures

The predictive nature of Eq. (7) is most useful for fabrication of MOFs. Equipped with the temperature and pressure offsets, our aim was to produce a fiber with a similar structure but smaller scale and core size, for which the cane and sleeve method [49] was required. The process is to first cane the preform to the order of millimeters, insert this cane into a rod (sleeve), and then draw down the cane and sleeve to fiber, which requires the successful application of the right combination of parameters in order to achieve the desired final fiber structure. Another preform was fabricated, as discussed in Sec. 2.2 and shown by Fig. 4(a), and drawn down to fiber using the cane and sleeve method.

For the cane, the feed rate needs to be greatly increased and the draw speed greatly reduced to achieve the lower draw down ratio. For this we chose a feed rate of 6.4 mm/min with the targeted outside diameter for the cane being Ø0.95 mm maximum. The aim was to pre-expand the holes during the caning process, for which we chose a geometry change ratio of $C = 1.55$. Using Eq. (7) the predicted pressure (p_f) needed to achieve this was 3.5 kPa at a furnace temperature of 1980 °C. A microscope image of the resulting cane structure is shown in Fig. 4(b), from which the outer diameter was measured as Ø0.91 mm with the hole region diameter Ø0.87 mm.

Applying the definition discussed in Sec. 2.4, the geometry change ratio (Eq. (5)) obtained for this cane was $C = 1.50$, which agrees well with the target $C = 1.55$.
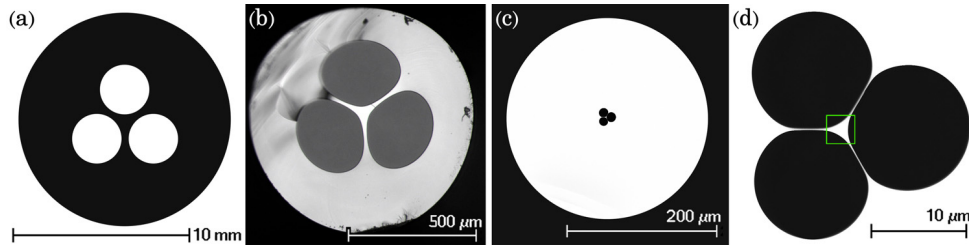
Fig. 4. (a) Cross section of the preform fabricated from Ø12 mm F300HQ silica rod; and, microscope image of (b) the cane; and, scanning electron microscope images of (c) the silica suspended-core fiber cross section measured to be Ø270 μm with (d) and enlarged image of the holes and core having effective diameters of 40.5 μm and 1.7 μm respectively.

A sleeve was made by drilling a Ø1 mm hole centrally located in Ø12 mm F300HQ silica rod into which the cane was placed. The setup of the cane and sleeve arrangement was made to ensure pressure was only applied to the three holes of the cane. The aim was to draw down the cane and sleeve to a suspended-core fiber with core size of Ø1.5-2.0 μm and target outside diameter of Ø270 μm. We chose a geometry change ratio of $C = 1.8$ to further expand the cane holes, for which Eq. (7) predicted the pressure (p_f) needed to achieve this was 2.7 kPa at a furnace temperature of 2000 °C and feed rate of 1.5 mm/min. A single 80 m long length of suspended-core fiber was fabricated using those parameters, as shown by the scanning electron microscope (SEM) images in Figs. 4(c)-4(d) from which the outer diameter was measured as being Ø270 μm with the hole region diameter Ø40.5 μm. Applying the definition discussed in Sec. 2.4, the geometry change ratio (Eq. (5)) obtained for this fiber was $C = 1.97$, which is ~10% deviation from what was calculated by the model. The core, shown by the green box in Fig. 4(d), was measured as having a effective diameter of Ø1.7 μm, defined as the diameter of a circle whose area is equal to a triangle that fits wholly within the core area [49].

3.2.2. Exposed-core fibers: asymmetric structures

A preform was fabricated, as discussed in Sec. 2.2, with a 1.8 mm wide slot cut along the length of one hole in order to fabricate a fiber with the core exposed along the length. These types of exposed-core fibers are useful in sensing applications where real time measurements and/or emptying and re-filling is required, or long lengths are needed for distributed sensing applications [27]. The aim was to produce this type of asymmetric structure to a final maximum outside diameter of 200 μm, by directly drawing down the preform to fiber. Looking at the series of fibers discussed in Sec. 3.1, we chose to use a furnace temperature of 2000 °C and aimed to expand the holes in order to achieve a geometry change ratio of $C = 1.4$. Using Eq. (7) the predicted pressure (p_f) needed to achieve this was 1.40 kPa, at a preform feed rate of 1.5 mm/min. A single 127 m long uncoated exposed-core fiber (Fig. 5(a)) was fabricated using a pressure of 1.40 kPa and the outside was measured from SEM images as being Ø202 μm (measured at the maximum) with the hole region diameter of the two holes being Ø143.1 μm.

As shown in Fig. 5(a), the outside of this asymmetric structure no longer resembles the preform from which it was made (Fig. 4(a) with 1.8 mm slot). This is caused by surface tension increasing the initial gap provided by the 1.8 mm slot in the preform and significantly changing the geometry, adding a degree of complexity not accounted for in the Fitt model or in the way the geometry is defined (Sec. 2.4). Therefore, C was not calculated from measurements
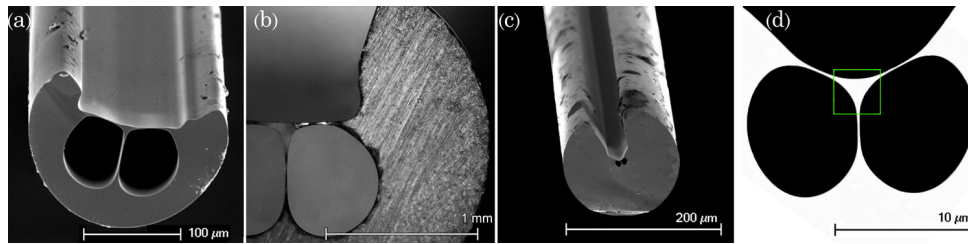
Fig. 5. Scanning electron microscope (SEM) image of (a) a asymmetric silica exposed-core fiber; and a microscope image of (b) the cross section of a cane which was used in a two step (cane and sleeve) process to produce a asymmetric silica exposed-core fiber shown by SEM images (c); and, (d) an enlarged image of the core having an effective diameter of 1.7 μm.

(Eq. (5)) and compared to the model, since a consistent method for such a measurement could not be found and further work is needed to understood, account for, and predict such geometry changes in the draw process. Nevertheless, since the outside diameter does not contribute in the calculation of C given by the Fitt model (Eq. (7)), it was still possible to predict the pressure needed, fabricate this asymmetric structure, and create a fiber useful for the intend application [50].

The above experiment used a one step drawing process from preform to fiber. It is also common to use two steps in the drawing of fibers, in order to achieve small core sizes [49,51], which requires the successful application of the right combination of parameters in order to achieve the desired final fiber structure. For this another preform was fabricated, as discussed above for the exposed-core fiber, and drawn down to fiber using the cane and sleeve method discussed in Sec. 3.2.1.

For the cane, we chose a feed rate of 7.5 mm/min with the targeted outside diameter for the cane being Ø2.9 mm maximum. The aim was to expand the holes slightly during the caning process, for which we chose a geometry change ratio of $C = 1.25$. Using Eq. (7) the predicted pressure (p_f) needed to achieve this was 1.64 kPa at a furnace temperature of 2000 °C. A microscope image of the resulting cane structure is shown in Fig. 5(b), which was measured as being Ø2.8 mm (measured at the maximum) with the hole region diameter Ø1.48 mm.

A sleeve was made by drilling a Ø2.9 mm hole centrally located in a Ø12 mm F300HQ silica rod and cutting a 1.8 mm wide slot along the length of the hole, into which the cane was placed ensuring that the sleeve slot lined up with the cane slot. The setup of the cane and sleeve arrangement was made to ensure that the cane would remain orientated correctly with the slot of the sleeve during drawing, as well as ensuring that pressure was only applied to the two holes of the cane. The aim was to draw down the cane and sleeve to a exposed-core fiber with a core size of Ø1.5-2.0 μm and target outside diameter of Ø150 μm. We chose a geometry change ratio of $C = 1.3$, since the holes of the cane were already expanded, for which Eq. (7) predicted the pressure (p_f) needed to achieve this was 1.80 kPa at a furnace temperature of 2000 °C and feed rate of 1.5 mm/min. A single 80 m long length of exposed-core fiber was fabricated using those parameters, as shown by the SEM images in Figs. 5(c)-5(d). This fiber outer diameter was measured using SEM images as being Ø152 μm (measured at the maximum) with the hole region diameter Ø19.1 μm. The core of this fiber, shown by the green box in Fig. 5(d), was measured as having a effective diameter of Ø1.7 μm. As discussed above, C was not calculated from measurements (Eq. (5)) and compared to the model, since this asymmetric structure no longer resembles the preform due to surface tension effects on the outside geometry.

These fabricated asymmetric exposed-core fiber structures have extremely non-

axisymmetric cross sectional wall thicknesses about the hole structure for which we use Eq. (7) to calculate the parameters. Since the Fitt model is independent of the outside diameter the parameters needed to make these structures could be predicted, within the geometry change ratio (C) limits of the types of asymmetric and symmetric multi-hole fiber structures we have shown.

4. Conclusion

The ability to predict the experimental drawing parameters needed to produce desired final MOF geometries requires a practical understanding of the draw process beyond what is achievable by trial and error. For the first time, we have described using the analytical model provided by Fitt *et al*. [26] to determine the draw conditions needed to produce multi-hole MOFs. Our results have shown that although the Fitt model describes a capillary draw process, it provides powerful and practical insights when applied to more complex multi-hole symmetric and asymmetric structures. By understanding the draw process, both in terms of the draw tower temperature profile and establishing a method to relate the geometry of a multi hole MOF to a capillary, it was found that analytical equations given by the Fitt model could predict the drawing conditions needed to produce the chosen structures.

For asymmetric structures it was found that the outside no longer resembles the preform from which it was made, due to surface tension effects. These effects add a degree of complexity not accounted for in the Fitt model or in the way the geometry is defined and further work is needed to understand and account for such geometry changes in the draw process.

APPENDIX C

Paper 3.

RSC Advances

PAPER

Nanoliter-scale, regenerable ion sensor: sensing with a surface functionalized microstructured optical fibre†

Sabrina Heng,* Mai-Chi Nguyen, Roman Kostecki, Tanya M. Monro and Andrew D. Abell

The first nanoliter-scale regenerable ion sensor based on a microstructured optical fibre (MOF) is reported. The air holes of the MOF are functionalized with a monoazacrown bearing spiropyran to give a switchable sensor that detects lithium ions down to 100 nM in nanoliter-scale volumes. Ion binding is turned on and off on upon irradiation with light, with the sensor being unaffected by multiple rounds of photoswitching. Unbound ions are flushed from the fibre in the 'off' state to allow the sensor to be reused. The integration of an ionophore into the sensor paves the way for the development of highly specific light-based sensing platforms that are readily adaptable to sense a particular ion simply by altering the ionophore design.

Introduction

With the advent of advanced medicine, early disease diagnosis often translates into better prognosis and treatment plans.[1–4] Given the intricate relationship between metal ions and human health,[5,6] there is a real need to develop new metal ion sensors that are user friendly, easily deployed, give rapid response and are affordable.[7] One important advance in this context would be to develop sensors that are reusable and/or capable of continuous or repeated measurements. Such a reusable sensor would maintain the sensing surface in a passive state, in-between measurements and *switch* to an active state under an external stimulus only when a measurement is required. When the measurement is completed, the target species would be expelled by a selected external stimulus, with the surface once again returning to its inactive form. This 'switchable' property makes it possible to return the sensing surface to its original state after a measurement is made, thereby potentially extending the sensor's useful lifetime.[8] Such sensors would allow for multiple measurements to be made on a single sample without the need to change the sensor. This may offer some advantage in remote applications and also in biochemical studies. Despite these needs and associated opportunities, little work has been done in this area.

The most basic switchable metal ion sensor of this type would consist of a molecular switch combined with a sensing platform that would ideally allow detection within nanoliter-samples. A suitable external stimulus (*e.g.* light) would change

or switch the structure and properties of the sensing platform in a non-invasive and reversible manner.

The use of an optical fibre as the sensing platform in this context offers attractive characteristics, such as low loss, high bandwidth, immunity to electromagnetic interference, small size, light weight, safety, relatively low cost, low maintenance, that make them very suitable and, in some cases, the only viable sensing solution.[9] Microstructured optical fibres (MOFs) offer the potential to improve performance relative to more traditional spectroscopic and fluorescence-based fibre sensors.[10] MOFs have air holes incorporated within their cross-section and these holes can be used to control the interactions between guided light and matter located within the holes while simultaneously acting as tiny sample chambers.[11,12] The amount of guided light that is available to interact with the material located within the holes of MOFs can be increased by manipulating the geometry of the fibre cross-section.[11,12] With an appropriate design, the cross-sectional structure of a MOF provides the broad range of optical properties demanded by different sensors. These characteristics have allowed MOFs to be used as sensing platforms for a variety of chemical and biological substrates.[13–15] In addition, integrating a photo-switchable molecule with MOFs as the sensor surface also means that light can be used to quantify the binding of analytes *via* absorption, fluorescence or label-free techniques.

From the plethora of photoswitchable molecules that are known, spiropyrans stand out as attractive candidates for sensor development for several reasons. Spiropyrans are characterized by two spectrally well-separated states that are thermally stable, with a high switching reliability, low fatigue to maximize the number of switching cycles the molecules can survive, and tunable switching rates.[16,17] Importantly, spiropyran undergoes a reversible structural isomerization between a colorless spiro (SP) form and a colored open form

Institute for Photonics & Advanced Sensing and School of Chemistry & Physics, The University of Adelaide, Adelaide, South Australia 5005, Australia.
E-mail: sabrina.heng@adelaide.edu.au; Fax: +61 8 83034380; Tel: +61 8 8313 6694
† Electronic supplementary information (ESI) available. See DOI: 10.1039/c3ra40321a

RSC Advances
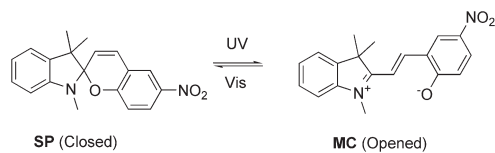
Fig. 1 Structures of spiropyran (**SP**, closed) and merocyanine (**MC**, opened).

Scheme 1 Reagents and conditions: i, 2-methyl-2-butanone, conc. H_2SO_4, EtOH, reflux, 12 h; ii, methyl iodide, toluene : acetonitrile 2 : 1, reflux, 14 h; iii, chloromethyl methyl ether, aluminium chloride, rt., 1 h then reflux, 2 h; iv, 1-aza-15-crown-5, Et$_3$N, THF, 0 °C–rt., 14 h then reflux 3 h; v, EtOH, reflux, 3 h.

(merocyanine or MC) upon irradiation with UV light and *vice versa* with visible light or heat (Fig. 1).[18,19] This substantial change in color between the two forms is due to the unavailability of the electron lone pair of the phenolate oxygen in MC, which contributes to the charge delocalization in the zwitterionic MC species.

A basic spiropyran structure can be readily functionalized with a suitable metal-binding site to provide an opportunity to affect the light-induced release of the metal ion to generate a re-generable sensing system. Indeed, spiropyran-based chemosensory systems for the detection of alkali and alkaline earth, lanthanides, transition and non-transition metals have been reported.[20,21] In particular, crowned spiropyrans have been developed as chemosensors for alkali metal ions, in which the metal ion binding in the crown ether moiety induces a large spectral change accompanied by isomerization to the merocyanine form.[22,23]

In this work we report the design, synthesis and operation of a novel photo-responsive, regenerable ion sensor for the detection of lithium ions (**Sensor-1**). Here, we chemically modified a known monoazacrown bearing spiropyran (**SP1**, Scheme 1) to enable it to be attached covalently to the glass surfaces inside the air holes of MOFs. When the optical fibres have been surface functionalized with **SP1**, the operation of the sensor was investigated through several key characteristics such as the minimum concentration of lithium ions detectable, photoswitching and sensor re-use. While various surface functionalized spiropyrans have been reported,[24–27] this study is the first demonstration of a surface functionalized spiropyran derivative with an ionophore attached to the molecular switch. Prior to this work, the ion sensing ability of surface functionalized spiropyran mainly relied on the metal chelating ability of the molecular switch during the SP to MC transition.[24,25,28] The integration of an ionophore to the sensor paves the way for the development of highly specific light-based sensing platforms that can be readily adapted to sense specific ions just by altering the ionophore design. In addition, this also represents the first reversible molecular switch that is functionalized within an optical fibre system. This integration of **SP1** and MOF results in a nanoliter-scale, light-driven ion sensor that can be turned on and off on demand in order to overcome the problem of a one-time use sensor.

Results and discussion

Synthesis of SP1

The synthesis of **SP1** with a monoazacrown moiety in the 8-position is based on the condensation of compounds **3** and **6**, as shown in Scheme 1. The key indole **3** was synthesized in two steps according to the literature.[29] In particular, the reaction of 4-hydrazinobenzoic acid (**1**) with isopropylmethylketone, followed by methylation with methyl iodide, gave the desired product. The crowned nitrosalicylaldehyde (**6**) was obtained in two steps by the chloromethylation of 5-nitrosalicyladehyde (**4**) in the presence of aluminum chloride followed by the reaction with 1-aza-15-crown-5. The subsequent condensation of (**3**) with (**6**) in ethanol under reflux gave **SP1**.
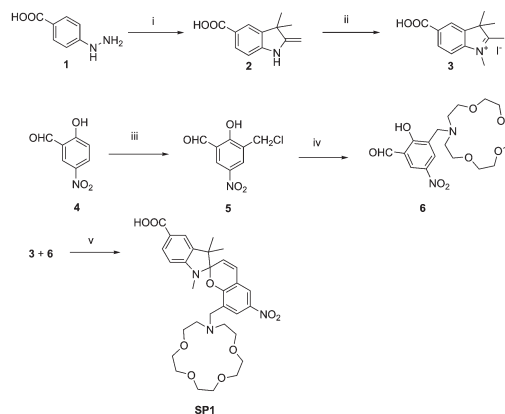
Solution studies

The photoswitchable ion sensor molecule (**SP1**) used for surface attachment and sensor development is based on a spiropyran system bearing a monoazacrown moiety at the 8-poisiton. Like most crown ethers, the rings of aza-crown ethers are rather flexible and provide some degree of structural freedom during complexation with metal ions. 1-Aza-15-crown-5 is known to have affinity towards alkali metal ions such as Li^+, Na^+ and K^+.[30] Although it is generally known that 1-aza-15-crown-5 prefers Na^+ to Li^+, the solution studies here seem to indicate that **SP1** does not strongly discriminate between Li^+ and Na^+ (Fig. 2a). This aberration from the norm can be explained by the additional interaction that the metal ion makes with the phenolic oxygen from the spiropyran molecule. It has been proposed that for this type of system, the metal ion sits approximately mid-way between the crown and the phenolic spiropyran oxygen.[31] This change in binding mode could explain why **SP1** does not strongly discriminate between Li^+ and Na^+. In fact, Kimura *et al.*[7] previously reported that with the 1-aza-15-crown-5 spiropyran analog, Li^+ gave a higher absorbance value when compared to Na^+ under the same condition. It is important to note that the objective of this study was not to develop a sensor for specific metal ions, rather it was directed at providing a first demonstration of an
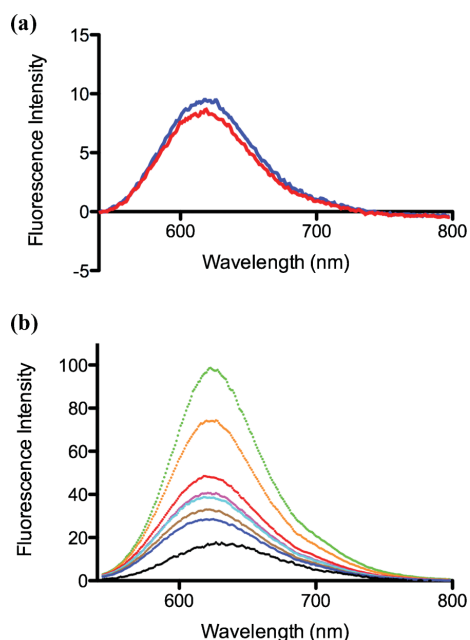
Fig. 2 (a) Cuvette fluorescence measurements for **SP1** (10 µM) in the presence of Li (1 µM, ——) and Na (1 µM, ——) ions respectively. (b) **SP1** (10 µM) with increasing Li^+ concentrations in acetonitrile (cuvette). Li concentrations were 0, 0.05, 0.2, 0.3, 0.4, 0.5, 0.8 and 1 µM respectively (from bottom to top). Each sample was exposed to UV light for 7 min before the fluorescence readings were obtained.
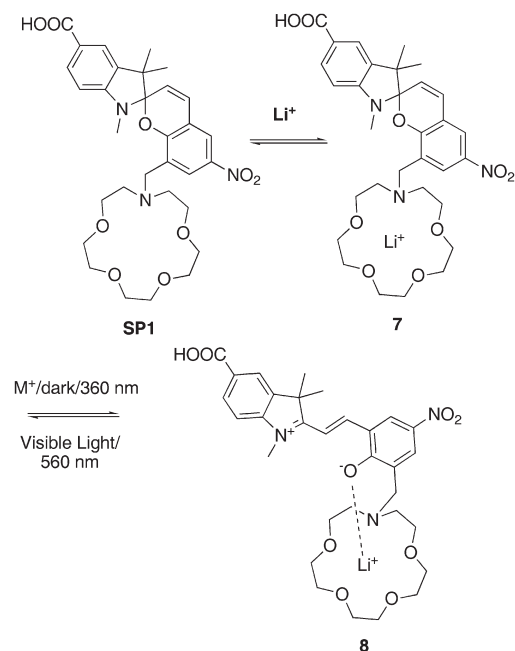
Fig. 3 Li^+ interaction with **SP1** according to the model proposed by Kimura *et al.*[7] Compound **7** represents the closed form of the SP–Li complex prior to irradiation with UV light ($\lambda = 365$ nm). Compound **8** represents the opened and fluorescent form of the SP–Li complex after irradiation with UV light for at least 5 min.

on/off sensor based on a photoswitch immobilized onto a MOF platform. As such we focused on understanding the operation of this new sensor without targeting a specific ion. For this reason, Li^+ was used in subsequent experiments to examine the operation of the sensor, as $LiClO_4$ is slightly more soluble in acetonitrile compared to the solubility of $NaClO_4$ in the same solvent. Fig. 2b shows the increase in fluorescence intensity with increasing Li^+ concentrations. From these experiments, two important observations can be made. The first is that the relationship between the closed (Fig. 3, compound **7**) and opened (Fig. 3, compound **8**) forms of **SP1**, in the presence of Li^+, is consistent with the model proposed by Kimura *et al.*,[7] where the ion would interact with compounds like **SP1** according to Fig. 3. Unlike the interaction of spiropyran with polar solvents (Fig. 3), the interaction of **SP1** with metal ions in an aprotic solvent does not result in the SP $\leftrightarrow$ MC transformation in the presence of white light (Fig. 1). Therefore, changes in fluorescence intensity were not observed upon adding more Li^+ to solutions of **SP1**. An increase in fluorescence intensity, corresponding to an increase in Li^+ concentrations was observed only when the respective **SP1–Li** solutions were exposed to UV light ($\lambda = 365$ nm) for at least 5 min (Fig. 2). The second characteristic is that the fluorescence of the ring-opened, complexed form (**8**) is more intense

compared to the free MC form, which fluoresces only weakly at these wavelengths ($\lambda_{ex} = 532$ nm, $\lambda_{em} \sim 630$ nm).

Microstructured optical fibre experiments

The MOF used for this study was fabricated in-house from undoped high purity fused silica, using the cane and jacket method[32] in combination with the process described by Kostecki *et al.*[33] Silica is ideal for this work as it has high transmission properties in the UV-vis–NIR spectral range.[34,35]

A single 80 m length of polymer coated ($n = 1.54$) fibre was fabricated and the dimensions of this fibre were measured using cross-sectional images from a scanning electron microscope (SEM). Fig. 4a shows the overall MOF structure with the coating removed, having an outside diameter of 270 µm. An enlargement of the core and holes region in the center of the fibre (structure known as a wagon wheel fibre) is shown in Fig. 4b, where the core of the fibre is the small triangular element in the center of the image (highlighted by the green box) suspended on three thin struts. The 3 black voids are the holes within the fibre cross-section, which form the cladding region used to provide the refractive index contrast needed for light confinement, and are used for this study as sample chambers, with each hole diameter being 12.4 µm, defined as the diameter of a circle whose area is equal to the cross
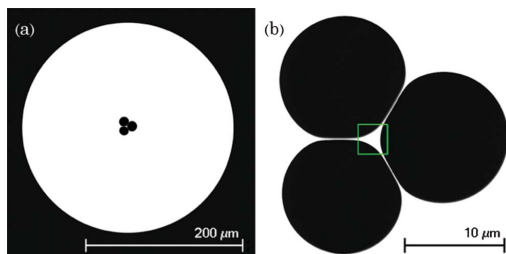
Fig. 4 Scanning electron microscopy images of (a) the silica microstructured optical fibre with an outside diameter of 270 μm and of (b) an enlarged image of the core and hole region, where the core is highlighted by the green box, having an effective diameter of 1.7 μm.

sectional area of the hole. The web thicknesses are a minimum of 0.16 μm, while the core has an effective diameter of 1.7 μm, defined as the diameter of a circle whose area is equal to a triangle that fits wholly within the core area.[32]

The power fraction of guided light protruding into the holes of this silica fibre was theoretically investigated,[36] using an air suspended rod approximation with a circular 1.7 μm core diameter. For the cladding region, the refractive index used was $n = 1.34$, being the refractive index of the analyte used in this study. It was found that at the excitation wavelength of 532 nm, this fibre can support 12 propagating modes, and with a coupled Gaussian beam waist of 1.7 μm, 2.1% of the total optical power of all 12 modes is located outside of the core, which is available to interact with a fluorophore functionalized on the surface.

Photostability studies on unfunctionalized MOFs

SP1 must possess high chemical stability and photostability under the conditions of the experiments if the sensor is to be useful. Any photochemical destruction of **SP1** can potentially impair the function of the sensor; therefore experiments were carried out to determine the intensity or time-span of light exposure that would cause a significant photobleaching of **SP1**.

The experimental set-up used for the in-fibre fluorescence measurements is shown in Fig. 5. The MOF was filled by immersing the left-hand tip into the solutions that were then
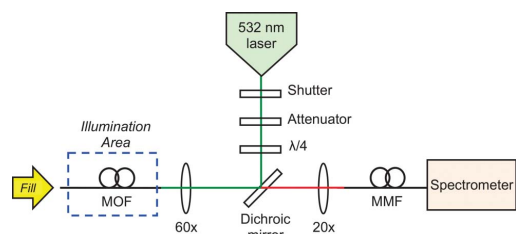
Fig. 5 Optical setup used to measure the fluorescence from a MOF. MMF is a multimode fibre.
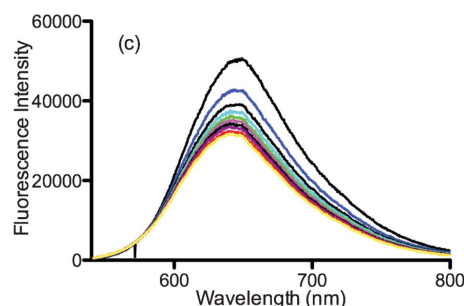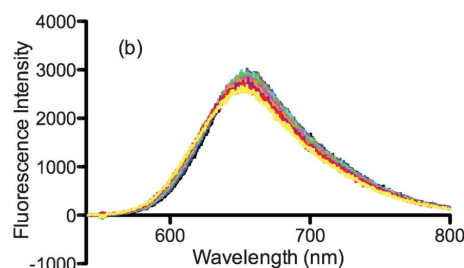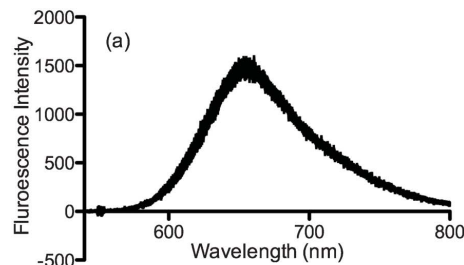
Fig. 6 Photobleaching experiments with **SP1** (1 μM in acetonitrile) absorbed onto a MOF using capillary action where (a) 10 × 16 ms, (b) 10 × 32 ms and (c) 10 × 1 s of exposure to the 532 nm laser, respectively.

left to fill *via* capillary forces. A UV lamp and a halogen light source were used to switch the molecules and were placed over the MOF. The area of illumination is shown by the dotted rectangle (Fig. 5). An empty fibre was thus filled with a solution of **SP1** (1 μM) in acetonitrile by capillary action. Once filled, the fibre was exposed to UV light for 7 min to convert all the absorbed **SP1** from its closed, non-fluorescent form to the opened, fluorescent MC form.

Photobleaching experiments were carried out by subjecting the **SP1** absorbed within the holes of the MOF to multiple exposures of the 532 nm laser (10 × 16 ms, 10 × 32 ms and 10 × 1 s, Fig. 6a, b, c respectively). As apparent in Fig. 6a, photobleaching was not observed for 10 × 16 ms of exposure, however photobleaching to approximately 60% fluorescence intensity was observed after 10 cycles of exposure to the laser at 1 s per exposure (Fig. 6c). Given that **SP1** was found to be

Paper
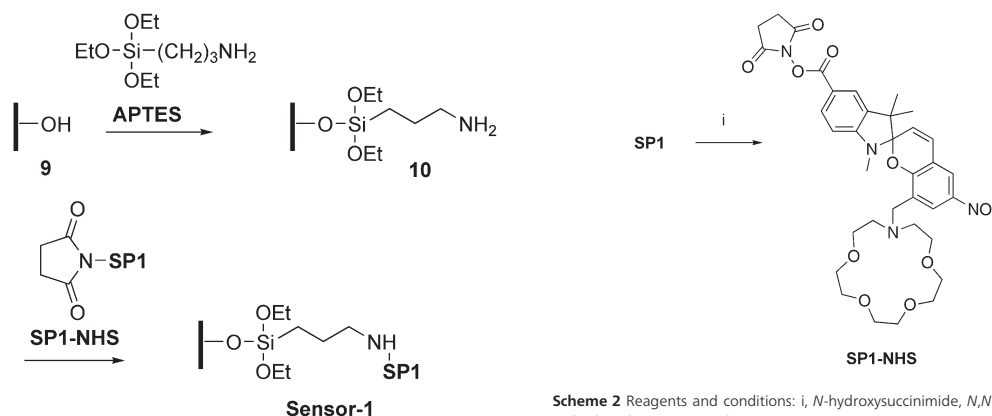
Fig. 7 Reaction scheme used to covalently attach **SP1** to the internal surface of the MOF. **9** represents the functionally inert silanols that line the surface of the silica glass. **10** represents a covalently attached APTES molecule with its amine group extending away from the surface. **Sensor-1** represents the completed sensor with molecules of **SP1** attached onto the internal surface (holes) of the MOF.

Scheme 2 Reagents and conditions: i, *N*-hydroxysuccinimide, *N,N′*-Diisopropyl-carbodiimide, THF, rt., 18 h.

robust and less prone to bleaching under these conditions, the time span of light-exposure to the 532 nm laser for all subsequent experiments were maintained at 10×16 ms.

Surface functionalization of a MOF with SP1

As mentioned previously, for the sensor to function as a regenerable ion sensor the molecular switch (**SP1**) must be covalently attached to the internal surface of the MOF. This then renders the sensing surface photo-responsive.

The procedure used to attach **SP1** onto the internal surface of the MOF is illustrated in Fig. 7. It is important that this methodology is reliable, repeatable, and capable of withstanding the conditions employed during ion binding and photoswitching. To do this, fibres were sealed into a metal chamber and the solutions were forced through the fibre *via* positive pressure using nitrogen gas. The fibres were coated with 5% APTES in toluene (w/w) for 2 h at 100 psi.[37,38] The next step usually involves pre-mixing the COOH-bearing molecule with excess coupling reagents (EDC/NHS) before applying the entire mixture to the amine-terminated silane surface (Fig. 7, 10). However, this approach is problematic in that it is hard to quantify the number of molecules that have been activated and are available to react with the surface. Secondly, long washing times are usually required to ensure that excess coupling reagents and by-products are completely flushed from the fibre. To eliminate having to perform the coupling reaction on the surface, **SP1** bearing a reactive succinimidyl ester moiety, for subsequent surface attachment, was first synthesized according to Scheme 2. **SP1** was reacted with *N*-hydroxysuccinimide (NHS)[39] in the presence of *N,N′*-diisopropylcarbodiimide (DIC) at room temperature to give **SP1–NHS** in 70% yield.

The fibres were then rinsed in preparation for coating with synthetic **SP1–NHS**. The fibres were prepared for coating by

initially flushing with toluene for 20 min, followed by drying with nitrogen for 20 min, a further flush with millipore water for 20 min and a final flush with nitrogen for 30 min. The fibres were then coated with a solution of **SP1–NHS** in acetonitrile (2 mM) for 2 h, and were flushed with acetonitrile, air and water for 20 min, respectively. In all of the above steps, 100 psi of pressure were used and the ends of the fibres were visually checked to ensure that the liquid/gas was flowing through.

The results in Fig. 8 reveal that, unlike an unfunctionalized fibre, the **SP1** functionalized fibre (**Sensor-1**, Fig. 7) has an inherent background fluorescence ($\lambda_{em} \sim 640$ nm). This is consistent with **SP1** having been successfully immobilized within the fibre's internal surface. Next, using only capillary forces, sections of **Sensor-1** were filled with lithium perchlorate solutions with concentrations ranging from 50 nM to 10 μM respectively. The respective sections were first exposed to white light for 2 min to ensure that all the fluorescent **SP1–MC**
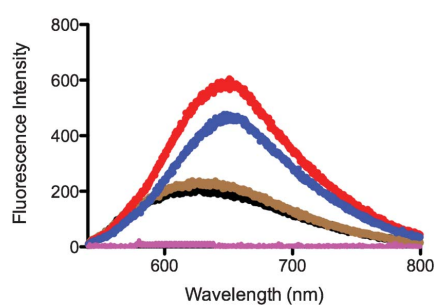
Fig. 8 (●) Empty fibre and (●) functionalized fibre (FF), not filled with Li⁺ solution after photo-irradiation with UV for 7 min and exposed to white light 2 min respectively. (●) FF, filled with 100 nM and 1 μM Li⁺ in ACN respectively, exposed to white light for 2 min. (●) FF, filled with 100 nM Li⁺ in ACN, exposed to UV ($\lambda = 360$ nm) for 7 min. (●) FF, filled with 1 μM Li⁺ in ACN, exposed to UV ($\lambda = 360$ nm) for 7 min.

forms was converted to the non-fluorescent **SP1–SP** forms. This was followed by exposure to UV light for 7 min with fluorescence measurements taken at regular intervals. This revealed that the maximum fluorescence was achieved after 7 min of UV exposure. Fig. 8 shows an increase in fluorescence intensity when the fibre was filled with solutions of 100 nM and 1 µM of Li^+, respectively. The signal-to-background ratio obtained for the 50 nM sample was approximately 1 (not shown in Fig. 8). This compared to the values of 1.9 and 2.5 signal-to-background ratios for the exposure to 100 nM and 1 µM of Li^+, respectively. The relatively poor signal-to-background ratio for concentrations lower than 100 nM is likely attributable to the high surface density of **SP1** on the fibre, which is common in surface-attachment experiments. This is not associated with the glass itself, as recently demonstrated by us in the sensing of CdSe quantum dots down to 10 pM in soft-glass microstructured optical fibres.[40] This was achieved using the same fibre concept. Thus, further optimization of the coating procedure can be done to reduce this background signal, but was beyond the scope of the proof-of-concept work presented in this paper.

MC ↔ SP transition in the presence of Li^+

It has been previously reported that the rate by which MC isomerizes back to SP is greatly influenced by exposure to metal ions.[7] In order to investigate light-induced reversion of the metal-complexed MC form to SP, a section of **Sensor-1**, filled with acetonitrile only, was exposed to white light and the emission spectra were recorded at regular intervals. The same piece of fibre was then irradiated with UV light to regenerate the fluorescent **SP1–Li** complex and this was again exposed to white light. Fig. 9b reveals that fluorescence decreased much more rapidly when **Sensor-1** is not chelated to Li ions, with the intensity falling below 50% in less than 2 min. In contrast, **Sensor 1** chelated to Li^+ demonstrated much slower photo-decolouration (Fig. 9a). There was little change in fluorescence intensity after 8 min of white light exposure. Once again this

result is consistent with the binding mode illustrated in Fig. 3, where the thermal stability of the crowned merocyanines is influenced by both the cation-complexing ability of the crown moiety and the strength of the intramolecular interaction between the crown-complexed metal ion and the phenolate anion. Although pseudo first order decolouration can be obtained for **Sensor 1** in the absence of any ions, we were unable to observe first-order decolouration for the metal bound complex. This observation is consistent with the work of Kimura *et al.*[7] where the authors were able to obtained the first order decolouration rates in THF at 40 °C but not in acetonitrile where the decolouration of the aza-crown spir-opyran analogs was too slow to follow. It has been proposed that these anomalies in the decolouration kinetics could be due complexing between the opened, metal-bound MC forms and the closed SP forms of the spiropyran fragments in the different solvents. However this interaction between solvent and photodecolouration of the metal-bound MC species is still far from a complete understanding[41] and is beyond the scope of this work.

It is well documented that the isomerization of spiropyrans is known to be highly dependent on solvent effects, with polar solvents stabilizing the opened MC form.[31] To investigate whether sensing can be performed in the presence of aqueous media, fluorescence data for **SP1** in varying percentages of water in acetonitrile was obtained (cuvette experiment). Fig. 10 shows the effect of 5% H_2O on fluorescence intensity. In the absence of any Li^+, a slight increase in fluorescence intensity for **SP1** in Solution 1 (5 : 95 H_2O:acetonitrile) (–) relative to that of **SP1** in acetonitrile alone (–) was observed. This increase in fluorescence agrees with the general observation that water stabilizes the open MC form. However, when **Solution 1** was exposed to white light, the MC → SP conversion occurred almost instantly, which is consistent with the data in Fig. 9b and the fluorescence intensity for both solutions are now similar.

Li^+ was then added to **Solutions 1** and **2**, respectively, and both solutions were exposed to UV light for 7 min. Fig. 10 shows that the fluorescence intensity for the Li^+ bound **SP1** in

Fig. 9 Photo-decolouration of **Sensor-1** in the absence and presence of Li ions. The points on the graphs are fitted using non-linear regression in GraphPad Prism version 5 (http://graphpad.com/help/prism5/prism5help.html). (a) (●) Cycle1. **Sensor 1** filled with 1 µM of Li^+ in acetonitrile, irradiated with UV for 7 min, followed by exposure to white light for 12 min. Pseudo R^2 = 0.9943. (▲) Cycle 2, second exposure to UV for 7 min, followed by second round of exposure to white light for 12 min. Pseudo R^2 = 0.9839. (b) (○) **Sensor 1** filled with acetonitrile only, exposed to white light. Pseudo R^2 = 0.9913.

Fig. 10 Comparison of the fluorescence intensity of **SP1** in 5 : 95 H_2O : acetonitrile (**Solution 1**) and in acetonitrile (**Solution 2**) with and without Li^+. (–) **Solution 1** prior to exposure to white light, (–) **Solution 1** exposed to white light for 2 min, (–) **Solution 2** exposed to white light for 2 min, (–) Solution 1 with 1 µM Li^+ exposed to UV for 7 min, (–) **Solution 2** with 1 µM Li^+ exposed to UV for 7 min, (–) **Solution 1** with 1 µM Li^+ exposed to white light for 2 min, (–) **Solution 2** with 1 µM Li^+ exposed to white light for 2 min.

Solutions **1** and **2** is identical. Both also demonstrated a much slower rate of photodiscolouration that is consistent with the model proposed for a metal bound complex (Fig. 9a). Finally, there is a subtle shift in $\lambda_{\max}$ from approximately 619 nm (**SP1**) to 625 nm for the **SP1–Li** complex. This wavelength shift is not observed for **Solution 1** in the absence of Li$^+$. These experimental results are reproducible up to solutions containing 30% water, above which **SP1** becomes non-dissolvable. Although acetonitrile was used in all fluorescence experiments in this work to minimize solvent related background fluorescence, it is clear that ion sensing experiments can still be performed in the presence of aqueous media. While polar solvents do produce the opened MC form, these studies demonstrate that the compound can be readily converted to the closed SP form by exposure to white light prior to the addition of any Li$^+$.

Photoswitching

The photoswitching process was next measured in the presence of 1 μM of Li$^+$ to show that ion binding and release could be optically controlled and measured by state-dependent fluorescence. Each "on-cycle" involved switching to the active merocyanine surface (fluorescent) upon exposure to UV light to allow the formation of the **SP1–Li** complex. Each "off-cycle" was generated upon exposure to white light to expel the Li ions back into solution to regenerate the passive spiropyran surface (non-fluorescent). The entire process occurred within the micron-scale holes of the MOFs. The resulting fluorescence spectra show that the binding process with **Sensor 1** can be repeated at least five times without problems (Fig. 11).

Sensor re-use

The potential reusability of the sensor after each measurement was investigated. A section of **Sensor 1** already filled with a 1 μM of Li$^+$ solution was removed from the optical set-up and placed back onto the fibre-filling chamber. The solution 1 μM of Li$^+$ was then expelled by successive flushing with air, acetonitrile and air. The fluorescence of the now 'empty' **Sensor 1** was then obtained as shown in Fig. 12. The emission spectrum obtained from this 'empty' **Sensor 1** is identical to

Fig. 12 Fluorescence emission to demonstrate sensor re-use. (—) Empty fibre. (—) First round of filling with 1 μM Li$^+$ in acetonitrile. (—) First round, after irradiation with UV light for 7 min. (—) After removing Li ions from **Sensor 1**. (—) Second round of filling with 1 μM Li$^+$, after irradiation with UV light for 7 min.

that of the fibre, which has not been surface functionalized with **SP1** (**empty fibre**, Fig. 12). This strongly indicated that Li ions were completely removed from the sensor during flushing. **Sensor 1** was then refilled with a fresh solution of 1 μM Li$^+$ ions, exposed to UV light (7 min) and the fluorescence spectra obtained. The resultant emission spectrum (Fig. 12, blue) is comparable to that obtained in the initial experiment (Fig. 12, red). This clearly shows that it is possible to empty the fibre of the ion solution and re-fill it with a fresh solution with negligible effect on the function of the sensor or the surface attached **SP1** molecules. Future work will involve constructing a more sophisticated process that would include the likes of a syringe pump to the optical set-up shown in Fig. 5 so that the fibre remains undisturbed. Importantly in practical devices, the interaction between ion binding and light can be further improved by guiding white light through the fibre instead. This will enable the sensor system to be kept in a light-tight enclosure to avoid unintended light-molecular switch interactions.

Conclusion

The ubiquitous nature of metal ions in the environment and biology presents a real need to develop new methodologies for their rapid and efficient detection. Such sensors would have applications in disease diagnosis and study, as well as environmental sensing. In an effort to meet this need, we have developed the first nanoliter-scale, regenerable ion sensor based on a microstructured optical fibre (MOF). The air holes of the MOF were functionalized with a monoaza-crown bearing spiropyran (**SP1**) to give a photo-switchable sensor that detects lithium ions down to 100 nM in nanoliter-scale volumes. The original compound reported by Kimura et al.[7] was not functionalized for surface attachment although the authors have recently reported the functionalization of silica with a similar crowned spirobenzopyran.[42] Using the original compound as a model, we thus designed and prepared a modified compound containing a carboxyl group

Fig. 11 Photoswitching of the surface functionalized MOF. Cycle 0 represents the state before **Sensor 1** was filled with a 1 μM Li$^+$ solution. Cycles 1, 3 and 5 represent each 'on-cycle' where **Sensor 1** was exposed to UV light (λ = 365 nm) for 7 min respectively. Cycles 2 and 4 represent each 'off-cycle' where **Sensor 1** was exposed to white light for 12 min respectively.

to allow attachment to the MOF and hence surface-based sensing. This enables the MOF's capacity to sense within small sample volumes (<10 nL) to be exploited.

The integration of a photoswitchable molecule bearing an ionophore within the MOF is new and we wished to understand the outcome of this integration and to then examine the operation of this novel sensing platform. We have demonstrated that ion binding is turned on and off upon irradiation with light, with the sensor being unaffected by multiple rounds of photoswitching. More importantly, we have showed that unbound ions are flushed from the fibre in the 'off' state to allow the sensor to be reused. The integration of an ionophore into the sensor paves the way for the development of highly specific light-based sensing platforms that are readily adaptable to sense a particular ion simply by altering the ionophore design. This work presents advances in both fibre sensing technology and in developing fast, sensitive "point of care" ion sensing methods that can be easily deployed, are disposable and affordable, particularly in the areas of disease diagnosis. Ongoing work is concerned with designing novel ionophores for binding specific ions and decreasing the detection limit of the sensor, with the aim of sensing down to the pM levels as recently demonstrated by our group where the detection of CdSe quantum dots down to 10 pM levels has been demonstrated.[40]

Experimental section

General Methods for Synthesis. All ^{13}C NMR spectra (75 MHz) and ^{1}H NMR spectra (300 MHz) were recorded on a Varian Gemini 2000 spectrometer in CDCl$_3$ or DMSO-d_6. Chemical shifts (δ) are reported in ppm. Chemical shifts of CDCl$_3$ (δ_C = 77.1 ppm), DMSO-d_6 (δ_C = 39.52 ppm) or TMS (δ_H = 0.0 ppm) were used as internal standards in all ^{13}C NMR and ^{1}H NMR experiments, respectively. HPLC grade acetonitrile (Scharlau) was used in all related experiments. Anhydrous THF was distilled in the presence of benzophenone and sodium. All lithium and sodium ions used in this work were in the form of perchlorate salt. All other reagents were purchased from Sigma-Aldrich and used without further purification.

3,3-Dimethyl-2-methyleneindoline-5-carboxylic acid (2)

A solution of 4-hydrazino benzoic acid (5.0 g, 33 mmol) and 2-methyl-2-butanone (3.9 mL, 36 mmol) in ethanol (15 mL) and conc. H$_2$SO$_4$ (1 mL) were heated under reflux for 18 h. After cooling to room temperature, the resultant precipitate was separated from the reaction mixture using vacuum filtration and saturated NaHCO$_3$ (30 mL). The resulting solution was extracted with CH$_2$Cl$_2$ (3 × 30 mL). The pH of the aqueous layer was adjusted to approximately 4 using 1 M HCl and the resultant aqueous layer was again extracted with CH$_2$Cl$_2$. Both organic layers were combined and excess solvent was removed under vacuum to yield 2 (6.5 g, 97%) as a brownish solid. ^{1}H NMR (CDCl$_3$, 300 MHz) δ 8.17 (d, J = 7.8 Hz, 1H), 8.09 (s, 1H), 7.73 (d, J = 7.8 Hz, 1H), 2.42 (s, 3H), 1.26 (s, 6H); ^{13}C NMR (75 MHz) δ 193.0, 171.1, 156.9, 145.7, 131.1,

127.8, 123.5, 119.8, 54.2, 23.1 (2C), 15.7; MS (*m/z*) for C$_{12}$H$_{13}$NO$_2$ + H ([M+H]$^+$) calcd 204.2; found 204.2.

1,3,3-Trimethyl-2-methyleneindoline-5-carboxylic acid (3)

Compound 2 (1.2 g, 5.9 mmol) and methyl iodide (368 µL, 5.9 mmol) were dissolved in a mixture of anhydrous toluene and acet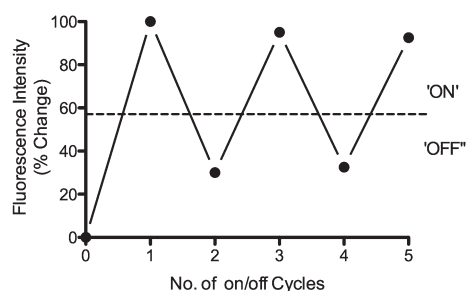onitrile (2 : 1, 30 mL) and were heated under reflux for 18 h. The reaction mixture was cooled to rt. and the dark red precipitate that formed was isolated using vacuum filtration. The solid was washed with minimal ethanol (approximately 5 mL) and hexane (30 mL) to yield 3 (900 mg, 70%) as a pale brown solid. ^{1}H NMR (DMSO-d_6, 300 MHz) δ 8.38 (s, 1H), 8.19 (d, J = 8.7 Hz, 1H), 8.02 (d, J = 8.7 Hz, 1H), 3.99 (s, 3H), 2.80 (s, 3H), 1.56 (s, 6H); ^{13}C NMR (75 MHz) δ 198.9, 166.4, 145.2, 141.9, 130.3, 129.8, 122.8, 115.3, 53.6, 35.0, 21.5 (2C), 14.5; MS (*m/z*) for C$_{13}$H$_{15}$NO$_2$ + H ([M + H]$^+$) calcd 218.2; found 218.2.

3-(Chloromethyl)-2-hydroxy-5-nitrobenzaldehyde (5)

2-Hydroxy-5-nitrobenzaldehyde (1.0 g, 6 mmol) was dissolved in dry chloromethyl methyl ether (10 mL). Sublimed aluminum chloride (4 g, 30 mmol) was added under nitrogen. The reaction mixture was stirred at rt. for 1 h then set to reflux for 2 h. Ice water was slowly added to the reaction mixture and the resultant light brown precipitate that formed was collected under vacuum filtration and purified *via* recrystallization using hot hexane to yield 5 (1.0 g, 77%) as a white solid. ^{1}H NMR (CDCl$_3$, 300 MHz) δ 12.08 (s, 1H), 10.02 (s, 1H), 8.58 (s, 1H), 8.56 (s, 1H), 4.72 (s, 2H); ^{13}C NMR (75 MHz) δ 195.4, 163.7, 140.4, 131.7, 129.4, 128.2, 119.4, 38.6. MS (*m/z*) for C$_8$H$_6$ClNO$_4$ + H ([M + H]$^+$) calcd 216.6; found 216.6.

8-((1,4,7,10-Tetraoxa-13-azacyclopentadecan-13-yl)methyl)-1′,3′,3′-trimethyl-6-nitrospiro [chromene-2,2′-indoline]-5′-carboxylic acid (SP1)

A solution of compound 5 (500 mg, 2.3 mmol) in anhydrous THF (15 mL) was added drop wise to a solution of 1-aza-15-crown-5 (489 mg, 2.3 mmol) and Et$_3$N (648 µL, 4.6 mmol) in anhydrous THF (10 mL) at 0 °C. The reaction mixture was allowed to warm to rt. gradually and was stirred at rt. for 18 h and finally set to reflux for 3 h. After removing the Et$_3$N.Cl salt that formed using filtration, excess solvent was removed under reduced pressure and the crude product (3-((1,4,7,10-tetraoxa-13-azacyclopentadecan-13-yl)methyl)-2-hydroxy-5-nitrobenz aldehyde (6)) was used in the next step without further purification. ^{1}H NMR (CDCl$_3$, 300 MHz) δ 10.18 (s, 1H), 8.27 (d, 1H, J = 3.3 Hz), 8.17 (d, 1H, J = 3.3 Hz), 3.63–3.60 (m, 2H), 3.58–3.54 (m, 7H), 3.25–3.16 (m, 9H), 2.93–2.90 (m, 4H); ^{13}C NMR (75 MHz) δ 189.4, 166.4, 138.3, 129.1, 126.3, 126.2, 125.0, 124.3, 70.8 (4C), 70.7 (2C), 67.5 (2C), 56.0 (2C). MS (*m/z*) for C$_{18}$H$_{26}$N$_2$O$_8$ + H ([M + H]$^+$) calcd 399.2; found 399.2. After which, compounds 3 (196 mg, 0.9 mmol) and 6 (355 mg, 0.9 mmol) were dissolved in anhydrous ethanol (15 mL) and set to reflux for 3 h. Excess solvent was removed under vacuum and the crude mixture was purified using C-18 reverse phase silica gel (30% acetonitrile in H$_2$O) to yield SP1 (450 mg, 85%) as a purple solid. ^{1}H NMR (DMSO-d_6, 300 MHz) δ 8.14 (s, 2H), 7.81 (d, J = 8.4 Hz, 1H), 7.69 (s, 1H), 7.25 (d, J = 10.5 Hz, 1H), 6.70 (d, J = 8.4 Hz, 1H), 6.01 (d, J = 10.2 Hz, 1H), 3.48–3.35 (m, 20H), 2.72 (s, 3H), 1.26 (s, 3H), 1.14 (s, 3H); ^{13}C NMR (75 MHz) δ 167.4, 156.6, 151.2, 140.2, 135.9, 130.8, 128.7, 127.0, 125.7, 122.9,

121.6, 121.4, 120.3, 118.4, 106.3, 105.8, 70.2, 69.7, 69.5, 69.4, 69.3, 69.2, 69.0, 53.8, 52.3, 51.2, 45.7, 28.3, 25.5, 19.4 (2C). MS (m/z) for + H ([M + H]$^+$) calcd $C_{31}H_{39}N_3O_9$ 598.3; found 598.0; ([M + Na]$^+$) calcd 620.3; found 620.3. HRMS (ESI, m/z) for ([M + H]$^+$ calcd 598.2765 found 598.2757. HPLC (20–100% acetonitrile over 20 min) retention time: 4.243 min.

To synthesize **SP1–NHS**, **SP1** (120 mg, 0.20 mmol) and 1-ethyl-3-(3-dimethylaminopropyl) carbodiimide (39 µL, 0.25 mmol) were suspended in anhydrous THF (10 mL) rt. *N*-hydoxysuccinimide (28 mg, 0.25 mmol) was added after 5 min and the reaction mixture was stirred at rt. for 18 h. Excess solvent was removed under vacuum and the crude reaction mixture was washed with minimal amount of water (approximately 5 mL) to remove any unreacted starting material and by-products to yield **SP1–NHS** (50 mg, 36%) as a pale yellow solid which was used in surface functionalization of the MOF without further purification. ^{1}H NMR (DMSO-d_6, 300 MHz) δ 8.03–8.0 (m, 2H), 7.87 (d, J = 2.4 Hz, 1H), 7.74 (s, 1H), 6.92 (d, J = 10.5 Hz, 1H), 6.53 (d, J = 8.4 Hz, 1H), 5.77 (d, J = 9.9 Hz, 1H), 3.69–3.42 (m, 14H), 2.84 (s, 2H), 2.76 (s, 2H), 2.57 (s, 4H), 1.25 (s, 3H), 1.14 (s, 3H). MS (m/z) for $C_{35}H_{42}N_4O_{11}$ + H ([M + H]$^+$ calcd 695.3; found 695.3; ([M + Na]$^+$) calcd 717.3; found 717.2.

Cuvette Measurements of **SP1**. **SP1** and lithium perchlorate were dissolved in HPLC grade acetonitrile respectively. A solution of the appropriate solvent containing similar concentrations of **SP1** and metal ion was prepared and exposed to UV light (8 W, 365 nm filtered) for 7 min. Fluorescence spectra were recorded on a Varian Cary Eclipse spectrofluorometer. The excitation and emission slit width were set at 5 mm. All measurements were recorded at 25 °C using 700 µL quartz cuvettes with an excitation path length of 10 mm. Photodecolouration experiments were performed by exposing the respective samples to white light (8 W, cool white).

Fibre fabrication. Undoped high purity fused silica is also known as Suprasil F300HQ (Heraeus Quarzglas GmbH & Co.KG). To draw the cane into microstructured optical fibre, a 6 m tower with graphite resistance furnace, a positive pressurization system and automated diameter control was used.

Acknowledgements

Notes and references

1 G. Costante and S. Filetti, *Oncologist*, 2011, **16**, 49.

2 J. Cymet-Ramirez, M. M. Alvarez-Martinez, G. Garcia-Pinto, R. Frias-Austria, A. Meza-Vernis, M. E. Rosales-Munoz, A. Isunza-Ramirez, O. D. Isunza-Alonso, J. A. Brito-Ramirez, M. Anaya-Garcia and A. Lizalde-Yanez, *Acta Ortopedica Mexicana*, 2011, **25**, 313.

3 J. F. Dartigues, *La Revue du Praticien*, 2011, **61**, 926.

4 G. Genoni, I. Demarchi, S. Bellone, A. Petri, F. Settanni, E. Dondi, M. Negro, L. Cortese, F. Prodam and G. Bona, *Minerva Pediatrica*, 2011, **63**, 425.

5 J. P. Glusker, A. K. Katz and C. W. Bock, *The Rigaku Journal*, 1999, **16**, 8.

6 K. H. Thompson and C. Orvig, *Science*, 2003, **300**, 936.

7 K. Kimura, T. Yamashita and M. Yokoyama, *J. Chem. Soc., Perkin Trans. 2*, 1992, 613.

8 B. Ruhland, T. H. Becker and G. Muller, *Sens. Actuators, B*, 1998, **50**, 85.

9 B. Lee, S. Roh and J. Park, *Opt. Fiber Technol.*, 2009, **15**, 209.

10 S. V. Afshar, Y. L. Ruan, S. C. Warren-Smith and T. M. Monro, *Opt. Lett.*, 2008, **33**, 1473.

11 T. M. Monro, W. Belardi, K. Furusawa, J. C. Baggett, N. G. R. Broderick and D. J. Richardson, *Meas. Sci. Technol.*, 2001, **12**, 854.

12 T. M. Monro, S. Warren-Smith, E. P. Schartner, A. Francois, S. Heng, H. Ebendorff-Heidepriem and S. Afshar, *Opt. Fiber Technol.*, 2010, **16**, 343.

13 F. V. Englich, T. C. Foo, A. C. Richardson, H. Ebendorff-Heidepriem, C. J. Sumby and T. M. Monro, *Sensors*, 2011, **11**, 9560.

14 S. C. Warren-Smith, S. Heng, H. Ebendorff-Heidepriem, A. D. Abell and T. M. Monro, *Langmuir*, 2011, **27**, 5680.

15 Y. Ruan, T. C. Foo, S. Warren-Smith, P. Hoffmann, R. C. Moore, H. Ebendorff-Heidepriem and T. M. Monro, *Opt. Express*, 2008, **16**, 18514.

16 U. Wiedemann, W. Alt and D. Meschede, *Opt. Express*, 2012, **20**, 12710.

17 G. Berkovic, V. Krongauz and V. Weiss, *Chem. Rev.*, 2000, **100**, 1741.

18 K. H. Shen, X. L. Li and D. H. Choi, *Chin. J. Chem.*, 2008, **26**, 935.

19 B. S. Lukyanov and M. B. Lukyanova, *Chem. Heterocycl. Compd.*, 2005, **41**, 281.

20 J. P. Phillips, A. Mueller and F. Przystal, *J. Am. Chem. Soc.*, 1965, **87**, 4020.

21 M. Natali and S. Giordani, *Chem. Soc. Rev.*, 2012, **41**, 4010.

22 S. Yagi, S. Nakamura, D. Watanabe and H. Nakazumi, *Dyes Pigm.*, 2009, **80**, 98.

23 K. Kruttwig, D. R. Yankelevich, C. Brueggemann, C. Tu, N. L'Etoile, A. Knoesen and A. Y. Louie, *Molecules*, 2012, **17**, 6605.

24 K. H. Fries, J. D. Driskell, G. R. Sheppard and J. Locklin, *Langmuir*, 2011, **27**, 12253.

25 R. J. Byrne, S. E. Stitzel and D. Diamond, *J. Mater. Chem.*, 2006, **16**, 1332.

26 S. Scarmagnani, Z. Walsh and F. B. Lopez, *e-J. Surf. Sci. Nanotechnol.*, 2009, **7**, 649.

27 E. Katz, B. Willner and I. Willner, *Biosens. Bioelectron.*, 1997, **12**, 703.

28 Y. Shiraishi, S. Sumiya, K. Manabe and T. Hirai, *ACS Appl. Mater. Interfaces*, 2011, **3**, 4649.

29 M. Tomasulo, S. L. Kaanumal, S. Sortino and F. M. Raymo, *J. Org. Chem.*, 2007, **72**, 595.

RSC Advances   **Paper**

30 H. Nakamura, M. Takagi and K. Ueno, *Talanta*, 1979, **26**, 921.

31 A. M. A. Salhin, M. Tanaka, M. Kamada, H. Ando, T. Ikeda, Y. Shibutani, S. Yajima, M. Nakamura and K. Kimura, *Eur. J. Org. Chem.*, 2002, 655.

32 H. Ebendorff-Heidepriem, S. C. Warren-Smith and T. M. Monro, *Opt. Express*, 2009, **17**, 2646.

33 R. Kostecki, H. Ebendorff-Heidepriem, C. Davis, G. McAdam, S. C. Warren-Smith and T. M. Monro, *Opt. Mater. Express*, 2012, **2**, 1538.

34 S. Kubodera, P. J. Wisoff, F. K. Tittel and R. A. Sauerbrey, *Appl. Opt.*, 1988, **27**, 1638.

35 K. Kawamura, *Anal. Sci.*, 2002, **18**, 715.

36 S. C. Warren-Smith, S. Afshar and T. M. Monro, *Opt. Express*, 2010, **18**, 9474.

37 T. Shimada, K. Aoki, Y. Shinoda, T. Nakamura, N. Tokunaga, S. Inagaki and T. Hayashi, *J. Am. Chem. Soc.*, 2003, **125**, 4688.

38 K. Wen, R. Maoz, H. Cohen, J. Sagiv, A. Gibaud, A. Desert and B. M. Ocko, *ACS Nano*, 2008, **2**, 579.

39 P. Zhang, J. B. Meng, X. L. Li, T. Matsuura and Y. M. Wang, *J. Heterocycl. Chem.*, 2002, **39**, 179.

40 E. P. Schartner, H. Ebendorff-Heidepriem, S. C. Warren-Smith, R. T. White and T. M. Monro, *Sensors*, 2011, **11**, 2961.

41 S. Zhang, Q. Zhang, B. Ye, X. Li, X. Zhang and Y. Deng, *J. Phys. Chem. B*, 2009, **113**, 6012.

42 Y. Nakahara, Y. Yamaguchi, H. Iwamoto, H. Sakamato and K. Kimura, *Anal. Methods*, 2012, **4**, 4025.

APPENDIX D

Paper 4.

Silica exposed-core microstructured optical fibers

Roman Kostecki,[1,*] **Heike Ebendorff-Heidepriem,**[1] **Claire Davis,**[2]
Grant McAdam,[2] **Stephen C. Warren-Smith,**[1] **and Tanya M. Monro**[1]

[1]*Centre of Expertise in Photonics, Institute for Photonics & Advanced Sensing,*
School of Chemistry & Physics, University of Adelaide, Adelaide, SA 5005, Australia
[2]*Defence Science and Technology Organisation, Fishermans Bend, Victoria, Australia*
[*]*roman.kostecki@adelaide.edu.au*

Abstract: We report the fabrication of silica microstructured optical fibers with the core exposed along the whole length, and characterize the stability of these new fibers when exposed to some typical sensing and storage environments. We show the fiber loss to be the best achieved to date for exposed-core fibers, while the deterioration in the transmission properties is up to ~2 orders of magnitude better than for the previously reported exposed-core fibers produced in soft glass. This opens up new opportunities for optical fiber sensors requiring long term and/or harsh environmental applications while providing real time analysis anywhere along the fibers length.

References and links

1. P. Kasier, E. A. J. Marcatili, and S. E. Miller, "A new optical fiber," Bell Sys. Tech. J. **52**, 265–269 (1973).
2. J. C. Knight, T. A. Birks, P. S. J. Russell, and D. M. Atkin, "All-silica single-mode optical fiber with photonic crystal cladding," Opt. Lett. **21**, 1547–1549 (1996).
3. T. M. Monro, W. Belardi, K. Furusawa, J. C. Baggett, N. G. R. Broderick, and D. J. Richardson, "Sensing with microstructured optical fibres," Meas. Sci. Technol. **12**, 854–858 (2001).
4. T. Monro, D. Richardson, and P. Bennett, "Developing holey fibres for evanescent field devices," Electron. Lett. **35**, 1188–1189 (1999).
5. O. S. Wolfbeis, "Fiber-optic chemical sensors and biosensors," Anal. Chem. **80**, 4269–4283 (2008).
6. T. M. Monro and H. Ebendorff-Heidepriem, "Progress in microstructured optical fibers," Annu. Rev. Mater. Res. **36**, 467–495 (2006).
7. J. Lægsgaard and A. Bjarklev, "Microstructured optical fibers—fundamentals and applications." J. Am. Ceram. Soc. **89**, 2–12 (2006).
8. T. M. Monro, S. Warren-Smith, E. P. Schartner, A. François, S. Heng, H. Ebendorff-Heidepriem, and S. Afshar V., "Sensing with suspended-core optical fibers," Opt. Fiber Technol. **16**, 343–356 (2010).
9. H. Ebendorff-Heidepriem, S. C. Warren-Smith, and T. M. Monro, "Suspended nanowires: fabrication, design and characterization of fibers with nanoscale cores," Opt. Express **17**, 2646–2657 (2009).
10. L. Tong, R. R. Gattass, J. B. Ashcom, S. He, J. Lou, M. Shen, I. Maxwell, and E. Mazur, "Subwavelength-diameter silica wires for low-loss optical wave guiding," Nature **426**, 816–819 (2003).
11. K. Kiang, K. Frampton, T. Monro, R. Moore, J. Tucknott, D. Hewak, D. Richardson, and H. Rutt, "Extruded singlemode non-silica glass holey optical fibres," Electron. Lett. **38**, 546–547 (2002).
12. H. Ebendorff-Heidepriem, P. Petropoulos, S. Asimakis, V. Finazzi, R. Moore, K. Frampton, F. Koizumi, D. Richardson, and T. Monro, "Bismuth glass holey fibers with high nonlinearity," Opt. Express **12**, 5082–5087 (2004).

13. J. Leong, P. Petropoulos, J. Price, H. Ebendorff-Heidepriem, S. Asimakis, R. Moore, K. Frampton, V. Finazzi, X. Feng, T. Monro, and D. Richardson, "High-nonlinearity dispersion-shifted lead-silicate holey fibers for efficient 1-μm pumped supercontinuum generation," J. Lightwave Technol. **24**, 183–190 (2006).

14. J. Jensen, P. Hoiby, G. Emiliyanov, O. Bang, L. Pedersen, and A. Bjarklev, "Selective detection of antibodies in microstructured polymer optical fibers," Opt. Express **13**, 5883–5889 (2005).

15. A. S. Webb, F. Poletti, D. J. Richardson, and J. K. Sahu, "Suspended-core holey fiber for evanescent-field sensing," Opt. Eng. **46**, 010503 (2007).

16. T. G. Euser, J. S. Y. Chen, M. Scharrer, P. S. J. Russell, N. J. Farrer, and P. J. Sadler, "Quantitative broadband chemical sensing in air-suspended solid-core fibers," J. Appl. Phys. **103**, 103108 (2008).

17. A. Mazhorova, A. Markov, A. Ng, R. Chinnappan, O. Skorobogata, M. Zourob, and M. Skorobogatiy, "Label-free bacteria detection using evanescent mode of a suspended core terahertz fiber," Opt. Express **20**, 5344–5355 (2012).

18. S. Afshar V., S. C. Warren-Smith, and T. M. Monro, "Enhancement of fluorescence-based sensing using microstructured optical fibres," Opt. Express **15**, 17891–17901 (2007).

19. E. P. Schartner, H. Ebendorff-Heidepriem, S. C. Warren-Smith, R. T. White, and T. M. Monro, "Driving down the detection limit in microstructured fiber-based chemical dip sensors," Sensors **11**, 2961–2971 (2011).

20. Y. Ruan, E. P. Schartner, H. Ebendorff-Heidepriem, P. Hoffmann, and T. M. Monro, "Detection of quantum-dot labelled proteins using soft glass microstructured optical fibers," Opt. Express **15**, 17819–17826 (2007).

21. H. Yan, J. Liu, C. Yang, G. Jin, C. Gu, and L. Hou, "Novel index-guided photonic crystal fiber surface-enhanced Raman scattering probe," Opt. Express **16**, 8300–8305 (2008).

22. A. Bjarklev, J. B. Jensen, J. Riishede, J. Broeng, J. Laegsgaard, T. T. Larsen, T. Sorensen, K. Hougaard, and O. Bang, "Photonic crystal structures in sensing technology," Proc. SPIE **5502**, 9–16 (2004).

23. J. E. Debs, H. Ebendorff-Heidepriem, J. S. Quinton, and T. M. Monro, "A fundamental study into the surface functionalization of soft glass microstructured optical fibers via silane coupling agents," J. Lightwave Technol. **27**, 576–582 (2009).

24. Y. L. Hoo, W. Jin, C. Shi, H. L. Ho, D. N. Wang, and S. C. Ruan, "Design and modeling of a photonic crystal fiber gas sensor," Appl. Opt. **42**, 3509–3515 (2003).

25. C. M. B. Cordeiro, C. J. S. de Matos, E. M. dos Santos, A. Bozolan, J. S. K. Ong, T. Facincani, G. Chesini, A. R. Vaz, and C. H. B. Cruz, "Towards practical liquid and gas sensing with photonic crystal fibres: side access to the fibre microstructure and single-mode liquid-core fibre," Meas. Sci. Technol. **18**, 3075–3081 (2007).

26. C. Martelli, P. Olivero, J. Canning, N. Groothoff, B. Gibson, and S. Huntington, "Micromachining structured optical fibers using focused ion beam milling," Opt. Lett. **32**, 1575–1577 (2007).

27. A. van Brakel, C. Grivas, M. N. Petrovich, and D. J. Richardson, "Micro-channels machined in microstructured optical fibers by femtosecond laser," Opt. Express **15**, 8731–8736 (2007).

28. J. P. Parry, B. C. Griffiths, N. Gayraud, E. D. McNaghten, A. M. Parkes, W. N. MacPherson, and D. P. Hand, "Towards practical gas sensing with micro-structured fibres," Meas. Sci. Technol. **20**, 075301 (2009).

29. F. M. Cox, R. Lwin, M. C. J. Large, and C. M. B. Cordeiro, "Opening up optical fibres," Opt. Express **15**, 11843–11848 (2007).

30. S. C. Warren-Smith, H. Ebendorff-Heidepriem, T. C. Foo, R. Moore, C. Davis, and T. M. Monro, "Exposed-core microstructured optical fibers for real-time fluorescence sensing," Opt. Express **17**, 18533–18542 (2009).

31. S. Warren-Smith, E. Sinchenko, P. Stoddart, and T. Monro, "Distributed fluorescence sensing using exposed core microstructured optical fiber," IEEE Photon. Technol. Lett. **22**, 1385–1387 (2010).

32. K. Peters, "Polymer optical fiber sensors—a review," Smart Mater. Struct. **20**, 013002 (2011).

33. H. Ebendorff-Heidepriem, K. Kuan, M. R. Oermann, K. Knight, and T. M. Monro, "Extruded tellurite glass and fibers with low OH content for mid-infrared applications," Opt. Mater. Express **2**, 432–442 (2012).

34. H. Ebendorff-Heidepriem and T. M. Monro, "Extrusion of complex preforms for microstructured optical fibers," Opt. Express **15**, 15086–15092 (2007).

35. S. C. Warren-Smith, H. Ebendorff-Heidepriem, S. Afshar V., G. McAdam, C. Davis, and T. Monro, "Corrosion sensing of aluminium alloys using exposed-core microstructured optical fibres," Mater. Forum **33**, 110–121 (2009).

36. K. Richardson, D. Krol, and K. Hirao, "Glasses for photonic applications," Int. J. Appl. Glass Sci. **1**, 74–86 (2010).

37. M. Li and D. Nolan, "Optical transmission fiber design evolution," J. Lightwave Technol. **26**, 1079–1092 (2008).

38. Heraeus Quarzglas GmbH & Co. KG, *Pure Silica Rods for Specialty Fiber Applications*, 1st ed. (2012), http://heraeus-quarzglas.com/.

39. D. Wildeboer, F. Jeganathan, R. G. Price, and R. A. Abuknesha, "Characterization of bacterial proteases with a panel of fluorescent peptide substrates," Anal. Biochem. **384**, 321–328 (2009).

40. M. Y. Sim and S. Gleixner, "Studying the etch rates and selectivity of SiO_2 and Al in BHF solutions," in *2006 16th Biennial University/Government/Industry Microelectronics Symposium* (2006), pp. 225–228.

41. C. J. Voyce, A. D. Fitt, and T. M. Monro, "Mathematical modeling as an accurate predictive tool in capillary and microstructured fiber manufacture: the effects of preform rotation," J. Lightwave Technol. **26**, 791–798 (2008).

42. M. Fujiwara, K. Toubaru and S. Takeuchi, "Optical transmittance degradation in tapered fibers," Opt. Express

19, 8596–8601 (2011).

43. D. Tallant, T. Michalske, and W. Smith, "The effects of tensile stress on the Raman spectrum of silica glass," J. Non-Cryst. Solids **106**, 380–383 (1988).

44. G. Brambilla, F. Xu, and X. Feng, "Fabrication of optical fibre nanowires and their optical and mechanical characterisation," Electron. Lett. **42**, 517–519 (2006).

45. G. Zhai and L. Tong, "Roughness-induced radiation losses in optical micro or nanofibers," Opt. Express **15**, 13805–13816 (2007).

46. R. Brandsch, G. Bar, and M.-H. Whangbo, "On the factors affecting the contrast of height and phase images in tapping mode atomic force microscopy," Langmuir **13**, 6349–6353 (1997).

1. Introduction

Microstructured optical fibers [1] (MOFs) are well-suited for sensing, as characteristic longitudinal air holes used to provide the effective refractive index needed for light confinement [2] can also act as tiny sample chambers [3]. The portion of guided light located within these holes can be used to provide the light-matter overlap needed for many fiber optic sensing applications [4,5]. Unlike conventional optical fibers, MOFs can be manufactured from a single material [6], and with the appropriate cross-sectional design, the structure can provide the broad range of optical properties demanded by sensors [7].

For MOFs, the portion of guided light (often described as "*evanescent field*") protruding into the holes of the structure is affected by the characteristics of the medium within these holes [4]. This light-matter overlap provides opportunities for exploiting the interaction of light with gases and liquids, where the absorption and fluorescence characteristics can be used to determine the composition and concentration of the analyte [5]. In this regard, the fiber geometry can provide extremely long interaction lengths without the need for large volumes. Of particular interest is the suspended-core fiber [8], which can have a significant fraction of the guided power located within the holes [9], since the geometry has a high air filling fraction with a small core suspended on a number of thin struts. Unlike glass nano-wires [10], this design provides a means for obtaining uniform micrometer-nanometer scale suspended 'wires' while protecting the highly sensitive core, and long lengths can be fabricated by drawing a structured preform.

The suspended-core fiber has been demonstrated in soft glasses [11–13], polymer [14] and silica [15] materials. Chemical [15, 16] and biological [17] suspended-core fiber absorption spectroscopy sensors, which exploit the absorbance characteristics of the light-matter overlap, provide opportunities for both environmental sensing and quantitative chemical analysis. Suspended-core fiber sensors using in-fiber excitation and recapturing [18] of fluorescent dyes [19] or quantum dots [20], as well as surface-enhanced Raman spectroscopy using nanoparticles [21], have also been shown to provide highly sensitive specificity of the analyte of interest.

In principle, the suspended-core fiber also offers the potential for easier filling compared to MOFs with hexagonally arranged cladding holes that provide a small air filling fraction when the core is small [22]. In practice, the time needed to fill suspended-core fibers depends on the required interaction length and size of the holes, such as $\sim$7 hrs for gas diffusion [15] or $\sim$100 min for water at standard temperature and pressure [23], along a 1 m length of fiber with Ø8 μm holes. This makes their use impossible for real time or distributed sensing applications and difficulty still exists when attempting to ensure stable optical coupling while filling. To overcome these problems, fabrication techniques which expose the core [24] have been demonstrated by micro-machining fluidic side-channels at several locations along the fiber length [25–28], which results in short exposed regions in the order of tens of microns. This provides access to the core by the analyte, making it useful for real time sensing applications. However, in applications where kinetic changes of the analyte need to be measured, where emp-

tying and re-filling is required, or long lengths are needed for distributed sensing applications, post processing methods to the fiber still remain impractical. Another technique to expose the core is by creating an opening at the preform stage of fiber fabrication. This provides a means to fabricate long lengths of exposed-core fiber, and has been demonstrated in polymer [29] (polymethylmethacrylate) and soft glass [30] (Schott F2) materials, where the geometry was shown to be practical for real time evanescent field and distributed sensing [31] applications, with the capacity for fast filling and quick response to kinetic changes of the analyte.

Both polymer and soft glasses have properties which makes them useful for particular applications [9, 32, 33], and their glass transition temperatures (T_g) are low enough to make them practical for extruding the structured preform [34]. Nevertheless, these materials are not transparent at UV wavelengths, where many biological molecules can absorb the light, and the soft glass exposed-core fiber deteriorated quickly [30, 35], making it impractical for long term and/or harsh environmental applications. On the other hand, silica is known to be reliable under a range of processing and use environments, with relatively better mechanical and thermal stability [36]. Highly homogeneous, high purity bulk material is commercially available, which has led to silica telecom fibers regularly being made with low loss (~ 0.2 dB/km at NIR wavelengths) [37]. Also, silica has a relatively low refractive index, which can improve the sensitivity of evanescent field sensors, since reducing the index contrast (Δn) at the core-cladding boundary increases the power fraction to the analyte or functionalized surface [19].

In this paper we demonstrate an alternative fabrication technique for glass exposed-core fibers, where the fabricated geometry is a useful platform for surface analysis of the core. We report, for the first time to the best of our knowledge, the fabrication of a silica microstructured fiber with the core exposed along the whole length, and characterize the stability of this new fiber when exposed to some typical sensing and storage environments.

2. Silica exposed-core fiber fabrication

2.1. Introduction to silica exposed-core fiber fabrication

The aim of this work was to develop silica exposed-core fibers (Fig. 1), which are asymmetric and therefore needed new fabrication methods to be established. These methods expand on a combination of work previously shown by Webb *et al.* [15] for fabricating silica suspended-core fibers (wagon wheel structure) by machining the preform, and Warren-Smith *et al.* [30] for cutting a thin slot into the side of the symmetric preform (soft glass) in order to expose the core region. High purity fused silica known as Suprasil F300HQ (Heraeus Quarzglas GmbH & Co.KG) was chosen because it is produced to be free from bubbles and made to tight geometric tolerances [38]. This material has high transmission in the UV-Vis-NIR spectral range making it suitable for (bio)chemical sensing applications since it allows for the efficient excitation of a range of fluorophores; for example quantum dot labeled proteins excited in the visible [20] and fluorogenic peptide substrates excited in the UV [39].

2.2. The preform

The exposed-core fiber preform was fabricated from Ø12 mm F300HQ silica rod, which was drilled with three holes, where the centers of the holes form an equilateral triangle. The preform was sonic cleaned in methanol and Milli-Q water, then etched for 30 minutes in a buffered hydrofluoric acid solution (BHF), made using 6 volumes of ammonium fluoride (NH_4F, 40% solution) to 1 volume of hydrofluoric acid (HF, 50% solution), which has a well known etch rate of 100–250 nm/min [40]. After etching, the preform was rinsed with de-ionized water and then sonic cleaned in methanol and Milli-Q water, after which it was dried with nitrogen. The only difference between suspended-core fiber and exposed-core fiber preforms, is that for the exposed-core fiber case a slot was cut along the length of one of the holes, as shown in Fig. 1(a).
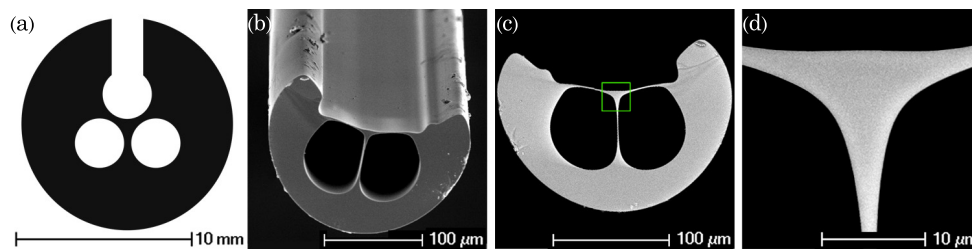
Fig. 1. (a) Cross section of the preform fabricated from Ø12 mm F300HQ silica rod; and, scanning electron microscope images of (b) the silica exposed-core fiber with (c) the cross section measured at the maximum to be Ø202 µm; and, (d) an enlarged image of the core having an effective diameter of 10.0µm.

2.3. Fiber drawing

To draw the preform to fiber a 6m tower with graphite resistance furnace, positive pressurization system and automated diameter control was used. By systematically using a series of temperatures and pressures, hole expansion and draw characteristics were investigated for the process of producing suspended-core fibers using the preform described in the previous section. These investigations showed that the exposed-core fiber could be produced using a temperature of 2000°C with pressure at 1.4 kPa, although one should consider that temperature and pressure profiles can vary between drawing towers and furnace designs [41].

A single 127 m long uncoated exposed-core fiber (Fig. 1(b)) was fabricated and the dimensions of this fiber were measured using cross-sectional images from a scanning electron microscope (SEM), shown in Figs. 1(b)–1(d), being Ø202 µm (measured at the maximum) with each hole being Ø66.0 µm, defined as the diameter of a circle whose area is equal to the cross sectional area of the hole. The central web thickness (between the holes) is 0.85 µm minimum, while the webs each side of the core are 1.10 µm minimum thickness. The core, shown by the green box in Fig. 1(c) and enlarged in Fig. 1(d), has an effective diameter of 10.0 µm, defined as the diameter of a circle whose area is equal to a triangle that fits wholly within the core area [9].

3. Silica exposed-core fiber characterization

3.1. Fiber loss & fluorescence

After fabrication, the exposed-core fiber was stored in the laboratory, exposed to air, on a high density Polyurethane foam drum with 1 m circumference. While the fiber was on the drum, cutback fiber loss measurements were performed by coupling the light from a 100 W halogen light bulb source with power curve of approximately Gaussian distribution and peak power at 800 nm, into one end of the exposed-core fiber. At the other end, the light from the core was imaged onto the grating of a Ando AQ6315E Optical Spectrum Analyzer (OSA) such that the power was maximized before each measurement. The fiber loss measurement results taken directly after fiber draw, shown by the red spectrum in Fig. 2(a), were 1.12±0.15 dB/m, 1.10±0.08 dB/m and 1.43±0.39 dB/m at 532 nm, 900 nm and 1550 nm respectively. Further work is required to determine the cause of the increased loss at longer wavelengths. For another fiber loss measurement taken 26 days after fiber draw, shown by the blue spectrum in Fig. 2(a), the results were observed to be the same within a 95% confidence interval. As a comparison, the fiber loss measurement results for a suspended-core fiber produced in the same way, with material from the same bulk stock, and with similar core, web and hole sizes as for the exposed-core fiber, is shown by the black spectrum in Fig. 2(a). This suspended-core fiber result, being
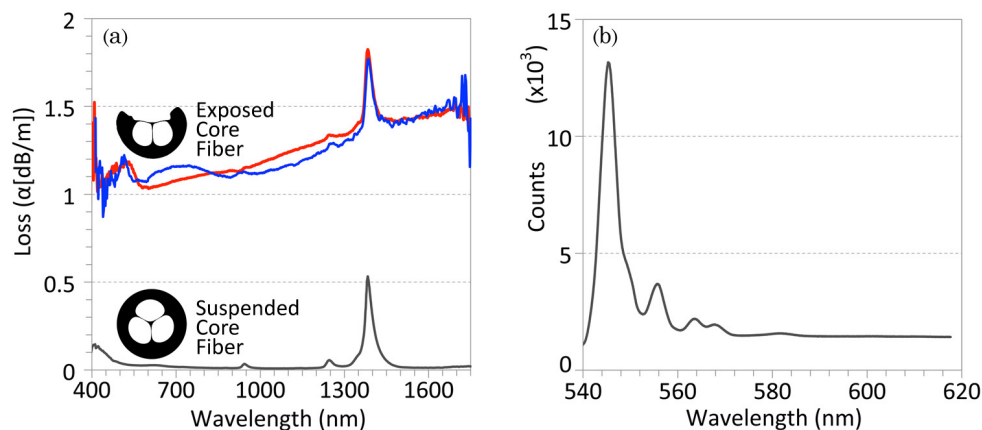
Fig. 2. (a) Loss of silica exposed-core fiber, broadband cutback measurements taken 26 days apart (red and blue) compared to silica suspended-core fiber with similar core size (black); and, (b) fiber Raman peaks at 532 nm.

~2 orders of magnitude lower compared to the exposed-core fiber, shows that confinement loss is negligible in the total loss of the exposed-core fiber, and therefore additional surface scattering loss, either from the process of cutting the slot or airborne particulates depositing on the surface of the core [42] before or after fiber drawing, is the most likely cause of the additional loss. For exposed-core fibers previously produced in Schott F2 lead silicate soft glass [30] ($n \sim 1.62$) with a core size of $\sim \varnothing 3\,\mu$m, the fiber loss measurements taken directly after fiber draw were 5.54 ± 0.20 dB/m, 2.25 ± 0.26 dB/m and 2.50 ± 0.34 dB/m at 532 nm, 900 nm and 1550 nm respectively. Further work is required to determine the effect that core size has on the fiber loss of the silica exposed-core fiber.

Another factor which can restrict the detection limit of a fiber optic sensor is the amount of Raman and fluorescence peaks generated within the glass [19] which depends on the wavelength and power of the light source. Given enough power and with a sensitive enough detector, the Raman spectrum corresponding to the energy of the probed vibrational modes of the silica is expected, whereas fluorescence is an indication of impurities and/or structural defects within the silica material. In order to detect the Raman and any potential fluorescence peaks, a 25 mW laser excitation light source at commonly used 532 nm was coupled into a 1 m long exposed-core fiber using a $60\times$ objective via a dichroic mirror. The signal collected from the fiber was imaged using the same objective, passed through the dichroic mirror and filtered using a 532 nm long pass filter, and measured using a Horiba iHR550 Imaging Spectrometer with Synapse CCD Detector. The peaks observed at 545 nm, 550 nm, 555 nm, 562 nm, 566 nm and 580 nm, shown in Fig. 2(b), correspond to well known Raman peaks of silica at 490 cm^{-1}, 605 cm^{-1}, 800 cm^{-1}, 1050 cm^{-1}, 1190 cm^{-1} and 1600 cm^{-1} respectively, previously used for sensing applications [43]. The absence of any fluorescence peaks shows that the silica material has negligible fluorescence at 532 nm for the excitation power and detector sensitivity used. For fluorescence or Raman spectroscopy sensing applications these peaks generated within the glass might affect the detection limit, depending on the excitation and emission wavelengths of interest.

3.2. Environmental stability

3.2.1. Introduction to environmental stability

Numerous sensing applications in health, the environment, agriculture and national security involve the detection of analyte typically suspended in a bulk liquid or gas; such as water or air. When preparing the fiber for these applications, solvents such as acetone, isopropanol, methanol and water are sometimes also used [44] to clean the core of dust or other particulates deposited on the surface. The silica exposed-core fiber serves as a unique platform for measuring any deterioration in the transmission properties when exposed to these typical sensing and processing environments, providing access to the core for post exposure surface analysis.

In previous studies, for the exposed-core fibers produced in F2 soft glass [30,35] with a $\sim \varnothing 3\,\mu\text{m}$ core, it was found that the fiber loss increased by $0.4\pm0.048\,\text{dBm}^{-1}\text{day}^{-1}$, even when stored in a dry nitrogen filled environment. It is thought that this deterioration in the transmission properties of the fiber occurs due to changes in the properties at the core surface, such as particulate deposits [42], micro-fracturing [44] and/or increased roughness [45] induced by exposure to the environment. Since the deterioration found in the F2 soft glass exposed-core fibers was rapid, it could easily be measured by comparing standard cutback loss measurements over time. However, as shown in the previous section no loss was observed after 26 days for the silica exposed-core fiber.

3.2.2. Exposure to air, water & methanol

To measure the exposure induced deterioration in the transmission properties of the silica exposed-core fiber, a length of fiber was setup as previously described for cutback loss measurements. Instead of performing cutbacks, the transmitted power spectrum, in dBm, was recorded from 350–1750 nm every two minutes. With the fiber in air, this setup was left long enough so that the measured power stabilized to within $\pm0.05\,\text{dBm}$, then used to take time based measures of the power. Then any changes over time in the transmission characteristics can be fitted to the equation,

$$P_{\lambda,t} = P_{\lambda,0}10^{-\xi t/10} \tag{1}$$

where ξ is the loss in dB/day. An assumption for these measurements is that the deterioration measured comes from changes along the exposed fiber length, not just the cleaved ends of the fiber, as the area exposed along the length is much greater than the area at the ends. As a sanity check, a laboratory-grade patch cord optical fiber assembly was setup in the same way, to ensure that the measured losses were not coming from the light source or other parts of the setup; where no deterioration was detected.

The result of ξ_λ (Eq.(1)) for a 4.2m length of the exposed-core fiber exposed to air for 180hrs is shown in Fig. 3(a), where the 95% confidence interval is also shown in black. This result shows that there is a sharp loss peak at 515 nm, equivalent to $0.043\,\text{dBm}^{-1}\text{day}^{-1}$, and a broad loss from $\sim$450 nm to $\sim$900 nm with a peak of $0.023\,\text{dBm}^{-1}\text{day}^{-1}$. At wavelengths $\sim$900 nm to $\sim$1340 nm the loss is at $\sim0.0043\,\text{dBm}^{-1}\text{day}^{-1}$, and drops below the detection limit of the experiment for wavelengths $> \sim$1340 nm. The air exposure induced deterioration in the transmission properties of the silica exposed-core fiber is lower than the confidence intervals for cutback measurements, as shown in Fig. 2(a), and $\sim$2 orders of magnitude better than for the previously reported exposed-core fibers produced in F2 soft glass.

This measurement was repeated for a 1m length of the silica exposed-core fiber with a 8cm centrally located section of the fiber submersed in Milli-Q water, shown in Fig. 3(b), where we observe that the transmission properties of the fiber is reduced by $\sim0.067\,\text{dBm}^{-1}\text{day}^{-1}$ for wavelengths shorter than 1450 nm. When this was repeated with methanol, it was observed that the transmission properties of the silica exposed-core fiber was significantly affected across all
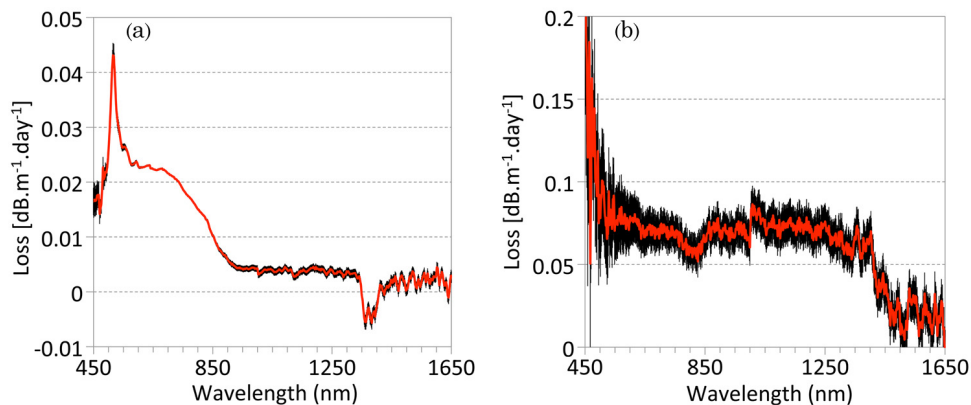
Fig. 3. Deterioration in the transmission properties of the silica exposed-core fiber when exposed to (a) air; and, (b) water.

the measured wavelengths (350–1750 nm), at a rate of 12.8–16.8 $dBm^{-1}hr^{-1}$.

This deterioration in the transmission properties is expected to come from changes in the mechanical and/or compositional characteristics at the core surface, causing light scattering effects. When the core diameter is reduced, these light scattering effects are expected to increase, as a greater portion of guided light travels outside the core. Further work is required to quantitatively determine the effect that core size has on the deterioration in the transmission properties of the silica exposed-core fiber.

3.2.3. Surface mechanical and compositional characteristics

In order to determine the differences between the mechanical and compositional characteristics of the exposed sample surfaces, nanometer-scale topographical and phase mapping of the exposed-core fiber core surfaces was performed using a NT-MDT Ntegra Solaris AFM with Smena head for Tapping Mode Atomic Force Microscopy (AFM).

Figures 4(a)–4(c), 4(d)–4(f) and 4(g)–4(i) show the AFM phase and topology results of a $25\,\mu m^2$ section across the core for the exposed-core fiber exposed to air for 19 days, Milli-Q water for 72 hrs and methanol for 2 hrs respectively. For the core area exposed to air, the nanometer scale spikes in the topology and phase shift suggest small hardened impurities within the surface structure, while the bulk of the material is homogeneous in composition with nanometer scale roughness. For the core exposed to water, large peaks measuring > 100 nm in height and several microns across the surface suggest that impurities from the water have been deposited onto the core. The darkest areas in the phase image show up on the topology to be slightly lower than the surrounding bulk, which may also be an indication of surface damage such as micro-fracturing [44]. The results for the core exposed to methanol shows micron scale areas with large phase shifts where the topology image indicates a increase in height. The methanol exposed-core area was further investigated using a ContourGT-K1 coherence scanning interferometer (CSI), shown in Fig. 4(j), which indicates micrometer scale pitted sections along the core instead of the increase in height observed by the AFM. It is known that topology height reversal can occur for AFM images when the tip is strongly affected by the capillary forces and also by the tip-sample van der Waals attraction [46]. In this interaction regime, the phase shift shows to be more negative on more hydrophilic regions, and suggests pitting or micro-fracturing of the methanol exposed sample, which is confirmed by the CSI results. Nevertheless, further experimental evidence would be needed to confirm these hypothesis.
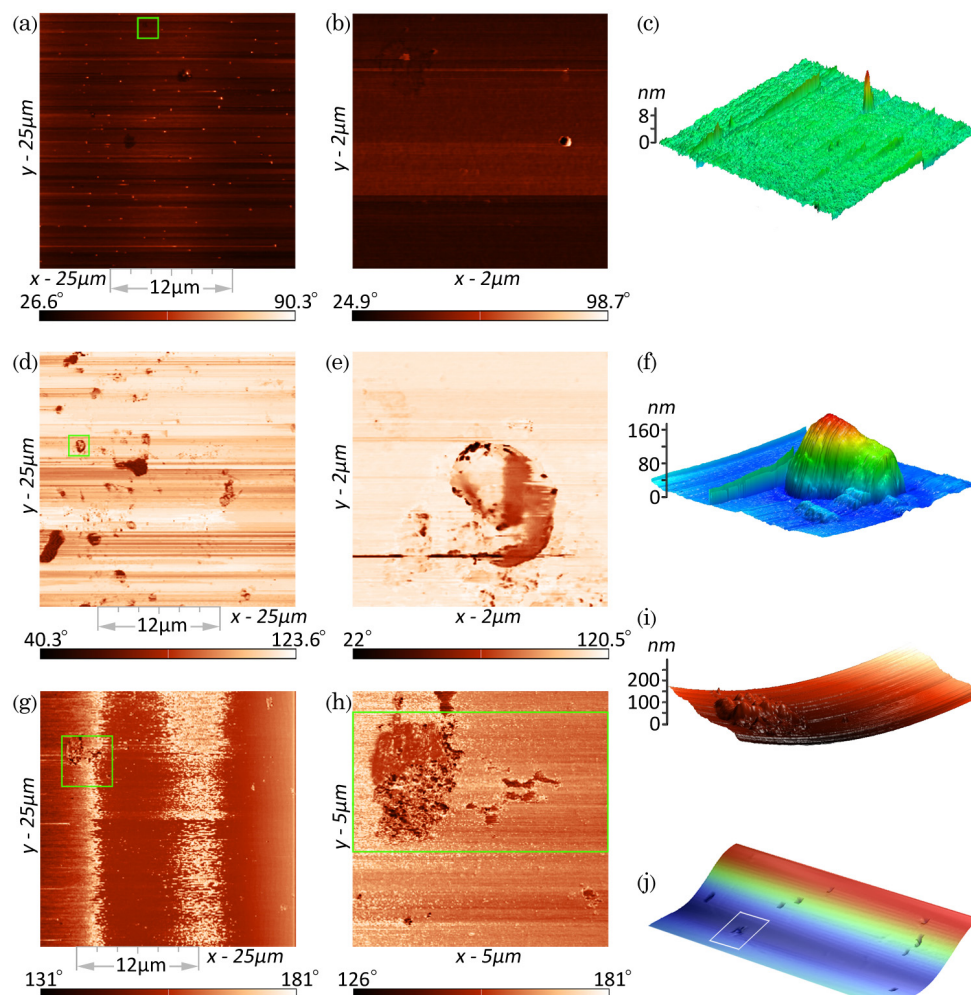
Fig. 4. Tapping Mode Atomic Force Microscopy images of the exposed-core fibers exposed to (a)–(c) air, (d)–(f) water and (g)–(i) methanol with (j) a coherence scanning interferometer image along the methanol exposed core region. (a), (d) and (g) show the phase images across the core region indicated by the $12\,\mu$m area on the x-axis, with [(b), (e) and (h) respectively] enlarged phase images of the area shown by the green box; and, (c), (f) and (i) showing their respective topologies.

4. Conclusion

A silica exposed-core fiber has been fabricated, for the first time to the best of our knowledge. We have demonstrated preform drilling as an alternative for fabricating glass exposed-core fibers, and shown the unique ability to perform surface analysis of the core with the silica exposed-core fiber geometry produced. We explored and characterized the new silica exposed-core fiber, showing it to have relatively low loss with deterioration in the transmission properties being ∼2 orders of magnitude better than for the previously reported exposed-core fibers produced in soft glass. Although the silica material shows good stability in air and water, the buildup of contaminates on the surface and micro-fracturing deteriorates the transmission prop-

erties, while significant degradation occurs with the use of methanol.

With high transmission properties in the UV-Vis-NIR spectral range, the silica material is suitable for (bio)chemical sensing applications. The exposed-core geometry serves as a versatile platform for real time evanescent field absorption or fluorescence spectroscopy, with capacity for fast filling and quick response to kinetic changes of the analyte. This opens up new opportunities for optical fiber sensors requiring long term and/or harsh environmental applications while providing long length light interaction with the analyte of interest.

In the future, further practical issues need to be solved, particularly in how to package the fiber such that it is sensitive to the chosen analyte but protected from the applied sensing environment.

Acknowledgments

┌─ **APPENDIX E** ───┐

Paper 5.

└──┘

Novel polymer functionalization method for exposed-core optical fiber

Roman Kostecki,[1*] **Heike Ebendorff-Heidepriem,**[1] **Shahraam Afshar V.,**[1] **Grant McAdam,**[2] **Claire Davis,**[2] **and Tanya M. Monro**[1]

[1]*ARC Centre of Excellence for Nanoscale BioPhotonics, and Institute for Photonics and Advanced Sensing, and the School of Chemistry and Physics, The University of Adelaide, Adelaide, South Australia, 5005, Australia*
[2]*Defence Science and Technology Organisation, Fishermans Bend, Victoria, Australia*
[*]*roman.kostecki@adelaide.edu.au*

Abstract: We report on a one step functionalization process for optical fiber sensing applications in which a thin film (∼50 nm) polymer doped with sensor molecules is applied to a silica exposed-core fiber. The method removes the need for surface attachment of functional groups, while integrating the polymer, silica and sensor molecule elements to create a distributed sensor capable of detecting an analyte of interest anywhere along the fiber's length. We also show that the thin film coating serves a protective function, reducing deterioration in the transmission properties of the silica exposed-core fiber, but increasing loss.

© 2014 Optical Society of America

References and links

1. R. Kostecki, H. Ebendorff-Heidepriem, C. Davis, G. McAdam, S. C. Warren-Smith, and T. M. Monro, "Silica exposed-core microstructured optical fibers," Opt. Mater. Express **2**, 1538 – 1547 (2012).
2. T. M. Monro, D. J. Richardson, and P. J. Bennett, "Developing holey fibres for evanescent field devices," Electron. Lett. **35**, 1188 – 1189 (1999).
3. S. Afshar V., S. C. Warren-Smith, and T. M. Monro, "Enhancement of fluorescence-based sensing using microstructured optical fibres," Opt. Express **15**, 17891 – 17901 (2007).
4. O. S. Wolfbeis, "Fiber-optic chemical sensors and biosensors," Anal. Chem. **80**, 4269 – 4283 (2008).
5. T. M. Monro, S. Warren-Smith, E. P. Schartner, A. François, S. Heng, H. Ebendorff-Heidepriem, and S. Afshar V., "Sensing with suspended-core optical fibers," Opt. Fiber Technol. **16**, 343 – 356 (2010).
6. C. Lodeiro, J. L. Capelo, J. C. Mejuto, E. Oliveira, H. M. Santos, B. Pedras, and C. Nunez, "Light and colour as analytical detection tools: A journey into the periodic table using polyamines to bio-inspired systems as chemosensors," Chem. Soc. Rev. **39**, 2948 – 2976 (2010).
7. S. Heng, M.-C. Nguyen, R. Kostecki, T. M. Monro, and A. D. Abell, "Nanoliter-scale, regenerable ion sensor: sensing with a surface functionalized microstructured optical fibre," RSC Adv. **3**, 8308 – 8317 (2013).
8. H. T. C. Foo, H. Ebendorff-Heidepriem, C. J. Sumby, and T. M. Monro, "Towards microstructured optical fibre sensors: surface analysis of silanised lead silicate glass," J. Mater. Chem. C **1**, 6782 – 6789 (2013).
9. B. Sciacca, A. François, M. Klingler-Hoffmann, J. Brazzatti, M. Penno, P. Hoffmann, and T. M. Monro, "Radiative-surface plasmon resonance for the detection of apolipoprotein E in medical diagnostics applications," Nanomed. - NBM **9**, 550 – 557 (2013).
10. A. François, H. Ebendorff-Heidepriem, C. J. Sumby, and T. M. Monro, "Comparison of surface functionalization processes for optical fibre biosensing applications," in "20th International Conference on Optical Fibre Sensors," vol. 7503 of *Proc. SPIE* (2009).

11. S. C. Warren-Smith, S. Heng, H. Ebendorff-Heidepriem, A. D. Abell, and T. M. Monro, "Fluorescence-based aluminum ion sensing using a surface-functionalized microstructured optical fiber," Langmuir **27**, 5680 – 5685 (2011).

12. M. Zhu, M. Z. Lerum, and W. Chen, "How to prepare reproducible, homogeneous, and hydrolytically stable aminosilane-derived layers on silica," Langmuir **28**, 416 – 423 (2012).

13. K. Richardson, D. Krol, and K. Hirao, "Glasses for photonic applications," Int. J. Appl. Glass Sci. **1**, 74 – 86 (2010).

14. K. Peters, "Polymer optical fiber sensors - a review," Smart Mater. Struct. **20**, 013002 (2011).

15. S. H. Law, M. A. van Eijkelenborg, G. W. Barton, C. Yan, R. Lwin, and J. Gan, "Cleaved end-face quality of microstructured polymer optical fibres," Opt. Commun. **265**, 513 – 520 (2006).

16. S. Atakaramians, K. Cook, H. Ebendorff-Heidepriem, S. Afshar V., J. Canning, D. Abbott, and T. M. Monro, "Cleaving of extremely porous polymer fibers," IEEE Photon. J. **1**, 286 – 292 (2009).

17. A. Stefani, K. Nielsen, H. K. Rasmussen, and O. Bang, "Cleaving of TOPAS and PMMA microstructured polymer optical fibers: Core-shift and statistical quality optimization," Opt. Commun. **285**, 1825 – 1833 (2012).

18. M. Li and D. A. Nolan, "Optical transmission fiber design evolution," J. Lightwave Technol. **26**, 1079 – 1092 (2008).

19. E. P. Schartner, H. Ebendorff-Heidepriem, S. C. Warren-Smith, R. T. White, and T. M. Monro, "Driving down the detection limit in microstructured fiber-based chemical dip sensors," Sensors **11**, 2961 – 2971 (2011).

20. S. C. Warren-Smith and T. M. Monro, "Exposed core microstructured optical fiber bragg gratings: refractive index sensing," Opt. Express **22**, 1480 – 1489 (2014).

21. K. J. Rowland, A. François, P. Hoffmann, and T. M. Monro, "Fluorescent polymer coated capillaries as optofluidic refractometric sensors," Opt. Express **21**, 11492 – 11505 (2013).

22. V. V. N. R. Kishore, A. Aziz, K. L. Narasimhan, N. Periasamy, P. S. Meenakshi, and S. Wategaonkar, "On the assignment of the absorption bands in the optical spectrum of Alq3," Synthetic Met. **126**, 199 – 205 (2002).

23. G. McAdam, P. J. Newman, I. McKenzie, C. Davis, and B. R. W. Hinton, "Fiber optic sensors for detection of corrosion within aircraft," Struct. Health Monit. **4**, 47 – 56 (2005).

24. J. Ščančar and R. Milačič, "Aluminium speciation in environmental samples: a review," Anal. Bioanal. Chem. **386**, 999 – 1012 (2006).

25. R. Kostecki, H. Ebendorff-Heidepriem, S. C. Warren-Smith, and T. M. Monro, "Predicting the drawing conditions for microstructured optical fiber fabrication," Opt. Mater. Express **4**, 29 – 40 (2014).

26. H. Ebendorff-Heidepriem, S. C. Warren-Smith, and T. M. Monro, "Suspended nanowires: fabrication, design and characterization of fibers with nanoscale cores," Opt. Express **17**, 2646 – 2657 (2009).

27. G. Brambilla, F. Xu, and X. Feng, "Fabrication of optical fibre nanowires and their optical and mechanical characterisation," Electron. Lett. **42**, 517 – 519 (2006).

28. G. Zhai and L. Tong, "Roughness-induced radiation losses in optical micro or nanofibers," Opt. Express **15**, 13805 – 13816 (2007).

29. M. Fujiwara, K. Toubaru, and S. Takeuchi, "Optical transmittance degradation in tapered fibers," Opt. Express **19**, 8596 – 8601 (2011).

30. S. C. Warren-Smith, E. Sinchenko, P. R. Stoddart, and T. M. Monro, "Distributed fluorescence sensing using exposed core microstructured optical fiber," IEEE Photon. Technol. Lett. **22**, 1385 – 1387 (2010).

31. G. S. He, H. Qin, and Q. Zheng, "Rayleigh, Mie, and Tyndall scatterings of polystyrene microspheres in water: Wavelength, size, and angle dependences," J. Appl. Phys. **105**, 023110 (2009).

32. P. J. Roberts, F. Couny, H. Sabert, B. J. Mangan, D. P. Williams, L. Farr, M. W. Mason, A. Tomlinson, T. A. Birks, J. C. Knight, and P. S. Russell, "Ultimate low loss of hollow-core photonic crystal fibres," Opt. Express **13**, 236 – 244 (2005).

33. K. Tajima, J. Zhou, K. Nakajima, and K. Sato, "Ultralow loss and long length photonic crystal fiber," J. Lightwave Technol. **22**, 7 – 10 (2004).

34. T. Kaino, M. Fujiki, S. Oikawa, and S. Nara, "Low-loss plastic optical fibers," Appl. Opt. **20**, 2886 – 2888 (1981).

35. T. Seydel, A. Madsen, M. Tolan, G. Grübel, and W. Press, "Capillary waves in slow motion," Phys. Rev. B **63**, 073409 (2001).

36. J. Jäckle and K. Kawasaki, "Intrinsic roughness of glass surfaces," J. Phys. - Condens. Mat. **7**, 4351 – 4358 (1995).

37. S. C. Xue, M. C. J. Large, G. W. Barton, R. I. Tanner, L. Poladian, and R. Lwin, "Role of material properties and drawing conditions in the fabrication of microstructured optical fibers," J. Lightwave Technol. **24**, 853 – 860 (2006).

38. J. Liu, H. Li, and J.-M. Lin, "Measurements of surface tension of organic solvents using a simple microfabricated chip," Anal. Chem. **79**, 371 – 377 (2007).

39. K. Boyd, H. Ebendorff-Heidepriem, T. M. Monro, and J. Munch, "Surface tension and viscosity measurement of optical glasses using a scanning CO_2 laser," Opt. Mater. Express **2**, 1101 – 1110 (2012).

1. Introduction

Exposed-core microstructured optical fibers (MOFs) made from silica open up new opportunities for creating sensors capable of withstanding long term use in harsh environments and for providing real time analysis anywhere along the fiber length [1]. The portion of guided light extending from the glass core, often described as 'evanescent field', is affected by the refractive index and absorption characteristics of the medium surrounding it [2,3]. This light-matter overlap provides opportunities for exploiting the interaction of light with gases and liquids, where absorption and/or fluorescence can be used to determine the composition and concentration of the analyte [4,5].

Although sensor molecules provide a method for fluorescence based analyte detection [6], existing staining and/or specimen sampling based methodology is not well suited for real-time, in situ, and/or remote sensing applications. For such applications it is necessary to immobilize sensor molecules on the glass surface of the MOF exposed core, which can then be used directly within the medium as a sensor without requiring prior pre-mixing of analyte with sensor molecules. Functionalization methods traditionally used include silanes [7,8] or polyelectrolytes [9,10], which provide a functional group on the surface to which the sensor molecules can be covalently attached. These processes require several steps that typically take many hours to perform, due to the incubation times needed to achieve consistent maximized binding efficiency [8,10]. Some important factors to consider when choosing a functionalization method are the conditions in which the sensor is to be used (for example polyelectrolytes have been found to wash off in acidic conditions [11]), and any additional optical losses that might occur as a result. Also, achieving uniform covalent binding of the sensor molecules along the constrained surface of MOFs in a consistent manner is challenging using silanes or polyelectrolytes [5,8], since results are highly dependent on experimental conditions (temperature, concentration, solvents, hydration and reaction time) as well as pre- and post-treatment processes [5, 10–12]. These factors can diminish sensor performance, reducing the achievable light-matter interactions, which in turn decreases sensitivity.

Both polymer and silica have properties that make them attractive for optical fiber sensing applications [13,14]. Poly(methyl methacrylate) (PMMA) polymer optical fibers (POFs) have high elastic strain limits, high fracture toughness, and high flexibility in bending, however high attenuation properties and difficulties with splicing, cleaving and coupling makes small core size POF sensors challenging [14–17]. On the other hand, silica is known to be reliable under a range of processing and use environments, with relatively better mechanical and thermal stability [13]. Highly homogeneous, high purity bulk material is commercially available, which has led to the development of low loss silica telecom fibers [18]. Silica has a relatively low refractive index, which can improve the sensitivity of evanescent field sensors, since reducing the index contrast (Δn) at the core-cladding boundary increases the power fraction to the analyte or functionalized surface [19]. Also, silica exposed-core MOF fibers can be spliced to single mode fiber for improved handling and integration with commercial interrogation units [20].

In this paper we demonstrate a one step functionalization process for optical fiber sensing applications, by applying thin film ($\sim$50 nm) PMMA doped with sensor molecules to a silica exposed-core MOF. This integrates the polymer, silica and sensor molecule elements to create a distributed sensor capable of detecting an analyte of interest anywhere along the fiber's length, while removing the need for surface attachment of functional groups. We show that the thin film coating also serves a protective function, which has the potential to solve some of the practical issues involved in functionalizing exposed-core MOFs where sensitivity to the chosen analyte as well as environmental protection is required. We also characterize the attenuation properties of the thin film functionalized fiber, and analyze the overall loss of the polymer layer. By normalizing the fiber loss before and after adding the polymer layer to the field distribution, we are

able to determine the source of added attenuation to be primarily due to surface roughness.

2.   One step functionalization process

The method used to coat silica exposed-core MOFs with PMMA is an extension of the method used for micron scale polymer coating in glass capillaries [21]. A clear cast acrylic rod (PMMA) with a density of 1.18 g/cm^3, also known as a 'plexiglass rod' (Professional Plastics Pte. Ltd. [Singapore]), was dissolved in dichloromethane (DCM) at a concentration of 12.3 g/L. 8-hydroxyquinoline (8-HQ), which is known to complex with aluminum ions (Al cations) and then fluoresce strongly with UV excitation [22], was dissolved in DCM and added to the dissolved PMMA solution making a concentration of $30_{(8-HQ)} : 100_{(PMMA)}$ by weight. The detection of Al cations is of particular interest as it provides a marker of aluminum corrosion [23] and is also an environmental hazard [24]. One end of the fabricated [25] silica exposed-core MOF (Fig. 1(a)), with an effective core diameter of 7.5 μm (defined as the diameter of a circle whose area is equal to a triangle that fits wholly within the core area [26]), was fed through a silicon septa fitted to the bottom of an open-end vial. This setup, shown by the schematic in Fig. 1(b), was then used to coat the outside of the MOF including the exposed core region. The PMMA+8-HQ DCM solution was placed into the vial (∼5 mm depth), and the fiber was pulled through the solution and silicon septa by hand (at ∼8 m/min) to leave behind a ∼50 nm coating of the doped PMMA on the core surface (Fig. 1(c)). Uniformity of the polymer layer is critically important for optical performance of the device. Measured results from scanning electron microscope (SEM) images of six samples, from the center and 10 cm in from the ends of two individually coated 1 m lengths of fiber, showed the coating thickness on the outside edge of the exposed-core to be in the range 43–46 nm with measurement uncertainty of ±9 nm. The coating procedure was performed in a laboratory chemical fume hood at room temperature (∼21°C), without additional curing.

3.   Characterization of thin film polymer layer

3.1.   Sensing measurements

To test the ability of the coated fiber to detect Al cations, an 18 mW laser excitation light source with a wavelength of 375 nm was coupled into the core of an 80 cm long PMMA+8-HQ functionalized fiber using an aspheric lens (f=2.75 mm, NA=0.55) via a dichroic mirror. The back
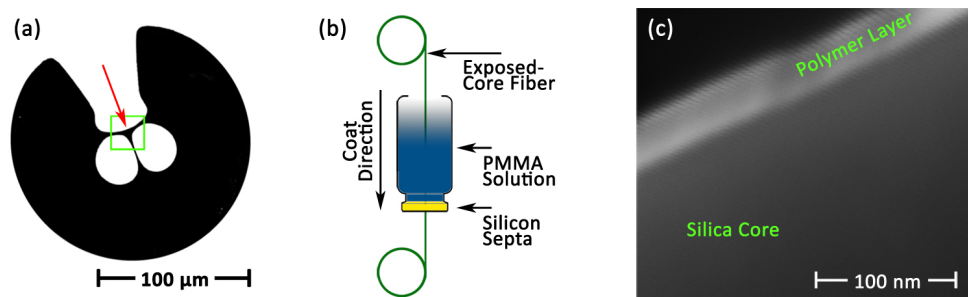
Fig. 1. (a) Contrast enhanced SEM image of (silica material shown in black) exposed-core MOF cross section, having an effective core diameter of 7.5 μm (core location shown by green box). (b) A schematic of the thin-film polymer coating method used to coat the outside of the MOF including the exposed core region. (c) Close-up SEM of the outside edge of the exposed core (red arrow in Fig. 1(a)) with 50 nm polymer coating (light grey).

reflected light collected from the coated fiber core was imaged using the same lens, passed through the dichroic mirror, 425 nm long pass filter and $\times 4$ objective, and characterized using a Horiba iHR550 Imaging Spectrometer with Synapse CCD Detector. The exposed-core region of the coupled fiber was then exposed to Al cations by immersing the outside of a 23 cm long central section of the fiber in a saturated solution of potassium aluminum sulfate (potassium alum, $KAl(SO_4)_2 \cdot 12H_2O$), and the back reflected spectra were measured immediately after immersion and again after 1 hour of immersion. The setup is shown by the schematic in Fig. 2(a). The measured result before immersion subtracted from the after immersion results is presented in Fig. 2(b), which shows the fluorescence peak of 8-HQ complexed with Al cations [22] increasing over time. This result demonstrates the ability of a thin polymer film functionalized fiber to detect Al cations, with the potential for corrosion detection, and confirms sufficient mobility of the 8-HQ within the polymer matrix to allow complexation with the Al cations.

3.2. Air exposure induced deterioration

The impact of deterioration on the transmission properties of the functionalized fiber, resulting from exposing the functionalized fiber to air, was measured using the same procedure detailed in [1] which is briefly outlined here. A 4 m long PMMA+8-HQ functionalized fiber was coupled to a 100 W halogen broadband source with an approximately Gaussian-distributed intensity profile and peak power at 800 nm. At the other end, the light from the core was imaged onto the detector of an Ando AQ6315E Optical Spectrum Analyzer (OSA) and the transmitted power spectrum, in dBm, was recorded from 350–1750 nm every two minutes. This procedure was performed in a laboratory at room temperature ($\sim 21°C$), with the fiber in air, where the setup was left long enough (~ 6 hours) so that the measured power stabilized to within ± 0.05 dBm, then used to take time based measures of the power for 180 hours. Any changes over time (t)
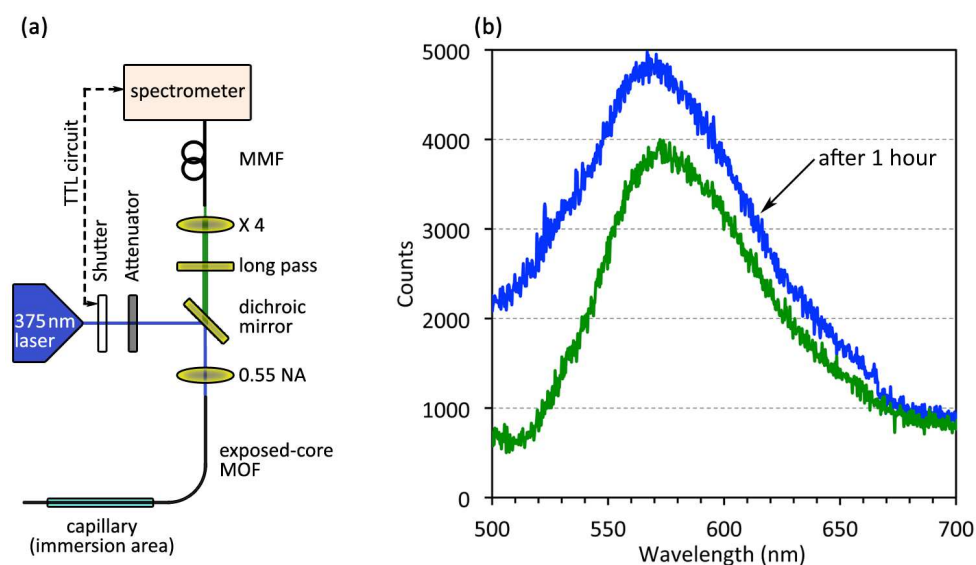
Fig. 2. (a) Setup used to test the ability of the coated fiber to detect Al cations (MMF is multimode fiber). (b) Back reflected spectra of the functionalized fiber directly after immersion in Al cations solution (green – ●) and after 1 hour of immersion in solution (blue – ●).

in the transmission characteristics were then fitted to the equation,

$$P(\lambda,t) = P(\lambda,0)10^{-\xi tz/10} \tag{1}$$

where ξ is the loss in dB m^{-1}day^{-1} and z is the fiber length in meters. For comparison the result in [1] for an uncoated exposed-core MOF, with 10 μm core diameter, is shown by the red line in Fig. 3. The result of $\xi(\lambda)$ (Eq. (1)) for the thin-film functionalized fiber, shown by the blue line in Fig. 3, shows a significant improvement compared to the uncoated fiber.

This deterioration in the transmission properties is expected to come from changes in the mechanical and/or compositional characteristics at the core surface, causing light scattering effects [27–29]. When the core diameter is reduced these light scattering effects are expected to increase, as a greater portion of guided light travels outside the core. However, this result shows less deterioration in transmission properties even though the core diameter of this functionalized fiber is smaller (7.5 μm) compared to the uncoated exposed-core MOF from [1] (10 μm). This shows that the thin film coating is providing a protective function for the core surface. For example, at $\lambda = 532$ nm the air induced deterioration in the transmission properties of the thin-film functionalized fiber (3×10^{-3} dB m^{-1}day^{-1}) is an order of magnitude better than for the previously reported uncoated result [1]. This is significant for optical fiber sensors requiring long term and/or harsh environmental applications while providing long length light interaction with the analyte of interest.

3.3. Functionalized fiber loss

To determine the impact of polymer coating on propagation loss, cutback fiber loss measurements were performed using a 100 W halogen broadband source with an approximately Gaussian-distributed intensity profile and peak power at 800 nm. The before and after polymer coating loss measurements are shown by the blue and red lines in Fig. 4 respectively, and
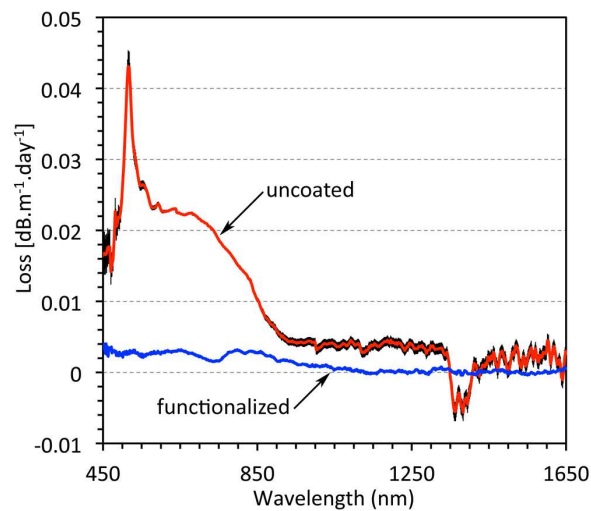
Fig. 3. Deterioration in the transmission properties of the air exposed uncoated (red – ●, from [1] with 10 μm core diameter) and thin-film polymer functionalized (blue – ●) silica exposed-core MOF. The 95% confidence interval is shown in black. For the thin-film polymer functionalized fiber result, the confidence interval is approximately the same as the line thickness.

summarized in Table 1 for 532 nm, 1064 nm, and 1550 nm wavelengths. These results show an increase of $\sim$10–20 times after applying the polymer layer. The difference between these coated and uncoated fiber loss measurements ($\alpha_{\text{after}} - \alpha_{\text{before}}$) is shown by the green line in Fig. 4.

Understanding the reasons the polymer layer adds to the overall loss, and finding ways to reduce these losses, can significantly improve the distributed sensor practical range [30]. The loss of a fiber is given by,

$$\alpha_{\text{fiber}}(\lambda) = \left(\frac{\varepsilon_0}{\mu_0}\right)^{\frac{1}{2}} \frac{\int_\infty n^{\text{r}} \alpha |\mathbf{E}|^2 \, dA}{\int_\infty \mathbf{E} \times \mathbf{H}^* \cdot \hat{\mathbf{z}} \, dA} \tag{2}$$

where $n^{\text{r}}(x,y)$ and $\alpha(x,y)$ are the refractive index and material loss distribution, $\mathbf{E}(x,y)$ and $\mathbf{H}(x,y)$ are the electric and magnetic field distributions, and $\mathbf{z}$ is along the optical axis of the fiber. This guided mode loss includes all loss mechanisms, such as absorption and scattering. The change in loss of the guided mode due to the addition of the polymer layer can be written
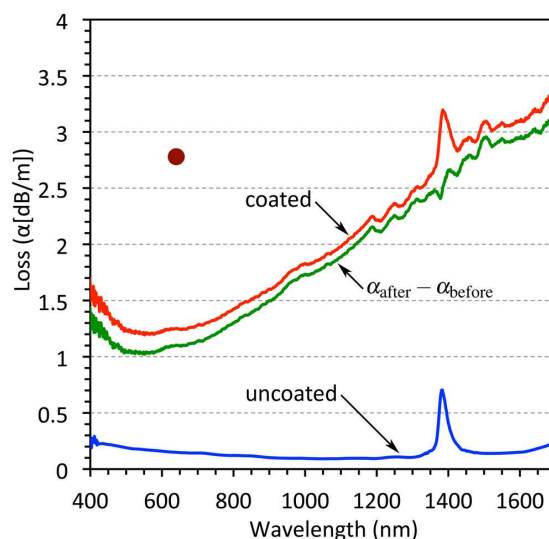
Fig. 4. Broadband cutback loss measurements of silica exposed-core MOF, before (blue – ●) and after polymer (PMMA+8HQ) coating (red – ●). The difference between the coated and uncoated fiber loss $\alpha_{\text{after}} - \alpha_{\text{before}}$ is shown in green (– ●). Cutback loss measurement at $\lambda = 640$ nm for un-doped PMMA coated exposed-core MOF (dark-red dot ●).

Table 1. Loss measurements for silica exposed-core MOF (Fig. 1(a))

Wavelength (nm)	Uncoated (dB/m)	Coated (dB/m)
532	0.178	1.04
1064	0.092	1.82
1550	0.141	2.94

as,

$$\alpha_{\text{after}} - \alpha_{\text{before}} = \left(\frac{\varepsilon_0}{\mu_0}\right)^{\frac{1}{2}} \frac{\int_{\text{layer}} n^{\text{r}} \alpha |\mathbf{E}|^2 \, dA}{\int_{\infty} \mathbf{E} \times \mathbf{H}^* \cdot \hat{\mathbf{z}} \, dA} \tag{3}$$

where we have assumed the mode distribution has not changed due to addition of the layer, since it is very thin (~ 50 nm). In Eq. (3), $\alpha(x, y)$ includes loss of polymer material, α_{m}, and any loss due to scattering or inhomogeneity added during fabrication, α_{f}, hence $\alpha(x, y) = \alpha_{\text{m}} + \alpha_{\text{f}}(x, y)$. As a result, Eq. (3) can be rewritten as,

$$\alpha_{\text{after}} - \alpha_{\text{before}} = \left(\frac{\varepsilon_0}{\mu_0}\right)^{\frac{1}{2}} \left(\frac{n^{\text{r}}_{\text{m}} \alpha_{\text{m}} \int_{\text{layer}} |\mathbf{E}|^2 \, dA}{\int_{\infty} \mathbf{E} \times \mathbf{H}^* \cdot \hat{\mathbf{z}} \, dA} + \frac{\int_{\text{layer}} n^{\text{r}}(x, y) \alpha_{\text{f}}(x, y) |\mathbf{E}|^2 \, dA}{\int_{\infty} \mathbf{E} \times \mathbf{H}^* \cdot \hat{\mathbf{z}} \, dA} \right) \tag{4}$$

or alternatively,

$$\left(\frac{\mu_0}{\varepsilon_0}\right)^{\frac{1}{2}} \frac{(\alpha_{\text{after}} - \alpha_{\text{before}}) \int_{\infty} \mathbf{E} \times \mathbf{H}^* \cdot \hat{\mathbf{z}} \, dA}{n^{\text{r}}_{\text{m}} \int_{\text{layer}} |\mathbf{E}|^2 \, dA}$$

$$= \alpha_{\text{m}} + \frac{\int_{\text{layer}} n^{\text{r}}(x, y) \alpha_{\text{f}}(x, y) |\mathbf{E}|^2 \, dA}{n^{\text{r}}_{\text{m}} \int_{\text{layer}} |\mathbf{E}|^2 \, dA}$$

$$= \alpha' \tag{5}$$

where α' is the overall layer loss. Equation (5) can be used to determine the loss induced from applying the polymer layer, as a function of the guided mode field distribution fraction, by measuring $\alpha_{\text{after}} - \alpha_{\text{before}}$ and calculating electric and magnetic fields of the fiber propagation mode. To calculate the electric and magnetic fields, numerical simulation was performed on the fiber core profile taken from an SEM image, with a 50 nm polymer layer added to the
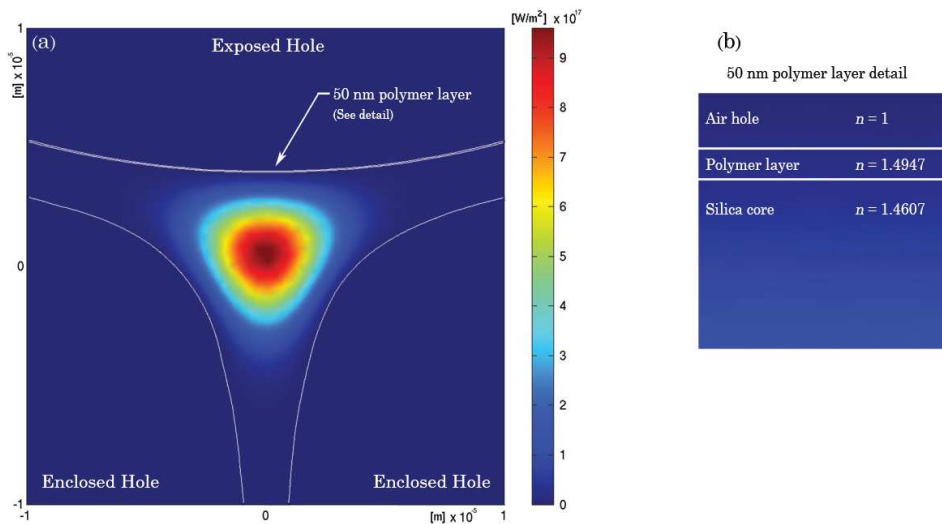
Fig. 5. (a) Numerical simulation result for the z-component power flow ($\mathbf{S}_z$) distribution at $\lambda = 532$ nm of the fundamental mode using full vector FEM. The fiber core profile (shown by white outline) taken from SEM image. (b) Detail of the of the refractive index profile used for the simulation.

exposed hole side of the core, using full vector finite element method (FEM) in the commercial package COMSOL 3.4. For example, Fig. 5(a) shows the FEM result for the z-component power flow ($\mathbf{S}_z = \mathbf{E} \times \mathbf{H}^* \cdot \hat{\mathbf{z}}$) distribution at $\lambda = 532$ nm of the fundamental mode, with refractive indices of the air holes, silica core, and polymer layer being $n_{\text{holes}} = 1$, $n_{\text{silica}} = 1.4607$, and $n_{\text{layer}} = 1.4947$ respectively (Fig. 5(b)). The cutback measurements (see Fig. 4) were used together with the fundamental mode FEM calculations with silica and PMMA material wavelength dependent refractive indices (n_{m}^{r}) to determine α' for 405 nm, 532 nm, 640 nm, 790 nm, 980 nm, 1064 nm, and 1550 nm wavelengths. The green dots in Fig. 6 plot the results for these seven wavelengths which show a trend of reducing attenuation with increased wavelength. To investigate this λ dependence, α' was fitted to the function,

$$\alpha' = \sum_{i=0}^{4} \frac{a_i}{\lambda^i} \tag{6}$$

which revealed the experimental values of α' could be fitted with either of the following two functions,

$$\alpha_1' = \left(\frac{2049.04}{\lambda} + \frac{413.27}{\lambda^4} + 6988.35 \right) \qquad \left[R^2 = 0.997 \right] \tag{7}$$

$$\text{and} \qquad \alpha_2' = \left(\frac{1272.97}{\lambda^3} + 8001.75 \right) \qquad \left[R^2 = 0.994 \right] \tag{8}$$

with λ in μm, and α' in dB/m units, shown by the red and blue lines respectively in Fig. 6. The fit of these functions could not be improved by allowing $a_2 \neq 0$.

Equation (7) shows wavelength dependencies of the form known to originate from intrinsic material light scattering. In general terms, material density changes cause intrinsic light scattering which is termed as Tyndall, Mie, and Rayleigh scattering originating from constituents
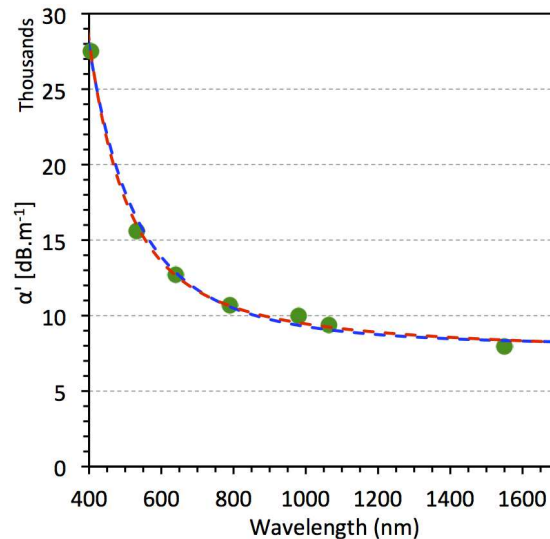
Fig. 6. (green ●) Plot of loss induced from applying the polymer layer, α' in Eq. (5), using cutback measurements ($\alpha_{\text{after}} - \alpha_{\text{before}}$, Fig. 4) for 405 nm, 532 nm, 640 nm, 790 nm, 980 nm, 1064 nm, and 1550 nm wavelengths. Plot of fitted λ dependent functions Eq. (7) (red - - ■) and Eq. (8) (blue - - ■).

of sizes $r > 40\lambda$, $\lambda/20 < r < 40\lambda$, and $r < \lambda/20$ respectively [31]. On the other hand, Eq. (8) has λ^{-3} dependence which is described by Roberts *et al.* [32] as applying to surface roughness at all length scales. For suspended and free-standing nanowires, increased field strength at the surface leading to larger roughness scattering type loss [28, 33] has also been shown to have core size dependence of $\alpha \propto d^{-3}$ [26].

The fact that both functions α'_1 and α'_2 fit the experimental data indicates that any function α' given by $\alpha' = \rho\alpha'_1 + (1-\rho)\alpha'_2$ where $\rho \in [0,1]$ fits the data as well. In order to determine ρ, we compare the coefficient of Rayleigh scattering that has been measured for bulk PMMA [34] with the coefficient of λ^{-4} in Eq. (7), which appears to be 5×10^6 times bigger than actual value as reported in [34]. To investigate the possibility that the added 8-HQ is contributing to additional Rayleigh scattering, another length of the exposed-core MOF was coated with a thin film (~ 50 nm) of un-doped PMMA using the same method as described above. The loss of this PMMA coated exposed-core MOF was measured at $\lambda = 640$ nm using the cutback method, which was found to be 2.78 dB/m compared to 1.25 dB/m measured for the PMMA+8-HQ, shown by the dark-red dot and red line in Fig. 4 respectively. This reveals that 8-HQ is not the cause of the additional loss from the thin film layer, instead helping to reduce the overall attenuation. Also, the λ^{-1} Mie type scattering in Eq. (7) cannot be due to intrinsic properties of the thin film, since this would suggest constituents with sizes orders of magnitude larger then the layer thickness. This implies that $\rho \approx 0$, since Eq. (7) cannot be describing intrinsic material properties of the thin film layer as being the predominant cause for the additional loss, and so does not contribute to the loss function α' in terms of intrinsic material light scattering.

To investigate surface roughness scattering type loss described by Eq. (8), a ContourGT-K1 coherence scanning interferometer was used to measure the roughness of the exposed-core MOF core surface before and after polymer coating. Before coating the roughness along a 20 μm length of the core was found to be $S_z = 0.394$ nm, whereas after coating $S_z = 0.873$ nm. The additional measured roughness at the core surface, together with Eq. (8) having an $\alpha \propto \lambda^{-3}$ dependence [32], indicates that the source of the added attenuation from the polymer layer is primarily due to surface roughness. Such roughness has been shown to arise from excited surface capillary waves (SCWs) [32], where small ripples on the surface are frozen in at the time of fiber fabrication. The amplitude of SCWs is dictated by equilibrium thermodynamics with surface tension (γ) providing a restoring force. During material phase transition these SCWs freeze [35], leaving a surface roughness proportional to inverse surface tension ($S_z \propto \gamma^{-1}$) [32, 36]. Both the PMMA ($\gamma = 0.032$ Nm^{-1} [37]) and DCM ($\gamma = 0.026$ Nm^{-1} [38]) used for the thin film coating have surface tensions an order of magnitude lower than for the silica ($\gamma = 0.31$ Nm^{-1} [39]) used to fabricate the exposed-core MOF. This relatively low surface tension for the polymer coating gives rise to higher amplitude SCWs, leading to additional surface roughness and therefore additional loss. Hence, improvements may be possible by finding ways to increase the surface tension of polymer mixtures used for the thin film coating.

4. Conclusion

By applying a thin polymer film ($\sim$50 nm) doped with sensor molecules to a silica exposed-core MOF, a one step functionalizing process for optical fiber sensing applications has been demonstrated, which eliminates the need for functional groups on the core surface for sensor molecule attachment and offers the prospect of being applied during the fiber drawing process. This method integrates the polymer, silica, and sensor molecule properties to create a distributed sensor capable of detecting an analyte of interest anywhere along the fiber length. The technique was successfully applied to the detection of Al cations in solution by doping the PMMA film with 8-HQ sensing molecules showing sufficient mobility in the PMMA matrix to allow interaction of the sensing molecules with the analyte of interest. This sensing reaction has

the potential to be applied to corrosion and environmental hazard detection where the benefits of a distributed sensor are significant.

The air induced deterioration in transmission properties of the coated exposed-core MOF was shown to be an order of magnitude reduced compared to the previously reported un-coated result. The protective function of this coating is a practical improvement for any use of these fibers, particularly for photonic applications were environmental protection is needed while maintaining access to the guided light. This improvement is attributed to the polymer matrix, however further work is needed to understand if the sensor molecules influence the protective function.

Cutback loss measurements showed an increase in the attenuation of $\sim$10–20 times after applying the polymer layer. Analyzing the overall loss of the polymer layer, by calculating the field distribution normalized attenuation of the layer, we were able to determine that the source of the added attenuation from the polymer layer is primarily due to surface roughness. Such roughness arises from excited SCWs, which become frozen in during material phase transition. Further work is needed to find ways of improving the functionalized surface, compare other surface coating methods, and exploit the method for more complex sensing molecules and applications.

Acknowledgments

APPENDIX F

Paper 6.

INTERNATIONAL JOURNAL OF

Applied Glass
SCIENCE

Taming the Light in Microstructured Optical Fibers for Sensing

Erik P. Schartner, Georgios Tsiminis, Alexandre François, Roman Kostecki, Stephen C. Warren-Smith, Linh Viet Nguyen, Sabrina Heng, Tess Reynolds, Elizaveta Klantsataya, Kris J. Rowland, Andrew D. Abell, and Heike Ebendorff-Heidepriem*,†

ARC Centre of Excellence for Nanoscale BioPhotonics, Institute for Photonics and Advanced Sensing and School of Physical Sciences, The University of Adelaide, Adelaide, SA 5005, Australia

Tanya M. Monro

ARC Centre of Excellence for Nanoscale BioPhotonics, Institute for Photonics and Advanced Sensing and School of Physical Sciences, The University of Adelaide, Adelaide, SA 5005, Australia

University of South Australia, Adelaide, SA 5000, Australia

In this review, we examine recent developments in the field of chemical and biological sensing utilizing suspended-core, exposed-core, and hollow-core microstructured optical fibers. Depending on the intended application, a host of sensing modalities have been utilized including labelled fluorescence techniques, and label-free methods such as surface plasmon resonance, fiber Bragg gratings, and Raman scattering. The use of various functionalization techniques adds specificity to both chemical ions and biological molecules. The results shown here highlight some of the important benefits that arise with the use of microstructured optical fibers compared to traditional techniques, including small sample volumes, high sensitivity, and multiplexing.

Introduction

Optical detection of chemical or biological species relies on the interaction between a target species and light, either to change the properties of the excitation light in a manner corresponding to the properties of the species or to generate a separate, measurable light signal that can be used as the detection mechanism.[1,2] Optical fibers are one platform which can exploit this mechanism

to create a sensor. These structures have well-defined optical guiding properties, an ability to guide light to areas of interest, and are compatible with an array of established excitation sources and detection devices.[1]

Conventional optical fibers, such as those used traditionally for optical communication, consist of two concentric solid glass materials forming the core and the cladding. Such fibers are exceptionally good at carrying light from one end of the fiber to the other and back with very low loss and have therefore been successful for applications where sensing is performed at the distal end of the fiber, known as extrinsic sensing.[2,3] However, solid core optical fibers do present some limitations in sensing applications, as the interaction area is limited to the fiber tip's cross section, with a diameter in the order of up to a few hundred micrometers.[2]

Many optical fiber designs have been proposed and demonstrated to achieve intrinsic sensing, where the optical fiber is not simply a light pipe but plays a significant role in the sensing. For chemical and biological sensing, this usually refers to accessing a portion of the optical field that propagates along the fiber, such as through tapering[4] or the use of D-shaped fibres.[5] This approach is attractive as it allows the integration of light–matter interactions along the fiber length. However, modification of the fiber geometry in this way leads to either fragile structures or very low sensitivity, depending on the amount of tapering or portion of the fiber cladding removed.

Microstructured optical fibers (MOFs) offer the advantage that the interaction between the light and chemical species can be extended along the entire length of the fiber, while maintaining the integrity of the device. In suspended-core MOFs (SCMOFs), the glass core is suspended in air by thin struts, allowing a portion of the guided light to extend outside the fiber core into the surrounding holes which serve as low-volume sample chambers.[6,7] For exposed-core MOFs (ECMOFs), the suspended core is partly open to the environment, enabling easy access to the fiber core and removing the need for sample filling.[8,9] Hollow-core MOFs (HCMOFs) have also been used for sensing, where the air core not only guides light but also serves as the sample chamber, allowing large overlap of the guided light with the sample.[10]

The overlap of the guided light means that properties such as the refractive index and the absorption characteristics of the medium can alter the properties of the guided light.[11,12] These fibers are an attractive platform for liquid sensing as they can enable strong light–matter interactions, long interaction lengths, and the use of small sample volumes.[6]

In this study, we review our recent progress exploiting the use of MOFs for optical sensing. Methods for the attachment of functional species to the surfaces of MOFs are discussed in the scope of describing how MOFs can function as active sensing elements. We focus on the different modalities of deploying MOFs in sensing applications, using both label-based fluorescence and label-free detection techniques. For label-based fluorescence sensing, we discuss the different chemical and physical mechanisms used for surface attachment of suitable marker molecules, the fiber geometries, and the varied target species which can be detected using MOF-based sensors. For label-free sensing, we explore whispering gallery modes, surface plasmon resonance detection of biological species, Bragg grating-based sensing, and Raman spectroscopy in MOFs, highlighting an additional toolset of sensing mechanisms for MOF-based chemical and biological sensing.

Surface Functionalization

One solution to adding chemical or biological specificity and selectivity using an optical fiber is to premix reagents with a sample containing the analyte of interest, a small volume of which is then interrogated by the fiber. A different approach is to bind reactive molecules or antibodies to the glass surface before the fiber interacts with the analyte. As most analytes of interest do not typically bind directly with the glass, it is first necessary to create a scaffold onto which the molecules can be bound, through either a grafting or physical functionalization procedure.

Grafting

Grafting, or linking, the sensing molecule of interest to the sensor surface is commonly achieved via covalent bonding to oxide surfaces,[13–15] polymers,[16] or metals.[17] A number of different attachment chemistries are available, including phosphonates, carboxylates, catechols, alkenes, alkynes, and amines, with a large body of work looking at attachment via silanization.[18]

For silanization, hydrolysis of the silane forms silanols, which attach to hydroxyl groups on the surface

via a condensation reaction. This allows for diverse functional groups to be utilized, including perfluoroalkyl, amino, and sulfhydryl for surface passivation or further sensing molecule immobilization.

The surface density of hydroxyl groups on the sensor surface has a large influence on the layer density, with techniques such as plasma activation[19] or treatment of the surface with acids used to increase the surface density.[20] A low surface density typically results in low reproducibility in the deposition process.[20,21]

Silanes can be deposited either in solution[20] or in vapor phase[22] with previous work in MOF functionalization focused on solution deposition. The solution deposition process typically involves dipping the freshly prepared sensor into the silane solution, yielding a full silane coating in minutes to hours.[20]

Physical Functionalization

Physical functionalization is a collective term for any approach by which the sensor molecules are attached to the surface by forces that are not chemical bonds, such as electrostatic forces. These methods have less dependence on the chemistry of the surface and can therefore be exploited on a wide variety of substrates including metals,[23] polymers,[24] glass,[25] and carbon nanotubes.[20]

One particular approach is to deposit layers of charged polymers, such as polyelectrolytes (PE) from solution. This involves a layer-by-layer process, wherein the PE is attached through electrostatic interaction. The first PE layer, with a charge opposite to the intrinsic surface charge of the substrate is deposited, rinsed, and a subsequent PE layer of the opposite charge deposited.[26] The process can be repeated multiple times to stack layers onto any substrate, resulting in an increased PE functional group density on the sensor surface.

Alternatively, a volume-doped polymer layer can be deposited, as shown in Fig. 1b.[27] This process can combine both the formation of a protective coating, along with functionalization of the fiber to the target species.[27] The thin polymer film functionalized fiber, shown in Figs. 1a and c, has been shown to be suitable for the detection of aluminum cations. This result also shows that the fluorophore (8-hydroxyquiniline) is not held too tightly within the polymer, allowing for multiligand binding so that three molecules can still complex with the aluminium.

Fluorescence-Based Sensing Methods

Once a method for attaching molecules to the surface of the MOF is established, functionality needs to be added to allow for specific detection of the target molecules, that either utilizes these surface attached methods, or involves premixing of chemicals and the subsequent use of the MOF for sample interrogation.

One of the primary ways that specificity can be achieved is through fluorescence-based sensing techniques. These typically excite fluorescent molecules or nanoparticles with light guided along the fiber, and analyze the emitted light captured using the same fiber. The captured light can be analyzed at either end of the fiber, with the back-captured emission both improving the practicality of the probe as well as potentially increasing the sensitivity of the device.[28] Examples of SCMOFs used for sensing are shown in Fig. 2.

Changing the geometry and material of the MOF allows the desired fiber parameters to be tailored to the specific application. Decreasing the core diameter increases the overlap of the optical field with the medium, which increases sensitivity.[31] Meanwhile, the hole size can either be made smaller to reduce the required
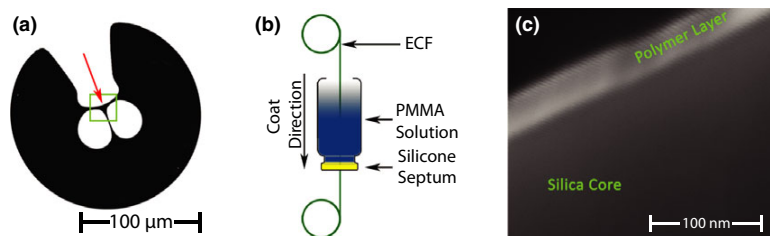
Fig. 1.   (a) Contrast enhanced scanning electron microscope image of ECMOF cross section, with core region highlighted in green. (b) Thin film polymer deposition method on ECMOFs. (c) Scanning electron microscope image of the outside edge of the exposed core, with a 50-nm polymer coating.[27]
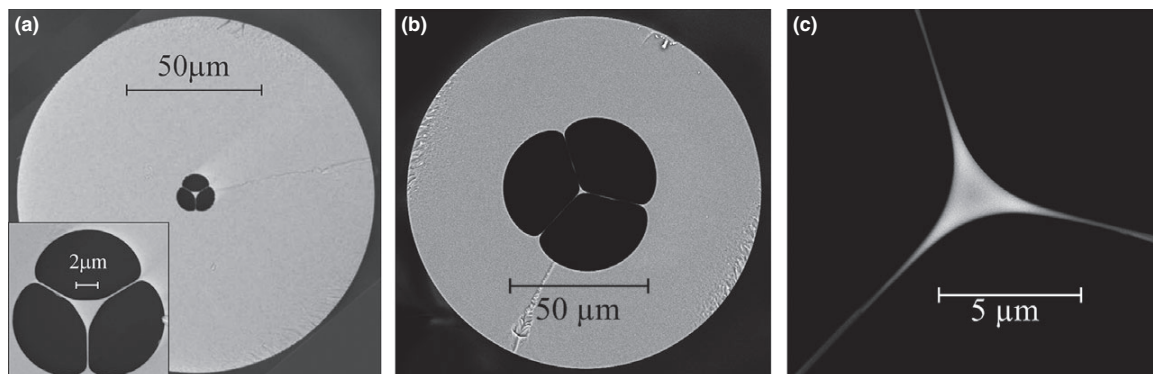
Fig. 2. Scanning electron microscope images of SCMOFs used for sensing applications made from (a) F2 Glass[29] and (b, c) Silica.[30]

sample volume, or larger to reduce filling time.[6] The fiber material can be selected to optimize the sensor, for example, increasing the glass refractive index (e.g., F2 glass [Fig. 2a] has a higher index than silica [Fig. 2b]) increases the numerical aperture of the fiber and thus the proportion of the fluorescence that can be re-captured.[31]

For SCMOFs, the fibers are filled using capillary action, which is approximately 5 min for a 20-cm length of fiber with an internal volume of 60 nL.[32]

Two primary fluorescence sensing avenues have been explored using MOFs. The first seeks to use fluorophores as labels for biomolecules, while the second looks at the emission from fluorophores and attempts to correlate the observed signals with concentrations of chemical species within the solution.

Fluorescence-Based Sensing of Biomolecules

By labeling target biomolecules with fluorescent markers, the detection of the biomolecule itself can be inferred from the detection of the fluorophore to which it is attached. The sensitivity of fluorescence-based MOF-biosensing is typically limited by either background fluorescence emissions, or photobleaching.

Previous work by Jensen *et al.*[33] utilizing Cy5 labelled DNA, looking at the absorption rather than the emission of the fluorophores restricting the detection limit to 0.1 μM. Smolka *et al.*[10] were able to observe concentrations as low as 1 nM by measuring the fluorescence emission of Rhodamine 6G using an HCMOF with a large light–matter overlap.

The use of alternative labels, such as semiconductor-based quantum dots (Qdots), allows for detection of biomolecules to be performed at much lower concentrations. Filling near infrared emitting Qdots within the holes of an SCMOF allowed for detection down to 1 nM of quantum dot labelled proteins,[34] which was further improved to 10 pM after modifications to the glass composition and fiber design.[29] This result was limited primarily by background fluorescence emissions from the glass.

Lanthanide-doped upconversion nanoparticles provide a significant advantage over alternative labels, as they emit at a shorter wavelength compared to the excitation source. The high brightness of these particles, combined with a significant reduction in competing background signals allows for an improvement in detection to 660 fM using erbium-/ytterbium-doped nanoparticles.[35] Using optimized thulium-ytterbium-doped nanoparticles allows further sensitivity improvements. These high brightness, highly doped nanoparticles along with the lack of competing background signals allows detection of single nanoparticles from one end of the fiber as they enter into the vicinity of the evanescent field inside a SCMOF from the fiber's other end.[36]

Another application where SCMOFs have also found use in is enzyme activity assays, where they have been shown to be able to detection of PC6 down to 50 U/mL using a sample size of 210 nL.[30] This is particularly important for potential *in vivo* applications, where difficulty removing larger samples restricts the total available volume leading to a particular advantage in using MOFs for these particular applications.

Further work has explored the use of these fibers for specific DNA detection[25] and genotyping, where molecular beacons have been multiplexed to differentiate between wild- and mutant-type sequences in MOFs.[37]

Fluorescence-Based Chemical Sensing

In addition to their use as biosensors, MOFs can also be applied to chemical sensing applications. These sensors typically function by detecting and amplifying the interaction of the desired substrate with a receptor, where the receptor is usually a small-molecule responsive fluorophore.

By choosing the appropriate fluorophore to react with the target species, these MOF-based sensors have been used to detect metal ions such as aluminum[38] through the use of a surface attached fluorophore layer, sodium ions,[39] or hydrogen peroxide.[40]

A recent advance in sensing technology involves the use of photoswitchable molecules and MOFs to create light-driven sensors that are capable of targeting the desired substrates selectively and reversibly among other unique characteristics. The photoswitchable component provides an ability to modulate reversible binding and release of the desired ion from the binding domain. Such a sensor would allow for multiple measurements to be made on a single sample without the need to change the sensor. This would then permit continual and noninvasive study of biological systems, with an associated increase in the sensors' useful lifetime. In this respect, the first nanoliter-scale regenerable ion sensor based on MOFs was recently reported,[41] where the air holes of the MOF are functionalized with a monoazacrown bearing spiropyran to give a switchable sensor that reversibly detects lithium ions down to 100 nM in nanoliter-scale volumes. Similar sensors for probing zinc[42] as well as multiple ions have also been demonstrated using MOFs, with a dual sensor for calcium and cadmium capable of detecting ion concentrations as low as 100 pM.[43]

The deposition of thin layers of reactive polymer layers gives an alternative to standard organic fluorophores, as the polymer layer itself can be used for detection. This has been demonstrated using poly[2-methoxy-5-(2-ethylhexyloxy)-1,4-phenylenevinylene] for explosives detection, showing a detection limit of 6.3 ppm using only 27 nL of sample volume.[44]

Label-Free Sensing Methods

Methods which do not require prior attachment of fluorescent molecules to perform detection are commonly referred to as label-free techniques. These encompass methods which either look at a refractive index change on a surface to correlate binding, typically of biomolecules, or methods such as Raman spectroscopy which look at vibrational modes of the molecules themselves.

In the optical domain, we have successfully exploited four different physical phenomena in conjunction with MOFs to create new sensing modalities.

Whispering Gallery Modes

Whispering Gallery Modes (WGMs) refer to a resonance mechanism that occurs when light is trapped within a microresonator by total internal reflection, and returns in phase after one or multiple roundtrip(s).[45] Multiple geometries of optical resonators have been investigated, including microspheres,[45,46] capillaries,[47] micro disks, and toroids.[48] WGMs have been widely used for refractive index sensing and biological sensing applications in particular via surface functionalization.[49] The amount of time the light remains circulating within the resonator determines the quality (Q) factor (i.e., the linewidth of the resonance features), with a higher Q-factor resulting in longer interaction lengths with the molecules as they bind to the surface.[50]

WGMs can be excited and interrogated through two different mechanisms. The first approach involves using a phase matched fiber taper or prism to couple light to the microresonator at one of the resonance wavelengths.[48] This approach runs the risk that a small deviation in the optimum position of the gap separating the resonator and the taper will not only affect the coupling conditions, but also be seen by the resonator as a change of local refractive index, yielding measurement error.[51]

The second approach relies on using microresonators which contain a gain medium such as a fluorescent dye, and through remote excitation of the dye the re-emitted light can be coupled back into the resonant modes. This allows for remote excitation and collection of the WGM-modulated spectra as seen in Fig. 3a, alleviating the limitation of the taper coupling requirements but at the cost of lower Q-factors.

We have initiated the use of SCMOFs for both the excitation and collection of the WGM signal emitted by a dye-doped polymer microsphere positioned onto the tip of the fiber, as shown in Fig. 3b.[52] Further work on this platform has shown a strong coupling mechanism between the microsphere and the SCMOF as a function of the diameter mismatch between the microsphere and the hole into which the microsphere is positioned, resulting in preferential enhancement of the
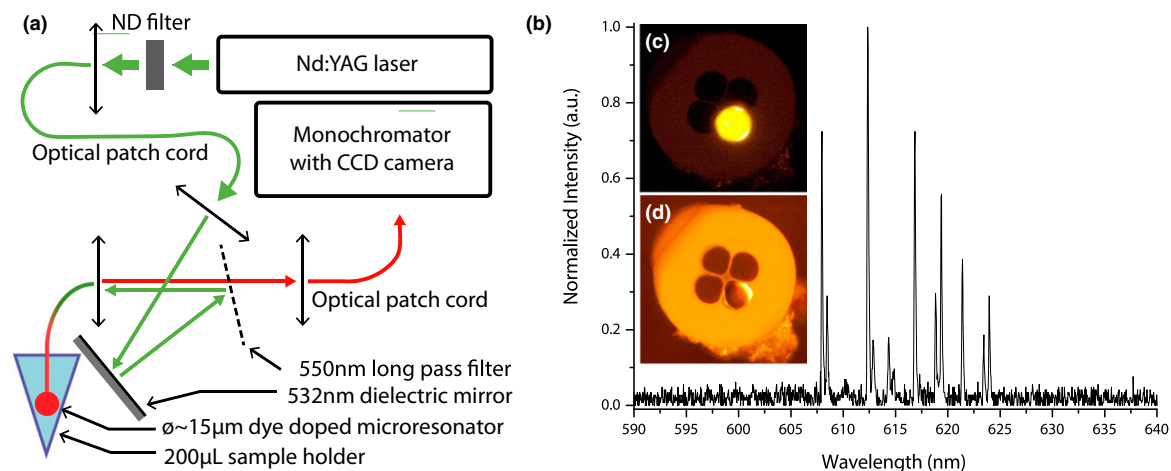
Fig. 3. (a) Optical setup used for the excitation and interrogation of a dye-doped microsphere on an SCMOF tip, (b) WGM spectra of a 15-µm diameter dye-doped polystyrene microsphere, (c, d) Bright field and fluorescence images of a microsphere positioned onto the tip of a silica SCMOF.[46]

WGM depending on their polarization[53]. This effect, combined with the operation of the dye-doped microspheres above their lasing threshold allowed to increase the stored energy within the resonator, increasing the Q-factor[45] by almost 6×, allowing for improved detection limits and the potential for *in-vivo* biosensing applications.[24]

Surface Plasmon Resonance

Surface plasmon resonance (SPR), which refers to the oscillation of free electrons in thin metallic coatings, is another refractive index sensing method that has been widely exploited for biosensing applications. The resonance wavelength depends on the different dielectric functions of the metallic coating and dielectric substrate, as well as the surrounding refractive index adjacent to the metallic coating.[54]

Although SPR methods initially used a prism to match the propagation constant of the monochromatic radiation with the propagation constant of the plasmons, a similar mechanism has as been demonstrated with optical fibers.[55] Hassani and Skorobogatiy[55] started investigating the use of SPR in a MOF, with theoretical work showing the potential for improved performance.

To circumvent observed issues with physical deposition methods inside MOFs, an electroless plating technique for silver deposition based on the Tollens reaction has been developed.[56] Initial work showed that scattering of the plasmonic wave induced by the higher surface roughness of silver thin film can be exploited on bare core optical fibers. This process essentially turns an intrinsically nonradiative process into a radiative one, with significant advantages compared with the standard transmission measurements in terms of signal-to-noise ratio, the potential for multiplexed and self-referencing sensing.[23,57,58]

Recently, we showed that a silver layer could be deposited on the core of an ECMOF (similar to that shown in Fig. 4a) by thermal evaporation. This fiber possessed a significantly smaller core diameter ($\varnothing_{core}$~10 µm) compared to the bare core fibers previously used ($\varnothing_{core}$~140 µm) and resulted in a reduction of the resonance linewidth by a factor 3, while the refractive index sensitivity ($\delta\lambda/\delta n$) remained constant,[59] improving the refractive index detection limit by the same factor.

Bragg Gratings

Fiber Bragg gratings (FBGs) are formed by creating a small periodic modulation of the optical fiber's refractive index along its length, which results in a narrow band reflection at a particular Bragg wavelength. FBGs are well known within the optical fiber sensing
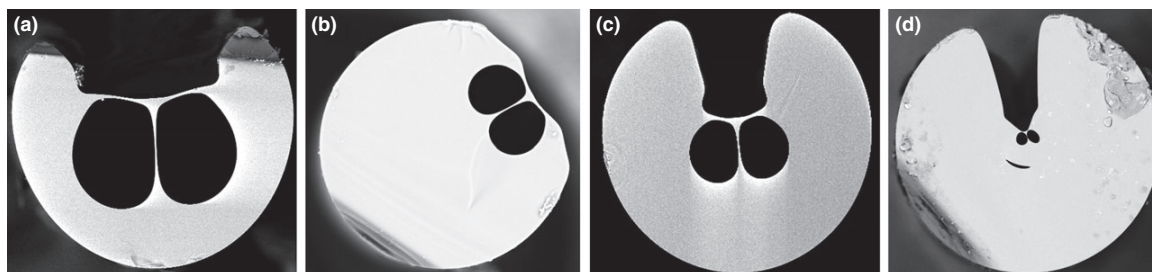
Fig. 4.   Scanning electron images of fabricated silica ECMOFs.[68] The fibers have core diameters of (a) 12.5 μm, (b) 9.3 μm, (c) 7.5 μm, and (d) 2.7 μm. The outer diameters of the fibers at the maximum point are (a) 200 μm, (b) 200 μm, (c) 160 μm, and (d) 200 μm.

community for their role in temperature and strain sensing, as the pitch is highly dependent on strain, while the effective refractive index of the fiber is dependent on temperature via the thermo-optic effect.[2]

In the case of refractive index sensing, the position of the Bragg wavelength depends on the fiber's effective index, which in-turn depends on the refractive index experienced by the evanescent field. For FBGs written on conventional optical fibers, the analyte is well isolated from the light guided within the fiber, and as such the fiber cladding needs to be thinned down to improve the refractive index sensitivity.[60,61]

There is particular advantage in using MOFs which can be tailored to enhance this light–matter overlap without weakening the fiber structure. For example, an ultra-violet written FBG in an SCMOF was shown to detect a refractive index variation of 3×10^{-5} refractive index units (RIU).[62]

Two challenges arise using SCMOFs for FBG-based biosensing. Firstly, they must be filled from the distal end to interact with analytes, and secondly, complexity can arise due to inscription methods being susceptible to scattering by the MOF geometry.[63]

To address these issues, ECMOFs have been developed where the core is accessible from one side along the length of the fiber. These have been fabricated from a diverse range of materials including polymer,[64] chalcogenide,[65] lead-silicate,[8] and silica.[9,66–68] Silica ECMOFs show good stability[9] and can be readily spliced to conventional single mode fiber for easy integration with commercial interrogation equipment.[67,68] ECMOFs have been fabricated with core diameters ranging from 2.7 to 12 μm, as seen in Fig. 4.[68]

Fiber Bragg gratings have been written onto the core of these ECMOFs using a femtosecond laser technique:

using sufficiently short duration pulses multiphoton absorption can lead to ionization of electrons and the physical removal of material, a process known as laser ablation.[63] An example of such gratings is shown in Figs. 5a and b for the 7.5 μm core diameter ECMOF from Fig. 4c. The Bragg reflection shift with respect to external refractive index is shown in Fig. 5c, and the shift with polyelectrolyte layer deposition shown in Fig. 5d.

While FBGs on ECMOFs are less sensitive than techniques based on surface plasmon resonance, with shifts reported in the range of 1.1 to 101 nm/RIU depending on core diameter, the capability to be multiplexed and operate in reflection mode makes them a particularly attractive research direction for label-free assays in *in-vivo* biosensing applications.

Raman Spectroscopy

Raman spectroscopy is a form of vibrational spectroscopy in which each Raman-active chemical bond vibrational mode changes the energy of incident photons from a laser source by a fraction equal to that mode's vibrational energy.[69] Raman spectroscopy has the great advantage of being a label-free technique that can uniquely identify chemical species in a sample without the need for target-specific chemistry or surface modification.[70] Optical fibers have been deployed for Raman-based optical sensing as, besides their advantages in terms of delivering and collecting light,[2] in the case of MOFs they can enhance the Raman signature from target molecules.[71,72]

We have shown that Raman spectroscopy in SCMOFs can be used as a method for detecting explosives in liquid samples.[32] We were able to detect explosive quantities as small as 1 μg (Fig. 6a) in a small
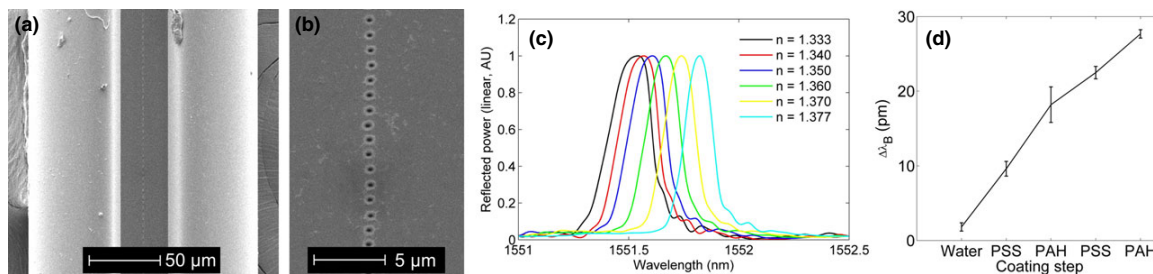
Fig. 5.   (a, b) Scanning electron images of the ECMOF from Fig. 4(c) with femtosecond laser ablation gratings written on the exposed-core. (c) Shift in the reflected Bragg wavelength when the ECMOF is immersed into liquids of varying refractive index. (d) Shift in the Bragg wavelength as polyelectrolyte layers are coated onto the ECMOF.[68]
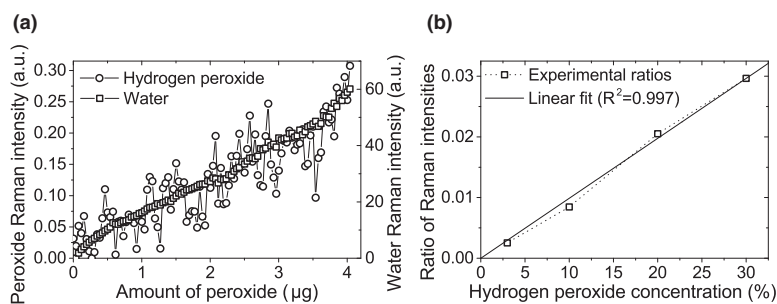
Fig. 6.   (a) Experimental data showing the Raman signal intensity for hydrogen peroxide and water for an aqueous solution of hydrogen peroxide (b) correlation between the hydrogen peroxide concentration in water and the ratio between the Raman signal intensities.

sample volume (60 nL). The sensor was tested using hydrogen peroxide (H_2O_2), a key ingredient in making triacetone triperoxide (TATP), a difficult to detect home-made explosive, as well as using 1,4-dinitrobenzene (DNB), a member of the nitroaromatic family of explosives and a substitute molecule for 2,4,6-trinitrotoluene (TNT). In addition, using the solvent's Raman signature as a calibration standard in the same measurement, we were able to quantify the amount of explosive in the sample (Fig. 6b).

Background Raman signal from the solid core of SCMOFs can, however, hamper the detection limit of these optical fiber sensors. HCMOFs can overcome this issue, as the light is guided within the sample region itself, therefore maximizing the Raman signal.[73] These HCMOFs are time consuming to fabricate, as they rely on capillary stacking.[74,75] Our work concentrated on single ring hollow core antiresonance reflection optical waveguiding fibers[76,77] fabricated using the extrusion technique.[78] This simple fabrication process was used to fabricate a lead-silicate glass (Schott F2HT) preform

that was directly drawn to a single ring HCMOF (loss spectrum shown in Fig. 7a) with a core diameter of 47 μm, and a central ring diameter of 1.5 μm (Fig. 7a inset).

After filling with ethanol, spectra showed a 4 times increase in the intensity of the ethanol Raman spectrum when coupled into the core compared to the signal from the bulk ethanol (Fig. 7b). The combination of ease-of-fabrication and enhanced Raman sensing performance highlights the potential of extruded single ring HCMOFs as Raman sensors.[79]

Conclusion

Optical fiber sensors have emerged as a very promising category of devices due to the combination of attractive physical properties, ease of integration with existing optical sources and detectors and the large number of compatible sensing modalities. Lowering the detection limits for analytes of interest and increasing the selectivity
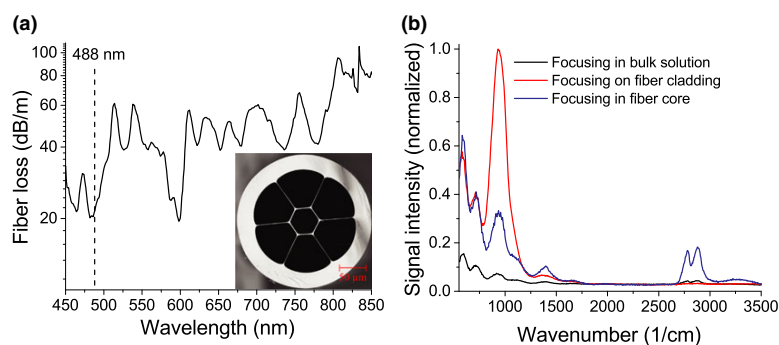
Fig. 7.   (a) Optical loss from an extruded single ring HCMOF, highlighting the excitation wavelength used for Raman experiments. The inset shows a scanning electron microscope image of a cross section of the fiber.[79] (b) Raman signal of ethanol collected with the excitation light coupled in a bulk quantity of solution, on the fiber cladding and finally in the core of the optical fiber.

of optical fiber sensors are the main challenges for deploying these sensors in real-world applications.

In this work, we have demonstrated the use of MOFs in a diverse range of sensing applications to answer these challenges. MOFs have unique optical and physical properties that can be tailored by controlling the fiber geometry during fabrication, allowing for control over the light–matter interaction. The structural geometries of SCMOFs or HCMOFs enable interaction between light and analyte along the entire length of the fiber, allowing for measurements to be performed on small sample volumes with lower detection limits.

The use of label-free techniques such as WGM/SPR, Bragg gratings or Raman, as well as surface attachment methods for fluorescence-based sensing enables these sensors to be used without perturbing the sample. Lower detection limits can be aided by self-referencing methods that reduce the effect of fluctuations in the performance of the sensors at small signal levels and offer the potential for quantification of analytes in a sample. This makes MOF-based sensors particularly useful for measurements of low concentrations of analytes in small volumes of sensitive biological samples and has the potential to enable nondestructive *in vivo* or *in vitro* measurements in real time.

Acknowledgments

References

1. X.-D. Wang and O. S. Wolfbeis, "Fiber-optic Chemical Sensors and Biosensors (2008–2012)," *Anal. Chem.*, 85 [2] 487–508 (2012).
2. B. Lee, "Review of the Present Status of Optical Fiber Sensors," *Opt. Fiber Technol.*, 9 [2] 57–79 (2003).
3. R. A. Potyrailo, S. E. Hobbs, and G. M. Hieftje, "Optical Waveguide Sensors in Analytical Chemistry: Today's Instrumentation, Applications and Trends for Future Development," *Fresenius J. Anal. Chem.*, 362 [4] 349–373 (1998).
4. L. Tong, *et al.*, "Subwavelength-Diameter Silica Wires for Low-Loss Optical Wave Guiding," *Nature*, 426 [6968] 816–819 (2003).
5. G. Stewart, W. Jin, and B. Culshaw, "Prospects for Fibre-Optic Evanescent-Field Gas Sensors Using Absorption in the Near-Infrared," *Sens. Actuators B. Chem.*, 38 [1] 42–47 (1997).
6. T. M. Monro, *et al.*, "Sensing with Suspended-Core Optical Fibers," *Opt. Fiber Technol.*, 16 [6] 343–356 (2010).
7. B. Lee, S. Roh, and J. Park, "Current Status of Micro-and Nano-Structured Optical Fiber Sensors," *Opt. Fiber Technol.*, 15 [3] 209–221 (2009).

8. S. C. Warren-Smith, *et al.*, "Exposed-Core Microstructured Optical Fibers for Real-Time Fluorescence Sensing," *Opt. Express*, 17 [21] 18533–18542 (2009).

9. R. Kostecki, *et al.*, "Silica Exposed-Core Microstructured Optical Fibers," *Opt. Mater. Express*, 2 [11] 1538–1547 (2012).

10. S. Smolka, M. Barth, and O. Benson, "Highly Efficient Fluorescence Sensing with Hollow Core Photonic Crystal Fibers," *Opt. Express*, 15 [20] 12783–12791 (2007).

11. T. M. Monro, *et al.*, "Holey Optical Fibers: An Efficient Modal Model," *J. Lightwave Technol.*, 17 [6] 1093 (1999).

12. T. M. Monro, D. Richardson, and P. Bennett, "Developing Holey Fibres for Evanescent Field Devices," *Electron. Lett.*, 35 [14] 1188–1189 (1999).

13. M. Qin, *et al.*, "Two Methods for Glass Surface Modification and Their Application in Protein Immobilization," *Colloids Surf. B*, 60 [2] 243–249 (2007).

14. H. T. Foo, *et al.*, "Towards Microstructured Optical Fibre Sensors: Surface Analysis of Silanised Lead Silicate Glass," *J. Mater. Chem. C*, 1 [41] 6782–6789 (2013).

15. S. P. Pujari, *et al.*, "Covalent Surface Modification of Oxide Surfaces," *Angew. Chem. Int. Ed.*, 53 [25] 6322–6356 (2014).

16. L. Basabe-Desmonts, D. N. Reinhoudt, and M. Crego-Calama, "Design of Fluorescent Materials for Chemical Sensing," *Chem. Soc. Rev.*, 36 [6] 993–1017 (2007).

17. R. Müller, *et al.*, "Surface Engineering of Stainless Steel Materials by Covalent Collagen Immobilization to Improve Implant Biocompatibility," *Biomaterials*, 26 [34] 6962–6972 (2005).

18. J. A. Howarter and J. P. Youngblood, "Optimization of Silica Silanization by 3-Aminopropyltriethoxysilane," *Langmuir*, 22 [26] 11142–11147 (2006).

19. S. Fiorilli, *et al.*, "Vapor-Phase Self-Assembled Monolayers of Aminosilane on Plasma-Activated Silicon Substrates," *J. Colloid Interface Sci.*, 321 [1] 235–241 (2008).

20. J. Cras, *et al.*, "Comparison of Chemical Cleaning Methods of Glass in Preparation for Silanization," *Biosens. Bioelectron.*, 14 [8] 683–688 (1999).

21. J. Brzoska, I. B. Azouz, and F. Rondelez, "Silanization of Solid Substrates: A Step Toward Reproducibility," *Langmuir*, 10 [11] 4367–4373 (1994).

22. R. D. Lowe, *et al.*, "Deposition of Dense Siloxane Monolayers from Water and Trimethoxyorganosilane Vapor," *Langmuir*, 27 [16] 9928–9935 (2011).

23. B. Sciacca, *et al.*, "Radiative-Surface Plasmon Resonance for the Detection of Apolipoprotein E in Medical Diagnostics Applications," *Nanomed. Nanotechnol. Biol. Med.*, 9 [4] 550–557 (2013).

24. A. François, T. Reynolds, and T. M. Monro, "A Fiber-Tip Label-Free Biological Sensing Platform: A Practical Approach toward In-Vivo Sensing," *Sensors*, 15 [1] 1168–1181 (2015).

25. L. V. Nguyen, *et al.*, "Molecular Beacons Immobilized Within Suspended Core Optical Fiber for Specific DNA Detection," *Opt. Express*, 20 [28] 29378–29385 (2012).

26. G. Decher, "Fuzzy Nanoassemblies: Toward Layered Polymeric Multicomposites," *Science*, 277 [5330] 1232–1237 (1997).

27. R. Kostecki, *et al.*, "Novel Polymer Functionalization Method for Exposed-Core Optical Fiber," *Opt. Mater. Express*, 4 [8] 1515–1525 (2014).

28. S. Afshar V, *et al.*, "Enhanced Fluorescence Sensing Using Microstructured Optical Fibers: A Comparison of Forward and Backward Collection Modes," *Opt. Lett.*, 33 [13] 1473–1475 (2008).

29. E. P. Schartner, *et al.*, "Driving down the Detection Limit in Microstructured Fiber-Based Chemical Dip Sensors," *Sensors*, 11 [3] 2961–2971 (2011).

30. S. C. Warren-Smith, *et al.*, "Enzyme Activity Assays Within Microstructured Optical Fibers Enabled by Automated Alignment," *Biomed. Opt. Express*, 3 [12] 3304–3313 (2012).

31. S. Afshar V, S. C. Warren-Smith and T. M. Monro, "Enhancement of Fluorescence-Based Sensing Using Microstructured Optical Fibres," *Opt. Express*, 15 [26] 17891–17901 (2007).

32. G. Tsiminis, *et al.*, "Identification and Quantification of Explosives in Nanolitre Solution Volumes by Raman Spectroscopy in Suspended Core Optical Fibers," *Sensors*, 13 [10] 13163–13177 (2013).

33. J. B. Jensen, *et al.*, "Photonic Crystal Fiber Based Evanescent-Wave Sensor for Detection of Biomolecules in Aqueous Solutions," *Opt. Lett.*, 29 [17] 1974–1976 (2004).

34. Y. Ruan, *et al.*, "Detection of Quantum-Dot Labelled Proteins Using Soft Glass Microstructured Optical Fibers," *Opt. Express*, 15 [26] 17819–17826 (2007).

35. E. P. Schartner, *et al.*, "Lanthanide Upconversion Within Microstructured Optical Fibers: Improved Detection Limits for Sensing and the Demonstration of a New Tool for Nanocrystal Characterization," *Nanoscale*, 4 [23] 7448–7451 (2012).

36. J. Zhao, *et al.*, "Single-Nanocrystal Sensitivity Achieved by Enhanced Upconversion Luminescence," *Nat. Nanotechnol.*, 8 [10] 729–734 (2013).

37. L. V. Nguyen, *et al.*, "Genotyping Single Nucleotide Polymorphisms Using Different Molecular Beacon Multiplexed within a Suspended Core Optical Fiber," *Sensors*, 14 [8] 14488–14499 (2014).

38. S. C. Warren-Smith, *et al.*, "Fluorescence-Based Aluminum Ion Sensing Using a Surface-Functionalized Microstructured Optical Fiber," *Langmuir*, 27 [9] 5680–5685 (2011).

39. F. V. Englich, *et al.*, "Photoinduced Electron Transfer Based Ion Sensing Within an Optical Fiber," *Sensors*, 11 [10] 9560–9572 (2011).

40. E. Schartner, *et al.*, "A hydrogen peroxide fibre optic dip sensor for aqueous solutions," *Proceedings of the Australasian Conference on Optics, Lasers and Spectroscopy and Australian Conference on Optical Fibre Technology in association with the International Workshop on Dissipative Solitons.* Adelaide, Australia, 61–62, 2009.

41. S. Heng, *et al.*, "Nanoliter-Scale, Regenerable Ion Sensor: Sensing with a Surface Functionalized Microstructured Optical Fibre," *RSC Adv.*, 3 [22] 8308–8317 (2013).

42. S. Heng, *et al.*, "Microstructured Optical Fibers and Live Cells: A Water-Soluble, Photochromic Zinc Sensor," *Biomacromolecules*, 14 [10] 3376–3379 (2013).

43. S. Heng, *et al.*, "Dual Sensor for Cd (II) and Ca (II): Selective Nanoliter-Scale Sensing of Metal Ions," *Anal. Chem.*, 86 [7] 3268–3272 (2014).

44. F. Chu, *et al.*, "Explosives Detection by Fluorescence Quenching of Conjugated Polymers in Suspended Core Optical Fibers," *Sens. Actuators B Chem.*, 199 22–26 (2014).

45. A. François, *et al.*, "Polymer Based Whispering Gallery Mode Laser for Biosensing Applications," *Appl. Phys. Lett.*, 106 [3] 031104 (2015).

46. A. François, *et al.*, "Combining whispering gallery mode lasers and microstructured optical fibers for in-vivo biosensing applications," Proc. SPIE, 8915 Photonics North, 891518, 2013.

47. S. Lane, *et al.*, "Protein Biosensing with Fluorescent Microcapillaries," *Opt. Express*, 23 [3] 2577–2590 (2015).

48. K. J. Vahala, "Optical Microcavities," *Nature*, 424 [6950] 839–846 (2003).

49. F. Vollmer and S. Arnold, "Whispering-Gallery-Mode Biosensing: Label-Free Detection Down to Single Molecules," *Nat. Methods*, 5 [7] 591–596 (2008).

50. A. M. Armani, *et al.*, "Label-Free, Single-Molecule Detection with Optical Microcavities," *Science*, 317 [5839] 783–787 (2007).

51. Z. Guo, H. Quan, and S. Pau, "Near-Field Gap Effects on Small Microcavity Whispering-Gallery Mode Resonators," *J. Phys. D: Appl. Phys.*, 39 [24] 5133 (2006).

52. A. François, K. J. Rowland, and T. M. Monro, "Highly Efficient Excitation and Detection of Whispering Gallery Modes in a Dye-Doped Microsphere Using a Microstructured Optical Fiber," *Appl. Phys. Lett.*, 99 [14] 141111 (2011).

53. A. François, *et al.*, "Enhancing the Radiation Efficiency of Dye Doped Whispering Gallery Mode Microresonators," *Opt. Express*, 21 [19] 22566–22577 (2013).

54. J. Homola, S. S. Yee, and G. Gauglitz, "Surface Plasmon Resonance Sensors: Review," *Sens. Actuators B Chem.*, 54 [1] 3–15 (1999).

55. A. Hassani and M. Skorobogatiy, "Design of the Microstructured Optical Fiber-Based Surface Plasmon Resonance Sensors with Enhanced Microfluidics," *Opt. Express*, 14 [24] 11616–11621 (2006).

56. J. Boehm, *et al.*, "Chemical Deposition of Silver for the Fabrication of Surface Plasmon Microstructured Optical Fibre Sensors," *Plasmonics*, 6 [1] 133–136 (2011).

57. A. François, *et al.*, "Collection Mode Surface Plasmon Fibre Sensors: A New Biosensing Platform," *Biosens. Bioelectron.*, 26 [7] 3154–3159 (2011).

58. B. Sciacca, *et al.*, "Multiplexing of Radiative-Surface Plasmon Resonance for the Detection of Gastric Cancer Biomarkers in a Single Optical Fiber," *Sens. Actuators B Chem.*, 183 454–458 (2013).

59. E. Klantsataya, *et al.*, "Exposed core microstructured optical fiber surface plasmon resonance biosensor," *Proceedings SPIE 8938, Optical Fibers and Sensors for Medical Diagnostics and Treatment Applications XIV*, 89380X, San Francisco, CA (2014).

60. W. Liang, *et al.*, "Highly Sensitive Fiber Bragg Grating Refractive Index Sensors," *Appl. Phys. Lett.*, 86 [15] 151122 (2005).

61. A. Iadicicco, *et al.*, "Thinned Fiber Bragg Gratings as High Sensitivity Refractive Index Sensor," *IEEE Photonics Technol. Lett.*, 16 [4] 1149–1151 (2004).

62. M. C. Phan Huy, *et al.*, "Three-Hole Microstructured Optical Fiber for Efficient Fiber Bragg Grating Refractometer," *Opt. Lett.*, 32 [16] 2390–2392 (2007).

63. J. Canning, *et al.*, "Gratings in Structured Optical Fibres," *Laser Chem.*, 2008 1–20 (2008).

64. F. M. Cox, *et al.*, "Opening Up Optical Fibres," *Opt. Express*, 15 [19] 11843–11848 (2007).

65. P. Toupin, *et al.*, "Comparison Between Chalcogenide Glass Single Index and Microstructured Exposed-Core Fibers for Chemical Sensing," *J. Non-Cryst. Solids*, 377 217–219 (2013).

66. R. Kostecki, *et al.*, "Predicting the Drawing Conditions for Microstructured Optical Fiber Fabrication," *Opt. Mater. Express*, 4 [1] 29–40 (2014).

67. S. C. Warren-Smith, and T. M. Monro, "Exposed Core Microstructured Optical Fiber Bragg Gratings: Refractive Index Sensing," *Opt. Express*, 22 [2] 1480–1489 (2014).

68. S. C. Warren-Smith, *et al.*, "Fabrication, Splicing, Bragg Grating Writing, and Polyelectrolyte Functionalization of Exposed-Core Microstructured Optical Fibers," *Opt. Express*, 22 [24] 29493–29504 (2014).

69. J. R. Ferraro, *Introductory Raman Spectroscopy*, Academic press, New York, 2003.

70. K. Kneipp, *et al.*, "Ultrasensitive Chemical Analysis by Raman Spectroscopy," *Chem. Rev.*, 99 [10] 2957–2976 (1999).

71. D. Pristinski and H. Du, "Solid-Core Photonic Crystal Fiber as a Raman Spectroscopy Platform with a Silica Core as an Internal Reference," *Opt. Lett.*, 31 [22] 3246–3248 (2006).

72. S. Hanf, *et al.*, "Fiber-Enhanced Raman Multigas Spectroscopy: A Versatile Tool for Environmental Gas Sensing and Breath Analysis," *Anal. Chem.*, 86 [11] 5278–5285 (2014).

73. A. Khetani, *et al.*, "Monitoring of Heparin Concentration in Serum by Raman Spectroscopy Within Hollow Core Photonic Crystal Fiber," *Opt. Express*, 19 [16] 15244–15254 (2011).

74. J. M. Fini, *et al.*, "Low-Loss Hollow-Core Fibers with Improved Single-modedness," *Opt. Express*, 21 [5] 6233–6242 (2013).

75. P. Ghenuche, *et al.*, "Kagome Hollow-Core Photonic Crystal Fiber Probe for Raman Spectroscopy," *Opt. Lett.*, 37 [21] 4371–4373 (2012).

76. A. D. Pryamikov, *et al.*, "Demonstration of a Waveguide Regime for a Silica Hollow-Core Microstructured Optical Fiber with a Negative Curvature of the Core Boundary in the Spectral Region> 3.5 µm," *Opt. Express*, 19 [2] 1441–1448 (2011).

77. L. V. Doronina-Amitonova, *et al.*, "Raman Detection of Cell Proliferation Probes with Antiresonance-Guiding Hollow Fibers," *Opt. Lett.*, 37 [22] 4642–4644 (2012).

78. H. Ebendorff-Heidepriem, S. C. Warren-Smith, and T. M. Monro, "Suspended Nanowires: Fabrication, Design and Characterization of Fibers with Nanoscale Cores," *Opt. Express*, 17 [4] 2646–2657 (2009).

79. G. Tsiminis, *et al.*, "Extruded single ring hollow core optical fibers for Raman sensing," *Proceedings SPIE 9157, 23rd International Conference on Optical Fibre Sensors*, 915782, Santander, Spain (2014).

APPENDIX G

Paper 7.

Fabrication, splicing, Bragg grating writing, and polyelectrolyte functionalization of exposed-core microstructured optical fibers

Stephen C. Warren-Smith[*]**, Roman Kostecki, Linh Viet Nguyen, and Tanya M. Monro**

Institute for Photonics and Advanced Sensing (IPAS) and ARC Centre of Excellence in Nanoscale BioPhotonics, The University of Adelaide, Adelaide 5005, Australia
[*]*stephen.warrensmith@adelaide.edu.au*

Abstract: Femtosecond laser written Bragg gratings have been written in exposed-core microstructured optical fibers with core diameters ranging from 2.7 µm to 12.5 µm and can be spliced to conventional single mode fiber. Writing a Bragg grating on an open core fiber allows for real-time refractive index based sensing, with a view to multiplexed biosensing. Smaller core fibers are shown both experimentally and theoretically to provide a higher sensitivity. A 7.5 µm core diameter fiber is shown to provide a good compromise between sensitivity and practicality and was used for monitoring the deposition of polyelectrolyte layers, an important first step in developing a biosensor.

©2014 Optical Society of America

References and links

1. T. A. Birks, J. C. Knight, and P. S. J. Russell, "Endlessly single-mode photonic crystal fiber," Opt. Lett. **22**(13), 961–963 (1997).
2. R. F. Cregan, B. J. Mangan, J. C. Knight, T. A. Birks, P. S. J. Russell, P. J. Roberts, and D. C. Allan, "Single-mode photonic band gap guidance of light in air," Science **285**(5433), 1537–1539 (1999).
3. W. J. Wadsworth, R. M. Percival, G. Bouwmans, J. C. Knight, T. A. Birks, T. D. Hedley, and P. S. J. Russel, "Very high numerical aperture fibers," IEEE Photonic. Tech. L. **16**, 843–845 (2004).
4. K. Furusawa, A. Malinowski, J. H. V. Price, T. M. Monro, J. K. Sahu, J. Nilsson, and D. J. Richardson, "Cladding pumped Ytterbium-doped fiber laser with holey inner and outer cladding," Opt. Express **9**(13), 714–720 (2001).
5. J. K. Sahu, C. C. Renaud, K. Furusawa, R. Selvas, J. A. Alvarez-Chavez, D. J. Richardson, and J. Nilsson, "Jacketed air-clad cladding pumped ytterbium-doped fibre laser with wide tuning range," Electron. Lett. **37**(18), 1116–1117 (2001).
6. J. Laegsgaard and A. Bjarklev, "Microstructured optical fibers-fundamentals and applications," J. Am. Ceram. Soc. **89**(1), 2–12 (2006).
7. A. S. Webb, F. Poletti, D. J. Richardson, and J. K. Sahu, "Suspended-core holey fiber for evanescent-field sensing," Opt. Eng. **46**(1), 010503 (2007).
8. X. Feng, A. K. Mairaj, D. W. Hewak, and T. M. Monro, "Nonsilica glasses for holey fibers," J. Lightwave Technol. **23**(6), 2046–2054 (2005).
9. H. Ebendorff-Heidepriem and T. M. Monro, "Extrusion of complex preforms for microstructured optical fibers," Opt. Express **15**(23), 15086–15092 (2007).
10. H. Ebendorff-Heidepriem, S. C. Warren-Smith, and T. M. Monro, "Suspended nanowires: Fabrication, design and characterization of fibers with nanoscale cores," Opt. Express **17**(4), 2646–2657 (2009).
11. S. C. Warren-Smith, H. Ebendorff-Heidepriem, T. C. Foo, R. Moore, C. Davis, and T. M. Monro, "Exposed-core microstructured optical fibers for real-time fluorescence sensing," Opt. Express **17**(21), 18533–18542 (2009).
12. S. Atakaramians, S. Afshar V, H. Ebendorff-Heidepriem, M. Nagel, B. M. Fischer, D. Abbott, and T. M. Monro, "THz porous fibers: design, fabrication and experimental characterization," Opt. Express **17**(16), 14053–15062 (2009).
13. T. M. Monro, S. C. Warren-Smith, E. P. Schartner, A. Francois, S. Heng, H. Ebendorff-Heidepriem, and S. V. Afshar, "Sensing with suspended-core optical fibers," Opt. Fiber Technol. **16**(6), 343–356 (2010).
14. T. M. Monro, D. J. Richardson, and P. J. Bennett, "Developing holey fibres for evanescent field devices," Electron. Lett. **35**(14), 1188–1189 (1999).

15. Y. Zhu, R. T. Bise, J. Kanka, P. Peterka, and H. Du, "Fabrication and characterization of solid-core photonic crystal fiber with steering-wheel air-cladding for strong evanescent field overlap," Opt. Commun. **281**(1), 55–60 (2008).

16. Y. Zhu, H. Du, and R. Bise, "Design of solid-core microstructured optical fiber with steering-wheel air cladding for optimal evanescent-field sensing," Opt. Express **14**(8), 3541–3546 (2006).

17. J. B. Jensen, L. H. Pedersen, P. E. Hoiby, L. B. Nielsen, T. P. Hansen, J. R. Folkenberg, J. Riishede, D. Noordegraaf, K. Nielsen, A. Carlsen, and A. Bjarklev, "Photonic crystal fiber based evanescent-wave sensor for detection of biomolecules in aqueous solutions," Opt. Lett. **29**(17), 1974–1976 (2004).

18. S. V. Afshar 5th, S. C. Warren-Smith, and T. M. Monro, "Enhancement of fluorescence-based sensing using microstructured optical fibres," Opt. Express **15**(26), 17891–17901 (2007).

19. T. Ritari, J. Tuominen, H. Ludvigsen, J. C. Petersen, T. Sørensen, T. P. Hansen, and H. R. Simonsen, "Gas sensing using air-guiding photonic bandgap fibers," Opt. Express **12**(17), 4080–4087 (2004).

20. C. J. Hensley, D. H. Broaddus, C. B. Schaffer, and A. L. Gaeta, "Photonic band-gap fiber gas cell fabricated using femtosecond micromachining," Opt. Express **15**(11), 6690–6695 (2007).

21. O. Frazão, J. L. Santos, F. M. Araujo, and L. A. Ferreira, "Optical sensing with photonic crystal fibers," Laser and Photonic Reviews **2**(6), 449–459 (2008).

22. S. C. Warren-Smith, S. Heng, H. Ebendorff-Heidepriem, A. D. Abell, and T. M. Monro, "Fluorescence-based aluminum ion sensing using a surface-functionalized microstructured optical fiber," Langmuir **27**(9), 5680–5685 (2011).

23. S. Heng, A. M. Mak, D. B. Stubing, T. M. Monro, and A. D. Abell, "Dual sensor for Cd(II) and Ca(II): selective nanoliter-scale sensing of metal ions," Anal. Chem. **86**(7), 3268–3272 (2014).

24. L. Rindorf, P. E. Høiby, J. B. Jensen, L. H. Pedersen, O. Bang, and O. Geschke, "Towards biochips using microstructured optical fiber sensors," Anal. Bioanal. Chem. **385**(8), 1370–1375 (2006).

25. Y. Ruan, T. C. Foo, S. Warren-Smith, P. Hoffmann, R. C. Moore, H. Ebendorff-Heidepriem, and T. M. Monro, "Antibody immobilization within glass microstructured fibers: a route to sensitive and selective biosensors," Opt. Express **16**(22), 18514–18523 (2008).

26. J. B. Jensen, P. E. Hoiby, G. Emiliyanov, O. Bang, L. H. Pedersen, and A. Bjarklev, "Selective detection of antibodies in microstructured polymer optical fibers," Opt. Express **13**(15), 5883–5889 (2005).

27. G. Emiliyanov, J. B. Jensen, O. Bang, P. E. Hoiby, L. H. Pedersen, E. M. Kjaer, and L. Lindvold, "Localized biosensing with Topas microstructured polymer optical fiber," Opt. Lett. **32**(5), 460–462 (2007).

28. M. Hautakorpi, M. Mattinen, and H. Ludvigsen, "Surface-plasmon-resonance sensor based on three-hole microstructured optical fiber," Opt. Express **16**(12), 8427–8432 (2008).

29. A. Wang, A. Docherty, B. T. Kuhlmey, F. M. Cox, and M. C. J. Large, "Side-hole fiber sensor based on surface plasmon resonance," Opt. Lett. **34**(24), 3890–3892 (2009).

30. A. Hassani and M. Skorobogatiy, "Design of the microstructured optical fiber-based surface plasmon resonance sensors with enhanced microfluidics," Opt. Express **14**(24), 11616–11621 (2006).

31. B. Gauvreau, A. Hassani, M. Fassi Fehri, A. Kabashin, and M. A. Skorobogatiy, "Photonic bandgap fiber-based surface plasmon resonance sensors," Opt. Express **15**(18), 11413–11426 (2007).

32. G. Emiliyanov, P. E. Høiby, L. H. Pedersen, and O. Bang, "Selective serial multi-antibody biosensing with TOPAS microstructured polymer optical fibers," Sensors (Basel) **13**(3), 3242–3251 (2013).

33. B. Culshaw, "Optical fiber sensor technologies: opportunities and-perhaps-pitfalls," J. Lightwave Technol. **22**(1), 39–50 (2004).

34. Y. Liu, C. Meng, A. P. Zhang, Y. Xiao, H. Yu, and L. Tong, "Compact microfiber Bragg gratings with high-index contrast," Opt. Lett. **36**(16), 3115–3117 (2011).

35. A. Iadicicco, A. Cusano, A. Cutolo, R. Bernini, and M. Giordano, "Thinned fiber Bragg gratings as high sensitivity refractive index sensor," IEEE Photonic. Tech. L. **16**(4), 1149–1151 (2004).

36. W. Liang, Y. Huang, Y. Xu, R. K. Lee, and A. Yariv, "Highly sensitive fiber Bragg grating refractive index sensors," Appl. Phys. Lett. **86**(15), 151122 (2005).

37. B. N. Shivananju, M. Renilkumar, G. R. Prashanth, S. Asokan, and M. M. Varma, "Detection limit of etched fiber Bragg grating sensors," J. Lightwave Technol. **31**(14), 2441–2447 (2013).

38. M. C. Phan Huy, G. Laffont, V. Dewynter, P. Ferdinand, P. Roy, J. L. Auguste, D. Pagnoux, W. Blanc, and B. Dussardier, "Three-hole microstructured optical fiber for efficient fiber Bragg grating refractometer," Opt. Lett. **32**(16), 2390–2392 (2007).

39. A. Candiani, A. Bertucci, S. Giannetti, M. Konstantaki, A. Manicardi, S. Pissadakis, A. Cucinotta, R. Corradini, and S. Selleri, "Label-free DNA biosensor based on a peptide nucleic acid-functionalized microstructured optical fiber-Bragg grating," J. Biomed. Opt. **18**, 057004 (2013).

40. S. C. Warren-Smith and T. M. Monro, "Exposed core microstructured optical fiber Bragg gratings: refractive index sensing," Opt. Express **22**(2), 1480–1489 (2014).

41. R. Kostecki, H. Ebendorff-Heidepriem, S. C. Warren-Smith, and T. M. Monro, "Predicting the drawing conditions for microstructured optical fiber fabrication," Opt. Mater. Express **4**(1), 29–40 (2014).

42. R. Kostecki, H. Ebendorff-Heidepriem, C. Davis, G. McAdam, S. C. Warren-Smith, and T. M. Monro, "Silica exposed-core microstructured optical fibers," Opt. Mater. Express **2**, 1538–1547 (2012).

43. R. Kostecki, H. Ebendorff Heidepriem, S. V. Afshar, G. McAdam, C. Davis, and T. M. Monro, "Novel polymer functionalization method for exposed-core optical fiber," Opt. Mater. Express **4**(8), 1515–1525 (2014).

44. G. Tsiminis, F. Chu, S. C. Warren-Smith, N. A. Spooner, and T. M. Monro, "Identification and quantification of explosives in nanolitre solution volumes by Raman spectroscopy in suspended core optical fibers," Sensors (Basel) **13**(10), 13163–13177 (2013).
45. K. Okamoto, *Fundamentals of Optical Waveguides* (Academic, 2000).
46. J. Wooler, S. R. Sandoghchi, D. Gray, F. Poletti, M. N. Petrovich, N. V. Wheeler, N. K. Baddela, and D. Richardson, "Overcoming the challenges of splicing dissimilar diameter solid-core and hollow-core photonic band gap fibers," Workshop on Specialty Optical Fibers and their Applications (2013).
47. L. Xiao, W. Jin, and M. S. Demokan, "Fusion splicing small-core photonic crystal fibers and single-mode fibers by repeated arc discharges," Opt. Lett. **32**(2), 115–117 (2007).
48. L. Xiao, M. S. Demokan, W. Jin, Y. Wang, and C.-L. Zhao, "Fusion splicing photonic crystal fibers and conventional single-mode fibers: microhole collapse effect," J. Lightwave Technol. **25**(11), 2563–2574 (2007).
49. G. V. Steenberge, P. Geerinck, S. V. Put, J. Watte, H. Ottevaere, H. Thienpont, and P. V. Daele, "Laser cleaving of glass fibers and glass fiber arrays," J. Lightwave Technol. **23**(2), 609–614 (2005).
50. K.-Y. Chu and A. R. Thompson, "Densities and refractive indices of alcohol-water solutions," J. Chem. Eng. Data **7**(3), 358–360 (1962).
51. Y. Zhang, H. Shibru, K. L. Cooper, and A. Wang, "Miniature fiber-optic multicavity Fabry-Perot interferometric biosensor," Opt. Lett. **30**(9), 1021–1023 (2005).
52. D. W. Kim, Y. Zhang, K. L. Cooper, and A. Wang, "Fibre-optic interferometric immuno-sensor using long period grating," Electron. Lett. **42**(6), 324–325 (2006).

1. Introduction

The advent of microstructured optical fibers (MOFs) has provided significant freedom in designing the optical and physical properties of optical fibers. Fibers can now be fabricated with features such as endlessly single mode guidance [1], air-guiding via the photonic bandgap effect [2], and high numerical aperture double clad structures for fiber lasers [3–5]. To achieve such structures numerous techniques have been developed such as capillary stacking [6], drilling [7, 8], and extrusion [9, 10]. Each technique has its own advantages, for example, capillary stacking can be used to create highly regular periodic structures, drilling can be used to form arbitrarily located circular features, while extrusion has the capacity to form non-circular features [11, 12]. Of particular interest here is the sensing ability of MOFs. It is well known that a portion of the guided modes can propagate within the holes of the fiber. This can be a significant fraction of the guided modes in the case of index-guiding solid-core structures, if the core diameter is sufficiently small [13–18]. Alternatively, close to 100% of the light can propagate within the air-core of photonic bandgap structures [19–21].

MOF sensors have gained particular attention in the literature for absorption and fluorescence based chemical and biological sensing. For example, gas sensing can be achieved by directly measuring the spectral features of an analyte that has been loaded into the MOF holes. For the measurement of chemical species without strong or distinguishable spectral features in the transmission window of silica glass it is common to make use of transduction molecules that provide a fluorescence enhancement (or quenching) upon binding with the target analyte. This has been demonstrated for species including aluminum ions [22], and cadmium and calcium ions [23]. Similarly, MOF biosensors can make use of either absorption [17, 24], fluorescence-based labelling techniques [25–27], or surface plasmon resonance for refractive-index based label free detection [28–31]. Unfortunately, the above methods of biosensing all suffer from negating one of the greatest strengths of the optical fiber sensing, which is the ability to perform significant wavelength division multiplexed measurements. While there are occasional examples of measuring two biomolecules [32], the broadband nature of fluorescence and surface plasmon resonance makes it prohibitive to perform the type of multiplexed assays routinely required in the life sciences.

Fiber Bragg gratings (FBGs) offer a straightforward approach to multiplexed sensing, and they are now used routinely to provide multiplexed temperature and strain measurements [33]. Due to their narrow bandwidth it is possible to perform significantly greater multiplexing than can be achieved on a single fiber with either surface plasmon resonance or fluorescence based biosensing. Refractive-index based sensing using Bragg gratings has focused on the use of micro/nano-fibers (e.g. tapered or etched optical fibers) [34–37] and, to a lesser extent, microstructured optical fiber Bragg gratings [38, 39]. Part of the challenge in

such work is to create a Bragg grating that is highly sensitive to changes outside the fiber core, which generally involves reducing the core diameter, while also allowing for: easy interaction with a liquid analyte, access to the core for Bragg grating inscription, integration with commercial interrogation equipment, and physical robustness for real-world applications.

In this work we advance the ability to use a new class of optical fiber, termed the exposed-core microstructured optical fiber (EC-MOF), by demonstrating how they can be inscribed with Bragg gratings for biosensing applications. Compared to an unclad micro/nano-fiber, this class of fiber provides the physical robustness of a standard fiber, while allowing a portion of the small, sensitive core to be externally accessible along its length for both Bragg grating inscription and ease of interacting with external analytes. Previously, we have reported the fabrication of Bragg gratings in a large core (12.5 μm) EC-MOF, which yielded a modest sensitivity averaging 1.7 nm/RIU over the refractive index range of 1.333 (water) to 1.377 (isopropanol) [40].

Here we investigate the fabrication, splicing, and Bragg grating inscription of smaller core EC-MOFs and demonstrate both experimentally and theoretically that smaller core fibers yield significantly higher sensitivity to changes in refractive index. In particular, we demonstrate experimentally a four-fold increase in sensitivity by using a 7.5 μm core diameter EC-MOF and a sixty-fold increase for a 2.7 μm core diameter fiber. The intermediate core size provides a good compromise between sensitivity and ease of use (e.g. splicing), and is demonstrated to be sufficiently sensitive to measure polyelectrolyte deposition, an important first step in developing a label-free biosensor.

2. Cross-sectional structure: fiber fabrication

The fabrication of microstructured optical fibers is generally a two-step technique [6]. First a preform is fabricated that has a macroscopic structure that closely resembles the desired fiber geometry. Some deformation of the structure will occur during fiber drawing depending on the draw parameters and effects related to surface tension and material viscosity. Secondly, the preform is drawn into fiber using a draw tower, where control of parameters such as temperature, internal pressurization, and feed and draw speeds allow some degree of fine-tuning of the final geometry. In some cases it is necessary to introduce an additional step where the preform is canned and then sleeved before finally drawing into fiber. This can allow for a reduction in size of the final features of the fiber, such as enabling the production of sub-micron core sizes [10].

2.1 Fiber preform

In this work we have used ultrasonic drilling and milling or cutting to prepare the preform. While the details of this fabrication process have been detailed elsewhere [41, 42], here we show the versatility of this technique to develop a range of different structures. The preforms were fabricated by first ultrasonic drilling three holes (2.8 mm in this work) into either 12 mm or 20 mm F300HQ (Heraeus) silica rods in an equilateral triangle pattern [Fig. 1]. This can either be done centrally in the preform [Figs. 1(a) and 1(c)] or offset from the center [Fig. 1(b)]. To create an exposed-core, the preform can either be milled [Fig. 1(b)] or cut with a diamond blade [Fig. 1(c)].
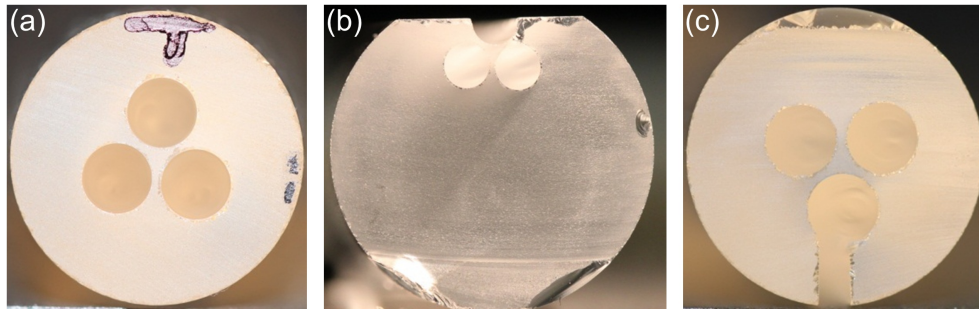
Fig. 1. Preforms demonstrating the various structures that can be utilized for exposed-core fiber fabrication. (a) Drilling, (b) milling, and (c) cutting. The diameter of the preforms are (a) 12 mm, (b) 12 mm, and (c) 20 mm.

2.2 Fiber drawing

The preforms were drawn into fiber using a 6 m tall drawing tower with a graphite resistance furnace and positive internal pressure. Detailed drawing conditions for the fibers in Figs. 2(a) and 2(d) can be found in [42] and [41], respectively. For both fibers in Figs. 2(b) and 2(c) the conditions used were: a draw temperature of 1976°C, a preform feed rate of 1.0 mm/min, and an internal pressure of 1100 Pa. Four different designs of EC-MOF were fabricated [Fig. 2] with different core diameters (12.5 µm, 7.5 µm, 9.3 µm, and 2.7 µm) and varying core accessibility. That is, the open wedge that exposes the core varies from open [Figs. 2(a) and 2(b)] to a more closed form [Figs. 2(c) and 2(d)].
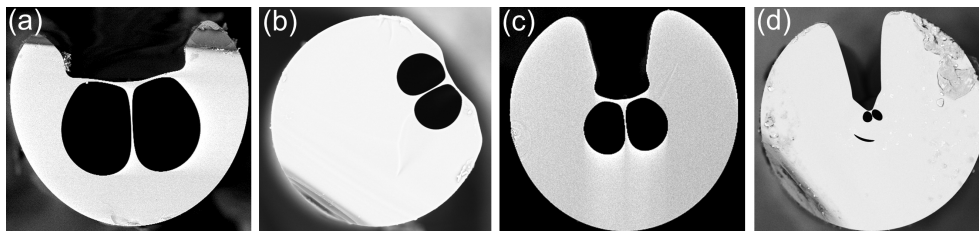
Fig. 2. Scanning electron images (SEMs) of the EC-MOFs that have been fabricated. The fibers have effective core diameters of (a) 12.5 µm [42], (b) 9.3 µm, (c) 7.5 µm [43], and (d) 2.7 µm [41]. The outer diameters at the maximum point of the fibers are (a) 200 µm, (b) 200 µm, (c) 160 µm, and (d) 200 µm.

2.3 Splicing to conventional single mode fiber: theory

One of the most important practical considerations when using EC-MOFs is the ability to splice such fibers to conventional single mode fiber (SMF). This both improves the coupling stability into the EC-MOF and allows for easier integration with commercial interrogation equipment.

One of the first considerations is matching the mode size (e.g. mode field diameter) of the single mode fiber with the EC-MOF. Thus, we have calculated the splice loss when coupling from the SMF into the fundamental mode of the EC-MOFs. Note that the EC-MOFs are multimode and thus the total coupling efficiency can be greater than that calculated here. Depending on the application, coupling into higher order modes may, or may not, be desirable and could be considered in future work. For the purposes of Bragg grating based sensing, we have observed experimentally that coupling into the fundamental mode provides the most stable signal as the Bragg grating peak associated with the fundamental mode is spectrally isolated from reflections associated with higher order modes, which tend to overlap each other.

The splice loss has been calculated using Eq. (1) [44].

$$\alpha_{SL} = -10 \log_{10} \left[\left| \frac{2(\int \vec{e}_S \times \vec{h}_E \cdot \vec{z} dA)(\int \vec{e}_E \times \vec{h}_S \cdot \vec{z} dA)}{\int\limits_{\infty} \vec{e}_S \times \vec{h}_E \cdot \vec{z} dA + \int\limits_{\infty} \vec{e}_E \times \vec{h}_S \cdot \vec{z} dA} \right|^2 \right] \qquad (1)$$

In Eq. (1), $\vec{e}$ and $\vec{h}$ are the electric and magnetic fields of the fundamental modes of the single-mode (S) and exposed-core (E) fibers, respectively, α_{SL} is the splice loss (in dB), and $\vec{z}$ is a unit vector along the fiber axis.

The electric and magnetic modes have been calculated using an analytic model for the step-index fiber [45] and the modes of the EC-MOFs where calculated by importing SEM images into COMSOL v3.4, as has been done previously for the EC-MOF in Fig. 2(a) [40]. The splice losses for the fibers shown in Fig. 2 are shown in Table 1, along with a summary of the fiber properties. Four commercially available types of single mode fiber are shown and include SMF28, 980HP, UHNA1, UHNA4 (Nufern), the core diameter (CD) and mode field diameter (MFD) are also shown. All calculations were performed at a wavelength of 1550 nm. Note that random polarization in the single mode fiber has been assumed and thus the values in Table 1 assume the total coupling from unpolarized light in the single mode fiber into both polarizations of the fundamental mode of the EC-MOF.

Table 1. Splice loss from SMF into EC-MOF

EC-MOF Description	D-shaped	Offset	Wedged	Small-core
Figure	2(a)	2(b)	2(c)	2(d)
Exposed-core fiber characteristics (µm)				
Outer diameter	200	200	160	200
Core diameter	12.5	9.3	7.5	2.7
Wedge angle (°)	113	158	50	33
MFD[a] (polarization 1)	8.62	6.75	5.18	2.19
MFD[a] (polarization 2)	8.26	6.56	5.07	2.72
Calculated splice loss for SMF to EC-MOF (dB)				
SMF28[b] (MFD = 10.3 µm) (CD = 9.2 µm)	0.49	1.22	2.48	8.28
980HP[b] (MFD = 6.19 µm) (CD = 3.6 µm)	0.55	0.44	0.70	4.07
UHNA1[b] (MFD = 4.51 µm) (CD = 2.5 µm)	1.18	0.66	0.45	2.33
UHNA4[b] (MFD = 3.48 µm) (CD = 2.2 µm)	2.27	1.32	0.65	1.27

[a]Numerically calculated value.
[b]Mode field diameter, core diameter, and refractive index data from: http://www.nufern.com/

It can be seen from Table 1 that the choice of single mode fiber can be used to optimize the splice loss, with values below 0.5 dB being possible for all fiber designs, except for the smallest core (2.7 µm) fiber considered here, where the minimum splice loss is 1.27 dB. If smaller splice losses are required in practice, then intermediate fibers or tapers would need to be introduced. These results serve as a useful guide for single mode fiber selection, noting that experimentally other factors become significant, most notably structural deformation of the EC-MOF upon heating, and alignment tolerances of the splicer.

2.4 Splicing to conventional single mode fiber: experimental

It was previously shown that the 12.5 µm exposed-core fiber can be spliced to conventional single mode fiber (SMF28e), with a loss as low as 3 dB [40]. In this work we have

concentrated our efforts on splicing to the wedged (7.5 µm core) EC-MOF using an arc splicer (Fujikura FSM-100P), motivated by the success in writing Bragg gratings into this fiber (see Sec. 3).

A number of techniques have been presented for optimizing splicing to MOFs, including reducing arc current, offsetting the arc position, and using a tack-sweep-pulse technique [46–48]. In this work we have spliced EC-MOF to SMF with only a small deviation from standard SMF splicing by optimizing the arc current, arc time, and overlap (the distance the two fibers are pushed together). The transmitted power obtained from the EC-MOF after splicing is shown in Fig. 3 relative to the transmitted power when butt-coupling at a gap of 5 µm. The results show that the splice can be optimized by decreasing the arc current while increasing the arc time. Transmission consistently better than the butt-coupled power was found for a current of 4.0 mA below the standard SMF setting, for a duration of 3.0 s (standard is 2.0 s). The results of Fig. 3 also show that an overlap of 2 µm below the standard overlap (10 µm) provides optimal splicing. These results are consistent with trying to minimize damage to the structured fiber. In future, further refinements could be made by further decreasing arc current and increasing arc discharge time. However, the optimized settings found here have proven to provide sufficient coupling for Bragg grating sensor measurements while still being physically robust enough for handling within a laboratory setting.
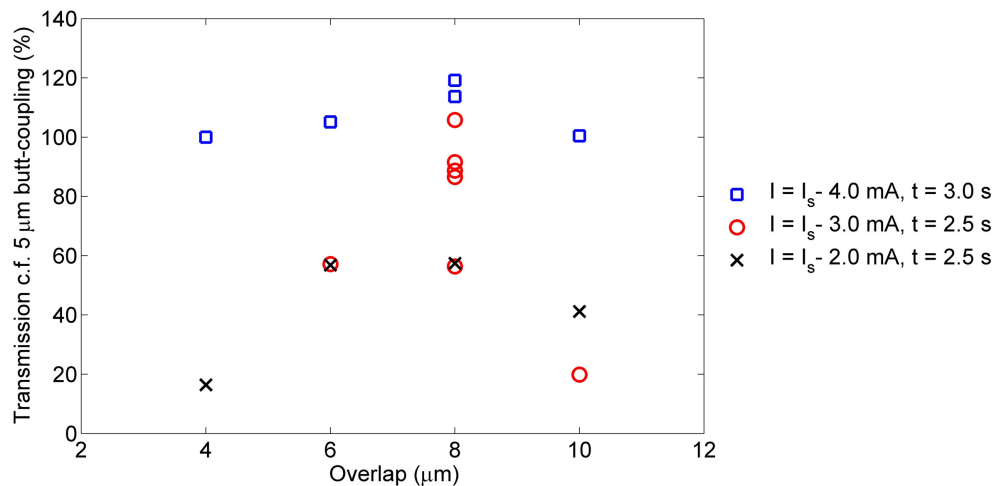
Fig. 3. Transmitted power through 7.5 µm core diameter EC-MOF spliced to 980HP single mode fiber. Power is relative to butt-coupled transmission with a 5 µm offset. I_s is the standard current used by the arc splicer after calibration, approximately 16.5 mA.

The splicing parameters determined in Fig. 3 are quite specific for the particular geometry of the microstructured fiber, the wedged (7.5 µm core) fiber in this case. For example, when splicing to the small-core (2.7 µm) EC-MOF is it much more likely that the fiber structure is damaged, particularly the fine struts. The best splice loss achieved for the small-core EC-MOF was approximately 16.5 dB (settings were: $I = I_s - 3.0$ mA, $t = 2.0$ s, overlap = 5 µm). For the offset (9.3 µm) core it was found to be difficult to produce a flat cleave using traditional crack cleaving approaches, particularly near the core region. In future this might be solved by utilizing laser cleaving techniques [49], but is beyond the scope of this study.

3. Longitudinal structure: fiber Bragg gratings

In previous work Bragg gratings were written into the D-shaped (12.5 µm core) EC-MOF [Fig. 1(a)] [40]. Briefly, the gratings were written by focusing a 200 nJ, 200 Hz, 800 nm femtosecond laser (Hurricane Ti:sapphire) pulses using a 50X long working distance

microscope objective while translating the fiber along its axis to yield 20 mm long, 1060 nm pitch second order Bragg gratings at 1550 nm.

Writing such structures into EC-MOFs that have an open and accessible core, such as the D-shaped and Offset geometries [Figs. 2(a) and 2(b)], is readily achieved as the focused beam is not obstructed by material. Of particular interest here is the ability to write gratings into exposed-core fiber structures that pose obstructions to the focused femto-second laser beam. For the wedged (7.5 μm core) fiber, which has a wedge angle of 50°, it was found that a femto-second laser pulse energy of 250 nJ was required in order to produce damage spots on the core. This level of obstruction from the fiber geometry does not have a significant impact on the focal point of the femtosecond laser, as shown by the grating produced in Figs. 4(a) and 4(b). Note that the settings used for this grating writing were the same as used for the D-shaped fiber, except that the pulse frequency was reduced from 200 Hz to 100 Hz in order to reduce the speed of the translation stage and improve stability. The length of the Bragg gratings were also varied, between 1 to 20 mm, with longer lengths being required for larger core diameter fibers due to the reduced overlap between the femtosecond laser ablation features and the propagating mode.

The small-core (2.7 μm) fiber with a wedge angle of 33° required a pulse energy of 440 nJ before any ablation occurred. Unfortunately, the ablation occurred at the thin struts holding the core (approximately 1 μm thick) rather than on the surface of the core, as shown in Fig. 4(c). Thus, laser ablation gratings could not be formed on this fiber without significant damage to the fiber structure. For this reason the sensing results that follow have primarily utilized the 7.5 μm core fiber. Gratings were also written into the offset (9.2 μm core) fiber. However, the difficulty found in cleaving and splicing the fiber meant that it could not be used for liquid-based experiments.
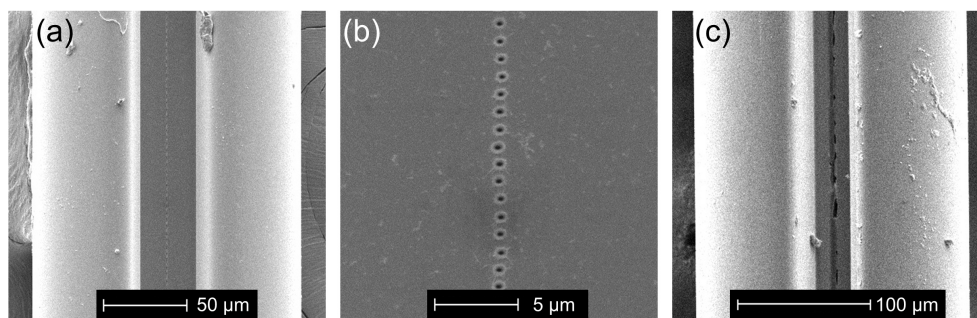
Fig. 4. (a) Femtosecond laser written Bragg gratings in the wedged (7.5 μm core) fiber, written directly on its core. (b) Magnified image of (a). Damage caused on the core of the small core (2.7 μm core) fiber, which results from aberrations to the femtosecond laser beam due to the narrow fiber geometry in combination with the thin struts that support the fiber core.

4. Sensitivity of FBGs to bulk refractive index

The fibers in Figs. 2(a), 2(c), and 2(d) have been characterized for their refractive index sensing performance. These fibers were first spliced to conventional single mode fiber (see Sec. 2.4 and [40]) and the Bragg reflections measured using an Optical Sensor Interrogator (OSI, National Instruments PXIe-4844). In all measurements where liquids were measured, the far end of the fiber was sealed using the arc splicer to prevent liquid ingress into the MOF holes. The spliced EC-MOF fibers were immersed into refractive index solutions by vertically holding the fibers and inserting into sealed Pasteur pipettes containing isopropanol in water solutions, with the refractive index calculated based on measurements performed by Chu *et al.* [50]. The reflection spectra contains multiple peaks due to higher order modes, however, the narrowest and strongest peak is generally the longest wavelength peak, which corresponds to coupling from the forward to the backward propagating fundamental mode. The spectra

obtained for the fundamental mode reflection of the wedged (7.5 µm core) fiber are shown in Fig. 5. As expected, the Bragg wavelength increases as the external refractive index is increased.
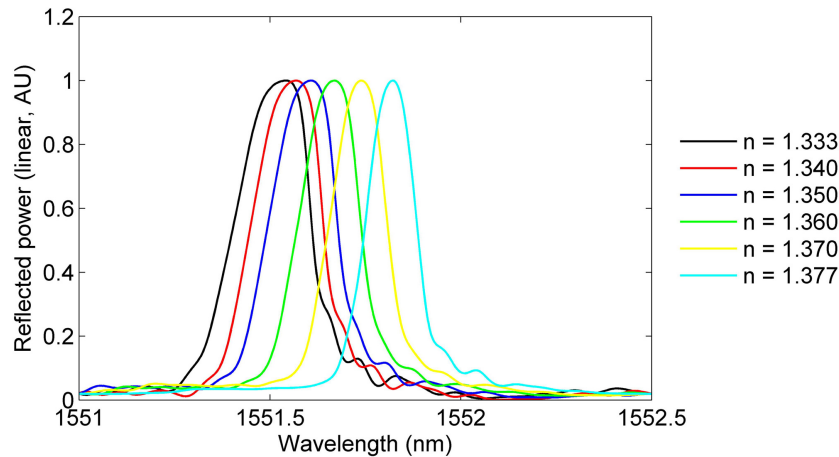
Fig. 5. The reflected Bragg grating spectra when the EC-MOF with a core diameter of 7.5 µm [Fig. 2(c)] was immersed in different refractive index liquids. The refractive index was varied by dissolving isopropanol in water. Only the longest wavelength is shown, which corresponds to the fundamental mode.

To compare the sensitivity of the various core diameters, both theoretically and experimentally, the fundamental mode Bragg wavelengths for refractive index solutions ranging from 1.0 (air) to 1.4 are shown in Fig. 6. The theoretical curves were generated by importing SEM images into COMSOL v3.4, as was done for the coupling efficiency, and varying the refractive index of the exposed region of the fiber. The Bragg grating pitch (Λ) was varied slightly in order to achieve the best fit with experiment (Λ = 1080 nm + (a) 1.03 nm, (b) 1.22 nm, (c) 1.00 nm). The experimental points for Fig. 6(a) were from [40] and those for Fig. 6(b) were obtained from Fig. 5. For the small-core (2.7 µm) EC-MOF a 2 mm long grating was used. In this case a particularly weak grating (< 1 dB) formed, due to a combination of the damage during the grating writing, high splice loss, and a high background reflection that resulted from the splice. Thus, the experimental results in Fig. 6(c) consist of only two data points, which were in air (n = 1.0) and water (n = 1.33). Attempts to measure the grating position for higher index solutions were unsuccessful, indicating a substantial challenge in using such small core fibers for measuring refractive index solutions using a Bragg grating approach.

The wedged (7.5 µm core) fiber grating shifted by approximately 0.28 nm over the refractive index range from 1.333 (water) to 1.377 (isopropanol). This corresponds to an average sensitivity over this range of 6.4 nm/RIU. This is a significant improvement compared to a shift of only 0.076 nm (1.7 nm/RIU) that was measured over the same range for the D-shaped (12.5 µm core) fiber [40]. Despite difficulties in coupling, the sensitivity of the small-core (2.7 µm) fiber, as shown by the numerically calculated curve and two closely fitting experimental points in Fig. 6(c), is much higher at 101 nm/RIU over the same range.
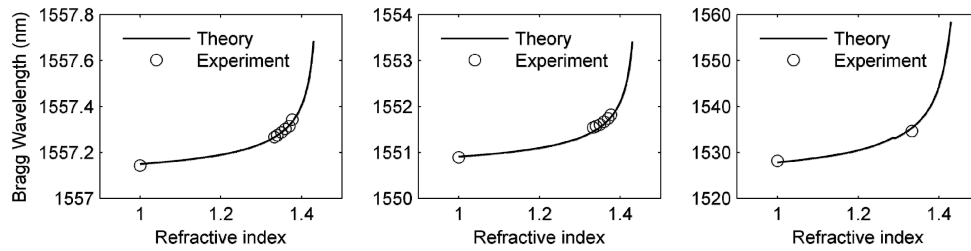
Fig. 6. Refractive index sensitivity curves for the (a) D-shaped (12.5 μm core), (b) wedged (7.5 μm core), and (c) small-core (2.7 μm) EC-MOFs, both theoretical (lines) and experimental (circles). The grating lengths used were (a) 20 mm, (b) 10 mm, and (c) 2 mm.

5. Characterizing the polyelectrolyte layer deposition

For biological sensing with silica fibers it is often desirable to modify the functional groups present on the glass surface in order to optimize binding of specific biological material. One versatile technique is to coat the surface with polyelectrolytes [13, 22, 51, 52]. These coatings are formed by stacking alternating charged layers of electrostatic polymers and can provide a host of functional groups on the surface such as amine or carboxylic acid groups. By using a technique that is capable of measuring refractive index on the surface it is possible not only to measure the layers being deposited but to also use this as a calibration curve for subsequent biological binding. Thus, measuring polyelectrolyte layer deposition is an important first step in developing this class of biosensor. Here we have coated the wedged (7.5 μm) core EC-MOF with two bi-layers of polyelectrolytes to demonstrate the potential use of the FBG written on EC-MOF for biosensing applications.

In this experiment the optical sensor interrogator was connected to an in-line polarizer and then polarization maintaining fiber (Nufern, PM980-XP). The polarization maintaining fiber was then spliced to the EC-MOF using the optimized conditions from Sec. 2.4. Fixing the polarization in this manner prevents the reflected spectra from being modified if the single mode fiber cable is moved during the course of the experiment. The Bragg grating used was 10 mm long with a second order reflection at approximately 1550 nm while the total length of the EC-MOF was 100 mm long with the grating in the center. The entire length of the EC-MOF was then inserted into a flow cell, which consisted of a silica capillary (approx. 1 mm inner diameter (ID)) with an inlet capillary (150 μm ID) that was connected to a syringe pump (Nanojet) and another outlet capillary (150 μm ID). In this experiment the syringe pump was set at 0.1 mL/min for all steps. Prior to polyelectrolyte deposition the flow cell, containing the EC-MOF, was rinsed with water (Millipore) for 50 minutes. Solutions of 2 mg/ml Poly(sodium styrene sulphonate) (PSS) and poly(allylamine hydrochloride) (PAH) in 1 M NaCl were then passed through the flow cell for 20 minutes alternatively, with a 30 minute minimum water rinsing time between each step.

The shift in the Bragg grating reflection associated with each polyelectrolyte layer is shown in Fig. 7(a). These values correspond to the measurements recorded once per minute during the last 10 minutes of the rinsing phase, after the signal had reached equilibrium. The shift was recorded in the rinsing phase rather than the coating phase as it is important to measure in the same refractive index solution (water in this case). The error bars in Fig. 7(a) refer to the standard deviation of the 10 spectra recorded over the 10 minutes of measurement. The shift in Bragg reflection was determined by calculating the weighted mean of the longest reflection peak (the fundamental mode reflection) as indicated in Fig. 7(b). The weighted mean of the Bragg reflection, λ_w, was calculated using Eq. (2).

$$\lambda_w = \frac{\int \lambda I_B(\lambda) d\lambda}{\int I_B(\lambda) d\lambda} \qquad (2)$$

In Eq. (2), the integrals were calculated over the wavelength range from $\lambda = 1551.4$ nm to $\lambda = 1552.0$ nm and I_B is the linear intensity of the Bragg reflection.

This allows the wavelength resolution to be improved over the 4 pm values provided by the instrumentation. The positive shift observed in Fig. 7(a) is consistent with polyelectrolyte layer deposition, which increases the refractive index on the surface of glass. Thus, we have demonstrated that the Bragg grating sensor formed from the 7.5 μm core EC-MOF is sufficiently sensitive to characterize the growth of polyelectrolyte layer deposition. This serves as a useful step towards turning an EC-MOF into a biological sensor as it is both sensitive and has the functional groups required (in this case amine groups) to allow for biological binding.
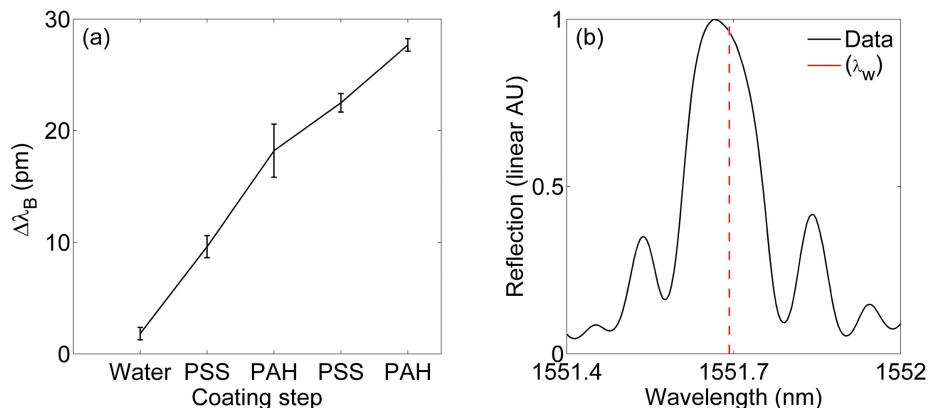
Fig. 7. (a) Shift in the Bragg wavelength as each polyelectrolyte coating is added. (b) Example spectra indicating the position of the weighted mean (λ_w), which was used to determine the values in (a).

6. Discussion and conclusions

We have demonstrated experimentally that reducing the core diameter of exposed-core microstructured optical fibers can improve the sensitivity for refractive index sensing using Bragg gratings, which is due to an increase in the portion of the guided mode that propagates externally to the optical fiber glass. By reducing the core diameter to 7.5 μm the experimentally measured sensitivity is increased to 6.4 nm/RIU over the refractive index range of 1.333 to 1.377, compared to the previously demonstrated result of 1.7 nm/RIU using a 12.5 μm core fiber. Theoretical modelling based on SEM images of fabricated fibers predict that sensitivities as high as 101 nm/RIU should be achievable using a 2.7 μm core fiber. While the sensitivity is unlikely to outperform techniques such as surface plasmon resonance, the capability of Bragg grating sensors to be multiplexed and operate in reflection mode makes them particularly attractive for performing label-free immunoassays in *in-vivo* biosensing applications.

The increase in sensitivity of smaller core fibers must then be traded against the practicality of these fibers. In particular, the ability to cleave and splice the fibers to conventional single mode fiber is critical in accessing the viability of the fiber to be used for sensing. The wedged (7.5 μm core) fiber was found to splice readily to SMF, and optimized settings have allowed for high transmission efficiencies. On the other hand, fibers that have an offset, or non-central, core or fibers with small cores were found to be challenging to splice with high efficiency or repeatability, despite low theoretical losses. This is likely attributed to the difficulty in obtaining a flat cleave at the core and struts, and thus advanced techniques such as laser cleaving may be required.

The next critical factor to consider is the ability to write gratings onto the core of these fibers. Open structures with unimpeded access to the core have been found to be well suited

to writing femtosecond laser ablated gratings. It is also possible to write gratings if the exposed section of the fiber is formed from a narrower slot, up to a point where the wedge is significantly obstructing the beam. In future, alternative techniques such as oil immersion or choice of a different focusing lens could be used to write gratings into narrower features.

Of the fibers considered here, the 7.5 μm exposed-core microstructured optical fiber has been found to be the best compromise between practicality and sensitivity when fabricating a refractive index sensor. In future it would be ideal to fabricate fibers with a similar geometry but with core diameters in the range of 4-5 μm that sit in the region between single-step and two-step preform fabrication using currently available facilities. Such fibers should exhibit improved sensitivity, while still being practical to handle, and thus allow for the direct measurement of biomolecule binding.

Acknowledgments

Paper 8.

Fiber Optic Approach for Detecting Corrosion

Roman Kostecki[a,b], Heike Ebendorff-Heidepriem[a,b], Claire Davis[c], Grant McAdam[c], Tianyu Wang[b], and Tanya M. Monro[a,b,d]

[a]ARC Centre of Excellence for Nanoscale BioPhotonics, The University of Adelaide, Adelaide, SA 5005, Australia
[b]Institute for Photonics and Advanced Sensing and School of Physical Sciences, The University of Adelaide, Adelaide, SA 5005, Australia
[c]Defence Science and Technology Group, Fishermans Bend, Victoria, Australia
[d]University of South Australia, Adelaide, SA 5001, Australia

ABSTRACT

Corrosion is a multi-billion dollar problem faced by industry. The ability to monitor the hidden metallic structure of an aircraft for corrosion could result in greater availability of existing aircraft fleets. Silica exposed-core microstructured optical fiber sensors are inherently suited towards this application, as they are extremely lightweight, robust, and suitable both for distributed measurements and for embedding in otherwise inaccessible corrosion-prone areas. By functionalizing the fiber with chemosensors sensitive to corrosion by-products, we demonstrate in-situ kinetic measurements of accelerated corrosion in simulated aluminum aircraft joints.

Keywords: Corrosion, Sensors, Smart structures, Nondestructive evaluation, Structural health monitoring, Fiber optic sensors, Microstructured fibers, Nanostructure fabrication, Optical sensing and sensors, Thin film devices and applications.

1. INTRODUCTION

Corrosion remains a multi-billion dollar problem in industry.[1,2] An increasing recognition of the potential cost savings derived from early warning of corrosion problems has led to an increasing focus on corrosion monitoring as part of a preventive and predictive maintenance regime. The high acquisition costs associated with modern military and civilian aircraft coupled with tighter budgets has resulted in the need for greater utilization of existing aircraft fleets. Typically, military aircraft have a planned life-of-type of 25–30 years. In Australia, in many cases, almost twice this time has been achieved before the aircraft is retired.[3] For civilian aircraft flying today, approximately 20% are considered to be aging, and as that number increases so does the need for heightened fleet monitoring by airlines and manufacturers[5] combined with intense focus and surveillance of these activities by regulatory agencies.[6]

Send correspondence to Roman Kostecki: roman.kostecki@adelaide.edu.au
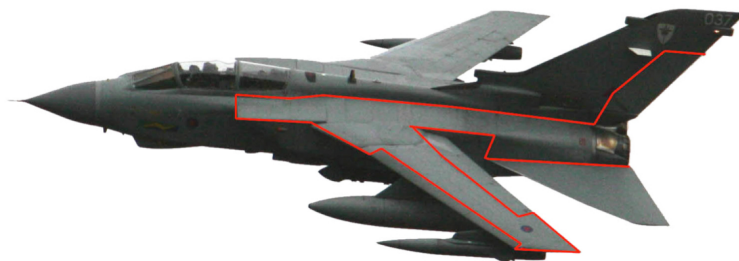
Figure 1: The concept of aircraft fitted with a distributed optical fiber sensor in ▌ – red, from Ref. 4.

With advancing aircraft age there is an increased possibility that protective coatings will break down or be damaged, resulting in exposure of the base material to the environment and an increased possibility of corrosion.[5] The operational loads on the structure also increase the possibility of structural fatigue damage, which constitutes one of the most significant safety concerns due to the potential for corrosion to reduce the fatigue life of the aircraft.[7] While attempts are made to prevent and reduce the effects of corrosion, in practice it is impossible to completely avoid. It is therefore essential that corrosion processes are monitored so that the inspection intervals are optimized and repair time and costs are minimized.

The detection of corrosion is particularly challenging in the sub-structure of an aircraft, such as lap joints, stiffeners and under sealant beads, since access to these areas usually requires time consuming and therefore costly disassembly.[3] Such areas are recognized as being particularly prone to corrosion, due to the possibility of creating a micro-environment within the crevices between the plates, accelerating the corrosion process.[7] Current non-destructive inspection methods, typically based on the use of a hand held ultrasonic probe, require a 5–10% section loss for corrosion to be reliably detected, at which stage the damage may be too severe to repair, and so the component often needs to be replaced.[3] Clearly a more proactive approach is needed to detect the initial onset of corrosion within these difficult to inspect areas.

Because corrosion can be very localized but can occur anywhere across a large structure, it is a broad area problem which requires a detection and/or monitoring system with the potential for distributed measurements, alerting the operator to the onset and location of corrosion. Optical fiber based sensors offer several inherent advantages when applied to structural platforms; they are immune to electro magnetic interference, easily net-worked, inherently suited to distributed sensing, and are typically in the order of only a few hundred microns in diameter making them very lightweight and suitable for embedment in inaccessible corrosion-prone areas. A number of fiber optic systems have been developed for single point corrosion monitoring, but only a few of these systems have exploited the capability of optical fibers for distributed measurements. Many of the aircraft fuselage components are fabricated from aluminum-based alloys, hence aluminium ions (Al^{3+}) are of particular interest because they are not only an indicator of the onset of corrosion,[3] but also have the potential to be an environmental hazard.[8] The concept of an aircraft fitted with a distributed optical fiber sensor is shown in Fig. 1.

2. PRINCIPLES AND BACKGROUND

Initial work on the fluorometric detection of Al^{3+} as an indicator of aluminum corrosion was conducted by the Australian Defence Science and Technology Group (DSTG), part of Australia's Department of Defence, in conjunction with Monash University in the early 2000s. These experiments focussed on the use of conventional large core multi-mode fibers (MMFs). As part of this research a range of different permeable polymer systems, doped with a compound that fluoresces in the presence of Al^{3+} were evaluated. The most promising of these, a flexible polyurethane the main constituent of which is a polyether,[3] was shown by McAdam *et al.* in 2005. The polymer was doped with a fluorescent compound, 8-HQ, which reacts with Al^{3+}. 8-HQ is an aromatic nitrogen compound characterized by a double-ring structure, containing a benzene fused to pyridine at two
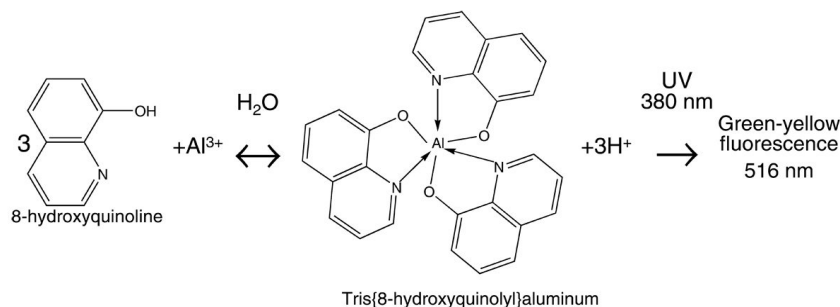
Figure 2: Reaction sequence for 8-HQ with Al^{3+} from Ref. 3.

adjacent carbon atoms, with the formula C_9H_7NO (Fig. 2(left)). This compound has a hydrogen atom that is replaceable by a metal, and gains its fluorescent nature by forming a dative bond between the metal and heterocyclic nitrogen atom, enabling formation of a five-membered chelate ring with Al^{3+}. It is a bidentate ligand which forms a stable multi-ligand complex with Al^{3+}.[9] A 3+ charge metal ion, as for the Al^{3+} case, forms a tris[8-hydroxyquinoline]metal(III), as shown in Fig. 2. The rigid octahedral complex that forms between three 8-HQ molecules and Al^{3+} fluoresces strongly at 516 nm (max) when excited by ultraviolet (UV) light in the range 360 to 390 nm,[10] although it has also been shown to work effectively when using a 405 nm excitation light source.[11]

The doped polymer was dip-coated onto the distal end of a MMF to create a sensing polymer bead at the fiber tip and placed into the channel of a simulated lap joint which was subjected to accelerated corrosion using a salt spray chamber. The measured back fluorescence from this optical fiber tip sensor increased as a function time, indicating an increasing presence of Al^{3+} due to progressing aluminum corrosion.[3] For this case, where the bead is attached to the end of an optical fiber, there are fewer physical constraints on the properties of the permeable coating used to contain the fluorescent species compared to a distributed sensor. Ideally, it would be preferable to create sensitivity to Al^{3+} by coating the fiber along the length, thus creating a distributed sensor rather than a local (point) sensor. In order to make distributed measurements the fraction of guided light propagating along the outside of the core needs to be accessed, which requires careful tailoring of the cladding refractive index and thickness to optimize the light/fluorophore interaction.

The concept of distributed detection of fluorescence from 8-HQ complex with Al^{3+} in solution was demonstrated by Sinchenko et al.[11] By using a large solid core (200 μm) MMF made from silica with the cladding removed, it was shown that optical time-domain reflectometry (OTDR) could be used to not only detect the presence of Al^{3+} in solution but also locate the position of this fluorescence 80 m along the fibers length. Figure 3(a) shows the setup, where photon counts were accumulated by time-gated electronics with a length resolution along the fiber of $\sim$0.2 m. The signal detected is shown in Fig. 3(b), which represents the time domain response of the detection system when the de-clad fiber section was immersed in a 5×10^{-3} M solution of the 8-HQ–Al^{3+} complex. This experiment, described in detail in Ref. 11, demonstrated the that distributed fluorescence detection of cations, and in particular Al^{3+}, is possible. The power fraction (PF) of guided light propagating along the outside of the glass core was able to be used to excite the 8-HQ complex and the fraction of emitted florescence recaptured by the fiber core could be measured by time-gated electronics. However, using such a large core MMF meant that less than 0.1% of the total optical power propagates outside the core, making it impractical

(a)   (b)
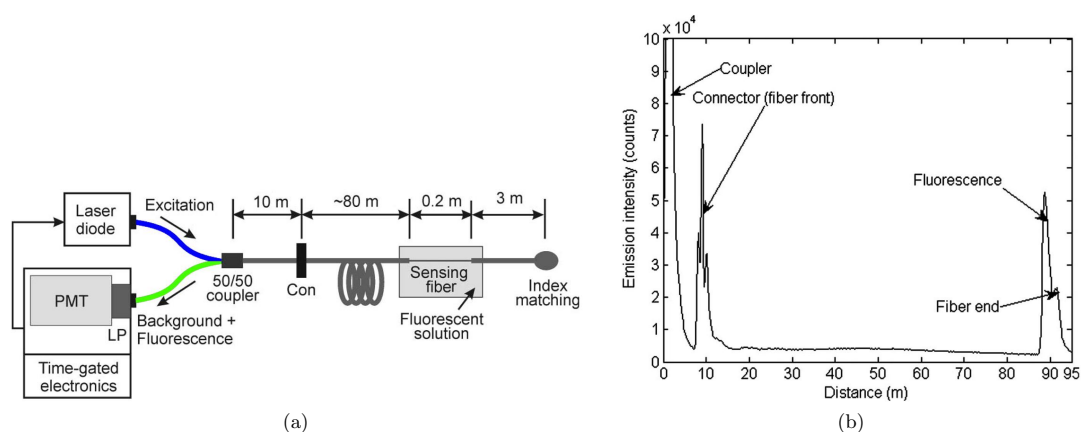
Figure 3: (a) OTDR setup for distributed measurements of Al^{3+} (LP, long pass; Con, connector) in solution using a MMF silica fiber with 200 μm core; with which the (b) time of flight resolved fluorescence response of the 8-HQ complex within solution corresponds to detection position along the fiber.[11]

for applications requiring low detection limits.[12] Nevertheless, it is possible to increase this power fraction by reducing the core diameter.

Figure 4 shows a theoretical estimate[13] of the PF outside a circular silica core, for core diameters from 460 nm to 10 μm. The excitation and fluorescence wavelengths used for this study were 375 nm and 516 nm respectively, being the excitation and fluorescence wavelengths of the 8-HQ–Al^{3+} complex, and for the region surrounding the silica core a refractive index of water ($n = 1.33$) was used. As a first approximation, the coupled incident beam waist was set at the same diameter as the core, which is reasonable for micron scale (> 1 μm) core diameters. The total PF of all propagating modes excited by the incident beam as a function of the core diameter is shown by the red curve in Fig. 4(a). This PF curve shows that for core diameters less than 4 μm the fraction of power available for fluorophore excitation starts to significantly increase, being 0.3 and 2.1% at 4 and 2 μm diameters respectively. For core sizes below 1 μm in diameter there is another significant PF increase, where the calculated values are 2.8 and 17% at 1 μm and 460 nm diameters respectively. The corresponding fluorescence capture fraction (FCF) is shown by the blue curve in Fig. 4(a). The FCF is defined as the fraction of fluorescent photons that are coupled to the guided mode(s) of the fiber. Although the total PF was used to calculate the FCF, for simplicity only the FCF into the fundamental mode (HE11) of the fiber was considered for the special case of an attenuation-free fiber of infinite length. This FCF curve varies from a minimum of 1.1% to a maximum of 1.7%.

The intensity of fluorescence that is measured from the backward propagating modes of the fiber is the result of both the incident excitation power and the number of fluorescence photons recaptured. These quantities can be brought together to provide a better understanding of the overall performance of the sensor as a function of the core diameter by defining a figure of merit (FOM), FOM=(PF)·(FCF).[12] This FOM is shown in Fig. 4(b), where we observe an order of magnitude increase in sensor performance between the peaks at 8 and 2 μm, and no significant change in performance from 2 to 1 μm. Another factor, which will influence the FOM, is the fiber loss, which increases with smaller core diameters (and therefore greater PF) due to the increased scattering resulting from surface imperfections. Hence, the goal was to create a robust small core fiber which can be placed in situ and be capable of detecting the onset and monitor the progress of corrosion anywhere along its length within the aircraft fuselage.

While glass nano-wires,[14] as shown in Fig. 5(a), provide a way of producing centimeter scale lengths of small cores from conventional fibers, they are fragile and not practical for a distributed sensor needing lengths in the

(a)   (b)
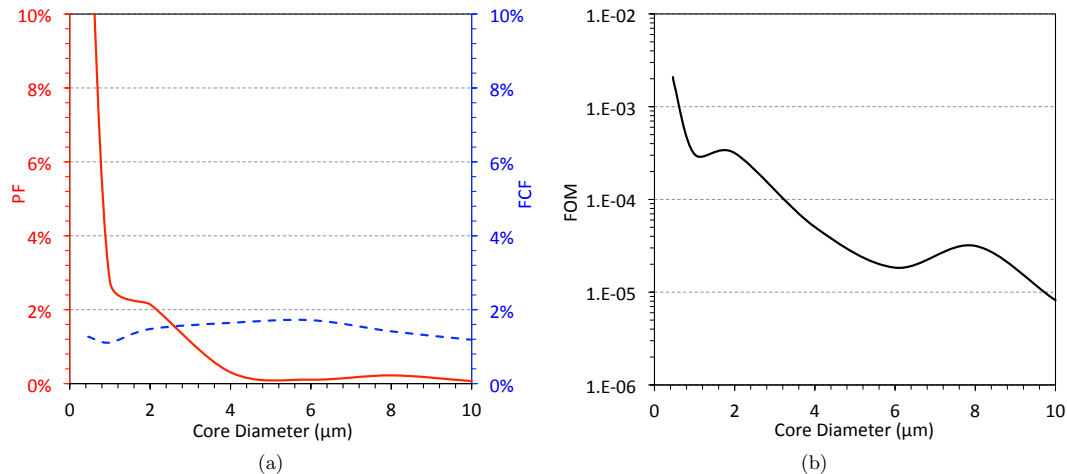
Figure 4: (a) [▊ - Red solid line] Fraction of guided light power propagating outside a silica core as a function of core diameter assuming Gaussian beam excitation, and [▊ - Blue dashed line] the corresponding fluorescence capture fraction into the fundamental mode; and (b) the figure of merit as a combination of both.

order of hundreds of meters. On the other hand, a microstructured optical fiber (MOF)[15] provides a means for obtaining long lengths of uniform micrometre-nanometre scale suspended and protected cores. In particular, the suspended-core MOF (SC-MOF)[16] design, which consists of a small glass core suspended by thin struts inside voids within the fiber, have dramatically improved fluorescence-based fiber sensors by making use of the increased PF provided by the micrometer scale core size and therefore increased sensor performance.[12, 17] Figure 5(b) shows a SC-MOF based on undoped high purity fused silica known as Heraeus Suprasil F300HQ silica (F300HQ), and Fig. 5(c) shows an enlargement of the core and holes region in the centre of the fiber, where the core of the fiber is the small triangular element in the centre of the image (highlighted by the green box), suspended on three thin struts.

While SC-MOFs have provided a highly sensitive sensing platform exploiting the significant fraction of guided power located within the holes,[12, 19–24] the closed structure makes it impossible to use them for distributed sensing applications. To overcome this an exposed-core MOF (EC-MOF) geometry was developed to allow interaction of guided light with the surrounding medium along its length.[25, 26] This was done by effectively opening up one of the voids within the preform before drawing to fiber. This method provides the ability to fabricate EC-MOFs hundreds of meters long with a fixed microstructured cross section. Warren-Smith showed that the EC-MOF has fast response and is capable of real-time sensing anywhere along the fiber length, making this type of fiber ideal for distributed sensing.[26] It was demonstrated that fluorescence emission coupled into the backward modes of a MOF core has higher efficiency compared to the forward modes.[13, 27] This means that fluorescence measurements are enhanced when evaluating the back reflected signal, as shown by the schematic in Fig. 6. Warren-Smith also demonstrated fluorescence based distributed sensing by performing OTDR measurements using EC-MOFs.[28]

Fabrication of these small-core EC-MOFs was a significant milestone in the development of a distributed fiber optic corrosion sensor. For the first time, small core distributed fluorescence measurements became possible,[28] where the increased PF from the guided light propagating outside the small core could be accessed anywhere along its length whilst still being supported by the outside structure. Unfortunately, it was found that the Schott F2 soft glass (F2) material was not suitable for long term use and/or harsh environments,[26, 29] where the loss and deterioration issues associated with the soft glass material precluded their long-term practical use under harsh conditions.[4] To produce a distributed fiber optic corrosion sensor capable of withstanding the intended harsh conditions, fiber materials other then soft glass were investigated. Both polymer and silica have material properties that made them attractive for optical fiber sensing applications.[30, 31] Poly(methyl methacrylate) (PMMA) polymer optical fibers (POFs) have high elastic strain limits, high fracture toughness, and high flexibility in bending, and so initial work was performed to establish the suitability of polymer to create a robust optical fiber based distributed corrosion sensor. It was found that the high attenuation properties and difficulties with splicing, cleaving and coupling made small core size exposed-core POFs sensors challenging.[31–34]

(a)   (b)   (c)
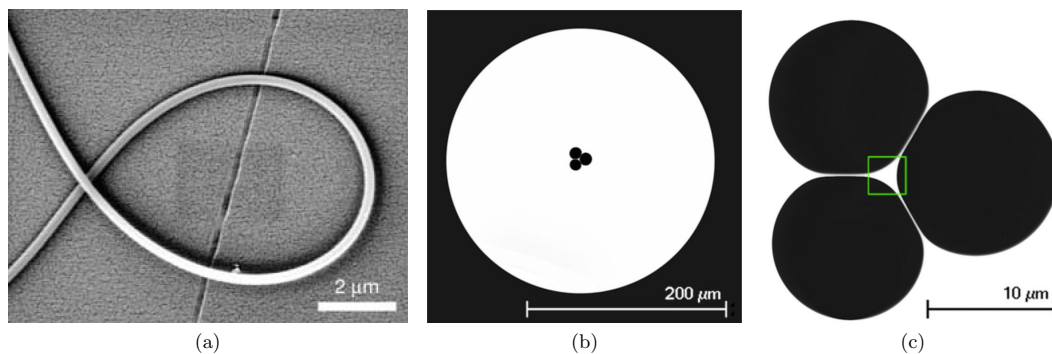
Figure 5: Scanning electron microscope (SEM) cross section images of (a) glass nano-wire from Ref. 14; (b) the silica SC-MOF (polymer coating removed) with an OD of 270 μm; and, (c) an enlarged image of the core and hole region, where the core is highlighted by the ▌ – green box, having an effective diameter of 1.7 μm.[18]

On the other hand, silica is known to be reliable under a range of processing conditions and applications, with relatively better mechanical and thermal stability compared to polymer or soft glass.[30] Highly homogeneous, high purity bulk material is commercially available, which has led to the development of low loss silica telecom fibers.[35] Silica has a relatively low refractive index, which can improve the sensitivity of evanescent field sensors, since reducing the index contrast (Δn) at the core-cladding boundary increases the PF.[12]

3. SILICA EXPOSED-CORE MICROSTRUCTURED OPTICAL FIBERS

As discussed in the previous section, the rationale behind producing silica EC-MOFs for long length distributed sensing of corrosion was to make a physically robust sensing element. The fabrication of a microstructured fiber with the core exposed along the whole length provides near-instantaneous measurements of fluorescence intensity while additionally allowing the opportunity for spatially distributed measurements along the length of the fiber through temporal detection methods such as OTDR.[26] High purity F300HQ fused silica was chosen because of its low hydroxide (OH^-) content and availability with tight geometric tolerances.[36] This material has high transmission in the UV–visible–near-infrared spectral range, making it suitable for a range of fluorophores. Unlike soft glass, the glass transition temperature of silica is high making it challenging to extrude, and since the EC-MOF are asymmetric, new fabrication methods needed to be established.

When fabricating structured optical fibers it is important to control the size and shape of the hole structure in a finished MOF. This is because when the MOF is drawn down to the typical 100–250 μm diameter from the typically 10–25 mm diameter preform, the structure experiences substantial external deformation under draw tension. Systematic experiments were performed and analytical equations worked out in order to understand how to reliably draw the EC-MOF geometry to optical fiber using silica.[37]

Figure 7(a) shows the geometry of an EC-MOF which was produced by drilling three holes in an equilateral triangle pattern and machining a slot along the length of one of the holes in an initial 20 mm diameter F300HQ silica rod.[38] This preform was then cleaned using acetone and water (ultra pure Milli-Q), then submersed in 70% nitric acid for 12 hours followed by a rinse with water and dried at 80°C. These methods expanded on a combination of work previously shown by Webb et al.[20] for fabricating a silica SC-MOF by drilling the preform, and Warren-Smith et al.[26] for cutting a thin slot into the side of the symmetric preform (soft glass) in order to expose the core region. The loss of this EC-MOF is shown in Fig. 7(b), with more then an order of magnitude less loss then the first silica EC-MOF we showed in Ref. 38. This relatively low loss has the potential to increase the OTDR distributed sensing range, where at 0.1–0.15 dB/m loss level the achievable distributed sensing range would be about 80 – 100 m at signal-to-noise ratio of 30.

The next step was to functionalize this silica EC-MOF into a sensing element for the detection of corrosion. Although the 8-HQ sensor molecules provide a method for fluorescence based Al^{3+} detection,[39] existing methods
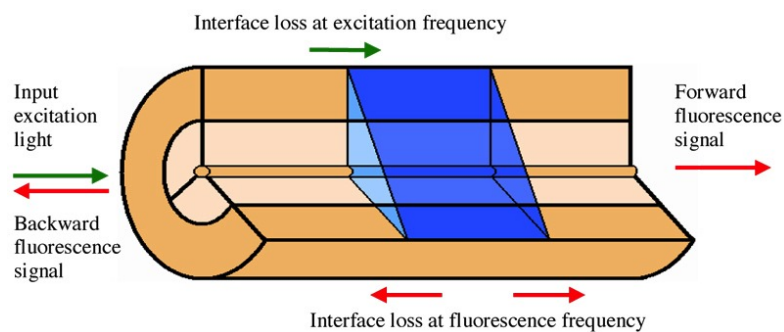
Figure 6: Schematic from Ref. 13 of an EC-MOF with a section immersed in a liquid. Liquid interface losses exist for the excitation light entering the liquid filled section and for the fluorescence exiting the liquid filled section.
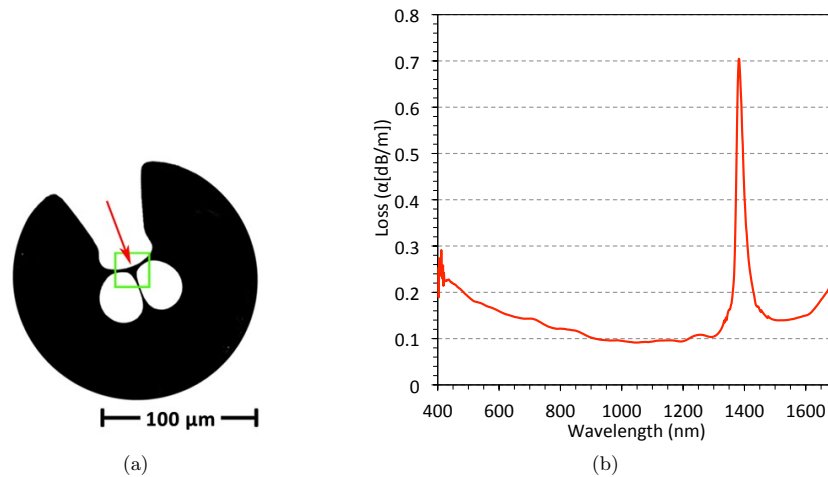
Figure 7: (a) Contrast enhanced SEM image of (silica material shown in black) EC-MOF cross section, having an effective core diameter of 7.5 μm (core location shown by ▮ – green box) and 160 μm outside diameter; and (b) loss (cutback) measurement of this fiber.

for premixing 8-HQ with the sample are not well suited for real-time, in situ, and/or remote sensing within a fuselage. For such applications it is necessary to immobilize sensor molecules on the glass surface of the EC-MOF exposed core, which can then be used directly as a sensing element without requiring prior pre-mixing of a sample with the sensor molecules. Functionalization methods traditionally used include silanes[18, 40] or polyelectrolytes,[41, 42] which provide a functional group on the surface to which the sensor molecules can be covalently attached. These processes require several steps that typically take many hours to perform, due to the incubation times needed to achieve consistent maximized binding efficiency.[40, 42] Also, results are highly dependent on experimental conditions (temperature, concentration, solvents, hydration and reaction time) as well as pre- and post-treatment processes.[16, 19, 42, 43] These factors can diminish sensor performance, reducing the achievable light-matter interactions, which in turn decreases sensitivity. Apart from these potential difficulties, it
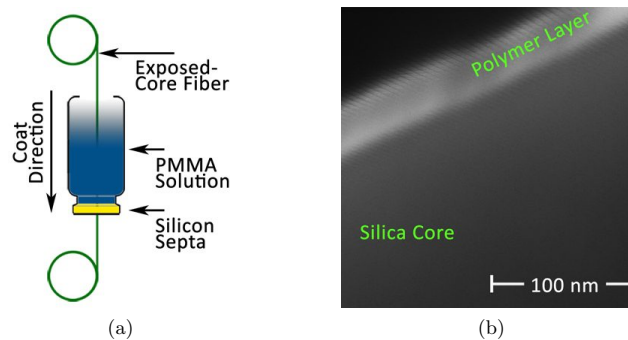
Figure 8: (a) A schematic of the thin-film polymer coating method used to coat the outside of the MOF including the exposed core region. (b) Close-up SEM of the outside edge of the exposed core (▮ – red arrow in Fig. 7(a)) with 50 nm polymer coating (light grey).

was found that when sensing molecules were covalently attached to the exposed core of a EC-MOF the ability for multiligand binding was negated, although single-ligand binding was still achievable.[44] As an alternative method where the sensing molecule is not covalently bound to the surface, a method of functionalizing EC-MOFs was developed by the authors using a thin film ($\sim$50 nm) PMMA doped with 8-HQ in free form for Al^{3+} detection.[45] This also has the potential to solve some of the practical issues[38] involved in packaging an exposed-core MOF so that it is sensitive to the chosen analyte but protected from the applied sensing environment without the need for surface attachment functional groups.

The method used to functionalize the silica EC-MOFs with thin film PMMA is an extension of the method used for micron scale polymer coating in glass capillaries.[46] A clear cast acrylic rod (PMMA) with a density of 1.18 g/cm^3, also known as a 'plexiglass rod' (Professional Plastics Pte. Ltd. [Singapore]), was dissolved in dichloromethane (DCM) at a concentration of 12.3 g/L. 8-HQ was dissolved in DCM and added to the dissolved PMMA solution making a concentration of $30_{(8\text{-}HQ)} : 100_{(PMMA)}$ by weight. One end of the fabricated[37] silica EC-MOF (Fig. 7(a)), with an effective core diameter of 7.5 μm (defined as the diameter of a circle whose area is equal to a triangle that fits wholly within the core area[47]), was fed through a silicon septa fitted to the bottom of an open-end vial. This setup, shown by the schematic in Fig. 8(a), was then used to coat the outside of the EC-MOF including the exposed core region. The PMMA+8-HQ DCM solution was placed into the vial ($\sim$5 mm depth), and the fiber was pulled through the solution and silicon septa by hand (at $\sim$8 m/min) to leave behind a $\sim$50 nm coating of the doped PMMA on the core surface (Fig. 8(b)). Uniformity of the polymer layer is critically important for optical performance of the device. Measured results from SEM images of six samples, from the center and 10 cm in from the ends of two individually coated 1 m lengths of fiber, showed the coating thickness on the outside edge of the exposed-core to be in the range 43–46 nm with measurement uncertainty of $\pm$9 nm. The coating procedure was performed in a laboratory chemical fume hood at room temperature ($\sim$21°C), without additional curing.

The impact of deterioration on the transmission properties of the functionalized fiber, resulting from exposing the functionalized fiber to air, was measured using the same procedure detailed in Ref. 38, and briefly described here. A 4 m long PMMA+8-HQ functionalized fiber was coupled to a 100 W halogen broadband source with an approximately Gaussian-distributed intensity profile and peak power at 800 nm. At the other end, the light from the core was imaged onto the detector of an Ando AQ6315E optical spectrum analyzer and the transmitted power spectrum, in dBm, was recorded from 350–1750 nm every two minutes. This procedure was performed in a
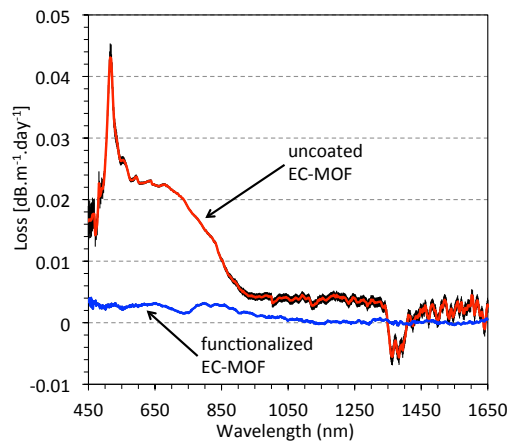
Figure 9: Deterioration in the transmission properties of the air exposed uncoated (▮ – red), from Ref. 38 with 10 μm core diameter) and thin-film polymer functionalized (▮ – blue) silica EC-MOFs. The 95% confidence interval is shown in black. For the thin-film polymer functionalized fiber result, the confidence interval is approximately the same as the line thickness.

laboratory at room temperature ($\sim$21°C), with the fiber in air. This setup was first left long enough ($\sim$6 hours) so that the measured power stabilized to within $\pm$0.05 dBm, then used to take time based measurements of the power for 180 hours. Any changes over time (t) in the transmission characteristics were then fitted to the equation,

$$P(\lambda, t) = P(\lambda, 0)10^{-\xi tz/10} \tag{1}$$

where ξ is the loss in dB m^{-1}day^{-1} and z is the fiber length in meters. For comparison the result in Ref. 38 for an uncoated EC-MOF, with 10 μm core diameter, is shown by the red line in Fig. 9. The result of $\xi(\lambda)$ (Eq. (1)) for the thin-film functionalized fiber, shown by the blue line in Fig. 9, shows a significant improvement compared to the uncoated fiber.

The deterioration in the transmission properties is expected to come from changes in the mechanical and/or compositional characteristics at the core surface, causing light scattering effects.[48–50] When the core diameter is reduced these light scattering effects are expected to increase, as a greater portion of guided light travels outside the core (increased PF). However, this result shows less deterioration in transmission properties even though the core diameter of this functionalized fiber is smaller (7.5 μm) compared to the uncoated EC-MOF from Ref. 38 (10 μm). This shows that the thin film coating is providing a protective function for the core surface. For example, at $\lambda = 532$ nm the air induced deterioration in the transmission properties of the thin-film functionalized fiber (3×10^{-3} dB m^{-1}day^{-1}) is an order of magnitude better than for the uncoated result and $\sim$3 orders of magnitude better than for the previously reported EC-MOFs produced in F2 soft glass.[38] This is significant for optical fiber sensors requiring long term exposure to harsh environmental conditions, such as structural corrosion detection. Further details and results showing the characterization of thin film polymer functionalization layer can be found in Ref. 45.

4. SENSING CORROSION

Measurements were performed to test the ability of the EC-MOF coated with the doped PMMA to detect Al^{3+}. The experimental setup of these measurements is shown in Fig. 10, which consisted of a 405 nm wavelength laser excitation light source coupled to the functionalized EC-MOF. The back reflected light collected from the core of the coated fiber was imaged using a 60$\times$ objective, passing through the dichroic mirror and 405 nm Raman long pass filter and 10$\times$ objective, and characterized using a Horiba iHR320 Imaging Spectrometer with Synapse CCD Detector. Each measurement was done with a 50 ms pulse of light from the laser. Two separate experiments were performed using this setup, the first of which was to immerse a section of the EC-MOF in a solution containing Al^{3+} and the second experiment used a second section of EC-MOF in a corroded simulated aluminum aircraft joint. For consistency, one longer length of EC-MOF was coated and then cut, with half used on each of the experiments.

For the first experiment the exposed-core region of the coupled EC-MOF was exposed to Al^{3+} by immersing a 23 cm long central section of the fiber in a saturated solution of potassium aluminum sulfate in a capillary. The back reflected spectra were measured before immersion, immediately after immersion and periodically over a 2 hour period. The measured result before immersion subtracted from the after immersion results is presented
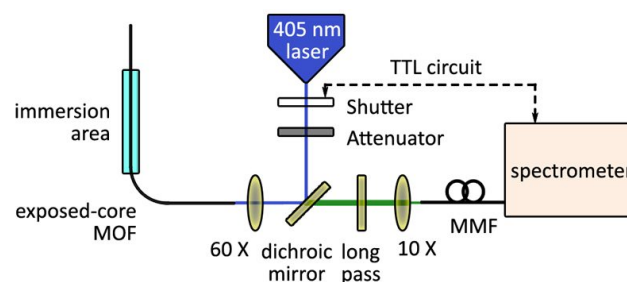
Figure 10: Setup used to test the ability of the coated EC-MOF to detect Al^{3+}.

(a)   (b)
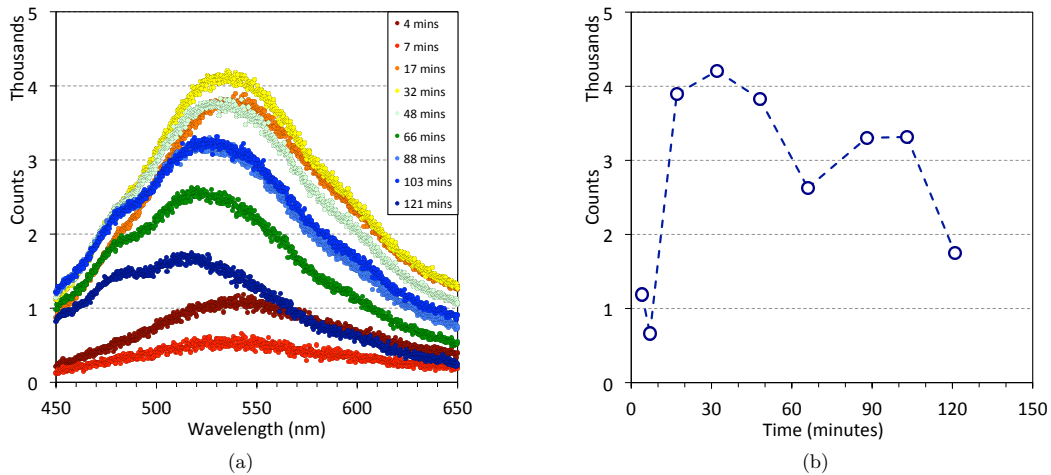
Figure 11: (a) Periodic measurements of the back reflected spectra of the functionalized fiber immersed in solution containing Al^{3+}, and (b) plot of the peak intensities from the measurements shown in Fig. 11(a) as a function of time.

in Fig. 11(a), which shows the fluorescence peaks of 8-HQ–Al^{3+} complex[10] for a series of immersion times. These in solution measurements demonstrates the ability of the thin polymer film functionalized fiber to detect Al^{3+}. However, over time the measurement deteriorated after peaking around half an hour after immersion, as shown by a plot of the peak intensities as a function of time in Fig. 11(b). The cause of this deterioration was not known, however it may be that the drying saturated solution causes salt crystal formation on the core at the air-liquid interface where the fiber enters and exits the solution.

For the second experiment, a 21 cm long aerospace grade aluminum plate was machined with 2 mm slots and covered with a top plate of 1 cm thick perspex to allow visualization of the corrosion. The perspex was drilled with 2 mm holes along the location of the slots so as to allow the ingress of the corrosive atmosphere to the aluminum. The plate was placed in the highly corrosive atmosphere of a salt spray chamber for four days to induce accelerated corrosion of the aluminum. The corroded plate, shown in Fig. 12(a) was allowed to dry and then the functionalized EC-MOF was placed inside one of the corroded slots, as shown in Fig. 12(b). For a

(a)   (b)
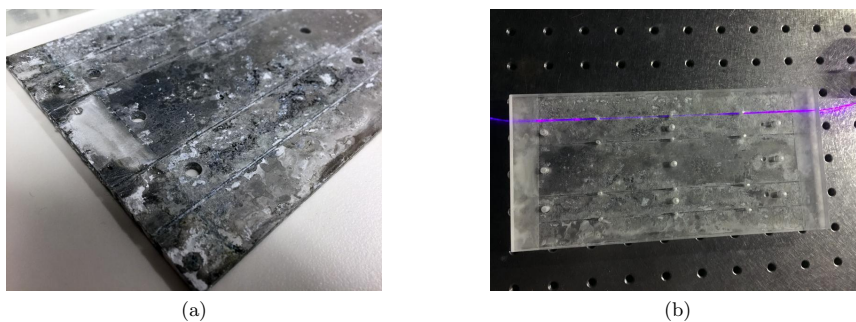
Figure 12: (a) Aerospace grade aluminum plate after four days in the highly corrosive atmosphere of a salt spray chamber. (b) The corroded plate with a functionalized EC-MOF (▌ – purple) inside one of the slots.
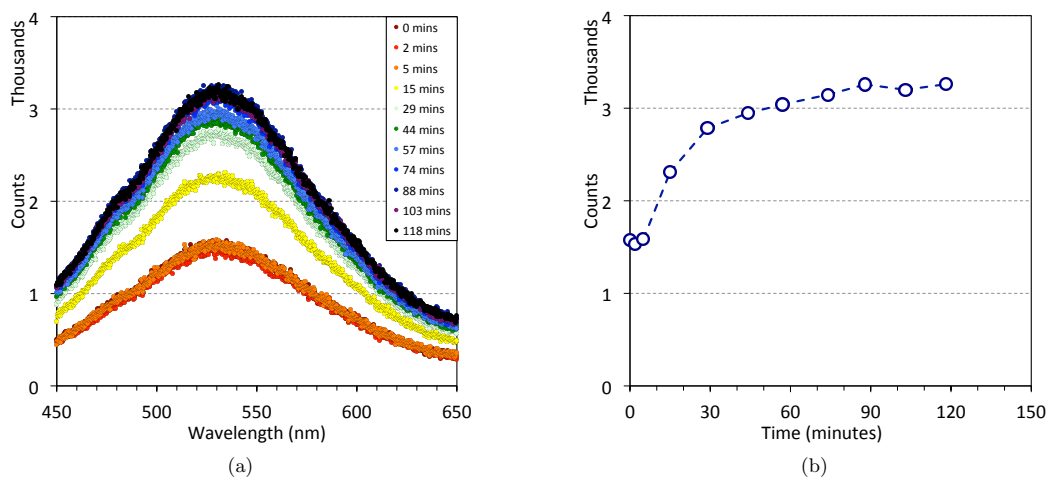
Figure 13: (a) Periodic measurements of the back reflected spectra of the functionalized fiber inside a corroded simulated aluminum aircraft joint, and (b) plot of the peak intensities from the measurements shown in Fig. 13(a) as a function of time.

background measurement, the back reflected spectra from the EC-MOF was measured while the plate was dry. The slot of the aluminum plate with the fiber inside was then filled with high purity MilliQ water and the back reflected spectra measured immediately and again periodically over a 2 hour period.

The measured results with background subtracted are presented in Fig. 13(a), which shows the fluorescence peaks of 8-HQ–Al^{3+} complex[10] for a series of time intervals after addition of the water. These simulated aluminum aircraft joint measurements demonstrate the ability of the EC-MOF functionalized with a thin polymer film to detect Al^{3+} as a byproduct of corrosion. Figure 13(b) is a plot of the peak intensities of these in plate measurements as a function of time, which shows that there was an immediate initial response from the functionalized fiber which then logarithmically increased over the two hour period.

5. CONCLUSION AND FUTURE WORK

We have summarized progress in the development of a fiber optic detection and monitoring system for corrosion, and have shown that functionalized EC-MOFs can detect Al^{3+} in a simulated aircraft joint. It has been shown in Ref. 51 that the silica EC-MOF fibers can be spliced to single mode fiber for improved handling and integration with commercial interrogation units. Methods are under development to fully connectorize the EC-MOF into a system which incorporates the interrogation and detection instrumentation for use as a field-portable demonstrator. Further work is also required to incorporate a distributed sensing capability so that the position where corrosion is occurring along the length of fiber can be located.

REFERENCES

[1] Lohner, H. and Hack, T., [*Aluminium Alloy Corrosion of Aircraft Structures: Modelling and Simulation*], WIT Press (2013).

[2] Broomfield, J. et al., "The strategic highway research program. Research on corrosion of steel in concrete.," *P. I. Civil Eng. – Str. B.* **104**(2), 211 – 218 (1994).

[3] McAdam, G., Newman, P. J., McKenzie, I., Davis, C., and Hinton, B. R. W., "Fiber optic sensors for detection of corrosion within aircraft," *Struct. Health Monit.* **4**, 47 – 56 (March 2005).

[4] Warren-Smith, S. C., *Fluorescence-Based Chemical Sensing Using Suspended-Core Microstructured Optical Fibres*, PhD thesis, The University of Adelaide (Oct 2010).

[5] Hall, J., "Corrosion prevention and control programs for boeing airplanes," Technical Paper 931259, SAE International (1993).

[6] Australian Government, "Corrosion prevention and control program (CPCP)," Civil Aviation Safety Regulations 1998 Part 39.001(1), AD/B737/52 Amdt 3, Infrastructure and Regional Development (2011).

[7] McKenzie, I. and Newman, P. J., "Methods for detection of corrosion in aircraft structures using fiber optic technology," in [*Tri-Service Corrosion Conference [15–19 Nov., Myrtle Beach, South Carolina]*], (Nov 1999).

[8] Ščančar, J. and Milačič, R., "Aluminium speciation in environmental samples: a review," *Anal. Bioanal. Chem.* **386**(4), 999 – 1012 (2006).

[9] Shar, G. A. and Soomro, G. A., "8-hydroxyquinoline as a complexing reagent for the determination of Cd(II) in micellar medium," *J. Chem. Soc. Pak.* **27**(5), 471 – 475 (2005).

[10] Kishore, V. V. N. R., Aziz, A., Narasimhan, K. L., Periasamy, N., Meenakshi, P. S., and Wategaonkar, S., "On the assignment of the absorption bands in the optical spectrum of Alq3," *Synthetic Met.* **126**(2–3), 199 – 205 (2002).

[11] Sinchenko, E., Gibbs, W. E. K., Davis, C. E., and Stoddart, P. R., "Characterization of time-resolved fluorescence response measurements for distributed optical-fiber sensing," *Appl. Opt.* **49**, 6385–6390 (Nov 2010).

[12] Schartner, E. P., Ebendorff-Heidepriem, H., Warren-Smith, S. C., White, R. T., and Monro, T. M., "Driving down the detection limit in microstructured fiber-based chemical dip sensors," *Sensors* **11**(3), 2961 – 2971 (2011).

[13] Warren-Smith, S. C., Afshar V., S., and Monro, T. M., "Theoretical study of liquid-immersed exposed-core microstructured optical fibers for sensing," *Opt. Express* **16**, 9034 – 9045 (Jun 2008).

[14] Tong, L., Gattass, R. R., Ashcom, J. B., He, S., Lou, J., Shen, M., Maxwell, I., and Mazur, E., "Subwavelength-diameter silica wires for low-loss optical wave guiding," *Nature* **426**, 816 – 819 (Dec 2003).

[15] Monro, T. M. and Ebendorff-Heidepriem, H., "Progress in microstructured optical fibers," *Annu. Rev. Mater. Res.* **36**(1), 467 – 495 (2006).

[16] Monro, T. M., Warren-Smith, S., Schartner, E. P., François, A., Heng, S., Ebendorff-Heidepriem, H., and Afshar V., S., "Sensing with suspended-core optical fibers," *Opt. Fiber Technol.* **16**(6), 343 – 356 (2010).

[17] Schartner, E. P., Tsiminis, G., François, A., Kostecki, R., Warren-Smith, S. C., Nguyen, L. V., Heng, S., Reynolds, T., Klantsataya, E., Rowland, K. J., Abell, A. D., Ebendorff-Heidepriem, H., and Monro, T. M., "Taming the light in microstructured optical fibers for sensing," *Int. J. Appl. Glass Sci.* **6**(3), 229 – 239 (2015).

[18] Heng, S., Nguyen, M.-C., Kostecki, R., Monro, T. M., and Abell, A. D., "Nanoliter-scale, regenerable ion sensor: sensing with a surface functionalized microstructured optical fibre," *RSC Adv.* **3**, 8308 – 8317 (2013).

[19] Warren-Smith, S. C., Heng, S., Ebendorff-Heidepriem, H., Abell, A. D., and Monro, T. M., "Fluorescence-based aluminum ion sensing using a surface-functionalized microstructured optical fiber," *Langmuir* **27**(9), 5680 – 5685 (2011).

[20] Webb, A. S., Poletti, F., Richardson, D. J., and Sahu, J. K., "Suspended-core holey fiber for evanescent-field sensing," *Opt. Eng.* **46** (Jan 2007).

[21] Euser, T. G., Chen, J. S. Y., Scharrer, M., Russell, P. S. J., Farrer, N. J., and Sadler, P. J., "Quantitative broadband chemical sensing in air-suspended solid-core fibers," *J. Appl. Phys.* **103**(10), 103108 (2008).

[22] Mazhorova, A., Markov, A., Ng, A., Chinnappan, R., Skorobogata, O., Zourob, M., and Skorobogatiy, M., "Label-free bacteria detection using evanescent mode of a suspended core terahertz fiber," *Opt. Express* **20**, 5344–5355 (Feb 2012).

[23] Afshar V., S., Warren-Smith, S. C., and Monro, T. M., "Enhancement of fluorescence-based sensing using microstructured optical fibres," *Opt. Express* **15**, 17891 – 17901 (Dec 2007).

[24] Ruan, Y., Schartner, E. P., Ebendorff-Heidepriem, H., Hoffmann, P., and Monro, T. M., "Detection of quantum-dot labelled proteins using soft glass microstructured optical fibers," *Opt. Express* **15**, 17819 – 17826 (Dec 2007).

[25] Cox, F. M., Lwin, R., Large, M. C. J., and Cordeiro, C. M. B., "Opening up optical fibres," *Opt. Express* **15**, 11843–11848 (Sep 2007).

[26] Warren-Smith, S. C., Ebendorff-Heidepriem, H., Foo, T. C., Moore, R., Davis, C., and Monro, T. M., "Exposed-core microstructured optical fibers for real-time fluorescence sensing," *Opt. Express* **17**, 18533 – 18542 (Oct 2009).

[27] Afshar V., S., Ruan, Y., Warren-Smith, S. C., and Monro, T. M., "Enhanced fluorescence sensing using microstructured optical fibers: a comparison of forward and backward collection modes," *Opt. Lett.* **33**, 1473 – 1475 (Jul 2008).

[28] Warren-Smith, S. C., Sinchenko, E., Stoddart, P. R., and Monro, T. M., "Distributed fluorescence sensing using exposed core microstructured optical fiber," *IEEE Photon. Technol. Lett.* **22**, 1385 – 1387 (Sep 2010).

[29] Warren-Smith, S. C., Ebendorff-Heidepriem, H., Afshar V., S., McAdam, G., Davis, C., and Monro, T., "Corrosion sensing of aluminium alloys using exposed-core microstructured optical fibres," *Mater. Forum* **33**, 110 – 121 (2009).

[30] Richardson, K., Krol, D., and Hirao, K., "Glasses for photonic applications," *Int. J. Appl. Glass Sci.* **1**(1), 74 – 86 (2010).

[31] Peters, K., "Polymer optical fiber sensors - a review," *Smart Mater. Struct.* **20**(1), 013002 (2011).

[32] Law, S. H., van Eijkelenborg, M. A., Barton, G. W., Yan, C., Lwin, R., and Gan, J., "Cleaved end-face quality of microstructured polymer optical fibres," *Opt. Commun.* **265**(2), 513 – 520 (2006).

[33] Atakaramians, S., Cook, K., Ebendorff-Heidepriem, H., Afshar V., S., Canning, J., Abbott, D., and Monro, T. M., "Cleaving of extremely porous polymer fibers," *IEEE Photon. J.* **1**, 286 – 292 (Dec 2009).

[34] Stefani, A., Nielsen, K., Rasmussen, H. K., and Bang, O., "Cleaving of TOPAS and PMMA microstructured polymer optical fibers: Core-shift and statistical quality optimization," *Opt. Commun.* **285**(7), 1825 – 1833 (2012).

[35] Li, M. and Nolan, D. A., "Optical transmission fiber design evolution," *J. Lightwave Technol.* **26**(9), 1079 – 1092 (2008).

[36] Heraeus Quarzglas GmbH & Co. KG, http://heraeus-quarzglas.com/, *Pure Silica Rods for Specialty Fiber Applications*, 1st edition ed. (Jan 2012).

[37] Kostecki, R., Ebendorff-Heidepriem, H., Warren-Smith, S. C., and Monro, T. M., "Predicting the drawing conditions for microstructured optical fiber fabrication," *Opt. Mater. Express* **4**, 29 – 40 (Jan 2014).

[38] Kostecki, R., Ebendorff-Heidepriem, H., Davis, C., McAdam, G., Warren-Smith, S. C., and Monro, T. M., "Silica exposed-core microstructured optical fibers," *Opt. Mater. Express* **2**, 1538 – 1547 (Nov 2012).

[39] Lodeiro, C., Capelo, J. L., Mejuto, J. C., Oliveira, E., Santos, H. M., Pedras, B., and Nunez, C., "Light and colour as analytical detection tools: A journey into the periodic table using polyamines to bio-inspired systems as chemosensors," *Chem. Soc. Rev.* **39**, 2948 – 2976 (2010).

[40] Foo, H. T. C., Ebendorff-Heidepriem, H., Sumby, C. J., and Monro, T. M., "Towards microstructured optical fibre sensors: Surface analysis of silanised lead silicate glass," *J. Mater. Chem. C* **1**, 6782 – 6789 (2013).

[41] Sciacca, B., François, A., Klingler-Hoffmann, M., Brazzatti, J., Penno, M., Hoffmann, P., and Monro, T. M., "Radiative-surface plasmon resonance for the detection of apolipoprotein E in medical diagnostics applications," *Nanomed. - NBM* **9**(4), 550 – 557 (2013).

[42] François, A., Ebendorff-Heidepriem, H., Sumby, C. J., and Monro, T. M., "Comparison of surface functionalization processes for optical fibre biosensing applications," in [*20th International Conference on Optical Fibre Sensors*], *Proc. SPIE* **7503** (2009).

[43] Zhu, M., Lerum, M. Z., and Chen, W., "How to prepare reproducible, homogeneous, and hydrolytically stable aminosilane-derived layers on silica," *Langmuir* **28**(1), 416 – 423 (2012).

[44] Kostecki, R., Heng, S., Ebendorff-Heidepriem, H., Abell, A. D., and Monro, T. M., "Functionalization of exposed core fibers with multiligand binding molecules for fluorescence based ion sensing," in [*23rd International Conference on Optical Fibre Sensors*], *Proc. SPIE* **9157** (2014).

[45] Kostecki, R., Ebendorff-Heidepriem, H., Afshar V., S., McAdam, G., Davis, C., and Monro, T. M., "A novel polymer functionalization method for exposed-core optical fiber," *Opt. Mater. Express* **4**, 1515 – 1525 (Aug. 2014).

[46] Rowland, K. J., François, A., Hoffmann, P., and Monro, T. M., "Fluorescent polymer coated capillaries as optofluidic refractometric sensors," *Opt. Express* **21**, 11492 – 11505 (May 2013).

[47] Ebendorff-Heidepriem, H., Warren-Smith, S. C., and Monro, T. M., "Suspended nanowires: fabrication, design and characterization of fibers with nanoscale cores," *Opt. Express* **17**, 2646 – 2657 (Feb 2009).

[48] Brambilla, G., Xu, F., and Feng, X., "Fabrication of optical fibre nanowires and their optical and mechanical characterisation," *Electron. Lett.* **42**, 517 – 519 (april 2006).

[49] Zhai, G. and Tong, L., "Roughness-induced radiation losses in optical micro or nanofibers," *Opt. Express* **15**, 13805 – 13816 (Oct 2007).

[50] Fujiwara, M., Toubaru, K., and Takeuchi, S., "Optical transmittance degradation in tapered fibers," *Opt. Express* **19**, 8596 – 8601 (Apr 2011).

[51] Warren-Smith, S. C., Kostecki, R., Nguyen, L. V., and Monro, T. M., "Fabrication, splicing, bragg grating writing, and polyelectrolyte functionalization of exposed-core microstructured optical fibers," *Opt. Express* **22**(24), 29493 – 29504 (2014).

Paper 9. (Prepared for Submission)

COMMUNICATION   **WILEY**-VCH

Control of Molecular Recognition with Nano-Environment Effects

Roman Kostecki,[a] Sabrina Heng,[a] Adrian M. Mak,[b] Tanya M. Monro,[a,c] Andrew D. Abell,[a] and Heike Ebendorff-Heidepriem[a]

Abstract: Here we report the design of a photo-switchable spiropyran-ionophore molecule and its use in defining the effect of the nano-environment on molecular recognition. The effects of solvation, conformational mobility and diffusion on the binding of cations to the molecule are compared. When the molecule is chemisorbed to a surface interface, conformational mobility of the molecule is restricted, and hence the ability to complex to cations. The mobility and dispersive properties of polymer restricts the ability of the sensing molecule to complex to relatively larger cations. This shows the potential for using nano-environments to control how cations interact with molecules, with practical implications for the development of highly selective and biologically or environmentally compatible interfaces.

The ability of small molecule ligands (host) to bind specifically to a related set of species (guest) is fundamental to molecular recognition chemistry and biology,[1] and the local molecular environment (nano-environment) is known to influence a molecule's binding property.[2] However, development of synthetic systems that control molecular recognition by varying the nano-environment remains a significant challenge. Therefore, the chemical structure of a host molecule instead of the nano-environment is typically changed for tailoring guest selectivity. Using nano-environments to specifically control and vary host molecule selectivity, without the need to change chemical structure, would be a real advantage. Here, we show that for the same host molecule, tailoring the nano-environment determines sensitivity and selectivity towards different analytes. In addition, we show that modulation of the nano-environment allows the same host molecule to be used for analytes in aqueous or organic solvents.

A spiropyran-ionophore host molecule (S-I) was chosen (Figure 1) as it was found to form a single-ligand complex with Ca^{2+}, and a dual-ligand complex with Al^{3+}, as described in Ref. ?. The spiropyran part of S-I acts as a photoswitch to allow reversible ion binding, with an ability to reversibly switch from a low-fluorescent spiro (SP) isomer (Figure 1a) to ring-opened merocyanine (MC) isomer (Figure 1b and c) which is highly fluorescent when an ion is bound to the ionophore.[1-3] This occurs with a high switching reliability and low fatigue to maximize the number of switching cycles between the two isomers. As such, appropriately functionalized spiropyrans have found wide use as a basis of reversible metal sensing and

scavenging, catalysis, and medicinal chemistry, with the ability to bind to metal ions,[4] amino acids[5] and other species such as cyanide ion[6]. A spiropyran also has the advantage of low background fluorescence as compared to non-photochromic fluorophores, such as those based on rhodamine.[8] A combination of a 1-aza-18-crown-6 substituent at C8' of the benzopyran ring[9], was used to promote affinity for M^{2+} ions such as Ca^{2+} in the MC as shown in Figure 1. In addition, a butanoic acid functionality was incorporated on the indole nitrogen in order to provide sufficient charge and conformational mobility for the molecule to form strong, yet reversible binding to more than one cation via single- and multi-ligand complexing (Figs. 1(b) and 1(c)). S-I also contains an aryl carboxylate to enable it to be attached covalently to solid surfaces.
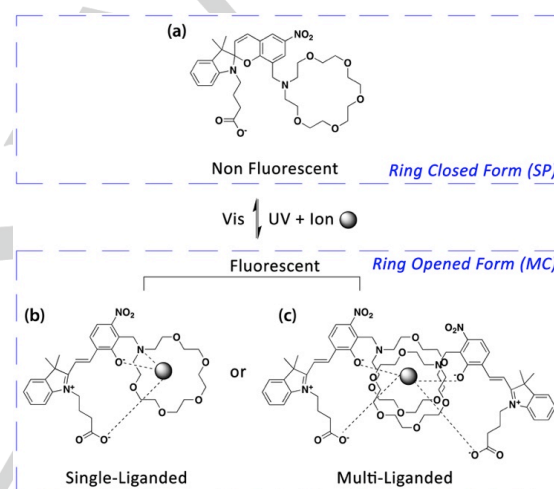
Figure 1. Cation interaction with spiropyran based molecule according to the model proposed by Kimura *et al.*[8] Spiropyran-ionophore molecule (S-I) (a) represents the SP ring-closed, non fluorescent form. S-I in (b) and (c) represent the ring-opened, fluorescent forms of MC-cation single- and multi-liganded complexes.

To measure the impact of three significantly different nano-environments on binding affinities of the MC isomer to Al^{3+} and Ca^{2+}, the fluorescence intensity of 2MC-Al^{3+} and MC-Ca^{2+} in acetonitrile (solution measurements) was compared with the chemisorbed and physisorbed arrangements of the MC isomer. In solution, the MC isomer and cation interaction equilibrium occurs in an environment of mobile molecules, which are free to displace when forming the complex[13] (Fig. 6(a)). When chemisorbed on a solid surface, the MC isomer has restricted mobility, and relies on cation and solvent displacement at the surface for complexation[14] (Fig. 6(b)). In between these highly mobile (in solution) and mobility restricted (on a solid surface) extremes is physical absorption of S-I into a polymer. Polymers can be thought of as a highly viscous fluid subject to molecular diffusion, so that within a thin-film polymer the mobility of the MC isomer and cation can be restricted by the polymer matrix[15] (Fig. 6(c)).

[a]   Mr. R. Kostecki,[*] Dr. S. Heng,[§] Prof. H. Ebendorff-Heidepriem,
        Prof. A. D. Abell, and Prof. T. M. Monro
        The ARC Centre of Excellence for Nanoscale BioPhotonics,
        and Institute for Photonics and Advanced Sensing and School of
        Physical Sciences, The University of Adelaide, Adelaide, Australia
        E-mail: [*]roman.kostecki@adelaide.edu.au,
        [§]sabrina.heng@adelaide.edu.au
[b]   Dr. A. M. Mak
        Institute of High Performance Computing, 1 Fusionopolis Way, No.
        16-16 Connexis, Singapore 138632
[c]   Prof. T. M. Monro
        University of South Australia, Adelaide, Australia

        Supporting information for this article is given via a link at the end of
        the document.

Silica exposed-core microstructured optical fibre (ECF) (cross section shown in Fig. 5(a)) was chosen as the platform for S-I to be chemisorbed onto a surface and physisorbed into polymer nano-environments. A portion of light guided by the ECF core (red square in Fig. 5(b)) is guided a few hundred nanometers outside of the glass surface[17] and interacts with whatever is put on the surface. When a fluorescent molecule, such as MC-cation complex, is excited by this guided light, some of the resulting emission is captured and guided by the same ECF core which can be collected and measured from either end of the fiber.[18] This principle improves the signal-to-noise ratio (SNR) compared to other techniques such as microscopy and thus was used to determine the impact of these significantly different nano-environments on binding affinities of the MC isomer to Al^{3+} and Ca^{2+}. The measurement setup is shown in Fig. 5 and detailed in the supporting information.

As the ECF provides direct access to the light guiding core, it is well suited for covalent bonding (chemisorption) or thin-film ($\sim$50 nm thickness) polymer (physisorption) application of S-I onto the core surface.[16] Silane, which covalently bonds to hydroxyl groups on the silica core surface, was used to provide free amine groups for covalent bonding with the carboxylic acid group of S-I. For the thin-film polymer method, S-I was added to poly(methyl methacrylate) (PMMA) dissolved in dichloromethane (DCM) which was then applied to the ECF to form a $\sim$50 nm thick coating of doped PMMA on the core surface. It has been reported that macromolecular polymer chains can hold relatively hydrophobic molecules[pmmaPaper] such as S-I. These different application methods yield the different nano-environments where molecular recognition between the MC isomer and cation occurs (Figs. 6(b) and 6(c)). The covalent bonding and thin film polymer procedures are detailed in the supporting information. For the solution based measurements, the experiments were performed using a 96 well plate via a plate reader and is detailed in the supporting information. The plate reader was used instead of the ECF to avoid anomalous results due to any physisorbed S-I on the ECF core surface.[xx]
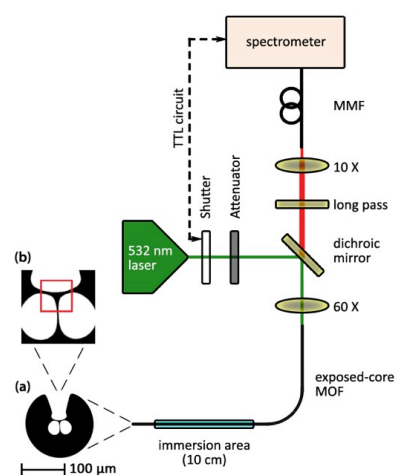
Figure 5. Schematic of the setup used to measure the fluorescence from MC-cation complexes at the surface of silica ECF core, including a scanning electron microscope (SEM) cross section (a) of the ECF, and enlarged view (b) of the core (7.5 µm effective diameter) indicated by the red square. MMF is multimode fiber.

The solution measurement results revealed that the MC isomer strongly fluoresced when single-ligand complexed with Ca^{2+}. In addition, the MC isomer had modest fluorescence when dual-ligand complexed with Al^{3+}, however the maximum fluorescence intensity obtained for Al^{3+} binding was an order of magnitude lower than that obtained with Ca^{2+}. Figure 6(d) shows the fluorescence intensity results of the MC isomer without cations, MC-Ca^{2+} complex, and 2MC-Al^{3+} complex.

The covalently bound (chemisorbed) SP isomer only showed weak fluorescence when immersed in acetonitrile solution, which was not affected by the presence of cations. The measured response from the chemisorbed MC isomer when immersed in an acetonitrile solution without any cations showed 3.8-fold increased fluorescence compared to the SP isomer (Fig. 6(e)). This is different from the results obtained in the experiments with the MC isomer dissolved in acetonitrile solution (Fig. 6(d)), which effectively had no fluorescence. When the ECF with covalently bound MC isomer was subsequently immersed in acetonitrile solution containing Ca^{2+} cations (10 µM), the response showed 5.6-fold increased fluorescence compared to the SP isomer, which does not bind to the cations (Fig. 6(e)). This significant increase in fluorescence intensity indicates binding of Ca^{2+} to MC isomer and is consistent with the results obtained in the experiments with MC isomer and Ca^{2+} in acetonitrile solution, which showed strong fluorescence (Fig. 6(d)). The same fiber that was immersed in the Ca^{2+} solution was then used to examine the affinity of the covalently bound MC isomer towards Al^{3+}. The Ca^{2+} cations were first rinsed from the ECF and replaced with Al^{3+}, as detailed in the supporting information. The results showed that covalently bound MC in the presence of Al^{3+} (Fig. 6(e)) did not result in an increase in fluorescence intensity, when compared to the cation-free MC isomer (Fig. 6(e)), indicating that Al^{3+} did not bind to the covalently bound MC isomer on the surface. This is significantly different from the experiments with MC isomer dissolved in acetonitrile (Fig. 6(d)), where both Ca^{2+} and Al^{3+} were found to form complexes with MC, leading to significant fluorescence increases relative to the dissolved MC isomer without cations.

These results indicate that when S-I is covalently bound (chemisorbed) to the surface it is unable to bind to Al^{3+}. As 2MC-Al^{3+} was found to bind at the 2:1 ratio, this implies dual-ligand binding is prevented when MC isomer is chemisorbed on a solid surface. We hypothesize that there is such a steric hindrance when MC isomer is chemisorbed on a solid surface that two MC molecules could not undergo conformational changes necessary to bind simultaneously to one Al^{3+} cation. This is an important observation for applications where control of host-guest interactions is needed, as it allows the selectivity to a single cation to be modulated without the need to alter the chemical structure of the host molecule itself.

To explore the relative binding affinities of Ca^{2+} and Al^{3+} with MC isomer physisorbed within a thin polymer film, water was used as solvent for the cations instead of acetonitrile to prevent the PMMA layer from dissolving and/or the S-I from leaching when exposed to acetonitrile solutions. To avoid contamination from the cations that may be trapped within the polymer matrix, a new ECF was used for each of the water only, Ca^{2+} and Al^{3+} experiments. As was observed with SP isomer covalently attached to the ECF core, the SP isomer physisorbed within the polymer only showed weak fluorescence, which was not affected by the presence of cations. In the absence of cations, the MC isomer also showed only weak fluorescence intensity (Fig. 6(f)).

COMMUNICATION

In the presence of Ca^{2+} (10 mM), the fluorescence intensity of the MC isomer increased 4-fold compared to the SP isomer (Fig. 6(f)). In the presence of Al^{3+} (10 mM) the fluorescence intensity of the MC isomer increased 8-fold compared to the SP isomer (Fig. 6(f)), demonstrating that Al^{3+} cations resulted in a 2-fold increase in fluorescence intensity compared to Ca^{2+}. This is significantly different from the results obtained when S-I was dissolved in solution or chemisorbed. In solution, Ca^{2+} resulted in 10-fold increased fluorescence intensity compared to Al^{3+} (Fig. 6(d)), and when chemisorbed only Ca^{2+} yielded change in fluorescence by the MC isomer, compared to Al^{3+} or without cation.

The observation of high fluorescence intensity in the presence of Ca^{2+} and Al^{3+} suggests that PMMA allows sufficient conformational mobility of MC to form complexes with cations. High degree of conformational mobility is in particular important to form the dual-ligand 2MC-Al^{3+} complex. The significantly higher fluorescence intensity for the MC isomer when embedded in PMMA and in the presence of Al^{3+} that have diffused into the PMMA, indicates that within PMMA the MC isomer can more easily bind to Al^{3+} compared to Ca^{2+}, indicating that binding to Ca^{2+} is hindered compared to Al^{3+}. The binding of two MC ligands simultaneously to one Al^{3+} cation within the polymer matrix implies that S-I has high conformational mobility within PMMA, whereas when covalently binding it to a surface the conformational mobility of the MC isomer decreases to such an extent that dual-ligand complexation with Al^{3+} becomes impossible. For MC isomer in solution, the higher fluorescence intensity for Ca^{2+} compared to Al^{3+} is consistent with the theory that the single-ligand MC-Ca^{2+} complex can form more easily compared to the dual-ligand 2MC-Al^{3+} complex. This is because the host-guest interaction for dual-ligand binding requires two MC isomers to diffuse to and complex simultaneously with one cation, which has a lower probability compared to the complexation of a cation with only one MC isomer.

The hindrance of Ca^{2+} binding to MC isomer in PMMA is surprising considering that single-ligand complexation of Ca^{2+} poses less demands on the mobility of the MC isomer compared to multi-molecule complexation with Al^{3+}, as described above. When S-I is embedded in polymer, the cations have to diffuse from the analyte solution to the surface of the polymer film and then into the polymer matrix to be bound to the MC isomer. If diffusion of the MC isomer would determine the rate of cation binding then it would be more greatly affected when binding with Al^{3+}, as two MC ligands have a reduced probability of binding compared to one MC ligand. However, it is not observed that Al^{3+} binding to MC isomer in PMMA is hindered in this way, compared to Ca^{2+}. Therefore, the hindrance of Ca^{2+} binding to MC isomer in PMMA is attributed not to a difference in MC isomer mobility but to a difference in the mobility of the cations. The larger ionic radius for Ca^{2+} (114 pm) compared to Al^{3+} (68 pm) is anticipated to relatively decrease the ability of Ca^{2+} to diffuse within the PMMA matrix, which would diminish the efficiency to form MC-Ca^{2+} complexes in PMMA. In comparison, in the experiments with MC isomer in solution or attached to a surface, Ca^{2+} or Al^{3+} are located within a solvation shell of acetonitrile, which enables easier diffusion for both Ca^{2+} and Al^{3+} compared with the diffusion that is occurring within the solvation shell which includes the polymer matrix.

To confirm that the spiropyran based molecules are sufficiently held by the polymer matrix, and therefore solvation is occurring within the polymer matrix, seventeen photoswitching cycles between the MC and SP isomers was explored with and without Ca^{2+} and Al^{3+}. The thin-film polymer coated ECF was also left for 17 hrs while immersed in the solution of water dissolved Al^{3+}. The results are included in the supporting information and show that the fluorescence intensity from the MC-cation complexes does not diminish over time between measurements which indicates that the spiropyran based molecules are trapped within the nano-environment of the polymer matrix. The fluorescence response from these complexes is maintained over many switching cycles in the polymer matrix, as is expected for switching experiments with spiropyrans in solution.
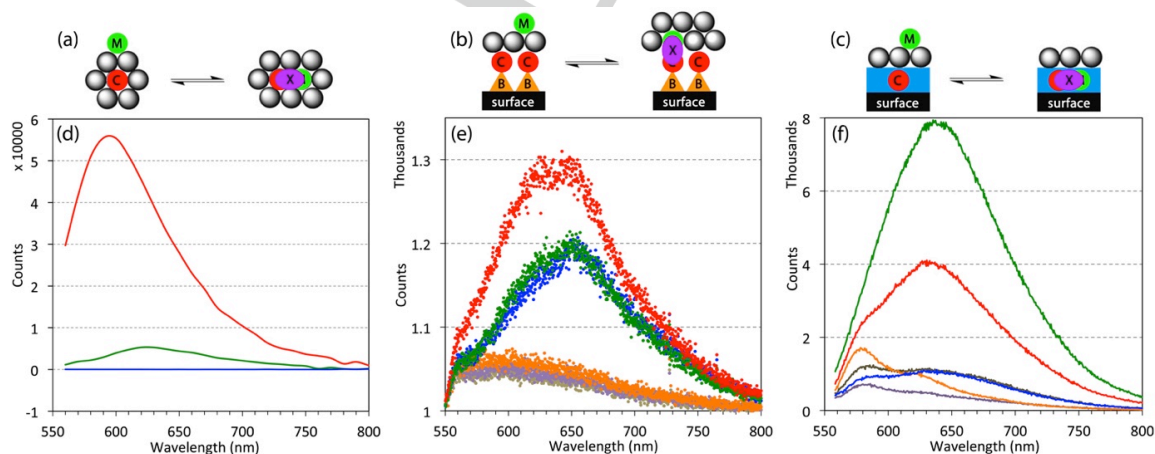
Figure 6. (a) Solution, (c) chemisorbed on solid surface, and (c) physisorbed in thin-film polymer, according to the model proposed by Hunter.[13] 'C' indicates MC isomer, 'M' indicates cation, 'B' indicates covalently attached silane, and 'X' indicates MC-cation complexation. The shaded balls indicate solvent molecules. (d-f) Comparison of fluorescence intensity from (-blue) MC isomer without cations, (-red) MC-Ca^{2+} complex, and (-green) 2MC-Al^{3+} complex, and (-violet) SP isomer without cations, (-orange) SP isomer with Ca^{2+} present, and (-brown) SP isomer with Al^{3+} present. (d) Shows results of MC isomer and cations in acetonitrile solution, (e) shows results from covalently bound (chemisorbed) SP and MC isomers with cations in acetonitrile solution, and (f) shows results from polymer doped (physisorbed) SP and MC isomers with cations in water.

COMMUNICATION   WILEY-VCH

In conclusion, we investigated a spiropyran ligand in three different nano-environments, namely in solution, covalently bound to a surface and embedded within polymer. The S-I molecule used here enabled different binding modes to Ca^{2+} and Al^{3+} in that it is single-liganded to Ca^{2+} and dual-liganded to Al^{3+}. We found that the different nano-environments have differing affects on the affinity for single-ligand and dual-ligand binding. Dual-ligand binding required high conformational mobility of S-I. Covalent binding onto a surface (chemisorption) restricts conformational mobility, preventing dual-ligand binding while still enabling single-ligand binding. Embedding S-I in polymer (physisorption) preserves conformational mobility so that dual-ligand binding is observed. In addition to the conformational mobility of the S-I ligand, host-guest interaction within a polymer matrix is affected by the mobility (diffusion) of the cation. While both Ca^{2+} and Al^{3+} appear to have high mobility when dissolved in an analyte solution, within the PMMA matrix the larger sized Ca^{2+} has as hindered diffusion compared with smaller Al^{3+}.

The results here show that impact of the nano-environment on diffusion and conformational mobility can be used to control host-guest interaction. For example, if Ca^{2+} selectivity is preferred, then S-I would be attached to a surface. However, if Al^{3+} selectivity is preferred, then embedding S-I into PMMA would be better. Adjustment of the PMMA film thickness might be able to further enhance selectivity to Al^{3+} due to enhanced hindrance of Ca^{2+} diffusion. The impact of the nano-environment can also be used to modulate which analyte solvent can be used. For organic solvents such as acetonitrile, MC can be dissolved or attached to a surface. However, for aqueous solution these methods cannot be used since MC is not water-soluble. However, by embedding the molecule in PMMA, an aqueous solution based analyte can be readily used since the SP and MC isomers are stable and solvated within the PMMA matrix, which also preserves the conformational mobility required for photoswitching and binding to cations.

Acknowledgements

Keywords: keyword 1 • keyword 2 • keyword 3 • keyword 4 • keyword 5

[1]   Lehn, J.-M. *Angew. Chem. Int. Ed.* **1988**, 27, 89 - 112.
[2]   (a) Slowing, I.; Trewyn, B.; Giri, S.; Lin, V.-Y. *Adv. Funct. Mater.* **2007**, 17, 1225 - 1236; (b) Chen, Y.; Wang, S.; Ye, J.; Li, D.; Liu, Z.; Wu, X. *Nanoscale* **2014**, 6, 9563 - 9567; (c) Yang, Y.-W.; Sun, Y.-L.; Song, N. *Accounts Chem. Res.* **2014**, 47, 1950 - 1960; (d) Okrut, A.; Runnebaum, R. C.; Ouyang, X.; Lu, J.; Aydin, C.; Hwang, S.-J.; Zhang, S.; Olatunji-Ojo, O. A.; Durkin, K. A.; Dixon, D. A.; Gates, B. C.; Katz, A. *Nat. Nano.* **2014**, 9, 459 – 465.
[3]   Mal, N. K.; Fujiwara, M.; Tanaka, Y. *Nature* **2003**, 421, 350 - 353.
[4]   Kittelmann, M.; Nimmrich, M.; Neff, J. L.; Rahe, P.; Greń, W.; Bouju, X.; Gourdon, A.; Kühnle, A. *J. Phys. Chem. C* **2013**, 117, 23868 - 23874.
[5]   Major, R. C.; Zhu, X.-Y. *J. Am. Chem. Soc.* **2003**, 125, 8454 - 8455.
[6]   Kresge, C. T.; Leonowicz, M. E.; Roth, W. J.; Vartuli, J. C.; Beck, J. S. *Nature* **1992**, 359, 710 - 712.
[7]   Corma, A. *Chem. Rev.* **1997**, 97, 2373 - 2420.
[8]   Kimura, K.; Yamashita, T.; Yokoyama, M. *J. Chem. Soc., Perkin Trans.* **1992**, 2, 613 - 619.
[9]   Bosque-Sendra, J. M.; Almansa-López, E.; Garćıa-Campaña, A. M.; Cuadros-Rodŕıguez, L. *Anal. Sci.* **2003**, 19, 1431 - 1439.
[10] Shao, Y. et al. *Phys. Chem. Chem. Phys.* **2006**, 8, 3172 - 3191.
[11] Perdew, J. P.; Burke, K.; Ernzerhof, M. *Phys. Rev. Lett.* **1996**, 77, 3865 - 3868.
[12] (a) Kirkwood, J. G. *J. Chem. Phys.* **1939**, 7, 911; (b) Kirkwood, J. G. *J. Chem. Phys.* **1934**, 2, 767; (c) Onsager, L. *J. Am. Chem. Soc.* **1936**, 58, 1486 - 1493.
[13] Hunter, C. A. *Angew. Chem. Int. Ed.* **2004**, 43, 5310 - 5324.
[14] Basabe-Desmonts, L.; Reinhoudt, D. N.; Crego-Calama, M. *Chem. Soc. Rev.* **2007**, 36, 993-1017.
[15] (a) Frank, B.; Gast, A. P.; Russell, T. P.; Brown, H. R.; Hawker, C. *Macromolecules* **1996**, 29, 6531 - 6534; (b) Fries, K. H.; Driskell, J. D.; Sheppard, G. R.; Locklin, J. *Langmuir* **2011**, 27, 12253 - 12260.
[16] (a) Heng, S.; Nguyen, M.-C.; Kostecki, R.; Monro, T. M.; Abell, A. D. *RSC Adv.* **2013**, 3, 8308 - 8317; (b) Kostecki, R.; Ebendorff-Heidepriem, H.; Afshar V., S.; McAdam, G.; Davis, C.; Monro, T. M. *Opt. Mater. Express* **2014**, 4, 1515 - 1525.
[17] Perrella, C.; Griesser, H. P.; Light, P. S.; Kostecki, R.; Stace, T. M.; Ebendorff-Heidepriem, H.; Monro, T. M.; White, A. G.; Luiten, A. N. *Phys. Rev. Applied* **2015**, 4, 014013.
[18] (a) Kostecki, R.; Ebendorff-Heidepriem, H.; Davis, C.; McAdam, G.; Warren-Smith, S. C.; Monro, T. M. *Opt. Mater. Express* **2012**, 2, 1538 - 1547; (b) Schartner, E. P.; Tsiminis, G.; François, A.; Kostecki, R.; Warren-Smith, S. C.; Nguyen, L. V.; Heng, S.; Reynolds, T.; Klantsataya, E.; Rowland, K. J.; Abell, A. D.; Ebendorff-Heidepriem, H.; Monro, T. M. *Int. J. Appl. Glass Sci.* **2015**, 6, 229 - 239.

Roman Kostecki,*,† Sabrina Heng,*,† Adrian M. Mak,‡ Heike Ebendorff-Heidepriem,†
Andrew D. Abell,† and Tanya M. Monro†

*ARC Centre of Excellence for Nanoscale BioPhotonics, and Institute for Photonics and Advanced Sensing,
and the School of Chemistry and Physics, The University of Adelaide, Adelaide, South Australia, 5005,
Australia, and Institute of High Performance Computing, 1 Fusionopolis Way, No. 16-16 Connexis,
Singapore 138632*

Received February 3, 2015; E-mail: roman.kostecki@adelaide.edu.au; sabrina.heng@adelaide.edu.au

Experimental

Analyte

Separate solutions of Al and Ca metal ions were prepared by dissolving potassium alum ($KAl(SO_4)_2$) and calcium perchlorate ($Ca(ClO_4)_2$) respectively.

General Methods for Synthesis

All ^{13}C NMR spectra (75 and 125 MHz) and ^1H NMR spectra (300 and 500 MHz) were recorded on a Varian Gemini spectrometers in $CDCl_3$, CD_3OD or $DMSO-d_6$. Chemical shifts (δ) are reported in ppm. Chemical shifts of $CDCl_3$ ($\delta C = 77.1$ ppm), $DMSO-d_6$ ($\delta C = 39.52$ ppm) or TMS ($\delta H = 0.0$ ppm) were used as internal standards in all ^{13}C NMR and ^1H NMR experiments, respectively. Signals are reported as s (singlet), d (doublet), t (triplet) or m (multiplet). Low resolution mass spectral data were analyzed using a Finnigan MAT LCQ spectrometer with MS/MS and ESI probe, utilizing XCalibur software. High-resolution mass spectral data were analyzed using an Ultimate 3000 RSL HPLC (Thermo Fisher Scientific Inc., MA) and an LTQ Orbitrap XL ETD using a flow injection method, with a flow rate of 5 μL/min. The HPLC flow is interfaced with the mass spectrometer using the Electrospray source (Thermo Fisher Scientific Inc., MA). Mass spectra were obtained over a range of $100 < m/z < 1000$. Data were analyzed using XCalibur software (Version 2.0.7, Thermo Fisher Scientific). The compounds were analyzed and purified by reverse phase HPLC, using an HP 1100 LC system equipped with a Phenomenex C18 column (250×4.6 mm) for analytical traces and a Phenomenex C18 column (250×21.2 mm) for purification, a photodiode array detector, and a Sedex evaporative light scattering detector. Water/TFA (100/0.1 by v/v) and ACN/TFA (100/0.08 by v/v) solutions were used as aqueous and organic buffers. HPLC grade acetonitrile (Scharlau) was used in all related experiments. All ions used in this work were in the form of perchlorate salt. All other reagents were purchased from Sigma-Aldrich and used without further purification.

Scheme 1. (1) 2,3,3-Trimethylindlenine $\xrightarrow{i}$ (2) 1-(4-ethoxy-4-oxobutyl)-2,3,3-trimethyl-3H-indol-1-ium bromide
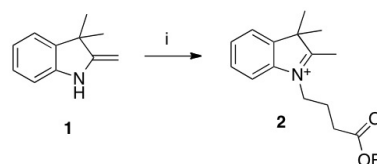
(2)   1-(4-ethoxy-4-oxobutyl)-2,3,3-trimethyl-3H-indol-1-ium bromide

(Scheme 1) 2,3,3-Trimethylindlenine (**1**, 1.36 mL, 8.5 mmol) and Ethyl 4-bromobutyrate (3.6 mL, 17 mmol) were dissolved in anhydrous chloroform (20 mL) and stirred under reflux for 48 h. The reaction was cooled to room temperature and excess solvent was removed under vacuo. The resultant pink solid was redissolved in a solution of methanol (1 mL) and diethyl ether (20 mL). The bright pink crystals that formed were collected and dried under vacuum to yield 1-(4-ethoxy-4-oxobutyl)-2,3,3-trimethyl-3H-indol-1-ium bromide (**2**, 800 mg, 35%). ^1H NMR ($CDCl_3$, 300 MHz) δ 7.99 (d, $J = 7.2$ Hz, 1H), 7.61 – 7.54 (m, 3H), 4.91 (t, $J = 8.1$ Hz, 2H), 4.11 (q, $J = 7.2$ Hz, 2H), 3.20 (s, 3H), 2.73 (app t, $J = 6.45$, 2H), 22.28 2.23 (m, 2H), 1.65 (s, 6H), 1.24 (t, $J = 7.2$ Hz, 3H); ^{13}C NMR (75 MHz) δ 196.9. 173.8, 141.9, 141.2, 129.4, 128.9, 123.6, 115.4, 56.0, 54.2, 47.1, 30.4, 22.5, 22.0 (3H), 14.2. MS (m/z) for $C_{17}H_{24}NO_2^+$ calcd 274.38 found 274.40.

(4)   3-((1,4,7,10,13-pentaoxa-16-azacyclooctadecan-16-yl)methyl)-2-hydroxy-5-nitro benzaldehyde

(Scheme 2)   3-(chloromethyl)-2-hydroxy-5-nitrobenzaldehyde* (**3**, 250 mg, 1.16 mmol), EtN_3 (324 μL, 2.32 mmol) and 1-aza-18-crown-6 were dissolved in anhydrous THF and set to reflux for 18 h. The reaction mixture was allowed to cool to room temperature and excess solvent was removed under vacuo. The crude mixture (**4**) was used in the next step without further purification. ^1H NMR ($CDCl_3$, 500 MHz) δ 10.35 (s, 1H), 8.49 (s, 1H), 8.03 (s, 1H), 4.18

---

†ARC Centre of Excellence for Nanoscale BioPhotonics, and Institute for Photonics and Advanced Sensing, and the School of Chemistry and Physics, The University of Adelaide, Adelaide, South Australia, 5005, Australia

‡Institute of High Performance Computing, 1 Fusionopolis Way, No. 16-16 Connexis, Singapore 138632

1

**Scheme 2.** **(3)** 3-(chloromethyl)-2-hydroxy-5-nitrobenzaldehyde*
$\xrightarrow{ii}$ **(4)** 3-((1,4,7,10,13-pentaoxa-16-azacyclooctadecan-16-yl)methyl)-2-hydroxy-5-nitro benzaldehyde
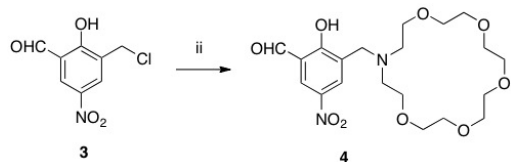
(s, 2H), 3.78 – 3.58 (m, 24H); ^{13}C NMR (125 MHz) δ 189.5, 172.4, 136.6, 129.4, 125.4, 123.5, 123.0, 70.8 (8C), 67.1 (2C), 57.5, 52.8 (2C). MS (m/z) $[C_{20}H_{30}N_2O_9 + H]^+$ calc 443.4; found 443.6.

(SP) 4-(8-((1,4,7,10,13-pentaoxa-16-azacyclo-octadecan-16-yl)methyl)-3',3'-dimethyl-6-nitrospiro [chromene-2,2'-indolin]-1'-yl)butanoic acid

Scheme 3. **(2 + 4)** $\xrightarrow{iii}$ **(5)** Ethyl 4-(8-((1,4,7,10,13-pentaoxa-16-azacyclooctadecan-16-yl)methyl)-3',3'-dimethyl-6-nitrospiro[chromene-2,2'-indolin]-1'-yl)butanoate $\xrightarrow{iv}$ **(SP)** 4-(8-((1,4,7,10,13-pentaoxa-16-azacyclooctadecan-16-yl)methyl)-3',3'-dimethyl-6-nitrospiro[chromene-2,2'-indolin]-1'-yl)butanoic acid
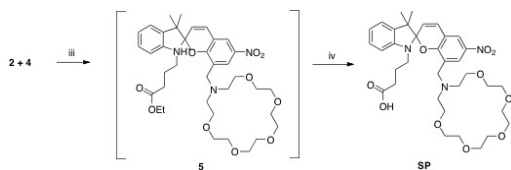
(Scheme 3) Compound **4** (181 mg, 0.41 mmol) and compound **2** (112 mg, 0.41 mmol) were dissolved in anhydrous ethanol (10 mL) and the reaction was set to reflux for 18 h. Excess solvent was removed under vacuum. The reaction was monitored via TLC and upon consumption of starting material, excess solvent was removed under vacuo and the crude product **5** Ethyl 4-(8-((1,4,7,10,13-pentaoxa-16-azacyclooctadecan-16-yl)methyl)-3',3'-dimethyl-6-nitrospiro[chromene-2,2'-indolin]-1'-yl)butanoate was used in the next step without further purification. The presence of the desired product was confirmed via mass spectrometry where MS (m/z) $[C_{37}H_{51}N_3O_{10} + H]^+$ calcd 698.8; found 698.1. Compound **5** was added to a solution of 2 M NaOH and methanol (5:10 mL) and set to stir at 50°C for 5 h. The reaction mixture was cooled to room temperature and excess solvent was removed under vacuo. The crude mixture was purified using C18 reverse phase silica gel beginning with 100% H$_2$O and gradually increasing the ratio of acetonitrile from 0 – 40%. The desired product eluded at 40:60 acetonitrile:water (purple solid, 40 mg, 42%). ^{1}H NMR (CD$_3$OD, 500 MHz) δ 8.18 (d, $J = 2.0$ Hz, 1H), 8.07 (d, $J = 3.0$ Hz, 1H), 7.17 – 7.08 (m, 3H), 6.84 (t, $J = 7.5$ Hz, 1H), 6.74 (d, $J = 8.0$ Hz, 1H), 6.06 (d, $J = 10.5$ Hz, 1H), 3.87 – 3.46 (m, 22H), 3.28 – 3.14 (m, 2H), 2.79 – 2.64 (m, 4H), 2.33 – 2.21 (m, 2H), 1.93 – 1.90 (app t, $J = 7.0$ Hz, 2H), 1.34 (s, 3H), 1.31 (s, 3H); 13C (CD$_3$OD 125 MHz) δ 181.1, 161.5, 147.1,

135.9, 128.3, 127.6, 127.4, 122.4, 122.0, 121.3, 119.2, 114.2 (2C), 106.6, 103.8, 69.9 (2C), 69.7 (2C), 69.6 (2C), 69.3 (2C), 56.4, 52.3 (2C), 47.8 (2C), 26.1, 25.1, 25.0, 18.8 (2C). HRMS (m/z) $[C_{35}H_{47}N_3O_{10} + H]^+$ calc 670.3334, found 670.3340.
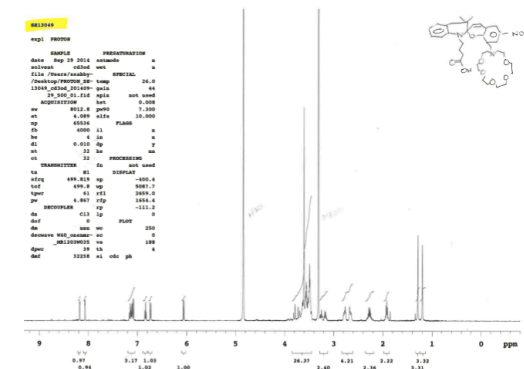
Figure 1. **SP** NMR spectra

Surface Measurements Setup

The optical fiber used was an exposed-core silica MOF, a cross section of which is shown by the scanning electron microscope (SEM) image in Fig. 2(a). This fiber was designed and fabricated in-house[1] (120 m) with an effective core diameter of 7.5 μm (defined as the diameter of a circle whose area is equal to a triangle that fits wholly within the core area[2]) shown by the red highlighted area of the enlargement in Fig. 2(b). A 15 mW laser excitation light source with wavelength at 532 nm is coupled into the core of the functionalized fibers using a 60$\times$ microscope objective (NA = 0.85) via a dichroic mirror. The back reflected light collected from the functionalized fiber core was imaged using the same objective, passed through the dichroic mirror and 550 nm long pass filter, and focused into a multimode patch fiber (MMF) with 200 μm diameter core using a 10$\times$ microscope objective (NA = 0.25). This signal being focused into the MMF was then characterized using a Horiba iHR550 Imaging Spectrometer with Synapse CCD Detector. Additional optics used, such as mirrors for beam alignment, have been omitted in Fig. 2 for clarity. In each case (**F1** and **F2**) a 60 cm coupled length of functionalized fiber was characterized with $\sim$ 10 cm long central section immersed in the analytes.

(F1) Covalent Functionalization of Exposed-Core MOF with SP

In order to couple the **SP** molecules to the exposed core surface, 3-aminopropyltriethoxysilane (APTES) was used which covalently bonds to hydroxyl groups on the silica core surface to provide free amine groups for covalent bonding with the **SP** carboxylic acid group.[3] A 80 cm length of fiber was prepared for APTES functionalization by flame sealing the holes at each end, then clean and hydroxylate the outer surface by immersion in 70% nitric acid for 16 hrs followed by 2 hrs in 70/30 piranha solution (concentrated sulfuric acid and hydrogen peroxide). After rinsing and drying, the
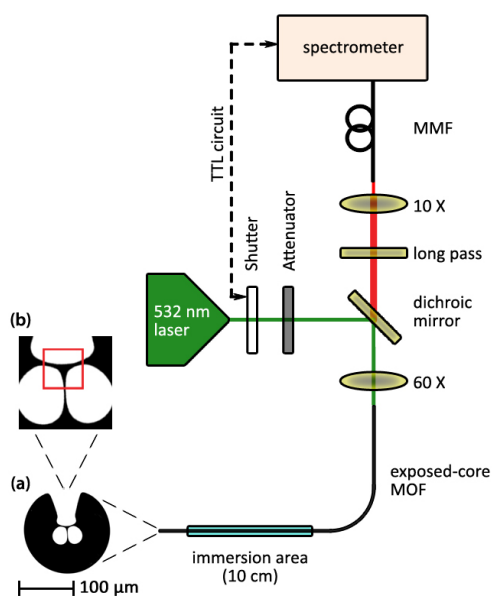
Figure 2. Sensing platform setup used to compare functionalization methods (MMF is multimode fiber), including a SEM cross section (a) of the silica exposed-core MOF, and enlarged view (b) of the core (Ø7.5 μm) indicated by the red square.

prepared fiber was immersed in 5% APTES–toluene solution for 2 hrs then rinsed with toluene and acetonitrile. This silane functionalized fiber was then immersed in a solution of **SP** + acetonitrile + 1-[Bis(dimethylamino)methylene]-1H-1,2,3-triazolo[4,5-b]pyridinium 3-oxid hexafluorophosphate (HATU) for 20 hrs and rinsed with acetonitrile, which gave the functionalized exposed-core fiber with **SP** covalently bound to the core (**F1**).

(F2) Thin Film Polymer Functionalization of Exposed-Core MOF with SP

Functionalization of the exposed-core MOF with thin film polymer followed the same procedure as detailed in Ref. 4 and briefly outlined here. Clear cast acrylic rod PMMA (1.18 g/cm³, *plexiglass rod* - Professional Plastics Pte. Ltd. [Singapore]), dissolved in dichloromethane (DCM) at a concentration of 12.3 g/L, was added to **SP** and DCM to make a concentration of $30_{(SP)} : 100_{(PMMA)}$ by weight. One end of a 1 m long exposed-core MOF was fed through a silicon septa fitted to the bottom of a open-end vial. With a few millimeters of PMMA+SP+DCM solution in the vial, the fiber was pulled through the solution and silica septa by hand at ∼ 8 m/min to leave behind a thin film coating of the **SP** doped PMMA on the outside of the fiber structure (**F2**). The thickness of the coating left behind for this particular mixture was not measured, however previous results show that this method typically applies a ∼ 50 nm layer to the surface of the MOF exposed core.[4] This procedure was performed in a laboratory chemical fume hood at room temperature, without additional curing.

Computational data – PBE/LANL2DZ optimized 3D xyz coordinates

SP-Al³⁺

N 0.41194 -0.19058 0.07445, C 0.12945 0.09108 1.52275, C 1.83552 -0.57596 -0.14707, C 0.06164 1.01038 -0.73625, C 1.98335 -1.16657 -1.55812, H 2.11061 -1.31017 0.62023, H 2.50715 0.29510 -0.03253, C -1.45344 1.16968 -0.74265, H 0.43730 0.86340 -1.76016, H 0.54106 1.92471 -0.33805, H 2.69667 -2.00359 -1.59809, H 2.28287 -0.40113 -2.29229, O 0.66800 -1.66914 -1.97483, O -2.01448 -0.17892 -0.78126, H -1.80878 1.73245 -1.62202, H -1.82513 1.67527 0.16493, H -0.94171 0.35307 1.59601, H 0.69447 0.99265 1.82904, C 0.44327 -1.04066 2.47140, C -3.34874 -0.22378 -0.20037, C 0.46298 -1.72835 -3.42434, C -1.00643 -1.40876 -3.62883, H 0.79463 -2.72027 -3.76758, H 1.09440 -0.95987 -3.90205, O -1.78764 -2.13662 -2.64416, H -1.34634 -1.65055 -4.64935, H -1.21887 -0.34528 -3.43634, C -3.79986 -1.66077 -0.29052, H -4.02748 0.43768 -0.76502, H -3.28791 0.12249 0.84755, H -4.11566 -1.93247 -1.31221, H -4.62295 -1.85634 0.41645, O -2.64296 -2.47342 0.07719, C -3.00092 -3.88965 0.18791, C -2.16422 -3.48855 -3.04386, C -1.73657 -4.70885 -0.03956, H -3.77855 -4.10023 -0.56613, H -3.42229 -4.06979 1.19112, H -1.99209 -5.73793 -0.34199, H -1.10619 -4.73476 0.85638, C -1.18165 -4.47879 -2.43609, H -2.19412 -3.56071 -4.14358, H -3.18974 -3.63740 -2.67099, H -0.20023 -4.47150 -2.93609, H -1.58171 -5.50638 -2.46536, O -0.91050 -4.08509 -1.06509, C 0.72373 -0.70563 3.80379, C 0.95389 -1.71833 4.73449, C 0.99296 -3.05049 4.34953, C 0.78602 -3.42218 2.99785, C 0.40826 -2.39601 2.05919, H 0.75065 0.33452 4.14474, N 1.19427 -1.35958 6.15827, H 1.23077 -3.80245 5.10787, C 1.05684 -4.81816 2.70317, O 0.05174 -2.74347 0.80541, C 1.37315 -5.43292 1.51100, C 1.77910 -6.80387 1.42353, H 1.11530 -5.42944 3.60791, H 1.37462 -4.83589 0.59402, N 2.16941 -7.36373 0.26015, C 1.87807 -7.85339 2.54205, C 2.54257 -8.72656 0.42420, C 2.30631 -6.69690 -1.04605, C 2.96156 -7.46598 3.59068, C 2.35851 -9.07041 1.77263, C 0.51027 -8.14267 3.21511, C 3.01477 -9.62685 -0.54002, C 2.64042 -10.36910 2.19553, C 3.10924 -11.29472 1.24617, C 3.29692 -10.92744 -0.10036, H 0.14108 -7.28387 3.79818, H 0.62832 -8.99030 3.90891, H -0.25283 -8.41957 2.46976, H 3.93094 -7.25514 3.11136, H 3.10121 -8.31323 4.28057, H 2.67087 -6.59026 4.19059, H 3.16835 -9.35087 -1.58690, H 2.50614 -10.67363 3.23842, H 3.33585 -12.31765 1.56006, H 3.66893 -11.66597 -0.81564, C 3.72031 -6.11275 -1.24041, H 1.53475 -5.92098 -1.14135, H 2.09232 -7.46506 -1.80718, H 3.81228 -5.17079 -0.67100, C 4.09972 -5.89289 -2.70815, H 4.45529 -6.81540 -0.81066, H 4.05608 -6.84205 -3.27562, H 5.15789 -5.58106 -2.77481, C 3.27503 -4.86616 -3.46792, O 3.74682 -4.73711 -4.70884, O 2.30801 -4.23835 -3.00612, C 3.10563 -3.78524 -5.61832, C 3.87428 -3.81190 -6.92391, H 3.13064 -2.78989 -5.13888, H 2.05156 -4.09234 -5.74330, H 4.92349 -3.51387 -6.77224, H 3.41650 -3.10577 -7.63614, H 3.85445 -4.81547 -7.37670, O 1.39234 -2.29689 6.93822, O 1.16980 -0.15507 6.43401, Al -0.76459 -1.91490 -0.59451

SP-Ca²⁺

N 0.96713 -1.64402 0.13772, C 0.91994 -0.24561 0.66178, C 2.22537 -1.93878 -0.58853, C -0.21906 -1.90138 -0.71354, C 2.31418 -3.41523 -0.98955, H 3.05775 -1.68155 0.08679, H 2.34258 -1.31619 -1.50145, C -1.52099 -1.83065 0.07120, H -0.12344 -2.91101 -1.14231, H -0.27785 -1.18123 -1.55859, H 3.37121 -3.70836 -1.11442, H 1.77740 -3.62609 -1.93489,

O 1.71270 -4.20163 0.06546, O -1.39136 -2.66592 1.24673, H -2.35778 -2.19394 -0.55415, H -1.76071 -0.79858 0.38960, H 0.06209 -0.20002 1.36219, H 0.68327 0.45325 -0.16829, C 2.14358 0.27660 1.38100, C -2.48359 -2.45275 2.16309, C 1.88977 -5.62232 -0.10710, C 0.99357 -6.30309 0.91083, H 2.95437 -5.87027 0.04894, H 1.58598 -5.92583 -1.12763, O 1.27629 -5.68157 2.18400, H 1.21956 -7.38500 0.95171, H -0.07958 -6.17346 0.66370, C -2.29778 -3.37736 3.34482, H -3.45095 -2.66486 1.66916, H -2.47833 -1.39580 2.49495, H -2.44099 -4.43874 3.05880, H -3.03574 -3.12189 4.12720, O -0.95488 -3.18741 3.83695, C -0.76793 -3.67628 5.17849, C 0.70650 -6.33704 3.32842, C 0.72247 -3.61122 5.46870, H -1.15018 -4.71390 5.25441, H -1.32936 -3.04772 5.89630, H 0.93605 -4.00898 6.47817, H 1.08256 -2.57051 5.41291, C 1.42763 -5.76220 4.54167, H 0.87688 -7.42963 3.27524, H -0.38779 -6.16001 3.36690, H 2.47232 -6.11754 4.54977, H 0.93873 -6.09499 5.47474, O 1.48207 -4.31858 4.46678, C 2.61903 1.53237 1.01074, C 3.63971 2.15960 1.74491, C 4.20578 1.53953 2.84312, C 3.79514 0.23767 3.23253, C 2.71712 -0.42330 2.50534, H 2.19717 2.07257 0.15754, N 4.10797 3.49725 1.33596, H 4.99969 2.05838 3.38907, C 4.53834 -0.34263 4.31465, O 2.27394 -1.60033 2.86329, C 4.58501 -1.66151 4.73200, C 5.46458 -2.14710 5.73492, H 5.21843 0.36493 4.80003, H 3.94679 -2.37565 4.20630, N 5.66619 -3.47526 5.91227, C 6.28558 -1.37464 6.77790, C 6.52982 -3.73904 7.01073, C 5.15146 -4.52416 5.02281, C 7.43132 -0.55104 6.12013, C 6.89778 -2.51106 7.58185, C 5.38717 -0.47284 7.65980, C 6.97298 -4.97066 7.50371, C 7.73357 -2.49325 8.69799, C 8.18381 -3.71869 9.22103, C 7.81154 -4.93773 8.62855, H 4.92872 0.33693 7.06974, H 5.99983 -0.01400 8.45279, H 4.58456 -1.05439 8.14163, H 8.02041 -1.16538 5.42029, H 8.11060 -0.19027 6.99695, H 7.05251 0.33152 5.58140, H 6.69480 -5.92597 7.04966, H 8.03582 -1.55023 9.16468, H 8.83529 -3.72334 10.09947, H 8.17973 -5.87840 9.04750, C 5.89787 -4.56017 3.67904, H 4.07405 -4.34255 4.86448, H 5.24604 -5.48241 5.55732, H 5.81622 -3.56543 3.20487, C 5.30724 -5.63055 2.73817, H 6.97108 -4.75295 3.84419, H 4.20503 -5.57954 2.73401, H 5.61255 -6.63915 3.06898, C 5.75943 -5.40020 1.30165, O 7.05837 -5.69413 1.14980, O 5.02917 -4.96110 0.41288, H 7.62639 -5.47341 -0.18878, C 9.07978 -5.89817 -0.14196, H 7.50144 -4.40616 -0.43764, H 7.03492 -6.06298 -0.90876, H 9.64843 -5.30299 0.59057, H 9.53638 -5.74660 -1.13389, H 9.17522 -6.96439 0.11872, O 5.00186 4.01691 2.01879, O 3.57101 3.99909 0.33681, Ca 0.91516 -3.18536 2.12912

SP

N 0.22137 0.27286 -0.11759, C 0.27538 0.28158 1.33438, C 1.28213 0.89148 -0.89386, C -1.07043 0.36045 -0.78201, C 2.68821 0.69909 -0.33795, H 1.15143 1.99317 -1.05007, H 1.25270 0.43953 -1.90649, C -2.22959 -0.25938 -0.01241, H -0.98213 -0.15340 -1.76124, H -1.38068 1.41112 -1.01261, H 2.80167 1.20093 0.64934, H 3.40427 1.19408 -1.03271, O 2.96717 -0.68828 -0.22788, O -1.98435 -1.64168 0.20521, H -3.16206 -0.11112 -0.60277, H -2.37447 0.26681 0.95643, H 1.28958 -0.03095 1.64374, H -0.35404 -0.54988 1.70352, C -0.12082 1.55184 2.07281, C -2.93739 -2.22355 1.07687, C 4.28359 -0.94202 0.22632, C 4.45890 -2.44088 0.39659, C 4.47850 -0.43030 1.19512, H 5.03832 -0.56914 -0.50465, O 3.70328 -2.87157 1.51974, H 5.54061 -2.67404 0.52924, H 4.11375 -2.95378 -0.52648, C -2.53945 -3.66201 1.35259, H -3.95736 -2.20790 0.62778, H -2.98506 -1.66633 2.03858, H -2.37841 -4.19307 0.38921, H -3.37695 -4.17264 1.88273, O

-1.35867 -3.67528 2.13765, C -0.94346 -4.99363 2.44649, C 3.72106 -4.28401 1.67664, C 0.41033 -4.95400 3.13386, H -0.86020 -5.61336 1.52668, H -1.68008 -5.49221 3.11945, H 0.59740 -5.94659 3.60728, H 0.39393 -4.19305 3.94547, C 2.71325 -4.68751 2.74025, H 4.73597 -4.63444 1.97502, H 3.45781 -4.78894 0.72269, H 2.79159 -3.99797 3.60732, H 2.95913 -5.71450 3.09990, O 1.41136 -4.65723 2.17682, C -0.39538 2.73966 1.43804, C -0.81095 3.89222 2.17555, C -0.96659 3.85935 3.54504, C -0.69738 2.66646 4.27407, C -0.23125 1.44934 3.53925, H -0.30819 2.83942 0.35483, N -1.08555 5.13284 1.45804, H -1.29699 4.76529 4.06263, C -0.89443 2.69677 5.67314, O 0.05745 0.36503 4.11275, C -0.65524 1.62181 6.54084, C -0.81579 1.58543 7.92484, H -1.25850 3.65218 6.07478, H -0.28658 0.72893 6.02760, N -0.51814 0.44849 8.63644, C -1.30259 2.66488 8.90310, C -0.71830 0.63326 10.01846, C 0.01934 -0.77013 8.02490, C -0.37205 3.90335 8.89051, C -1.20157 1.93704 10.23653, C -2.76694 3.07070 8.60252, C -0.50232 -0.26665 11.06814, C -1.49128 2.36115 11.53149, C -1.28809 1.47028 12.60284, C -0.79791 0.17620 12.36815, H -2.84789 3.57404 7.62546, H -3.12885 3.76478 9.38000, H -3.42752 2.18862 8.59435, H 0.67522 3.61518 9.07766, H -0.68079 4.60853 9.68111, H -0.41766 4.43013 7.92373, H -0.11342 -1.27488 10.89794, H -1.86830 3.37275 11.71873, H -1.51041 1.79061 13.62505, H -0.63780 -0.50426 13.21030, C 1.51751 -0.64514 7.68907, H -0.56696 -0.96994 7.11109, H -0.17505 -1.60559 8.71654, H 1.71777 0.37355 7.31593, C 1.94561 -1.64428 6.61109, H 2.12857 -0.76649 8.59930, H 1.36269 -1.49195 5.68346, H 1.76806 -2.69180 6.92408, C 3.41970 -1.49001 6.26733, O 3.71835 -2.20844 5.15353, O 4.21976 -0.80290 6.88752, C 5.07944 -2.08311 4.64782, C 5.98993 -3.13533 5.26482, H 5.43853 -1.06546 4.87089, H 4.96041 -2.21367 3.56095, H 6.10384 -2.96615 6.34787, H 6.99041 -3.08503 4.80103, H 5.58711 -4.14979 5.10402, O -1.45436 6.12636 2.11632, O -0.93531 5.13076 0.21916

References

(1) Kostecki, R.; Ebendorff-Heidepriem, H.; Warren-Smith, S. C.; Monro, T. M. Predicting the drawing conditions for Microstructured Optical Fiber fabrication. *Opt. Mater. Express* **2014**, *4*, 29 – 40.

(2) Ebendorff-Heidepriem, H.; Warren-Smith, S. C.; Monro, T. M. Suspended nanowires: fabrication, design and characterization of fibers with nanoscale cores. *Opt. Express* **2009**, *17*, 2646 – 2657.

(3) Foo, H. T. C.; Ebendorff-Heidepriem, H.; Sumby, C. J.; Monro, T. M. Towards microstructured optical fibre sensors: Surface analysis of silanised lead silicate glass. *J. Mater. Chem. C* **2013**, *1*, 6782 – 6789.

(4) Kostecki, R.; Ebendorff-Heidepriem, H.; Afshar V., S.; McAdam, G.; Davis, C.; Monro, T. M. A Novel Polymer Functionalization Method for Exposed-Core Optical Fiber. *Opt. Mater. Express* **2014**, *4*, 1515 – 1525.

APPENDIX J

Paper 10.

Demonstration of an Exposed-Core Fiber Platform for Two-Photon Rubidium Spectroscopy

C. Perrella,[1,*] H. P. Griesser,[1] P. S. Light,[1] R. Kostecki,[1,2] T. M. Stace,[3,4] H. Ebendorff-Heidepriem,[1,2]
T. M. Monro,[1,5] A. G. White,[4,6] and A. N. Luiten[1]

[1]*Institute for Photonics and Advanced Sensing (IPAS) and the School of Physical Sciences,*
The University of Adelaide, Adelaide, Australia
[2]*ARC Center of Excellence for Nanoscale Biophotonics, Australia*
[3]*ARC Centre for Engineered Quantum Systems, Australia*
[4]*School of Mathematics and Physics, University of Queensland, Brisbane, Australia*
[5]*The University of South Australia, Adelaide, Australia*
[6]*ARC Centre for Quantum Computing and Communication Technology, Australia*

We demonstrate a promising fiber architecture for generating strong photon-photon interactions. Exposed-core silica optical fibers possess low-loss guidance between 400 and 1700 nm crucial for quantum-logic applications. The potential of this fiber is demonstrated by exciting a two-photon transition within a rubidium vapor using an exposed-core silica optical fiber. Transit-time broadened spectral features enable measurement of the evanescent-field scale length of (120 ± 20) nm which shows excellent agreement with the characteristics of the modeled fiber mode (118 ± 2) nm. We observe a two-photon absorption coefficient of 8.3 cm^{-1} for one optical mode in response to a transmitted power of 1.3 mW in the second mode. A clear pathway to an exposed-core fiber exhibiting substantial absorption mediated by a single photon is identified.

I. INTRODUCTION

Strong photon-photon interactions are a key ingredient to produce the on-demand and deterministic entanglement necessary for a scalable, universal set of quantum-photonic-logic devices [1,2]. The most promising results to date are generated from resonantly enhanced systems [3–5], which recently demonstrated a near-ideal two-photon π phase shift [6]. The resonant nature of these platforms places tight constraints on the interacting photon's frequency and bandwidth. Nonresonant (traveling-wave) systems avoid such restrictions and demonstrate all-optical switching with a few hundred photons [7] and broadband single-photon memories [8,9]. One promising path to creating nonresonant strong photon-photon interactions is the use of two-photon transitions within atomic vapors [10–14]. The efficiency of these higher-order atom-light interactions is directly proportional to optical intensity; thus, an optical arrangement capable of generating high optical intensities at the single-photon level is required.

Two main approaches are used to generate these high-intensity traveling optical fields within atomic vapors. Solid-core optical waveguides [14–20] with core areas of approximately 0.1 μm^2 produce optical fields outside their core with peak intensities in the range of approximately 6 GW m^{-2} per milliwatt of guided power [21]. Such devices are capable of atom trapping [16,17] and driving two-photon transitions [14]. These nanoscale cores offer large optical

intensities but only short interaction lengths [20], can be fragile, and potentially suffer failure after prolonged operation [19]. A second approach confines a vapor within hollow-core optical waveguides [10–13,22–24]. The minimum core area demonstrated for hollow-core waveguides to date is approximately 16 μm^2 [25], leading to a maximum peak intensity in the range of approximately 125 MW m^{-2} per milliwatt of guided power, capable of driving two- and three-photon transitions [10–14,23]. Hollow-core waveguides offer long interaction lengths, although this comes at the cost of long vapor-loading times [12,23].

II. EXPOSED-CORE FIBER

Here we present an exposed-core fiber (ECF) architecture that exhibits many of the best features of the aforementioned approaches. Light is guided within the ECF's core, shown in Fig. 1(a), which is suspended from the outer jacket by three struts. An opening through the jacket (which extends along the length of the fiber) allows the surrounding medium access to the optical field that propagates outside the silica core. The peak intensity of the optical field in the surrounding medium is 0.25 MW m^{-2} per milliwatt of guided power for the fiber used here. While currently not demonstrating the same strong evanescent fields of a tapered fiber, the ECF's suspended core architecture offers superior mechanical strength, enabling long fiber lengths to be used which compensate for their lower intensity. In this paper, a 30-cm length of fiber is used, which is 60 times longer than typical tapered-fiber approaches [14]. The exposed-core

architecture alleviates the months required to load hollow-core waveguides [12,23,25], with absorption or fluorescence signatures observed within minutes to hours of exposure to atomic vapor. These attributes make the ECF architecture promising for use in quantum-photonic-logic devices which is demonstrated here via production of photon-photon interactions.

The ECF is manufactured via ultrasonic milling of an F300HQ silica rod to form a preform, which is drawn down into the final fiber diameter on a 6-m fiber tower [26,27]. The resulting ECF has an effective core diameter of 7.5 μm and demonstrates low-loss guidance between 400 and 1700 nm, measured by using a cutback technique over a length of 6.7 m; see Fig. 1(b). The fiber presents a low (0.12 ± 0.02) dB m^{-1} loss at the wavelengths used in this experiment, which is crucial for single-photon quantum applications. Finite element modeling of the ECF shows the electric field of the fundamental guided mode decays exponentially outside the silica core with a $1/e^2$ intensity scale length of $d = (118 \pm 2)$ nm and $1/e^2$ intensity area of $A = (0.77 \pm 0.05)$ μm^2 for the wavelengths used here; see Fig. 1(c). Experimental near-field mode images observed from this fiber matched numerical modeling well [see Fig. 1(e)], and power outside the core is due to imaging artifacts. The integrated power in the evanescent field on the exposed side of the core is 7×10^{-5} of the fundamental mode's power.

III. EXPERIMENTAL SETUP

To mediate photon-photon interactions, the fiber is surrounded by a rubidium (Rb) vapor which possesses a strong two-photon transition; see Fig. 2(a). The $5S_{1/2} \rightarrow 5D_{5/2}$ two-photon transition of Rb is enhanced via stepwise excitation through the intermediate $5P_{3/2}$ state of linewidth $\Gamma_{5P} = 6.1$ MHz. Lasers at 780 and 776 nm, frequencies ω_{780} and ω_{776}, respectively, are tuned to the $5S_{1/2} \rightarrow 5P_{3/2}$ and $5P_{3/2} \rightarrow 5D_{5/2}$ transitions, frequencies ω_{SP} and ω_{PD}, respectively. The $5D_{5/2}$ excited state has a lifetime of 238 ns (linewidth of $\Gamma_{5D} = 666$ kHz) with a 7.5% probability of decay via the $6P_{3/2} \rightarrow 5S_{1/2}$ transition to produce 420-nm fluorescence [28]. The 420-nm fluorescence provides a measure of the transition rate into the excited state and thus enables inference of the 780-nm absorption caused by the two-photon transition. Direct observation of the 780-nm absorption is masked by backscattered infrared light from the ECF faces and vacuum windows.

Figure 2(b) shows the optical setup. The 780-nm laser is an extended cavity diode laser, and the 776-nm laser is a titanium:sapphire laser. The 776-nm laser is typically held at a fixed frequency, while the 780-nm is scanned over 10 GHz.

The chamber, containing a $l = 30$ cm length of the ECF, is heated to a temperature of $T = (85 \pm 5)\,°$C to increase the Rb vapor density to $N = (2.2 \pm 0.8) \times 10^{18}$ atoms m^{-3}. The two lasers are launched into either end of the ECF to produce counterpropagating fields enabling Doppler-free spectroscopy of the two-photon transition. The beams are coupled through windows at either end of the chamber using 20-mm aspheric lenses. Initially, the transmission through the ECF is $(12.5 \pm 2.5)\%$. The ECF's low loss implies that this is due to poor coupling efficiency from optical-mode mismatch. Exposure to the Rb vapor over a period of 2 months degraded the transmission to $(1.0 \pm 0.2)\%$, associated with a Rb metallic layer on the surface of the fiber's exposed core generating an additional loss of 0.37 dB cm^{-1}. Similar effects are observed with a

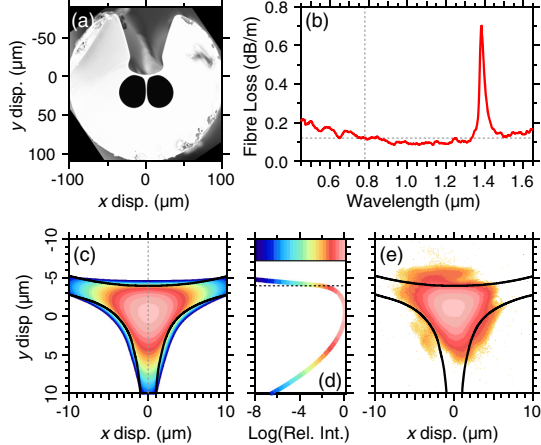
FIG. 1. (a) A scanning electron microscope image of the exposed-core fiber. (b) Cutback loss measurement of ECF showing < 0.2 dB m^{-1} loss from 450 to 1650 nm. An OH$^-$ absorption is visible at 1360 nm. Dashed lines indicate the operating wavelength and loss. (c) Finite element model of the power distribution of the fundamental mode. (d) Cross section through the optical mode at $x = 0$, indicated by the dashed line in (c). The horizontal line indicates the edge of the silica core. The scale bar shows color scaling for (c)–(e). (e) Experimental near-field mode image observed from the ECF.
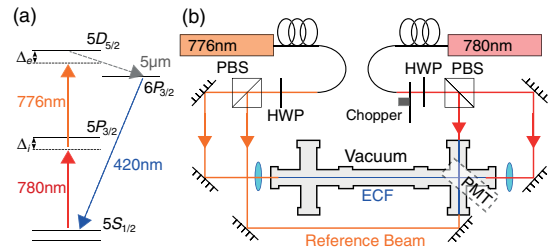

FIG. 2. (a) Energy-level diagram of the two-photon transition used. Excitation lasers (solid lines) and relevant decay paths (dashed) are indicated. (b) Experimental setup: PBS, polarization beam splitter; HWP, half-wave plate; ECF, exposed-core fiber; PMT, photomultiplier tube.

tapered optical fiber [19]. A second pair of laser beams (reference beams) passes through the vacuum chamber to measure the two-photon transition in a free-space vapor.

Two-photon fluorescence from either the ECF or the reference beams is detected by using a photomultiplier tube (PMT) positioned above a vacuum window. A dichroic filter prevents detection of scattered infrared light. During measurements of the fiber, the reference beams are blocked to eliminate background fluorescence. Synchronous detection is used to improve rejection of unwanted backgrounds and increase sensitivity. The 780-nm laser is amplitude modulated with a mechanical beam chopper at 3 kHz which is detected by the PMT as an amplitude modulation imprinted on the two-photon fluorescence. A lock-in amplifier demodulates the PMT output to measure the amplitude of the two-photon fluorescence.

IV. MODELING

The two-photon fluorescence is modeled by using a five-level atomic model, consisting of the intermediate and excited states $|5P\rangle$ and $|5D\rangle$, a decay path $|6P\rangle$, and the two ground states arising from hyperfine splitting, $|5S_1\rangle$ and $|5S_2\rangle$; see Fig. 2(a). In the atomic frame, detuning from the intermediate and two-photon state is expressed as $\Delta_i = \omega_{SP} - \omega_{780}(1 - v_z/c)$ and $\Delta_e = (\omega_{SP} + \omega_{PD}) - \omega_{780}(1 - v_z/c) - \omega_{776}(1 + v_z/c)$, respectively; see Fig. 2(a). States $|5S_1\rangle$ and $|5P\rangle$ are coupled by a laser with Rabi frequency $\Omega_{sp}(t)$, while a laser of strength $\Omega_{pd}(t)$ couples the states $|5P\rangle$ and $|5D\rangle$. The $|5P\rangle$, $|5D\rangle$, and $|6P\rangle$ states decay into the ground-state manifold with known branching ratios [28,29]. The evolution of a particular atom crossing an optical mode is governed by the optical Bloch master equations [30]:

$$\dot{\rho} = -i[H, \rho]$$
$$+ \sum_{5S_i}(\Gamma_{5S_i}^{5P}\mathcal{D}[|5P\rangle\langle 5S_i|]\rho + \Gamma_{5S_i}^{6P}\mathcal{D}[|6P\rangle\langle 5S_i|]\rho)$$
$$+ \Gamma_{5P}^{5D}\mathcal{D}[|5D\rangle\langle 5P|]\rho + \Gamma_{6P}^{5D}\mathcal{D}[|5D\rangle\langle 6P|]\rho \quad (1)$$

with interaction Hamiltonian

$$H = \Delta_e|5D\rangle\langle 5D| + \Delta_i|5P\rangle\langle 5P|$$
$$+ \left(\frac{\Omega_{sp}(t)}{2}|5P\rangle\langle 5S_1| + \frac{\Omega_{pd}(t)}{2}|5D\rangle\langle 5P| + \text{H.c.}\right)$$
$$+ \omega_{6P}|6P\rangle\langle 6P| + \omega_{5S_2}|5S_2\rangle\langle 5S_2|. \quad (2)$$

The two-photon scattering rate at a given time t is proportional to $S(t) = NAl\Gamma_{5D}\langle 5D|\rho(t)|5D\rangle$, where N is the number density of the Rb vapor, A is the optical-mode area, l is the interaction length, $\Gamma_{5D} = \Gamma_{5P}^{5D} + \Gamma_{6P}^{5D}$ is the excited-state decay rate, and the excited-state population is $\langle 5D|\rho(t)|5D\rangle$.

For conditions where the light-field crossing time is much shorter than the excited-state lifetime, the thermal motion of the atoms cannot be ignored [31,32]. Atoms with different speeds and trajectories will experience different time-dependent Rabi frequencies $\Omega_{sp}(t)$ and $\Omega_{pd}(t)$. We average the absorption over the Maxwell-Boltzmann distribution similar to that presented in Ref. [32] by using $\mathcal{F} = F_{v_0}^{(z)}(v_z)F_{v_0}^{(t)}(v_t)$, where $F_{v_0}^{(z)}(v_z)$ is the atoms' axial Maxwell-Boltzmann velocity distribution and $F_{v_0}^{(t)}(v_t)$ is the atoms' transverse Maxwell-Boltzmann speed distribution with $v_0 = (2k_B T/m)^{1/2}$. For a Gaussian beam, the final scattering-rate expression, averaging over axial velocity v_z and transverse speed v_t, takes the form

$$S(\Delta_i, \Delta_e) = \int_{-r}^{r}\int_0^{2\pi}\int_0^\infty\int_{-\infty}^\infty \mathcal{F}\bar{S}(v_t)dv_t dv_z d\theta dx, \quad (3)$$

where r is the Gaussian mode's electric field $1/e$ half-width. The averaged scattering rate $\bar{S}$ is evaluated by transformation of its parameter space to that of the atomic transit time using the relationship $v_t = d/\tau$, where d is the length of the chord through the Gaussian mode's electric field that the atom passes through, such that $\bar{S}(\tau) = \int_0^\tau S(t)dt$.

In contrast, the elongated aspect ratio of the evanescent field allows us to treat all atoms as if they are leaving the fiber traveling parallel to the y axis of Fig. 1 from $x = 0$. The final scattering rate, averaging over axial velocity v_z and transverse speed v_t, takes the form

$$S(\Delta_i, \Delta_e) = \int_0^\infty\int_{-\infty}^\infty \mathcal{F}\bar{S}(v_t)dv_t dv_z. \quad (4)$$

We calculate the expected line shape from Eqs. (3) and (4) for the two situations, free-space excitation and ECF excitation:

$$S(\Delta_i, \Delta_e) \propto NAl I_{780}I_{776}e^{-(\Delta_i/\sigma_D)^2}L(\Delta_e), \quad (5)$$

where I_{780} and I_{776} are the intensities of the 780- and 776-nm laser, respectively, and $\sigma_D = \omega_{SP}v_0/c$ is the Doppler broadening of the intermediate state. The line-shape function takes the form

$$L(\Delta_e) = \begin{cases} e^{-n|\Delta_e\bar{\tau}|} & \Gamma_{5D}\bar{\tau} \ll 1, \\ V(\Delta_e, \Gamma_{5P} + \Gamma_{5D}, \sigma_{PT}) & \Gamma_{5D}\bar{\tau} \gg 1, \end{cases} \quad (6)$$

where the average transit time is $\bar{\tau}$, $V(\Delta_e, \Gamma_{5P} + \Gamma_{5D}, \sigma_{TP})$ is a Voigt profile with detuning Δ_e, the Lorentzian component full width at half maximum of $\Gamma_{5P} + \Gamma_{5D}$, and $\sigma_{TP} = v_0(\omega_{PD} - \omega_{SP})/c$ is the Doppler broadening Gaussian $1/e$ half-width. For atoms that experience a decaying exponential evanescent-field profile, such as the mode profile of the ECF, $n = 2$, whereas $n = 1$ for a Gaussian optical-mode profile [31].
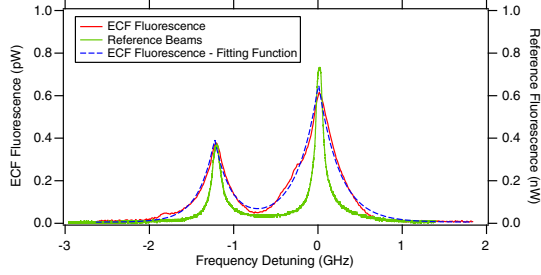
FIG. 3. Fluorescence spectra from the ECF (red line) with fit of the form in Eq. (5) (dashed blue line), the reference beam (green line) as a function of 780-nm detuning from the ^{85}Rb $F_g = 3 \rightarrow F' = 4$ D_2 transition. The ECF spectra show transit-time broadening, whereas the reference is a Voigt profile, both expected from Eq. (6). A frequency shift between the two spectra is subtracted, a result of spectra acquired at different times.

V. RESULTS

A. Spectral line shape

Figure 3 presents experimental measurements of the fluorescence resulting from excitation via free-space reference beams (green line) and with beams guided by the ECF (red line). The spectral line shapes are seen to be consistent with Eqs. (5) and (6): The ECF excitation shows a broadened line shape characteristic of transit-time-limited light-atom interactions, while the free-space excitation shows a more conventional Voigt profile. The free-space vapor fluorescence line shape shows a Voigt profile, with a full width at half maximum of (135 ± 15) MHz produced through strong power broadening of the intermediate $5P_{3/2}$ state, producing an effective broadening of Γ_{5P} [33–35]. Equations (3) and (4) are evaluated in the low-optical-power limit, where $\Omega_{sp}(t), \Omega_{pd}(t) < \Gamma_{5D}$ and $\Omega_{sp}(t), \Omega_{pd}(t) < \Gamma_{5S_i}^{5P}$. Extending this theory to higher powers produces power broadening on the $|5S_i\rangle \rightarrow |5P\rangle$ transition with a similar dependence reported within Refs. [33–35]:

$$\Gamma_{FWHM} = \Gamma_{5D} + s\Gamma_{5P}\sqrt{1 + \Omega_{sp}/\Omega_{sat}}, \qquad (7)$$

where $s = (\omega_{SP} - \omega_{PD})/\omega_{SP}$, for this configuration is $s \approx 0.005$, the intermediate, $|5P\rangle$, state decay rate is $\Gamma_{5P} = \Gamma_{5S_1}^{5P} + \Gamma_{5S_2}^{5P}$, and Ω_{sat} is the transition's effective saturation Rabi frequency. Power broadening of this two-photon transition has previously been experimentally investigated within a hollow-core fiber geometry [12] showing agreement with Eq. (7).

The main feature in Fig. 3 is fluorescence from the Doppler-free two-photon transition excited from the counterpropagating beams. Weaker features are evident when detuning from double resonance ($\Delta_i = 0$, $\Delta_e = 0$), indicated by arrows in Fig. 4. These features originate from the
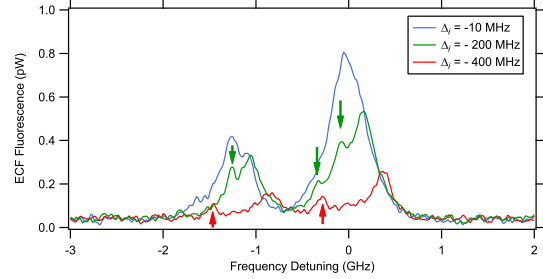
FIG. 4. Fluorescence from the ECF detected at the PMT showing the presence of copropagating fluorescence (indicated by arrows) alongside counterpropagating fluorescence for difference intermediate-state detunings. The frequency axis is relative to the ^{85}Rb D_2 $F_g = 3 \rightarrow F' = 4$ transition.

two-photon transition being excited from copropagating beams originating from backreflections off the fiber end faces. When on resonance with the excited state, the copropagating fluorescence occurs when

$$\Delta_e = \delta_{SP} + \delta_{PD} + \frac{v_z}{c}(\omega_{780} + \omega_{776}) = 0, \qquad (8)$$

where $\delta_{SP} = \omega_{SP} - \omega_{780}$ and $\delta_{PD} = \omega_{PD} - \omega_{776}$. The 780-nm laser is on resonance with the velocity class v_z for the intermediate transition $\delta_{SP} = -\omega_{780}v_z/c$. As a result, Eq. (8) shows that the only atoms that can be excited to the two-photon state are the atoms with a velocity of v_z: $\delta_{PD} = -\omega_{780}v_z/c$. This tight constraint placed on the atom's velocity due to the copropagating two-photon transition produces narrow velocity-selective spectra.

The co- and counterpropagating contributions tune differently with the driving laser frequencies due to the different laser configurations, seen in Fig. 4. The copropagating fluorescence satisfies Eq. (8), whereas the counterpropagating excitation satisfies the equation

$$\Delta_e = \delta_{SP} + \delta_{PD} + \frac{v_z}{c}(\omega_{780} - \omega_{776}) = 0. \qquad (9)$$

The result is that the ratio of detunings for the copropagating case follows $\delta_{SP}/\delta_{PD} = 1$, whereas the counterpropagating case follows $\delta_{SP}/\delta_{PD} = -1$ due to energy conservation.

When doubly resonant, the copropagating and counterpropagating contributions lie at the same frequency, distorting the line shape. This leads to a distortion of the observed transition strength and spectral linewidth which is highlighted in Fig. 5 and discussed below.

B. Transit-time broadening

The Doppler-free counterpropagating two-photon fluorescence signals, shown in Fig. 3, are fitted with Eq. (5), giving an estimate for the average transit time as
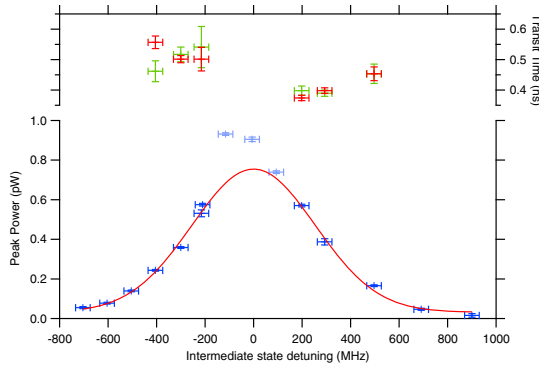
FIG. 5. Transit-time measurements for ^{85}Rb (green) and ^{87}Rb (red) for different intermediate-state detunings Δ_i. Fluorescence amplitude detected at the PMT for the ^{85}Rb $F_g = 3 \to F'$ transition manifold as a function of intermediate-state detuning Δ_i, for fixed laser intensities I_{780} and I_{776} and $\Delta_e = 0$. Highlighted points are excluded from the Gaussian fit; see the text.

$\bar{\tau} = (470 \pm 80)$ ps. We obtain the same value of $\bar{\tau}$ for both Rb isotopes, and little statistically significant variation is seen as a function of intermediate-state detuning; see Fig. 5. Spectra near resonance with the intermediate transition are not shown, as the results are skewed by the presence of copropagating features overlapping the counterpropagating spectra; see Fig. 4. Combining the measured transit time with the mean thermal velocity $v_0 = (262 \pm 2)$ ms^{-1} at $T = (85 \pm 5)$ °C predicts an evanescent-field scale length of $d = (120 \pm 20)$ nm, in excellent agreement with the modeled field extent of $d = (118 \pm 2)$ nm.

C. Transition strength

The transition strength is investigated as a function of intermediate-state detuning Δ_i for fixed laser intensities I_{780} and I_{776} and $\Delta_e = 0$; see Fig. 5. It is evident that the transition strength has a predominately Gaussian profile in accord with Eq. (5) associated with inhomogeneous Doppler broadening of the intermediate transition. The three measurements that are doubly resonant ($\Delta_i = 0$, $\Delta_e = 0$, shown lighter in Fig. 5) show additional fluorescence. This effect is due to multiple excitation paths into the excited state that are opened through weak backreflections in the apparatus, seen in Fig. 4. By excluding these points, we find a Gaussian $1/e$ half-width of (360 ± 17) MHz. This behavior is expected from the thermal distribution of Rb atoms in combination with the intermediate-state hyperfine structure, which predicts an intermediate $1/e$ Gaussian half-width of (350 ± 2) MHz.

Figure 6 shows the dependence of the fluorescence on the transmitted powers when driving the ^{85}Rb $F_g = 3$ and ^{87}Rb $F_g = 2$ transitions in double resonance, $\Delta_i = 0$ and $\Delta_e = 0$. The fluorescence shows proportionality to the product of the laser intensities, as expected from Eq. (5).
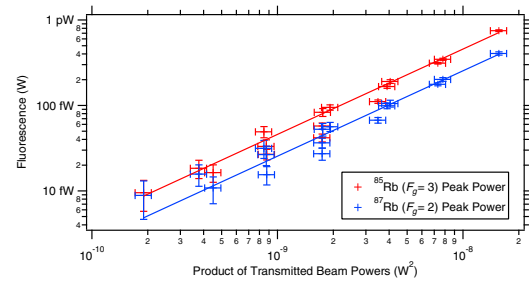
FIG. 6. Fluorescence power detected at the PMT as a function of the product of transmitted laser beam powers.

D. Fiber absorption strength

The key figure of merit for this highly nonlinear platform is the cross sensitivity of the absorption coefficient in one mode to power in the second mode. We need estimates of the fraction of power from each mode that are coupled to the Rb vapor as well as the effective absorption coefficient for the 780-nm beam from the observed fluorescence.

We calculate the absorbed power for the highest powers used in the experiment, which is 12 μW and 1.3 mW of transmitted power for the 780- and 776-nm beam, respectively. At these powers, the PMT measures (750 ± 50) fW of 420-nm fluorescence (see Fig. 6), corresponding to 14 nW of fluorescence emitted along the ECF length, accounting for the PMT collection efficiency of 5.4×10^{-5}. The two-photon transition rate is calculated from this by allowing for various decay branches from the excited state: a nonradiative decay branch of 50% due to collision with the silica fiber structure; and only 7.5% of the radiative decays result in 420-nm fluorescence [28]. This yields an absorbed power of 0.2 μW corresponding to a fractional absorption of $\mathcal{A} = 1.7\%$ relative to the transmitted 780-nm beam. This corresponds to each atom within the evanescent field scattering an average of 0.4 photons per excited-state lifetime Γ_{5D}.

The absorption coefficient of the two-photon transition, α_{TP}, is related to the fiber's transmission $\mathcal{T}$, which is expressed in a modified Beer-Lambert law:

$$\mathcal{T} = \mathcal{T}_F / \mathcal{T}_0 (1 - \mathcal{A}) = e^{-l(\alpha_{\mathrm{Rb}} + \alpha_{\mathrm{TP}} F)}, \qquad (10)$$

where $\mathcal{T}_F = (1.0 \pm 0.2)\%$ is the transmission of the fiber when detuned from both the two-photon and intermediate transitions, $\mathcal{A} = 1.7\%$ is the two-photon fractional absorption, $\mathcal{T}_0 = (12.5 \pm 2.5)\%$ is the original transmission prior to ECF exposure to Rb, $l = 0.3$ m is the fiber length, $\alpha_{\mathrm{Rb}} = 0.084$ cm^{-1} (corresponding to 0.37 dB cm^{-1}) is the fiber loss due to Rb degradation, and $F = 7 \times 10^{-5}$ is the fraction of the guided mode on the exposed side of the core. Equation (10) suggests that the two-photon absorption coefficient within the evanescent field is

$\alpha_{TP} = 8.3$ cm^{-1} for the 780-nm beam at the largest powers shown in Fig. 6.

We find that this agrees with that reported in a tapered-fiber experiment [14]. Taking into account a different fraction of power within the evanescent field, interaction length, rubidium vapor temperature, evanescent-field area, and probing power, we find agreement between the two experiments within the knowledge of experimental parameters to show a ratio of $1.0^{+0.9}_{-0.5}$.

VI. DISCUSSION

A clear pathway towards a platform of high utility to the quantum information community can be seen. The next generation of ECF to be manufactured with an effective core size of 1 μm would generate intensities outside the silica core of 500 MW m^{-2} per milliwatt of guided power [36,37]. These ECFs would deliver a substantial improvement when compared to the 7.5-μm fiber described here: A 1-μm ECF has a smaller evanescent-field area $A = (0.11 \pm 0.02)$ μm^2 and a fraction of the guided mode on the exposed side of the core, $F = 2 \times 10^{-2}$, resulting in approximately 2240 times stronger interaction with the Rb vapor. An additional increase in absorption strength can be gained by elevating the operating temperature to $T = 200$ °C to increase the Rb density. Under these conditions, a single photon in the 776-nm guided mode per atomic transit time will deliver an absorption coefficient of $\alpha_{TP} \approx 1$ cm^{-1} in the 780-nm mode resulting in near 50% absorption over the same length fiber. Implementing techniques such as light-induced atomic desorption and fiber heating are shown to eject Rb off fiber surfaces, thus potentially decreasing the fiber loss due to Rb deposition [19,25,38]. Furthermore, separate work shows low-loss splicing of ECF to a conventional solid-core single-mode fiber [39], opening the way to a convenient architecture for generating a strong light atom and, thus, photon-photon interactions via two-photon interactions. A demonstration of this nature would be highly significant for quantum photonics.

VII. CONCLUSION

In conclusion, we demonstrate that ECFs possess low-loss guidance between 400 and 1700 nm, crucial for quantum-logic applications. The potential of this fiber for use in quantum-logic applications is further demonstrated through generating strong photon-photon interactions utilizing the Rb two-photon transition $5S_{1/2} \rightarrow 5D_{5/2}$. A two-photon absorption coefficient of 8.3 cm^{-1}, corresponding to a total absorption of 1.7%, is observed in one laser mode when the second mode is driven with 1.3 mW. Two-photon spectra enable measurement of the evanescent-field scale length to be (120 ± 20) nm, in excellent agreement with the modeled fiber mode (118 ± 2) nm. Projection to a 1-μm core fiber

shows that a single 776-nm photon per atomic transit time would result in approximately 50% absorption of a 780-nm photon. This architecture offers great promise in the field of all-optical switching or for quantum-logic gates where two-photon absorption at low power levels is required.

[1] P. Kok, K. Nemoto, T. C. Ralph, J. P. Dowling, and G. J. Milburn, Linear optical quantum computing with photonic qubits, Rev. Mod. Phys. **79**, 135 (2007).

[2] H. J. Kimble, The quantum internet, Nature (London) **453**, 1023 (2008).

[3] T. G. Tiecke, J. D. Thompson, N. P. de Leon, L. R. Liu, V. Vuletić, and M. D. Lukin, Nanophotonic quantum phase switch with a single atom, Nature (London) **508**, 241 (2014).

[4] S. M. Hendrickson, C. N. Weiler, R. M. Camacho, P. T. Rakich, A. I. Young, M. J. Shaw, T. B. Pittman, J. D. Franson, and B. C. Jacobs, All-optical-switching demonstration using two-photon absorption and the Zeno effect, Phys. Rev. A **87**, 023808 (2013).

[5] J. Goldwin, M. Trupke, J. Kenner, A. Ratnapala, and E. A. Hinds, Fast cavity-enhanced atom detection with low noise and high fidelity, Nat. Commun. **2**, 418 (2011).

[6] J. Volz, M. Scheucher, C. Junge, and A. Rauschenbeutel, Nonlinear pi phase shift for single fiber-guided photons interacting with a single atom, Nat. Photonics **8**, 965 (2014).

[7] M. Bajcsy, S. Hofferberth, V. Balic, T. Peyronel, M. Hafezi, A. S. Zibrov, V. Vuletic, and M. D. Lukin, Efficient All-Optical Switching Using Slow Light within a Hollow Fiber, Phys. Rev. Lett. **102**, 203902 (2009).

[8] M. R. Sprague, D. G. England, A. Abdolvand, J. Nunn, X.-M. Jin, W. Steven Kolthammer, M. Barbieri, B. Rigal, P. S. Michelberger, T. F. M. Champion, P. St. J. Russell, and I. A. Walmsley, Efficient optical pumping and high optical

depth in a hollow-core photonic-crystal fibre for a broadband quantum memory, New J. Phys. **15**, 055013 (2013).

[9] M. R. Sprague, P. S. Michelberger, T. F. M. Champion, D. G. England, J. Nunn, X.-M. Jin, W. S. Kolthammer, A. Abdolvand, P. St. J. Russell, and I. A. Walmsley, Broadband single-photon-level memory in a hollow-core photonic crystal fibre, Nat. Photonics **8**, 287 (2014).

[10] V. Venkataraman, K. Saha, and A. L. Gaeta, Phase modulation at the few-photon level for weak-nonlinearity-based quantum computing, Nat. Photonics **7**, 138 (2013).

[11] V. Venkataraman, K. Saha, P. Londero, and A. L. Gaeta, Few-Photon All-Optical Modulation in a Photonic Band-Gap Fiber, Phys. Rev. Lett. **107**, 193902 (2011).

[12] C. Perrella, P. S. Light, J. D. Anstie, T. M. Stace, F. Benabid, and A. N. Luiten, High-resolution two-photon spectroscopy of rubidium within confined geometry, Phys. Rev. A **87**, 013818 (2013).

[13] C. Perrella, P. S. Light, J. D. Anstie, F. Benabid, T. M. Stace, A. G. White, and A. N. Luiten, High-efficiency cross-phase modulation in a gas-filled waveguide, Phys. Rev. A **88**, 013819 (2013).

[14] S. M. Hendrickson, M. M. Lai, T. B. Pittman, and J. D. Franson, Observation of Two-Photon Absorption at Low Power Levels Using Tapered Optical Fibers in Rubidium Vapor, Phys. Rev. Lett. **105**, 173602 (2010).

[15] M. Kohnen, M. Succo, P. G. Petrov, R. A. Nyman, M. Trupke, and E. A. Hinds, An integrated atom-photon junction, Nat. Photonics **5**, 35 (2011).

[16] A. Goban, K. S. Choi, D. J. Alton, D. Ding, C. Lacroûte, M. Pototschnig, T. Thiele, N. P. Stern, and H. J. Kimble, Demonstration of a State-Insensitive, Compensated Nanofiber Trap, Phys. Rev. Lett. **109**, 033603 (2012).

[17] E. Vetsch, D. Reitz, G. Sagué, R. Schmidt, S. T. Dawkins, and A. Rauschenbeutel, Optical Interface Created by Laser-Cooled Atoms Trapped in the Evanescent Field Surrounding an Optical Nanofiber, Phys. Rev. Lett. **104**, 203603 (2010).

[18] D. E. Jones, J. D. Franson, and T. B. Pittman, Saturation of atomic transitions using subwavelength diameter tapered optical fibers in rubidium vapor, J. Opt. Soc. Am. B **31**, 1997 (2014).

[19] M. Lai, J. D. Franson, and T. B. Pittman, Transmission degradation and preservation for tapered optical fibers in rubidium vapor, Appl. Opt. **52**, 2595 (2013).

[20] L. Stern, B. Desiatov, I. Goykhman, and U. Levy, Nanoscale light-matter interactions in atomic cladding waveguides, Nat. Commun. **4**, 1548 (2013).

[21] T. M. Monro, W. Belardi, K. Furusawa, J. C. Baggett, N. G. R. Broderick, and D. J. Richardson, Sensing with microstructured optical fibres, Meas. Sci. Technol. **12**, 854 (2001).

[22] W. Yang, D. B. Conkey, B. Wu, D. Yin, A. R. Hawkins, and H. Schmidt, Atomic spectroscopy on a chip, Nat. Photonics **1**, 331 (2007).

[23] G. Epple, K. S. Kleinbach, T. G. Euser, N. Y. Joly, T. Pfau, P. St. J. Russell, and R. Löw, Rydberg atoms in hollow-core photonic crystal fibres, Nat. Commun. **5**, 4132 (2014).

[24] S. Okaba, T. Takano, F. Benabid, T. Bradley, L. Vincetti, Z. Maizelis, V. Yampol'skii, F. Nori, and H. Katori, Lamb-Dicke spectroscopy of atoms in a hollow-core photonic crystal fibre, Nat. Commun. **5**, 4096 (2014).

[25] A. D. Slepkov, A. R. Bhagwat, V. Venkataraman, P. Londero, and A. L. Gaeta, Generation of large alkali vapor densities inside bare hollow-core photonic band-gap fibers, Opt. Express **16**, 18976 (2008).

[26] R. Kostecki, H. Ebendorff-Heidepriem, C. Davis, G. McAdam, S. C. Warren-Smith, and T. M. Monro, Silica exposed-core microstructured optical fibers, Opt. Mater. Express **2**, 1538 (2012).

[27] R. Kostecki, H. Ebendorff-Heidepriem, S. Afshar V., G. McAdam, C. Davis, and T. M. Monro, Novel polymer functionalization method for exposed-core optical fiber, Opt. Mater. Express **4**, 1515 (2014).

[28] D. Sheng, A. Pérez Galván, and L. A. Orozco, Lifetime measurements of the 5d states of rubidium, Phys. Rev. A **78**, 062506 (2008).

[29] D. Adam Steck, Rubidium 87 D line data, http://steck.us/ alkalidata (revision 2.1.4, 23 December 2010).

[30] D. F. Walls and G. J. Milburn, *Quantum Optics* (Springer-Verlag, Berlin, 2008).

[31] S. N. Bagayev, V. P. Chebotayev, and E. A. Titov, Saturated absorption lineshape under the transit-time conditions, Laser Phys. **4**, 224 (1994).

[32] T. M. Stace and A. N. Luiten, Theory of spectroscopy in an optically pumped effusive vapor, Phys. Rev. A **81**, 033848 (2010).

[33] J. E. Bjorkholm and P. Liao, Line shape and strength of two-photon absorption in an atomic vapor with a resonant or nearly resonant intermediate state, Phys. Rev. A **14**, 751 (1976).

[34] M. Tanasittikosol, C. Carr, C. S. Adams, and K. J. Weatherill, Subnatural linewidths in two-photon excited-state spectroscopy, Phys. Rev. A **85**, 033830 (2012).

[35] T. T. Grove, V. Sanchez-Villicana, B. C. Duncan, S. Maleki, and P. L. Gould, Two-photon two-color diode laser spectroscopy of the Rb $5D_{5/2}$ state, Phys. Scr. **52**, 271 (1995).

[36] S. C. Warren-Smith, G. Nie, E. P. Schartner, L. A. Salamonsen, and T. M. Monro, Enzyme activity assays within microstructured optical fibers enabled by automated alignment, Biomed. Opt. Express **3**, 3304 (2012).

[37] R. Kostecki, H. Ebendorff-Heidepriem, S. C. Warren-Smith, and T. M. Monro, Predicting the drawing conditions for microstructured optical fiber fabrication, Opt. Mater. Express **4**, 29 (2014).

[38] S. Ghosh, A. R. Bhagwat, C. K. Renshaw, S. Goh, A. L. Gaeta, and B. J. Kirby, Low-Light-Level Optical Interactions with Rubidium Vapor in a Photonic Band-Gap Fiber, Phys. Rev. Lett. **97**, 023603 (2006).

[39] S. C. Warren-Smith, R. Kostecki, L. Viet Nguyen, and T. M. Monro, Fabrication, splicing, Bragg grating writing, and polyelectrolyte functionalization of exposed-core microstructured optical fibers, Opt. Express **22**, 29493 (2014).

APPENDIX K

Paper 11.

Microstructured Optical Fiber-based Biosensors: Reversible and Nanoliter-Scale Measurement of Zinc Ions

Sabrina Heng,[*][†] Christopher A. McDevitt,[‡] Roman Kostecki,[†] Jacqueline R. Morey,[‡] Bart A. Eijkelkamp,[‡] Heike Ebendorff-Heidepriem,[†] Tanya M. Monro,[§] and Andrew D. Abell[†]

[†]ARC Center of Excellence for Nanoscale BioPhotonics, Institute for Photonics and Advanced Sensing, Department of Chemistry, School of Physical Sciences, The University of Adelaide, Adelaide, South Australia 5005, Australia

[‡]Research Center for Infectious Diseases, School of Biological Sciences, The University of Adelaide, Adelaide, South Australia 5005, Australia

[§]The University of South Australia, Adelaide, South Australia 5000, Australia

ⓢ *Supporting Information*

ABSTRACT: Sensing platforms that allow rapid and efficient detection of metal ions would have applications in disease diagnosis and study, as well as environmental sensing. Here, we report the first microstructured optical fiber-based biosensor for the reversible and nanoliter-scale measurement of metal ions. Specifically, a photoswitchable spiropyran Zn^{2+} sensor is incorporated within the microenvironment of a liposome attached to microstructured optical fibers (exposed-core and suspended-core microstructured optical fibers). Both fiber-based platforms retains high selectivity of ion binding associated with a small molecule sensor, while also allowing nanoliter volume sampling and on/off switching. We have demonstrated that multiple measurements can be made on a single sample without the need to change the sensor. The ability of the new sensing platform to sense Zn^{2+} in pleural lavage and nasopharynx of mice was compared to that of established ion sensing methodologies such as inductively coupled plasma mass spectrometry (ICP-MS) and a commercially available fluorophore (Fluozin-3), where the optical-fiber-based sensor provides a significant advantage in that it allows the use of nanoliter (nL) sampling when compared to ICP-MS (mL) and FluoZin-3 (μL). This work paves the way to a generic approach for developing surface-based ion sensors using a range of sensor molecules, which can be attached to a surface without the need for its chemical modification and presents an opportunity for the development of new and highly specific ion sensors for real time sensing applications.

KEYWORDS: *biosensor, microstructured optical fiber, photoswitch, liposome, zinc, nanoscale*

■ INTRODUCTION

The ability to detect the on/off binding of a metal ion to a complementary surface-bound receptor provides a basis for real-time sensing applications in fields such as environmental monitoring and in clinical diagnostics. Small-molecule "on/off" sensors for metal ions, such as those based on rhodamine[1−3] or other fluorophores,[4,5] can exhibit high selectivity for a given ion and as a result have found wide use in this context. However, chemically modifying these small molecules to allow surface attachment, while retaining efficient sensing capability, can be problematic from both a synthesis viewpoint and an operational viewpoint as the immobilized molecule may lose functionality.[6] Sensing can also be achieved using a larger biological receptor such as a protein or nucleic acid capable of binding an ion of interest.[7] While these systems allow for better surface attachment through standard coupling with a component amino acid or another biomolecule within, these biological receptors are typically only weakly selective for a given ion. Although this can be improved somewhat by genetic modification, this approach is time-consuming and lacks broad generality.[7,8] A generic and biocompatible approach to attach highly selective small molecule sensors to surfaces, without the need for chemical modification, would offer significant advantages over these methods.

Here, we report such an approach where the phospholipids and a photochromic sensor molecule are assembled to form a novel liposome-based sensing material and attached this to the surfaces of microstructured optical fibers. This new sensing platform retains high selectivity of ion binding associated with a small molecule sensor, while also allowing sampling of small volumes and an opportunity for on/off switching. Liposomes were chosen because they can be readily made from a range of natural lipids and are nontoxic and biodegradable.[9] Detection of Zn^{2+} was incorporated into the design of this new sensing platform because of the essential role of Zn^{2+} in a range of cellular processes[10] such as antioxidant enzyme activity,[11] DNA structural integrity, oocytes maturation, and fertilization,[12] while disruption of its homeostasis is associated with numerous disease states including Alzheimer's,[13] diabetes,[14] and cancer.

A photoswitchable spiropyran-based ion chelator (SP2) was chosen for embedding within the surface of the microstructured optical fiber-bound liposome as shown in Figure 1. SP2 contains an aryl carboxylate group for improved aqueous solubility and the bis(2-pyridylmethyl)amine functionality was
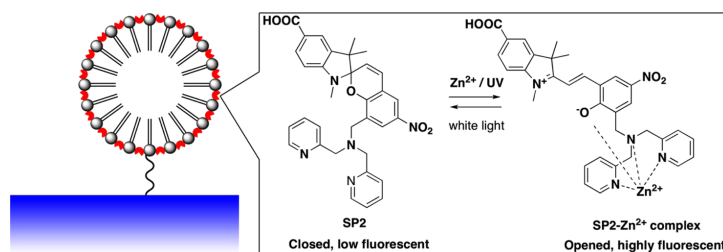
Figure 1. Schematic of the optical fiber-based sensing architecture, where a photoswitchable spiropyran (SP2, red) is embedded within a liposome (gray). This structure (SP2-liposome) is covalently attached to the surface of an ECF or SCF (blue). The inset shows the isomeric structures of spiropyran SP2 (closed, nonfluorescent spiropyran isomer), and the metal-induced ring-opened Zn^{2+} complex (opened, fluorescent merocyanine isomer). The spiropyran-Zn^{2+} sensing mechanism depicted here was modeled by Rivera-Fuentes et al.[24] on a similar analog using density functional theory calculations.[24] The ring-opened isomer is induced by binding to Zn^{2+} or by exposure to UV light (λ_{em} = 320−350 nm), while the ring-closed isomer is induced by exposure to white light (broad spectrum).

chosen as the ionophore in this work as it is known to selectively form a complex with Zn^{2+} over other biologically relevant ions in solutions (Supporting Information Figure S1).[15] The photoswitching of spiropyran on surfaces[16] and semicondensed phase[17−19] are well-characterized and in this context, exposure of this compound to Zn^{2+} (by sampling through the optical fiber) gives rise to a ring-opened and fluorescent merocyanine isomer that is stabilized by specific binding through the appended phenoxide and bis-pyridyl functionalities.[15] This switching can also be induced on illumination with UV through the fiber. Irradiation with white light regenerates the ring closed spiropyran isomer with release of Zn^{2+}, resulting in a switchable sensing platform. In all cases, fluorescence is both induced and measured through the microstructured optical fibers, which are exposed to the 532 nm excitation light 10 times for 10 ms. The long interaction length between the evanescent tails of the guided light and the material attached to the surface of the optical fiber maximizes the fluorescence signal to give improved sensitivity of detection relative to more traditional spectroscopic and fluorescence-based fiber sensors.[20] Two different types of microstructured optical fibers were used in these experiments. The first is an exposed-core microstructured optical fibers (ECF) that has a suspended micron-scale core partially exposed to the external environment[21,22] (Figure 2 left), which allows consistent washing, drying and refilling of the biosensor during its use. The second type of fiber has air holes within its cross section and is known as a suspended-core microstructured optical fibers

(SCF;[23] Figure 2 right). These air holes confine light to the solid core and allow it to be guided along the length of the fiber. The holes also act as micro sample chamber to allow nanoscale sampling,[20] a real advance in biological sensing.

RESULTS AND DISCUSSION

Optimum conditions for the generation of a functional and stable integrated spiropyran-liposome system (SP2-liposome) were initially investigated, where liposome-based materials are known to be unstable when dehydrated. Liposomal stability is especially important for reusable sensors of the type developed here since measurement would require cycles of washing and air-drying between readings. Dehydration of the liposome could also occur during long-term storage of the sensor. Such factors have limited the development of liposome-based sensors to date.[9,25] With this in mind, a solution of SP2 in DMSO was mixed with a solution of total *Escherichia coli* lipids extracts in buffer containing various amounts of maltose or trehalose (0, 5, 10 or 20%, weight/vol) and 20 mM 3-(N-morpholino)-propanesulfonic acid (MOPS) at pH 7.2. The formation of hydrogen bonds between the sugar and surrounding polar residues of liposomes was expected to help prevent collapse and loss of function under the dehydrating conditions.

Samples of the above solutions were then placed on a glass microscope slide, initial fluorescence was measured by irradiating with the 532 nm laser using a Typhoon imager, and aqueous zinc chloride (100 μM) was added to each, the droplets were again irradiated (532 nm), and the resulting fluorescence of the complexed ring opened merocynine isomer measured, see Figure 3 and Supporting Information for detail. Each droplet was then irradiated with white light to expel Zn^{2+} ions and regenerate the passive spiropyran (nonfluorescent) isomer. The samples were then left to air-dry for 18 h, rehydrated with further aqueous zinc chloride, and a subsequent off/on cycle was performed as above.

Samples prepared with 20% of maltose and 10% and 20% of trehalose precipitated upon addition of Zn^{2+} and as such these conditions were deemed unsuitable for subsequent experiments. Importantly, the results shown in Figure 4 demonstrate that SP2-liposomes constituted with maltose 5% and 10% remained functional and underwent a second round of photoswitching after air-drying for 18 h and rehydration. In contrast, fluorescence emission of SP2-liposome prepared with 5% trehalose did not return to intensity levels reflective of the
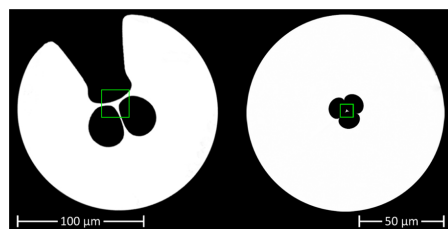
Figure 2. Scanning electron microscopy images of the microstructured optical fibers used in this work. (Left) The silica ECF and (right) the silica SCF with effective core diameters of 7.5 and 1.5 μm, respectively. The green box highlights the core of each fiber.
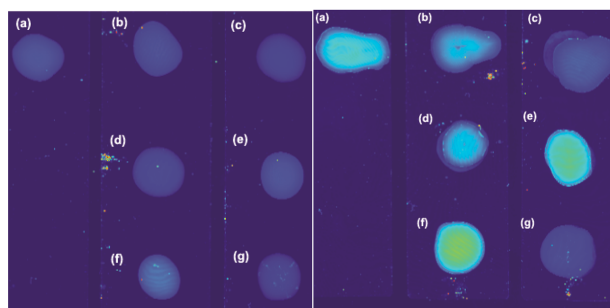
Figure 3. Initial studies were carried out on readily available silicate glass slides as a simple model for the microstructured optical fibers (F300 silica glass), where both are silicate glasses with wettable (hydrophilic) surfaces. Images were taken using a Typhoon Imager (λ_{Ex} = 532 nm, $\lambda_{Ex} \sim$ 640 nm). On each slide: 5 μL droplets constituted with (a) 10% maltose, (b) 20% trehalose, (c) 5% trehalose, (d) 10% trehalose, (e) 5% maltose, (f) 20% maltose, and (g) 0% disaccharide. The glass slide on the left and right represent the droplets before and after the addition of 100 μM Zn, respectively.
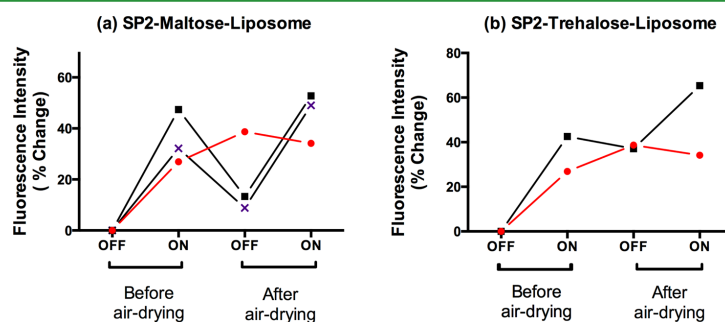
Figure 4. Photoswitching of the SP2-liposome on glass slide reconstituted with (red ●) 0%, (■) 5% and (X) 10% maltose (panel a) and (fx2) 0%, (■) 5% trehalose (panel b), respectively. The experiments were performed on glass slides and resultant fluorescence was recorded using the Typhoon Imager (λ_{ex} = 532 nm). Each "off-cycle" represents the fluorescence emission (λ_{em} approximately = 640 nm) of the ring-closed spiropyran without Zn^{2+} chelated and after the droplets were irradiated with white light for 10 min. Each "on-cycle" represents the resultant fluorescence emission (λ_{em} approximately = 640 nm) of ring-opened merocyanine isomer in the presence of 100 μM Zn^{2+} (SP2-Zn^{2+}). The fluorescence emission of the second "off/on cycle" was obtained after the droplets had been air-dried for 18 h.
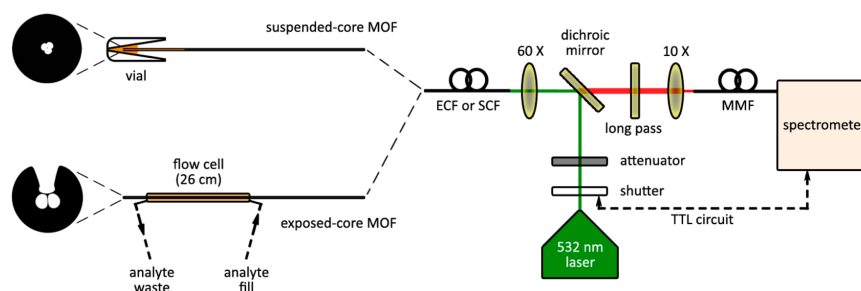
Figure 5. Setup used for fluorescence measurements using (top) suspended-core fiber and (bottom) exposed-core fibers.

ring-closed spiropyran when exposed to white light. The SP2-liposome samples lacking disaccharide were unable to photoswitch and functionality was not restored after rehydration, i.e. no modulation of fluorescence emission was observed (Figure 4, red). Based on these results samples for subsequent experiments were prepared using the minimum amount of maltose (5%) that provided protection against drying (SP2-maltose-liposome).

SP2-maltose-liposomes were next prepared with added succinyl PE lipid (as detailed in the Supporting Information), where the component carboxylic acid would be expected to be exposed in the liposome structure to allow attachment to both
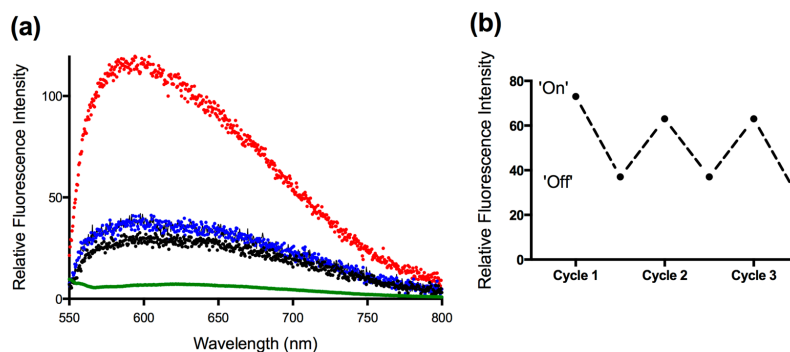
Figure 6. (a) Fluorescence emission spectra of exposed-core fiber functionalized with SP2-maltose-liposome after excitation with 532 nm laser; (green) Empty fiber, unfunctionalized, (black) exposed core based sensor in flow cell filled only with acetonitrile and no Zn^{2+}, (red) sensor filled 10 μM Zn^{2+} in acetonitrile and exposed to UV for 1 h, (blue) sensor, exposed to white light and rinsed with acetonitrile, to release Zn^{2+} from the sensor. (b) Photoswitching of functionalized exposed core-based sensor. Each cycle consist of filling the sensor with Zn^{2+} in acetonitrile (10 μM, "On") followed by irradiating the sensor with white light for 30 min ("Off"). Fluorescence emission for each cycle was obtained by irradiation with the 532 nm laser.

exposed and suspended core microstructured fibers. Each fiber was precleaned and hydroxylated by immersion in nitric acid followed by piranha solution and then functionalized with alternating layers of poly(allylamine hydrochloride) (PAH), poly(acrylic acid) (PAA) and further PAH[26] for the exposed core fiber and APTES for the suspended core fiber.[27] The SP2-maltose-liposomes were then coupled onto to the surface-bound free amines using standard coupling conditions[27] (HATU/DIPEA; Supporting Information) to give the functionalized exposed core and suspended core sensors.

The ability of the exposed core fiber-based sensor to bind and detect Zn^{2+} was studied using the optical set up depicted in Figure 5. A 5 mW laser excitation light source with a wavelength of 532 nm was coupled into the core of the functionalized fibers lengths using a 60× objective via a diachroic mirror to excite the sensing molecules and induce fluorescence at the surface of the core. The sensor was placed in a flow-cell filled with acetonitrile (Figure 5, exposed-core fiber, bottom) and then excited using a 532 nm laser (10 × 10 ms pulses), and the resulting fluorescence was measured. Figure 6a shows that the functionalized fiber (Figure 6a, black) possessed significant background fluorescence (λ_{em} = 640 nm) relative to the unfunctionalized fiber (Figure 6a, green), as would be expected for spiropyran immobilized within the fiber's internal surface. Next, the flow cell was drained of acetonitrile and then air-dried and refilled with a solution of Zn^{2+} in acetonitrile (10 μM). The fluorescence was again measured by excitation with the 532 nm laser (10 × 10 ms), and the resulting fluorescence emission intensity increased 2.5 fold (Figure 6a, red), which is consistent with the formation of the highly fluorescent SP2-Zn^{2+} complex (Figure 1).[15] Next, the sensor was irradiated with white light in order to release the bound Zn^{2+} and reform the ring-closed spiropyran isomer.[15] As expected, subsequent excitation of the sensor with the 532 nm laser showed the intensity of resultant fluorescence emission (Figure 6a, blue) returned to that of the sensor before Zn^{2+} was added (Figure 6a, black). After washing with acetonitrile to remove all Zn^{2+} the flow cell was again filled with solution of Zn^{2+} in acetonitrile (10 μM) and fluorescence measured as before in order to determine the reusability of the sensor. Again, fluorescence

emission increased approximately 2.5 fold in the presence of Zn^{2+}. Irradiating the sensor with white-light, and subsequently, excitation with the 532 nm laser once again returned the fluorescence emission of the sensor to the level similar to that before the addition of Zn^{2+} (Figure 6a, black). The procedure was repeated for a third time, and the results are summarized in Figure 6b. Importantly, attempted photoswitching of the microstructured optical fibers functionalized with SP2-liposomes, lacking disaccharide, failed to regenerate once the fibers had been drained of solution and left to air-dry.

Finally, the ability of the new sensing platform to sense Zn^{2+} in pleural lavage and nasopharynx of mice was compared to that of established ion sensing methodologies such as inductively coupled plasma mass spectrometry (ICP-MS) and solution fluorescence based (Fluozin-3) in order to validate its use in a biological setting. These two biological systems contain low endogenous Zn^{2+} concentrations, which results in poor signal-to-background ratios and a necessity to use of large sample volumes when using traditional ion-sensing techniques. Here we assessed the Zn^{2+} abundance in 8 separate murine samples using ICP-MS, Fluozin-3[28] and SCF sensor. Again the micron-sized air holes within the cross-section of the SCF allow control of the interactions between light guided within the fiber core and sensor located within the holes, while simultaneously acting as micro sample chambers. The experiments for ICP-MS and Fluozin-3 used established techniques[29] and are described in detail in the Supporting Information. The functionalized suspended core-based sensor experiments were performed as follows; one end of the SCF was dipped into the biological sample and this mixture (20 nL) was drawn into the fiber air holes by capillary action (Figure 5, suspended core fiber, top). The fluorescence was measured by excitation with a 532 nm laser (10 × 10 ms pulses) in each case and the resultant emission was recorded and shown in Figure 7. An approximate 3.5- and 4-fold increase in fluorescence intensities was observed for the nasopharyngeal (Figure 7, red) and pleural lavages (Figure 7, blue) samples, respectively. The sensing experiment was repeated using water in place of the biological samples as a negative control. No significant change in fluorescence was apparent in this case (Figure 7, black), which confirms that the
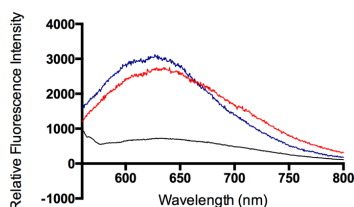
ACS Applied Materials & Interfaces

Figure 7. Representative fluorescence emission results from SCF sensor with biological samples. The emission data in the graph were obtained from (black) water only, (blue) filled with solution from the pleural lavages, and (red) filled with solution from the nasopharyngeal wash. Emission data for all samples can be found in the Supporting Information, Figure S2.

earlier changes in fluorescence were due to the formation of the highly fluorescent SP2-Zn^{2+} species. An analysis of the pleural lavage across eight murine samples showed that the optical fiber method was capable of detecting Zn^{2+} ions (uM levels, Figure 8a). Zn^{2+} concentrations were also quantified by Fluozin-3 (0.8−1.3 μM; Figure 8b) and ICP-MS (1.8−2.1 μM; Figure 8c). The results show that the narrow range of variation across the samples observed for the fiber-based approach (1.5−3.5 RFUs) correlates closely with the results for Fluozin-3. Minor differences in the absolute concentrations determined between ICP-MS and the fluorophore-based methods (Fluozin-3 and SCF-based sensor) were not unexpected as ICP-MS is based on a denaturing approach that releases ions from the biological material, while Fluozin-3 and the fiber-based approach use nondenaturing fluorophores that interact with the labile Zn^{2+} content in the biological samples. Importantly, the optical fiber based sensor provides a significant advantage in that it allows the use of nL sampling, which compares to ICP-MS (mL) and FluoZin-3 (μL).

CONCLUSION

Metal ions are ubiquitous in the environment and in biology, and as such, there is a real need to develop new sensing platforms for their rapid and efficient detection. Such sensors would have applications in disease diagnosis and study, as well as environmental sensing. Here, we report the first instance where phospholipids and a photochromic sensor molecule are assembled to form a novel liposome-based sensing material. This was then coupled to microstructured optical fibers to create nanoscale biosensors that are capable of sensing Zn^{2+}

ions in biological samples. These new sensing platforms retain high selectivity of ion binding associated with a small molecule sensor, while also allowing sampling of small volumes and on/off switching. We have demonstrated that multiple measurements can be made on a single sample without the need to change the sensor. This is particularly attractive for biological experiments, where sample availability and volumes often limit the number of experiments that can be performed. More significantly, this work paves the way to a generic approach for developing surface-based ion sensors using a range of sensor molecules, which can be attached to a surface without the need for its chemical modification. This presents an opportunity for the development of new and highly specific ion sensors for real-time sensing applications.

ASSOCIATED CONTENT

Ⓢ Supporting Information

The Supporting Information is available free of charge on the ACS Publications website at DOI: 10.1021/acsami.6b03565.

SP2-liposome generation; preparation of SP2-maltose-liposomes; attachment of biosensor material to surface of suspended-core fiber; and biological assays. (PDF)

AUTHOR INFORMATION

Corresponding Author
*E-mail: Sabrina.heng@adelaide.edu.au.

Author Contributions
The manuscript was written through contributions of all authors. All authors have given approval to the final version of the manuscript.

Notes
The authors declare no competing financial interest.
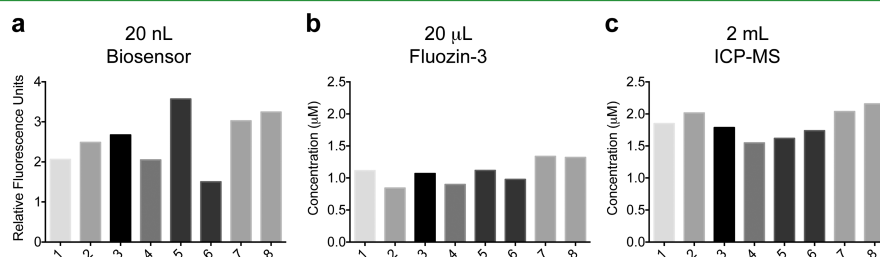

Figure 8. Analysis of Zn^{2+} in the pleural lavage samples obtained across 8 mice (numbered 1−8). (a) SCF direct detection of Zn^{2+} using nanolitre volumes (∼20 nL) of sample. (b) Fluozin-3 detection of Zn^{2+} in biological sample using microliter volumes with added fluorophore (∼20 μL). (c) ICP-MS determination of Zn^{2+} using 2 mL of processed sample.

ACS Applied Materials & Interfaces   Research Article

■ REFERENCES

(1) Kaewtong, C.; Wanno, B.; Uppa, Y.; Morakot, N.; Pulpoka, B.; Tuntulani, T. Facile Synthesis of Rhodamine-Based Highly Sensitive and Fast Responsive Colorimetric and Off-on Fluorescent Reversible Chemosensors for Hg2+: Preparation of a Fluorescent Thin Film Sensor. *Dalton Trans* **2011**, *40*, 12578−12583.

(2) Goswami, S.; Sen, D.; Das, N. K.; Fun, H. K.; Quah, C. K. A New Rhodamine Based Colorimetric 'Off-on' Fluorescence Sensor Selective for Pd2+ Along with the First Bound X-Ray Crystal Structure. *Chem. Commun. (Cambridge, U. K.)* **2011**, *47*, 9101−9103.

(3) Zhou, Y.; Wang, F.; Kim, Y.; Kim, S. J.; Yoon, J. Cu2+-Selective Ratiometric and ″Off-on″ Sensor Based on the Rhodamine Derivative Bearing Pyrene Group. *Org. Lett.* **2009**, *11*, 4442−4445.

(4) de Silva, A. P.; Gunaratne, H. Q.; Gunnlaugsson, T.; Huxley, A. J.; McCoy, C. P.; Rademacher, J. T.; Rice, T. E. Signaling Recognition Events with Fluorescent Sensors and Switches. *Chem. Rev.* **1997**, *97*, 1515−1566.

(5) Heng, S.; Mak, A. M.; Stubing, D. B.; Monro, T. M.; Abell, A. D. Dual Sensor for Cd(Ii) and Ca(Ii): Selective Nanoliter-Scale Sensing of Metal Ions. *Anal. Chem.* **2014**, *86*, 3268−3272.

(6) Byrne, R. J.; Stitzel, S. E.; Diamond, D. Photo-Regenerable Surface with Potential for Optical Sensing. *J. Mater. Chem.* **2006**, *16*, 1332−1337.

(7) Aragay, G.; Pons, J.; Merkoci, A. Recent Trends in Macro-, Micro-, and Nanomaterial-Based Tools and Strategies for Heavy-Metal Detection. *Chem. Rev.* **2011**, *111*, 3433−3458.

(8) Kirsch, J.; Siltanen, C.; Zhou, Q.; Revzin, A.; Simonian, A. Biosensor Technology: Recent Advances in Threat Agent Detection and Medicine. *Chem. Soc. Rev.* **2013**, *42*, 8733−8768.

(9) Liu, Q.; Boyd, B. J. Liposomes in Biosensors. *Analyst* **2013**, *138*, 391−409.

(10) Tomat, E.; Lippard, S. J. Imaging Mobile Zinc in Biology. *Curr. Opin. Chem. Biol.* **2010**, *14*, 225−230.

(11) Orlova, M. A.; Orlov, A. P. Role of Zinc in an Organism and Its Influence on Processes Leading to Apoptosis. *British Journal of Medicine & Medical Research* **2011**, *1*, 239−305.

(12) Picco, S. J.; Anchordoquy, J. M.; de Matos, D. G.; Anchordoquy, J. P.; Seoane, A.; Mattioli, G. A.; Errecalde, A. L.; Furnus, C. C. Effect of Increasing Zinc Sulphate Concentration During in Vitro Maturation of Bovine Oocytes. *Theriogenology* **2010**, *74*, 1141−1148.

(13) Bjorklund, N. L.; Sadagoparamanujam, V. M.; Taglialatela, G. Selective, Quantitative Measurement of Releasable Synaptic Zinc in Human Autopsy Hippocampal Brain Tissue from Alzheimer's Disease Patients. *J. Neurosci. Methods* **2012**, *203*, 146−151.

(14) Miao, X.; Sun, W.; Fu, Y.; Miao, L.; Cai, L. Zinc Homeostasis in the Metabolic Syndrome and Diabetes. *Front Med.* **2013**, *7*, 31−52.

(15) Heng, S.; McDevitt, C. A.; Stubing, D. B.; Whittall, J. J.; Thompson, J. G.; Engler, T. K.; Abell, A. D.; Monro, T. M. Microstructured Optical Fibers and Live Cells: A Water-Soluble, Photochromic Zinc Sensor. *Biomacromolecules* **2013**, *14*, 3376−3379.

(16) Del Canto, E.; Natali, M.; Movia, D.; Giordani, S. Photo-Controlled Release of Zinc Metal Ions by Spiropyran Receptors Anchored to Single-Walled Carbon Nanotubes. *Phys. Chem. Chem. Phys.* **2012**, *14*, 6034−6043.

(17) Miskolczy, Z.; Biczok, L. Photochromism in Cucurbit[8]Uril Cavity: Inhibition of Hydrolysis and Modification of the Rate of Merocyanine-Spiropyran Transformations. *J. Phys. Chem. B* **2011**, *115*, 12577−12583.

(18) Nilsson, J. R.; Parente Carvalho, C.; Li, S.; Da Silva, J. P.; Andreasson, J.; Pischel, U. Switching Properties of a Spiropyran-Cucurbit[7]Uril Supramolecular Assembly: Usefulness of the Anchor Approach. *ChemPhysChem* **2012**, *13*, 3691−3699.

(19) Kundu, P. K.; Olsen, G. L.; Kiss, V.; Klajn, R. Nanoporous Frameworks Exhibiting Multiple Stimuli Responsiveness. *Nat. Commun.* **2014**, *5*, 3588.

(20) Monro, T. M.; Warren-Smith, S.; Schartner, E. P.; Francois, A.; Heng, S.; Ebendorff-Heidepriem, H.; Afshar, S. Sensing with Suspended-Core Optical Fibers. *Opt. Fiber Technol.* **2010**, *16*, 343−356.

(21) Kostecki, R.; Ebendorff-Heidepriem, H.; Davis, C.; McAdam, G.; Warren-Smith, S. C.; Monro, T. M. Silica Exposed-Core Microstructured Optical Fibers. *Opt. Mater. Express* **2012**, *2*, 1538−1547.

(22) Warren-Smith, S. C.; Sinchenko, E.; Stoddart, P. R.; Monro, T. M. Distributed Fluorescence Sensing Using Exposed Core Microstructured Optical Fiber. *IEEE Photonics Technol. Lett.* **2010**, *22*, 1385−1387.

(23) Monro, T. M.; Belardi, W.; Furusawa, K.; Baggett, J. C.; Broderick, N. G. R.; Richardson, D. J. Sensing with Microstructured Optical Fibres. *Meas. Sci. Technol.* **2001**, *12*, 854−858.

(24) Rivera-Fuentes, P.; Lippard, S. J. Spirozin1: A Reversible and Ph-Insensitive, Reaction-Based, Red-Fluorescent Probe for Imaging Biological Mobile Zinc. *ChemMedChem* **2014**, *9*, 1238−1243.

(25) Reimhult, E.; Kumar, K. Membrane Biosensor Platforms Using Nano- and Microporous Supports. *Trends Biotechnol.* **2008**, *26*, 82−89.

(26) Warren-Smith, S. C.; Kostecki, R.; Nguyen, L. V.; Monro, T. M. Fabrication, Splicing, Bragg Grating Writing, and Polyelectrolyte Functionalization of Exposed-Core Microstructured Optical Fibers. *Opt. Express* **2014**, *22*, 29493−29504.

(27) Heng, S.; Nguyen, M.; Kostecki, R.; Monro, T. M.; Abell, A. D. Nanoliter-Scale, Regenerable Ion Sensor: Sensing with a Surface Functionalized Microstructured Optical Fiber. *RSC Adv.* **2013**, *3*, 8308−8317.

(28) Gee, K. R.; Zhou, Z. L.; Ton-That, D.; Sensi, S. L.; Weiss, J. H. Measuring Zinc in Living Cells. A New Generation of Sensitive and Selective Fluorescent Probes. *Cell Calcium* **2002**, *31*, 245−251.

(29) Begg, S. L.; Eijkelkamp, B. A.; Luo, Z.; Counago, R. M.; Morey, J. R.; Maher, M. J.; Ong, C. L.; McEwan, A. G.; Kobe, B.; O'Mara, M. L.; Paton, J. C.; McDevitt, C. A. Dysregulation of Transition Metal Ion Homeostasis Is the Molecular Basis for Cadmium Toxicity in Streptococcus Pneumoniae. *Nat. Commun.* **2015**, *6*, 6418.

Supporting Information

Microstructured Optical Fiber-based Biosensors: Reversible and Nanoliter-Scale Measurement of Zinc Ions.

Sabrina Heng,[1]* Christopher A. McDevitt,[2] Roman Kostecki,[1] Jacqueline R. Morey,[2] Bart A. Eijkelkamp,[2] Tanya M. Monro[3] and Andrew D. Abell[1]

[1]ARC Center of Excellence for Nanoscale BioPhotonics, Institute for Photonics and Advanced Sensing, School of Physical Sciences, The University of Adelaide, Adelaide, South Australia 5005, Australia.

[2]Research Center for Infectious Diseases, School of Biological Sciences, The University of Adelaide, Adelaide, South Australia 5005, Australia.

[3]University of South Australia, South Australia 5005, Australia.

*Corresponding author: sabrina.heng@adelaide.edu.au

General Methods and Materials. HPLC grade Acetonitrile was used in all related experiments. All zinc ions used in this work were in the form of perchlorate, sulphate and chloride salts.[1]
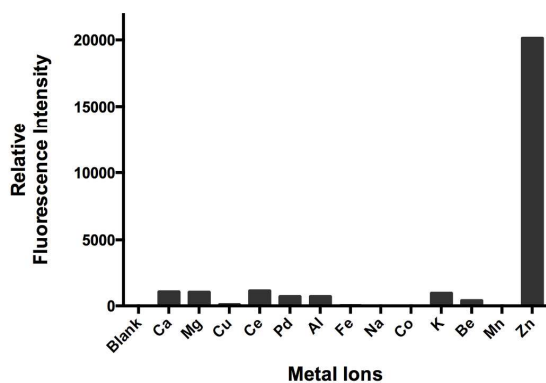
Figure S1. Selectivity of **SP2-liposome** against biologically relevant ions (100 μM).

SP2-liposome Generation

SP2-liposome was then generated by dissolving SP2 (Figure S.1) in DMSO (40 mg.ml-1) and mixing it with a solution containing 0.04 mg of total *Escherichia coli* total lipids extracts in 20 mM 3-(N-morpholino)propanesulfonic acid (MOPS), pH 7.2, supplemented to a final concentration of 0%, 5%, 10% or 20% (weight/vol) maltose or trehalose. Liposomes were generated by successive rounds of sonication and vortexing. The unreconstituted SP2 was removed by a low-speed centrifugation step (18,000 x *g*, 35 min, 25°C) and the liposomes isolated by ultracentrifugation (200,000 x *g*, 60 min, 25°C). The liposomal pellet was resuspended in in 20 mM MOPS, pH 7.2, and unilamellar SP2 liposomes were generated by extruding the mixture through a 0.1 μm membrane to generate SP2-liposome.

Glass slide experiment

A 5 μL sample of each glycosylated SP-liposome (Figure 3, 7 samples in total) was place on a slide and the droplets were subsequently mixed with an aqueous solution of Zn^{2+} (100 μM). The resulting ring opened merocyanine isomer was irradiated at 532 nm, using the Typhoon Imager (GE Healthcare), and Zn^{2+} induced fluorescence was recorded.

Preparation of SP2-maltose-liposomes

SP2-maltose-liposome was prepared as described above with 1,2-dipalmitoyl-*sn*-glycero-3-phosphoethanolamine-N-(succinyl) (Figure S2) used instead of *E.coli* total lipids. The buffer used was 20 mM MOPS pH 7.2, 5 % Maltose, filtered using 0.45 u filter.
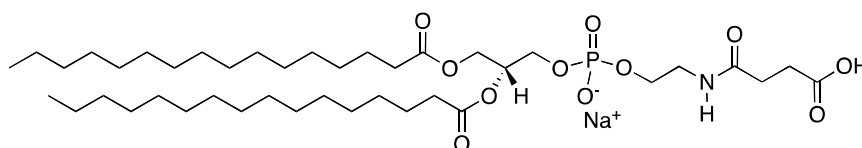
Figure S2. 1,2-dipalmitoyl-*sn*-glycero-3-phosphoethanolamine-N-(succinyl).

Attachment of biosensor material to surface of suspended-core fiber

To attach **SP2-maltose-liposomes** to the core surface of the suspended-core fiber, a pressurized filling station with sealed nitrogen chamber was used with procedures modified from previous work. Specifically, (3-aminopropyl)triethoxysilane (APTES) was used which covalently bonds to hydroxyl groups on the silica core surface to provide free amine groups for covalent bonding with the biosensor carboxylic acid group. One-meter lengths of fiber were prepared for APTES functionalization by cleaning and hydroxylation of the inner surface with 70% nitric acid for 16 h followed by 2 h in 70/30 piranha solution (concentrated sulfuric acid and hydrogen peroxide). After water and acetone rinsing then drying under nitrogen flow for 16 h, the prepared fiber was filled with 5% w/w APTES in anhydrous toluene for 2 h then rinsed with toluene and acetonitrile. This silane functionalized fiber was then filled with a mixture of acetonitrile, modified lipids, and coupling reagent for 20 h and rinsed with 25% w/w acetonitrile in water, which gave the functionalized suspended-core fiber with **SP2-maltose-liposomes** covalently bound to the core surface. The air-holes of the functionalized fiber was then dried under nitrogen flow for 1 day before experiments with biological samples. The coupling reagent used to form amide bonds was 1-[Bis(dimethylamino)methylene]-1H-1,2,3-triazolo[4,5-b]pyridinium 3-oxid hexafluorophosphate (HATU) with 100 μM N,N-diisopropylethylamine (DIPEA).

Murine serum and pleural lavage

23Outbred 5- to 6-week old female CD1 (Swiss) mice were used in all animal experiments. Mice were anaesthetized by intraperitoneal injection of pentobarbital sodium (Nembutal; Rhone- Merieux) at a dose of 66 μg per g of body weight. Blood was collected by syringe from the posterior vena cava. The pleural cavity was lavaged with 1 ml sterile PBS containing 2 mM EDTA introduced through the diaphragm.[2-3] All procedures performed in this study were conducted with a view to minimizing the discomfort of the animals, and used the minimum numbers to generate reproducible and statistically significant data. All experiments were approved by the University of Adelaide Animal Ethics Committee (Animal Welfare Assurance number A5491-01; project approval number S-2013-053) and were performed in strict adherence to guidelines dictated by the Australian Code of Practice for the Care and Use of Animals for Scientific Purpose

Metal ion analyses using ICP-MS and Fluozin-3

Murine samples were prepared essentially as described in previous work.2 Briefly, murine samples were supplemented with 3.5% HNO_3 (final concentration) and boiled for 60 min at 370 K. Samples were then cooled and centrifuged for 20 min at 14,000 g. The supernatant was analysed by inductively coupled plasma mass spectrometry (ICP-MS) on an Agilent 7500cx ICP- MS (Adelaide Microscopy, University of Adelaide), and the metal concentration determined.[4-5] The fluorescence data were collected by on a PHERAStar Omega (BMG Labtech) at 301 K using black half-volume 384-well microtitre plates (Greiner Bio One). All experiments were performed in 20 mM MOPS (pH 6.7), 50 mM NaCl with Fluozin-3 (Thermo Fisher Scientific) at a concentration of 50 nM. Deionized water and buffers were prepared and treated with Chelex- 100 (Sigma-Aldrich) to avoid metal contamination. Filters used for Fluozin-3 were excitation (485 ± 10 nm) and emission (520 ± 5 nm). After subtraction of the background fluorescence from the buffer, the fluorescence intensity of the murine samples were determined and the concentration derived by comparison with a standard curve using known concentrations of $ZnSO_4$.[6]

Results from suspended core based-sensor experiments with pleural lavage and nasopharynx.
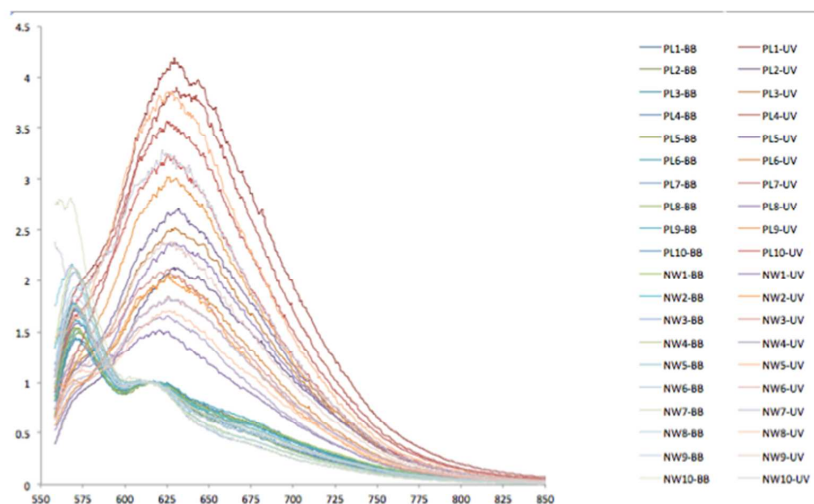
Figure S3. Fluorescence emission results from suspended core fiber sensor with biological samples. NW represents nasopharynx samples, PL represents pleural lavage samples.   BB represents emission data obtained when the samples were exposed to white light. UV represents emission data obtained after the samples were exposed to UV (320 – 350 nm).

References

1.   Maret, W., Analyzing Free Zinc(Ii) Ion Concentrations in Cell Biology with Fluorescent Chelating Molecules. *Metallomics* **2015,** *7*, 202-211.

2.   Plumptre, C. D.; Eijkelkamp, B. A.; Morey, J. R.; Behr, F.; Counago, R. M.; Ogunniyi, A. D.; Kobe, B.; O'Mara, M. L.; Paton, J. C.; McDevitt, C. A., Adca and Adcaii Employ Distinct Zinc Acquisition Mechanisms and Contribute Additively to Zinc Homeostasis in Streptococcus Pneumoniae. *Mol Microbiol* **2014,** *91*, 834-851.

3.   McDevitt, C. A.; Ogunniyi, A. D.; Valkov, E.; Lawrence, M. C.; Kobe, B.; McEwan, A. G.; Paton, J. C., A Molecular Mechanism for Bacterial Susceptibility to Zinc. *PLoS Pathog* **2011,** *7*, e1002357.

4.   Begg, S. L.; Eijkelkamp, B. A.; Luo, Z.; Counago, R. M.; Morey, J. R.; Maher, M. J.; Ong, C. L.; McEwan, A. G.; Kobe, B.; O'Mara, M. L.; Paton, J. C.; McDevitt, C. A., Dysregulation of Transition Metal Ion Homeostasis Is the Molecular Basis for Cadmium Toxicity in Streptococcus Pneumoniae. *Nat Commun* **2015,** *6*, 6418.

5.   Counago, R. M.; Ween, M. P.; Begg, S. L.; Bajaj, M.; Zuegg, J.; O'Mara, M. L.; Cooper, M. A.; McEwan, A. G.; Paton, J. C.; Kobe, B.; McDevitt, C. A., Imperfect Coordination Chemistry Facilitates Metal Ion Release in the Psa Permease. *Nat Chem Biol* **2014,** *10*, 35-41.

6.   Pederick, V. G.; Eijkelkamp, B. A.; Begg, S. L.; Ween, M. P.; McAllister, L. J.; Paton, J. C.; McDevitt, C. A., Znua and Zinc Homeostasis in Pseudomonas Aeruginosa. *Sci Rep* **2015,** *5*.

APPENDIX L

Paper 12.

Third harmonic generation in exposed-core microstructured optical fibers

STEPHEN C. WARREN-SMITH,[1,*] JINGXUAN WIE,[1,2] MARIO CHEMNITZ,[1,2] ROMAN KOSTECKI,[3] HEIKE EBENDORFF-HEIDEPRIEM,[3] TANYA M. MONRO,[3,4] AND MARKUS A. SCHMIDT[1,2,5]

[1]Leibniz Institute of Photonic Technology (IPHT Jena), Albert-Einstein-Straße 9, 07745 Jena, Germany
[2]Abbe Center of Photonics, Friedrich Schiller University Jena, Max-Wien-Platz 1, 07743 Jena, Germany
[3]ARC Centre of Excellence for Nanoscale BioPhotonics and Institute for Photonics and Advanced Sensing (IPAS), The University of Adelaide, Adelaide 5005, Australia
[4]University of South Australia, Adelaide, SA 5000, Australia
[5]Otto Schott Institute of Materials Research (OSIM), Friedrich Schiller University of Jena, Fraunhoferstrasse 6, 07743 Jena, Germany
[*]stephen.warrensmith@leibniz-ipht.de

Abstract: Inter-modal phase-matched third harmonic generation has been demonstrated in an exposed-core microstructured optical fiber. Our fiber, with a partially open core having a diameter of just 1.85 µm, shows efficient multi-peak third-harmonic generation between 500 nm and 530 nm, with a maximum visible-wavelength output of 0.96 µW. Mode images and simulations show strong agreement, confirming the phase-matching process and polarization dependence. We anticipate this work will lead to tailorable and tunable visible light sources by exploiting the open access to the optical fiber core, such as depositing thin-film coatings in order to shift the phase matching conditions.

References and links

1. J. C. Knight, "Photonic crystal fibres," Nature **424**(6950), 847–851 (2003).
2. P. S. J. Russell, "Photonic-crystal fibers," J. Lightwave Technol. **24**(12), 4729–4749 (2006).
3. M. A. Schmidt, A. Argyros, and F. Sorin, "Hybrid optical fibers - an innovative platform for in-fiber photonic devices," Adv. Opt. Mater. **4**(1), 13–36 (2016).
4. T. M. Monro, D. J. Richardson, and P. J. Bennett, "Developing holey fibres for evanescent field devices," Electron. Lett. **35**(14), 1188–1189 (1999).
5. T. M. Monro, S. Warren-Smith, E. P. Schartner, A. François, S. Heng, H. Ebendorff-Heidepriem, and S. Afshar, "Sensing with suspended-core optical fibers," Opt. Fiber Technol. **16**(6), 343–356 (2010).
6. E. P. Schartner, G. Tsiminis, A. François, R. Kostecki, S. C. Warren-Smith, L. V. Nguyen, S. Heng, T. Reynolds, E. Klantsataya, K. J. Rowland, A. D. Abell, H. Ebendorff-Heidepriem, and T. M. Monro, "Taming the light in microstructured optical fibers for sensing," Int. J. Appl. Glass Sci. **6**(3), 229–239 (2015).
7. T. G. Euser, J. S. Y. Chen, M. Scharrer, P. S. J. Russell, N. J. Farrer, and P. J. Sadler, "Quantitative broadband chemical sensing in air-suspended solid-core fibers," J. Appl. Phys. **103**(10), 103108 (2008).
8. H. Ebendorff-Heidepriem, S. C. Warren-Smith, and T. M. Monro, "Suspended nanowires: fabrication, design and characterization of fibers with nanoscale cores," Opt. Express **17**(4), 2646–2657 (2009).
9. M. Liao, C. Chaudhari, X. Yan, G. Qin, C. Kito, T. Suzuki, and Y. Ohishi, "A suspended core nanofiber with unprecedented large diameter ratio of holey region to core," Opt. Express **18**(9), 9088–9097 (2010).
10. S. Afshar V, W. Q. Zhang, H. Ebendorff-Heidepriem, and T. M. Monro, "Small core optical waveguides are more nonlinear than expected: experimental confirmation," Opt. Lett. **34**(22), 3577–3579 (2009).
11. L. Fu, B. K. Thomas, and L. Dong, "Efficient supercontinuum generations in silica suspended core fibers," Opt. Express **16**(24), 19629–19642 (2008).
12. N. Granzow, M. A. Schmidt, W. Chang, L. Wang, Q. Coulombier, J. Troles, P. Toupin, I. Hartl, K. F. Lee, M. E. Fermann, L. Wondraczek, and P. S. J. Russell, "Mid-infrared supercontinuum generation in As_2S_3-silica "nano-spike" step-index waveguide," Opt. Express **21**(9), 10969–10977 (2013).
13. N. Granzow, S. P. Stark, M. A. Schmidt, A. S. Tverjanovich, L. Wondraczek, and P. S. J. Russell, "Supercontinuum generation in chalcogenide-silica step-index fibers," Opt. Express **19**(21), 21003–21010 (2011).
14. G. P. Agrawal, *Nonlinear Fiber Optics (Third Edition)* (Academic, 2001).

15. P. D. Maker, R. W. Terhune, M. Nisenoff, and C. M. Savage, "Effects of dispersion and focusing on the production of optical harmonics," Phys. Rev. Lett. **8**(1), 21–22 (1962).
16. J. M. Gabriagues, "Third-harmonic and three-wave sum-frequency light generation in an elliptical-core optical fiber," Opt. Lett. **8**(3), 183–185 (1983).
17. K. Bencheikh, S. Richard, G. Mélin, G. Krabshuis, F. Gooijer, and J. A. Levenson, "Phase-matched third-harmonic generation in highly germanium-doped fiber," Opt. Lett. **37**(3), 289–291 (2012).
18. A. Borne, T. Katsura, C. Félix, B. Doppagne, P. Segonds, K. Bencheikh, J. A. Levenson, and B. Boulanger, "Ince-gauss based multiple intermodal phase-matched third-harmonic generations in a step-index silica optical fiber," Opt. Commun. **358**, 160–163 (2016).
19. A. Borne, T. Katsura, C. Félix, B. Doppagne, P. Segonds, K. Bencheikh, J. A. Levenson, and B. Boulanger, "Anisotropy analysis of third-harmonic generation in a germanium-doped silica optical fiber," Opt. Lett. **40**(6), 982–985 (2015).
20. A. Coillet and P. Grelu, "Third-harmonic generation in optical microfibers: from silica experiments to highly nonlinear glass prospects," Opt. Commun. **285**(16), 3493–3497 (2012).
21. V. Grubsky and J. Feinberg, "Phase-matched third-harmonic UV generation using low-order modes in a glass micro-fiber," Opt. Commun. **274**(2), 447–450 (2007).
22. A. Efimov, A. Taylor, F. Omenetto, J. Knight, W. Wadsworth, and P. Russell, "Phase-matched third harmonic generation in microstructured fibers," Opt. Express **11**(20), 2567–2576 (2003).
23. F. Omenetto, A. Efimov, A. Taylor, J. Knight, W. Wadsworth, and P. Russell, "Polarization dependent harmonic generation in microstructured fibers," Opt. Express **11**(1), 61–67 (2003).
24. F. G. Omenetto, A. J. Taylor, M. D. Moores, J. Arriaga, J. C. Knight, W. J. Wadsworth, and P. S. J. Russell, "Simultaneous generation of spectrally distinct third harmonics in a photonic crystal fiber," Opt. Lett. **26**(15), 1158–1160 (2001).
25. J. Nold, P. Hölzer, N. Y. Joly, G. K. L. Wong, A. Nazarkin, A. Podlipensky, M. Scharrer, and P. S. J. Russell, "Pressure-controlled phase matching to third harmonic in Ar-filled hollow-core photonic crystal fiber," Opt. Lett. **35**(17), 2922–2924 (2010).
26. T. Lee, Y. Jung, C. A. Codemard, M. Ding, N. G. R. Broderick, and G. Brambilla, "Broadband third harmonic generation in tapered silica fibres," Opt. Express **20**(8), 8503–8511 (2012).
27. W. Gao, T. Cheng, D. Deng, X. Xue, T. Suzuki, and Y. Ohishi, "Third-harmonic generation with a more than 500 nm tunable spectral range in a step-index tellurite fiber," Laser Phys. Lett. **11**(9), 095106 (2014).
28. R. Kostecki, H. Ebendorff-Heidepriem, S. C. Warren-Smith, and T. M. Monro, "Predicting the drawing conditions for microstructured optical fiber fabrication," Opt. Mater. Express **4**(1), 29–40 (2014).
29. R. Kostecki, H. Ebendorff-Heidepriem, C. Davis, G. McAdam, S. C. Warren-Smith, and T. M. Monro, "Silica exposed-core microstructured optical fibers," Opt. Mater. Express **2**(11), 1538–1547 (2012).
30. R. Kostecki, H. Ebendorff-Heidepriem, S. Afshar V, G. McAdam, C. Davis, and T. M. Monro, "Novel polymer functionalization method for exposed-core optical fiber," Opt. Mater. Express **4**(8), 1515–1525 (2014).
31. S. C. Warren-Smith, R. Kostecki, L. V. Nguyen, and T. M. Monro, "Fabrication, splicing, Bragg grating writing, and polyelectrolyte functionalization of exposed-core microstructured optical fibers," Opt. Express **22**(24), 29493–29504 (2014).
32. C. Perrella, H. P. Griesser, P. S. Light, R. Kostecki, T. M. Stace, H. Ebendorff-Heidepriem, T. M. Monro, A. G. White, and A. N. Luiten, "Demonstration of an exposed-core fiber platform for two-photon rubidium spectroscopy," Phys. Rev. Appl. **4**(1), 014013 (2015).
33. L. V. Nguyen, K. Hill, S. Warren-Smith, and T. Monro, "Interferometric type optical biosensor based on exposed-core microstructured optical fiber," Sensor. Actuat. Biol. Chem. **221**, 320–327 (2015).
34. S. C. Warren-Smith, R. M. André, C. Perrella, J. Dellith, and H. Bartelt, "Direct core structuring of microstructured optical fibers using focused ion beam milling," Opt. Express **24**(1), 378–387 (2016).

Introduction

Microstructured optical fibers (MOFs) are a class of optical fiber that is constructed of micro- or even nanometer-size longitudinal air holes that run along the entire fiber length [1–3]. Perhaps the simplest MOF design is the suspended-core fiber where a central glass core is surrounded by a small number of air holes, typically three, which is a close approximation to a glass rod suspended in air [4–6] and allows guidance in very small cores due to the high index contrast between glass and air. Core diameters as small as 800 nm have been achieved by using fused silica glass [7]. Even smaller diameters have been achieved using soft glasses with higher refractive indices, such as 420 nm in lead-silicate glass [8], 480 nm in tellurite glass [9], and 450 nm in bismuth glass [10]. These extreme dimensions provide new opportunities for nonlinear interactions, such as supercontinuum generation [11–13], given that the nonlinear parameter is inversely proportional to the effective area of the propagating mode [14].

Third harmonic generation (THG) is a phase matched nonlinear process that is typically achieved in crystalline structures by controlling polarization within a birefringent material in order to compensate the material dispersion [15]. In optical fibers this is not possible and thus

inter-modal phase matching, typically of the fundamental mode to modes of higher order, is usually required in order to counter the material and waveguide dispersion. THG was first demonstrated in step-index fibers by Gabriagues in 1983, though the phase matching conditions were not specifically engineered or analyzed [16]. Inter-modal phase matched THG has since been demonstrated in configurations such as highly germanium doped fibers [17–19], tapered silica microfibers [20,21], silica suspended-core fiber [22–24], and argon-filled hollow-core photonic crystal fiber [25]. Furthermore, broadband THG has been demonstrated in tapered silica fibers [26]. Alternatively, weak third harmonics can be generated outside of phase matching conditions directly into the fundamental mode by using highly nonlinear material such as tellurite glass, which has been demonstrated for both solid step-index fibers [27] and suspended-core fibers [9].

In this paper we demonstrate inter-modal phase-matched THG in a new class of suspended core fiber referred to as an exposed-core fiber (ECF), where part of the cladding has been removed in order to provide direct access to the evanescent field of the core [28,29]. Such fibers have recently been demonstrated in a host of sensing related experiments such as fluorescence sensing [30], fiber Bragg grating refractometry [31], rubidium spectroscopy [32], and multimode [33] and Fabry-Perot [34] interferometry. Nonlinear light generation in these fibers, in particular THG, will open up new opportunities for tuning and tailoring modal and pulse dispersion and thus the nonlinear interaction, as the open core can easily be modified via post-processing (e.g. coating) with a wide range of materials.

2. Third harmonic generation experiment

Fused silica glass exposed-core fibers, with a continuous length of 80 meters, was fabricated using a ultrasonic drilled preform as detailed in a previous publication (cross-sectional scanning electron microscope (SEM) image shown in Fig. 1) [28]. The fiber has an outer diameter of 145 µm [Fig. 1(a)] and an effective core diameter of 1.85 µm [Fig. 1(b)], using the definition of core diameter in [8].
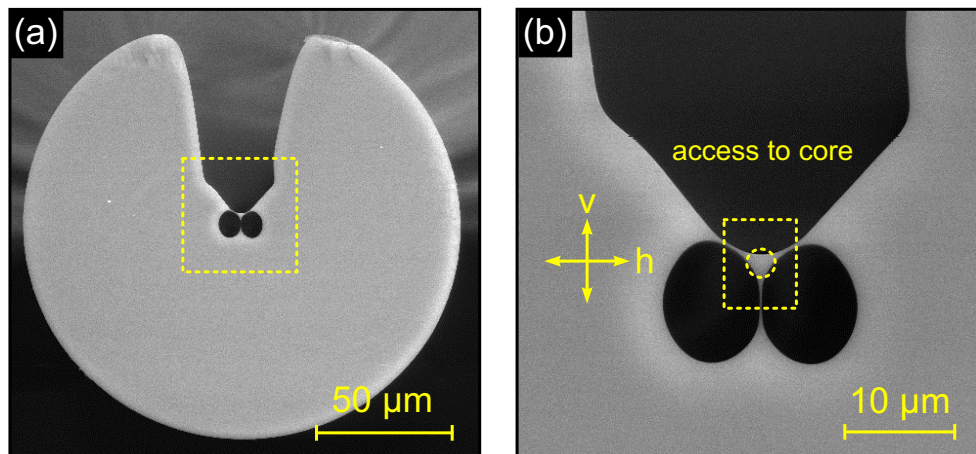
Fig. 1. Scanning electron microscope images of the silica glass exposed-core fiber. (a) The full cross-sectional geometry is shown. (b) The core region from within the yellow dashed line in (a). The yellow dashed square indicates the portion of the SEM that was used for numerical modelling (see Sec. 3). The arrows indicate the definition for horizontal (h) and vertical (v) polarization direction described in the following experimental and numerical work. The dashed yellow circle indicates the core diameter of 1.85 µm.

To demonstrate THG in the ECF we used a 1560 nm femtosecond laser (Toptica, FemtoFiber pro IRS, 80 MHz, <40 fs pulses, average power 220 mW) as the pump source. We controlled both the input pump power and polarization using a combination of a rotating half wave plate and a polarizer. The pump beam was then focused into the exposed-core fiber using an aspheric lens (Thorlabs, C230TM-C). A short length of fiber was used (3.3 mm) in

order to reduce the probability of contamination of the exposed-core (e.g. dust) leading to increased fiber loss. However, no increase in fiber loss was measured during the course of the experiment. The output was imaged using a 40X microscope objective and a camera in order to confirm coupling into the fiber core. Coupling efficiencies into the ECF core were in the range of 15-20%. The variation was primarily due to adjustment of the half-wave plate during the experiment, which slightly alters the pump beam path, and the consequent impact on coupling into the small 1.85 μm core. Once optimal coupling was achieved the output was coupled into a graded-index multi-mode fiber using a 4X microscope objective and connected to an optical spectrum analyzer (ANDO 6315A). The output spectra of the third harmonic (TH) signals for vertical input polarization are shown in Fig. 2, while the inset shows the corresponding transmitted input infra-red (IR) spectra.
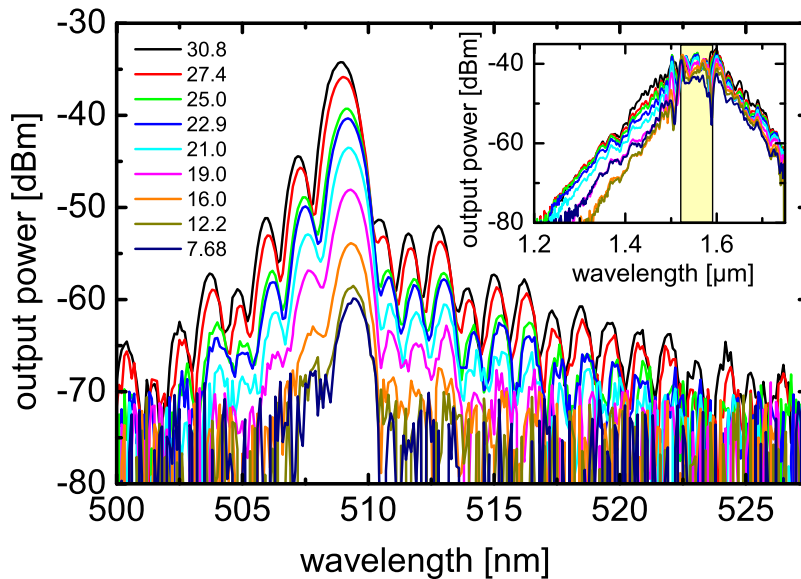
Fig. 2. Spectral distribution of the output power (generated third harmonic wavelengths) for various input power for vertical input polarization [defined in Fig. 1(b)] in the green part of the visible spectrum. The average transmitted infra-red pump power, as measured on a power meter, is indicated in the legend (mW). Inset: Spectral domain of the laser pump wavelength (near IR domain). The yellow column indicates the wavelength range that is relevant for the observed THG-process.

We observe a series of well-separated peaks in the spectral distribution of the output power between 500 nm and 530 nm with a power maximum power at 509 nm. The spectral shape is preserved for different input powers for the THG wavelengths, indicating the absence of other nonlinear effects influencing the phase matching process. Even though ultra-short optical pulses are used here, no nonlinear effects are observed in the domain of the IR pump wavelength (i.e. shape of the spectral power distribution remains constant), indicating separation between the zero-dispersion wavelength of the group velocity dispersion, and the pump and TH wavelengths. In particular, no other generated wavelengths were measured above the detection noise limit (−80 dBm) for the range 350-1750 nm.
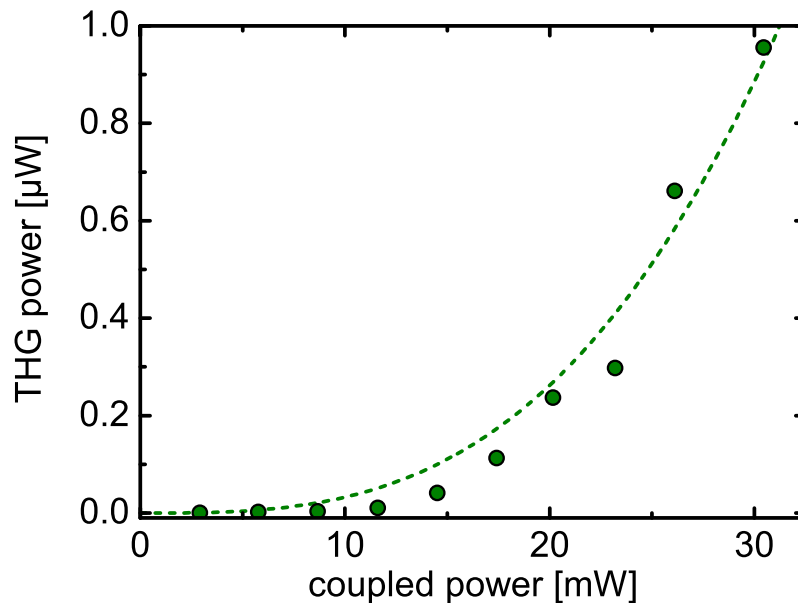
Fig. 3. Measured average third harmonic generated power for different coupled pump powers. A cubic polynomial fit of the form $P_{THG} = A + BP_{IN}^3$ is shown ($R^2 = 0.98$), where P_{THG} is the third harmonic generated power and P_{IN} is the input power from the femtosecond laser.

The integration (total power) of the spectra in Fig. 2 is shown in Fig. 3 against the femtosecond laser power that was coupled into the fiber core. In particular, the experimentally measured power displays a cubic relationship with input power, adding evidence that the visible spectra in Fig. 2 results from third harmonic generation. From Fig. 3, the maximum efficiency of converting coupled power into THG was 3.1×10^{-5} (0.96 µW generated from 30.5 mW coupled power) while the maximum overall system efficiency was 4.5×10^{-6} (210 mW total fs laser power). This compares well with previously reported values of overall system THG conversion efficiency, such as in silica microfibers (e.g. 2.5×10^{-7} [20] and 2×10^{-6} [21]) and highly germanium-doped step-index fibers (3×10^{-7} [17]).

The exposed-core fiber structure is highly asymmetric (Fig. 1) and thus it is expected that polarization of the input beam should have a significant impact on the phase-matching conditions and thus the resulting TH-signal. Figure 4 shows the TH-spectra for two orthogonal input polarizations, corresponding to the orientations shown in Fig. 1(b). It can be seen that the TH-signal for vertically orientated polarization is over one order of magnitude stronger than for the horizontal polarization (coupled power v- and h-pol.: 29.0mW and 30.8mW). As will be explained in the following section, this can be a result of both phase matching conditions and modal overlap. Note also that for the horizontal polarization there are two distinct peaks rather than a series of peaks seen in the vertical case, which correspond to two phase matched visible modes.
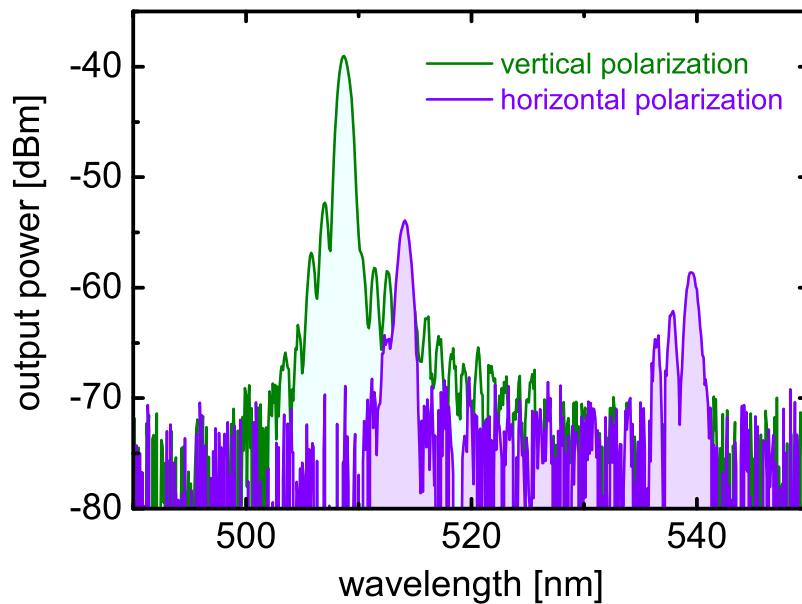
Fig. 4. Spectral distribution of the generated third harmonics for two orthogonal input polarizations (green: vertical polarization, purple: horizontal polarization). The polarization orientation corresponds to that shown in Fig. 1(b).

3. Numerical modeling

We simulated the different propagating modes using finite element modeling (COMSOL v5) on the structure indicated by the white dashed box of Fig. 1(b) in order to understand the phase matching conditions responsible for the measured TH-signals. A rectangular perfectly matched layer (PML) boundary condition was applied to prevent spurious modes from forming at the termination of the ECF struts. The dispersion values for the relevant eigenmodes were calculated in the range of the THG [450-550 nm, Fig. 5(a)] and the IR pumping range [1500-1600 nm, Fig. 5(b)]. As a result of the PML boundary conditions the calculated effective indices include an imaginary component, indicating how well confined the mode is to the fiber core. In the visible (THG) wavelength region only modes for which the imaginary part was less than 10^{-3} (approx. 100 dB/mm) are shown in Fig. 5(a). Also note that four other modes exist for the IR wavelengths, below $n_{eff} = 1.25$.

Figure 5(a) shows that there is a high density of modes that exist at the TH-wavelengths, providing high probability for inter-modal phase matching. This is expected given the high numerical aperture of the air-clad fiber geometry. In addition to phase matching, THG also requires polarization and modal overlap between the modes at the pump and generated wavelengths. To a first approximation, the THG modes should exhibit peak intensities at the center of the fiber core with a polarization matching that of the mode at the fundamental wavelength. All such modes that are close in effective index (< 1.0%) to the fundamental mode are highlighted in Fig. 5(a) (purple: horizontal modes, green: vertical modes). There are two such TH-modes that have predominantly vertically orientated polarization at the center [Figs. 6(b) and 6(c)] and two that are predominantly horizontally polarized at the center [Figs. 6(f) and 6(g)], which matches the polarization of the corresponding mode at the fundamental wavelength [v: Fig. 6(a), h: Fig. 6(e)].
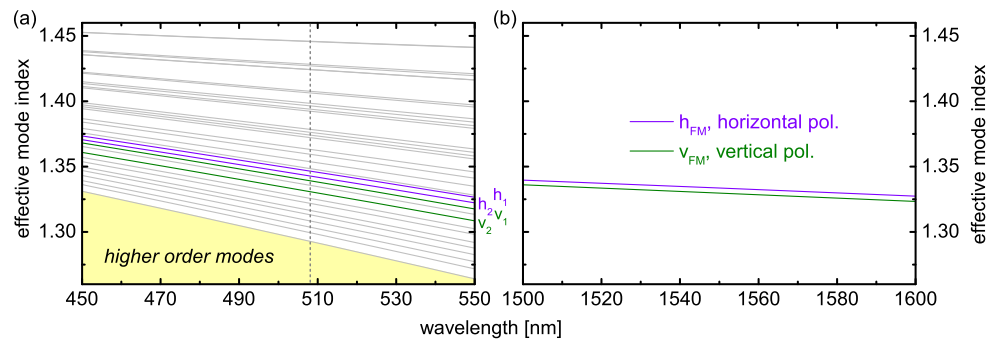
Fig. 5. (a) Effective index dispersions of the various modes in the exposed core fiber in the visible part of the spectrum. The modes with a strong horizontal (vertical) polarization components in the center of the fiber are shown in purple (green). Modes outside of 1% phase matching conditions and with no local intensity peak at the center, which are not relevant for the discussion here, are shown in light gray. The vertical dashed gray line indicates the wavelength at which the mode patterns in Fig. 6 are calculated. (b) Effective index dispersions of the two orthogonal fundamental eigenmodes in the spectral domain of the pump laser.

The experimentally recorded mode images of the TH-signal, after filtering of the IR pump wavelengths, are shown in Figs. 6(d) and 6(h). Comparison between the simulated vertically polarized mode images and the measured THG mode shows that the mode labeled by v2 in Fig. 5(a) is responsible for the inter-modal phase matching. The difference in effective index between the IR and THG wavelengths is $\Delta n_{eff} = 0.0023$ (0.17%), which is likely attributed to errors associated with recording the SEM image and importing it into COMSOL, rather than an actual significant phase difference. A potential contribution of a pump induced nonlinear phase shift has been calculated to be less than 0.7% and thus can be neglected here.
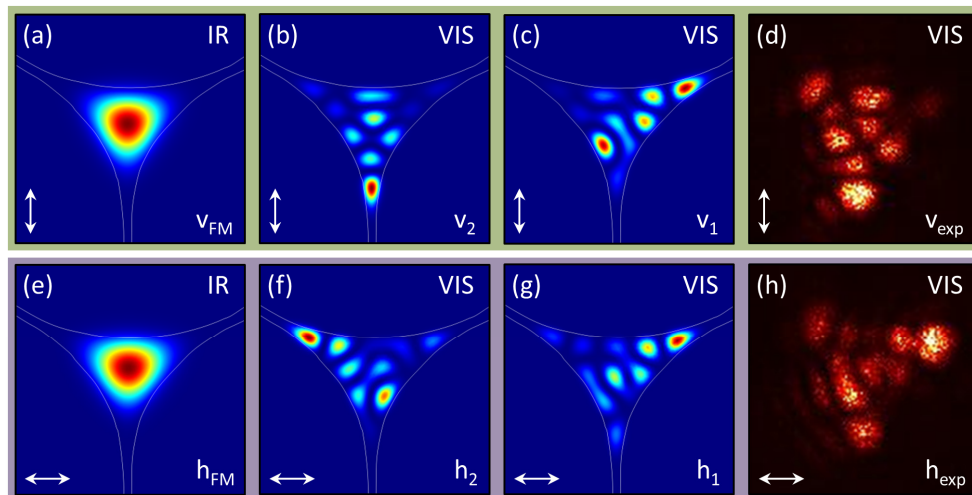
Fig. 6. Comparison of simulated mode patterns with the intensity distributions obtained in the experiment (top (bottom) row: refers to vertical (horizontal) input polarization, arrows in the lower-left corners indicate polarization as shown in Fig. 1). The fundamental and higher-order TH-modes have been calculated at 1527 nm (IR) and 509 nm (VIS), respectively. (a) Fundamental vertically-polarized mode. (b-c) Higher-order TH-modes with preferential vertical polarization in the center of the mode [(b) and (c) refer to modes labeled by v2 and v1 in Fig. 5(a)]. (d) Experimental measured image of the corresponding output mode. (e) Horizontal-polarized fundamental mode. (f-g) Higher-order horizontal TH-modes [(f) and (g) refer to modes labeled by h2 and h1 in Fig. 5(a)]. (h) Corresponding measured near-field pattern.

Understanding the THG-process in the horizontal polarization is more complex considering there are two peaks present in the TH-spectrum (Fig. 4). The measured mode image [Fig. 6(h)] exhibits features from both of the two modes shown in Figs. 6(f) and 6(g). In any case, the multi-lobed structure of the measured mode images in Figs. 6(d) and 6(h), and the strong agreement with simulations particularly for the vertical polarization, provides strong evidence that the visible emission observed in Fig. 2 is indeed inter-modal phase-matched third harmonic generation.

4. Discussion and conclusions

We have demonstrated inter-modal phase-matched third harmonic generation in an exposed-core microstructured optical fiber. Our fiber has a core diameter of only 1.85 μm leading to a strong field confinement for both the fundamental and third harmonic waves. We observe efficient multi-peak third-harmonic generation between 500 nm and 530 nm with a maximum generated average power at visible wavelengths of 0.96 μW. This corresponds to a total system efficiency of 4.5×10^{-6}, comparable to previous reports of THG in microfibers. The experimental results agree well with modal simulations, including the mode patterns, effect of polarization, and phase difference between the IR and THG wavelengths.

The use of an exposed-core structure will open up opportunities in tuning and tailoring nonlinear light generation in fibers using post-processing steps that would otherwise be difficult to achieve in conventional enclosed microstructured optical fiber geometries. In future, thin-film coatings can be deposited along the entire exposed core of the fiber in order to tailor the modal and pulse dispersion and hence the phase-matching conditions. Alternatively, the open channel can be filled with liquids in order to enhance the nonlinearity, though care would need to be taken to ensure guidance is still achieved. Such techniques may be used for improving the THG efficiency or to allow the generation of light at specific wavelengths and within specific spatial modes that otherwise could not be achieved by controlling only the fiber fabrication (i.e. preform geometry and fiber drawing conditions), thus balancing out production inaccuracies via post-fabrication processing. The open channel also allows for accessing ultrafast excitations propagating in the core (e.g. solitons and dispersive waves) via the evanescent field, which can be useful for investigating the spatial dependence of nonlinear processes and might enable new schemes for pump-probe spectroscopy.

This work may provide a path for the reverse process of triple photon generation (TPG) for quantum optics applications in a fiber integrated device. The challenge of inter-modal phase-matching for TPG is to efficiently launch light into the higher order modes of an optical fiber. The exposed-core fiber offers a potential solution by advancing recently demonstrated surface relief fibre Bragg gratings (FBGs) [31]. By adapting such FBGs as grating-couplers, side launching with an appropriate angle could be used to satisfy the phase-matching condition for launching directly into specific higher order modes. The ability to tailor the dispersion as described above may also be critical as the inter-modal phase matching condition may be adjusted for optimal operation at wavelengths available from commercial high peak power sources (e.g. 532 nm).

Funding

[1] R. Kostecki, H. Ebendorff-Heidepriem, C. Davis, G. McAdam, S. C. Warren-Smith, and T. M. Monro, "Silica exposed-core microstructured optical fibers," Opt. Mater. Express **2**, 1538 – 1547 (2012).

[2] S. C. Warren-Smith, G. Nie, E. P. Schartner, L. A. Salamonsen, and T. M. Monro, "Enzyme activity assays within microstructured optical fibers enabled by automated alignment," Biomed. Opt. Express **3**, 3304 – 3313 (2012).

[3] S. Heng, M.-C. Nguyen, R. Kostecki, T. M. Monro, and A. D. Abell, "Nanoliter-scale, regenerable ion sensor: sensing with a surface functionalized microstructured optical fibre," RSC Adv. **3**, 8308 – 8317 (2013).

[4] S. Heng, C. A. McDevitt, D. B. Stubing, J. J. Whittall, J. G. Thompson, T. K. Engler, A. D. Abell, and T. M. Monro, "Microstructured optical fibers and live cells: A water-soluble, photochromic zinc sensor," Biomacromolecules **14**, 3376 – 3379 (2013).

[5] S. C. Warren-Smith and T. M. Monro, "Exposed core microstructured optical fiber bragg gratings: refractive index sensing," Opt. Express **22**, 1480 – 1489 (2014).

[6] S. Heng, A. M. Mak, D. B. Stubing, T. M. Monro, and A. D. Abell, "Dual sensor for Cd(II) and Ca(II): Selective nanoliter-scale sensing of metal ions," Anal. Chem. **86**, 3268 – 3272 (2014).

[7] S. C. Warren-Smith, R. Kostecki, L. V. Nguyen, and T. M. Monro, "Fabrication, splicing, bragg grating writing, and polyelectrolyte functionalization of exposed-core microstructured optical fibers," Opt. Express **22**, 29493–29504 (2014).

[8] C. Perrella, H. P. Griesser, P. S. Light, R. Kostecki, T. M. Stace, H. Ebendorff-Heidepriem, T. M. Monro, A. G. White, and A. N. Luiten, "Demonstration of an exposed-core fiber platform for two-photon rubidium spectroscopy," Phys. Rev. Applied **4**, 014013 (2015).

[9] S. Heng, C. A. McDevitt, R. Kostecki, J. R. Morey, B. A. Eijkelkamp, H. Ebendorff-Heidepriem, T. M. Monro, and A. D. Abell, "Microstructured optical fiber-based biosensors: Reversible and nanoliter-scale measurement of zinc ions," ACS Appl. Mater. Interfaces **8**, 12727 – 12732 (2016).

[10] G. Tsiminis, F. Chu, S. C. Warren-Smith, N. A. Spooner, and T. M. Monro, "Identification and quantification of explosives in nanolitre solution volumes by raman spectroscopy in suspended core optical fibers," Sensors **13**, 13163 – 13177 (2013).

[11] L. V. Nguyen, S. Giannetti, S. Warren-Smith, A. Cooper, S. Selleri, A. Cucinotta, and T. Monro, "Genotyping single nucleotide polymorphisms using different molecular beacon multiplexed within a suspended core optical fiber," Sensors **14**, 14488 – 14499 (2014).

[12] H. Lohner and T. Hack, *Aluminium Alloy Corrosion of Aircraft Structures: Modelling and Simulation* (WIT Press, 2013).

[13] J. Broomfield *et al.*, "The strategic highway research program. Research on corrosion of

steel in concrete." P. I. Civil Eng. – Str. B. **104**, 211 – 218 (1994).

[14] G. McAdam, P. J. Newman, I. McKenzie, C. Davis, and B. R. W. Hinton, "Fiber optic sensors for detection of corrosion within aircraft," Struct. Health Monit. **4**, 47 – 56 (2005).

[15] J. Hall, "Corrosion prevention and control programs for boeing airplanes," Technical Paper 931259, SAE International (1993).

[16] Australian Government, "Corrosion prevention and control program (CPCP)," Civil Aviation Safety Regulations 1998 Part 39.001(1), AD/B737/52 Amdt 3, Infrastructure and Regional Development (2011).

[17] I. McKenzie and P. J. Newman, "Methods for detection of corrosion in aircraft structures using fiber optic technology," in "Tri-Service Corrosion Conference [15–19 Nov., Myrtle Beach, South Carolina]," (1999).

[18] J. Ščančar and R. Milačič, "Aluminium speciation in environmental samples: A review," Anal. Bioanal. Chem. **386**, 999 – 1012 (2006).

[19] TC156, "ISO8044:1999 corrosion of metals and alloys – basic terms and definitions," International Organization for Standardization (1999).

[20] S. D. Cramer and B. S. Covino, *Corrosion: Fundamentals, Testing, and Protection*, vol. 13A (ASM International, 2003).

[21] D. A. Krohn, *Fiber Optic Sensors: Fundamentals and Applications* (Instrument Society of America, 2000), 3rd ed.

[22] E. A. Mendoza, R. A. Lieberman, J. D. Prohaska, and D. P. Robinson, "Distributed fiber optic chemical sensors for detection of corrosion in pipelines and structural components," in "Nondestructive Evaluation of Utilities and Pipelines II," , vol. 3398 of *Proc. SPIE* (1998), vol. 3398 of *Proc. SPIE*, pp. 136 – 143.

[23] E. A. Mendoza, A. N. Khalil, Z. Sun, D. P. Robinson, S. J. Syracuse, C. O. Egalon, M. F. Gunther, and R. A. Lieberman, "Embeddable distributed moisture and ph sensors for nondestructive inspection of aircraft lap joints," in "Nondestructive Evaluation of Aging Aircraft, Airports, Aerospace Hardware, and Materials," , vol. 2455 (Proc. SPIE, 1995), vol. 2455, pp. 102 – 112.

[24] B. Culshaw and A. Kersey, "Fiber-optic sensing: A historical perspective," J. Lightwave Technol. **26** (2008).

[25] S. C. Warren-Smith, "Fluorescence-based chemical sensing using suspended-core microstructured optical fibres," Ph.D. thesis, The University of Adelaide (2010).

[26] B. Culshaw, "Chapter 24 - Principles of fiber optic sensors," in "Guided Wave Optical Components and Devices," , B. P. Pal, ed. (Academic Press, Burlington, 2006), pp. 371 – 387.

[27] H. S. Saini and A. Wason, "Role of optic sensors in engineering and technology," Int. J. IT Eng. Appl. Sci. Res. **1** (2012).

[28] D. Inaudi and B. Glisic, "Long-range pipeline monitoring by distributed fiber optic sens-

ing," J. Press. Vess. - T. ASME **132** (2010). International Pipeline Conference (IPC 2006), Calgary, CANADA, SEP 25-29, 2006.

[29] K. C. Kao and G. A. Hockham, "Dielectric-fibre surface waveguides for optical frequencies," Proc. IEE **113**, 1151 – 1158 (1966).

[30] D. B. Keck, R. D. Maurer, and P. C. Schultz, "On the ultimate lower limit of attenuation in glass optical waveguides," Appl. Phys. Lett. **22**, 307 – 309 (1973).

[31] J. B. MacChesney, P. B. O'Connor, and H. M. Presby, "A new technique for the preparation of low-loss and graded-index optical fibers," Proc. IEEE **62**, 1280 – 1281 (1974).

[32] M. Li and D. A. Nolan, "Optical transmission fiber design evolution," J. Lightwave Technol. **26**, 1079 – 1092 (2008).

[33] P. Kasier, E. A. J. Marcatili, and S. E. Miller, "A new optical fiber," Bell Sys. Tech. J. **52**, 265 – 269 (1973).

[34] E. Yablonovitch, "Inhibited spontaneous emission in solid-state physics and electronics," Phys. Rev. Lett. **58**, 2059 – 2062 (1987).

[35] S. John, "Strong localization of photons in certain disordered dielectric superlattices," Phys. Rev. Lett. **58**, 2486 – 2489 (1987).

[36] E. Yablonovitch and T. J. Gmitter, "Photonic band structure: The face-centered-cubic case," Phys. Rev. Lett. **63**, 1950 – 1953 (1989).

[37] E. Yablonovitch and T. J. Gmitter, "Photonic band structure: The face-centered-cubic case," J. Opt. Soc. Am. A **7**, 1792 – 1800 (1990).

[38] E. Yablonovitch, T. J. Gmitter, and K. M. Leung, "Photonic band structure: The face-centered-cubic case employing nonspherical atoms," Phys. Rev. Lett. **67**, 2295 – 2298 (1991).

[39] J. C. Knight, T. A. Birks, P. S. J. Russell, and D. M. Atkin, "All-silica single-mode optical fiber with photonic crystal cladding," Opt. Lett. **21**, 1547 – 1549 (1996).

[40] T. A. Birks, P. J. Roberts, P. S. J. Russell, D. M. Atkin, and T. J. Shepherd, "Full 2-D photonic bandgaps in silica/air structures," Electron. Lett. **31**, 1941 – 1943 (1995).

[41] T. M. Monro and H. Ebendorff-Heidepriem, "Progress in microstructured optical fibers," Annu. Rev. Mater. Res. **36**, 467 – 495 (2006).

[42] R. F. Cregan, B. J. Mangan, J. C. Knight, T. A. Birks, P. S. J. Russell, P. J. Roberts, and D. C. Allan, "Single-mode photonic band gap guidance of light in air," Science **285**, 1537 – 1539 (1999).

[43] W. Q. Zhang, H. Ebendorff-Heidepriem, T. M. Monro, and S. Afshar V., "Fabrication and supercontinuum generation in dispersion flattened bismuth microstructured optical fiber," Opt. Express **19**, 21135 – 21144 (2011).

[44] M. Oermann, H. Ebendorff-Heidepriem, D. Ottaway, D. Lancaster, P. Veitch, and T. Monro, "Extruded microstructured fiber lasers," IEEE Photon. Technol. Lett. **24**, 578 – 580 (2012).

[45] S. Atakaramians, S. Afshar V., H. Ebendorff-Heidepriem, M. Nagel, B. M. Fischer, D. Abbott, and T. M. Monro, "THz porous fibers: design, fabrication and experimental characterization," Opt. Express **17**, 14053 – 15062 (2009).

[46] N. A. Issa, "High numerical aperture in multimode microstructured optical fibers," Appl. Opt. **43**, 6191 – 6197 (2004).

[47] B. Gauvreau, F. Desevedavy, N. Guo, D. Khadri, A. Hassani, and M. Skorobogatiy, "High numerical aperture polymer microstructured fiber with three super-wavelength bridges," J. Opt. A. – Pure Appl. Op. **11**, 085102 (2009).

[48] K. Mukasa, K. Imamura, M. Takahashi, and T. Yagi, "Development of novel fibers for telecoms application," Opt. Fiber Technol. **16**, 367 – 377 (2010).

[49] T. M. Monro, D. J. Richardson, N. G. R. Broderick, and P. J. Bennett, "Holey optical fibers: An efficient modal model," J. Lightwave Technol. **17**, 1093 – 1102 (1999).

[50] T. M. Monro, D. J. Richardson, and P. J. Bennett, "Developing holey fibres for evanescent field devices," Electron. Lett. **35**, 1188 – 1189 (1999).

[51] T. M. Monro, W. Belardi, K. Furusawa, J. C. Baggett, N. G. R. Broderick, and D. J. Richardson, "Sensing with microstructured optical fibres," Meas. Sci. Technol. **12**, 854 – 858 (2001).

[52] T. M. Monro, Y. D. West, D. W. Hewak, N. G. R. Broderick, and D. J. Richardson, "Chalcogenide holey fibres," Electron. Lett. **36**, 1998 – 2000 (2000).

[53] M. van Eijkelenborg, M. Large, A. Argyros, J. Zagari, S. Manos, N. Issa, I. Bassett, S. Fleming, R. McPhedran, C. M. de Sterke, and N. A. Nicorovici, "Microstructured polymer optical fibre," Opt. Express **9**, 319 – 327 (2001).

[54] T. M. Monro, K. M. Kiang, J. H. Lee, K. Frampton, Z. Yusoff, R. Moore, J. Tucknott, D. W. Hewak, H. N. Rutt, and D. J. Richardson, "High nonlinearity extruded single-mode holey optical fibers," in "Optical Fiber Communications Conference," (2002), p. FA1.

[55] K. M. Kiang, K. Frampton, T. M. Monro, R. Moore, J. Tucknott, D. W. Hewak, D. J. Richardson, and H. N. Rutt, "Extruded singlemode non-silica glass holey optical fibres," Electron. Lett. **38**, 546 – 547 (2002).

[56] J. C. Knight, G. Cheung, F. Jacques, and T. A. Birks, "Phase-matched excitation of whispering-gallery-mode resonances by a fiber taper," Opt. Lett. **22**, 1129 – 1131 (1997).

[57] L. Tong, R. R. Gattass, J. B. Ashcom, S. He, J. Lou, M. Shen, I. Maxwell, and E. Mazur, "Subwavelength-diameter silica wires for low-loss optical wave guiding," Nature **426**, 816 – 819 (2003).

[58] H. Ebendorff-Heidepriem, P. Petropoulos, S. Asimakis, V. Finazzi, R. Moore, K. Frampton, F. Koizumi, D. Richardson, and T. Monro, "Bismuth glass holey fibers with high nonlinearity," Opt. Express **12**, 5082 – 5087 (2004).

[59] H. Ebendorff-Heidepriem, P. Petropoulos, R. Moore, K. Frampton, D. J. Richardson, and T. M. Monro, "Fabrication and optical properties of lead silicate glass holey fibers," J.

Non-Cryst. Solids **345–346**, 293 – 296 (2004).

[60] J. B. Jensen, L. H. Pedersen, P. E. Hϕiby, L. B. Nielsen, T. P. Hansen, J. R. Folkenberg, J. Riishede, D. Noordegraaf, K. Nielsen, A. Carlsen, and A. Bjarklev, "Photonic crystal fiber based evanescent-wave sensor for detection of biomolecules in aqueous solutions," Opt. Lett. **29**, 1974 – 1976 (2004).

[61] J. B. Jensen, P. Hϕiby, G. Emiliyanov, O. Bang, L. Pedersen, and A. Bjarklev, "Selective detection of antibodies in microstructured polymer optical fibers," Opt. Express **13**, 5883–5889 (2005).

[62] L. Rindorf, P. E. Hϕiby, J. B. Jensen, L. H. Pedersen, O. Bang, and O. Geschke, "Towards biochips using microstructured optical fiber sensors," Anal. Bioanal. Chem. **385**, 1370 – 1375 (2006).

[63] Y. L. Hoo, W. Jin, C. Shi, H. L. Ho, D. N. Wang, and S. C. Ruan, "Design and modeling of a photonic crystal fiber gas sensor," Appl. Opt. **42**, 3509–3515 (2003).

[64] G. Pickrell, W. Peng, and A. Wang, "Random-hole optical fiber evanescent-wave gas sensing," Opt. Lett. **29**, 1476 – 1478 (2004).

[65] V. P. Minkovich, D. Monzón-Hernández, J. Villatoro, and G. Badenes, "Microstructured optical fiber coated with thin films for gas and chemical sensing," Opt. Express **14**, 8413 – 8418 (2006).

[66] A. S. Webb, F. Poletti, D. J. Richardson, and J. K. Sahu, "Suspended-core holey fiber for evanescent-field sensing," Opt. Eng. **46** (2007).

[67] S. Afshar V., S. C. Warren-Smith, and T. M. Monro, "Enhancement of fluorescence-based sensing using microstructured optical fibres," Opt. Express **15**, 17891 – 17901 (2007).

[68] S. Afshar V., Y. Ruan, S. C. Warren-Smith, and T. M. Monro, "Enhanced fluorescence sensing using microstructured optical fibers: a comparison of forward and backward collection modes," Opt. Lett. **33**, 1473 – 1475 (2008).

[69] S. K. Bhatia, L. C. Shriver-Lake, K. J. Prior, J. H. Georger, J. M. Calvert, R. Bredehorst, and F. S. Ligler, "Use of thiol-terminal silanes and heterobifunctional crosslinkers for immobilization of antibodies on silica surfaces," Anal. Biochem. **178**, 408 – 413 (1989).

[70] Y. Ruan, T. C. Foo, S. Warren-Smith, P. Hoffmann, R. C. Moore, H. Ebendorff-Heidepriem, and T. M. Monro, "Antibody immobilization within glass microstructured fibers: A route to sensitive and selective biosensors," Opt. Express **16**, 18514 – 18523 (2008).

[71] J. Zhao, D. Jin, E. P. Schartner, Y. Lu, Y. Liu, A. V. Zvyagin, L. Zhang, J. M. Dawes, P. Xi, J. A. Piper, E. M. Goldys, and T. M. Monro, "Single-nanocrystal sensitivity achieved by enhanced upconversion luminescence," Nat. Nano. **8**, 729 – 734 (2013).

[72] J. H. Ali, W. B. Wang, P. P. Ho, and R. R. Alfano, "Detection of corrosion beneath a paint layer by use of spectral polarization optical imaging," Opt. Lett. **25**, 1303–1305 (2000).

[73] S. A. Wade, C. D. Wallbrink, G. McAdam, S. Galea, B. R. W. Hinton, and R. Jones, "A

fibre optic corrosion fuse sensor using stressed metal-coated optical fibres," Sensors Actuat. B-Chem. **131**, 602 – 608 (2008).

[74] J. Namkung, M. Hoke, and A. Schwartz, "Evanescent wave absorption measurements of corroded materials using optical fibers as remote probes," in "Photonics in the Transportation Industry: Auto to Aerospace III," , vol. 7675 (SPIE, 2010), vol. 7675.

[75] J. S. Namkung, M. Hoke, R. S. Rogowski, and S. Albin, "Optical fiber FTIR evanescent wave absorption spectroscopy of natural aluminum corrosion," SPIE: Optical Remote Sensing for Environmental and Process Monitoring, Proceedings of a Symposium **2883**, 655 (1996).

[76] J. S. Namkung, M. L. Hoke, R. S. Rogowski, and S. Albin, "Detection of aluminum corrosion by evanescent wave absorption spectroscopy with optical fibers," Smart Structures and Materials 1995: Smart Sensing, Processing, and Instrumentation (Proceedings of SPIE) **2444** (1995).

[77] X. Yang, Z. Tanaka, R. Newhouse, Q. Xu, B. Chen, S. Chen, J. Z. Zhang, and C. Gu, "Portable fiber sensors based on surface-enhanced Raman scattering," Rev. Sci. Instrum. **81** (2010).

[78] J. C. Lázaro, A. R. de Paula Jr., L. M. Moreira, J. P. Lyon, M. T. T. Pacheco, and C. J. de Lima, "Automated diagnosis and treatment by lasers employing Raman spectroscopy and catheter with optical fibers," Spectroscopy **25**, 147 – 154 (2011).

[79] A. Pesapane, A. Lucotti, and G. Zerbi, "Fiber-optic SERS sensor with optimized geometry: Testing and optimization," J. Raman Spectrosc. **41**, 256 – 267 (2010).

[80] J. M. Corres, I. R. Matias, I. del Villar, and F. J. Arregui, "Design of pH sensors in long-period fiber gratings using polymeric nanocoatings," IEEE Sensors J. **7**, 455 – 463 (2007).

[81] J. L. Elster, *Long Period Grating-Based pH Sensors For Corrosion Monitoring* (Virginia Polytechnic Institute and State University, 2009).

[82] W. C. Michie, B. Culshaw, I. McKenzie, M. Konstantakis, N. B. Graham, C. Moran, F. Santos, E. Bergqvist, and B. Carlstrom, "Distributed sensor for water and ph measurements using fiber optics and swellable polymeric systems," Opt. Lett. **20**, 103–105 (1995).

[83] E. Grinzato, V. Vavilov, P. G. Bison, and S. Marinetti, "Hidden corrosion detection in thick metallic components by transient IR thermography," Infrared Phys. Techn. **49**, 234 – 238 (2007).

[84] Q. Liu, K.-T. Wu, M. Kobayashi, C.-K. Jen, and N. Mrad, "In situ ice and structure thickness monitoring using integrated and flexible ultrasonic transducers," Smart Mater. Struct. **17**, 045023 (2008).

[85] I. Ozolinsh, I. Pavelko, V. Pavelko, M. Wevers, and H. Pfeiffer, "Some results of ultrasonic detection of uniform corrosion in thin Al2024-T3 sheets," in "EU Project Meeting on

Aircraft Integrated Structural Health Assessment (AISHA)," (NDT, 2007).

[86] H. Tsuda, "Bragg wavelength-insensitive fiber bragg grating ultrasound detection system based on a fiber ring laser," in "SPIE: 21st International Conference on Optical Fiber Sensors," , vol. 7753 (2011), vol. 7753.

[87] Z. Kral and W. Horn, "Detection of damage in metal lap joint by combined passive and active methods," in "In Proceedings: 4th Annual Symposium: Graduate Research and Scholarly Projects," (Wichita State University. Graduate School., 2008), 4, pp. 33–34.

[88] Z. Haiyan, S. Xiuli, Q. Xuerui, L. Xiao, and L. DongHui, "Ultrasonic lamb wave inspection using fiber bragg gratings," Microwave Conference, 2008 China-Japan Joint pp. 805–808 (2008).

[89] N. Rajic, C. Davis, and A. Thomson, "Acoustic-wave-mode separation using a distributed bragg grating sensor," Smart Mater. Struct. **18**, 125005 (2009).

[90] C. C. C. Lam, R. Mandamparambil, T. Sun, K. T. V. Grattan, S. V. Nanukuttan, S. E. Taylor, and P. A. M. Basheer, "Optical fiber refractive index sensor for chloride ion monitoring," IEEE Sensors J. **9**, 525 – 532 (2009).

[91] F. H. Muhammad, R. H. Y. Subban, S. R. Majid, T. Winie, and A. K. Arof, "Characterisation of Al_2O_3 doped hexanoyl chitosan-$LiCF_3SO_3$-EC polymer electrolytes," Mater. Res. Innov. **13**, 249 – 251 (2009).

[92] C. Yang, Z. Wu, and Y. Zhang, "Structural health monitoring of PC structures with novel types of distributed sensors," in "SPIE: Nondestructive Characterization for Composite Materials, Aerospace Engineering, Civil Infrastructure, and Homeland Security," , vol. 7649 (2010), vol. 7649.

[93] F. Bastianini, M. Cargnelutti, A. D. Tommaso, and M. Toffanin, "Distributed brillouin fiber optic strain monitoring applications in advanced composite materials," in "SPIE: Smart Structures and Materials 2003: Smart Systems and Nondestructive Evaluation for Civil Infrastructures," , vol. 5057 of *478* (2003), vol. 5057 of *478*.

[94] B. Ward and J. Spring, "Finite element analysis of brillouin gain in sbs-suppressing optical fibers with non-uniform acoustic velocity profiles," Opt. Express **17**, 15685–15699 (2009).

[95] K. Y. Song, S. Chin, N. Primerov, and L. Thevenaz, "Time-domain distributed fiber sensor with 1 cm spatial resolution based on brillouin dynamic grating," J. Lightwave Technol. **28**, 2062 – 2067 (2010).

[96] K. Y. Song, M. Kishi, Z. He, and K. Hotate, "High-repetition-rate distributed brillouin sensor based on optical correlation-domain analysis with differential frequency modulation," Opt. Lett. **36**, 2062–2064 (2011).

[97] C. Murner and J. P. Hansen, "Buried corrosion detection in multi-layer airframe structures using pulsed eddy current," in "17th World Conference on Nondestructive Testing," (2008).

[98] E. Juzeliūnas, Y. P. Ma, and J. P. Wikswo, "Magnetometric corrosion sensing under hydrodynamic conditions," J. Solid State Electr. **10**, 700 – 707 (2006).

[99] W. G. Jenks, S. S. H. Sadeghi, and J. P. Wikswo Jr, "SQUIDs for nondestructive evaluation," J. Phys. D: Appl. Phys. **30**, 293 – 323 (1997).

[100] S. Saha, S. Mukhopadhyay, U. Mahapatra, S. Bhattacharya, and G. P. Srivastava, "Empirical structure for characterizing metal loss defects from radial magnetic flux leakage signal," NDT&E Int. **43**, 507 – 512 (2010).

[101] M. Hautefeuille, C. O'Mahony, B. O'Flynn, K. Khalfi, and F. Peters, "A MEMS-based wireless multisensor module for environmental monitoring," Microelectron. Reliab. **48**, 906 – 910 (2008).

[102] A. Kumar, L. D. Stephenson, J. Hale, J. Murray, and M. Timonium, "Sensors for measurement of corrosion rates and detection of corrosion under coatings," in "Tri-Service Corrosion Conference," U. S. Army Engineer Research & Development Center (Department of Defence, United States of America, 2007).

[103] S. Kainuma, K. Sugitani, Y. Ito, and I. T. Kim, "Evaluation method for time-dependent corrosion behavior of carbon steel plate using atmospheric corrosion monitoring sensor," Key Eng. Mat. **417–418**, 417 – 420 (2010).

[104] H. Kozako, J. Sakurai, N. Mukai, Y. Ohnuma, T. Takahashii, and S. Hata, "Corrosion resistance consolidation of a diaphragm type vacuum sensor," in "IEEE 24th International Conference on Micro Electro Mechanical Systems (MEMS)," (2011), pp. 400–403.

[105] J. Zhang and W. Zhao, "Electrochemical noise analysis of pitting corrosion of J55 steel in $NaCl + NaHCO_3$ electrolytes," Surf. Interface Anal. **43**, 1018 – 1021 (2011).

[106] A. M. Fekry and R. H. Tammam, "Corrosion and impedance studies on magnesium alloy in oxalate solution," Mater. Sci. Eng. B **176**, 792 – 798 (2011).

[107] Z. F. Yin, Y. R. Feng, W. Z. Zhao, C. X. Yin, and W. Tian, "Pitting corrosion behaviour of 316L stainless steel in chloride solution with acetic acid and CO_2," Corros. Eng. Sci. Techn. **46**, 56 – 63 (2011).

[108] J. K. Saha, P. K. Mitra, S. Paul, and D. D. N. Singh, "Performance of different organic coatings on steel substrate by accelerated and in atmospheric exposure tests," Indian J. Chem. Techn. **17**, 102 – 110 (2010).

[109] K. Habib, K. Al-Muhana, and A. Habib, "Holographic interferometry as electrochemical emission spectroscopy of carbon steel in seawater with low concentration of RA-41 corrosion inhibitor," Opt. Laser Eng. **46**, 149 – 156 (2008).

[110] B. J. Connolly, D. A. Horner, S. J. Fox, A. J. Davenport, C. Padovani, S. Zhou, A. Turnbull, M. Preuss, N. P. Stevens, T. J. Marrow, J.-Y. Buffiere, E. Boller, A. Groso, and M. Stampanoni, "X-ray microtomography studies of localised corrosion and transitions to stress corrosion cracking," Mat. Sci. Tech. **22**, 1076 – 1085 (2006).

[111] N. N. Qaddoumi, W. M. Saleh, and M. Abou-Khousa, "Innovative near-field microwave nondestructive testing of corroded metallic structures utilizing open-ended rectangular waveguide probes," IEEE Trans. Instrum. Meas. **56**, 1961 – 1966 (2007).

[112] D. Zimdars, G. Fichter, and A. Chernovsky, "Rapid time domain terahertz axial computed tomography for aerospace non-destructive evaluation," in "33rd International Conference on Infrared, Millimeter and Terahertz Waves, 2008. IRMMW-THz," (2008), pp. 1–3.

[113] E. I. Madaras, R. F. Anastasi, S. W. Smith, J. P. Seebo, J. L. Walker, J. K. Lomness, P. E. Hintze, C. C. Kammerer, W. P. Winfree, and R. W. Russell, "Application of terahertz radiation to the detection of corrosion under the shuttle's thermal protection system," AIP Conference Proceedings **975**, 421–428 (2008).

[114] M. K. Barnoski and S. M. Jensen, "Fiber waveguides: a novel technique for investigating attenuation characteristics," Appl. Opt. **15**, 2112 – 2115 (1976).

[115] R. Lieberman, L. Blyler, and L. Cohen, "A distributed fiber optic sensor based on cladding fluorescence," J. Lightwave Technol. **8**, 212 – 220 (1990).

[116] J. P. Dakin, "Multiplexed and distributed optical fibre sensor systems," J. Phys. E: Sci. Instrum. **20**, 954 – 967 (1987).

[117] L. L. Blyler, Jr., J. A. Ferrara, and J. B. MacChesney, "A plastic-clad silica fiber chemical sensor for ammonia," in "Optical Fiber Sensors," (Optical Society of America, 1988), p. FAA7.

[118] R. A. Potyrailo and G. M. Hieftje, "Optical time-of-flight chemical detection: Spatially resolved analyte mapping with extended-length continuous chemically modified optical fibers," Anal. Chem. **70**, 1453 – 1461 (1998).

[119] E. Sinchenko, W. E. K. Gibbs, C. E. Davis, and P. R. Stoddart, "Characterization of time-resolved fluorescence response measurements for distributed optical-fiber sensing," Appl. Opt. **49**, 6385–6390 (2010).

[120] E. Sinchenko, "Fibre optic distributed corrosion sensor," Ph.D. thesis, Swinburne University of Technology (2013).

[121] E. P. Schartner, H. Ebendorff-Heidepriem, S. C. Warren-Smith, R. T. White, and T. M. Monro, "Driving down the detection limit in microstructured fiber-based chemical dip sensors," Sensors **11**, 2961 – 2971 (2011).

[122] T. M. Monro, S. Warren-Smith, E. P. Schartner, A. François, S. Heng, H. Ebendorff-Heidepriem, and S. Afshar V., "Sensing with suspended-core optical fibers," Opt. Fiber Technol. **16**, 343 – 356 (2010).

[123] S. C. Warren-Smith, S. Heng, H. Ebendorff-Heidepriem, A. D. Abell, and T. M. Monro, "Fluorescence-based aluminum ion sensing using a surface-functionalized microstructured optical fiber," Langmuir **27**, 5680 – 5685 (2011).

[124] H. Ebendorff-Heidepriem, S. C. Warren-Smith, and T. M. Monro, "Suspended nanowires: fabrication, design and characterization of fibers with nanoscale cores," Opt. Express **17**, 2646 – 2657 (2009).

[125] T. G. Euser, J. S. Y. Chen, M. Scharrer, P. S. J. Russell, N. J. Farrer, and P. J. Sadler, "Quantitative broadband chemical sensing in air-suspended solid-core fibers," J. Appl.

Phys. **103**, 103108 (2008).

[126] A. Mazhorova, A. Markov, A. Ng, R. Chinnappan, O. Skorobogata, M. Zourob, and M. Skorobogatiy, "Label-free bacteria detection using evanescent mode of a suspended core terahertz fiber," Opt. Express **20**, 5344–5355 (2012).

[127] Y. Ruan, E. P. Schartner, H. Ebendorff-Heidepriem, P. Hoffmann, and T. M. Monro, "Detection of quantum-dot labelled proteins using soft glass microstructured optical fibers," Opt. Express **15**, 17819 – 17826 (2007).

[128] A. Bjarklev, J. B. Jensen, J. Riishede, J. Broeng, J. Laegsgaard, T. T. Larsen, T. Sorensen, K. Hougaard, and O. Bang, "Photonic crystal structures in sensing technology," in "Second European Workshop on Optical Fibre Sensors," , vol. 5502 of *Proc. SPIE* (2004), vol. 5502 of *Proc. SPIE*, pp. 9 – 16.

[129] J. E. Debs, H. Ebendorff-Heidepriem, J. S. Quinton, and T. M. Monro, "A fundamental study into the surface functionalization of soft glass microstructured optical fibers via silane coupling agents," J. Lightwave Technol. **27**, 576 – 582 (2009).

[130] C. M. B. Cordeiro, C. J. S. de Matos, E. M. dos Santos, A. Bozolan, J. S. K. Ong, T. Facincani, G. Chesini, A. R. Vaz, and C. H. B. Cruz, "Towards practical liquid and gas sensing with photonic crystal fibres: side access to the fibre microstructure and single-mode liquid-core fibre," Meas. Sci. Technol. **18**, 3075 (2007).

[131] C. Martelli, P. Olivero, J. Canning, N. Groothoff, B. Gibson, and S. Huntington, "Micromachining structured optical fibers using focused ion beam milling," Opt. Lett. **32**, 1575–1577 (2007).

[132] A. van Brakel, C. Grivas, M. N. Petrovich, and D. J. Richardson, "Micro-channels machined in microstructured optical fibers by femtosecond laser," Opt. Express **15**, 8731–8736 (2007).

[133] J. P. Parry, B. C. Griffiths, N. Gayraud, E. D. McNaghten, A. M. Parkes, W. N. MacPherson, and D. P. Hand, "Towards practical gas sensing with micro-structured fibres," Meas. Sci. Technol. **20**, 075301 (2009).

[134] S. C. Warren-Smith, H. Ebendorff-Heidepriem, T. C. Foo, R. Moore, C. Davis, and T. M. Monro, "Exposed-core microstructured optical fibers for real-time fluorescence sensing," Opt. Express **17**, 18533 – 18542 (2009).

[135] F. M. Cox, R. Lwin, M. C. J. Large, and C. M. B. Cordeiro, "Opening up optical fibres," Opt. Express **15**, 11843–11848 (2007).

[136] H. Ebendorff-Heidepriem and T. M. Monro, "Extrusion of complex preforms for microstructured optical fibers," Opt. Express **15**, 15086 – 15092 (2007).

[137] S. C. Warren-Smith, S. Afshar V., and T. M. Monro, "Theoretical study of liquid-immersed exposed-core microstructured optical fibers for sensing," Opt. Express **16**, 9034 – 9045 (2008).

[138] S. C. Warren-Smith, E. Sinchenko, P. R. Stoddart, and T. M. Monro, "Distributed fluorescence sensing using exposed core microstructured optical fiber," IEEE Photon. Technol.

Lett. **22**, 1385 – 1387 (2010).

[139] S. C. Warren-Smith, H. Ebendorff-Heidepriem, S. Afshar V., G. McAdam, C. Davis, and T. Monro, "Corrosion sensing of aluminium alloys using exposed-core microstructured optical fibres," Mater. Forum **33**, 110 – 121 (2009).

[140] A. D. Fitt, K. Furusawa, T. M. Monro, C. P. Please, and D. J. Richardson, "The mathematical modelling of capillary drawing for holey fibre manufacture," J. Eng. Math. **43**, 201 – 227 (2002).

[141] K. Richardson, D. Krol, and K. Hirao, "Glasses for photonic applications," Int. J. Appl. Glass Sci. **1**, 74 – 86 (2010).

[142] H. Ebendorff-Heidepriem and T. M. Monro, "Analysis of glass flow during extrusion of optical fiber preforms," Opt. Mater. Express **2**, 304 – 320 (2012).

[143] Y. Zhu, R. T. Bise, J. Kanka, P. Peterka, and H. Du, "Fabrication and characterization of solid-core photonic crystal fiber with steering-wheel air-cladding for strong evanescent field overlap," Opt. Commun. **281**, 55 – 60 (2008).

[144] H. E. Hamzaoui, L. Bigot, G. Bouwmans, I. Razdobreev, M. Bouazaoui, and B. Capoen, "From molecular precursors in solution to microstructured optical fiber: a sol-gel polymeric route," Opt. Mater. Express **1**, 234 – 242 (2011).

[145] P. McNamara, D. Lancaster, R. Bailey, A. Hemming, P. Henry, and R. Mair, "A large core microstructured fluoride glass optical fibre for mid-infrared single-mode transmission," J. Non-Cryst. Solids **355**, 1461 – 1467 (2009).

[146] J. Lægsgaard and A. Bjarklev, "Microstructured optical fibers – fundamentals and applications," J. Am. Ceram. Soc. **89**, 2 – 12 (2006).

[147] A. D. Pryamikov, A. S. Biriukov, A. F. Kosolapov, V. G. Plotnichenko, S. L. Semjonov, and E. M. Dianov, "Demonstration of a waveguide regime for a silica hollow - core microstructured optical fiber with a negative curvature of the core boundary in the spectral region > 3.5 μm," Opt. Express **19**, 1441 – 1448 (2011).

[148] K. Peters, "Polymer optical fiber sensors - a review," Smart Mater. Struct. **20**, 013002 (2011).

[149] Schott AG, http://www.schott.com/advanced_optics/english/download/schott-optical-glass-pocket-catalog-europe-october-2011-eng.pdf, *Schott Optical Glass Description of Properties 2011* (2011).

[150] H. Ebendorff-Heidepriem, Y. Li, and T. M. Monro, "Reduced loss in extruded soft glass microstructured fibre," Electron. Lett. **43**, 1343 – 1345 (2007).

[151] Professional Plastics, http://www.professionalplastics.com/professionalplastics/content/castacrylic.pdf, *Typical Properties of Cast Acrylic* (2015).

[152] Professional Plastics, http://www.professionalplastics.com/professionalplastics/content/AcryliteFFDataSheet.pdf, *Physical Properties of Acrylite*, CYRO 1121D-0601-10MG ed. (2001).

[153] E. A. Grulke, J. Brandrup, and E. H. Immergut, *Polymer Handbook* (Wiley New York, 1999), 4th ed.

[154] J. Ballato, "Spotlight summary: Silica exposed-core microstructured optical fibers," (2012).

[155] Heraeus Quarzglas GmbH & Co. KG, http://www.gmassoc.com/pdf/heraeus-basic-materials-division.pdf, *Basic Materials* (2002).

[156] P. P. Bihuniak, A. Calabrese, and E. M. Erwin, "Effect of trace impurity levels on the viscosity of vitreous silica," J. Am. Ceram. Soc. **66**, C–134 – C–135 (1983).

[157] Heraeus Quarzglas GmbH & Co. KG, http://heraeus-quarzglas.com/, *Pure Silica Rods for Specialty Fiber Applications*, 1st ed. (2012).

[158] A. W. Snyder and J. D. Love, *Optical Waveguide Theory* (Chapman and Hall, 1983).

[159] S. C. Warren-Smith, S. Afshar V., and T. M. Monro, "Fluorescence-based sensing with optical nanowires: a generalized model and experimental validation," Opt. Express **18**, 9474 – 9485 (2010).

[160] H. Ebendorff-Heidepriem, T. M. Monro, M. A. van Eijkelenborg, and M. C. J. Large, "Extruded high–NA microstructured polymer optical fibre," Opt. Commun. **273**, 133 – 137 (2007).

[161] C. J. Voyce, A. D. Fitt, J. R. Hayes, and T. M. Monro, "Mathematical modeling of the self-pressurizing mechanism for microstructured fiber drawing," J. Lightwave Technol. **27**, 871 – 878 (2009).

[162] G. Yang, T. Rouxel, J. Troles, B. Bureau, C. Boussard-Plèdel, P. Houizot, and J.-C. Sangleboeuf, "Viscosity of As_2Se_3 glass during the fiber drawing process," J. Am. Ceram. Soc. **94**, 2408 – 2411 (2011).

[163] S. Roy Choudhury and Y. Jaluria, "Thermal transport due to material and gas flow in a furnace for drawing an optical fiber," J. Mater. Res. **13**, 494 – 503 (1998).

[164] S. H. Law, M. A. van Eijkelenborg, G. W. Barton, C. Yan, R. Lwin, and J. Gan, "Cleaved end-face quality of microstructured polymer optical fibres," Opt. Commun. **265**, 513 – 520 (2006).

[165] S. Atakaramians, K. Cook, H. Ebendorff-Heidepriem, S. Afshar V., J. Canning, D. Abbott, and T. M. Monro, "Cleaving of extremely porous polymer fibers," IEEE Photon. J. **1**, 286 – 292 (2009).

[166] S. E. Rosenberg, H. Papamichael, and I. N. Miaoulis, "A 2-dimensional analysis of the viscous problem of a glass preform during the optical-fiber drawing process," Glass Technol. **35**, 260 – 264 (1994).

[167] A. Mawardi and R. Pitchumani, "Optical fiber drawing process model using an analytical neck-down profile," IEEE Photon. J. **2**, 620 – 629 (2010).

[168] S. C. Xue, R. I. Tanner, G. W. Barton, R. Lwin, M. C. J. Large, and L. Poladian, "Fabrication of microstructured optical fibers – Part 1 & 2," J. Lightwave Technol. **23**, 2245 –

2266 (2005).

[169] G. Luzi, P. Epple, M. Scharrer, K. Fujimoto, C. Rauh, and A. Delgado, "Influence of surface tension and inner pressure on the process of fibre drawing," J. Lightwave Technol. **28**, 1882 – 1888 (2010).

[170] C. J. Voyce, A. D. Fitt, and T. M. Monro, "Mathematical modeling as an accurate predictive tool in capillary and microstructured fiber manufacture: The effects of preform rotation," J. Lightwave Technol. **26**, 791 – 798 (2008).

[171] R. Kostecki, E. P. Schartner, H. Ebendorff-Heidepriem, P. C. Henry, and T. M. Monro, "Fabrication of suspended and exposed core silica fibres for sensing applications," in "37th Australian Conference on Optical Fibre Technology," (2012).

[172] S. H. K. Lee and Y. Jaluria, "Simulation of the transport processes in the neck-down region of a furnace drawn optical fiber," Int. J. Heat Mass Tran. **40**, 843 – 856 (1997).

[173] R. M. Wynne, "A fabrication process for microstructured optical fibers," J. Lightwave Technol. **24**, 4304 – 4313 (2006).

[174] C. Voyce, A. Fitt, and T. Monro, "Mathematical model of the spinning of microstructured fibres," Opt. Express **12**, 5810 – 5820 (2004).

[175] C. J. Voyce, A. D. Fitt, and T. M. Monro, "The mathematical modelling of rotating capillary tubes for holey-fibre manufacture," J. Eng. Math. **60**, 69 – 87 (2008).

[176] G. Luzi, P. Epple, M. Scharrer, K. Fujimoto, C. Rauh, and A. Delgado, "Asymptotic analysis of flow processes at drawing of single optical microfibres," Int J. Chem. Reactor Eng. **9** (2011).

[177] U. C. Paek and R. B. Runk, "Physical behavior of the neck-down region during furnace drawing of silica fibers," J. Appl. Phys. **49**, 4417 – 4422 (1978).

[178] G. Urbain, Y. Bottinga, and P. Richet, "Viscosity of liquid silica, silicates and alumino-silicates," Geochim. Cosmochim. Ac. **46**, 1061 – 1072 (1982).

[179] R. H. Doremus, "Viscosity of silica," J. Appl. Phys. **92**, 7619 – 7629 (2002).

[180] N. M. Parikh, "Effect of atmosphere on surface tension of glass," J. Am. Ceram. Soc. **41**, 18 – 22 (1958).

[181] W. D. Kingery, "Surface tension of some liquid oxides and their temperature coefficients," J. Am. Ceram. Soc. **42**, 6 – 10 (1959).

[182] K. Boyd, H. Ebendorff-Heidepriem, T. M. Monro, and J. Munch, "Surface tension and viscosity measurement of optical glasses using a scanning CO_2 laser," Opt. Mater. Express **2**, 1101 – 1110 (2012).

[183] A. D. Fitt, K. Furusawa, T. M. Monro, and C. P. Please, "Modeling the fabrication of hollow fibers: capillary drawing," J. Lightwave Technol. **19**, 1924 – 1931 (2001).

[184] R. Kostecki, H. Ebendorff-Heidepriem, S. C. Warren-Smith, G. McAdam, C. Davis, and T. M. Monro, "Optical fibres for distributed corrosion sensing – architecture and characterisation," Key Eng. Mat. **558**, 522 – 533 (2013).

[185] R. Kostecki, H. Ebendorff-Heidepriem, S. C. Warren-Smith, and T. M. Monro, "Predicting the drawing conditions for microstructured optical fiber fabrication," Opt. Mater. Express **4**, 29 – 40 (2014).

[186] G. Brambilla, F. Xu, and X. Feng, "Fabrication of optical fibre nanowires and their optical and mechanical characterisation," Electron. Lett. **42**, 517 – 519 (2006).

[187] G. Zhai and L. Tong, "Roughness-induced radiation losses in optical micro or nanofibers," Opt. Express **15**, 13805 – 13816 (2007).

[188] M. Fujiwara, K. Toubaru, and S. Takeuchi, "Optical transmittance degradation in tapered fibers," Opt. Express **19**, 8596 – 8601 (2011).

[189] D. D. Wackerly, W. Mendenhall III, and R. L. Scheaffer, *Mathematical Statistics with Applications* (Cengage Learning, 2002), 6th ed.

[190] K. Muktavat and A. K. Upadhayaya, *Applied Physics* (IK International Pvt Ltd, 2010).

[191] P. D. Dragic, C. G. Carlson, and A. Croteau, "Characterization of defect luminescence in Yb doped silica fibers: part I NBOHC," Opt. Express **16**, 4688 – 4697 (2008).

[192] D. R. Tallant, T. A. Michalske, and W. L. Smith, "The effects of tensile stress on the Raman spectrum of silica glass," J. Non-Cryst. Solids **106**, 380 – 383 (1988).

[193] R. Leach *et. al.*, *Guide to the Measurement of Smooth Surface Topography using Coherence Scanning Interferometry*, National Physical Laboratory (2008).

[194] R. Brandsch, G. Bar, and M.-H. Whangbo, "On the factors affecting the contrast of height and phase images in tapping mode atomic force microscopy," Langmuir **13**, 6349–6353 (1997).

[195] R. M. Pope and E. S. Fry, "Absorption spectrum (380–700 nm) of pure water. II. integrating cavity measurements," Appl. Opt. **36**, 8710 – 8723 (1997).

[196] ISS, Inc., http://www.iss.com/resources/reference/data_tables/LifetimeDataFluorophores.html, *Lifetime Data of Selected Fluorophores* (2015).

[197] F. L. Arbeloa, P. R. Ojeda, and I. L. Arbeloa, "Flourescence self-quenching of the molecular forms of Rhodamine B in aqueous and ethanolic solutions," J. Lumin. **44**, 105 – 112 (1989).

[198] E. P. Schartner, G. Tsiminis, A. François, R. Kostecki, S. C. Warren-Smith, L. V. Nguyen, S. Heng, T. Reynolds, E. Klantsataya, K. J. Rowland, A. D. Abell, H. Ebendorff-Heidepriem, and T. M. Monro, "Taming the light in microstructured optical fibers for sensing," Int. J. Appl. Glass Sci. **6**, 229 – 239 (2015).

[199] R. Suárez, B. Horstkotte, C. M. Duarte, and V. Cerdà, "Fully-automated fluorimetric determination of aluminum in seawater by in-syringe dispersive liquid–liquid microextraction using lumogallion," Anal. Chem. **84**, 9462 – 9469 (2012).

[200] H. T. C. Foo, H. Ebendorff-Heidepriem, C. J. Sumby, and T. M. Monro, "Towards microstructured optical fibre sensors: Surface analysis of silanised lead silicate glass," J. Mater. Chem. C **1**, 6782 – 6789 (2013).

[201] B. Sciacca, A. François, M. Klingler-Hoffmann, J. Brazzatti, M. Penno, P. Hoffmann, and

T. M. Monro, "Radiative-surface plasmon resonance for the detection of apolipoprotein E in medical diagnostics applications," Nanomed. - NBM **9**, 550 – 557 (2013).

[202] A. François, H. Ebendorff-Heidepriem, C. J. Sumby, and T. M. Monro, "Comparison of surface functionalization processes for optical fibre biosensing applications," in "20th International Conference on Optical Fibre Sensors," , vol. 7503 of *Proc. SPIE* (2009), vol. 7503 of *Proc. SPIE*.

[203] A. E. Martell, R. D. Hancock, R. M. Smith, and R. J. Motekaitis, "Coordination of Al(III) in the environment and in biological systems," Coordin. Chem. Rev. **149**, 311 – 328 (1996).

[204] R. A. Yokel, "Aluminum chelation principles and recent advances," Coordin. Chem. Rev. **228**, 97 – 113 (2002).

[205] P. C. H. Hollman, J. M. P. van Trijp, and M. N. C. P. Buysman, "Fluorescence detection of flavonols in HPLC by postcolumn chelation with aluminum," Anal. Chem. **68**, 3511 – 3515 (1996).

[206] A.-C. Boudet, J.-P. Cornard, and J.-C. Merlin, "Conformational and spectroscopic investigation of 3-hydroxyflavone–aluminium chelates," Spectrochim. Acta A **56**, 829 – 839 (2000).

[207] G. A. Shar and G. A. Soomro, "8-hydroxyquinoline as a complexing reagent for the determination of Cd(II) in micellar medium," J. Chem. Soc. Pak. **27**, 471 – 475 (2005).

[208] V. V. N. R. Kishore, A. Aziz, K. L. Narasimhan, N. Periasamy, P. S. Meenakshi, and S. Wategaonkar, "On the assignment of the absorption bands in the optical spectrum of Alq3," Synthetic Met. **126**, 199 – 205 (2002).

[209] K. Kina and N. Ishibashi, "Effect of the nonionic surfactant on the fluorometric determination of gallium using lumogallion," Microchem. J. **19**, 26 – 31 (1974).

[210] M. S. Shuman, "Dissociation pathways and species distribution of aluminum bound to an aquatic fulvic acid," Environ. Sci. Technol. **26**, 593 – 598 (1992).

[211] T. Kataoka, M. Mori, T. Nakanishi, S. Matsumoto, and A. Uchiumi, "Highly sensitive analytical method for aluminum movement in soybean root through lumogallion staining," J. Plant Res. **110**, 305 – 309 (1997).

[212] R. S. Becker, *Theory and interpretation of fluorescence and phosphorescence* (Wiley Interscience, 1969).

[213] R. Byrne and D. Diamond, "Chemo/bio-sensor networks," Nat. Mater. **5**, 1476 – 1122 (2006).

[214] M. Inouye, M. Ueno, T. Kitao, and K. Tsuchiya, "Alkali metal recognition induced isomerization of spiropyrans," J. Am. Chem. Soc. **112**, 8977 – 8979 (1990).

[215] K. Kimura, T. Yamashita, and M. Yokoyama, "Syntheses, cation complexation, isomerization and photochemical cation-binding control of spirobenzopyrans carrying a monoazacrown moiety at the 8-position," J. Chem. Soc., Perkin Trans. **2**, 613 – 619 (1992).

[216] M. Natali and S. Giordani, "Molecular switches as photocontrollable "smart" receptors,"

Chem. Soc. Rev. **41**, 4010 – 4029 (2012).

[217] R. J. Byrne, S. E. Stitzel, and D. Diamond, "Photo-regenerable surface with potential for optical sensing," J. Mater. Chem. **16**, 1332 – 1337 (2006).

[218] S. P. Pujari, L. Scheres, A. T. M. Marcelis, and H. Zuilhof, "Covalent surface modification of oxide surfaces," Angew. Chem. Int. Ed. **53**, 6322 – 6356 (2014).

[219] M. Qin, S. Hou, L. Wang, X. Feng, R. Wang, Y. Yang, C. Wang, L. Yu, B. Shao, and M. Qiao, "Two methods for glass surface modification and their application in protein immobilization," Colloid Surface B **60**, 243 – 249 (2007).

[220] K. S. Lee and R. J. Ram, "Plastic-PDMS bonding for high pressure hydrolytically stable active microfluidics," Lab Chip **9**, 1618 – 1624 (2009).

[221] R. Müller, J. Abke, E. Schnell, F. Macionczyk, U. Gbureck, R. Mehrl, Z. Ruszczak, R. Kujat, C. Englert, M. Nerlich, and P. Angele, "Surface engineering of stainless steel materials by covalent collagen immobilization to improve implant biocompatibility," Biomaterials **26**, 6962 – 6972 (2005).

[222] S. Fiorilli, P. Rivolo, E. Descrovi, C. Ricciardi, L. Pasquardini, L. Lunelli, L. Vanzetti, C. Pederzolli, B. Onida, and E. Garrone, "Vapor-phase self-assembled monolayers of aminosilane on plasma-activated silicon substrates," J. Colloid Interface Sci. **321**, 235 – 241 (2008).

[223] J. Cras, C. Rowe-Taitt, D. Nivens, and F. Ligler, "Comparison of chemical cleaning methods of glass in preparation for silanization," Biosens. Bioelectron. **14**, 683 – 688 (1999).

[224] U. Jönsson, G. Olofsson, M. Malmqvist, and I. Rönnberg, "Chemical vapour deposition of silanes," Thin Solid Films **124**, 117 – 123 (1985).

[225] K. C. Popat, R. W. Johnson, and T. A. Desai, "Characterization of vapor deposited thin silane films on silicon substrates for biomedical microdevices," Surf. Coat. Tech. **154**, 253 – 261 (2002).

[226] J. Zhang, J. Hoogboom, P. H. J. Kouwer, A. E. Rowan, and T. Rasing, "Uniform N-(2-Aminoethyl)(3-aminopropyl)trimethoxysilane monolayer growth in water," J. Phys. Chem. C **112**, 20105 – 20108 (2008).

[227] R. D. Lowe, M. A. Pellow, T. D. P. Stack, and C. E. D. Chidsey, "Deposition of dense siloxane monolayers from water and trimethoxyorganosilane vapor," Langmuir **27**, 9928 – 9935 (2011).

[228] S. A. Habay, "The synthesis and characterization of water soluble hydroindole-based nanostructures of designed three-dimensional architectures," Ph.D. thesis, University of Pittsburgh (2005).

[229] M. Michel, V. Toniazzo, D. Ruch, and V. Ball, "Deposition mechanisms in layer-by-layer or step-by-step deposition methods: From elastic and impermeable films to soft membranes with ion exchange properties," ISRN Mater. Sci. **2012**, 1 – 13 (2012).

[230] G. Decher, "Fuzzy nanoassemblies: Toward layered polymeric multicomposites," Science

277, 1232 – 1237 (1997).

[231] B. Sciacca, A. François, P. Hoffmann, and T. M. Monro, "Multiplexing of radiative-surface plasmon resonance for the detection of gastric cancer biomarkers in a single optical fiber," Sensors Actuat. B-Chem. **183**, 454 – 458 (2013).

[232] A. François, J. Boehm, S. Y. Oh, T. Kok, and T. M. Monro, "Collection mode surface plasmon fibre sensors: A new biosensing platform," Biosens. Bioelectron. **26**, 3154 – 3159 (2011).

[233] A. François, T. Reynolds, and T. M. Monro, "A fiber-tip label-free biological sensing platform: A practical approach toward in-vivo sensing," Sensors **15**, 1168 – 1181 (2015).

[234] L. V. Nguyen, S. C. Warren-Smith, A. Cooper, and T. M. Monro, "Molecular beacons immobilized within suspended core optical fiber for specific DNA detection," Opt. Express **20**, 29378 – 29385 (2012).

[235] K. J. Rowland, A. François, P. Hoffmann, and T. M. Monro, "Fluorescent polymer coated capillaries as optofluidic refractometric sensors," Opt. Express **21**, 11492 – 11505 (2013).

[236] B. Frank, A. P. Gast, T. P. Russell, H. R. Brown, and C. Hawker, "Polymer mobility in thin films," Macromolecules **29**, 6531 – 6534 (1996).

[237] K. C. Tseng, N. J. Turro, and C. J. Durning, "Molecular mobility in polymer thin films," Phys. Rev. E **61**, 1800 – 1811 (2000).

[238] T. Beck, S. Schloer, T. Grossmann, T. Mappes, and H. Kalt, "Flexible coupling of high-Q goblet resonators for formation of tunable photonic molecules," Opt. Express **20**, 22012 – 22017 (2012).

[239] T. Kobayashi and N. Byrne, "Plastic evanescent microlaser," Appl. Phys. Lett. **99**, 153307 (2011).

[240] J. Huang, V. Bekiari, P. Lianos, and S. Couris, "Study of poly(methyl methacrylate) thin films doped with laser dyes," J. Lumin. **81**, 285 – 291 (1999).

[241] G. S. He, H. Qin, and Q. Zheng, "Rayleigh, Mie, and Tyndall scatterings of polystyrene microspheres in water: Wavelength, size, and angle dependences," J. Appl. Phys. **105**, 023110 (2009).

[242] P. J. Roberts, F. Couny, H. Sabert, B. J. Mangan, D. P. Williams, L. Farr, M. W. Mason, A. Tomlinson, T. A. Birks, J. C. Knight, and P. S. Russell, "Ultimate low loss of hollow-core photonic crystal fibres," Opt. Express **13**, 236 – 244 (2005).

[243] K. Tajima, J. Zhou, K. Nakajima, and K. Sato, "Ultralow loss and long length photonic crystal fiber," J. Lightwave Technol. **22**, 7 – 10 (2004).

[244] T. Kaino, M. Fujiki, S. Oikawa, and S. Nara, "Low-loss plastic optical fibers," Appl. Opt. **20**, 2886 – 2888 (1981).

[245] T. Seydel, A. Madsen, M. Tolan, G. Grübel, and W. Press, "Capillary waves in slow motion," Phys. Rev. B **63**, 073409 (2001).

[246] J. Jäckle and K. Kawasaki, "Intrinsic roughness of glass surfaces," J. Phys. - Condens.

Mat. **7**, 4351 – 4358 (1995).

[247] S. C. Xue, M. C. J. Large, G. W. Barton, R. I. Tanner, L. Poladian, and R. Lwin, "Role of material properties and drawing conditions in the fabrication of microstructured optical fibers," J. Lightwave Technol. **24**, 853 – 860 (2006).

[248] J. Liu, H. Li, and J.-M. Lin, "Measurements of surface tension of organic solvents using a simple microfabricated chip," Anal. Chem. **79**, 371 – 377 (2007).

[249] I. Slowing, B. Trewyn, S. Giri, and V.-Y. Lin, "Mesoporous silica nanoparticles for drug delivery and biosensing applications," Adv. Funct. Mater. **17**, 1225 – 1236 (2007).

[250] Y. Chen, S. Wang, J. Ye, D. Li, Z. Liu, and X. Wu, "Insights into the effect of nanoconfinement on molecular interactions," Nanoscale **6**, 9563 – 9567 (2014).

[251] Y.-W. Yang, Y.-L. Sun, and N. Song, "Switchable host–guest systems on surfaces," Accounts Chem. Res. **47**, 1950 – 1960 (2014).

[252] N. K. Mal, M. Fujiwara, and Y. Tanaka, "Photocontrolled reversible release of guest molecules from coumarin-modified mesoporous silica," Nature **421**, 350 – 353 (2003).

[253] M. Kittelmann, M. Nimmrich, J. L. Neff, P. Rahe, W. Greń, X. Bouju, A. Gourdon, and A. Kühnle, "Controlled activation of substrate templating in molecular self-assembly by deprotonation," J. Phys. Chem. C **117**, 23868 – 23874 (2013).

[254] R. C. Major and X.-Y. Zhu, "The surface chelate effect," J. Am. Chem. Soc. **125**, 8454 – 8455 (2003).

[255] C. T. Kresge, M. E. Leonowicz, W. J. Roth, J. C. Vartuli, and J. S. Beck, "Ordered mesoporous molecular sieves synthesized by a liquid-crystal template mechanism," Nature **359**, 710 – 712 (1992).

[256] A. Corma, "From microporous to mesoporous molecular sieve materials and their use in catalysis," Chem. Rev. **97**, 2373 – 2420 (1997).

[257] F. Ciardelli, D. Fabbri, O. Pieroni, and A. Fissi, "Photomodulation of polypeptide conformation by sunlight in spiropyran-containing poly(L-glutamic acid)," J. Am. Chem. Soc. **111**, 3470 – 3472 (1989).

[258] W. Tian and J. Tian, "An insight into the solvent effect on photo-, solvato-chromism of spiropyran through the perspective of intermolecular interactions," Dyes Pigments **105**, 66 – 74 (2014).

[259] J. M. Bosque-Sendra, E. Almansa-López, A. M. García-Campaña, and L. Cuadros-Rodríguez, "Data analysis in the determination of stoichiometries and stability constants of complexes," Anal. Sci. **19**, 1431 – 1439 (2003).

[260] H. Takeuchi, T. Arai, and I. Harada, "Structures of 18-crown-6, 15-crown-5 and their metal complexes in methanol solution as studied by raman spectroscopy," J. Mol. Struct. **146**, 197 – 212 (1986).

[261] R. Kostecki, H. Ebendorff-Heidepriem, S. Afshar V., G. McAdam, C. Davis, and T. M. Monro, "A novel polymer functionalization method for exposed-core optical fiber," Opt.

Mater. Express **4**, 1515 – 1525 (2014).

[262] F. Floris and J. Tomasi, "Evaluation of the dispersion contribution to the solvation energy. a simple computational model in the continuum approximation," J. Comput. Chem. **10**, 616 – 627 (1989).

[263] P. Lahiri, K. B. Wiberg, P. H. Vaccaro, M. Caricato, and T. D. Crawford, "Large solvation effect in the optical rotatory dispersion of norbornenone," Angew. Chem. Int. Ed. **53**, 1386 – 1389 (2014).